

Tsu-Yang Wu · Shaoquan Ni ·  
Shu-Chuan Chu · Chi-Hua Chen ·  
Margarita Favorskaya *Editors*



# Advances in Smart Vehicular Technology, Transportation, Communication and Applications

Proceedings of VTCA 2021

# **Smart Innovation, Systems and Technologies**

Volume 250

## **Series Editors**

Robert J. Howlett, Bournemouth University and KES International,  
Shoreham-by-Sea, UK

Lakhmi C. Jain, KES International, Shoreham-by-Sea, UK

The Smart Innovation, Systems and Technologies book series encompasses the topics of knowledge, intelligence, innovation and sustainability. The aim of the series is to make available a platform for the publication of books on all aspects of single and multi-disciplinary research on these themes in order to make the latest results available in a readily-accessible form. Volumes on interdisciplinary research combining two or more of these areas is particularly sought.

The series covers systems and paradigms that employ knowledge and intelligence in a broad sense. Its scope is systems having embedded knowledge and intelligence, which may be applied to the solution of world problems in industry, the environment and the community. It also focusses on the knowledge-transfer methodologies and innovation strategies employed to make this happen effectively. The combination of intelligent systems tools and a broad range of applications introduces a need for a synergy of disciplines from science, technology, business and the humanities. The series will include conference proceedings, edited collections, monographs, handbooks, reference books, and other relevant types of book in areas of science and technology where smart systems and technologies can offer innovative solutions.

High quality content is an essential feature for all book proposals accepted for the series. It is expected that editors of all accepted volumes will ensure that contributions are subjected to an appropriate level of reviewing process and adhere to KES quality principles.

Indexed by SCOPUS, EI Compendex, INSPEC, WTI Frankfurt eG, zbMATH, Japanese Science and Technology Agency (JST), SCImago, DBLP.

All books published in the series are submitted for consideration in Web of Science.

More information about this series at <https://link.springer.com/bookseries/8767>

Tsu-Yang Wu · Shaoquan Ni · Shu-Chuan Chu ·  
Chi-Hua Chen · Margarita Favorskaya  
Editors

# Advances in Smart Vehicular Technology, Transportation, Communication and Applications

Proceedings of VTCA 2021

 Springer

*Editors*

Tsu-Yang Wu  
College of Computer Science  
and Engineering  
Shandong University of Science  
and Technology  
Qingdao, China

Shu-Chuan Chu  
College of Computer Science  
and Engineering  
Shandong University of Science  
and Technology  
Qingdao, China

Margarita Favorskaya  
Institute of Informatics  
and Telecommunications  
Reshetnev Siberian State University  
of Science and Technology  
Krasnoyarsk, Russia

Shaoquan Ni  
School of Transportation and Logistics  
Southwest Jiaotong University  
Chengdu, Sichuan, China

Chi-Hua Chen  
College of Computer and Data Science  
Fuzhou University  
Fuzhou, China

ISSN 2190-3018

ISSN 2190-3026 (electronic)

Smart Innovation, Systems and Technologies

ISBN 978-981-16-4038-4

ISBN 978-981-16-4039-1 (eBook)

<https://doi.org/10.1007/978-981-16-4039-1>

© The Editor(s) (if applicable) and The Author(s), under exclusive license to Springer Nature Singapore Pte Ltd. 2022

This work is subject to copyright. All rights are solely and exclusively licensed by the Publisher, whether the whole or part of the material is concerned, specifically the rights of translation, reprinting, reuse of illustrations, recitation, broadcasting, reproduction on microfilms or in any other physical way, and transmission or information storage and retrieval, electronic adaptation, computer software, or by similar or dissimilar methodology now known or hereafter developed.

The use of general descriptive names, registered names, trademarks, service marks, etc. in this publication does not imply, even in the absence of a specific statement, that such names are exempt from the relevant protective laws and regulations and therefore free for general use.

The publisher, the authors and the editors are safe to assume that the advice and information in this book are believed to be true and accurate at the date of publication. Neither the publisher nor the authors or the editors give a warranty, expressed or implied, with respect to the material contained herein or for any errors or omissions that may have been made. The publisher remains neutral with regard to jurisdictional claims in published maps and institutional affiliations.

This Springer imprint is published by the registered company Springer Nature Singapore Pte Ltd. The registered company address is: 152 Beach Road, #21-01/04 Gateway East, Singapore 189721, Singapore

# Preface

This volume composes the proceedings of the Fourth International Conference on Smart Vehicular Technology, Transportation, Communication and Applications (VTCA 2021), which is hosted by Shandong University of Science and Technology and is held in Chengdu, Sichuan Province, China, on May 22–24, 2021. VTCA 2021 is technically co-sponsored by Springer, Southwest Jiaotong University (SWJTU), Shandong University of Science and Technology, Fujian University of Technology (FJUT), Minjiang University, Superconductivity and New Energy R&D Center (SWJTU), Fujian Provincial Key Lab of Big Data Mining and Applications, and National Demonstration Center for Experimental Electronic Information and Electrical Technology Education (FJUT). It aims to bring together researchers, engineers, and policymakers to discuss the related techniques, to exchange research ideas and to make friends.

Forty-one regular papers were accepted in this proceeding. We would like to thank the authors for their tremendous contributions. We would also express our sincere appreciation to the reviewers, program committee members, and the local committee members for making this conference successful. Finally, we would like to express our special thanks for the great help from Southwest Jiaotong University for locally organizing the conference.

Qingdao, China  
Chengdu, China  
Qingdao, China  
Fuzhou, China  
Krasnoyarsk, Russia  
May 2021

Tsu-Yang Wu  
Shaoquan Ni  
Shu-Chuan Chu  
Chi-Hua Chen  
Margarita Favorskaya

# Contents

## Part I Intelligent Transportation Systems

<b>1</b>	<b>Deep Learning Short-Time Interval Passenger Flow Prediction Based on Isomap Algorithm</b> .....	<b>3</b>
	Junxi Chen, Kaihan Yu, Kangjie Wu, and Jinshan Pan	
<b>2</b>	<b>Prediction of Subway Interchange Passenger Flow Based on Recurrent Neural Network Time Characteristic Model</b> .....	<b>11</b>
	Xiao Chen, Junxi Chen, Yi Liu, Zichen Zhan, and Jinglan Lei	
<b>3</b>	<b>Research on Dynamic Passenger Flow Distribution of Rail Transit Based on Multi-dimensional Euclidean Distance</b> .....	<b>19</b>
	Qianqian Wu, Lin Sun, Furong Jia, Yi Liu, and Zichen Zhan	
<b>4</b>	<b>Study on Valid Travel Route Selection of Integrated Passenger Transportation</b> .....	<b>27</b>
	Yao Yang, Chenyan Kan, and Dingjun Chen	
<b>5</b>	<b>Loading and Reinforcing Safety Evaluation of Railway Out-Of-Gauge Freight Considering the Dynamic Transportation Process</b> .....	<b>39</b>
	Hao Chen, Wenxian Wang, Min Zhou, and Xueqin Li	
<b>6</b>	<b>Design of Rail Freight Products in the Arduous Mountainous Area on the Plateau Under the Concept of Modern Logistics</b> .....	<b>55</b>
	Shiwei Yang, Qingchen Yao, Can Yang, Miaomiao Lv, and Mengyuan Yue	

## Part II Smart Vehicular Technology

<b>7</b>	<b>An Estimation of Vehicle Vertical Dynamics Using Inverse Method</b> .....	<b>67</b>
	Dong-Cherng Lin, Trong-The Nguyen, Jeng-Shyang Pan, and Chang-Der Lee	

<b>8</b>	<b>An Enhanced Flower Pollination Algorithm for Power System Economic Load Dispatch</b> .....	<b>77</b>
	Hung-Peng Lee, Trong-The Nguyen, Thi-Kien Dao, Van-Dinh Vu, and Truong-Giang Ngo	
<b>9</b>	<b>Distribution Vehicle Routing Optimization Based on 3D Loading</b> .....	<b>87</b>
	Xuan Luo, Jin Zhang, Tingyu Yin, Hongxing Zhu, and Mingyue Qiu	
<b>10</b>	<b>Robust and Fast Registration for Lidar Odometry and Mapping</b> .....	<b>99</b>
	Wenbo Liu and Wei Sun	
<b>11</b>	<b>Collaborative Control of Unmanned Vehicle Matrix Formation Based on Autonomous Neighborhood Negotiation</b> .....	<b>113</b>
	KaiXuan Wang, YuTing Shen, FuQuan Zhang, Jianglong Yu, Zhang Ren, and Liang Zhuo	
<b>12</b>	<b>Unmanned Vehicle Task Scheduling Method Based on Iterative Cognitive Interaction</b> .....	<b>125</b>
	Yuting Shen, Xin Meng, Kaixuan Wang, Fuquan Zhang, Yueqing Gao, and Lulu Chen	
<b>13</b>	<b>Event Sequence T-Way Test Strategy for Events Driven System</b> ....	<b>135</b>
	Yuqi Liu, Daming Pei, and Shiyuan Fang	
<b>Part III Artificial Intelligence</b>		
<b>14</b>	<b>QUasi-Affine TRansformation Evolutionary Algorithm for Feature Selection</b> .....	<b>147</b>
	Zhi-Gang Du, Tien-Szu Pan, Jeng-Shyang Pan, and Shu-Chuan Chu	
<b>15</b>	<b>Advanced QUasi-Affine TRansformation Evolutionary (QUATRE) Algorithm and Its Application for Neural Network</b> ....	<b>157</b>
	Pei Hu, Jeng-Shyang Pan, and Shu-Chuan Chu	
<b>16</b>	<b>An QUasi-Affine TRansformation Evolution (QUATRE) Algorithm for Job-Shop Scheduling Problem by Mixing Different Strategies</b> .....	<b>167</b>
	Qing-Yong Yang, Shu-Chuan Chu, Chien-Ming Chen, and Jeng-Shyang Pan	
<b>17</b>	<b>QUasi-Affine TRansformation Evolution Algorithm for Optimal Power Flow of Integrated Electrical Network Combining Thermal Power with Wind Power</b> .....	<b>177</b>
	Jianpo Li, Min Gao, Shu-Chuan Chu, Geng-Chen Li, and Jeng-Shyang Pan	



- 18 Hybrid Optimization Algorithm Based on QUATRE and ABC Algorithms** ..... 187  
Xin Zhang, Linlin Tang, Shu-Chuan Chu, Shaowei Weng,  
and Jeng-Shyang Pan
- 19 Joint Adaptive Reception Algorithm with Ant Colony Optimization for Asynchronous Cooperation Transmission Systems** ..... 199  
Aiyong Zhang, Changjie Liu, and Pengfei Qin
- 20 Multiple Data-Dependent Kernel Learning for Circuit Fault Diagnosis** ..... 209  
Wang Jianfeng, Wu Meixi, and Li Hanzhi
- 21 Calculation of Spacecraft Transfer Trajectory Based on Modified Differential Evolution Algorithm** ..... 219  
Gui-bo Zheng, Qing Yin, Guan-qun Wu, and Ke-yan Huang
- 22 Channel Pruning and Quantization-Based Learning for Object Detection with Computing Source Limited Application** ..... 229  
Fei Zhao, Huanyu Liu, Moufa Hu, and Yingjie Deng
- 23 Retinal Vessels Segmentation Based on Multi-scale Hybrid Convolutional Network** ..... 239  
Rui Li, Zuoyong Li, Xinrong Cao, and Shenghua Teng
- 24 Location Optimization of Service Centers for Seniors Based on an Improved Particle Swarm Optimization Algorithm** ..... 249  
Wei-Feng Wang, Ruo-Bin Wang, Shuo Yin, Zhi-Wei An,  
and Lin Xu
- 25 IBPO: Solving 3D Strategy Game with the Intrinsic Reward** ..... 257  
Huale Li, Rui Cao, Xiaohan Hou, Xuan Wang, Linlin Tang,  
Jijia Zhang, and Shuhan Qi
- 26 An Operation with Crossover and Mutation of MPSO Algorithm** ..... 265  
Yuxin Zhong, Yuxin Chen, Chen Yang, and Zhenyu Meng
- 27 Deep Learning on 3D Point Cloud for Semantic Segmentation** ..... 275  
Zhihan Ning, Linlin Tang, Shuhan Qi, and Yang Liu
- 28 An Improved Arithmetic Optimization Algorithm with a Strategy Balancing Exploration and Exploitation** ..... 283  
Ruo-Bin Wang, Shuo Yin, Wei-Feng Wang, Zhi-Wei An,  
and Lin Xu

**Part IV Networks and Security**

**29 MPSiam: A Fast Multiplexing Siamese Tracking Network** ..... 295  
 Donghao Li, Ce Shen, Jinxing Hu, and Diping Yuan

**30 A Single-Phase-to-Ground Fault Location Method Based on Deep Belief Network** ..... 303  
 Jia-Min Li, Shi-Jian Liu, Xiang Shao, and Jeng-Shyang Pan

**31 A Data Fusion Scheme in Wireless Sensor Network Based on Optimizing Parameters of Neural Network** ..... 315  
 Thi-Kien Dao, Trong-The Nguyen, Van-Dinh Vu, and Truong-Giang Ngo

**32 Cluster-Based Two-Level Mesh Routing Protocol for Wireless Sensor Network** ..... 325  
 Qi-yuan Zhang, Bo Sun, Jian-ming Xu, Jian He, and Ji-liang Mu

**33 PD Detection and Analysis of Cross-Bonded Cable Based on Broadband Sensor and Three-Phase Amplitude Relation Analysis Method** ..... 333  
 Liwei Wang, Bingwei Liu, Bin Wang, Xutao Han, Zhentao Liu, and Wei Sun

**34 A Dynamic and Fair Timeout Heartbeat Detection Technique for Server Clusters Using Nginx Reverse Proxy** ..... 341  
 Beiping Ma and Wei Zhang

**35 Visually Meaningful Image Encryption Algorithm Based on Parallel Compressive Sensing and Cellular Neural Network** .... 351  
 Renxiu Zhang, Donghua Jiang, Wei Ding, Ya Wang, Yanan Wu, Yerui Guang, and Qun Ding

**36 Comments on “A Robust User Authentication Protocol with Privacy-Preserving for Roaming Service in Mobility Environments”** ..... 361  
 Xinglan Guo, Lei Yang, Tsu-Yang Wu, Lili Chen, and Chien-Ming Chen

**Part V Video, Image, and Others**

**37 Research on Construction Method of Massive Geographic Image Database for Power Grid EIA** ..... 371  
 Yu Wu, Zun Li, Yang Guo, Songyang Zhang, Zhiguo Zhang, Zhentao Liu, Xutao Han, and Wei Sun

**38 Automatic Director of Live Sport Based on Motion State** ..... 381  
 Juan Wang and Longfei Zhang

**39 Image Dehazing Network Based on Multi-scale Feature Extraction** ..... 391  
Ting Feng, Fuquan Zhang, Zhaochai Yu, and Zuoyong Li

**40 Research on the Challenges and Strategies of Enterprises in Reverse Logistics Cost Control Under B2C Mode** ..... 401  
Chengxiao Ju

**41 Research on the Training Path of Big Data Application-Oriented Talents in Chinese Colleges and Universities** ..... 411  
Xiaohong Ju

**Author Index** ..... 421

# About the Editors

**Tsu-Yang Wu** received the Ph.D. degree in the Department of Mathematics, National Changhua University of Education, Taiwan (R.O.C.). Currently, he is Associate Professor at the College of Computer Science and Engineering, Shandong University of Science and Technology, China. In the past, he was Assistant Professor at Harbin Institute of Technology, Shenzhen Campus, and Associate Professor at Fujian University of Technology, China. He serves Executive Editor in the *Journal of Network Intelligence* (JNI) and Associate Editor in *Data Science and Pattern Recognition* (DSPR). His research interests include cryptography and network security.

**Shaoquan Ni** (born 1967, Hubei, China), is a male, Professor, and Director of Southwest Jiaotong University Train Diagram R&D training Center and Transportation Information and Technology Institute. He has presided over 60 research projects, published 3 monographs and more than 160 academic papers, and won 17 awards.

**Shu-Chuan Chu** received the Ph.D. degree in 2004 from the School of Computer Science, Engineering and Mathematics, Flinders University of South Australia. She joined Flinders in December 2009 after 9 years at the Cheng Shiu University, Taiwan. She has been Research Fellow in the College of Science and Engineering of Flinders University, Australia, from 2009. Currently, she is Research Fellow and Ph.D. Supervisor in the College of Computer Science and Engineering of Shandong University of Science and Technology. Her research interests are mainly in evolutionary computation, swarm intelligence, and wireless sensor networks.

**Chi-Hua Chen** (Senior Member, IEEE) received his Ph.D. degree in information management from National Chiao Tung University in 2013. He was Research Fellow at Chunghwa Telecom from 2014 to 2018. He has been Full Professor with the College of Computer and Data Science at Fuzhou University from 2018. He has also serves as Chair Professor with the Navigation College at Dalian Maritime University and Consultant with IF-Tek Inc. from 2019. He has published over 300 journal articles, conference articles, and patents. His contributions were published in

*IEEE Internet of Things Journal*, *IEICE Transactions on Fundamentals of Electronics, Communications and Computer Sciences*, *IEICE Transactions on Information and Systems*, *Journal of Enterprise Information Management*, *Physica A: Statistical Mechanics and its Applications*, *Transactions on Emerging Telecommunications Technologies*, *Wireless Communications and Mobile Computing*, *WWW'20*, *SIGIR 2020*, and so on. Some of his publications have been recognized as highly cited papers on Web of Science using data from Essential Science Indicators. He serves as Editor for several international journals (e.g., *Scientific Data* (i.e. one of Nature Research Journals), *IEEE Access*, *IEICE Transactions on Information and Systems*, *Scientific Reports* (i.e. one of Nature Research Journals), *PLOS ONE*, *Journal of Database Management*, *Journal of Applied Statistics*, *International Journal of Ad Hoc and Ubiquitous Computing*, *Journal of Organizational and End User Computing*, *Journal of Medical Imaging and Health Informatics*, *Intelligent Automation and Soft Computing*, *Wireless Communications and Mobile Computing*, *Mobile Information Systems*, *EURASIP Journal on Wireless Communications and Networking*, *International Journal of Distributed Sensor Networks*, *ISPRS International Journal of Geo-Information*, *Discrete Dynamics in Nature and Society*, *Mathematical Problems in Engineering*, and so on). He also serves as Chair for several international conferences (e.g., *AAAI-22 Workshop* (i.e. a top conference in computer sciences), *WWW'21 Workshop* (i.e. a top conference in computer sciences), *IEEE BIBM 2021 Workshop*, *IEEE TrustCom 2021 Workshop*, *IEEE BigData 2021 Workshop*, *IEEE APNOMS 2020*, *IEEE ICC 2020*, *IEEE BIBM 2020 Workshop*, *IEEE TrustCom 2020 Workshop*, *IEEE BigData 2020 Workshop*, *IEEE ICCE-TW 2020*, *IEEE IS3C 2020*, *DASFAA Workshop 2021*, *IEEE ICCCBDA 2021*, *IEEE BCD 2021*, and so on). His research interests include the Internet of things and machine learning.

**Dr. Margarita Favorskaya** is Professor and Head of Department of Informatics and Computer Techniques at Reshetnev Siberian State University of Science and Technology, Russian Federation. Prof. Favorskaya is Member of KES organization since 2010, the IPC Member, and Chair of invited sessions of over 30 international conferences. She serves as Reviewer in international journals (*Neurocomputing*, *Knowledge Engineering and Soft Data Paradigms*, *Pattern Recognition Letters*, and *Engineering Applications of Artificial Intelligence*), Associate Editor of *Intelligent Decision Technologies Journal*, *International Journal of Knowledge-Based and Intelligent Engineering Systems*, *International Journal of Reasoning-based Intelligent Systems*, Honorary Editor of the *International Journal of Knowledge Engineering and Soft Data Paradigms*, Reviewer, Guest Editor, and Book Editor (Springer). She is Author/Co-Author of 200 publications and 20 educational manuals in computer science/engineering. She co-authored/co-edited seven books for Springer recently. She supervised nine Ph.D. candidates and presently supervising four Ph.D. students. Her main research interests are smart systems design, digital image and videos processing, remote sensing, pattern recognition, fractal image processing, artificial intelligence, and information technologies.

**Part I**  
**Intelligent Transportation Systems**

# Chapter 1

## Deep Learning Short-Time Interval Passenger Flow Prediction Based on Isomap Algorithm



Junxi Chen, Kaihan Yu, Kangjie Wu, and Jinshan Pan

**Abstract** With the increasing complexity of subway lines, people's demand for subway travel is also increasing. Reasonable regulation of vehicles on different zones can not only improve the efficiency of people's travel but also lay the foundation for future short-time zone passenger flow prediction. The Isomap algorithm is used to represent the high-dimensional data by the low-dimensional method after transformation, and then the low-dimensional data are sorted from small to large, which results in the ordered OD data pairs. The ordered OD data pairs are then sorted in the database one by one for the last month, the corresponding data sets are constructed, and then the data are trained using the recurrent neural network model GRU to derive the passenger flow prediction results for the following week.

### 1.1 Introduction

With the rapid development of economy, people's living standard is gradually improved. At the same time, rail transportation as the key transportation mode of national development, more and more people choose to travel by subway or high-speed rail because it has the advantages of convenience, speed, cheap price, low impact on the environment, etc. that many other transportation modes cannot compete with it. However, with the gradual development of railroad system, the operation route map of subway is becoming more and more complicated. How to improve the efficiency of people's travel through reasonable scheduling in a complex roadmap without increasing the maximum speed of vehicles and ensuring safety has become a hot topic of passenger flow prediction nowadays.

---

J. Chen · K. Yu · K. Wu

College of Information Engineering, Sichuan Agricultural University, Ya'an City 625014, Sichuan Province, China  
e-mail: [201803768@stu.sicau.edu.cn](mailto:201803768@stu.sicau.edu.cn)

J. Pan (✉)

Southwest Jiaotong University, Chengdu City 610031, Sichuan Province, China  
e-mail: [jshpan@swjtu.cn](mailto:jshpan@swjtu.cn)

Accurate prediction of future changes in passenger flow helps to make reasonable subway scheduling and maximize the use of human and material resources without excessive waste, so the requirements for passenger flow prediction accuracy are generally high. If the predicted passenger flow is too small compared with the actual passenger flow, the railroad department cannot quickly adapt to the impact caused by the change of larger passenger flow and cannot effectively evacuate passengers in time when encountering an accident, nor can it reach the operation effect; if the predicted passenger flow is too large compared with the actual passenger flow, the frequent train movement will cause a large waste of human and material resources. It can be seen that the prediction results with higher accuracy are urgently needed, and the passenger flow prediction has very important practical significance.

The Isomap algorithm is able to predict the passenger flow of the OD pair, which can reflect the amount of passenger flow on the OD pair, so that the railroad department can quickly make reasonable train scheduling by comparing with the predicted passenger flow of other OD pairs. Then, it can facilitate better comparison of OD pairs by railroad authorities [1].

At present, neural network has been proved to be able to approximate any nonlinear model, with good adaptiveness, self-organization, and strong learning ability, which is more suitable for passenger flow prediction of nonlinear and more complex data. In the network architecture design, GRU, which is more concise in expression and more computationally efficient, is chosen in this paper. The model is evaluated using root mean square error (RMSE) and mean absolute error (MAE).

## 1.2 Isomap Algorithm

Isomap algorithm is a nonlinear unsupervised dimensionality reduction algorithm, which is a method to represent nonlinear structured high-dimensional data in low dimensions. Isomap algorithm first uses the shortest path in the popular space to find the approximate geodesic distance, and then inputs it to the multi-dimensional scale analysis (MDS) for processing, and then finds the low-dimensional coordinates embedded in the high-dimensional space [2].

Isomap algorithm is described as follows.

1. Input: sample set in high-dimensional ( $m$  dimensional) space  $X = \{x_1, x_2, \dots, x_n\}$ ; nearest neighbor parameter  $y$ ; dimension  $k$  in low-dimensional space.
2. Output: projection of the sample  $x$  is set  $Z = \{z_1, z_2, \dots, z_n\}$  in the  $k$  dimensional space.
3. Algorithm steps.
  - (1) for  $i = 1, 2, \dots, n$  do.
  - (2) determine the  $y$  nearest neighbors of  $x_i$ .



- (3) distance between  $x_i$  and  $y$  nearest neighbor points is Euclidean distance  $\Omega_{ij} = \sqrt{\sum_{t=1}^m (x_{it} - x_{jt})^2}$ , and distance from other points is set to  $+\infty$ .
- (4) end for.
- (5) call the shortest path algorithm  $d_{ij}$  to calculate the distance of any two sample points.
- (6) generate the distance matrix  $D = [d_{ij}]_{n \times n}$ .
- (7) construct the matrix  $A = [a_{ij}]_{n \times n} = \left[-\frac{1}{2}d_{ij}^2\right]_{n \times n}$ .
- (8) calculate the inner product matrix  $B = [b_{ij}]_{n \times n} = \left[a_{ij} - \bar{a}_{i.} - \bar{a}_{.j} + \bar{a}_{..}\right]_{n \times n}$ .
- (9) find the eigenvalues and eigenvectors of  $B$ .
- (10) construct the matrix  $Z = \left[E_k \Lambda_K^{1/2}\right]_{n \times k}$ , where  $E_k$  is the matrix consisting of the previous eigenvectors of the matrix  $B$  and  $\Lambda$  is the diagonal matrix consisting of  $k$  eigenvalues.
- (11) :return  $Z_{n \times k}$ ;

The dimensionality reduction algorithm implements OD feature reduction: the input is three-dimensional: [O-point site number, D-point site number, shortest travel time]; the output is one-dimensional feature.

The advantage of Isomap algorithm is that it is able to combine global and local information of the data, which generally gives better results than MDS algorithm. However, the disadvantages exist in the following aspects: (1) large computational and spatial complexity, firstly, the distance matrix  $D$  of  $N \times N$  in the data set [computational complexity  $O(N^2)$ ], then the shortest path  $DN$  between the data [computational complexity  $O(kN^2 \log N)$ ], and then the dimensionality reduction mapping using the MDS algorithm on  $DN$ , which requires the computation of the eigenvalue eigenvector [computational complexity  $O(N^3)$ ]. The Isomap algorithm has a space complexity  $O(N^2)$ , (2) the neighborhood is difficult to determine, (3) new data points cannot be downscaled online.

Based on the above characteristics of Isomap algorithm, it is reasonable to use Isomap algorithm for data preprocessing algorithm of short-time interval passenger flow prediction, and it plays a very critical role in the ranking of OD pairs of locations [3].

The Isomap algorithm plays a very critical role in the ranking of OD pairs [4]. In this paper, we believe that although it is still possible to forecast the passenger flow of OD pairs without the Isomap algorithm, the accuracy of the results will not be too high and the data processing time may be very different from that without the Isomap algorithm, so this paper chooses to add the algorithm to the data preprocessing session before the forecast.

### 1.3 GRU

The gated recurrent unit (GRU) is a very effective variant of LSTM network, which is simpler and more effective than the structure of LSTM network, so it is also a very popular network at present. GRU, since it is a variant of LSTM, is also able to solve the long dependency problem in RNN network [5]. In LSTM, three gate functions are introduced: input gate, forgetting gate, and output gate. In GRU, on the other hand, there are only two gates: the update gate and the reset gate (Fig. 1.1).

The entire forward propagation process of GRU is given by this [6]:

$$r_t = \sigma(W_r x_t + U_r h_{t-1} + b_r)$$

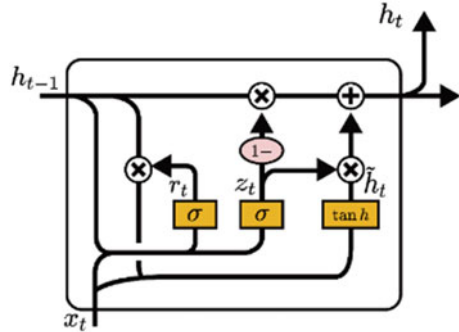
$$z_t = \sigma(W_z x_t + U_z h_{t-1} + b_z)$$

$$\hat{h}_t = \tanh(W_h x_t + U_h (r_t \odot h_{t-1}) + b_h)$$

$$h_t = z_t \odot h_{t-1} + (1 - z_t) \odot \hat{h}_t$$

GRU is a new generation of RNN network, very similar to LSTM. Instead of using unit states, GRU uses hidden states to transmit information. The update gate of GRU decides what information to discard and what new information to add, while the reset gate is another gate used to decide how much past information to forget [7]. Therefore, for subway passenger flow prediction, GRU can satisfy the reduced computation with a large amount of data, and the training speed is generally faster than other RNN networks.

Fig. 1.1 Cell of GRU



## 1.4 Isomap + GRU

In this paper, we take the ten pairs of OD pairs of Chongqing subway as an example. The ten pairs of OD pairs [O-point station number, D-point station number, shortest travel time] all need to be complete, and none of the data should be missing. And in order to ensure Isomap can work properly, the data of the three dimensions need to be all numeric and no Chinese station names can appear.

The three-dimensional data are calculated using Isomap algorithm, and finally, the one-dimensional results are obtained, stitched with the previous three-dimensional data, and the results are processed in ascending order as follows (Table 1.1):

At this point, the Isomap algorithm has been processed, and the OD pairs have been sorted according to the original idea. Next, from the first to the last row, take out the O-point station number and D-point station number in turn, enter the database to find the OD pair fixed by the corresponding O-point station number and D-point station number in turn, and find the data of the OD pair for almost 1 month (finally, only the first 28 days, i.e., 4 weeks, will be used). The passenger flow interval forecast will finally use the first three weeks to forecast the future week's data, so the extracted data need to be constructed as a dataset.

In the dataset construction stage, the first time period of the first week, the first time period of the second week, the first time period of the third week and the first time period of the fourth week are all extracted, and combined into one set using the create\_dataset function written in advance. The first three are used as the input to the model, the last one is used as the output of the model, and each next set of data is constructed according to the above method. Once each set of data for 28 days is constructed in this way, it is time to enter the GRU training and prediction process.

In this paper, we use keras to generate various layers, which is much more convenient than building the network manually. The model incorporates GRU layer, dense layer, epochs of 15,000 times (10 OD pairs), batch\_size of 512, and verbose of 2. The model uses AdamOptimizer optimizer to evaluate the model performance metrics

**Table 1.1** Data of three dimensions are reduced to one dimension by ISOMAP algorithm

O-point site number	D-point site number	Minimum travel time	Isomap downscaling results
287	48	960	- 107.7159
293	57	960	- 99.4005
283	57	960	- 99.1637
274	59	960	- 97.1621
288	62	960	- 94.8112
276	65	960	- 91.8444
273	271	850	141.5317
271	273	850	143.3674
290	277	850	146.4942
277	290	850	158.7046

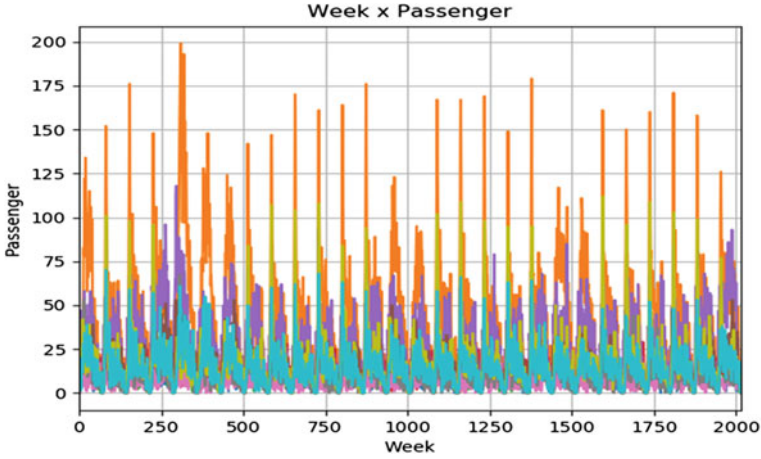


**Fig. 1.2** Raw passenger flow data for four weeks

root mean square error (RMSE) and mean absolute error (MAE) [8] (Fig. 1.2).

$$\text{RMSE} = \sqrt{\frac{1}{N} \sum_{i=1}^N (y_i - \hat{y}_i)^2}$$

$$\text{MAE} = \frac{1}{N} \sum_{i=1}^N |y_i - \hat{y}_i|$$

All original data for four weeks are as follows:

It can be seen that the data for the 10 OD pairs are relatively even overall, with the higher numbers on the OD pairs generally having higher numbers within four weeks and the lower numbers on the OD pairs generally having lower numbers within four weeks (Fig. 1.3).

The predicted results are as follows:

The predicted results are for one week, and the images show that the predicted results are still more uniform, and the OD pairs with more people have more predicted numbers compared to other OD pairs, and the same for the ones with less people, which shows that the Isomap-GRU model is more reasonable.

## 1.5 Conclusion

In this paper, a model combining Isomap algorithm and GRU recurrent neural network has been proposed for interval passenger flow prediction, and it has achieved good results from the results. However, there are still problems that need to be solved,

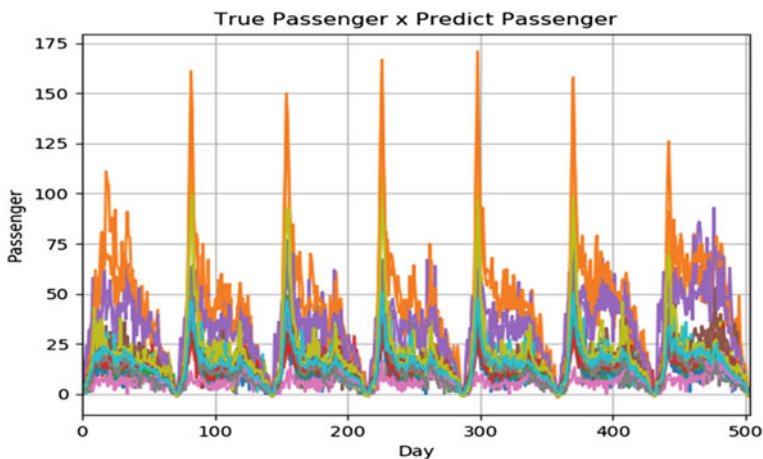


**Fig. 1.3** Passenger flow prediction data for the week

such as the fact that the prediction results will be poor and the network will easily collapse if a large number of OD pairs are flooded into the model at once, which can be better handled in the subsequent learning.

## References

1. Liu, Q., Cai, Y., Jiang, H., et al.: Traffic state prediction using ISOMAP manifold learning. **506**, 532–541 (2018)
2. Shi, L., Guo, L., Hao, Z., Zhang, J.: Spark-based parallel ISOMAP algorithm. *J. Univ. Sci. Technol. China* **49**(10), 842–850 (2019)
3. He, B.: Analysis of the advantages and disadvantages of Isomap and LLE in dimensionality reduction. *Capital Univ. Econ. Bus.* (2016)
4. Zhang, S., Gong, Z., Liao, H.: A nonlinear dimensionality reduction method integrating LLE and ISOMAP. *Comput. Appl. Res.* **31**(01), 277–280 (2014)
5. Wang, C.J., Zhang, W.J., Liu, S.J.: Turning traffic flow combination prediction based on EMD-GRU recurrent neural network. *Ind. Control Comput.* **33**(12), 73–76 (2020)
6. Tan, X., Zhang, X.: Short-term railroad freight volume forecasting based on GRU depth network. *J. Railway* **42**(12), 28–35 (2020)
7. Yuan, H., Chen, Z.: Short-time traffic flow prediction algorithm based on temporal convolutional neural network. *J. South China Univ. Technol. (Nat. Sci. Edn.)* **48**(11), 107–113+122 (2020)
8. Feng, S., Feng, C., Shen, H.: Research on short-time traffic flow prediction based on K-means and GRU. *Comput. Technol. Dev.* **30**(07), 125–129 (2020)

# Chapter 2

## Prediction of Subway Interchange Passenger Flow Based on Recurrent Neural Network Time Characteristic Model



Xiao Chen, Junxi Chen, Yi Liu, Zichen Zhan, and Jinglan Lei

**Abstract** With the rapid development of social economy, urban rail transit has become the mainstream of people's travel mode. For the reasonable dispatch of vehicles, rail transit operation departments have an increasing demand for short-term passenger flow forecasting. Through the analysis of the passenger flow data of Chongqing Metro from October 1, 2018, to October 15, 2018, the GRU neural network is used to analyze the Chongqing Metro stations from October 16, 2018, to October 30, 2018, to predict the arrival passenger flow data, and use the logit model-based transfer method selection combination model to obtain the transfer sharing rate, and finally obtain the predicted passenger flow of each transfer method. The comparison with other models and optimization algorithms shows that this model has better prediction accuracy, stability, and robustness. GRU neural network has associative memory function, simple structure, small amount of calculation, and anti-noise ability, so it is worth popularizing in subway passenger flow prediction applications.

### 2.1 Introduction

With the rapid development of social economy and urban modernization, urban rail transit has increasingly become the main mode of travel for urban residents, and the expansion and improvement of rail transit networks have become one of the development content of cities. As an important part of urban rail transit, the subway has developed rapidly. With the increase of subway lines, the structure of subway lines has become more and more complex, and the passenger flow has gradually increased. Among them, passenger flow is one of the main factors affecting subway operation and dispatch. In passenger flow forecasting, short-term passenger flow has gradually become a research focus. The forecast of short-term passenger flow can

---

X. Chen · J. Chen · Y. Liu · Z. Zhan · J. Lei (✉)  
College of Information Engineering, Sichuan Agricultural University, Ya'an City, Sichuan Province 625014, China  
e-mail: [lejinglan123@163.com](mailto:lejinglan123@163.com)

effectively improve the level of vehicle dispatch, evacuate passenger flow, and ensure safe travel of citizens. The current short-term passenger flow forecasting mainly includes historical averages, sequence-based methods (such as SARIMA model), neural network methods based on machine learning, K-nearest neighbor methods, support vector machine methods, etc. Each type of prediction method includes several forecast models. Due to the large randomness of subway passenger flow, machine learning-based methods are good at processing such data. Therefore, this article uses the subway credit card data provided by Chongqing Metro from October 1, 2018, to October 15, 2018. The statistics, analysis, and research of the total inbound and outbound passenger flow in units of 30 min, the use of Python language, GRU neural network model and logit model to predict the outbound passenger flow and the passenger flow for each transfer mode.

## 2.2 Introduction to Models and Methods

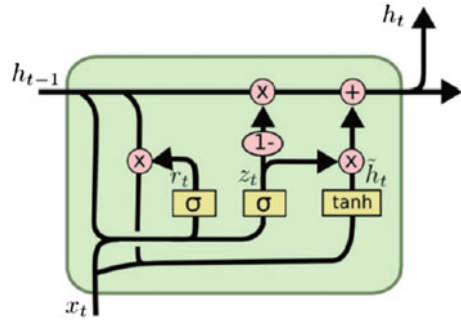
### 2.2.1 Introduction to Prediction Models

Long short-term memory model (LSTM) is a special structure type of RNN model. Compared with RNN model, LSTM adds three control units: input gate, output gate, and forget gate. When information is input into this model, the control unit in LSTM will judge the information, the information that meets the rules will be left for use, and the non-compliant information will be forgotten. Based on this principle, the problem of long sequence dependence in the neural network can be solved. With the widespread application of LSTM, the shortcomings of LSTM neural network models such as long training time, many parameters, and complex internal calculations are gradually exposed. In 2014, Cho et al. further proposed a simpler GRU model. In the LSTM network, the input gate and the forget gate are in a complementary relationship. As a variant of LSTM, GRU combines the forget gate and the input gate into a single update gate. It also mixes the cell state and the hidden state. With some other changes, the final model is more streamlined than the standard LSTM model. Therefore, as a more popular variant of LSTM, GRU maintains the effect of LSTM that can retain and update historical information. The long-term dependence of RNN, the ability to filter invalid information, a simpler structure, fewer parameters, and a better convergence model are more suitable for real-time calculation problems of subway passenger flow prediction. Its network structure is shown in Fig. 2.1: where  $h_t$  is the current state,  $h_{t-1}$  is the historical state,  $x_t$  is the current input,  $\tilde{h}_t$  is the candidate state at the current moment,  $r_t \in [0, 1]$  is the reset gate,  $z_t \in (0, 1)$  is the update gate.

The update method of the GRU model is:

$$r_t = \sigma(W_r x_t + U_r h_{t-1} + b_r) \quad (2.1)$$

**Fig. 2.1** Schematic diagram of GRU neural network structure



where  $\sigma()$  is the sigmoid function,  $W_r$  is the state-input weight matrix,  $U_r$  is the state-state weight matrix, and  $b_r$  is the deviation vector.

$$\tilde{h}_t = \tanh(W_c x_t + U_c (r_t \cdot h_{t-1}) + b_c) \quad (2.2)$$

Among them,  $\tanh()$  is the hyperbolic tangent activation function.

$$z_t = \sigma(W_z x_t + U_z h_{t-1} + b_z) \quad (2.3)$$

Among them,  $\sigma()$  is the sigmoid function, as the threshold number of the neural network, mapping the variable between 0 and 1,  $W_r$  is the state-input weight matrix,  $U_r$  is the state-state weight matrix, and  $b_r$  is the deviation vector.

$$h_t = z_t \cdot h_{t-1} + (1 - z_t) \cdot \tilde{h}_t \quad (2.4)$$

### 2.2.2 Calculation Method of Transfer Sharing Rate

First, based on the analytic hierarchy process, the passenger's satisfaction with the station transfer environment is obtained; then, the satisfaction is regarded as a type of variable in the non-aggregated model to form the station transfer environment characteristics obtained by combining the personal characteristics of passengers and the satisfaction model. Form a combined model to solve the utility function of each transfer mode, and solve the selection probability of each transfer mode.

## 2.3 Data Introduction

The data comes from the 15-day Chongqing Metro credit card data records from October 1, 2018, to October 15, 2018. According to the time period of arrival



DATA_DT	START_TIME	END_TIME	XFER_STATION_ID	TRAF_IN_LINE_ID	TRAF_OUT_LINE_ID	TRAF_SIN_SOUT	T
2018-10-01 00:00:00	2018-10-23 08:00:00	2018-10-23 08:30:00	180	10号线	3号线	364.87259741012542	
2018-10-01 00:00:00	2018-10-23 08:00:00	2018-10-23 08:30:00	201	1号线	27号线	0	
2018-10-01 00:00:00	2018-10-23 08:00:00	2018-10-23 08:30:00	276	10号线	3号线	52.039495297561665	
2018-10-01 00:00:00	2018-10-23 08:00:00	2018-10-23 08:30:00	130	5号线	6号线	658.42402790859524	
2018-10-01 00:00:00	2018-10-23 08:00:00	2018-10-23 08:30:00	45	5号线	2号线	475.73995007311748	
2018-10-01 00:00:00	2018-10-23 08:00:00	2018-10-23 08:30:00	172	3号线	26号线	187.70308458392546	
2018-10-01 00:00:00	2018-10-23 08:00:00	2018-10-23 08:30:00	254	3号线	环线	20.44153603141039	
2018-10-01 00:00:00	2018-10-23 08:00:00	2018-10-23 08:30:00	20	2号线	1号线	0	
2018-10-01 00:00:00	2018-10-23 08:00:00	2018-10-23 08:30:00	274	1号线	3号线	403.47934141726381	
2018-10-01 00:00:00	2018-10-23 08:00:00	2018-10-23 08:30:00	210	3号线	1号线	77.309635231020764	
2018-10-01 00:00:00	2018-10-23 08:00:00	2018-10-23 08:30:00	286	1号线	2号线	672.6328086226772	
2018-10-01 00:00:00	2018-10-23 08:00:00	2018-10-23 08:30:00	109	6号线	5号线	0	
2018-10-01 00:00:00	2018-10-23 08:00:00	2018-10-23 08:30:00	128	3号线	6号线	3184.3070704422062	
2018-10-01 00:00:00	2018-10-23 08:00:00	2018-10-23 08:30:00	109	2号线	5号线	7180.8664039706428	
2018-10-01 00:00:00	2018-10-23 08:00:00	2018-10-23 08:30:00	277	3号线	26号线	77.124673742191149	
2018-10-01 00:00:00	2018-10-23 08:00:00	2018-10-23 08:30:00	66	4号线	4号线	3474.78036565294276	

Fig. 2.2 Partial data of prediction input

passenger flow, for a more refined observation, half an hour is used as the time. Statistics are performed on segments, and the data fields include date and time, start time point, end time point of the time period, station ID, entry and exit lines, and passenger flow (unit: person) data. Some data are shown in Fig. 2.2.

## 2.4 Model Performance Evaluation

In order to compare the prediction effect of the GRU neural network, it is necessary to select appropriate evaluation indicators to objectively evaluate all models, but now, it is impossible to find an absolute advantage indicator to evaluate, so this article selects two evaluation methods: average absolute error (MAE), mean square. The root error (RMSE) comprehensively evaluates the prediction results of the model. The specific calculation formulas are shown in Formulas (2.5) and (2.6).

$$\text{MAE} = \frac{1}{N} \times \sum_{i=1}^N |y_i - \hat{y}_i| \quad (2.5)$$

$$\text{RMSE} = \left( \frac{1}{N} \times \sum_{i=1}^N (y_i - \hat{y}_i)^2 \right)^{1/2} \quad (2.6)$$

Among them,  $y_i$  and  $\hat{y}_i$  represent the actual value and the predicted value, respectively, and  $N$  represent the number of predicted samples. According to the calculation formula of the above evaluation index, the higher the average absolute error (MAE) and root mean square error (RMSE) index values are, the worse the prediction effect is, which means the greater the deviation between the prediction result and the actual value.

### 2.5 Model Prediction Process

Choose 50% of the experimental data as the training set, 50% of the data as the test set, and segment the original data according to 7:00–9:00 and 9:00–24:00. This paper uses the Formula (2.7) maximum-minimum normalization to compress the data to the interval [0,1]. After the model training and performance evaluation are completed, Formula (2.8) is used for denormalization.

$$x'_i = \frac{x_i - \min_{x_i}}{\max_{x_i} - \min_{x_i}} \tag{2.7}$$

Among them,  $x_i$  represents the  $i$ -th variable,  $\max_{x_i}$  and  $\min_{x_i}$  represent the maximum and minimum values, respectively.

$$\hat{y}_i^* = y_i^*(\max_{x_i} - \min_{x_i}) + \min_{x_i} \tag{2.8}$$

Among them,  $y_i^*$  is the predicted value obtained after model training.

Using the passenger flow arrival data of Chongqing Metro stations from October 1st to 15th, 2018, predict the passenger flow arrivals and the passenger flow of the transfer method at the same station from October 16, 2018, to October 30, 2018. The results are as follows Fig. 2.3, 2.4, 2.5, and 2.6.

The results show that the root mean square error of the training set from 7:00 to 9:00 is 2.98, the average absolute error is 1.51, the root mean square error of the test set is 2.40, the average absolute error is 1.42, and the relative error is stable

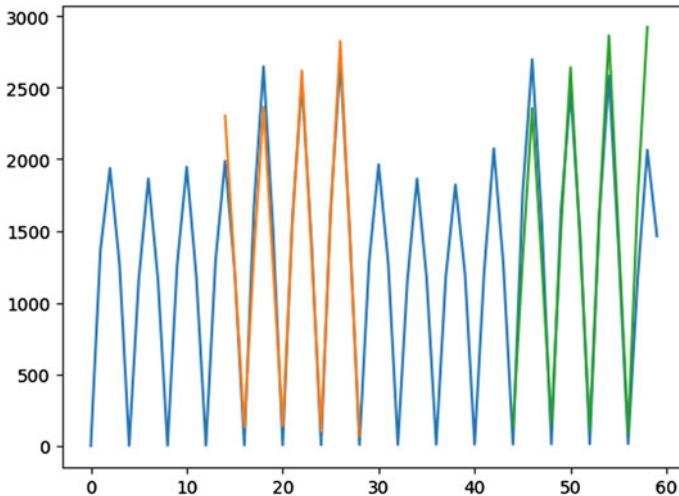
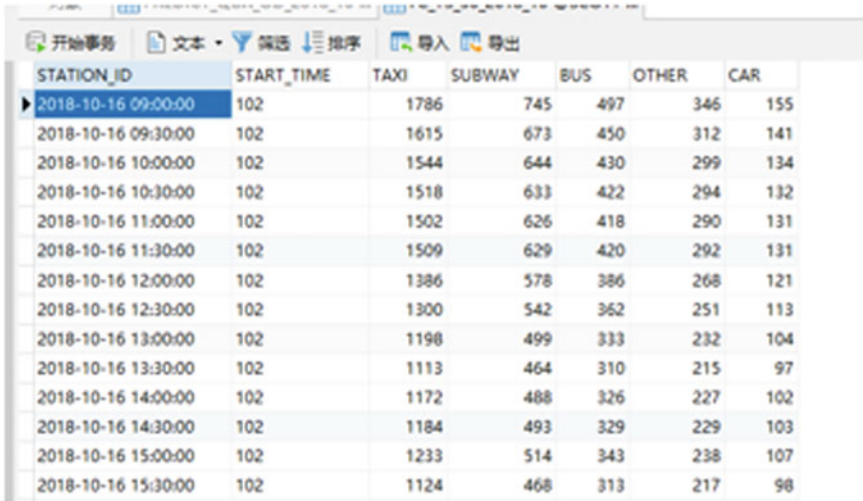


**Fig. 2.3** Forecast results of arrival passenger flow. Blue is the original data, green is the predicted value of the training set, and orange is the predicted value of the test set



STATION_ID	START_TIME	TAXI	SUBWAY	BUS	OTHER	CAR
2018-10-16 09:00:00	102	1786	745	497	346	155
2018-10-16 09:30:00	102	1615	673	450	312	141
2018-10-16 10:00:00	102	1544	644	430	299	134
2018-10-16 10:30:00	102	1518	633	422	294	132
2018-10-16 11:00:00	102	1502	626	418	290	131
2018-10-16 11:30:00	102	1509	629	420	292	131
2018-10-16 12:00:00	102	1386	578	386	268	121
2018-10-16 12:30:00	102	1300	542	362	251	113
2018-10-16 13:00:00	102	1198	499	333	232	104
2018-10-16 13:30:00	102	1113	464	310	215	97
2018-10-16 14:00:00	102	1172	488	326	227	102
2018-10-16 14:30:00	102	1184	493	329	229	103
2018-10-16 15:00:00	102	1233	514	343	238	107
2018-10-16 15:30:00	102	1124	468	313	217	98

Fig. 2.4 Passenger flow forecast for each transfer mode

Fig. 2.5 MAE and RMSE values of prediction results

```
Train Score :2.98 RMSE
Test Score :2.40 RMSE
Train Score :1.51 MAE
Test Score :1.42 MAE
```

Fig. 2.6 Relative error of prediction results

```
Epoch 94/100
- 0s - loss: 0.0102
Epoch 95/100
- 0s - loss: 0.0103
Epoch 96/100
- 0s - loss: 0.0103
Epoch 97/100
- 0s - loss: 0.0104
Epoch 98/100
- 0s - loss: 0.0104
Epoch 99/100
- 0s - loss: 0.0106
Epoch 100/100
- 0s - loss: 0.0105
```

to about 0.01, and for non-holiday data, select the SARIMA model that includes periodicity. For holiday data, use a combination of fluctuation coefficient models to predict passenger flow as shown in Table 2.1 [1]. Use random forest and lightgbm models to predict passenger flow. The results are shown in Table 2.2 [2], and the results of passenger flow prediction by other models are shown in Table 2.3 [3]. The comparison shows that the error of the prediction result obtained by using the GRU

**Table 2.1** Result of passenger flow prediction using the combined model of SARIMA and fluctuation coefficient

Date	Actual value	Predicted value	Relative error	Date	Actual value	Predicted value	Relative error
2016/3/11	5782	5660.39089	0.02103235	2016/3/16	3996	3401.29210	0.1488258
2016/3/12	4993	5746.34509	0.15088025	2016/3/17	4595	4372.35911	0.04845285
2016/3/13	5210	5467.62310	0.04944781	2016/3/18	6587	5693.19412	0.13569240
2016/3/14	3852	3777.06416	0.01945374	2016/3/19	5633	5604.54228	0.00505196
2016/3/15	3863	3346.86569	0.13360970	2016/3/20	5135	5370.62102	0.04588530

**Table 2.2** Results of using random forest and lightgbm model to predict passenger flow

	Model	MAE
January 25	Lightgbm	69.4
	Random forest	74.3
	Lightgbm linear fusion	65.5
	Random forest linear fusion	69.6
January 24	Lightgbm	59.3
	Random forest	62.6
January 20	Lightgbm	66.3
	Random forest	53.9

**Table 2.3** Results of passenger flow prediction by other various models

Predictive model	Class A passenger flow		Class B passenger flow		Class C passenger flow	
	RMSE	MAPE	RMSE	MAE	RMSE	MAPE
ARIMA	142.3214	0.2532	135.8471	0.2571	122.3214	0.2375
BP	96.8631	0.1582	97.7832	0.1632	91.2367	0.1512
GA-SVM	83.7291	0.1365	85.7353	0.1395	82.9632	0.1235
PSO-SVM	74.6521	0.1075	71.3561	0.1123	72.8531	0.1169
FA-SVM	71.5628	0.0821	68.3829	0.0792	69.8622	0.0771
GA_BP combination	65.4329	0.0747	63.8642	0.0751	63.7521	0.0738
DACFA-SVM	57.9646	0.0724	53.7143	0.0727	53.9821	0.0715

network is kept at a small level, so it shows that the model obtained by fitting can better predict the fluctuation of passenger flow.

## 2.6 Conclusion

The GRU neural network model inherits the advantages of the RNN neural network model with associative memory function and solves the long-term dependence problem of RNN. Its gate structure is similar to the LSTM model, which can filter out useless information and improve the accuracy of prediction. Compared with other models Recursive network, the gate structure of GRU is simple, the amount of calculation is small, and the prediction speed is faster. It is more suitable for real-time prediction such as subway passenger flow prediction; and GRU fully establishes the connection between various time series and can mine the internal connection between the series. Therefore, the GRU network structure has achieved good results on the problem of passenger flow prediction, and it is worthy of promotion in applications.

## References

1. Duan, R., Pang, J., Zhang, L.: Research on passenger flow prediction of railway stations based on SARIMA model. *Math. Pract. Knowl.* **49**(09), 1–10 (2019)
2. Zhang, S., Xie, X.: Analysis of characteristics and forecast of passenger flow in Hangzhou metro. *Value Eng.* **38**(19), 65–67 (2019)
3. Zhang, H., Ma, W.: Metro passenger flow prediction based on temporal and spatial characteristics. *Comput. Sci.* **46**(07), 292–299 (2019)

# Chapter 3

## Research on Dynamic Passenger Flow Distribution of Rail Transit Based on Multi-dimensional Euclidean Distance



Qianqian Wu, Lin Sun, Furong Jia, Yi Liu, and Zichen Zhan

**Abstract** With the rapid development of urban rail transit, choosing subway for short-distance transportation has become the primary plan for many residents. The passenger flow distribution of urban rail transit has an important reference for improving ride comfort and urban rail transit operation management. This paper starts from the historical passenger flow data in and out of the station, uses the original data of the urban rail transit automatic fare collection system, and is based on the multi-dimensional Euclidean distance formula. Dynamic passenger flow distribution is performed on OD (Origin-Destination) data to obtain section passenger flow data. The result of dynamic passenger flow allocation can provide basic data for the passenger flow forecasting module on the one hand, and provide certain guidance for the planning and designing of rail transit on the other hand.

### 3.1 Introduction

With the construction and improvement of the urban subway rail transit system, the traditional “The Four-step Method of Traffic Planning” for rail passenger flow forecasting is facing the challenge of new demands. On the one hand, the rail network, the encryption of stations, and the improvement of transfer conditions make passengers to face more travel options, not just constrained to choosing the nearest station; on the other hand, under the realistic background of the continuous use of new lines in various cities, the passenger flow changes of existing rail stations have become one of the important contents of demand forecasting. Therefore, based on the multi-dimensional Euclidean distance of rail transit dynamics, this paper takes the AFC data of Chongqing in recent two months as the reference data and studies the fluctuation prediction of section passenger flow.

---

Q. Wu (✉) · L. Sun · F. Jia · Y. Liu · Z. Zhan  
College of Information Engineering, Sichuan Agricultural University, Ya’an 625014, Sichuan, China

The research content of this paper mainly focuses on the dynamic passenger flow distribution of rail transit based on Euclidean distance. The current research status is summarized as follows:

Chen [1] proposed an improved logit model in the research of urban rail transit passenger flow distribution method based on the improved logit model, which improved the accuracy of passenger flow distribution. Song [2] studied the urban rail transit passenger flow analysis platform with big data analysis and processing capabilities on the spark based urban rail transit passenger flow analysis platform, which can provide dynamic analysis basis and decision support for daily operation management and passenger flow organization, to realize the improvement of transportation maintenance efficiency and service level. Zhai [3] established a passenger flow distribution model and algorithm that can accurately reflect the result of passenger flow distribution in the rail transit network in the modeling and application research of the dynamic distribution form of rail transit passenger flow. On the basis of theoretical research, the ticket sorting and passenger flow guidance system based on passenger flow distribution are developed. Liu [4] proposed the estimation method of passenger boarding selection probability and the estimation method of passenger travel time distribution in the research of urban rail transit passenger flow distribution method based on AFC data. Hu et al. [5] in the research of dynamic passenger flow assignment of urban rail transit with limited network capacity, this paper focuses on the dynamic passenger flow assignment considering time variables and analyzes the influence of road network transportation capacity and dynamic passenger flow density on the decision-making of passenger travel path selection.

### 3.2 Problem Analysis

Nowadays, the amount of statistical data that can be obtained by each system of subway rail transit is very large, and the data volume growth trend is also very rapid. With the rapid development of the Internet and cloud computing, according to the technical characteristics of the era of big data, it can be known that the use of multi-dimensional Euclidean distance calculation methods will successfully realize the dynamic passenger flow distribution of rail transit. Euclidean distance, also called Euclidean metric or Euclidean distance, is a commonly used distance definition, which is the true distance between two points in  $m$ -dimensional space. Taking the three-dimensional distance formula between two points as an example, the variables are the transfer time cost spent on each path, the interval running time cost, the difference between the crowding degree time cost and the OD entry and exit time interval, which can be used for path selection. The path calculated at this time, that is, the path selected by each OD under the conditions of congestion, transfer, and shortest path in turn, has subjective and objective temporal and spatial consistency.

### 3.3 System Design

This system mainly uses Java language and Scala for development work, and Oracle database and Hive database for data storage. The technical framework involved in the system mainly includes Spring Boot and Hadoop [6]. In addition, the system also integrates Kafka and Spark [7]. Kafka has the characteristics of high throughput, low latency, fault tolerance, and high concurrency; spark is a unified analysis engine for large-scale data processing and provides high performance for batch data. The function realization of the system is shown in Fig. 3.1.

The execution steps in Linux are as follows:

- (1) enter HiveQL statements;
- (2) parse it into an abstract syntax tree (Abstract Syntax Tree, AST) through the Thrift interface;
- (3) obtain metadata through Metastore and perform semantic analysis on AST to obtain a tree conforming to the Hive operator;
- (4) use Hive on Spark to optimize and adjust the syntax;
- (5) access Hive's Metastore through Hive Metastore Catalog in Spark, and generate RDD from the access results;
- (6) the RDD is generated through the function relationship, and the final RDD is obtained after multiple base-level RDDs undergo this series of conversions;
- (7) submit the final RDD to the Spark cluster for calculation.

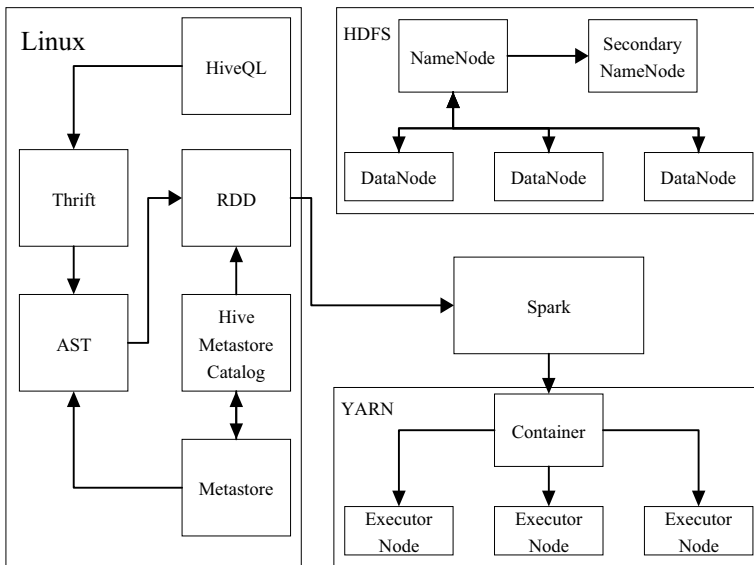


Fig. 3.1 System architecture diagram



Hadoop parallel computing uses its infrastructure HDFS and YARN. Each storage node of HDFS runs a DataNode process that manages data blocks of the host. Among them, we design to run Secondary NameNode and NameNode on the same host to assist NameNode data recovery in special circumstances. And YARN will be used as the running carrier of Spark to facilitate quick access to data in HDFS. In addition, YARN will also provide the Executor Node framework to execute SparkTask. When YARN performs resource scheduling, it runs its own tasks in the Container at the same time, and finally returns the calculated results to HDFS, which ends the entire process started by HiveQL.

### 3.4 Passenger Flow Distribution

The passenger flow of the section refers to the passenger flow passing through a certain place on the line within a unit time (full day, one hour, half an hour, 15 min), and its essence refers to the passenger flow passing through the section where the section is located. According to the different operating directions of urban rail transit, the cross-sectional passenger flow can be divided into the upstream cross-sectional passenger flow and the downstream cross-sectional passenger flow. Generally, the passenger flow in the upstream and downstream directions of each line is usually not equal [8]. Inter-section passenger flow distribution is an important function in the entire dynamic passenger flow distribution system. It has a key impact on the operation of urban rail transit and the choice of travel routes by passengers. The structure of the section passenger flow distribution table is shown in Table 3.1.

The distribution of passenger flow in section sections is mainly divided into static distribution and dynamic distribution. Static section distribution does not consider user perception (such as station congestion, running time, ticket cost) and only considers the physical path length for passenger flow distribution. Dynamic interval allocation needs to consider user perception, platform perception, behavior analysis, risk analysis and other factors, and then integrate physical length, and assign weights to all influencing factors into time parameters for passenger flow allocation.

**Table 3.1** Example structure of passenger flow allocation table for section

Field name	Field type	Length
DATA_DT	DATE	4
SECTION_ID	VARCHAR	30
START_STATION_ID	VARCHAR	30
END_STATION_ID	VARCHAR	30
START_TIME	DATE	4
END_TIME	DATE	4
PASGR_FLOW_QTTY	DECIMAL	18

In this system, according to the AFC entry and exit data, the selected time granularity is: static 15, 30, and 60 min; dynamic 15, 30, and 60 min for section passenger flow distribution. The static and dynamic passenger flow allocation steps are as follows:

(1) 15 min time granularity static passenger flow distribution steps

- Step 1 Pass the matched and cleaned OD data to the big data computing system, first perform  $K$  short-circuit calculation (calculation of  $K$  shortest paths for a single-source point) to obtain the shortest  $K$  between each incoming station and out-going station paths.
- Step 2 Perform physical interval division for each path, and get the start and end station number of each interval;
- Step 3 Divide the time according to the physical length of the interval. At this time, each interval can get a more accurate time length;
- Step 4 Calculate the intermediate value of the interval time length, this intermediate value falls into a certain 15 min interval to get the 15 min interval allocation data.

(2) 30 and 60 min static passenger flow allocation steps

- Step 1 Input the OD data that has been sliced by the OD matching system, and at a granularity of 30 min (60 min), first aggregate the recurring sites within a certain period of time and then perform  $K$  short-circuit allocation in the system;
- Step 2 At this time, after  $K$  short-circuit distribution, the intervals are divided according to the physical length, and the distribution data of 30 and 60 min can be directly obtained.

(3) 15-min time granularity dynamic passenger flow distribution steps

Input OD data and perform  $K$  short-circuit calculation. At this time,  $K$  short-circuit calculation needs to consider the impact of user perception factors such as congestion, travel risk, travel price, etc., and incorporate the impact into the risk calculation in the form of parameters. The remaining steps are the same as the static 15 above. The passenger flow distribution between minutes is consistent. The data representation of the dynamic interval section with a granularity of 15 min is shown in Fig. 3.2:

(4) 30 and 60-min time granularity dynamic passenger flow allocation steps

- Step 1 Input the OD data sliced through the OD pairing system. According to the granularity of 30 min (60 min), the recurring sites within a certain period of time are first aggregated, and then the  $K$  that considers the impact of user perception is performed in this system. Short-circuit distribution;
- Step 2 Same as the passenger flow distribution in the static interval, the OD data after the  $K$  short-circuit distribution at this time is directly divided into the intervals according to the physical length, and the 30 and 60 min interval distribution data can be directly obtained.

Data date	Interval ID	Inbound	IC	Outbound	Starting time	End Time	Number of people in the interval
2018/10/17 0:00	545	253	254		2018/10/17 15:15	2018/10/17 15:30	5.40E+00
2018/10/17 0:00	365	167	168		2018/10/17 9:15	2018/10/17 9:30	2.29E+02
2018/10/17 0:00	84	41	40		2018/10/17 8:45	2018/10/17 9:00	1.18E+02
2018/10/17 0:00	110	54	53		2018/10/17 10:45	2018/10/17 11:00	4.51E+02
2018/10/17 0:00	79	38	39		2018/10/17 10:30	2018/10/17 10:45	1.34E+02
2018/10/17 0:00	123	59	60		2018/10/17 15:45	2018/10/17 16:00	7.47E+02
2018/10/17 0:00	139	64	65		2018/10/17 8:45	2018/10/17 9:00	8.66E+02
2018/10/17 0:00		109	141		2018/10/17 13:00	2018/10/17 13:15	1.14E+03
2018/10/17 0:00	527	244	245		2018/10/17 7:00	2018/10/17 7:15	2.36E+01
2018/10/17 0:00	230	102	101		2018/10/17 16:45	2018/10/17 17:00	1.05E+03
2018/10/17 0:00	191	86	77		2018/10/17 8:45	2018/10/17 9:00	7.85E+01
2018/10/17 0:00	176	81	80		2018/10/17 15:15	2018/10/17 15:30	2.45E+02
2018/10/17 0:00		276	275		2018/10/17 6:30	2018/10/17 6:45	3.36E+02
2018/10/17 0:00	468	214	213		2018/10/17 9:30	2018/10/17 9:45	5.62E+02
2018/10/17 0:00	369	169	170		2018/10/17 9:45	2018/10/17 10:00	3.03E+02
2018/10/17 0:00	147	67	68		2018/10/17 10:30	2018/10/17 10:45	6.27E+02
2018/10/17 0:00	280	124	123		2018/10/17 9:30	2018/10/17 9:45	1.20E+03
2018/10/17 0:00	454	282	20		2018/10/17 13:30	2018/10/17 13:45	2.95E+02
2018/10/17 0:00	482	221	220		2018/10/17 14:45	2018/10/17 15:00	5.06E+02
2018/10/17 0:00	79	38	39		2018/10/17 17:30	2018/10/17 17:45	3.02E+02

Fig. 3.2 Example of 15 min section passenger flow

### 3.5 Conclusion Analysis

The dynamic passenger flow distribution system designed in this paper mainly uses the AFC data of the Chongqing rail transit system in the past two months and uses the corresponding data to calculate the multi-dimensional European distance. From this level, the dynamic passenger flow distribution of regional rail transit is carried out to a large extent. The above provides references for passenger travel and route planning, makes outstanding contributions to the development and improvement of the regional rail transit system, and provides new development ideas for the development of land transportation and maritime transportation.

**Authors’ Contributions** Lin Sun identified the problem. Furong Jia, Yi Liu and Zichen Zhan contributed to solving the problem. Lin Sun implemented the method and drafted the manuscript. All authors have read and approved the manuscript.

### References

1. Chen, P.: Research on urban rail transit passenger flow distribution method based on improved logit model. Beijing Jiaotong University (2018)
2. Song, X.: Research on urban rail transit passenger flow analysis platform based on spark. Beijing Jiaotong University (2017)
3. Zhai, H.: Modeling and application research on the dynamic distribution of rail transit passenger flow. Dalian Maritime University (2012)
4. Liu, Y.: Research on urban rail transit passenger flow distribution method based on AFC data. Beijing Jiaotong University (2019)
5. Hu, Y., Wen, D., Lv, H.: Research on dynamic passenger flow distribution of urban rail transit limited by road network capacity. *Comprehensive Transp.* **42**(08), 61–67+120 (2020)

6. Xu, H., Wang, L., Fan, G.: Metadata storage and query of hive based on hadoop distributed platform. Springer International Publishing: 2019-04-25
7. Wang, J., Wang, W., Chen, R.: Distributed data streams processing based on flume/kafka/spark. In: Proceedings of the 3rd International Conference on Mechatronics and Industrial Informatics (2015)
8. Huang, Y., Luo, Y.: Improved urban road congestion discrimination algorithm based on data distribution characteristics. Highway **63**(01), 124–131 (2018)

# Chapter 4

## Study on Valid Travel Route Selection of Integrated Passenger Transportation



Yao Yang, Chenyan Kan, and Dingjun Chen

**Abstract** With the vigorous development of the integrated transportation network, the choice of passenger travel route is becoming more and more diversified. Therefore, it is important to build the integrated transportation network by establishing the cost function of valid travel route to measure the route that passengers may choose. Based on passenger travel demand, an optimization model of valid route selection for integrated transportation network was established based on generalized travel cost. According to the characteristics of the model, an improved BFS algorithm based on dynamic updating generalized cost function and determining valid travel route by key nodes was designed to solve the valid route. Finally, a simulation was given to verify the effectiveness of the model and algorithm.

### 4.1 Introduction

Transportation is one of the basic supporting industries of China's national economy. With the rapid development of infrastructure on railway, highway, aviation and water transportation, a relatively complete transportation network system has been formed. Passenger connecting transportation is an organization mode to realize convenient and efficient travel of passengers through the overall planning and integrated transportation organization of different modes. As passengers, it is particularly important to choose an effective, economic, fast, comfortable way of travel. As far as the transportation department is concerned, a crucial problem to be solved by transportation

---

Y. Yang · C. Kan (✉) · D. Chen

School of Transportation and Logistics, Southwest Jiaotong University, Chengdu 610031, China  
e-mail: [swjtu113301@163.com](mailto:swjtu113301@163.com)

D. Chen

National and Local Joint Engineering Laboratory of Comprehensive Intelligent Transportation, Southwest JiaoTong University, Chengdu 610031, China

National Engineering Laboratory of Integrated Transportation Big Data Application Technology, Chengdu 610031, China

departments is how to allocate several different modes with the limited resources and make them to play with the maximum benefits.

For the optimization problem of road network, most researches focus on the urban traffic network. For example, LeBlanc [1] proposed that the optimization problem of road network can be solved by using the bi-level programming model, together with the bound of branch method; Zhao et al. [2] used the non-aggregate model to calculate the sharing of various transportation modes and established another minimum optimization model. Modesti and Sciomachen [3] raised the shortest path searching method which is based on multi criteria in the urban traffic networks by minimizing the total path cost. Nowadays, most of the domestic and foreign studies have not discussed the problem of the balance between different modes, and there are few targeted studies on the design of integrated channel network.

There have been many achievements in effective path selection, but so far, there is no good solution in the enumeration of effective paths. Li and Huang [4] proposed the definition of simple effective path without loop and proposed the corresponding hierarchical algorithm to solve it. However, a large number of invalid routes are included in the solution of the effective route constraints. Therefore, based on the definition of simple-acyclic path, He and Yan [5] proposed a new effective path definition by adding constraints to reduce some unnecessary algorithm calculation.

This paper analyzes the characteristics of passenger travel behavior with ticket price, travel time, safety and comfort as the main factors, and takes aviation, ordinary speed railway, high-speed railway, waterway transportation and highway transportation as the choice of passenger transportation mode, constructs the generalized cost function of passenger travel. According to the characteristics of road network and passenger travel, the constraints of effective path are formulated to limit the alternatives of effective path. BFS algorithm is used to search for effective path, trying to find the best solution to make the whole network efficiency achieve to be optimal, obtains the shortest path for passengers with different preferences. The feasibility of the model and algorithm is verified by an example.

## **4.2 Optimization Model of Passenger Effective Route Selection Based on Comprehensive Transportation Network**

According to the characteristics of path selection of passengers in the comprehensive transportation network, the travel cost can be divided into price cost, time cost, comfort cost and transfer cost. The four different cost units are unified and expressed as the same value. The generalized cost function model is established, and the comprehensive generalized cost value is used to measure the shortest route.

### 4.2.1 Price Cost

$$C_{\text{cost}} = C_O + C_R + C_D \quad (4.1)$$

$C_{\text{cost}}$  means the total price cost on the way;

$C_R$  represents ticket of various modes of transportation;

$C_O$  means the price cost from the starting point O to the departure transfer hub;

$C_D$  is the price cost from terminal to destination D.

### 4.2.2 Time Cost

$$C_{\text{time}} = (T_{\text{os}} + T_{S_s S_e} + T_{\text{SD}})V(T) \quad (4.2)$$

$C_{\text{time}}$  means the total time cost on the way;

$V(T)$  means the travel time cost parameter,  $V(T) = \text{GDP}/(T \times P)$ , GDP is gross domestic product, and  $T$  and  $P$  are average working hours and population, respectively;

$T_{\text{os}}$  means the travel time from the starting point to the departure hub;

$T_{S_s S_e}$  means the travel time between several transfer hubs;

$T_{\text{SD}}$  is the travel time from the terminal to the destination.

### 4.2.3 Comfort Cost

Travel comfort mainly depends on the type of transportation mode, seat type, travel time, travel conditions, etc. Assuming that the highest comfort score is 10, the comfort coefficient is defined as a constant A.

$$C_{\text{comfortable}} = A(10 - X_i) \quad (4.3)$$

$X_i$  means the comfort value of a class of seats in a certain mode of transportation.

The types of comfort value of passengers with different modes of transportation and different levels of seats can be found in Ref. [6].

### 4.2.4 Transfer Cost

In the process of travel, the total transfer cost is the transfer cost within the transfer station between various modes of transportation.

$$C_{\text{transfer}} = C_{\text{transfer}}^{S_1} + C_{\text{transfer}}^{S_2} + C_{\text{transfer}}^{S_3} \quad (4.4)$$

(1)  $C_{\text{transfer}}^{S_i}$  calculation

$$C_{\text{transfer}}^{S_i} = C_{\text{transfer}}^{\text{night}} + V(T)T_{\text{transfer}}^{S_i} + C_{\text{transfer}}^{\text{cost}} \quad (4.5)$$

$C_{\text{transfer}}^{S_i}$  refers to the transfer cost generated at the transfer hub (different stations in the same city) or station (the same station) in the whole transfer process.

$T_{\text{transfer}}^{S_i}$  is the time between arrival and departure from the transportation facility.

$C_{\text{transfer}}^{\text{night}}$  is the accommodation cost of the city where the transfer node is located.

$C_{\text{transfer}}^{\text{night}} = \varphi$ ,  $\varphi$  is the accommodation fee and transportation fee of unsuccessful transfer when the transfer is unsuccessful. When the transfer is,  $\varphi = 0$ .

$C_{\text{transfer}}^{\text{cost}}$  refers to the transportation cost during the transfer of two modes of transportation at the same transfer hub.

(2)  $T_{\text{transfer}}^{S_i}$  calculation

Suppose that the passenger chooses the route  $k$ ,  $x_k$  represents the transfer times and  $N$  represents the total transfer times, then the total transfer time of the passenger on route  $k$  is expressed as:

$$\begin{cases} T_{\text{transfer}}^{S_{ik}} = \sum_{x_k=1}^N x_k T_{\text{transfer}}^{S_i} (x_k > 0) \\ T_{\text{transfer}}^{S_{ik}} = 0 (x_k = 0) \end{cases} \quad (4.6)$$

All above are quantified by time cost, and the time value coefficient is normalized. Finally, a unified dimension is adopted for these four types of generalized costs, and the total generalized cost is defined as:

$$C = C_{\text{cost}} + C_{\text{time}} + C_{\text{transfer}} + C_{\text{comfortable}} \quad (4.7)$$

### 4.3 Improved BFS Algorithm

When searching for an effective route, it is normal that there are numbers of effective paths contained a lot of useless data. In this paper, Ref. [7], constraints are applied in the process of solving the effective route to redefine the comprehensive traffic effective route, so as to reduce unnecessary calculation.

#### 4.3.1 Improvement Strategy

Definition of comprehensive traffic effective route:



$L_k^{se}$  means the effective routes from the beginning to the end;  
 $V_k^{se} = \{V_1^{se}, V_2^{se}, \dots, V_n^{se}\}$  is the set of nodes that make up the path;  
 $T_k^{se} = \{T_1^{se}, T_2^{se}, \dots, T_n^{se}\}$  is the interval between arrival and departure time in a node,  
 $S_k^{se} = \{S_1^{se}, S_2^{se}, \dots, S_m^{se}\}$  is a collection of all road sections that make up the path.  
 $J_{se}$  is the collection of effective routes  $L^{se}$ ;  
 $C_k^{se}$  is the generalized travel cost function  $C_{se}^{min} = \min_{L_k^{se} \in J_{se}} \{C_k^{rs}\}$  of the path k.

The effective route satisfies the following conditions,

- (1)  $\forall S_i^{se}, S_j^{se} \in S_k^{se}, S_i^{se} \neq S_j^{se}$ ;
- (2)  $\forall V_i^{se}, V_j^{se} \in V_k^{se}, V_i^{se} \neq V_j^{se}$ ;

Restrictions on transfer times: Transfer times shall not exceed the maximum transfer times,  $x_k \leq N_{max}$   $N_{max}$  is different for different road network and travel.  
 $\forall T_i^{se} \in T_k^{se}, T_i^{se} > q$ ,  $q$  is transfer time in this node.

Condition 1 guarantees no repetition of road sections, condition 2 guarantees non repetition of nodes, condition 3 limits the number of transfer trips, and condition 4 guarantees the principle of limiting timetable. All the above conditions can reflect the actual road network situation.

### 4.3.2 Improvement

- (1) The generalized cost function is updated dynamically to judge the valid route condition. The improved algorithm updates the latest route generalized cost function to judge the effectiveness of the path every time it traverses to the transfer node, unlike the previous search algorithm, which searches all the routes first and then calculates the generalized cost function uniformly. If a route no longer meets the judgment condition of valid route, it can stop traversing in this direction in time and delete this branch, which can greatly reduce the complexity and steps of path search.
- (2) The valid route is determined by the key nodes. BFS algorithm marks every node that has been checked in the process of searching. The transfer node and the start and end node, which play a key role in the path determination, can also be called the key node. Therefore, the passenger's travel route can be obtained as long as the key node is marked, which reduces the complexity of the algorithm.

### 4.3.3 Improved BFS Algorithm

- Step 1 initialize the extension coefficient value  $h$  of a valid route. Reasonable setting of transmission time between maximum and minimum limits.  $\tau_h, \tau_{min} \leq \tau_h \leq \tau_{max}$ .

- Step 2 search all routes. The generalized cost of the first route is set as the lowest cost after calculating all the routes between the generalized costs of OD pairs based on each transportation mode. If a smaller cost is found, the lowest one is replaced. After repeated calculation, the strategy is updated to obtain the minimum generalized cost of the five transportation modes. Set all direct paths to set  $A$ , select all valid routes  $R_{S,S_e}$  settings as the judgment criteria.
- Step 3 search all transfer routes. In the comprehensive transportation network, there are two types of transfer that is the internal transfer of a certain mode of transportation and the transfer between different modes of transportation. For all these transfers, the criterion of effective path is the constraint of transmission time.
- Step 3.1 find the internal transfer route. If the transfer times and transfer time meet the specific standard range, all transfer routes with stations between OD will be searched. Similarly, the strategy is updated to obtain the minimum generalized cost of the five transportation modes of internal transfer among highway  $C_{\min}^R$ , ordinary speed railway  $C_{\min}^K$ , high-speed railway  $C_{\min}^G$ , aviation  $C_{\min}^F$  and waterway  $C_{\min}^L$ . The path determined to be a feasible path is added to set  $A$ .
- Step 3.2 find the external transfer path. Different from internal transfer, external transfer needs additional consideration for transfer plans of different stations in the same city. Based on the timetable of different modes of transportation, search the public platform (a certain station, ordinary speed train and high-speed train station or airport), and then find all possible transfers at the mixed station (or transfer city), and set all the routes found in the combination  $A$ .
- Step 3.3 determine a valid path in set  $A$ . For internal transfer routes, each mode of transportation judged by the  $C_{\min}$  value of each mode. For external transfer routes,  $(C_{\min}^R + C_{\min}^K + C_{\min}^G + C_{\min}^F + C_{\min}^L)/5$  is regarded as the judgment standard to determine whether it is an effective path. All valid paths can be placed in the collection  $R_{S,S_e}$ .
- Step 4 get all feasible route group  $A$  and effective path group  $R_{S,S_e}$  between specified OD pairs.

## 4.4 Simulation

The section from E'mei to Lianyungang is selected to form a comprehensive transportation network (Fig. 4.1). The valid routes from E'mei to Lianyungang are studied and the generalized cost is calculated according to needs of different groups, and the shortest path of different passenger's choice preference is obtained.

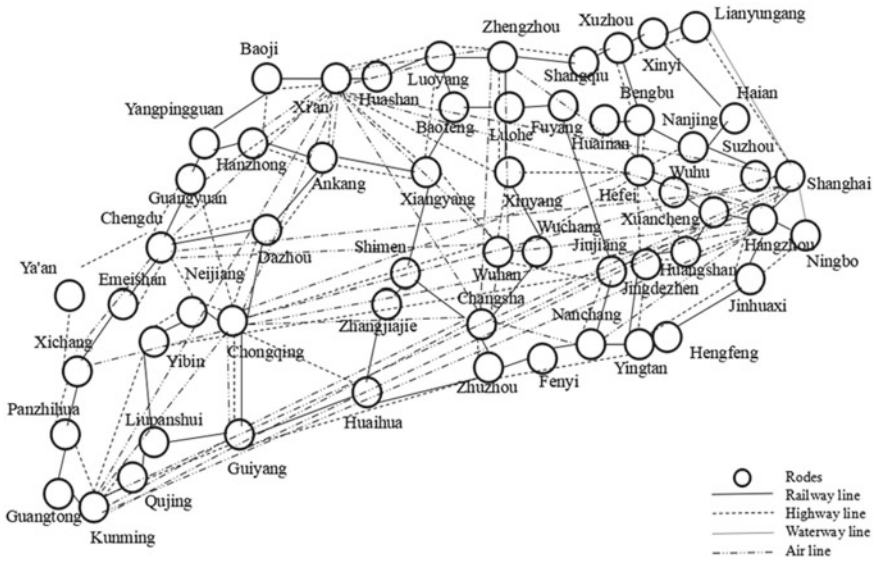


Fig. 4.1 Integrated transportation network from E'mei to Lianyungang

### 4.4.1 The Shortest Route in General

According to the calculation results, in the comprehensive route, the route with the lowest ticket price is No. 53 with a total of 448 yuan. The route with shortest total travel time is No. 181 with a total time of 467 min. The route with the highest comprehensive comfort is No. 196, corresponding to two transfers, and the seats are first class and business class. In general, the shortest route for passenger travel is the route corresponding to No. 151. The specific data are shown in Table 4.1.

### 4.4.2 Effective Routes with Different Transfer Preferences

Different passengers have different preferences for transfer, which is mainly reflected in different ages. The shortest route for two transfers is No. 151 as shown above, for one transfer, is No. 6, and for other transfers, is No. 49.

- (1) The shortest route of one transfer  
 In the case of one transfer, the shortest comprehensive route is No. 6 effective route which is first class seat and soft berth, with a total cost of 873.5 yuan. The total travel time is 1581 min. It can be found that when the number of transfer is reduced under long-distance trip, the impact of seat type on comfort is increasing, which is greater than the impact of ticket price on cost.
- (2) The shortest route of transfer three times

**Table 4.1** Valid routes for general condition

No.	Effective routes	Transfer hub		Cost (CNY)			Travel time (min)			Transfer		
		C1	C2	T1	T2	T3	Time1	Time2	Time3	Transfer over night	Transfer 1	Transfer 2
53	C6260(second), G1710(second), I148(hard)	Chengdu	Xi'an	62.0	263.0	118.5	81	230	879	N	31 min, Same station transfer	2 h17 min, Xi'an North → Xi'an
181	C6304(second), D1851(second), CA4019(economy)	Chengdu	Chongqing	62.0	121.0	760.0	73	122	135	N	37 min, Same station transfer	1 h40 min, Chongqing West → Jiangbei T2
196	C6262(first), 3U5056(business), MU2891(business)	Chengdu	Nanjing	99.0	1400.0	390.0	75	155	60	Y	3 h41 min, Chengdu East → Shuangliu T2	10 h30 min, Same station transfer
151	D1912(second), G1833(first), 9H8367(economy)	Xi'an	Xianyang	328.0	15.0	320.0	296	12	120	N	42 min, Same station transfer	2 h41 min, Xianyang Qindu → Xianyang T2

The shortest comprehensive route in the case of three transfers is No. 49 effective route with the total cost of 873.5 yuan. The total travel time is 886 min. The price and time are more than two transfers. When two transfers have the best route, no passengers choose three transfers in most cases.

#### ***4.4.3 Effective Route of Different Comfort Preferences***

Passengers with different incomes have different preferences for time and comfort. By adjusting the corresponding comfort coefficient, following results are shown: The shortest effective route of passengers with monthly income less than 2000 yuan is No. 149, with monthly income between 2000 and 3000 yuan is NO.151, with monthly income between 3000 and 8000 yuan is No. 155, and with monthly income more than 8000 yuan is corresponding to No. 188, the specific data are shown in Table 4.2.

As the income increases, the seat types are second and economy class, second, first and economy class, first and economy class and first and business class. The total cost is 672.5, 678, 875 and 1222 yuan. The total travel time is 631, 631, 631 and 467 min with two transfers.

It is indicated that with the increase in income, passenger's demand for price becomes lower, and their demand for time and comfort increases.

### **4.5 Conclusion**

With the continuous expansion of the scale of comprehensive transportation network and the continuous improvement of the network structure, the construction of comprehensive transportation network will flourish and the characteristics of comprehensive transportation network become more and more complex. On the way to travel, passengers can change their travel mode through the transfer choice in the transportation hub, and the passenger route choice will be more diversified. Therefore, it is an important means to determine the effective route that passengers may choose by analyzing the factors affecting the passenger route choice to better construct the comprehensive transportation network. It is important to understand passenger's choices of transportation mode and their effective paths to predict the future comprehensive traffic flow, reasonably arrange the facilities and equipment, plan the comprehensive line network, organize the operation, coordinate and cooperate with different transportation departments.

**Table 4.2** Valid travel routes for different comfort levels

No.	Effective routes	Transfer hub		Cost (CNY)			Travel time (min)			Transfer	
		C1	C2	T1	T2	T3	Time1	Time2	Time3	Transfer 1	Transfer 2
149	D1912(second), G1833(second), 9H8367(economy)	Xi'an	Xianyang	328.0	9.5	320.0	296	12	120	42 min, Same station transfer	2 h41 min, Xianyang Qindu → Xianyang T2
151	D1912(second), G1833(first), 9H8367(economy)	Xi'an	Xianyang	328.0	15.0	320.0	296	12	120	42 min, Same station transfer	2 h41 min, Xianyang Qindu → Xianyang T2
155	D1912(first), G1833(first), 9H8367(economy)	Xi'an	Xianyang	525.0	15.0	320.0	296	12	120	42 min, Same station transfer	2 h41 min, Xianyang Qindu → Xianyang T2
188	C6304(first), D1851(first), CA4019(business)	Chengdu	Chongqing	99.0	193.0	910.0	73	122	135	37 min, Same station transfer	1 h40 min, Chongqing West → Jiangbei T2

**Acknowledgements** This research was supported by the National Key R&D Program of China (2017YFB1200702), National Natural Science Foundation of China (Project No. 52072314; 71971182), Sichuan Science and Technology Program (Project No. 2020YFH0035; 2020YJ0268; 2020YJ0256; 2020JDRC0032; 2021YFQ0001; 2021YFH0175), Chengdu Science and Technology Plan Research Program (Project No. 019-YF05-01493-SN; 2020-RK00-00036-ZF; 2020-RK00-00035-ZF), Science and Technology Plan of China Railway Corporation (Project No. P2018T001, 2019KY10), Natural Science Foundation of Zhejiang Province, China (LQ18G030012) and the Humanities and Social Sciences Fund of Ministry of Education, China (18YJC630190).

## References

1. LeBlanc, L.J.: An algorithm for the discrete network design problem. *Transp. Sci.* **9**, 183–199 (1975)
2. Zhao, H., He, S., Song, R.: Network design for regional transportation corridors. *Chin. Civil Eng. J.* **40**, 74–78 (2007)
3. Modesti, P., Sciomachen, A.: A utility measure for finding multiobjective shortest paths in urban multimodal transportation networks. *Eur. J. Oper. Res.* **111**(3), 495–508 (1998)
4. Li, Z., Huang, H.: Determining the efficient paths in stochastic traffic assignment. *J. Transp. Syst. Eng. Inf. Technol.* **3**, 28–32 (2003)
5. He, S., Yan, L.: Searching the route of orientation in transportation network. *J. Univ. Shanghai Sci. Technol.* **26**, 356–359 (2004)
6. Nasitu, S.M.: A Study of Using Game Theory to Model the Competition Between High-Speed Train and Air Transport. Beijing Jiaotong University (2019)
7. Guo, Y.: Research on Effective Path of Urban Rail Transit. Beijing Jiaotong University (2011)

# Chapter 5

## Loading and Reinforcing Safety Evaluation of Railway Out-Of-Gauge Freight Considering the Dynamic Transportation Process



Hao Chen, Wenxian Wang, Min Zhou, and Xueqin Li

**Abstract** In order to evaluate the safety of loading and reinforcing scheme of railway out-of-gauge freight from the perspective of dynamic transportation process, the SIMPACK simulation model is established to collect the dynamic data during the transportation process, and safety factors are summarized into four indexes: wagon derail coefficient, wagon capsize coefficient, freight slip coefficient and freight capsize coefficient. On this basis, combine with the principle of neural network evaluation, this paper constructs a safety evaluation model of loading and reinforcing of railway out-of-gauge freights with the above-mentioned transportation process safety factors as the input layer and the comprehensive safety degree as the corresponding output layer. The results show that the lateral shift of gravity center for car loaded the gravity center height for car loaded and the longitudinal shift of gravity center for car loaded have the greatest impact on transportation process safety, and the influence degree is 0.52, 0.32, 0.35, respectively. And the classification of out-of-gauge freight and the length of protruding end have less impact. Other factors have relatively little impact.

---

H. Chen · M. Zhou

School of Economics and Business Administration, Yibin University, Yibin 644000, China  
e-mail: [2019114013@yibinu.edu.cn](mailto:2019114013@yibinu.edu.cn)

M. Zhou

e-mail: [2019114015@yibinu.edu.cn](mailto:2019114015@yibinu.edu.cn)

W. Wang (✉)

School of Railway Tracks and Transportation, Wuyi University, Wuyi 529020, China

X. Li

School of Transportation and Logistics, Southwest Jiaotong University, Chengdu 611756, China



## 5.1 Introduction

Out-of-gauge freights refer to the freights whose calculated width exceeds the basic outline of clearance of rolling stock when the rolling stocks stays on a horizontal straight line or passes through a curve with a radius of 300 m after loading [1]. Compared with ordinary freights, out-of-gauge freights have the characteristics of “indecomposable, over length, over width, over height and overweight.” Out-of-gauge, freights are often the key transport freights of major projects or national defense construction. Loading and reinforcing are the necessary premise of transportation process. A good loading reinforcement scheme can not only improve the safety of out-of-gauge freights in the transportation process, but also reduce the transportation time and the cost to a certain extent.

In the transportation network of various countries in the world, the status and organization mode of railway transportation are different. At the same time, the size of rolling stock, the railway lines and clearance are also different. Therefore, the importance and research level of railway freight transport in different countries are not the same.

In the United States, due to its well-developed road transportation, perfect highway infrastructure, high-carrying capacity of wagons, large freights are generally handed over to highway transport companies, so the United States has less research on the transportation theory of railway out-of-gauge freights. Russia, Germany, Austria and other countries pay more attention to improving the transport speed and increasing the wagon loading capacity of railway out-of-gauge freight trains. Russia’s optimization plan is to increase the running speed of freight train from 80 to 90 km/h. The optimization plan of Germany and Austria is to increase the design speed of 500 ton Schnabel car to 90–100 km/h, and the maximum speed of loaded railway freight car to 65–90 km/h. In addition to the 500 ton Schnabel car, Russia also plans to develop 36-axle oversize commodity cars with a loading capacity of 700 t, and the United States plans to develop supersized rolling stock with a loading capacity of 807 t. In order to realize the “door-to-door” transportation service of railway out-of-gauge freights, German railway has also specially researched and developed oversize commodity car for road and rail dual-use, and put them into short-distance transportation. In 1989, the Former Soviet Union (FSU) began to use the unified classification method for out-of-gauge freights on the railways of Bulgaria, Hungary, Poland, Romania, Czech Republic and FSU. Firstly, the maximum allowable contour and minimum contour of out-of-gauge freights are determined according to the construction gauge and rolling stock gauge, respectively, and then the “free space” between the two contours is divided into several grades [2]. The international railway union has determined the method for determining the dynamic gauge of international intermodal power vehicles, analyzed the influence of vehicle structure and line conditions on the space clearance required by vehicle operation, and determined the specific calculation formula for the lateral offset caused by the lateral travel of vehicle running gear. The lateral vibration offset caused by vehicle operation is considered in the safety reserve, and the specific value is determined by each country [3, 4]. In terms of safety research

on loading and reinforcing of out-of-gauge railway freights in China, Ma Guofeng, Chen Hao, Wang Pei, Huang Jujie, Liu Hui, etc., analyzed various risk factors of overload and unbalanced load, and summarized the safety problems existing in the loading and reinforcing of railway freights, such as insufficient management, backward monitoring means and testing equipment [5–9]. Xu analyzed the force situation during the transportation of out-of-gauge freights, as well as the force generated by the speed and direction change of vehicles passing through curves and ramps [10]. Wen improved the theoretical system of loading safety and the system of regulations and standards, and considered the method of using new freight reinforcing materials and equipment to ensure transportation safety [11]. Liu studied the safety of railway freight loading and reinforcing under the condition of mixed running of wagon and coach in view of the reconstruction of existing lines in China [12].

It is not difficult to find that the existing research mainly focuses on the analysis of the influencing factors or the formulation, optimization and evaluation of the loading and reinforcing scheme for specific freights. However, in the actual transportation of out-of-gauge freights, accidents are almost not in the static loading process, but more often in the transportation process. Due to the influence of various forces on the car bodies and freights in the dynamic transportation process, the freights are more likely to have potential safety hazards, including derail and capsize [13–16]. Based on the above analysis, this paper analyzes the force of the freights in the transportation process, and combines the neural network algorithm, proposes a dynamic safety evaluation simulation model in the railway out-of-gauge freights transportation process, and studies it based on MATLAB to confirm the influence of dynamic transportation process.

## 5.2 Dynamic Simulation and Data Acquisition in Transportation Process

In order to collect the dynamic data in the transportation process, simulation model should be established in SIMPACK. The model consists of three parts: freights, wagons and lines. According to the characteristics of out-of-gauge freights, it is necessary to choose suitable wagon and simulate a curve line. Three parts of cargo, vehicle and line are established. The force analysis point is established by the interaction between the freights and the upper plane of the car body. Finally, three modules of freights, wagons and lines and several force analysis points are established. There is force a relationship between bogie, wheel and line. Connect lines module and vehicles module with wheel–rail relationship module, and a simulation system model including freights, wagons and line is constructed. The model basic structure is shown in Fig. 5.1.

Through the establishment of each module of the simulation model, the freight-wagon-line model is finally established in SIMPACK as shown in Fig. 5.2.

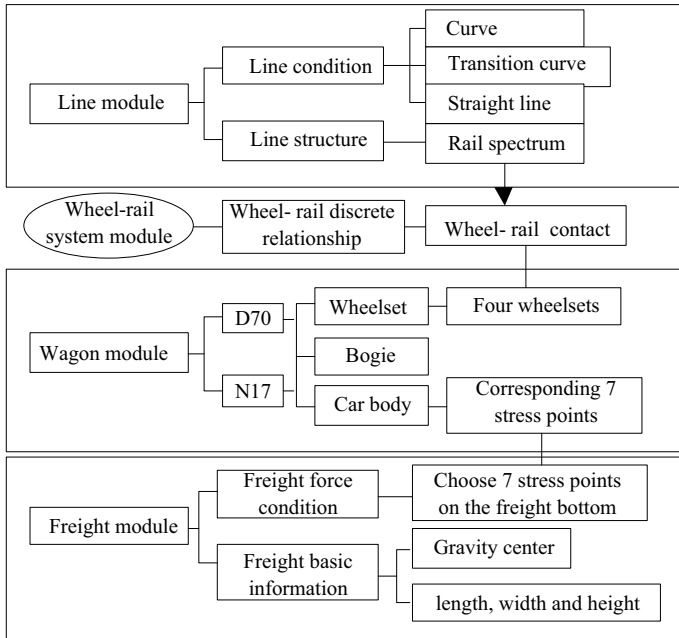


Fig. 5.1 Structure diagram of wheel/rail simulation model

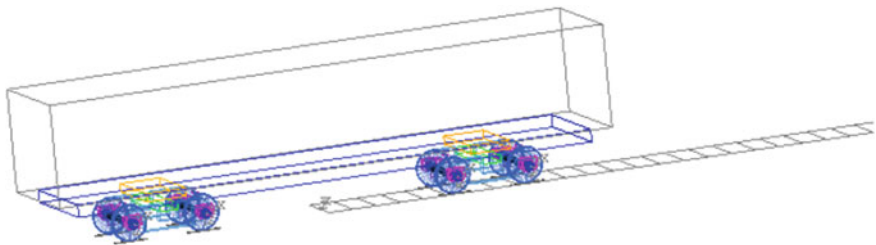


Fig. 5.2 Freight-wagon-rail model in SIMPACK

The simulation model simulates the transportation process of N17 and D70 wagons on a 500 m curve line (The line consists of a 100 m curve line with a radius of 400 m, two 100 m straight lines and two 100 m transition curve lines.), and the transportation speed is 20 m/s. Finally, the filtered data and corresponding real-time force images are obtained. The generated data are used for scheme analysis and evaluation.

### 5.3 Safety Evaluation Factors in Transportation Process

Referring to “railway freight loading and reinforcing rules” and “railway out-of-gauge freights transport rules,” the derail coefficient, wagon capsize coefficient, freight slip coefficient and freight capsize coefficient are taken as the analysis indexes of dynamic evaluation in transportation process.

(1) Wagon capsize coefficient

When the train passes through a curve line, if the train speed does not match the super elevation, the train may capsize. The calculation of train capsize coefficient is complex, but in the SIMPACK simulation process, only the overall force analysis can be carried out, which can be simply understood as the force between the same wheelset and the railway rail. When the interaction force between the wheel and the rail on one side is 0 at a certain time, it is considered that there is no contact between the wheel and the rail, and the capsize probability during the driving process is as follows:

$$D_1 = \left| \frac{P_R - P_L}{P_R + P_L} \right| \tag{5.1}$$

where  $D_1$  is the capsize coefficient of the wheelset;  $P_R$  is the vertical force between the right wheel and the rail;  $P_L$  is the vertical force between the left wheel and the rail.

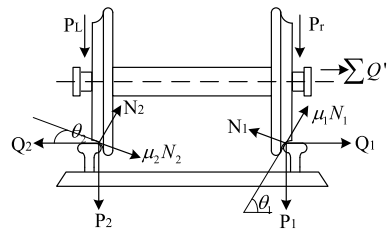
(2) Wagon derail coefficient

In the transportation process, when the train passes through curve line, it is easy to derail due to the combined effects of centrifugal force, wind force, transverse vibration force and gravity. If these forces are in the most unfavorable combination, the vehicle may derail (Fig. 5.3).

For this wheelset, the force balance formula of the non-derailed side is  $Q_2/P_2 = (\tan \theta_2 + \mu_2)/(1 - \mu_2 \tan \theta_2)$ . When  $\theta_2$  approaches 0, the derail coefficient of the derailed side is:

$$D_2 = \frac{Q}{P} = \frac{Q_1}{P_1} = \frac{\sum Q' + Q_2}{P_1} = \frac{\sum Q' + \mu_2 P_2}{P_1} \tag{5.2}$$

Fig. 5.3 Force between wheelset and rail



In the formula (5.2),  $\theta_1$  is the angle between the right flange and the horizontal line;  $\theta_2$  is the angle between the left wheel tread and the horizontal line;  $\mu_1$  is the friction coefficient between the right flange and the rail;  $\mu_2$  is the friction coefficient between the left wheel tread and the rail;  $P_2$  is the vertical force between the wheel and the rail on the non-derailed side,  $kN$ ;  $P_1$  is the vertical force between the wheel and the track on the derailed side,  $kN$ ;  $Q_2$  is the lateral force of the wheel on the non-derailed side acting on contact point B,  $kN$ ;  $Q_1$  is the lateral force of the wheel on the derailed side acting on contact point A,  $kN$ .

(3) Freight slip coefficient

In the transportation process, the inertia force of freights in the horizontal direction is generally greater than the friction force. If there are no reinforcement measures, the freights are prone to horizontal slip. The probability formula of horizontal slip of freights is as follows:

$$D_3 = \max\left(\frac{\sum F^x}{f_x^f}, \frac{\sum F^y}{f_y^f}\right) \quad (5.3)$$

where  $\sum F^y$  is the resultant force in the vertical direction,  $\sum F^x$  is the resultant force in the horizontal direction,  $f_y^f$  is the friction force in the vertical direction, and  $f_x^f$  is the friction force in the horizontal direction;

(4) Freight capsize coefficient

In the transportation process, different positions of freight are subject to different vertical forces, which may cause the freight capsize. Formula (5.4) can be obtained by analogy with the force situation of wagon capsize.

$$D_4 = \left| \frac{\sum F_R^z - \sum F_L^z}{\sum F_R^z + \sum F_L^z} \right| \quad (5.4)$$

where  $D_4$  is the freight capsize probability,  $\sum F_L^z$  is the resultant force in the vertical direction on the left side of the freight, and  $\sum F_R^z$  is the resultant force in the vertical direction on the right side of the freight.

According to the relevant regulations [17], the maximum allowable value of capsize coefficient is 0.8, i.e.,  $D_1 \leq 0.8$ . The derail coefficient  $D_2$ , the freight slip coefficient  $D_3$  and the freight capsize coefficient  $D_4$  are also specified. The calculation parameters of the above four coefficients are all taken from the simulation results. Part of the parameter values is shown in Fig. 5.4.

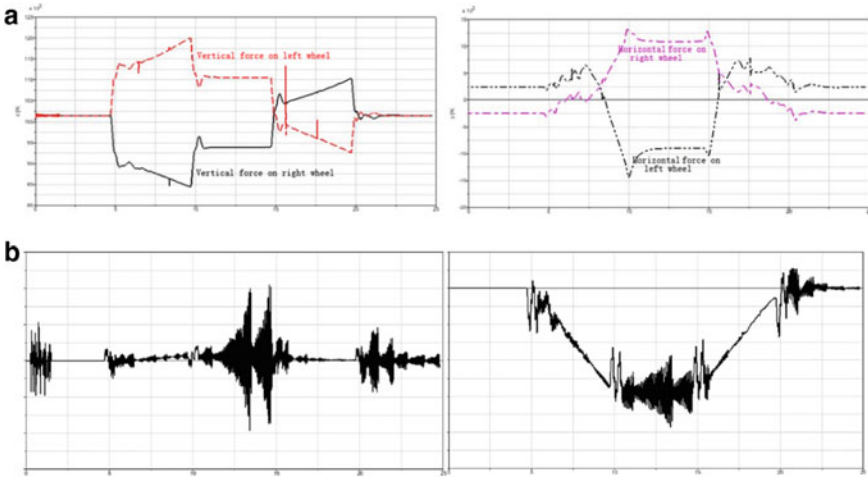


**Fig. 5.4** a Vertical force and horizontal force on the first set of front wheels. b Vertical and horizontal stress diagram of freight contact point

### 5.4 Safety Evaluation Method of Transportation Process

In this paper, the evaluation model of transportation process is established based on BP neural network, and the safety degree and result analysis of loading reinforcement scheme in transportation process are obtained by multiple transportation models. The transport factor designed in the simulation scheme is taken as the input layer, and the safety degree calculated by simulation is taken as the corresponding output layer. By analyzing the potential rules between the input–output data, and adjusting the weights of the hidden layer and the output layer, the evaluation model can be constructed. Finally, according to these rules and adjusted weights, new scheme data can be input to obtain new results. The specific steps of the evaluation process are as follows:

Step 1: Suppose there are  $n$  neuron nodes in input layer,  $q$  neuron nodes in hidden layer and  $m$  neuron nodes in output layer. This paper defines:

Input vector:  $X = (x_1, x_2, \dots, x_i, \dots, x_n)^T, x_i = \{\text{wagon type; loading mode ... minimum curve radius}\};$

Hidden layer input vector:  $Z^{\text{in}} = (z_1^{\text{in}}, z_2^{\text{in}}, \dots, z_k^{\text{in}}, \dots, z_q^{\text{in}})^T;$

Hidden layer output vector:  $Z^{\text{out}} = (z_1^{\text{out}}, z_2^{\text{out}}, \dots, z_k^{\text{out}}, \dots, z_q^{\text{out}})^T;$

Input vector of output layer:  $Y^{\text{in}} = (y_1^{\text{in}}, y_2^{\text{in}}, \dots, y_j^{\text{in}}, \dots, y_m^{\text{in}})^T;$

Output vector of output layer:  $Y^{\text{out}} = (y_1^{\text{out}}, y_2^{\text{out}}, \dots, y_j^{\text{out}}, \dots, y_m^{\text{out}})^T, y_i = \{\text{wagon capsize, wagon derail, freight slip, freight capsize}\};$

Expected output vector:  $T = (t_1, t_2, \dots, t_j, \dots, t_m)^T;$

Error function:  $E = \frac{1}{2} \sum_{j=1}^m (t_j - y_j^{\text{out}}), j = 1, 2, \dots, m.$

Step 2: Calculate the values of neurons in each layer.

Hidden layer input value:  $Z^{\text{in}} = \sum_{i=0}^n V_{ki}x_i$ ,  $k = 1, 2, \dots, q$ ;

Hidden layer output value:  $Z^{\text{out}} = f_1(Z^{\text{in}}) = f_1(\sum_{i=0}^n V_{ki}x_i)$ ,  $k = 1, 2, \dots, q$ ;

Output layer input value:  $Y^{\text{in}} = \sum_{j=0}^m W_{jk}z_j^{\text{out}}$ ,  $j = 1, 2, \dots, m$ ;

Output layer output value:  $Y^{\text{out}} = f_2(Y^{\text{in}}) = f_2(\sum_{j=0}^m W_{jk}z_j^{\text{out}})$ ,  $j = 1, 2, \dots, m$ .

Step 3: According to the actual output value and the expected output value, the partial derivative of the error function to neurons in the output layer can be obtained.

$$\frac{\partial E}{\partial W_{jk}} = \frac{\partial E}{\partial Y^{\text{in}}} \frac{\partial Y^{\text{in}}}{\partial W_{jk}} \quad (5.5)$$

$$\frac{\partial E}{\partial Y^{\text{in}}} = \frac{\partial \left[ \frac{1}{2} \sum_{j=0}^m (t_j - y_j^{\text{out}})^2 \right]}{\partial Y^{\text{in}}} = -(T - Y^{\text{out}}) \cdot (Y^{\text{out}})' = -(T - Y^{\text{out}}) \cdot f_2'(Y^{\text{in}}) \quad (5.6)$$

$$\frac{\partial Y^{\text{in}}}{\partial W_{jk}} = \frac{\partial \left[ \sum_{j=0}^m (W_{jk} \cdot z_k^{\text{out}}) \right]}{\partial W_{jk}} = Z^{\text{out}} \quad (5.7)$$

Let  $-(T - Y^{\text{out}}) \cdot f_2'(Y^{\text{in}}) = -\delta_y$ , where  $\delta_y$  is the error signal of the output layer.

Step 4: Obtain  $\frac{\partial E}{\partial W_{jk}} = \frac{\partial E}{\partial Y^{\text{in}}} \cdot \frac{\partial Y^{\text{in}}}{\partial W_{jk}} = -\delta_y \cdot Z^{\text{out}}$  from step 3, and then use the hidden layer to get the weight of the output layer and the output of the hidden layer, which can similarly calculate the partial derivative of the error function to the neurons in the hidden layer.

$$\frac{\partial E}{\partial V_{ki}} = \frac{\partial E}{\partial Z^{\text{in}}} \frac{\partial Z^{\text{in}}}{\partial V_{ki}} \quad (5.8)$$

$$\frac{\partial Z^{\text{in}}}{\partial V_{ki}} = \frac{\partial \left[ \sum_{i=0}^n (V_{ki} \cdot x_i) \right]}{\partial V_{ki}} = \sum x_i = X \quad (5.9)$$

$$\begin{aligned} \frac{\partial E}{\partial Z^{\text{in}}} &= \frac{\partial \left[ \frac{1}{2} \sum_{j=0}^m (t_j - y_j^{\text{out}})^2 \right]}{\partial Z^{\text{out}}} \cdot \frac{\partial Z^{\text{out}}}{\partial Z^{\text{in}}} = \frac{\partial \left[ \frac{1}{2} \sum_{j=0}^m (t_j - f_2(Y^{\text{in}}))^2 \right]}{\partial Z^{\text{out}}} \cdot \frac{\partial Z^{\text{out}}}{\partial Z^{\text{in}}} \\ &= \frac{\partial \left\{ \frac{1}{2} \sum_{j=0}^m \left[ t_j - f_2 \left( \sum_{j=0}^m (W_{jk} \cdot z_k^{\text{out}}) \right) \right]^2 \right\}}{\partial Z^{\text{out}}} \cdot \frac{\partial Z^{\text{out}}}{\partial Z^{\text{in}}} \end{aligned}$$

$$\begin{aligned}
&= - \sum_{j=0}^m [T - f_2(Y^{\text{in}})]^2 \cdot f_2' \left( \sum_{j=0}^m (W_{jk} \cdot z_k^{\text{out}}) \right) \cdot W_{jk} \cdot \frac{\partial Z^{\text{out}}}{\partial Z^{\text{in}}} \\
&= - \sum_{j=0}^m [T - f_2(Y^{\text{in}})]^2 \cdot f_2'(Y^{\text{in}}) \cdot W_{jk} \cdot \frac{\partial Z^{\text{out}}}{\partial Z^{\text{in}}} \\
&= - \sum_{j=0}^m \delta_y \cdot W_{jk} \cdot f_1'(Z^{\text{in}}) \tag{5.10}
\end{aligned}$$

Let  $-\sum_{j=0}^m \delta_y \cdot W_{jk} \cdot f_1'(Z^{\text{in}}) = -\delta_k$ , where  $\delta_k$  is the error signal of the hidden layer.

Step 5: Use the error signal  $\delta_j$  of the output layer and the output value of neurons in the hidden layer to modify the connection weight:

$$\Delta W_{jk} = -\eta \cdot \frac{\partial E}{\partial W_{jk}} = -\eta \cdot \frac{\partial E}{\partial Y^{\text{in}}} \cdot \frac{\partial Y^{\text{in}}}{\partial W_{jk}} = \eta \cdot \delta_j \cdot Z^{\text{out}} \tag{5.11}$$

By the same reason, there is another correction weight:

$$\Delta V_{ki} = -\eta \cdot \frac{\partial E}{\partial V_{ki}} = -\eta \cdot \frac{\partial E}{\partial Z^{\text{in}}} \cdot \frac{\partial Z^{\text{in}}}{\partial V_{ki}} = \eta \cdot \delta_k \cdot X \tag{5.12}$$

Step 6: As shown in formula (5.11) and (5.12), calculate the global error. When the calculated global error value is within the preset accuracy, then end the cycle. Otherwise, choose a new learning sample and enter the next round of learning.

## 5.5 Case Analysis

### 5.5.1 Basic Parameter Design

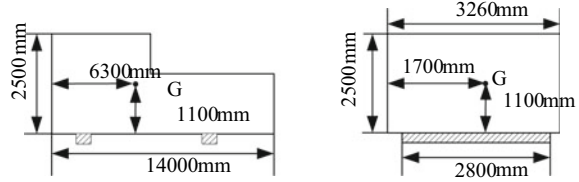
An out-of-gauge freight weighs 48 t, the total length is 14,000 mm, the gravity center is 6300 mm away from one end, the height of gravity center is 1100 mm and the height of horizontal cushion is 170 mm. The profile and cross section of the freight are shown in Fig. 5.5.

When one end of the freight is flush with the edge of the wagon, the other end protrudes from the car body by 1000 mm. When the freight gravity center falls on the wagon transverse center line, one end of the freight is 200 mm inside the edge of the wagon, and the other end is 1200 mm out of the wagon edge.

When the freight gravity center falls on the wagon longitudinal center line, there is no lateral deviation, but the freight external width is 1700 mm. When the freight



**Fig. 5.5** Schematic diagrams of freight profile and cross section



geometric center falls on the wagon longitudinal center line, the lateral offset is 70 mm and the freight external width is 1630 mm.

When using an idle car, the height of the lateral pedestal is calculated by  $H_m = 0.031a \pm h_{\Delta} + f + 80$ ,  $a$  is the distance from the protruding end to the vertical plane of the axle center of the nearest wheel axle,  $h_{\Delta}$  is the height difference between the wagon floor and idle car floor, and  $f$  is the deflection of the protruding end. Therefore,  $H_m = 0.031 \times 3000 \pm 0 + 0 + 80 \approx 170$  mm.

Based on Refs. [18–20], the following alternatives are combined by the extremum that can be taken within the range (Table 5.1).

### 5.5.2 Target Input and Output of Evaluation Index

(1) Target input

There are 11 evaluation indexes in the transportation process: (1) Wagon type; (2) Loading mode; (3) Gravity center transverse deviation; (4) Gravity center longitudinal deviation; (5) Height of transverse cushion; (6) Gravity center height for car loaded; (7) Length of freight protruding end; (8) Concentrated weight freight; (9) Classification of out-of-gauge freight; (10) Transportation speed; (11) Minimum line curve radius.

(2) Target output

In the transportation process, wagon capsize, wagon derail, freight slip and freight tumble are the four output indexes to quantify the safety degree of out-of-gauge freights transportation.

### 5.5.3 Sample Input and Data Output

The input evaluation index and output index of the sample can be obtained from the previous influence factor analysis, and the instantaneous state value of the worst time point in the simulation example is taken as the index data. In the evaluation indicators, quantitative indexes can obtain an accurate value, while qualitative indexes need to be obtained by other methods. Table 5.2 shows the 11 sample data of six sample evaluation indicators.

**Table 5.1** Alternatives

	Scheme 1	Scheme 2	Scheme 3	Scheme 4	Scheme 5	Scheme 6
Wagon types	N17	N17	N17	N17	D70	D70
Loading mode	Add an idle car	Add an idle car	Add an idle car	Add an idle car	No idle car	No idle car
Lateral shift (mm)	70	0	0	70	0	70
Longitudinal shift (mm)	200	200	0	0	0	0
Height of horizontal cushion (mm)	170	170	170	170	0	0
Gravity center height for car loaded (mm)	1894	1894	1894	1894	1699	1699
Length of protruding end (mm)	1000	1000	1200	1200	0	0
Concentrated weight	0	0	0	0	0	0
Classification of out-of-gauge freight	Level one	Level two	Level three	Level two	one-level	/
Transport speed (m/s)	20	20	20	20	20	20
Minimum curve radius (m)	400	400	400	400	400	400

The relevant parameters of the vehicle are as follows:

- (1) Type: N17, wagon weight 20.4 t, carrying capacity 60 t. The floor is 13,000 mm long, 2980 mm wide and 1209 mm high from the rail surface. The empty car gravity center is 690 mm high;
- (2) Type: D70, wagon weight 26.6 t, carrying capacity 70 t. The floor is 19,460 mm long, 2950 mm wide and 1169 mm high from the rail surface. The empty car gravity center is 798 mm high.

**Table 5.2** Safety evaluation sample indexes of out-of-gauge freight

No	1	2	3	4	5	6
Wagon types	0	0	0	0	1	1
Loading mode	2	2	2	2	1	1
Lateral shift	70	0	0	70	0	70
Longitudinal shift	200	200	0	0	0	0
Height of horizontal cushion	170	170	170	170	0	0
Gravity center height for car loaded	1894	1894	1894	1894	1699	1699
Length of protruding end	1000	1000	1200	1200	0	0
Concentrated weight	0	0	0	0	0	0
Classification of out-of-gauge freight	1	2	3	2	1	0
Transport speed	20	20	20	20	20	20
Minimum curve radius	400	400	400	400	400	400

**Table 5.3** Safety index of transportation process

No	1	2	3	4	5	6
Wagon capsize coefficient	0.1851	0.1768	0.1706	0.1801	0.1534	0.1588
Wagon derail coefficient	0.1689	0.1566	0.1511	0.1595	0.1336	0.1383
Freight slip coefficient	2.3480	2.2861	2.2059	2.3284	2.1228	2.1977
Freight capsize coefficient	0.0680	0.0637	0.0615	0.0649	0.0553	0.0573

The output layer takes four safety indexes in the transportation process as the target vector, and the four safety indexes can objectively quantitative the safety degree value. When calculating the safety value, this paper considers that the target vectors of the four outputs have the same importance, so only the weighted average is carried out to obtain the comprehensive quantitative evaluation value of the safety degree. The output matrix of sample safety index is shown in Table 5.3.

### 5.5.4 Calculation Results of BP Neural Network

The BP neural network algorithm is calculated in MATLAB.

- (1) Build sample  
Build 20 groups samples, each containing  $X_1, X_2, \dots, X_{11}; Y_1, Y_2, \dots, Y_4$ . The sample groups are shown in Fig. 5.6. The former six groups were used as calculation samples, and the other 14 groups were randomly applied to other loading models to verify the test data.
- (2) Data reading and assignment

	A	B	C	D	E	F	G	H	I	J	K	L	M	N	O
1	X1	X2	X3	X4	X5	X6	X7	X8	X9	X10	X11	Y1	Y2	Y3	Y4
2	0	2	70	200	170	1894	1000	0	1	20	400	0.1851	0.1689	2.348	0.068
3	0	2	0	200	170	1894	1000	0	2	20	400	0.1768	0.1566	2.2861	0.0637
4	0	2	0	0	170	1894	1200	0	3	20	400	0.1706	0.1511	2.2059	0.0615
5	0	2	70	0	170	1894	1200	0	2	20	400	0.1801	0.1595	2.3284	0.0649
6	1	1	0	0	0	1699	0	0	1	20	400	0.1534	0.1336	2.1228	0.0553
7	1	1	70	0	0	1699	0	0	0	20	400	0.1588	0.1389	2.1977	0.0573
8	0	2	0	200	200	1914	1000	0	2	15	400				
9	0	2	0	160	0	1780	1040	0	2	20	500				

Fig. 5.6 Build sample data

In MATLAB, the data in Excel table is read by xlsread function, and the data is read as  $20 \times 15$  matrix:

```
num = xlsread ('test.xlsx','Sheet2','A2: O7');
input_train = num ( 2: 7, 1: 11)';
output_train = num ( 2: 7, 12: 15)';
input_test = num ( 8: 21, 1: 11)';
```

- (3) Sample data normalization processing method

Normalize the sample data:

```
[inputn, inputs] = mapminmax (input_train);
[outputn, outputs] = mapminmax (output_train).
```

- (4) BP neural network training design

Initialize the BP neural network and design the calculation parameters. Training network with data.

```
net = newff ( inputn, output, 5);
net.trainParam.epochs = 100;
net.trainParam.lr = 0.1;
net.trainParam.goal = 0.00004;
net = train ( net, inputn, output);
```

- (5) Results anti-normalization processing

Anti-normalization processing is carried out to the results calculated by BP neural network.

```
inputn_test = mapminmax ("apply," input_test,inputs);
an = sim (net, inputn_test);
BPoutput = mapminmax ("reverse," an, outputs);
```

The sample data is calculated by MATLAB, and the corrected output value is shown in Table 5.4.

After calculating by BP neural network, other input schemes can be calculated and obtain output s. The output s of each scheme can be quantified quickly, and the safety degree of schemes can be compared. The safety degree of each scheme can be compared intuitively. Through the corrected four objective coefficients, it can be seen that Scheme 5 is the safest, Scheme 6 is the second, and Scheme 1 is the worst.

For the calculation of sensitive of parameters, the change of parameters is often the result of joint change of multiple factors. Such as the lateral shift for freight

**Table 5.4** Correction value of safety index

No	1	2	3	4	5	6
Wagon capsizes coefficient	0.1901	0.1780	0.1784	0.1850	0.1560	0.1605
Wagon derail coefficient	0.1701	0.1589	0.1552	0.1601	0.1341	0.1411
Freight slip coefficient	2.4208	2.3227	2.3140	2.4099	2.2035	2.2680
Freight capsizes coefficient	0.0692	0.0668	0.0637	0.0680	0.0561	0.0591

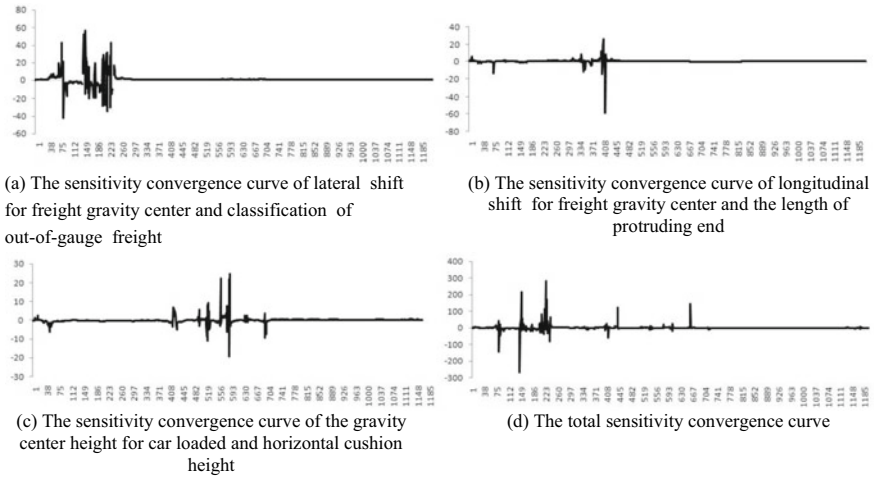


**Fig. 5.7** Parameter sensitivity convergence curves

gravity center and classification of out-of-gauge freight, generally speaking, these two factors are changed at the same time. Therefore, the sensitivity of parameters should also be calculated in groups. The parameters with greater influence include: the sensitivity of lateral shift for freight gravity center and classification of out-of-gauge freight is about 0.52; the sensitivity of longitudinal shift for freight gravity center and the length of protruding end is about 0.32; the sensitivity of the gravity center height for car loaded and horizontal cushion height is about 0.35. The total sensitivity is about 1.1, and its convergence is shown in Fig. 5.7.

## 5.6 Conclusion

- (1) The lateral shift for freight gravity center, center height of gravity for car loaded and longitudinal shift for freight gravity center have the greatest influence on the safety in the transportation process, followed by the classification of out-of-gauge freight and the length of protruding end.

- (2) When simulate the reliability of out-of-gauge freights during transportation in SIMPACK, the design of transportation environment under unfavorable working conditions will affect the calculation results to a certain extent, especially for the simulation of different wagon types, there may be obvious errors. However, in the case of the same wagon type and only changing other factors, the fluctuation of calculation result curve is basically the same, which has a certain accuracy.
- (3) When BP neural network is used to correct the output value, the larger the number of input samples, the larger the number of training and verification, and it is easier to obtain appropriate network results. But the calculation time is longer, and the calculated network has low-generalization ability.
- (4) When calculating the convergence of the parameters sensitivity, the larger the number of input samples, the better the convergence effect of output. However, when the number of samples exceeds 700, all the influencing parameters converge, and there is no obvious effect to expand the samples number.

**Fund Support** Sichuan Province 2011 Collaborative Innovation Center Yangtze River Upstream Shipping Logistics Collaborative Innovation Center Project “Research on the Coordinated Development of the Yangtze River Upstream Port Logistics Industry Cluster and Regional Economy (XTCX2020A06)”.

## References

1. Peng, Y.-Z., Lang, M.-X., Liu, J.-T.: Summary on the research off loading and reinforcing of chinese railway goods with exceptional dimensions. *Logist. Technol.***28**(11), 31–35 (2009)
2. Ju, D.: Research on the Basic Theory and Application of Out of Gauge Cargo Transportation, p. 21. Northern Jiaotong University, China (1997)
3. Zhou, Y., Zhu, Q.: Compilation of Foreign High Speed Railway Standards and Regulations. Academy of Railway Sciences, Beijing (1994)
4. Zeng, F.: UIC Regulations, p. 35. China Railway Press, Beijing (1977)
5. Ma, G.-F.: Consideration and exploration on the safety of current freight loading. *Railw. Freight Transp.* **4**(4), 40–43 (2004)
6. Chen, H.: Study on Theory and Method of Railway Out-of-gauge Freight Transportation of Reliability, p. 46. Southwest Jiaotong University, China (2017)
7. Wang, P.: Measures to improve the safety of cargo loading and reinforcement. *Railw. Freight Transp.* **6**(6), 27–28 (2008)
8. Huang, J.-J.: Analysis and measures affecting the safety factors of railway large cargo loading and reinforcement. *Technol. Market* **22**(5), 120–121 (2015)
9. Liu, H.: Research on Safety Risk Management of the Loading and Fastening of Railway Goods, p. 24. Beijing Jiaotong University, China (2013)
10. Xu, S.-S.: Railroad Transportation of Cargo Loading and Fastening Program Selection and Risk Assessment, p. 17. Jilin University, China (2014)
11. Wen, K.-X., Li, X.-H.: Retrospect and prospect of railway freight loading and reinforcement safety innovation practice. *Railw. Freight Transp.* **2**(2), 5–11 (2011)
12. Liu, T.-S.: Impact of cargo loading and reinforcement on train operation safety. *Railw. Freight Transp.* **2**(2), 29–30 (2009)

13. Mei, H.: Evaluation on safety of out-gauge goods transport by railway. *Proc. Saf. Sci. Technol.* **1**(1), 1029–1033 (2002)
14. Tan, Z.-M.: Research on the Optimization and Decision Support about Loading and Reinforcement of Railway Exceptional Dimension Freight, p. 36. Southwest Jiaotong University, China (2016)
15. Wang, W.-J.: Research on safety and reliability of key components for railway flat car loading and reinforcement. *Railw. Locomot. Car* **6**(6), 21–24+37 (2012)
16. Wang, C.-S.: The Study on Packaging Condition demanded in Dangerous Cargo Transport using Container and on Loading and Binding Measures, p. 19. Xi'an University of Technology, China (2003)
17. National Bureau of standards: Code for Evaluation and Test Evaluation of Dynamic Performance of Railway Vehicles (GB5599-85). National Bureau of Standards (1985)
18. Zhong, X.-Y.: On the Method of Evaluating the Loading and Securing Plan of Railway Exceptional Dimension Freight, p. 22. Southwest Jiaotong University, China (2011)
19. Li, X.-Q., Feng, W., Cai, M.-X.: Analysis of the factors affecting the safety and evaluation of large cargo loading. *Railw. Transp. Econ.* **30**(3), 32–34 (2008)
20. Li, X.-Q.: Research on Some Load Technique Problems of the Railway Out-of-gauge Freights, p. 54. Southwest Jiaotong University, China (2009)

# Chapter 6

## Design of Rail Freight Products in the Arduous Mountainous Area on the Plateau Under the Concept of Modern Logistics



Shiwei Yang, Qingchen Yao, Can Yang, Miaomiao Lv, and Mengyuan Yue

**Abstract** The railroad construction in the arduous mountainous area on the plateau is gradually improved. As the main channel of passenger and cargo transportation in and out of the difficult and dangerous mountainous areas on the plateau, how to develop cargo transportation on the basis of completing passenger transportation tasks and meet the transportation needs of resident's living and production materials is an urgent problem to be solved. Based on the demand for railway freight transportation in the arduous dangerous mountainous areas on the plateau, this paper combines modern logistics concepts and accurately locates customer needs on the premise of fully adapting to the characteristics of freight transportation in the arduous dangerous mountainous areas on the plateau. Based on the product genealogy, the railway freight system in the arduous dangerous mountainous areas is designed with refined product design, to promote the improvement of railway freight capacity.

### 6.1 Introduction

Railroad in the mountainous areas of the plateau is located in areas with severe undulations and harsh environments on the plateau. Cargo transportation is mainly for production and living materials, and it also undertakes the task of transporting bulk materials such as major mining and construction and ore along the line. When designing transportation products, it is necessary to take into account the transportation needs of various goods, for rail plays the main task of the basic people's livelihood project in the mountainous area of the plateau. The rail freight transportation promotes the overall upgrading of regional economic industries, and accelerate

---

S. Yang · Q. Yao (✉) · C. Yang · M. Lv · M. Yue  
CRRC Meishan Co., Ltd., Meishan 620010, China

S. Yang  
e-mail: [msysw126@126.com](mailto:msysw126@126.com)

M. Lv  
e-mail: [lvmiaomiao@swjtu.cn](mailto:lvmiaomiao@swjtu.cn)



the integration in the arduous mountainous area of plateau into the new pattern of national economic development.

There are few researches on railway freight transportation in plateau and difficult mountainous areas, mainly including intelligent and freight platform construction based on the Internet of Things technology. Research on products is relatively scarce [1–3]. The genealogical design of railway freight products generally needs to analyze the product requirements and level segmentation and then carry out subdivision design to form a genealogical product system [4, 5]. With the continuous deepening of the integration of railway freight transportation and modern logistics, results have been achieved in terms of changing service concepts, optimizing transportation organization, and optimizing the allocation of transportation resources, and the railway logistics model is gradually improving [6–8].

Since the construction of railroad network in the arduous mountainous areas of the plateau is incomplete and the organization of rail freight has not formed a specific model, there are few studies on rail product design and other aspects in the arduous mountainous area on the plateau. Especially, it is difficult to get the actual demand of customers from local cargo owners under the condition that the construction of railroad infrastructure in the arduous mountainous area on the plateau has not been well developed. Based on the above analysis, this paper designs the product system of rail freight in the arduous mountainous area on the plateau based on product spectrum design, combined with modern logistics concept.

## **6.2 The Impact of Modern Logistics Concept on Freight Product Design**

### **6.2.1 Full-Service**

With the integration and transformation of railway freight transportation to modern logistics, the transportation chain of products has become more and more complete. The services provided by freight companies have gradually developed to door-to-door transportation. The scope of transportation products has become larger and larger, and the logistics transformation of freight companies has become obvious, and gradually developed from the rail station-to-station transport for door-to-door transport services way.

### **6.2.2 Transportation Integration**

#### **(1) Transport mode integration**

Due to the limitations of the railroad construction network, railway transportation cannot achieve the true sense of the “door-to-door” transport services.

As the technical and economic characteristics of various modes of cargo transportation are not the same, rail freight service products under the modern logistics concept to cope with the more diversified and dynamic transport needs, should make full use of the characteristics of various modes of transportation to develop multimodal transport, especially in the mountainous areas of the plateau whose railroad infrastructure is not well developed, rail freight more should cooperate with road freight to develop public-rail intermodal transport services.

(2) **Transportation function integration**

Based on the development of modern logistics concept, rail freight functions should be integrated to achieve the integrated development of transport functions, including transportation, storage, warehousing and information consulting, establish a unified transport standard for the whole process, breaking industry barriers, precise positioning of customer needs to achieve efficient transportation of goods.

### ***6.2.3 Product Design Modularity***

Facing the dynamic development of freight market demand, cargo owners for freight service needs of the differentiation more and more differentiated, and it is difficult to satisfy the demands of customers with unchanging products. Modular product design can design specialized transport products for different demand modules, for customers to make their own choice, which can meet customer's product transportation needs more. Modular design method can satisfy customer customization and speed up the response of freight transport enterprises. It will ultimately achieve the scale benefits of rail freight through the production of specialized way.

## **6.3 Rail Freight Product Spectrum Design in the Arduous Mountainous Area on the Plateau Under the Modern Logistics Concept**

### ***6.3.1 Rail Freight Product Spectrum Design Method***

Railroad freight product spectrum design is a serialization study based on a clear understanding of railroad freight product demand, evolution lineage and development characteristics. It is designed in three dimensions: product demand spectrum, product evolution spectrum and product feature spectrum. It is a product design method that fully reflects customer needs, attaches importance to product evolution, comprehensively reflects development trends and can quickly respond to changing product development needs as shown in Fig. 6.1.

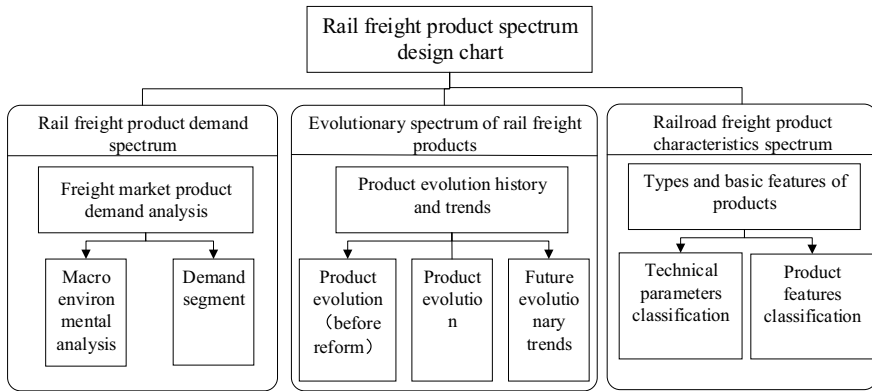


Fig. 6.1 Rail freight product spectrum design method

### 6.3.2 Rail Freight Product Demand Spectrum Design in the Arduous Mountainous Area on the Plateau

Due to the harsh climatic conditions and complex terrain conditions, transportation infrastructure is relatively scarce in the arduous mountainous area on the plateau. Railway assumes the backbone role of transportation of various production and living materials in the region. The market demand for railroad cargo transportation is high, so it is extremely important to promote the comprehensive development of railroad transportation products in the arduous mountainous area on the plateau, to promote the development process of local industrial and agricultural industries and improve living standards.

Combined with the characteristics of railroad and the classification of railroad transportation goods in the arduous mountainous area on the plateau, to meet the organization mode of railroad cargo transportation, the product requirement spectrum is designed as shown in Fig. 6.2.

### 6.3.3 Rail Freight Product Evolutionary Spectrum Design

Since the railroad construction in the mountainous areas on the plateau is not yet been completed, the evolution of railroad freight products is not enough to form a system. Here, the evolution spectrum of rail freight products in China is borrowed to provide a basis for the spectrum of design and development of railroad freight products in the arduous mountainous area on the plateau. Based on the review of existing data, the evolutionary spectrum of China’s railroad freight products is constructed from the perspective of product evolutionary relationships as shown in Fig. 6.3, from which it can be seen that the development trend of rail freight products has the following characteristics:

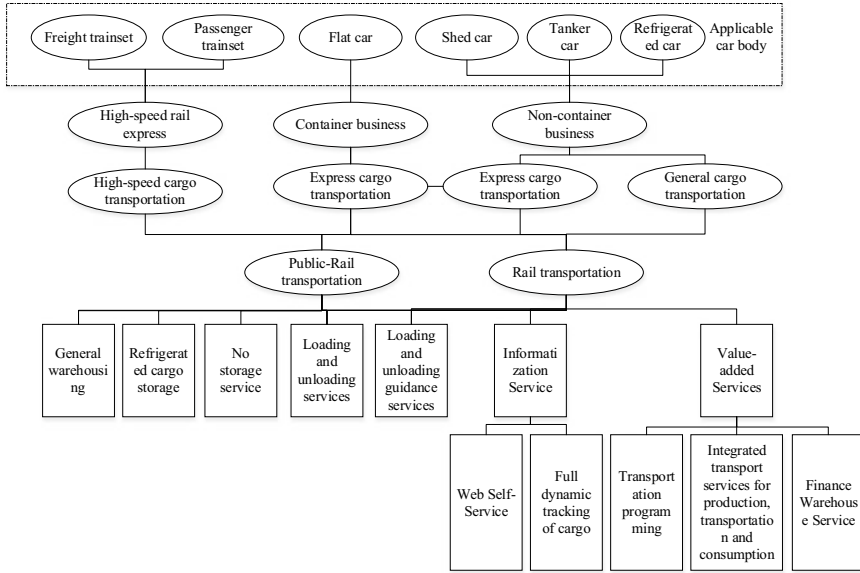


**Fig. 6.2** The spectrum of demand for railroad cargo transportation products in arduous mountainous areas on the plateau

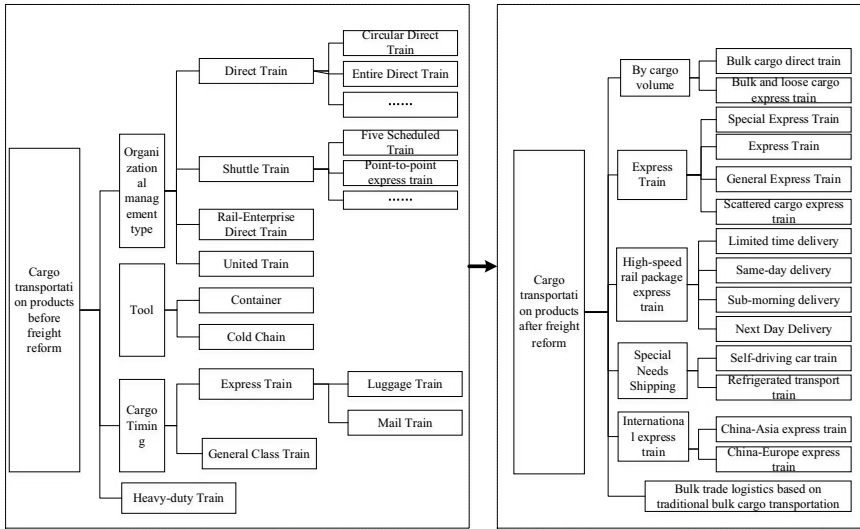


**Fig. 6.3** Evolutionary spectrum of rail freight products in China

1. Transport efficiency improved significantly, the rapid transport products gradually rich;
2. The development trend of integration with modern logistics industry is obvious, freight products logistics services to enhance the level;
3. Further refinement of transport products, freight product system is more abundant.

### ***6.3.4 The Design of Railroad Freight Product System Based on Modern Logistics Concept in the Arduous Mountainous Area on the Plateau***

According to the modular design method, the railroad freight products in the arduous mountainous area of the plateau are divided into three modules of core, form and additional products, and the rail freight product system is designed with three modules for the characteristics of rail freight products in the arduous mountainous area of the plateau as shown in Fig. 6.4.

1. Core product module  
The core product of rail freight transport in the arduous mountainous area of the plateau is the spatial displacement provided for various goods.
2. Form product module
  - (1) Divided by the freight category  
Considering the types of cargos, the railway in the arduous mountainous area on the plateau should focus on increasing the volume of container transport, and divide them into two types of products: container transport and non-container transport.
  - (2) Divided by the highest operating speed  
At present, the railway freight department has been improving the “door-to-door” pick-up and delivery product type. The railroad as the main body in the situation of incomplete rail cargo transportation infrastructure in the mountainous areas of the plateau, constructs “door-to-door” pick-up and delivery services. For cargos that do not require “door-to-door” service, we can provide “station-to-station” and “station-to-door” transportation services.
  - (3) Divided by arrival time  
According to the demands of customers along the railroad line in the arduous mountainous area on the plateau, the initial design of rail freight is divided into next-day, next two-day and multi-day delivery products. Among them, next-day delivery is mainly for small-volume high-value-added goods, such as express delivery and electronic information products like cell phones; next two-day delivery is mainly for goods with slightly lower requirements on time efficiency; multi-day delivery is mainly for goods with low requirements on delivery time efficiency.

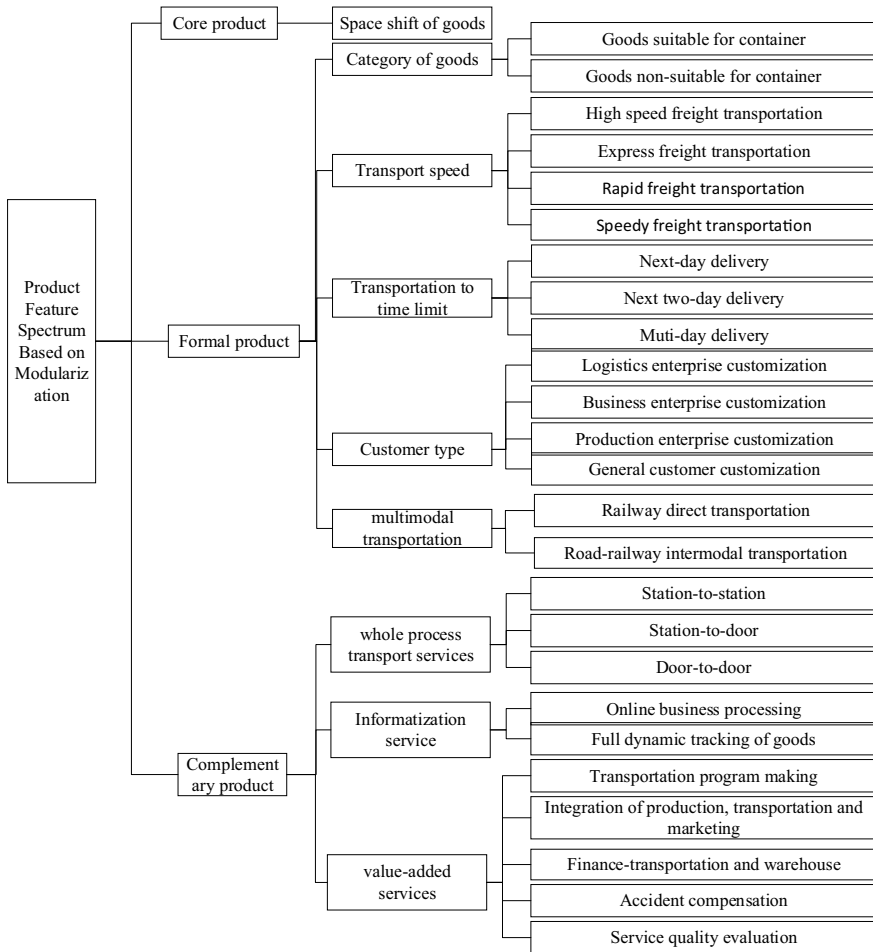


Fig. 6.4 Railway freight product spectrum based on modular design approach

(4) Divided by the type of customer

For different customer types, railway in the arduous mountainous area on the plateau can provide customized product services. For example, it can design exclusive customized trains for industrial and mining enterprises and industrial parks with stable production capacity along the rail line, and design special trade logistics trains similar to e-commerce trains for the resident’s shopping needs along the route.

(5) Divided by the demand of multimodal transportation

With the further improvement of the railway network, the backbone position of rail transportation in the freight market will be more prominent. However, it is difficult to provide transport products that require door-to-door pick-up and

delivery service by rail freight alone, so the development design of public-rail intermodal transport products should be focused on.

### 3. Additional product design

#### (1) Provide full transport services

At present, the railway freight department has been improving the "door-to-door" pick-up and delivery product type, especially in the situation of incomplete rail cargo transportation infrastructure in the arduous mountainous area on the plateau, the railroad should assume more social responsibility. The railroad as the main body, constructs "door-to-door" pick-up and delivery services in the mountainous areas of the plateau. For cargos that do not require "door-to-door" service, we can provide "station to station" and "station to door" transportation services.

#### (2) Informatization of service approaches

Based on the characteristics of rail cargo transportation in the arduous mountainous area of the plateau, the development of information-based service means is not only to improve the efficiency of freight transport, but also to be restricted by local environmental factors and the need to protect the efficiency and safety of railroad freight management and staff. Among the information-based service means provided, there should be online business processing functions including: customer order placement, fund settlement, transportation consulting and product service display. It is necessary to provide dynamic tracking function of the transportation process, and comprehensively improve the integration, intelligence and visualization construction of railroad service function in the arduous mountainous area on the plateau.

#### (3) Complete value-added services

Large-scale production enterprises on both sides of the rail line can be provided integrated transport services for production, transportation and consumption, to promote the development and upgrading of industrial and mining enterprises. It also needs to provide integrated financing warehouse services, providing logistics finance, insurance, warehouse leasing and other businesses; provide comprehensive after-sales management services, such as the establishment of a well-developed accident compensation mechanism and service quality evaluation mechanism, to achieve further improvement in the quality of rail freight services.

## 6.4 Conclusion

Based on the related research of railway freight transportation, this paper analyzes the current situation of railway freight products in the arduous mountainous area on the plateau. After determining the pedigree design method of railway freight products, combined with the integration development status of modern logistics and railway

freight, eventually form a complete product system for railway freight transport in the arduous mountainous area on the plateau.

**Acknowledgements** This paper is supported by Sichuan Science and Technology Program (2019ZYZF0034).

## References

1. Yan, J.: Discussion on the application of video surveillance technology in Sichuan-Tibet railway. *High-Speed Railw. Technol.* **11**(03), 51–54 (2020)
2. Li, G., Kong, C., Zhang, J.: Study on the application research on the integration of Sichuan-Tibet railway freight management and internet of things technology innovation. *Railw. Comput. Appl.* **29**(04), 37–41 (2020)
3. Zhang, J., Xu, J., Guo, J., Long, W.: Design and research on the overall architecture of intelligent Sichuan-Tibet railway system. *Comprehensive Transp.* **42**(01), 100–107 (2020)
4. Dahmus, J.B., Gonzale-Zugasti, J.P.: Modular product architecture. *Des. Stud.* **22**(5), 409–424 (2000)
5. Chen, C., Hong, Y., Ye, F., Tang, H.: Product spectrum design for rail cargo trains. *Freight Transp. Mark.* **38**(12), 26–31+43 (2020)
6. David, J.B.: *Introduction to Integrated Logistics Management*. Mechanic Industry Press, Beijing (2003)
7. Wang, Y., Chen, T.: Exploration on the logistics development of railway bulk cargo transportation. *Railw. Freight* (12), 8–10 (2008)
8. Guo, Y.: Research on the development of modern logistics in railway freight transport. *Railw. Transp. Econ.* **32**(02), 10–13 (2010)



**Part II**  
**Smart Vehicular Technology**

# Chapter 7

## An Estimation of Vehicle Vertical Dynamics Using Inverse Method



Dong-Cherng Lin, Trong-The Nguyen, Jeng-Shyang Pan,  
and Chang-Der Lee

**Abstract** The well-defined input to the vehicle or simulation model is one of the essential requirements to test driving ride comfort typically. This work suggests an approach to determining vehicle vertical dynamics, wheel vertical forces, and pitch torques based on an inverse direction methodology. The simple Kalman filter is used to form a filter that generates the residual innovation sequences with a recursive estimator. A least-squares algorithm is applied to compute the load's magnitudes from the car systems measured dynamic response data. In numerical simulations, we analyze the current strategy's feasibility and precision with a model driving estimation of wheel loads of a half-car over deterministic and random road profiles. The results from the simulation show that the proposed approach correctly measures the vertical dynamics of the vehicle.

### 7.1 Introduction

Serious problems for the driver and passengers are caused by the vibration produced due to the unevenness of the road profile, which has shown vibration on the ride's comfort [1]. Moreover, to interpret the driving environment and be road safety [2], the driving behavior of vehicles and artificial intelligence-based vision is necessary [3], so vertical dynamic estimation plays an important role [4]. A vehicle

---

D.-C. Lin (✉)

School of Computer Science and Mathematics, Fujian University of Technology, Fuzhou 350118, China

T.-T. Nguyen

University of Management and Technology Haiphong, Haiphong, Vietnam  
e-mail: [vnthe@hpu.edu.vn](mailto:vnthe@hpu.edu.vn)

J.-S. Pan

College of Computer Science and Engineering, Shandong University of Science and Technology, Qingdao 266590, China

C.-D. Lee

School of Information Engineering, Wuchang University of Technology, Wuchang 430223, China

driving over deterministic profiles or random road profiles demonstrates that these road profiles serve as a basic excitement system. So, since we do not use force sensors/transducers but use device responses, estimating road profiles is also input estimation, an overview of the force estimation problem for a linear vibration system [5].

An approach suggested Kalman inverse filtering using a Kalman filter [6] to deconvolve the forces acting from vehicle response measurements at the tire–road interface. The basic Kalman filter with the recursive least-squares estimator has been applied to classify tons of different structures [7, 8].

For a 2 DOF half-car model driving over three forms of road profile with an estimate of wheel vertical forces and pitch torques, this work suggests an inverse method of estimating vertical vehicle dynamics, investigating the feasibility accuracy of the proposed method through computational model simulations. The results from the simulation show that the proposed approach correctly measures the vertical dynamics of the vehicle.

### 7.2 Kalman Filter with Recursive Least-Squares Estimator

This section derives the discrete-time state equations of the half-car model subjected to the loads. The inverse analysis of wheel vertical loads in half-car model is presented as follows. A half-car model can be used and suited perfectly with a single-track road model [9]. This work, modeling of the system assumptions, the effects of the tires are negligible, and the left side and the right of the car symmetric, shown in Fig. 7.1.

Newton’s law gives the equation of motions of the half-car model that is expressed as follows.

$$\sum F_z = m\ddot{z} = -F_{S_R} - F_{S_F} - F_{C_R} - F_{C_F} \tag{7.1}$$

where

$$F_{S_R} = K_R(z - L_R\theta - Z_R), F_{S_F} = K_F(z + L_F\theta - z_F) \tag{7.1a}$$

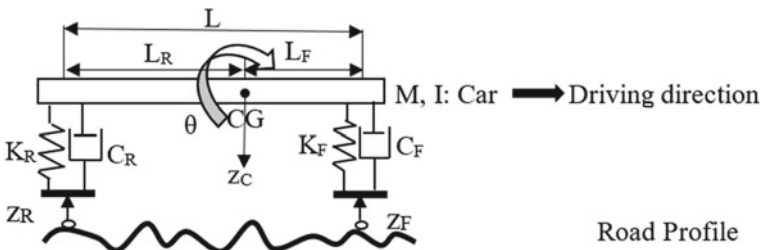


Fig. 7.1 Two-degree-of-freedom half-car model lay out

$$F_{C_R} = C_R(\dot{z} - L_R\dot{\theta} - \dot{z}_R), F_{C_F} = C_F(\dot{z} + L_F\dot{\theta} - \dot{z}_F) \quad (7.1b)$$

and Euler's equation

$$\sum M_{CG} = I\ddot{\theta} = F_{S_R}L_R + F_{S_R}L_R - F_{C_R}L_F - F_{C_F}L_F \quad (7.2)$$

If we put (7.1), (7.2) in matrix format

$$\begin{aligned} \begin{bmatrix} m & 0 \\ 0 & I \end{bmatrix} \begin{bmatrix} \ddot{z} \\ \ddot{\theta} \end{bmatrix} + \begin{bmatrix} C_F + C_R & C_FL_F - C_RL_R \\ C_FL_F - C_RL_R & C_FL_F^2 + C_RL_R^2 \end{bmatrix} \begin{bmatrix} \dot{z} \\ \dot{\theta} \end{bmatrix} \\ + \begin{bmatrix} K_F + K_R & K_FL_F - K_RL_R \\ K_FL_F - K_RL_R & K_FL_F^2 + K_RL_R^2 \end{bmatrix} \begin{bmatrix} z \\ \theta \end{bmatrix} \\ = \begin{bmatrix} C_F\dot{z}_F + C_R\dot{z}_R + K_Fz_F + K_Rz_R \\ C_FL_F\dot{z}_F - C_RL_R\dot{z}_R + K_FL_Fz_F - K_RL_Rz_R \end{bmatrix} \end{aligned} \quad (7.3)$$

Where

$$F_V = C_F\dot{z}_F + C_R\dot{z}_R + K_Fz_F + K_Rz_R \quad (7.3a)$$

$$T_\theta = C_FL_F\dot{z}_F - C_RL_R\dot{z}_R + K_FL_Fz_F - K_RL_Rz_R \quad (7.3b)$$

In the formula:  $F_V$  and  $T_\theta$  are wheel vertical force and pitch torque;  $\ddot{z}$ ,  $\dot{z}$ ,  $z$  and  $\ddot{\theta}$ ,  $\dot{\theta}$ ,  $\theta$  are the vertical acceleration, velocity, displacement, angular acceleration, angular velocity, angle of the chassis, respectively;  $m$  and  $I$  are the mass of the chassis and moment of inertia, respectively;  $K_F, K_R, C_F, C_R, L_F, L_R$  are spring constants, damping constants in front and rear;  $L_F, L_R$  are length of front and rear to C.G., respectively. With the  $F_V, T_\theta$ , this work determined them by the road profiles estimation. We set the state variables as  $X_1 = z, X_2 = \dot{z}, X_3 = \theta, X_4 = \dot{\theta}$  when adapting the motion equations with this the state variable notation. A system with the state and measure equations of the continuous time can be stated as follows.

$$\dot{\mathbf{X}}(t) = \mathbf{F}\mathbf{X}(t) + \mathbf{G}\mathbf{u}(t), \quad (7.4)$$

$$\mathbf{Z}(t) = \mathbf{H}\mathbf{X}(t) \quad (7.5)$$

Where

$$\mathbf{X}(t) = [X_1 X_2 X_3 X_4]^T, \mathbf{u}(t) = [F_V T_\theta]^T, u(t) = [F_V T_\theta]^T$$

$$\mathbf{F} = \begin{bmatrix} 0 & 1 & 0 & 0 \\ \frac{-(K_F+K_R)}{m} & \frac{-(C_F+C_R)}{m} & \frac{-(K_FL_F-K_RL_R)}{m} & \frac{-(C_FL_F-C_RL_R)}{m} \\ 0 & 0 & 0 & 1 \\ \frac{-(K_FL_F-K_RL_R)}{I} & \frac{-(C_FL_F-C_RL_R)}{I} & \frac{-(K_FL_F^2+K_RL_R^2)}{I} & \frac{-(C_FL_F^2+C_RL_R^2)}{I} \end{bmatrix}, \mathbf{G} = \begin{bmatrix} 0 & 0 \\ \frac{1}{m} & 0 \\ 0 & 0 \\ 0 & \frac{1}{I} \end{bmatrix}$$

$$\mathbf{H} = \begin{bmatrix} 1 & 0 & 0 & 0 \\ 0 & 0 & 1 & 0 \end{bmatrix}. \text{ In which we converted the Eqs. (7.4) and (7.5) into discrete}$$

ones with  $\Delta T$  length of period times, and based on the inputs of noise process with fictitious [10]. Then, Eq. (7.4) can be expressed as follows.

$$\mathbf{X}(k+1) = \Phi \mathbf{X}(k) + \Gamma [\mathbf{u}(k) + \mathbf{w}(k)] \quad (7.6)$$

$$\mathbf{X}(k) = [X_1(k) X_2(k) X_3(k) X_4(k)]^T, \Phi = \exp(F\Delta T)$$

$$\Gamma = r \int_{k\Delta T}^{(k+1)\Delta T} \exp\{\mathbf{F}[(k+1)\Delta T - \tau]\} \mathbf{G} d\tau$$

$$\mathbf{W}(k) = [w_1(k)w_2(k)]^T, \mathbf{u}(t) = [F_v T_\theta]^T$$

where  $\mathbf{u}(k)$ ,  $\Gamma$ , and  $\mathbf{X}(k)$  are the wheel loads, input matrix, and state vector;  $\Phi$  is the matrix of the state transition; and  $w(k)$  is the vector of noise. The mean is assumed as zero and variance white with  $E\{w(k)w^T(j)\} = Q\delta_{kj}$ , in which  $\delta_{kj}$  expresses as the delta function. The statistical measurement noise equation of Eq. (7.5) can be expressed as follows.

$$\mathbf{Z}(k) = \mathbf{H}\mathbf{X}(k) + \mathbf{v}(k) \quad (7.7)$$

$$\mathbf{Z}(k) = [Z_1(k)Z_2(k)]^T, \mathbf{v}(k) = [v_1(k)v_2(k)]^T$$

where  $\mathbf{H}$  and  $\mathbf{Z}(k)$  are the measured variable matrix, and observed vector, respectively;  $\mathbf{v}(k)$  is the vector of measured noise, where  $\mathbf{v}(k)$  is supposed as zero with white noise its mean; and its variance is set as  $E\{v(k)v^T(j)\} = \mathbf{R}\delta_{kj}$ , and  $\mathbf{R} = \sigma^2$ , where  $\sigma$  is the standard deviation of the measured noise. The magnitudes of the  $F_v$ ,  $T_\theta$ , are wheel vertical force and pitch torque can be estimated from the car model responses.

### 7.3 Numerical Simulations and Results

The section uses the driven half-car model with a constant velocity, e.g., 30 km/hr. Three types of road profiles: sine-shaped bump, rectangular cleat, and random ISO

**Table 7.1** Setting parameters of a model for half car

Parameters	Values	Parameters	Values	Parameters	Values	Values	Parameters
$m$	2000 (kg)	$C_F$	500 (Ns/m)	$L$	2 (m)	$L_F$	0.8 (m)
$I$	600 (kgm <sup>2</sup> )	$C_R$	500 (Ns/m)	$h_0$	0.1 (m)	$L_R$	1.2 (m)
$K_F$	5000 (N/m)	$K_R$	5000 (N/m)	$D$	1 (m)		

8608 road profile, are used to test the inputs system. The setting parameters for the half-car model are indicated in Table 7.1.

The parameters of simulation consists of a sampling interval of  $\Delta T$  is set to 0.001 s, and a final time  $t_f$  is set to 1.2 s. The exact and loads estimations validate the proposed approach with its error metric as defined expression as follows.

$$\text{Error} = \frac{\sqrt{\sum_{k=1}^n u_{\text{Exact}}^2(k)} - \sqrt{\sum_{k=1}^n \hat{u}_{\text{Est}}^2(k)}}{\sqrt{\sum_{k=1}^n u_{\text{Exact}}^2(k)}} \times 100\% \tag{7.8}$$

The estimated error (NEE) in Eq. (7.8) is termed the normalized one to obtain the optimal estimated NEE of dynamic wheel loads. The fading factor  $ftr$  in  $Q$  is assumed to  $1E2$ , two levels of measurement noise  $\sigma = 1E-7.5$  and  $1E-8$ . The choosing  $Q$  and  $\sigma$  are not easy to optimize in real engineering problems. In the work, the initial conditions for the approach are given by: the state vector is a 4-by-1 zero matrix, the filter’s error covariance matrix is a 4-by-4 diagonal matrix of  $1E10$  for the Kalman filter, the error covariance is a 2-by-2 diagonal matrix of  $1E8$ , the sensitivity matrix is a 4-by-4 zero matrix, and wheel load is a 2-by-1 as zero matrix to which the least squares algorithms are applied.

Three dynamic wheel load type’s NEE values figured out model driven over sine-shaped bump and rectangular cleat vary less than random road profile when  $ftr = 0.1$  (Figs. 7.2, 7.3 and 7.4). Moreover, the estimation results for the wheel vertical force and pitch torque in the car driven over the three different road profile types are good, and all NEE values are within 5.33% at  $\sigma = 1E-8$  with  $Q = 1 E2$ , when  $ftr = 0.1$  (in Table 7.2). The fading factor  $ftr$  discards old data by weighting data according to the occurred data time. The measurement noise covariance must have been increased in comparison with the previous measurements, e.g., the estimated optimization method [11].

### 7.3.1 Simulation Results

1. Dynamic wheel loads are estimated in the half-car model crossing the three different road profile types, Figs. 7.2, 7.3, and 7.4 show estimated results.

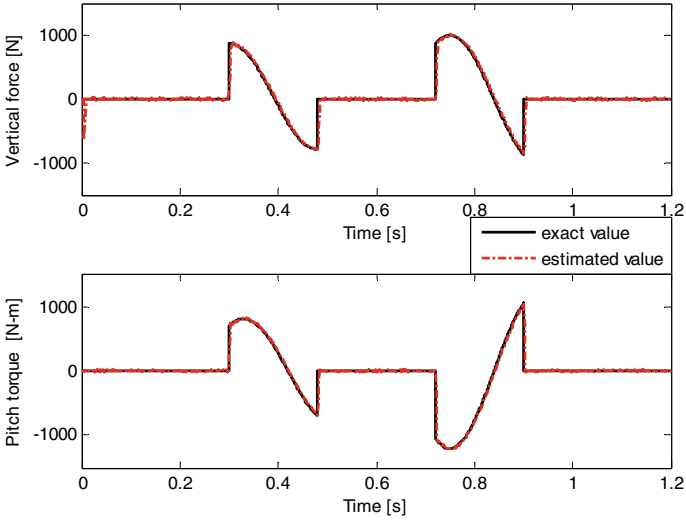


**Fig. 7.2** Vertical force and pitch torque estimation of the half-car model driven over sine-shaped bump

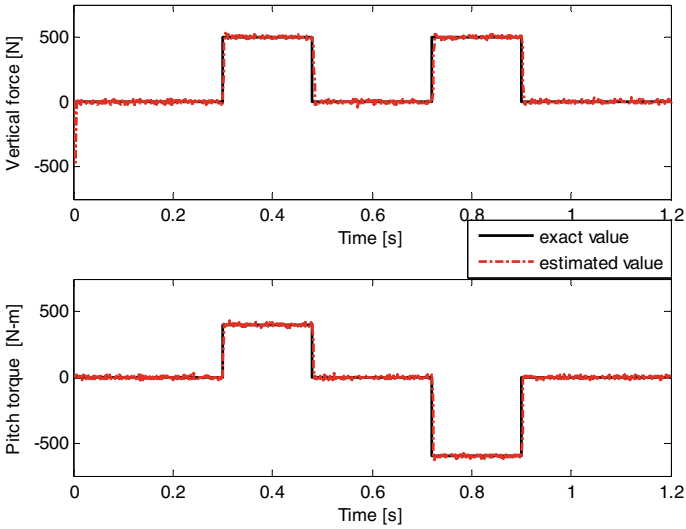


**Fig. 7.3** Vertical force and pitch torque estimation of the half-car model driven over rectangular cleat

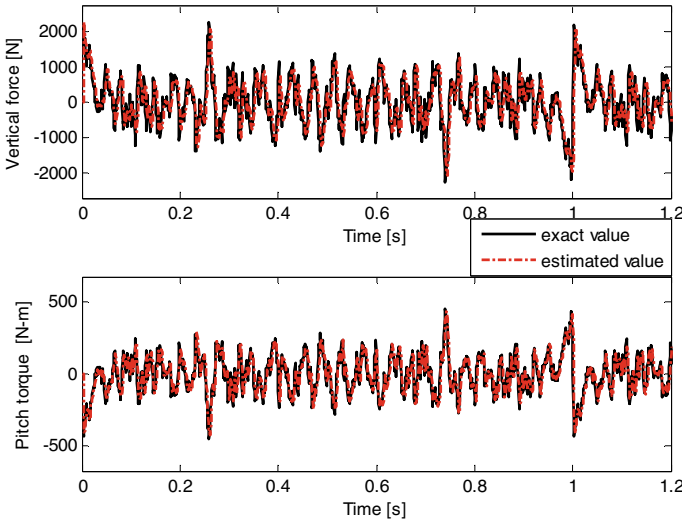


**Fig. 7.4** Vertical force and pitch torque estimation of the half-car model driven over random road profile

**Table 7.2** NEE of wheel loads estimation for the half-car model is driven over different road profiles

Types of road profile	Wheel load type	ftr = 0.1	ftr = 0.9
Sine-shaped bump	Vertical force	1.22%	0.81%
	Pitch torque	0.70%	1.24%
Rectangular cleat	Vertical force	0.78%	1.36%
	Pitch torque	0.91%	1.76%
Random	Vertical force	5.33%	42.85%
	Pitch torque	2.24%	43.03%

Figures 2a, b, 3a, b, and 4a, b reveal the simulation results with  $ftr = 0.1$ , for the wheel vertical forces and pitch torques, respectively.

- Table 7.2 summarizes the NEEs of the dynamic wheel load types for the half-car model in the three road profiles. The NEE of wheel loads type are within 5.33% with  $ftr = 0.1$ . The NEE of wheel load type in the half-car model crossing sine-shaped bump and rectangular cleat are within 1.76%, and crossing random road profile are within 43.03% with when  $ftr = 0.9$ .
- From front to back, pitching is an oscillating motion. In other words, if the front axle drops into a depression while the rear pushes up to a bump, or vice versa (Figs. 2b and 3b), a car pitches if the wavelengths of road unevenness are such that the vertical motions of the front and rear are in phase opposition.



### 7.3.2 Simulation Discussions

1. The proposed method had very large errors in initial estimated, but after a few time step, the estimated rapidly converge to the exact values (Figs. 2a, 3a, and 4a), these simulation results reveal that the proposed scheme can correct the error in the initial estimate by using very large values of the filter's error covariance and the error covariance.
2. For comparing estimated results with  $\sigma = 1E-7.5$  and  $1E-8$ , investigated that the determined results for  $\sigma = 1E-7.5$  have larger NEEs than those for  $\sigma = 1E-8$  (Table 7.2). The estimated accuracy is reduced, and this is because of considerable measurement noise. For  $\sigma = 1E-8$ , high precision measurement sensor is needed.
3. The dynamic wheel loads estimation for the half-car model driven over three different road profile types, the NEEs of wheel vertical forces are 1.12%, 0.78%, and 5.33%; pitch torques are 0.70%, 0.91%, and 2.24% with  $f_{tr} = 0.1$ , respectively (Table 7.2). There are not change abruptly for estimated loads in the rectangular cleat (Fig. 7.3), the loads estimated error results less than estimated loads in sine-shaped bump and random road profile (Table 7.2). Additionally, the estimated results are pitch torques better than vertical forces.
4. Oscillating pitching movement is likely to occur when the wheelbase of the vehicle is an odd multiple of half the road surface wavelength unevenness [12]. In the task, the half-car model's wheelbase is 2 m, the sine-shaped bump and rectangular cleat wavelength is 1 m, and the car is pushed over the road profiles. So, at figs, there are pitching appearances in 2(b), and 2(b) (b).
5. The aim of vertical dynamics is the tuning of body suspension and damping to guarantee good ride comfort, respectively, a minimal stress of the load at sufficient safety. According to the simulation estimated results, these body suspension spring force and damping force in Eqs. (1a), (1b), can also be estimated, using the inverse method. After all, they can be estimate the input (this is, road profile) from the system output.

## 7.4 Conclusions

The vertical dynamics of the half-car model was determined using the inverse method. The examples verify the accuracy of the wheel vertical force's estimation results and pitch torques for the method with a  $f_{tr} = 0.1$ . They could be perfected by tracking the random vertical dynamics. In simulations, the current strategy's feasibility and precision were analyzed with a model driving estimation of wheel loads of a half-car over deterministic and random road profiles. The results from the simulation show that the proposed approach correctly measures the vertical dynamics of the vehicle. Future work will apply to a variety of fields [13, 14], e.g., vibration and noise guidance.

## References

1. Rouillard, V., Sek, M.A., Perry, T.: Analysis and simulation of road profiles. *J. Transp. Eng.* **122**, 241–245 (1996)
2. Chen, S.-H., Pan, J.-S., Lu, K., Xu, H.: Driving behavior analysis of multiple information fusion based on adaboost. In: *Genetic and Evolutionary Computing*, pp. 277–285. Springer (2015)
3. Pan, J.-S., Lu, K., Chen, S.-H., Yan, L.: Driving behavior analysis of multiple information fusion based on SVM. In: *International Conference on Industrial, Engineering and Other Applications of Applied Intelligent Systems*, pp. 60–69. Springer (2014)
4. Chen, S.-H., Pan, J.-S., Lu, K.: Driving behavior analysis based on vehicle OBD information and adaboost algorithms. In: *Proceedings of the International Multiconference of Engineers and Computer Scientists*, pp. 18–20 (2015)
5. Stevens, K.K.: Force identification problems an overview. In: *Proceedings of the 1987 SEM Spring Conference on Experimental Mechanics*, Houston, TX, USA, pp. 838–844 (1987)
6. Kalman, R.E.: A new approach to linear filtering and prediction problems. (1960)
7. Chan, Y.T., Hu, A.G.C., Plant, J.B.: A kalman filter based tracking scheme with input estimation. *IEEE Trans. Aerosp. Electron. Syst.* 237–244 (1979)
8. Ma, C.-K., Lin, D.-C.: Input forces estimation of a cantilever beam. *Inverse Probl. Eng.* **8**, 511–528 (2000)
9. Bruscella, B., Rouillard, V., Sek, M.: Analysis of road surface profiles. *J. Transp. Eng.* **125**, 55–59 (1999)
10. Mendel, J.M.: *Lessons in Estimation Theory for Signal Processing, Communications, and Control*. Pearson Education (1995)
11. Gelb, A.: *Applied Optimal Estimation*. MIT Press (1974)
12. Michelin: *The Tyre Mechanical and Acoustic Comfort*. Societe de Technology Michelin
13. Dao, T., Nguyen, T., Pan, J., Qiao, Y., Lai, Q.: Identification failure data for cluster heads aggregation in WSN based on improving classification of SVM. *IEEE Access.* **8**, 61070–61084 (2020). <https://doi.org/10.1109/ACCESS.2020.2983219>
14. Dao, T., Yu, J., Nguyen, T., Ngo, T.: A hybrid improved MVO and FNN for identifying collected data failure in cluster heads in WSN. *IEEE Access.* **8**, 124311–124322 (2020). <https://doi.org/10.1109/ACCESS.2020.3005247>

# Chapter 8

## An Enhanced Flower Pollination Algorithm for Power System Economic Load Dispatch



Hung-Peng Lee, Trong-The Nguyen, Thi-Kien Dao, Van-Dinh Vu,  
and Truong-Giang Ngo

**Abstract** This research proposes a solution to the economic load dispatch (ELD) problem using the enhanced flower pollination algorithm (EFPA). The EFPA has captured advanced features, e.g., simple structure, quick search, and implementation, due to introducing a random jump perturbation in the global pollination phase and updating the switching probability according to the optimal global value of each iteration. The mathematically expressed ELD is described as a typical problem of multi-constraint nonlinear optimization. Two case calculation experiments will be used to assess and evaluate the proposed system's optimization efficiency from multi-dimensional economic perspectives with its feasibility and efficacy solution. The validation results show that the proposed scheme has more convergence speed and robustness than the other comparative methods.

### 8.1 Introduction

The aim of optimizing the power system's economic load distribution (ELD) issue is to fairly distribute the load of each unit in a power system such that the cost of power generation is reduced under the load and operating constraints [1, 2]. The linear programming methods, dynamic programming methods, and other methods are

---

H.-P. Lee · T.-K. Dao

School of Computer Science and Mathematics, Fujian University of Technology, Fuzhou 350118, Fujian Province, China

T.-T. Nguyen

Haiphong University of Management and Technology, Haiphong, Vietnam  
e-mail: [vnthe@hpu.edu.vn](mailto:vnthe@hpu.edu.vn)

V.-D. Vu

Information Power Technology Faculty, Electric Power University, Hanoi, Vietnam  
e-mail: [dinhvv@epu.edu.vn](mailto:dinhvv@epu.edu.vn)

T.-G. Ngo (✉)

Faculty of Computer Science and Engineering, Thuyloi University, Hanoi, Vietnam  
e-mail: [giangnt@tlu.edu.vn](mailto:giangnt@tlu.edu.vn)

also complicated to solve these problems [3] virtually. As metaheuristic algorithms [4] are named, many intelligent algorithms are developed with the development of artificial intelligence technology, such as a genetic algorithm [5], particles swarms' algorithm [6], etc. These metaheuristic algorithms have been used to successfully overcome ELD problems [1, 7]. The enhanced flower pollination algorithm (EFPA) is inspired by estimating plenty of flowering plants in nature and can be seen everywhere with abstracted from the pollination mechanism [4]. A random jump perturbation in the global and local pollination updating phases are used switching probability according to the optimal global value of each iteration. Additional features of the adaptation algorithm, simple structure, quick search, and implementation easily, the EPFA are paid much attention from community research [8]. Since the metaheuristic method's intelligent algorithm has greater robustness, the net loss, and valve point effect overlooked by conventional methods can also be measured, thus enhancing its accuracy and practicality [9].

This paper proposes a solution to the ELD problem using on the EFPA. A technique, e.g., the less-square programming, is used as a standard multi-constraint nonlinear optimization problem to model mathematical optimization for the objective optimization function. Two separate case studies of ELD scenarios to verify the performance enhancement of the proposed schemes.

## 8.2 The Economic Load Distribution Statement

### 8.2.1 Objective Function

The schematic diagram with the system's minimum total cost of generating power  $C$  as the optimal goal of dispatch [1, 10–12] can be expressed as follows.

$$C = \min \sum_{i=1}^n F_i(PW_i) \quad (8.1)$$

In the formula,  $n$  is the number of grid-connected generators in the system.  $PW_i$  is the active power of the  $i$ -th generator, and  $F_i(PW_i)$  is the consumption characteristic curve of the  $i$ -th generator, the power generation cost function can be expressed as.

$$\min \sum_{i=1}^n F_i(PW_i) = \sum_{i=1}^n (\alpha_i PW_i^2 + \beta_i PW_i + \gamma_i) \quad (8.2)$$

In the formula,  $\alpha_i, \beta_i$ , and  $\gamma_i$  are the power generation cost coefficients of the  $i$ -th generator.

### 8.2.2 Objective Function's Constraints

The power balance constraint is expressed as follows:

$$\sum_{i=1}^n (PW_i) = PW_{\text{Load}} + PW_{\text{Loss}} \quad (8.3)$$

In the formula,  $PW_i$  is the active power of the  $i$ -th generator;  $PW_{\text{Load}}$  is the total load demand of the system;  $PW_{\text{Loss}}$  is the total network loss of the system, which is generally obtained by the  $B$  coefficient method [1, 10].

$$PW_{\text{Loss}} = \sum_{i=1}^n \sum_{j=1}^n PW_i B_{ij} PW_j + \sum_{i=1}^n B_{0i} PW_i + B_{00} \quad (8.4)$$

In the formula,  $B_{ij}$ ,  $B_{0i}$ , and  $B_{00}$  are network loss coefficients, which are generally constants. The generator output constraint is stated as follows:

$$PW_i^{\min} \leq PW_i \leq PW_i^{\max} \quad (8.5)$$

In the formula,  $PW_i^{\min}$  is the lower limit of the active power of the  $i$ -th generator;  $PW_i^{\max}$  is the upper limit of the active power of the  $i$ -th generator. The generator ramp rate constraint is presented as follows. When the output increases, it is expressed:

$$PW_i - PW_i^0 \leq UR_i \quad (8.6)$$

When the output decreases, it is:

$$PW_i^0 - PW_i \leq DR_i \quad (8.7)$$

In the formula,  $PW_i^0$  is the active power of the  $i$ -th generator at the previous moment;  $UR_i$  and  $DR_i$  are the limit of the increase and decrease in the active power of the  $i$ -th generator per unit time, respectively.

The generator output constraint and the slope rate constraint can be written as:

$$\max(PW_i^{\min}, PW_i^0 - DR_i) \leq PW_i \leq \min(PW_i^{\max}, PW_i^0 + UR_i) \quad (8.8)$$

Next section, we will apply the equation for the optimization problem that can be solved by the intelligent algorithm.

### 8.3 Enhanced Flower Pollination Algorithm for ELD Problem

#### 8.3.1 Flower Pollination Algorithm

A metaheuristic algorithm is the flower pollination algorithm (FPA), and in this article, we suggest an enhanced flower pollination algorithm (EFPA). By adding a random jump disturbance in the global pollination process, we enhance the global search capability of FPA and update the switching probability according to the optimal global value of each iteration. The global pollination of FPA is modeled as follows [4].

$$\text{Pol}_i^{t+1} = \text{Pol}_i^t + \text{Levy}_{\text{step}} \times (\text{Pol}_i^t - \text{Pol}_*^t) \quad (8.9)$$

where  $\text{Pol}_i^{t+1}$  is the  $i$ -th pollen of the  $t$ th iteration,  $\text{Pol}_*$  is the best pollen of the current iteration among all pollens. In this paper  $\text{Levy}_{\text{step}} > 0$  and draw from Levy distribution. FPA's local pollination for exploiting is modeled as follows [4].

$$\text{Pol}_i^{t+1} = \text{Pol}_i^t + \varphi_{\text{rand}} \times (\text{Pol}_p^t - \text{Pol}_q^t) \quad (8.10)$$

where  $\text{Pol}_q^t$  and  $\text{Pol}_p^t$  are pollens from the identical plant diverse flowers, and  $\varphi_{\text{rand}}$  is the uniform distribution number in  $[0,1]$ .

#### 8.3.2 Enhanced Flower Pollination Algorithm

As mentioned, FPA has good practicality in terms of self-pollination and long-distance pollination. However, it also has some disadvantages, such as a sluggish convergence rate and more insufficient accuracy. A random jump disturbance operator in the global pollination process is added for improving global searchability of FPAs, and a novel updating strategy for switching probability that uses global optimum to control the probability of switching. To prevent its convergence from being too late, it is also restricted to a one-step leap. The improved global formula for pollination is as follows.

$$\text{Pol}_i^{t+1} = \text{Pol}_i^t + \text{Levy}_{\text{step}} \times (\text{Pol}_i^t - \text{Pol}_*^t) + \alpha \times (\text{Pol}_i^t - \text{Pol}_k^t) \quad (8.11)$$

where  $\alpha$  is the random integer number in  $[-1,0,1]$ , and  $\text{Pol}_k$  is the random pollen different from  $\text{Pol}_i^t$ . The switching likelihood regulates the proportion of global pollination and local pollination. If a switching possibility is greater, the global search capacity of the FPAs is improved with shunning the optimal local solution, local

pollination is weakened, and the low-optimization precision; otherwise, the chance of switching is lower.

### 8.3.3 Applied EFPA for ELD

The ELD is a problem with discrete, multi-constrained, nonlinear, and other characteristics [12]. Its constraints include equality constraints and inequality constraints. All individuals must satisfy constraints in the solution space. Therefore, before calculating each individual's objective function value, it needs to be processed to satisfy all constraints. In this paper, a penalty function is used to deal with the constraints, and the objective function is rewritten as:

$$C = \min \sum_{i=1}^n F_i(PW_i) + q \left( \sum_{i=1}^n PW_i - PW_{Load} - PW_{Loss} \right)^2 \quad (8.12)$$

In the formula,  $q$  is the penalty factor, which is always 1000 during the simulation.

The necessary steps for the ELD problem based on the EFPA algorithm are as follows:

- Step 1** Set the EFPA algorithm parameters and ELD model coefficients.
- Step 2** Initialize the population. Calculate the fitness value of each pollination and get the pollination in the optimal global position.
- Step 3** Determine the time control function, choose to follow the proportion of global pollination and local pollination, or move in the local pollination to update the pollination position.
- Step 4** If you are moving in the pollination group, select passive or active movement to update the position of the pollination.
- Step 5** Calculate the fitness value of each pollination and update the pollination in the optimal global pollination position.
- Step 6** If the algorithm does not meet the optimization end conditions, turn to Step3; otherwise, the optimization process ends.
- Step 7** Output the optimal solution.

## 8.4 Experimental Results

Two scenarios of ELD problems with different dimensions of six units and fifteen units are used to check the feasibility and efficacy of the method proposed as its performing simulation experiments. The simulation considers the effect of power loss to suit the real ELD problem. The proposed algorithm is compared with other algorithms, namely the optimization of particle swarms (PSO) [11], the algorithm of sine cosine (SCA) [13], and the algorithm of whale optimization (WOA) [14].

**Table 8.1** Coefficients setting for a six-unit system

Units	$\gamma$ (\$/MW <sup>2</sup> )	$\beta$ (\$/MW)	$\alpha$ (\$)	$P_{\min}$ (MW)	$P_{\max}$ (MW)
1	0.0072	7.7	241.0	101.0	501.0
2	0.0096	10.01	201.0	51.0	201.0
3	0.0091	8.50	221.0	81.0	301.0
4	0.0091	11.01	201.0	51.0	151.0
5	0.0081	10.52	221.0	51.0	201.0
6	0.0076	12.22	191.0	51.0	121.0

To ensure fairness, all algorithms uniformly set the number of search agents to 25, and the maximum number of iterations is 1000 in the simulation process. Take the average value after several runs to get the simulation result.

A. Case study of six units

Taking a six-unit system as an example, the generator’s total load is 1264 MW, and the dimension  $d$  is taken as six. The parameters of the six-unit test system are shown in Table 8.1.

The power loss factor  $B_{ij}$  is set as follows.

$$B_{ij} = \begin{bmatrix} 0.0018 & 0.0012 & 0.0008 & -0.0002 & -0.0006 & -0.0003 \\ 0.0012 & 0.0014 & 0.0009 & 0.0001 & -0.0006 & -0.0002 \\ 0.0007 & 0.0009 & 0.0032 & 0.0000 & -0.0010 & -0.0007 \\ -0.0001 & 0.0002 & 0.0000 & 0.0024 & -0.0006 & -0.0009 \\ -0.0005 & -0.0007 & -0.0010 & -0.0006 & 0.0129 & -0.0003 \\ -0.0002 & -0.0007 & -0.0006 & -0.0008 & -0.0002 & 0.0151 \end{bmatrix}$$

$$B_0 = 10^{-3}[-0.3908 - 0.12790.70470.05910.2161 - 0.6635], B_{00} = 0.057$$

The proposed method’s comparative results are shown in Table 8.2 with PSO, SCA, and WOA are six-unit system. The solution has six-generator outputs, including P1 to P6. In addition, the total cost of power generation, the real power loss, and the respective calculation time.

Figure 1a describes the comparison of using EFPA and other algorithms (PSO, SCA, and WOA) to solve the six-unit system scheduling problem under the same conditions.

B. Case study of fifteen units

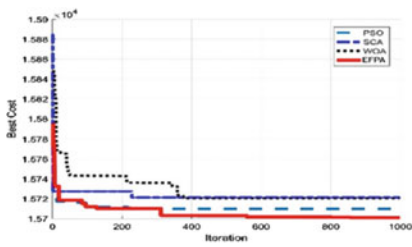
Table 8.3 lists the parameters of the fifteen-unit system. The total load borne by the generator is 2630 MW, and the dimension  $d$  is 15.

The comparative results of the proposed applied IFPA algorithm and other algorithms (such as PSO [11], SCA [13], and WOA [14]) under the same conditions for solving the ELD’s fifteen-unit power grid scheduling are described in Table 8.4. This

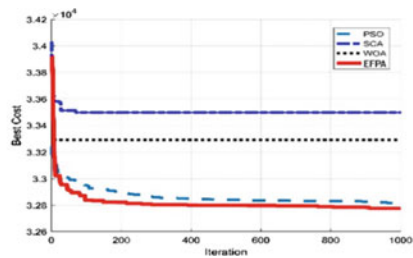


**Table 8.2** The best power outputs for a six-generator grid system

Outputs	PSO [11]	SCA [13]	WOA [14]	EFPA
P <sub>1</sub>	465.9059	461.6460	481.2798	456.4659
P <sub>2</sub>	186.2893	176.3008	190.9744	187.1464
P <sub>3</sub>	240.02	240	240.023	265.0121
P <sub>4</sub>	149.9782	133.2271	133.6215	150.021
P <sub>5</sub>	168.3705	180.5467	154.1544	157.7478
P <sub>6</sub>	85.021	105.0286	105.01	92.9818
Total power output (MW)	1294.5639	1295.7488	1295.0301	1294.3820
Total generation cost (\$/h)	15,709.6236	15,721.4026	15,720.2586	15,700.7846
Power loss (MW)	31.5639	32.7366	32.0302	31.350811
Total CPU times (sec)	1.7382295	1.3081542	1.5615731	1.3051715



a) A scheduling six-unit power grid system



b) A scheduling fifteen-unit power grid system

**Fig. 8.1** Comparison of the use of the proposed EFPA scheme and PSO [11], SCA [13], and WOA [14] for solving the six-unit and fifteen-unit scheduling system problems under the same conditions

table includes the solution’s statistical performance, cost of power generation, loss of power from the network, and average CPU time.

In terms of expense, power consumption, and time consumption, it can be seen from table that the system used has better output outcomes than other techniques. The comparison of the use of EFPA and various algorithms (PSO, SCA, and WOA) to solve the six-unit device scheduling problem under the same conditions as defined in Fig. 1b.

It can be seen from figure that in terms of convergence speed and time consumption, the quality output observation results indicate that the optimization approach used is superior to other techniques.

**Table 8.3** Coefficients setting for a fifteen-unit system

Units	$\gamma$ (\$/MW <sup>2</sup> )	$\beta$ (\$/MW)	$\alpha$ (\$)	$P_{\min}$ (MW)	$P_{\max}$ (MW)
1	0.000298	10.1	671	150	455
2	0.000191	10.2	574	150	455
3	0.001125	8.8	374	20	130
4	0.001125	8.8	374	20	130
5	0.000205	10.4	461	150	470
6	0.000301	10.1	630	135	460
7	0.000364	9.8	548	135	465
8	0.000338	11.2	227	60	300
9	0.000807	11.2	173	23	162
10	0.001203	10.7	175	23	160
11	0.003586	10.2	186	20	80
12	0.005513	9.9	230	20	80
13	0.000371	13.1	225	25	85
14	0.001929	12.1	309	15	55
15	0.004447	12.4	323	15	55

**Table 8.4** The best power output for a fifteen-generator grid system

Outputs	PSO [11]	SCA [13]	WOA [14]	EFPA
P1	453.8913	419.5333	446.3137	455.0342
P2	377.2665	339.4666	373.4275	380.012
P3	129.9198	111.4374	124.7734	130.0321
P4	129.7971	107.7066	104.9709	129.9865
P5	166.9779	168.9997	157.5359	169.9508
P6	455.0012	430.061	395.012	460.012
P7	429.7784	389.4666	405.9198	430.023
P8	66.5485	139.7333	134.7823	60.01
P9	107.6787	143.0415	147.2498	104.8355
P10	113.9893	132.2346	113.0699	131.6601
P11	80.0213	75.3339	70.6940	79.4695
P12	79.9886	67.8400	65.02	80.021
P13	25.021	75.0168	63.7854	25.0435
P14	35.5363	46.4698	44.7592	15.021
P15	15.01	46.8933	34.4970	15.021
Total power output (MW)	2667.3723	2694.1725	2683.7690	2665.9659
Total generation cost (\$/h)	32,814.4965	33,497.5476	33,293.0176	32,773.7531
Power loss (MW)	37.0661	63.0077	52.7689	35.93571
Total CPU time (sec)	1.8027188	1.2727662	2.0873071	1.3112389

## 8.5 Conclusion

In this paper, by applying a new metaheuristic algorithm called the enhanced flower pollination algorithm (EFPA), we proposed a solution to the economic load distribution problem (ELD). With the benefits of the new metaheuristic algorithm of the EFPA algorithm, such as speed, convergence, robustness, and ease of implementation, the proposed scheme could have achieved the solution's goal. In the experiment section, two calculation examples check the suggested scheme output with four angles of economy, speed, convergence, and robustness. The preliminary findings are compared with other literature, e.g., particle swarm optimization (PSO), sine cosine algorithm (SCA), and whale optimization algorithm (WOA) schemes show that local search and global search can be effectively taken into account by the proposed scheme, demonstrating high competition and efficient method of problem solving for the ELD problem.

## References

1. Tsai, C.F., Dao, T.K., Pan, T.S., Nguyen, T.T., Chang, J.F.: Parallel bat algorithm applied to the economic load dispatch problem. *J. Internet Technol.* **17**, 761–769 (2016). <https://doi.org/10.6138/JIT.2016.17.4.20141014c>
2. Nguyen, T.-T., Wang, M.-J., Pan, J.-S., Dao, T.-K., Ngo, T.-G.: A load economic dispatch based on ion motion optimization algorithm. (2020). [https://doi.org/10.1007/978-981-13-9710-3\\_12](https://doi.org/10.1007/978-981-13-9710-3_12).
3. Sun, J., Palade, V., Wu, X.J., Fang, W., Wang, Z.: Solving the power economic dispatch problem with generator constraints by random drift particle swarm optimization. *IEEE Trans. Ind. Informatics* **10**, 222–232 (2014). <https://doi.org/10.1109/TII.2013.2267392>
4. Nguyen, T.T., Pan, J.S., Dao, T.K.: An Improved flower pollination algorithm for optimizing layouts of nodes in wireless sensor network. *IEEE Access* **7**, 75985–75998 (2019). <https://doi.org/10.1109/ACCESS.2019.2921721>
5. The parallel genetic algorithm as function optimizer. *Parallel Comput.* **17**, 619–632 (1991). [https://doi.org/10.1016/S0167-8191\(05\)80052-3](https://doi.org/10.1016/S0167-8191(05)80052-3).
6. Shi, Y., Eberhart, R.: A modified particle swarm optimizer. In: 1998 IEEE International Conference on Evolutionary Computation Proceedings. IEEE World Congress on Computational Intelligence (Cat. No.98TH8360), pp. 69–73 (1998). <https://doi.org/10.1109/ICEC.1998.699146>
7. Nguyen, T.-T., Wang, M.-J., Pan, J.-S., Dao, T., Ngo, T.-G.: A load economic dispatch based on ion motion optimization algorithm. In: *BT-Advances in Intelligent Information Hiding and Multimedia Signal Processing*, Presented at the Singapore (2020)
8. Pan, J.-S., Dao, T.-K., Pan, T.-S., Nguyen, T.-T., Chu, S.-C., Roddick, J.F.: An improvement of flower pollination algorithm for node localization optimization in WSN. *J. Inf. Hiding Multimed. Signal Process* **08**, 500–509 (2017)
9. Nguyen, T.-T., Shieh, C.-S., Horng, M.-F., Dao, T.-K., Ngo, T.-G.: Parallelized flower pollination algorithm with a communication strategy. In: *Proceedings—2015 IEEE International Conference on Knowledge and Systems Engineering, KSE 2015* (2016). <https://doi.org/10.1109/KSE.2015.22>.
10. Al-Sumait, J.S., Sykulski, J.K., Al-Othman, A.K.: Solution of different types of economic load dispatch problems using a pattern search method. *Electr. Power Components Syst.* **36**, 250–265 (2008). <https://doi.org/10.1080/15325000701603892>

11. Park, J.-B., Lee, K.-S., Shin, J.-R., Lee, K.Y.: A particle swarm optimization for economic dispatch with nonsmooth cost functions. *IEEE Trans. Power Syst.* **20**, 34–42 (2005). <https://doi.org/10.1109/TPWRS.2004.831275>
12. Warsono, D.J.K., Özveren, C.S., Bradley, D.A.: Economic load dispatch optimization of renewable energy in power system using genetic algorithm. In: 2007 IEEE Lausanne POWERTECH, Proceedings (2007). <https://doi.org/10.1109/PCT.2007.4538655>.
13. Gonidakis, D., Vlachos, A.: A new sine cosine algorithm for economic and emission dispatch problems with price penalty factors. *J. Inf. Optim. Sci.* **40**, 679–697 (2019)
14. Kumar, A., Bhalla, V., Kumar, P., Bhardwaj, T., Jangir, N.: Whale optimization algorithm for constrained economic load dispatch problems—a cost optimization. In: *Ambient Communications and Computer Systems*, pp. 353–366. Springer (2018).

# Chapter 9

## Distribution Vehicle Routing Optimization Based on 3D Loading



Xuan Luo, Jin Zhang, Tingyu Yin, Hongxing Zhu, and Mingyue Qiu

**Abstract** The rapid development of e-commerce leads to increasingly fierce competition in the logistics industry. Cost reduction and efficiency has become the key issue for logistics enterprises to survive. Loading optimization and path optimization are the two core issues in distribution activities, and they are inseparable and related. The joint optimization of the two is more in line with the actual distribution optimization needs. Based on the analysis of the interaction between routing and loading, this paper proposes a multi-objective optimization model with the minimum distribution cost, the minimum number of vehicles and the maximum customer satisfaction as the objectives. A hybrid nesting algorithm based on NSGAI algorithm is designed, in which the packing module is designed by tree search algorithm combined with the deepest and leftmost algorithm. Finally, the real data of China Railway Express Chengdu branch are taken as a case to verify the feasibility of the model and algorithm. Combined with the results of the algorithm, some suggestions are put forward.

---

X. Luo (✉) · J. Zhang · T. Yin · H. Zhu · M. Qiu

School of Transportation and Logistics, Southwest Jiaotong University, Chengdu 611756, China

J. Zhang

e-mail: [zhjswjtu@home.swjtu.edu.cn](mailto:zhjswjtu@home.swjtu.edu.cn)

H. Zhu

e-mail: [zhx\\_202103@163.com](mailto:zhx_202103@163.com)

J. Zhang

National Engineering Laboratory of Integrated Transportation Big Data Application Technology, Southwest Jiaotong University, Chengdu 611756, China

Comprehensive Transportation Big Data Application Technology Laboratory, Chengdu 611756, China

## 9.1 Introduction

Terminal distribution is the last link in logistics activities to connect with end customers, which directly affects customers' experience of logistics services. With the deepening of marketization, the diversification of customers' requirements for distribution services and the intensification of homogeneous competition in the industry have caused the distribution costs of logistics enterprises to rise continuously. The high logistics costs limit the competitiveness of enterprises, and cost reduction and efficiency improvement have become the key issues for enterprises to make profits in the logistics field. Most enterprises are still stuck in the traditional logistics mode, still using the traditional manual row of vehicles mode to arrange distribution, the process of logistics is not strictly supervised, the distribution process is regularly low vehicle loading rate, roundabout driving and other problems, resulting in a waste of resources, the total cost of logistics due to the above problems account for nearly 60% of the cost of fees. Whether the distribution path is excellent and the packing is reasonable directly affects the cost and efficiency of the enterprise. Therefore, it is necessary to consider the route selection and packing jointly, rationalize the distribution route, optimize loading, improve customer satisfaction and reduce costs.

Gendrea et al. proposed the vehicle path problem with three-dimensional loading capacity constraints in 2006, which combined the crating problem and the path problem [1]. The difficulty of this problem is that the crating process and the path process are interrelated and constrained, when the customer's delivery order is decided, the order of cargo loading is determined, and similarly, the crating is optimized when the path is affected. Guenther et al. designed an algorithm with an ant colony algorithm as the main body to solve the combined optimization problem [2]. Mahvash et al. constructed a joint 3D loading and path optimization model with stability factors, considering back-out advanced, and used column generation heuristic algorithms to solve the path first and then verify the loading [3]. Junqueira et al. constructed a 3D loading and path optimization model considering vertical stability, updated the algorithm and simulated annealing algorithm to solve it [4]. Luis Miguel et al. divided the joint optimization problem into two phases: the first phase solves the path problem using a cut-set optimization approach and the second phase validates the crating using a greedy stochastic adaptive algorithm [5].

## 9.2 Basic Assumptions

Some assumptions are made to facilitate the use of the model to reflect the actual problem. The following assumptions are added to the general vehicle path problem and loading problem model assumptions.

It is assumed that the goods have cartons as the outer packing, and the packing shape is a regular cuboid. It is not allowed to load the goods upside down, and at least three sides of the goods are parallel to the carriage. The outer package of goods has a certain hardness, which can support multilayer stacking. The bottom surface of each layer of goods is 100% in contact with the floor of the carriage or the upper plane of the next layer of goods, and there is no suspension. In order to prevent the goods from toppling, the bottom of the goods placed above is not allowed to be suspended. The time of unloading at the customer's point is ignored. Vehicles arriving early or late will be punished. The unit time penalty of early arrival is less than that of delayed arrival. The goods must be placed in accordance with the principle of first in and then out, that is, if the customer is on the same service route, the goods required by the first service customer cannot be blocked or pressed by the goods required by the second service customer.

### 9.3 Parameter Description

According to the model established, the specific symbols are described as follows.  $i, j$  represent a customer,  $k$  represents a vehicle, and  $m$  represents a good (Table 9.1).

Decision variables  $x_{ij}^k, y_i^k$  are the zero-one variables, when  $x_{ij}^k$  equals 1 means that the  $k$ th vehicle travels from customer  $i$  to customer  $j$ , when  $x_{ij}^k$  equals 0 means that the  $k$ th vehicle does not travel from customer  $i$  to customer  $j$ , when  $y_i^k$  equals 1 means that the  $k$ th vehicle completes the delivery of customer  $i$ , and when  $y_i^k$  equals 0 means that the  $k$ th vehicle does not complete the delivery of customer  $i$ .

$$\text{Time window penalty value } P_{(t_i)} = \begin{cases} c_2(ET_i - T_i), & T_i \leq ET_i \\ 0, & ET_i < T_i \leq LT_i \\ c_3(T_i - LT_i), & T_i > LT_i \end{cases}$$

In addition,  $s_i = \sum_{k=1}^K \sum_{m=1}^{M_i} l_{Y_{im}^k} w_{Y_{im}^k} h_{Y_{im}^k}, d_{ij} = v \cdot t_{ij}, (a', a''), (b', b''), (c', c'')$  shows the range of the center of gravity of the delivery vehicle carriage, where each parameter value is determined by the carriage specification of the delivery vehicle.

### 9.4 Vehicle Path and Loading Optimization Model

The multi-objective optimization mathematical model for 3D crating and vehicle path optimization is shown in Eqs. (9.1)–(9.22).

**Table 9.1** Model parameter

Parameter	Description	Parameter	Description
$K$	Number of vehicles	$v$	Vehicle speed
$ET_i$	Earliest arrival time	$LT_i$	Latest arrival time
$T_i$	Actual reach time	$c_0$	Driver's salary
$c_{ij}^k$	Transportation cost per unit distance	$c_1$	Single vehicle depreciation charge
$c_2$	Early arrival punishment	$c_3$	Tardiness punishment
$P_{(t_i)}$	Time window penalty function	$e^k$	Number of accompanying persons
$d_{ij}$	Distance between customers	$t_{ij}$	Driving time between customers
$L, W, H$	Carriage length, width and height	$G$	Maximum vehicle weight
$V$	Maximum vehicle volume	$g_i$	Customer $i$ Total weight of goods
$s_i$	Customer $i$ Total volume of goods	$M_i$	Customer $i$ Quantity of goods
$Y_{im}^k$	The $m$ th shipment of customer $i$ on the $k$ th vehicle	$g_{im}$	Weight of the goods
$l_{Y_{im}^k}$	Length of goods	$w_{Y_{im}^k}$	Width of goods
$h_{Y_{im}^k}$	Height of goods	$(x_{Y_{im}^k}, y_{Y_{im}^k}, z_{Y_{im}^k})$	Center of gravity of cargo
$(\bar{x}_{Y_{im}^k}, \bar{y}_{Y_{im}^k}, \bar{z}_{Y_{im}^k})$	Coordinates of the upper right corner of the back (near the door side of the car)	$(\underline{x}_{Y_{im}^k}, \underline{y}_{Y_{im}^k}, \underline{z}_{Y_{im}^k})$	Coordinates of the lower left corner of the front of the item (near the front side of the car)

$$\min f_1 = \sum_{k=1}^K \sum_{j=0}^n \sum_{i=0}^n c_{ij}^k x_{ij}^k d_{ij} + \sum_{k=1}^K c_0 e^k + \sum_{k=1}^K c_1 \quad (9.1)$$

$$\min f_2 = \sum_{k=1}^K \sum_{i=1}^n x_{0i}^k \quad (9.2)$$

$$\min f_3 = \sum_{i=1}^n (c_2 \cdot \max(ET_i - T_i, 0) + c_3 \cdot \max(LT_i - T_i, 0)) \quad (9.3)$$

$$x_{ij}^k + x_{ji}^k \leq 1 \quad (9.4)$$

$$\sum_{k=1}^K \sum_{j=0}^n x_{ij}^k = 1, i = 0, 1, \dots, n; i \neq j \quad (9.5)$$



$$\sum_{i=0}^n x_{il}^k = \sum_{j=0}^n x_{ij}^k, l = 1, 2, \dots, n; k = 1, 2, \dots, K; l \neq i; i \neq j \quad (9.6)$$

$$\sum_{j=1}^n x_{ij}^k = y_i^k, i = 0, 1, \dots, n; k = 1, 2, \dots, K; i \neq j \quad (9.7)$$

$$\sum_{i=1}^n x_{0i}^k = \sum_{j=1}^n x_{j0}^k, k = 1, 2, \dots, K \quad (9.8)$$

$$\sum_{k=1}^K \sum_{i=1}^n Y_{im}^k = M_i \quad (9.9)$$

$$T_i + t_{ij} = T_j, i, j = 0, 1, \dots, n; i \neq j \quad (9.10)$$

$$\sum_{i=1}^n y_i^k g_i \leq G, k = 1, 2, \dots, K \quad (9.11)$$

$$\sum_{i=1}^n y_i^k s_i \leq V, k = 1, 2, \dots, K \quad (9.12)$$

$$\text{when } x_{ij}^k = 1, \underline{z}_{Y_{im}^k} > \underline{z}_{Y_{jm}^k}, \underline{x}_{Y_{im}^k} > \underline{x}_{Y_{jm}^k}, i, j = 0, 1, 2, \dots, n \quad (9.13)$$

$$\bar{z}_{Y_{im}^k} - \underline{z}_{Y_{im}^k} = h_{Y_{im}^k}, k = 1, 2, \dots, K \quad (9.14)$$

$$[(\bar{x}_{Y_{im}^k} - \underline{x}_{Y_{im}^k}) - l_{Y_{im}^k}][(\bar{y}_{Y_{im}^k} - \underline{y}_{Y_{im}^k}) - l_{Y_{im}^k}] = 0 \quad (9.15)$$

$$\text{或} [(\bar{x}_{Y_{im}^k} - \underline{x}_{Y_{im}^k}) - w_{Y_{im}^k}][(\bar{y}_{Y_{im}^k} - \underline{y}_{Y_{im}^k}) - w_{Y_{im}^k}] = 0$$

$$a' \leq \frac{\sum_{i=1}^n \sum_{m=1}^{M_i} g_{im} x_{Y_{im}^k} y_i^k}{\sum_{i=1}^n \sum_{m=1}^{M_i} g_{im} y_i^k} \leq a'' \quad (9.16)$$

$$b' \leq \frac{\sum_{i=1}^n \sum_{m=1}^{M_i} g_{im} y_{Y_{im}^k} y_i^k}{\sum_{i=1}^n \sum_{m=1}^{M_i} g_{im} y_i^k} \leq b'' \quad (9.17)$$

$$c' \leq \frac{\sum_{i=1}^n \sum_{m=1}^{M_i} g_{im} z_{Y_{im}^k} y_i^k}{\sum_{i=1}^n \sum_{m=1}^{M_i} g_{im} y_i^k} \leq c'' \quad (9.18)$$

$$\underline{x}_{Y_{im}^k} \geq 0, \bar{x}_{Y_{im}^k} \leq L, i = 1, 2, \dots, n; m = 1, 2, \dots, M_i; k = 1, 2, \dots, K \quad (9.19)$$

$$\underline{y}_{Y_{im}^k} \geq 0, \bar{y}_{Y_{im}^k} \leq W, i = 1, 2, \dots, n; m = 1, 2, \dots, M_i; k = 1, 2, \dots, K \quad (9.20)$$

$$z_{Y_{im}^k} \geq 0, \bar{z}_{Y_{im}^k} \leq H, i = 1, 2, \dots, n; m = 1, 2, \dots, M_i; k = 1, 2, \dots, K \quad (9.21)$$

$$x_1^p = \min(\bar{x}_{Y_{im}^k}, \bar{x}_{Y_{uv}^k}^p), x_2^p = \max(\underline{x}_{Y_{im}^k}, \underline{x}_{Y_{uv}^k}^p), y_1^p = \min(\bar{y}_{Y_{im}^k}, \bar{y}_{Y_{uv}^k}^p), y_2^p = \max(\underline{y}_{Y_{im}^k}, \underline{y}_{Y_{uv}^k}^p).$$

$B(u, v)$  denotes the  $v$ th shipment of customer  $u$

$$\sum_{(u,v) \in B, p \in P} (x_1^p - x_2^p)(y_1^p - y_2^p) = l_{Y_{im}^k} w_{Y_{im}^k} \quad (9.22)$$

Equation (9.1) indicates that the vehicle's transportation costs are minimal (including vehicle power consumption costs, vehicle depreciation and labor costs). Equation (9.2) indicates that the minimum number of vehicles required also reflects the maximum loading rate. Equation (9.3) indicates the minimum penalty for not arriving on time. Equation (9.4) indicates that a road can be passed only once. Equation (9.5) indicates that all customer points are visited only once. Equation (9.6) indicates that a vehicle arrives at a customer point and then leaves from that customer point. Equation (9.7) indicates that each customer point is served by one and only one vehicle. Equation (9.8) indicates that the vehicle must return to the distribution center from the distribution center. Equation (9.9) indicates that all customers' goods must be delivered. Equation (9.10) indicates that the time for the vehicle to reach the next customer is the time to reach the previous customer plus the travel time on the road. Equations (9.11) and (9.12) indicate that the sum of the weight and volume of the goods loaded in the distribution vehicle must not exceed the rated weight and volume of the vehicle. Equation (9.13) indicates that the goods delivered later cannot block the goods delivered first. Equation (9.14) indicates that the goods can only be placed correctly with the open side facing upwards and are not allowed to be inverted. Equation (9.15) indicates that the cargo has at least 3 sides parallel to the carriage, i.e., each side of the cargo must be parallel or perpendicular to the carriage. When adjusting the angle after placing the cargo, it can be rotated by  $90^\circ$  only on the side parallel to the bottom of the carriage. Equations (9.16)–(9.18) indicate that the overall center of gravity of all cargo does not exceed the center of gravity of the car after each car is loaded. Equations (9.19)–(9.21) indicate that each cargo loaded in each car is located inside the carriage and cannot exceed the boundary range. Equation (9.22) indicates that the bottom surface of each layer of cargo is in 100% contact with the floor of the carriage or the upper plane of the next layer of cargo, without overhang.

## 9.5 Algorithm Design

The NSGA II-based hybrid nesting algorithm flow is as follows.

1. Read the customer location, demand information, distribution cost information and, using the greedy algorithm, generate the initial solution and verify the loading scheme for the initial path. If it is feasible, proceed to the next step, and if the loading cannot be completed, regenerate the path solution.
2. Perform selection, crossover and mutation operations for the initial population to generate a new population of children.
3. Check whether the constraints are satisfied, if not, replace the individuals again, and if the constraints are satisfied, proceed to the next step.
4. Verify the boxing for the newly generated paths, record the loading scheme of each individual and give a high penalty to the individuals that cannot complete the boxing.
5. Perform fitness calculation, non-dominance ranking and crowding calculation for all individuals, and generate new parent population for crating verification using elite strategy.
6. Perform genetic operation to generate new offspring individuals, and if the number of iterations is reached, proceed to the next step, otherwise return to step 3.
7. Output the solution to show the path and the loading of each vehicle.

The main tree search algorithm combining 3D loading constraints proceeds as follows:

1. Initialize the vehicle  $k$  internal space and add the initial test space to the available space list.
2. Add the first customer's  $m$  cargoes to the cargo list and select the target space in the initial space, giving priority to the following spaces in order, higher position, inward and left. In the list of goods, priority is given to the goods with higher weight (less than the weight of the target space). Assuming that these  $m$  goods have  $M$  positional relations in the available space, and since each goods is not invertible, but can be rotated by  $90^\circ$ , each goods has two placement directions, there are  $2M$  first branches (first level sub-nodes).
3. Keep the information about the location of each cargo, i.e., the geometric center coordinates. Filter the first level sub-node according to the size and weight of the goods, and if it can fit the goods of the second customer, the space list of this sub-node will be the available space list, otherwise it will be deleted.
4. The initial space where the first customer's goods are loaded is cut into multiple subspaces along the horizontal and vertical planes, and the projected area of the "pro-space" on the XOY plane for different placement schemes is compared, and the nodes are sorted according to the area from smallest to largest, and the list of available space for the first level of sub-nodes is updated.

5. Under node  $c_j$  ( $j$  starts from 1), empty the cargo list and add the cargo of the second customer to the cargo list. Select the target space among the available spaces and filter the list of spaces according to the cargo size and weight. If it can fit the third customer's cargo, add it to the list of available spaces, otherwise discard the solution. Prioritize the available spaces and update the list of spaces in the second level sub-nodes.
6. Let  $j = j + 1$ , go to step 5 until the child node of layer  $i$ .
7. Repeat the above steps iteratively until all customers' goods are loaded into the carriage, recording information on the location of the goods in the optimal solution, the load space utilization and the load weight.

## 9.6 Case Verification

The data of part of the end delivery business of China Railway Express Chengdu Branch on a certain day is selected as the basis. According to the research data, it is determined that the end distribution vehicles of China Railway Express Chengdu Branch are uniformly 4.2 m long, 1.8 m wide and 1.6 m high electric box trucks. The average speed of distribution is 40 km/h. The average electricity consumption per kilometer is about 0.2°, and the service fee is about 1.8 RMB per degree of electricity plus service fee when charging. The depreciation cost of each vehicle is 3600 yuan/month, and the average salary of delivery personnel is 8000 yuan/month, calculated on the basis of 30 days per month, that is, a total of 387 yuan of fixed delivery cost exists per vehicle per day. Railroad express daily arrival cargo will be unified in the next day to arrange distribution. The delivery personnel start to load the car early in the morning every day, and according to the regulations, the delivery will start at 10:00 am sharp. The penalty value is 2 for every hour the vehicle arrives early and 3 for every hour it is late. There are up to eight delivery vehicles that can be called in this area (Table 9.2).

Many Pareto solutions are obtained by solving the algorithm, and three solutions are selected for demonstration. Option 1 chooses the compromise solution where all objectives are not optimal, Option 2 takes customer satisfaction as the primary and pursues the maximum customer satisfaction, and Option 3 chooses the solution with the lowest transportation cost and number of vehicles (Table 9.3).

Solution 2 has the highest customer satisfaction, Solution 3 has the best transportation cost, number of vehicles used and loading, and Solution 1 is a random Pareto solution. There exist many such solutions, each of which has a focus on each of the three objectives, i.e., at least one of the objectives is better than the others, i.e., each solution does not have all three objectives inferior to the others. When the enterprise pursues the maximum loading utilization rate or the lowest transportation cost, it can choose the optimization with one objective as the main body like scheme 3. When it needs to consider several objectives comprehensively, it can choose any

**Table 9.2** Distribution Cargo Information

Customer	<i>L</i> (mm)	<i>W</i> (mm)	<i>H</i> (mm)	Quality (kg)	Quantity	Time requirements
1	400	360	250	18.3	16	(11: 00–12: 00)
2	400	350	250	17.5	18	(10: 00–12: 00)
3	500	450	350	27.5	18	(12: 00–15: 00)
4	600	500	300	30.4	10	(10: 00–16: 00)
5	500	400	300	21.6	19	(10: 00–12: 30)
6	400	400	300	19.0	14	(10: 30–13: 30)
7	450	300	300	18.6	22	(11: 00–12: 00)
8	450	350	350	21.3	18	(10: 00–12: 00)
9	400	400	350	21.6	15	(12: 00–15: 00)
10	450	450	250	19.8	12	(10: 00–16: 00)
11	500	500	250	23.2	18	(10: 00–12: 30)
12	1800	400	300	48.0	8	(10: 30–13: 30)
13	700	600	350	38.0	6	(11: 00–12: 00)
14	450	400	300	20.0	12	(10: 00–12: 00)
15	500	500	250	24.0	14	(12: 00–15: 00)
16	500	400	250	19.5	13	(10: 00–16: 00)
17	450	400	300	20.5	13	(10: 00–12: 30)
18	450	400	350	24.2	18	(10: 30–13: 30)
19	550	450	350	28.8	15	(11: 00–12: 00)
20	550	450	300	27.2	18	(10: 00–12: 00)
21	500	350	350	22.6	12	(12: 00–15: 00)
22	430	380	300	19.2	14	(10: 00–11: 00)
23	300	300	230	16.0	20	(10: 00–12: 30)
24	420	360	250	18.4	16	(10: 30–13: 30)
25	500	400	350	25.9	12	(11: 00–12: 00)
26	450	400	350	24.8	11	(10: 00–12: 00)
27	600	520	350	35.7	7	(12: 00–15: 00)
28	490	400	350	25.8	13	(10: 00–16: 00)
29	450	400	250	18.8	16	(10: 00–12: 30)
30	500	420	400	28.6	8	(10: 30–13: 30)
31	500	400	300	21.7	14	(11: 00–12: 00)
32	600	500	350	33.0	14	(10: 00–12: 00)
33	550	420	400	31.0	13	(12: 00–15: 00)
34	400	380	230	18.2	20	(10: 00–16: 00)
35	500	500	350	30.2	4	(10: 00–12: 30)
36	500	400	310	22.7	13	(10: 30–13: 30)

(continued)

**Table 9.2** (continued)

Customer	L (mm)	W (mm)	H (mm)	Quality (kg)	Quantity	Time requirements
37	500	450	350	27.1	13	(11: 00–12: 00)
38	400	350	250	17.2	14	(10: 00–12: 00)
39	600	540	370	36.5	8	(12: 00–15: 00)
40	450	400	300	20.7	16	(10: 00–16: 00)

**Table 9.3** Solutions

Solution number	Travel path	cost	Average loading rate (%)	Penalty
1	0–5–35–13–15–1–28–25–3–0	2527.9	71.88	3.43
	0–8–29–31–6–30–32–4–0			
	0–22–40–19–0			
	0–2–34–11–23–37–27–39–0			
	0–16–17–26–7–38–21–36–33–0			
	0–20–12–10–9–14–18–24–0			
2	0–2–10–11–5–0	2536.1	71.88	2.27
	0–22–14–1–16–8–9–0			
	0–19–40–12–28–25–3–0			
	0–23–24–6–26–37–38–31–35–21–4–0			
	0–32–18–34–13–27–39–36–33–0			
	0–30–29–7–17–15–20–0			
3	0–24–37–14–39–29–17–35–33–28–0	2125.3	86.25	4.73
	0–11–40–32–23–20–19–0			
	0–25–16–18–6–2–12–9–3–0			
	0–5–13–15–26–27–38–36–22–4–0			
	0–34–31–30–7–1–8–10–21–0			

compromise solution, which also has bias in each objective, and the enterprise can choose the scheme according to its own needs, and according to the actual bias, output multiple schemes to meet the needs according to the demand (Fig. 9.1).

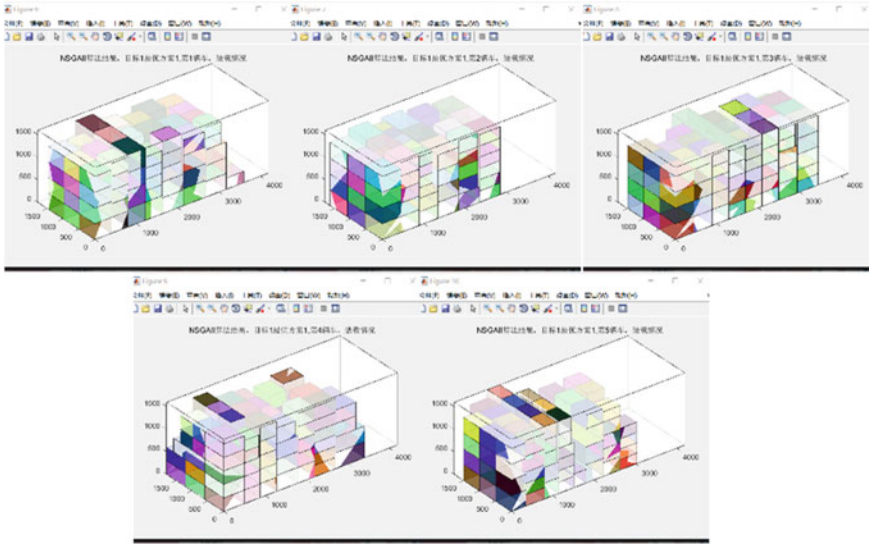


Fig. 9.1 Scheme 3 packing display

### References

1. Gendreau, M., Iori, M., Laporte, G., Martello, S.: A tabu search algorithm for a routing and container loading problem. *Transp. Sci.* **40**, 342–350 (2006)
2. Guenther, F., Doerner, K.F., Hartl, R.F., Iori, M.: Metaheuristics for vehicle routing problem with three-dimensional loading constraints. *Eur. J. Oper. Res.* **201**(3), 751–759 (2010)
3. Mahvash, B., Awasthi, A., Chauhan, S.: A column generation based heuristic for the capacitated vehicle routing problem with three-dimensional loading constraints. *Int. J. Prod. Res.* **55**(6), 1730–1747 (2015)
4. Junqueira, L., Morabito, R.: Heuristic algorithms for a three-dimensional loading capacitated vehicle routing problem in carrier. *Comput. Ind. Eng.* **88**, 110–130 (2015)
5. Luis Miguel, E.-F., David Á.-M., Mauricio G.-E., John W.-E., Rubén Augusto R.-L.: A matheuristic algorithm for the three-dimensional loading capacitated vehicle routing problem (3L-CVRP). *Revista Facultad de Ingeniería, Universidad de Antioquia* **78**, 9–20 (2016)
6. Ke, P.: *Research on Vehicle Path Problem Based on Multi-objective Evolutionary Algorithm*, p. 111. Wuhan University, Wuhan (2013)
7. Zhang, H.: *Application Research of Vehicle Path Optimization Problem Based on Genetic Algorithm*, p. 72. Tianjin University of Science and Technology, Tianjin (2016)
8. Hu, G., Lv, L.: Modeling and optimization of three-dimensional loading problem of transportation vehicles. *Logist. Technol.* **34**(11), 133–135 (2015)
9. Lian, Z.G., Lin, W.T., Cao, Y., Ji, C.H.L.: Optimization research of container loading model based on class particle swarm algorithm. *J. Chongqing Jiaotong Univ. (Nat. Sci. Ed.)* **33**(02), 126–130+134 (2014)

# Chapter 10

## Robust and Fast Registration for Lidar Odometry and Mapping



Wenbo Liu and Wei Sun

**Abstract** Outliers, such as sensor noise, abnormal measurements, or dynamic objects, can damage the overall accuracy of a Simultaneous Localization and Mapping (SLAM) system. Aiming at to improve the performance of Lidar SLAM systems in urban scenes containing a large number of outliers, we propose a real-time, feature-based, and outliers-rejection Lidar SLAM system. By embedding an outlier elimination method based on 4-points congruent sets into a state-of-the-art SLAM framework and further optimizing the traditional single-step registration to coarse-to-fine registration, we can solve the problem of time-consuming, high motion drift, and wrong mapping caused by the current Lidar SLAM systems which cannot effectively detect and eliminate the outliers in surrounding environment.

### 10.1 Introduction

Simultaneous Localization and Mapping (SLAM) is the most basic prerequisite of intelligent robots and the necessary ability of driverless vehicles. Although there are many accurate and effective solutions to SLAM problems, such as the methods based on vision [1] or Lidar [2, 3], or integrating their advantages [4], most of the existing methods [5, 6], including them, are based on the assumption of a static world, which greatly limits the scope of application of these excellent methods. The typical method to estimate Lidar ego-motion is to apply the iterative closest point (ICP) method to the point clouds of adjacent frames [7]. However, Lidar-based methods can work even in the dark, and many 3D Lidars can capture the details of the environment over a long distance [6]. Therefore, this work focuses on the use of 3D Lidar to deal with the problem of SLAM in urban environment containing complex outliers.

---

W. Liu · W. Sun (✉)  
Xidian University, Xi'an, China  
e-mail: [wsun@xidian.edu.cn](mailto:wsun@xidian.edu.cn)



The main contributions of this paper are as follows:

- We integrate a robust outliers elimination method based on 4-point congruence set into a state-of-the-art SLAM framework to further improve the accuracy and robustness of odometry and mapping.
- We use a reasonable coarse-to-fine registration method to replace the traditional single-step registration method to further reduce computation of the registration part, so as to reduce total runtime consumption of the system.

The rest of the paper is organized as follows: we introduce the related work in Sect. 10.2, describe the proposed method in Sect. 10.3, compare our method with the most advanced method in Sect. 10.4, and summarize our work and put forward the prospect in Sect. 10.5.

## 10.2 Related Work

### 10.2.1 Point Cloud Registration

The overlap rate of two point clouds to be registered is a key parameter, which is usually inversely proportional to the number of outliers. If two point clouds have a large overlap rate or obvious point correspondence, then their registration can be achieved by the iterative closest point [8] and various improved algorithms without initialization. ICP will fall into the local optimal solution. Go-ICP [9] and Gogma [10] use branch and bound in six-dimensional space to achieve global registration of point clouds without corresponding points. Because branch and bound method has exponential complexity, these methods are computationally expensive, and they often diverge due to small overlap [15].

The common rough registration methods are divided into hypothesis, test methods are represented by Random Sample Consensus (RANSAC), and geometric feature-based methods are represented by 4PCS [11]. RANSAC and its improved algorithm have cubic complexity and are not suitable for large-scale point clouds. Mellado et al. [13] reduced the complexity to quadratic and linear successively by matching the congruent four-point sets in two point clouds. Theiler et al. [12] use the set of key points for matching, which reduces the size of the set to be searched. Mohamad et al. [14] generalize the construction of coplanar four-point basis, which further improves the efficiency of point cloud registration. Raposo and Barreto [15] only use the topological relationship and normal vector between two points to construct matching rules, which greatly improves the registration efficiency and is suitable for point clouds with smaller overlap ratio. On the basis of the initial solution of coarse registration, precise registration is used to locally minimize the nonconvex error function to obtain the exact solution. Shan and Englot [6] suggest searching rotation and translation separately to reduce the registration complexity.

There are a lot of related works, but they either cannot fully meet the requirements of real-time, robustness, and high-precision in Lidar SLAM or have not carried out systematic experiments on Lidar point cloud dataset.

## 10.2.2 Lidar Odometry and Mapping

LOAM [2], rank second in the odometry evaluation project of KITTI vision benchmark [16], has a very low drift in the short-trajectory scenarios, and LOAM has greatly promoted the development of Lidar SLAM field. However, LOAM has no loop closure detection to eliminate the continuous accumulation of errors, so it may produce significant errors in the case of long trajectory. More importantly, LOAM does not consider dynamic objects, resulting in incorrect results in dynamic scenes. LeGo-LOAM [6] optimizes LOAM by adding loop closure detection to reduce motion drift, adding clustering and segmentation modules to filter out clusters with less than 30 points to realize filtering of noise. LOL [17] improves odometry accuracy by detecting the geometric similarity between online 3D point clouds and prior offline maps.

## 10.3 Proposed System

### 10.3.1 Task Description and Definitions

The problem addressed in this work is how to use the point cloud observed by 3D Lidar to estimate its ego-motion and build a global map for the traversed environment.

We define the point cloud measured as  $P$ , Lidar pose as  $X$ , global map as  $M$ , use the upper right corner to represent the time stamp and define the  $K$ -scan point cloud as  $\mathbf{P}^k$ , where a point is  $p_i^k$ , that is,  $\mathbf{P}^k = (p_1^k, p_2^k, \dots, p_n^k)$ ,  $p_i^k = (x_i^k, y_i^k, z_i^k)$ , where  $n$  is the size of the point cloud,  $k \in \mathbb{N}^+$ .

Under the above definition, the problem can be modeled as: Given map  $M^{t-1}$ , Lidar pose  $X^{t-1}$  at time  $t-1$ , and point cloud  $\mathbf{P}^t$  at time  $t$ , to update  $X^t$  and  $M^t$ , as can be shown in (10.1) and (10.2).

$$X^t = \mathbb{F}(X^{t-1}, \mathbf{P}^t) = \mathbb{F}(X^{t-1}, \mathbb{W}(\mathbf{P}^{*t}, W^t)) \quad (10.1)$$

$$M^t = \mathbb{G}(M^{t-1}, \mathbf{P}^t) = \mathbb{G}(M^{t-1}, \mathbb{W}(\mathbf{P}^{*t}, W^t)) \quad (10.2)$$

where  $\mathbf{P}^{*t}$  is the description of the real scene in the field of vision at time  $t$ .  $W^t = (w_1^t, w_2^t, \dots, w_i^t)$  is the sum of many interference factors such as sensor noise, abnormal measurement values, or dynamic objects.  $\mathbb{W}$  is the unknown noise

function that transforms the real scene into the measurement point cloud. Next, we define the set of outliers in point cloud caused by  $W^t$  that are harmful to registration as  $\mathbf{P}_{out}$ , and the remaining points are  $\mathbf{P}_{in}$ , namely,

$$\mathbf{P} = \mathbf{P}_{out} \cup \mathbf{P}_{in} = \mathbb{W}(\mathbf{P}^*, W) \quad (10.3)$$

The task of this paper is to find the optimal function  $\mathbb{F}$  and  $\mathbb{G}$ , and the core procedure is to find and eliminate  $\mathbf{P}_{out}$  to optimize them.

### 10.3.2 Segmentation

The input of the segmentation module is the original 3D LIDAR point cloud  $\mathbf{P} = \{p_1, p_2, \dots, p_n\}$ , the output is  $m$  clusters  $\{P_{C_1}, P_{C_2}, \dots, P_{C_m}\}$  and corresponding cluster label vector  $L = (l_1, l_2, \dots, l_n)$ , where  $l_i \in [-1, m] \cap \mathbb{Z}$ , label  $-1$  represents the point belongs to the ground, and the positive integer represents the serial number of non-ground clusters.

The point cloud  $\mathbf{P}^k$  is first projected onto the circular range image  $P_{U,V} \triangleq \{p_{(u,v)} | u \in [1, 360^\circ/R_{\text{hori}}] \cap \mathbb{Z}, v \in [1, N_{\text{scan}}] \cap \mathbb{Z}\}$  of size  $N_{\text{pixel}} = 360^\circ/R_{\text{hori}} * N_{\text{scan}}$ . The row index  $\text{row}_i$  of  $p_i$  is shown in (10.4), and the column index  $\text{col}_i$  is shown in (10.5).

$$\text{row}_i = \left( \tan^{-1} \frac{z_i}{\sqrt{x_i^2 + y_i^2}} + \text{Pit}_{\text{bottom}} \right) / R_{\text{vert}} \quad (10.4)$$

$$\text{col}_i = \tan^{-1} \frac{y_i}{x_i} / R_{\text{hori}} \quad (10.5)$$

The value of the image is the distance from  $p_i$  to the Lidar  $r_i = \sqrt{x_i^2 + y_i^2 + z_i^2}$ , where  $R_{\text{hori}}$  is the horizontal resolution of the Lidar,  $R_{\text{vert}}$  is the vertical resolution of the Lidar,  $\text{Pit}_{\text{bottom}}$  is the minimum pitch of the Lidar Lidar beam, and  $N_{\text{scan}}$  is the number of Lidar lines. After the projection, a point  $p_{u,v+1}$  and  $p_{u,v}$ ,  $v \in [1, \frac{1}{2}N_{\text{scan}}] \cap \mathbb{Z}$  in  $P$  can be uniquely identified by the row index and column index, denoted by:

$$p_i \equiv p_{(u,v)} = (x_{(u,v)}, y_{(u,v)}, z_{(u,v)}) \quad (10.6)$$

Then the ground is extracted from the range image  $P_{U,V}$ . For points  $p_{u,v+1}$  and  $p_{u,v}$ , where  $v \in [1, \frac{1}{2}N_{\text{scan}}] \cap \mathbb{Z}$ ; if the pitch of adjacent rows  $\text{Pit}_{v,v+1}$  (as shown in (10.7)) are less than  $10^\circ$ , they are denoted as ground points.

$$\text{Pit}_{v,v+1} = \tan^{-1} \frac{z_{u,v+1} - z_{u,v}}{\sqrt{(x_{u,v+1} - x_{u,v})^2 + (y_{u,v+1} - y_{u,v})^2}} \quad (10.7)$$

Finally, the segmentation clustering method based on range image [18] was applied to cluster the points into several clusters. Points from the same cluster are assigned a unique label. After this process, for  $p_i^k \in \mathbf{P}^k$ , we get  $l_i$ ,  $\text{row}_i$ ,  $\text{col}_i$ , and  $r_i$ , where  $i \in [1, N_{\text{pixel}}] \cap \mathbb{Z}$ .  $\mathbf{P}^k$  is divided into a ground point set and some non-ground point sets, that is,  $\mathbf{P}^k = \mathbf{P}_g \cup \mathbf{P}_{ng}$ , and it is worth noting that both types of points may contain outliers. The extraction of features from non-ground points can reduce time-consuming and improve the accuracy of registration through label matching and noise filtering.

### 10.3.3 Feature Extraction

In order to reduce the computation amount of registration, we extract the representative feature points to reduce the number of the points to be registered. The feature extraction method is similar to that used in LeGo-LOAM. We first used (10.8) to evaluate the curvature  $c_i$  of point  $p_i$ , defining points whose curvature is greater than threshold  $c_{\text{thre}}$  as edge features and points whose curvature is less than  $c_{\text{thre}}$  as plane features.

$$c_i = \frac{1}{|\mathcal{S}||r_i|} \left\| \sum_{j \in \mathcal{S}, j \neq i} (r_j - r_i) \right\| \quad (10.8)$$

where  $\mathcal{S}$  is a set of continuous points on the same row from the image, points in  $\mathcal{S}$  are uniformly distributed on both sides of  $p_i$ , and  $|\mathcal{S}|$  is the number of points in  $\mathcal{S}$ .

### 10.3.4 Lidar Odometry

The input of Lidar odometry module is the feature point in the point cloud, which includes estimating the Lidar motion between adjacent scans and eliminating the motion distortion of the point cloud through feature matching. Looking for the Lidar of the adjacent scanning motion—by looking for rotation matrix  $\tilde{\mathbf{R}} \in \text{SO}(3)$  and translation vector  $\tilde{t} \in \mathbb{R}^3$  to minimize the point cloud registration error, such as (10.9).

$$\tilde{\mathbf{T}} \triangleq (\tilde{\mathbf{R}}, \tilde{t}) = \arg \min \left( \sum_i \|\tilde{\mathbf{R}}^t p_i^t + \tilde{t} - q_i^{t-1}\| \right) \quad (10.9)$$

where  $q_i^{t-1}$  is the corresponding point at  $t - 1$  found by  $p_i^t$ .

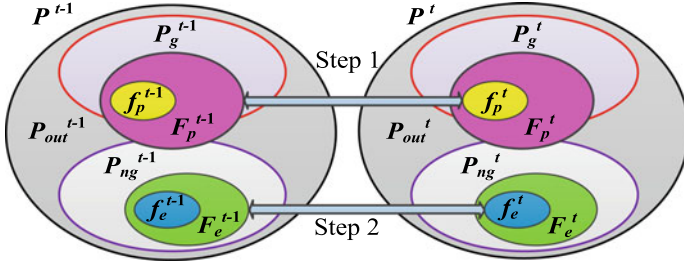


Fig. 10.1 Corresponding relation of feature points at adjacent moments

The LOAM details  $\mathbb{F}$ , and LeGo-LOAM optimizes it. For brevity, this chapter focuses on further optimization based on these methods, which is achieved by matching only valid feature points in the adjacent frames. The optimization process can be defined as:

$$\min \|\tilde{\mathbf{T}}^t - \mathbf{T}^{*t}\| \quad \text{s.t. } p_i^t \in \mathbf{F}_{in}^t \quad (10.10)$$

There is the optimal transformation matrix from  $\mathbf{P}^t$  to  $\mathbf{P}^{t-1}$ ,  $\mathbf{R}^*$  and  $tr^*$  are the corresponding rotation matrix and the translational vectors, and  $\mathbf{F}_{in}^t$  is the set of effective feature points at time  $t$ , namely  $\mathbf{F}^t = (\mathbf{F}_{out}^t \cup \mathbf{F}_{in}^t)$ . The process of finding the corresponding relationship is shown in Fig. 10.1, that is, the transformation is found in the plane feature point set and the edge feature point set, respectively, and the computational effort is reduced by reducing the candidate range of corresponding points. We focus on two strategies, outlier elimination and weight compensation of feature point.

**(1) Outlier elimination:** To solve this problem, we use the two-step coarse-to-fine registration strategy, that is, rough registration is first used to detect outliers, and then the outliers are avoided to participate in the L-M algorithm. We can express the outlier feature point  $\mathbf{F}_{out}$  as:

$$\mathbf{F}_{out}^t = \{p_i^t \mid \|\mathbf{R}^* p_i^t + tr^* - q_i^{t-1}\| > \varepsilon \wedge p_i^t \in \mathbf{F}^t\} \quad (10.11)$$

where  $q_i^{t-1}$  is the feature point corresponding to  $p_i^t$ . We first define feature descriptor  $\mathbf{d}^t$  and then use  $\mathbf{d}^t$  and  $\mathbf{d}^{t-1}$  to calculate pose transformation  $\tilde{\mathbf{T}}_{rough}$  as follows:

- (1) Finding the first point in the four-point basis: We select the feature point  $f_{(u_1, v_1)}^t \in \mathbf{F}^t$  as the first point  $a_1^t$  in the  $i$ th range image, namely  $a_1^t \triangleq f_{(u_1, v_1)}^t$ , where  $u_1^t \in \left[1 + \frac{360^\circ * (i-1)}{N_{sub} * R_{horiz}}, \frac{360^\circ * i}{N_{sub} * R_{horiz}}\right] \cap \mathbb{Z}$  and  $v_1^t \in \left[\frac{N_{scan}}{4}, \frac{N_{scan}}{2}\right] \cap [v_1^{t-1} - 1, v_1^{t-1} + 1] \cap \mathbb{Z}$ .

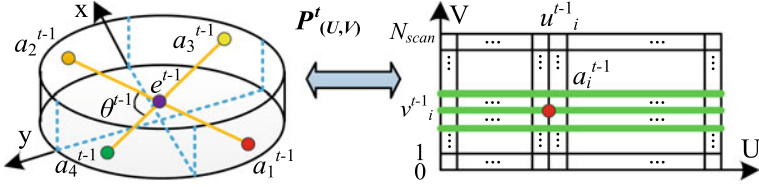


**Fig. 10.2** Schematic diagram of four-point base selection

- (2) Finding the second point: We select  $a_2^t \triangleq f_{(u_2, v_2)}^t$  in the sub-image farthest from  $a_1^t$ , where  $u_2^t \in \left[ 1 + \frac{360^\circ * (i-1 + \frac{N_{div}}{2})}{N_{sub} * R_{horiz}}, \frac{360^\circ * (i + \frac{N_{div}}{2})}{N_{sub} * R_{horiz}} \right] \cap \mathbb{Z}$ ,  $f_{(u_2, v_2)}^t \in P_{(U, V)_{i+\frac{1}{2}N_{sub}}}^t$ , the line segment defined with  $a_1^t$  and  $a_2^t$  as endpoints is  $l_1^t \triangleq a_1^t a_2^t$ .
- (3) Constructing feature descriptors: We select  $a_3^t$  and  $a_4^t$  from the sub-images excepting  $a_1^t$  and  $a_2^t$  to satisfy the conditions that  $l_2^t \triangleq a_3^t a_4^t$  is coplanar with  $l_1^t$ ,  $|l_2^t| > \frac{|l_1^t|}{4}$ , and  $\angle(l_1^t, l_2^t) > \frac{180^\circ}{N_{sub}}$ . The intersection of  $l_1^t$  and  $l_2^t$  is  $e^t$ . Then we record feature descriptor  $d^t$ ,  $d^t \triangleq (d_1^t, d_2^t)$  when the above three conditions are true, otherwise,  $d^t \triangleq (d_1^t, d_3^t)$ , where  $d_1^t \triangleq (a_1^t, a_2^t)$ ,  $d_2^t \triangleq (a_3^t, a_4^t, e^t, \angle(l_1^t, l_2^t))$ , and  $d_3^t \triangleq (c_{a_1}^t, c_{a_2}^t)$ .
- (4) Matching feature descriptors: If the condition in (10.3) is true, and we use Super4PCS [13] to match  $d^t$  and  $d^{t-1}$ ; otherwise, we use 2PNS [15].

The process of the second L-M step is similar to that in the first step, but the edge feature points is used instead, and the number of rows of feature points in (1) and (2) is no longer limited (Fig. 10.2).

**(2) Weight compensation of feature point:** LeGo-LOAM gives the feature points a weight  $s_i$  which is inversely proportional to the distance between Lidar and points in the iteration process of L-M algorithm. The difference is that we also consider the influence of the point cloud holes in the background caused by the occlusion of dynamic objects on the stability of the system. Therefore, we reduce the weight of the feature points within a certain range of the dynamic cluster.

$$\tilde{s}_i = s_i * \left( 1 - \frac{R_{horiz}}{|\theta_{yaw}|} \right) \quad (10.12)$$

where  $\tilde{s}_i$  is the new feature weight and  $\theta_{yaw}$  is the minimum yaw difference between a feature point and a dynamic object.

### 10.3.5 Lidar Mapping

Let us review the mapping model  $\mathbb{G}$  (10.2), which is to use  $M^{t-1}$  and  $P^t$  to build  $M^t$  because the global map contains a lot of feature information, and the earlier information contains less error. The Lidar mapping module further optimizes the pose estimation by matching the  $F^t$  with the submap  $M_{\text{sub}}^{t-1}$  around the Lidar. Please refer to the description in [20] for detailed matching and optimization procedures. We use the map storage method in LeGo-LOAM to store only the feature point set  $F^t$ .

$$M^{t-1} \triangleq \left\{ \underbrace{\{F^1\}, \{F^2\}, \dots, \{F^{t-k2}\}}_{M_{\text{hist}}^{t-1}}, \dots, \underbrace{\{F^{t-k}\}, \dots, \{F^t\}}_{M_{\text{sub}}^{t-1}} \right\} \quad (10.13)$$

In addition, the optional function is to further eliminate the error of the mapping module by detecting the loop closure. In LeGo-LOAM, if  $F^t$  can find corresponding feature in earlier map  $M_{\text{hist}}^{t-1}$  or recent features by ICP, a new constraint is added. The difference is that we use coarse-to-fine registration strategy in odometry module again to replace single-step ICP.

Then, the estimated pose of the sensor is updated by sending the pose map to the optimized system (e.g., [19]).

## 10.4 Experiments

All experiments were performed on a laptop equipped with a 2.5 GHz Intel i7-4700 processor, 16 GB of RAM.

### 10.4.1 Feature Extraction

Figure 10.3 shows a frame of point cloud and feature points (in green) in scenario 1, including five moving pedestrians (circled in white box), where Fig. 10.3a shows the wrong feature extraction results of LeGo-LOAM. It can be seen that many feature points are distributed on unstable outliers belong to pedestrians, while our result (Fig. 10.3b) is more reasonable because we detect outliers and avoid extracting feature points from them to avoid the incorrect odometry and mapping results caused by wrong matching of feature points. To be concise, we only show the feature edge points that are sufficient to illustrate the problem.

The results show that our method has the advantage of effective feature extraction in scenes containing a large proportion of outliers (Table 10.1).

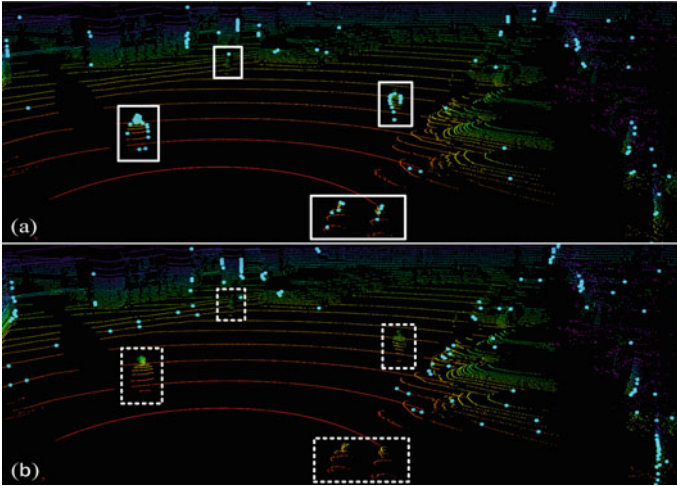


**Fig. 10.3** Feature extraction results of LeGo-LOAM and ours

**Table 10.1** Comparison of effective features ratio between LeGo-LOAM and ours

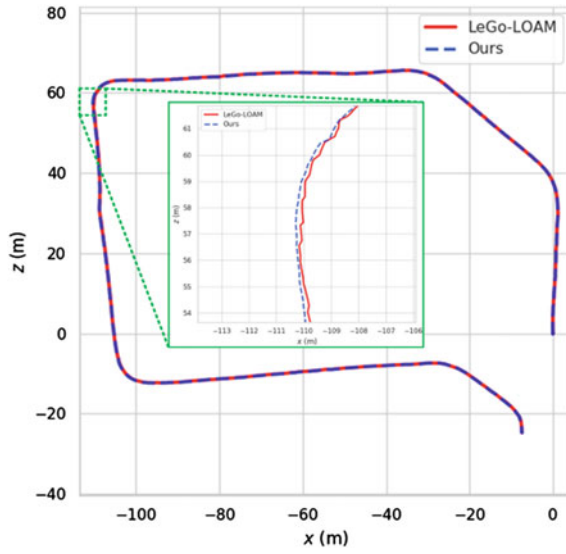
Scenario	$F_e$		$f_e$		$F_p$		$f_p$	
	Ours	LeGo-LOAM	Ours	LeGo-LOAM	Ours	LeGo-LOAM	Ours	LeGo-LOAM
1	0.96	0.57	0.97	0.59	0.99	0.52	0.98	0.83
2	0.98	0.82	0.98	0.83	0.99	0.80	0.99	0.94

### 10.4.2 Odometry

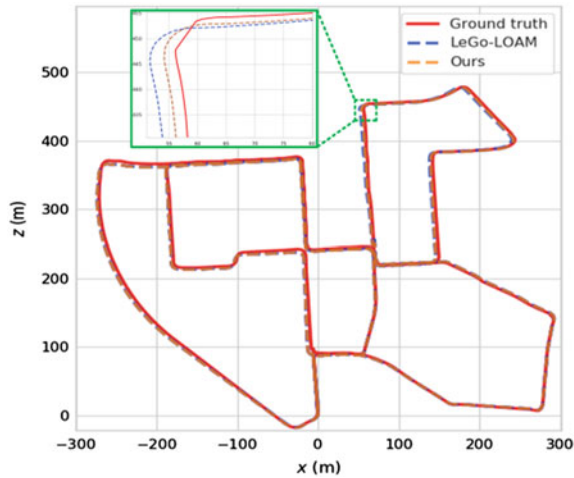
Figure 10.4 shows the odometry comparison results of scenario 1, where the red curve is the result of LeGo-LOAM, while the blue one is ours. The results of the two methods have little difference from a global perspective, but there are quite differences in detail. We choose the most representative location (upper left corner of scenario 1, where pedestrians gathering here) to show the contrast, as can be seen from the green box, and the red line has a distinct jagged edge, which is exactly the wrong odometry estimation caused by the outliers, while the blue line has no such problem.

Figure 10.5 shows the comparison result between the two methods and the true value in scenario 2, and we can see from Fig. 10.5 that the accuracy can still be maintained in the long trajectory scene (with a length of about 3730 m). The relative pose estimation error is calculated by comparing the final pose and the initial pose. Rotation errors and translation errors of LeGo-LOAM are  $5.65^\circ$  and 3.19 m, while our results are  $4.52^\circ$  and 2.75 m. These two groups of experiments illustrate the advantage of our method in odometry estimation.





**Fig. 10.4** Odometry comparison results in scenario 1 between the two methods, where the green box is enlarged to highlight the differences. Ours is smoother and more accurate than that of LeGo-LOAM



**Fig. 10.5** Odometry comparison results in scenario 2 between the two methods. Green box is enlarged to highlight the differences

### 10.4.3 Mapping

The results of representative scenarios indicate that LeGo-LOAM will produce wrong mapping results because they do not consider outliers, as shown from Figs. 10.6, 10.7, 10.8, and 10.9.

Figure 10.6 shows the mapping result of scenario 1, where Fig. 10.6a is the LeGo-LOAM mapping result. Figure 10.7 shows the details of the mapping result of scene 1, where (a), (b), and (c) are the result of incorrect mapping caused by incorrect

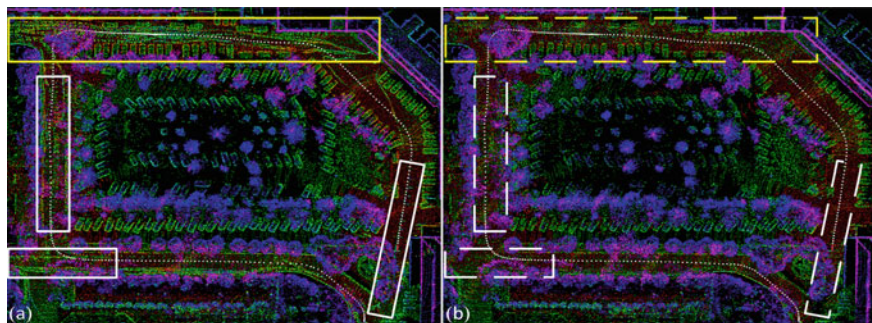


**Fig. 10.6** Mapping result of scenario 1. **a** The result of LeGo-LOAM, we can clearly see the shadow left by outliers. **b** Our result, we get a clean map by identifying outliers and avoiding extracting feature points and mapping using them

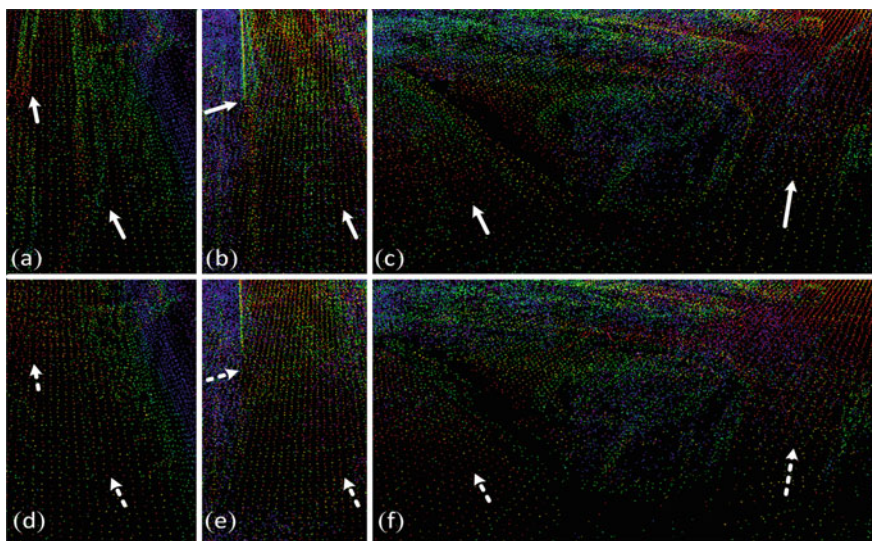


**Fig. 10.7** Details comparison in scenario 1. **a**, **b**, and **c** are the results of LeGo-LOAM. **d**, **e**, and **f** are the results of our method. The white arrows highlight the differences

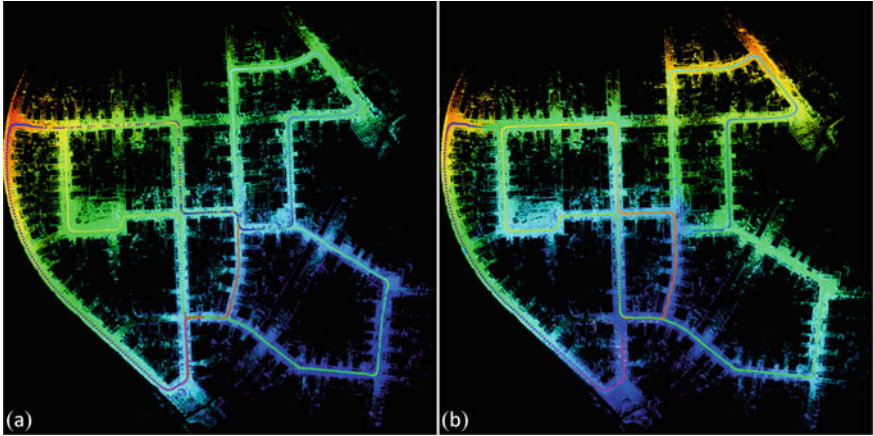


**Fig. 10.8** Mapping result of scenario 2. **a** The result of LeGO-LOAM. **b** The result of our method

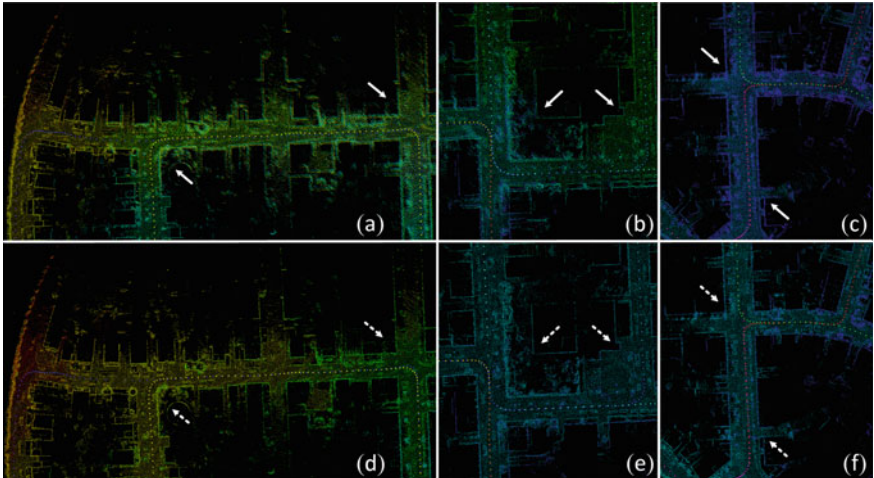


**Fig. 10.9** Details comparison in scenario 2. **a**, **b**, and **c** are the results of LeGo-LOAM. **d**, **e**, and **f** are the results of our method. The white arrow highlights the differences

feature extraction. Dynamic pedestrians and vehicles participate in feature extraction and association and are thus added to the map, leaving obvious residual shadows. Among them, Fig. 10.7a is the enlarged result on the top of the map, and the residual shadow is the movement track left by four pedestrians moving forward. Figure 10.7b is a local enlarged image on the left of the map, and the residual shadow is the movement track left by an upward moving vehicle. Figure 10.7c is a local enlarged image of the lower right part of the map, and the residual shadow is left by a moving car. Different from LeGO-LOAM, we first detect and eliminate outliers and focus

**Table 10.2** Runtime (ms) comparison of one frame between LeGo-LOAM and ours

Scenario	Lidar odometry		Lidar mapping	
	Ours	LeGO-LOAM	Ours	LeGO-LOAM
1	9.2	10.7	217.5	311.0
2	12.1	14.0	200.4	294.2

on extracting effective features, so we have obvious advantages when mapping in dynamic scenarios.

Figure 10.8 shows the mapping result of scenario 2, when we zoom in on the local map near the loop closure, as shown in Fig. 10.9, we can see the obvious differences as indicated by the white arrows, and the buildings in map of LeGO-LOAM have obviously offset, while ours remains globally consistent, which benefits from two-step of coarse-to-fine registration strategy.

#### 10.4.4 Runtime

The running time of odometry module and mapping module between our method and LeGo-LOAM is shown in Table 10.2. The time consumption of odometry module is reduced by about 15%, while that of mapping module is about 31%. The results demonstrate the advantage of our approach in terms of time consumption, which is because we use two-step coarse-to-fine registration strategy to replace single-step registration.

## 10.5 Conclusions and Future Works

Future works include further improving the accuracy of SLAM system in complex and highly dynamic scenes, because we find the proposed system will still produce unsatisfactory performance when there are many and dense moving objects around the Lidar. Some methods to solve the problem of robot kidnapping may be the solutions to the raised problems. We will also try to deploy SLAM system on multiple base stations to make up for the deficiency caused by the serious occlusion of a single base station by mobile objects through cooperative tasks. Therefore, we will further combine the semantic information and motion information of the scene, which will also provide a new idea for the construction of semantic map.

**Acknowledgements** This work was supported by National Nature Science Foundation of China (NSFC) under Grants No. 61671356, Science and Technology Program of Shaanxi Province under Grants No. 2020GY-136 and 2019ZDLGY14-02-03.

## References

1. Zhang, J., Henein, M., Mahony, R.E., Ila, V.: VDO-SLAM: a visual dynamic object-aware SLAM system. *Int. J. Robot. Res.* (2020) [Online]. <https://arxiv.org/abs/2005.11052>
2. Zhang, J., Singh, S.: LOAM: Lidar odometry and mapping in real time. *Proc. Robot.: Sci. Syst.* (2014)
3. Zhang, J., Singh, S.: Low-drift and real-time lidar odometry and mapping. *Auton. Robot.* **41**(2), 401–416 (2017)
4. Zhang, J., Singh, S.: Visual-lidar odometry and mapping: low-drift, robust, and fast. In: 2015 IEEE International Conference on Robotics and Automation (ICRA), pp. 2174–2181 (2015)
5. Shan, T., Englot, B., Meyers, D., Wang, W., Ratti, C., Rus, D.: LIO-SAM: tightly-coupled Lidar inertial odometry via smoothing and mapping. In: 2020 IEEE/RSJ International Conference on Intelligent Robots and Systems (IROS), Oct 2020
6. Shan, T., Englot, B.: LeGO-LOAM: lightweight and ground-optimized lidar odometry and mapping on variable terrain. In: 2018 IEEE/RSJ International Conference on Intelligent Robots and Systems (IROS), pp. 4758–4765 (2018)
7. Cadena, C., Carlone, L., Carrillo, H., Latif, Y., Scaramuzza, D., Neira, J., Reid, I., Leonard, J.J.: Past, present, and future of simultaneous localization and mapping: towards the robust-perception age. *IEEE Trans. Robot. (TRO)* 1309–1332 (2016)
8. Besl, P.J., McKay, N.D.: A method for registration of 3-D shapes. *IEEE Trans. Pattern Anal. Mach. Intell.* **14**(2), 239–256 (1992)
9. Yang, J., Li, H., Campbell, D., Jia, Y.: Go-ICP: a globally optimal solution to 3D ICP point-set registration. *IEEE Trans. Pattern Anal. Mach. Intell.* **38**(11), 2241–2254 (2016)
10. Campbell, D., Petersson, L.: Gogma: Globally-optimal gaussian mixture alignment. In: 2016 IEEE Conference on Computer Vision and Pattern Recognition (CVPR), pp. 5685–5694 (2016)
11. Aiger, D., Mitra, N.J.: Cohen-Or D.4-points congruent sets for robust pairwise surface registration. *ACM Trans. Graphics* **27**(3), 85, 1–10 (2008)
12. Theiler, P.W., Wegner, J.D., Schindler, K.: Keypoint-based 4-points congruent sets—automated marker-less registration of laser scans. *ISPRS J. Photogramm. Remote Sens.* **96**, 149–163 (2014)
13. Mellado, N., Aiger, D., Mitra, N.J.: Super 4PCS fast global pointcloud registration via smart indexing. *Comput. Graphics Forum* **33**(5), 205–215 (2015)
14. Mohamad, M., Ahmed, M.T., Rappaport, D., Greenspan, M.: Super generalized 4PCS for 3D registration. In: 2015 International Conference on 3D Vision, pp. 598–606 (2015)
15. Raposo, C., Barreto, J.P.: Using 2 point+normal sets for fast registration of point clouds with small overlap. In: 2017 IEEE International Conference on Robotics & Automation (ICRA), pp. 5652–5658 (2017)
16. Geiger, A., Lenz, P., Urtasun, R.: Are we ready for autonomous driving? The KITTI vision benchmark suite. In: 2012 IEEE Conference on Computer Vision and Pattern Recognition (CVPR), pp. 3354–3361 (2012)
17. Rozenberszki, D., Majdik, A.L.: LOL: Lidar-only odometry and localization in 3D point cloud maps. In: 2020 IEEE International Conference on Robotics and Automation (ICRA), Paris, France, pp. 4379–4385 (2020)
18. Bogoslavskyi, I., Stachniss, C.: Fast range image-based segmentation of sparse 3D Lidar scans for online operation. In: Proceedings of the IEEE/RSJ International Conference on Intelligent Robots and Systems, pp. 163–169 (2016)
19. Kaess, M., Johannsson, H., Roberts, R., Ila, V., Leonard, J.J., Dellaert, F.: iSAM2: incremental smoothing and mapping using the Bayes tree. *Int. J. Robot. Res.* **31**(2), 216–235 (2012)
20. Quigley, M., Conley, K., Gerkey, B., Faust, J., Foote, T., Leibs, J., Wheeler, R., Ng, A.Y.: ROS: an open-source robot operating system. In: IEEE ICRA Workshop on Open Source Software (2009)

# Chapter 11

## Collaborative Control of Unmanned Vehicle Matrix Formation Based on Autonomous Neighborhood Negotiation



**KaiXuan Wang, YuTing Shen, FuQuan Zhang, Jianglong Yu, Zhang Ren, and Liang Zhuo**

**Abstract** In large-scale activities or performances, the formation of unmanned vehicles on the large platform has become a shocking means of artistic expression. How to achieve low-cost and reliable cooperative control and highly reliable formation in a limited observation area with viewing Angle constraints is a very valuable area of research. This paper puts forward a kind of driving control method of unmanned vehicle formation with matrix arrangement based on a small-scale region driving consultation. An observation and neighborhood negotiation topology is designed, which can realize the automatic maintenance of unmanned vehicle formation in the leader-slave mode with a single leader. This method can provide a low-cost and high-reliability cooperative control scheme for large-scale unmanned vehicle formation performance.

---

K. Wang · L. Zhuo

China Academy of Launch Vehicle Technology, Beijing 100076, P.R. China

e-mail: [kingkaixuan@126.com](mailto:kingkaixuan@126.com)

L. Zhuo

e-mail: [liangzhuo\\_nust@163.com](mailto:liangzhuo_nust@163.com)

K. Wang · J. Yu · Z. Ren

School of Automation Science and Electrical Engineering, Beihang University, Beijing 100191, P.R. China

e-mail: [yujianglong@163.com](mailto:yujianglong@163.com)

Z. Ren

e-mail: [renzhang@buaa.edu.cn](mailto:renzhang@buaa.edu.cn)

Y. Shen

National Space Science Center, Chinese Academy of Sciences, Beijing 100190, P.R. China

University of Chinese Academy of Sciences, Beijing 100039, P.R. China

The 54th Research Institute of China Electronics Technology Group Corporation, Shijiazhuang 050000, P.R. China

F. Zhang (✉)

Fujian Provincial Key Laboratory of Information Processing and Intelligent Control, Minjiang University, Fuzhou 350121, P.R. China

## 11.1 Preface

With the development of automatic control technology, artificial intelligence technology, and collaborative control technology, the formation performance of large-scale unmanned equipment has become a kind of shocking artistic expression means, which is applied in large-scale open stage performance. Unmanned vehicles are the most common carrier in large-scale performances based on ground stages. Driving in formation is the most common form.

In the environment of unmanned vehicle performance, the environment of the performance area is complex, and the performance of driverless car is affected by sound, light, electricity, and other noises. According to the way of active positioning, accurate point location information of each unmanned car can be obtained. However, active localization requires many support conditions, its technical implementation is complex, and the high probability will be disturbed.

The autonomous detection method, which only measures the relative distance, is a low-cost and high-reliable relative positioning method. In the process of autonomous detection of unmanned vehicle, the relative distance is easy to measure, and the measured value is accurate. In the case of complete autonomy without reference, the relative Angle is difficult to measure, and there is a certain degree of measurement error. In the common engineering application, the low-cost range finder is usually fixed on the car body and has a certain field of view. Therefore, how to achieve reliable cooperative control and maintain formation under the condition of restricted viewing Angle and limited detection area is a very worthy direction of research.

When the ranging detection device is fixed on the unmanned vehicle body, the unmanned vehicles on the edge of the matrix can only measure the distance of one neighbor cannot maintain the formation with the support of only one relative distance data. In the absence of global information sharing, it is necessary to share information with neighbor nodes in a small range and maintain formation through agent region negotiation of some edge nodes. Therefore, the small-scope regional negotiation of edge nodes is also an important problem to solve the formation maintenance of autonomous formation of unmanned vehicles.

## 11.2 Solution Overview

Grassé, a French biologist, first proposed the concept of consensus autonomy, that is, an indirect coordination mechanism between individuals, which can accomplish complex intelligence activities without any centralized planning and direct communication [1]. In the natural environment, the biological group can realize the autonomous control of the group through the individual autonomous decision, under the condition of limited range perception and limited range communication. The pigeons' flock model is proposed by Vicsek's team [2], and the geese 'flock model is

discovered by Wieselsberger [3]. All of these models can achieve cluster autonomous control.

The matrix formation of unmanned vehicles is an example of group autonomous cooperation, which can be realized by using group consistency theory, autonomous detection position perception method, and group cooperative control method. In this research direction, Tian Daxin's team mainly focused on formation forming, formation switching, and formation keeping and made an in-depth study and summarized some research directions of formation control in the future [4]. Zhang Lang's team studied the formation control of unmanned vehicles based on the pilot-follow method, designed a controller to control the acceleration of unmanned vehicles and eliminate distance errors, and designed three types of formation of unmanned vehicles: rectangle, circle, and triangle [5]. Yang Xiuxia et al. proposed a minimum rigid formation communication topology generation algorithm for multi-agent system based on the network complexity of formation communication topology [6]. Liu Guobo used rigid graph theory to study the master-slave formation control of multi-agent [7]. Liu Shuanjun et al. proposed a formation control method of UAV based on distributed consistency [8]. The formation control based on the lead mode is easy to implement, but it is greatly affected by the communication delay in the global information sharing mode. The formation control based on consistency can complete the task well, but it needs to add the Angle measurement information based on the ranging data. The method based on rigid graph can realize formation control in the case of measuring distance only, but each individual needs to be in a rigid unit.

Therefore, under the guidance of consistency theory, this study integrated rigid graph and regional negotiation method to realize the formation control of unmanned vehicles with only distance data.

### 11.3 Consistent Control

In group consistency control, algebraic graph theory can be used to describe the interaction between the individuals in the cluster, and the adjacency matrix of the graph can be represented by non-negative matrix

$$W = [w_{ij}] \in \mathbb{R}^{N \times N}.$$

$w_{ij}$  represents the weight of an edge  $e_{ij}$ .  $w_{ij} > 0$  represents the existence of an edge  $e_{ij}$ , i.e.,  $e_{ij} \in \mathcal{E}(G)$ . The set of neighbors is defined as

$$N_i = \{v_j \in V(G) : (v_j, v_i) \in \mathcal{E}(G)\}$$

If an edge  $e_{ij}$  exists,  $v_j$  is called a neighbor of  $v_i$ . The entry degree of nodes can be expressed as



$$\text{deg}_{\text{in}}(v_i) = \sum_{j=1}^N w_{ij}$$

The Laplace matrix of the graph,  $L = D - W$  where  $D$  is the entry diagonal matrix of each node of diagonal element,  $W$  is the entry matrix of. In a directed graph, the existence of a spanning tree means that at least one root node exists and all other nodes have a directed path. For a directed graph  $G$ , if there is a spanning tree, 0 is a single eigenvalue of  $L$ , and the real parts of the other eigenvalues are positive. For a first-order linear time-invariant cluster system

$$\dot{x}(t) = -Lx(t)$$

Its stability depends on the position of eigenvalues in the complex plane of  $L$ . If a directed graph  $G$  is strongly connected, there is a control protocol to keep it consistent.

In engineering applications, the unmanned vehicle cooperative formation can be simplified as a first-order linear time-invariant system cluster, matrix formation, for example, if there is no car in fixed gaze direction distance detection condition of limited field of view angle, the unmanned vehicle only observable in front and left, in front of the vehicle in front of the relative position to correct their own position. This is shown in Fig. 11.1.

The formation can be represented as a directed graph with spanning tree [9], and the topology can be consistent according to the properties of Laplace matrix. In formation control, formation consistency can be achieved by adding formation deviation matrix  $K$ . According to the rigid graph theory, there is a minimum triangular stable structure in the topological structure shown in Fig. 11.1, which can realize formation structure maintenance. Therefore, the matrix formation of the entire unmanned vehicle cluster can be realized by active or program control of the unmanned vehicle in the upper left corner. According to formation consistency theory and rigid graph theory, formation travel control can be realized as long as formation consistency and stable structure exist.

## 11.4 Autonomous Positioning

In the low-cost unmanned vehicle cluster system with autonomous perception ability, large-scale carless people can travel in formation by dispersing the limited range of autonomous perception and small-scale collaborative control.

In the autonomous perception of the unmanned vehicle, the following conditions are considered:

1. Vehicles travel in matrix formation.
2. Only one vehicle is controlled by active or autonomous driving.

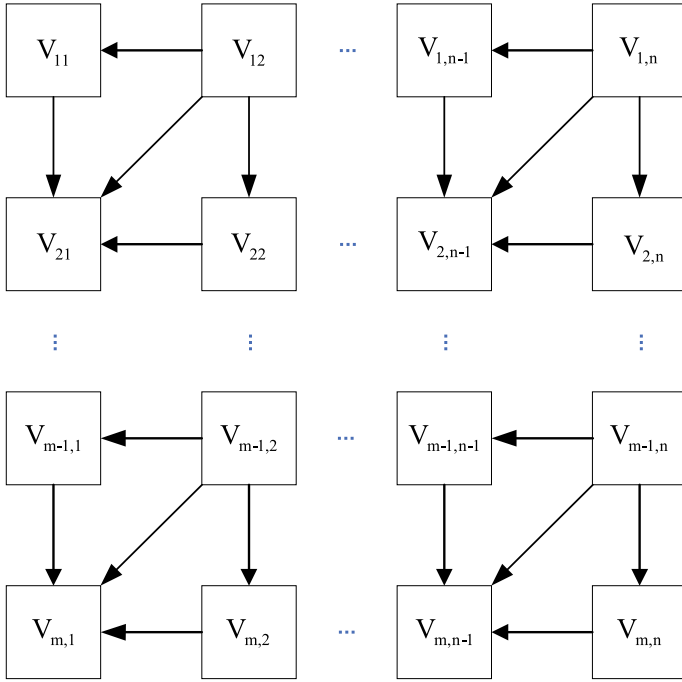


**Fig. 11.1** Topological relation of matrix formation

3. There is line of sight occlusion in the moving plane, so the vehicle cannot detect the whole scene.
4. The detection device is fixedly connected to the vehicle body, so the unmanned vehicle can only observe in a fixed sight direction and under the condition of limited field of view.
5. Detection device can only detect relative distance, not relative Angle.

In the matrix arrangement structure shown in Fig. 11.2,  $v_{1,n}$  serves as A single lead node, and the remaining nodes are follow nodes. Due to the constraint of position relationship, the entry degree of nodes is located at the upper edge, and the right edge is 1. In the absence of relative Angle support, the relative distance of the reference object cannot be relied on to complete the positioning. Therefore, regional negotiation should be carried out based on the detection results of sub-edge nodes, so as to complete the estimation of the motion vector of the reference node. The negotiation model is shown in Fig. 11.2.

According to the principle of minimizing negotiation and minimizing communication, as shown by the dashed arrow in Fig. 11.2, negotiation communication is conducted in accordance with the following principles.

$$e_{ij} = \begin{cases} v_{i+1,j} \rightarrow v_{ij} & (i = 1, j < n) \\ v_{i,j-1} \rightarrow v_{ij} & (i < m, j = n) \end{cases}$$

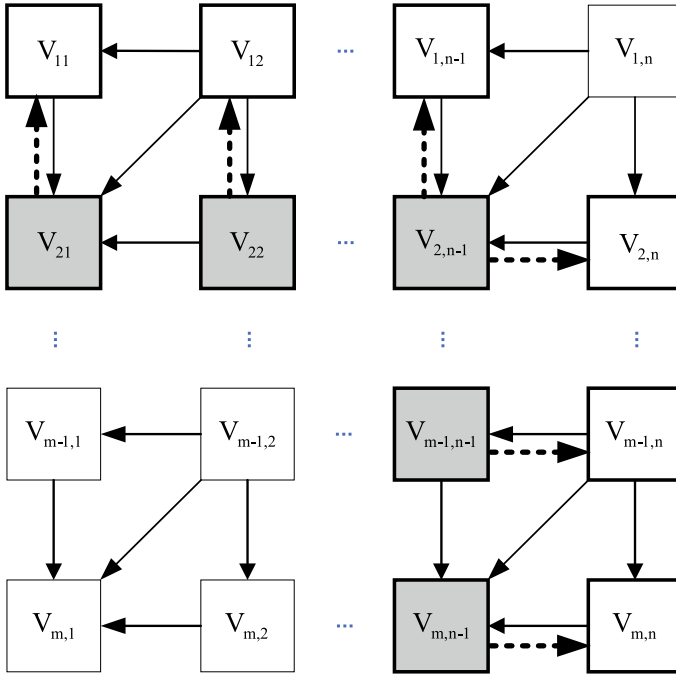


Fig. 11.2 Matrix formation topological relationship with edge negotiation

The negotiation is the distance relative to the node at the top right.

$$K_{ij} = \begin{cases} L(v_{i+1,j}, v_{i,j+1}) & (i = 1, j < n) \\ L(v_{i,j-1}, v_{i+1,j}) & (i < m, j = n) \end{cases}$$

$L(a, b)$  is the distance from  $a$  to  $b$ .

Other nodes rely only on their own detection devices, without regional negotiation. According to the different topologies and negotiation modes of the nodes in the formation, the following nodes can be divided into three types: the node located at the upper edge  $v_{up} : i = 1, j < n$ , the node located at the right edge  $v_{right} : i < m, j = n$  and the other non-negotiating following nodes  $v_{norm}$ .

### 11.4.1 Upper Edge Node

For the node  $v_{up} : i = 1, j < n$  on the upper edge as shown in Fig. 11.3a,  $l_0 = L(v_{i,j}, v_{i+1,j})$  is a known item of the matrix queue.  $v_{i,j}$  relies on its own detection device to obtain the detection distance  $l_1 = L(v_{i,j}, v'_{i,j+1})$  from  $v'_{i,j+1}$ , and  $v_{i,j}$  obtains the detection distance  $l_2 = L(v_{i+1,j}, v'_{i,j+1})$  from  $v'_{i,j+1}$  through negotiation

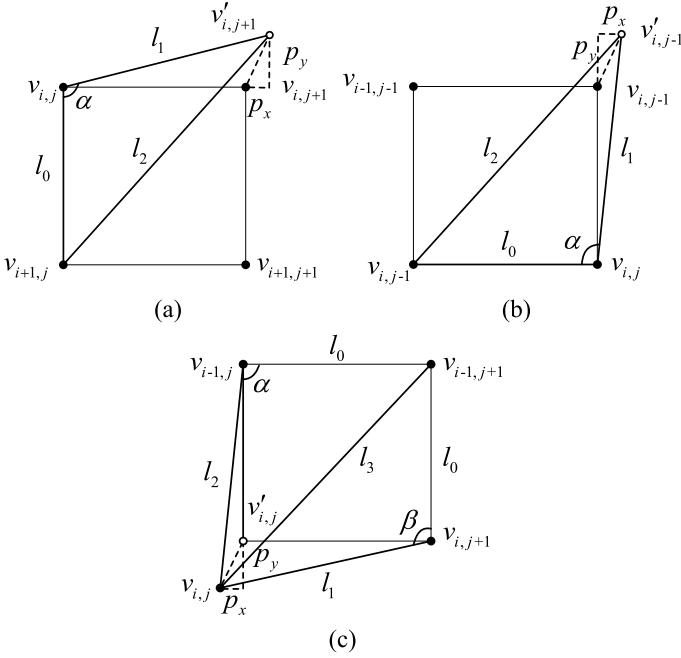


**Fig. 11.3** Structure diagram of autonomous detection and regional negotiation

with A. According to the theorem of triangle cosines, the Angle between  $l_0$  and  $l_1$  can be obtained:

$$\alpha = a \cos\left(\frac{l_0^2 + l_1^2 - l_2^2}{2l_0l_1}\right)$$

In matrix formation, in order to maintain its rectangular structure, the Angle between,  $v_{i+1,j}$ ,  $v_{i,j}$ , and  $v_{i+1,j}$  is assumed as  $\pi/2$ . The movement vector of  $v_{i,j+1}$  is obtained by autonomic computation of node  $v_{i,j}$  by

$$p_y = l_1 \sin(\alpha - \pi/2)$$

$$p_x = l_1 \cos(\alpha - \pi/2) - l_0$$

$$P(v_{i,j+1}, v'_{i,j+1}) = (l_1 \cos(\alpha - \pi/2) - l_0, l_1 \sin(\alpha - \pi/2))$$

Therefore, node  $v_{i,j}$  can be guaranteed to be consistent with node  $v_{i,j+1}$  by moving along vector  $P(v_{i,j+1}, v'_{i,j+1})$  through its own calculation.

### 11.4.2 Right Edge Node

For the right edge node  $v_{\text{right}} : i < m, j = n$  as shown in Fig. 11.3b, the movement vector  $v_{i,j-1}$  can be obtained by

$$P(v_{i,j-1}, v'_{i,j-1}) = (l_1 \sin(\alpha - \pi/2), l_1 \cos(\alpha - \pi/2) - l_0)$$

Therefore, node  $v_{i,j}$  can be guaranteed to be consistent with node  $v_{i,j-1}$  by moving along vector  $P(v_{i,j-1}, v'_{i,j-1})$  through its own calculation.

### 11.4.3 No Negotiation Node

For other nodes, as shown in Fig. 11.3c, since each node has three references, no regional negotiation is required. In order to reduce the influence of noise, the weighted summation method is used to obtain its offset vector by

$$P(v_{i,j}, v'_{i,j}) = \left( \frac{l_2 \sin(\alpha - \pi/2) + l_1 \cos(\beta - \pi/2) - l_0}{2}, \frac{l_2 \cos(\alpha - \pi/2) - l_0 + l_1 \sin(\beta - \pi/2)}{2} \right)^T$$

Therefore, node  $v_{i,j}$  can be guaranteed to be consistent with three nodes by moving along vector  $P(v_{i,j}, v'_{i,j})$  through its own calculation.

## 11.5 Cooperative Control Method

For the  $i$ th unmanned vehicle node, its position tracking error is considered as  $p_{y,i}$  and  $p_{x,i}$ .

Then the motion error model of the unmanned vehicle can be written as:

$$\begin{cases} \dot{x}_{e,i} = V_i \cos \theta_i - \dot{p}_{x,i} \\ \dot{y}_{e,i} = V_i \sin \theta_i - \dot{p}_{y,i} \\ \dot{\theta}_{e,i} = \omega_i - \dot{\theta}_{d,i} \end{cases}$$

where  $x_{e,i}$  and  $y_{e,i}$  represent position tracking error, and its expressions are as follows:

$$x_{e,i} = x_i - p_{x,i}, y_{e,i} = y_i - p_{y,i}.$$

Based on this, two virtual control quantities are taken, as shown below:

$$\begin{cases} V_i \cos \theta_i = u_{1,i} \\ V_i \sin \theta_i = u_{2,i} \end{cases}$$

For the first subsystem  $\dot{x}_{e,i} = u_{1,i} - \dot{p}_{x,i}$ , in order to make its tracking error converge to zero, we may as well take the following virtual control law:

$$u_{1,i} = \dot{p}_{x,i} - k_x x_{e,i}$$

Among them,  $k_x > 0$ . Similarly, for the second tracking error subsystem, we also choose a similar control law:

$$u_{2,i} = \dot{p}_{y,i} - k_y y_{e,i}$$

Among them, it can be proved that the position tracking error subsystem can asymptotically converge to the origin under the action of the two virtual control laws. Take Lyapunov function  $E_{1,i} = \frac{1}{2}(x_{e,i}^2 + y_{e,i}^2)$ , substitute the designed control law in, and take the derivative of Lyapunov function, we can get:

$$\begin{aligned} \dot{E}_{1,i} &= x_{e,i} \dot{x}_{e,i} + y_{e,i} \dot{y}_{e,i} = -k_x x_{e,i}^2 - k_y y_{e,i}^2 \\ &\leq -2k_0 E_{1,i} \end{aligned}$$

where  $k_0 = \min\{k_x, k_y\}$ . According to Lyapunov stability theorem, the system is asymptotically stable.

In order to obtain the above control law  $\omega_i$ , we need another control quantity. According to Equation, if the attitude Angle is controlled as the internal loop, the ideal control instruction is as follows:

$$\theta_{d,i} = \arctan \frac{u_{2,i}}{u_{1,i}}$$

Obviously, the domain of  $\theta_{d,i}$  is  $(-\pi/2, \pi/2)$ , and the desired tracking instruction can be obtained in this domain. However, this is only the attitude Angle instruction that is expected to track. We also need to design a control law for attitude control. Next, we will use the sliding mode control method to design the inner loop attitude controller. First, the sliding mode surface is defined, then the governing equation of the inner loop is  $\dot{s}_i = \dot{\theta}_{e,i} = \omega_i - \dot{\theta}_{d,i}$ . According to the sliding mode control theory, the control law is  $\omega_i = \dot{\theta}_{d,i} - k_\theta s_i - \eta_\theta \text{sgn}(s_i)$ , where  $k_\theta > 0$ ,  $\eta_\theta > 0$ .

Lyapunov stability theory is used for stability analysis. Take the Lyapunov function as  $E_{2,i} = \frac{1}{2}s_i^2$  and take the derivative with respect to time:

$$\dot{E}_2 = -k_\theta s_i^2 - \eta_\theta |s_i| \leq -k_\theta s_i^2$$

Obviously, the tracking deviation of the unmanned vehicle will converge to the origin within a limited time.

**Fig. 11.4** Simulation node topology structure

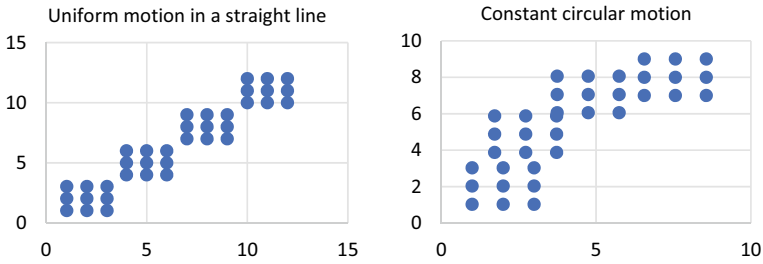
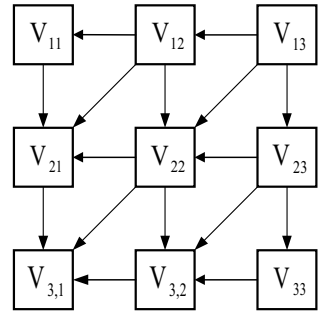


**Fig. 11.5** Simulation node topology structure

### 11.6 Simulation

In order to verify the effectiveness of the topology of the unmanned vehicle and the feasibility of the autonomous position awareness method, an ideal model of the unmanned vehicle is established in the simulation scene. The distance between the unmanned vehicles is 1 m, and the arrangement is as  $3 \times 3$ . The unmanned vehicle  $v_{1,3}$  is the leaders in the upper left corner, and the others are the followers, as shown in Fig. 11.4.

The leader makes uniform linear or uniform circular motion, the speed is (3, 3) m/s, and the simulation period is 0.01 s. After 300 simulation cycles, the following results can be obtained (Fig. 11.5).

Through simulation, it can be concluded that the consistent topology structure and the autonomous position awareness method in this paper are effective and feasible.

### 11.7 Conclusion

This paper analyzes the demand of unmanned vehicle formation in large-scale performance. Based on the principle of minimizing cost and communication, a detection and negotiation topology is designed under the conditions of limited range,

limited viewing Angle and edge node negotiation, and the general control method of unmanned vehicle was analyzed. Through simulation, this paper proposes that the topology structure can realize matrix formation control of unmanned vehicles, which has a high engineering guiding significance.

## References

1. Grasse, P.P.: La reconstruction du Nids et les coordinations inter-individuelles chez *bellicositermes natalensis* et *Cubitermes* sp. La theorie de La stigmergie: Essi d 'interpretation des termites constructeurs. In *Ins. Soc.* **6**, 41–83 (1995)
2. Shao, J., Zheng, W.X., Huang, T., Bishop, A.N.: On leader—follower consensus with switching topologies: an analysis inspired by pigeon hierarchies, *IEEE Trans. Autom. Control* **63**(10), 3588–3593 (2018). <https://doi.org/10.1109/TAC.2018.2797205>
3. Zhou, Z., Duan, H., Fan, Y.: *Sci. China: Technol. Sci.* **47**(03), 230–238 (2017). (in Chinese)
4. Tian, D., Huang, M., Li, J., Duan, X.: Summary of formation control methods and applications of vehicle formation. *Mob. Commun.* **44**(11), 52–57 (2020)
5. Zhang, L., Niu, Y., Liu, Z.: Research on formation control of unmanned vehicle based on pilot-following method. *Chin. Inst. Command Control: Chin. Soc. Command Control* **202**, 6
6. Yang, X., Yan, X., Zhang, Y.: Communication topology generation of minimum rigid formation based on network complexity. *J. Nanjing Univ. Aeronaut. Astronaut.* **52**(06), 855–860 (2020)
7. Liu, G.: Research on Master-slave Formation Control of Multi-agent Based on Azimuth-rigidity. Southwest Jiaotong University (2019)
8. Liu, Z., He, M., Ma, Z., Gu, L.: Control of UAV formation based on distributed consistency. *Comput. Eng. Appl.* **56**(23), 146–152 (2020)
9. Horng, G.-J., Chang, T.-Y., Wu, H.-T.: The adaptive node-selection mechanism scheme in solar-powered wireless sensor networks. *J. Netw. Intell.* **3**(1), 58–73 (2018)



# Chapter 12

## Unmanned Vehicle Task Scheduling Method Based on Iterative Cognitive Interaction



**Yuting Shen, Xin Meng, Kaixuan Wang, Fuquan Zhang, Yueqing Gao, and Lulu Chen**

**Abstract** At present, in the field of autonomous driving, the application of unmanned vehicles has made considerable progress. However, there are still a large number of engineering problems to be solved in practical application. For example, the ability of multi-vehicle interactive autonomous operation in high-dynamic and time-sensitive environment is not sufficient for large-scale application. These kinds of problems restrict the effective integration of unmanned intelligent transportation

---

Y. Shen · X. Meng (✉)

National Space Science Center, Chinese Academy of Sciences, Beijing 100190, China  
e-mail: [mengxin@nssc.ac.cn](mailto:mengxin@nssc.ac.cn)

University of Chinese Academy of Sciences, Beijing 100039, P.R. China

Y. Shen

e-mail: [rebeccashenstudy@yeah.net](mailto:rebeccashenstudy@yeah.net)

Y. Shen · Y. Gao · L. Chen

The 54th Research Institute of China Electronics Technology Group Corporation, Shijiazhuang 050000, P.R. China

K. Wang

China Academy of Launch Vehicle Technology, Beijing 100076, P.R. China  
e-mail: [kingkaixuan@126.com](mailto:kingkaixuan@126.com)

School of Automation Science and Electrical Engineering, Beihang University, Beijing 100191, P.R. China

F. Zhang

Fujian Provincial Key Laboratory of Information Processing and Intelligent Control (Minjiang University), Fuzhou 350121, P.R. China  
e-mail: [8528750@qq.com](mailto:8528750@qq.com)

Y. Gao

Beijing Jiaotong University, Beijing, China  
e-mail: [18111069@bjtu.edu.cn](mailto:18111069@bjtu.edu.cn)

L. Chen

Center for Future Multimedia and School of Computer Science and Engineering, University of Electronic Science and Technology of China, Chengdu 610051, China  
e-mail: [nechlu@163.com](mailto:nechlu@163.com)

system and current traffic system. Facing the problems described above, this paper focuses on introducing knowledge-driven and experiential memory decision-making process for agents, which is based on the research on the process characteristics of human brain cognitive reasoning under the condition of dynamic changes in the observation results of multi-agent clusters. Thus, the method of unmanned vehicles tasks scheduling method based on iterative cognitive interaction is proposed in this paper. In view of the behavior and decision-making process of multi-vehicle in aspects of cognition, interaction, and association, the analysis and research on the time scale will provide a research route for solving the continuous autonomous operation of multi-vehicle system in a high dynamic environment. Contribution of this paper can provide theoretical basis and practical value for multi-application fields.

## 12.1 Background

Along with sustainable development of the unmanned vehicle related technologies, in the unmanned automatic logistics, automatic unmanned patrol, and unmanned automatic, applications of UGVs have begun to take effect in the field of autonomous vehicles. However, there are still a lot of practical problems to be solved in practical application. For example, it is difficult to realize multi-vehicle interactive autonomous operation in high-dynamic and time-sensitive environment. These restriction limits the integrative development between unmanned intelligent transportation with the current transportation system [1].

Aiming at the above problems, this paper abstracts the problem of multi-vehicle interactive autonomous operation into a distributed decision problem of multi-agent system with dynamic and diversified objectives. This paper focuses on the nature of autonomous behavior adjustment and optimization of the multi-agent cluster under the condition of dynamic change of observation results, and tries to introduce a knowledge-driven decision process integrating experience memory for a single agent based on the study of process characteristics of human cognitive reasoning. The actual content of this paper is the iterative interactive task dynamic scheduling decision-making process of multi-unmanned vehicles. Based on the dynamic topology changes of multi-unmanned vehicles, an agent cognitive model and an iterative cognitive framework are studied and established. This research result enables the agent to have the extensible local complete information of each agent and its state within the cluster, and forms the iterative cognitive information interaction ability of multi-unmanned vehicles, which can guide the decision-making and scheduling processes of multi-unmanned vehicles. Finally, this paper carries out the relevant simulation verification work.

The rest of this paper is arranged according to the following structure: Firstly, related research work is introduced in the second part. The third part introduces the related technologies of dynamic scheduling of unmanned vehicle tasks based on iterative cognitive interaction. The fourth part introduces the design and verification

of relevant simulation experiments. The fifth part summarizes the conclusion and future work plan.

## 12.2 Related Work

In essence, a multi-unmanned vehicle system is a collection of multiple intelligent individuals with the same or different abilities, that is, a multi-unmanned vehicle system can be regarded as a cluster of agents mixed with isomorphic and heterogeneous agents. Multi-agent system (MAS) is a kind of computing system composed of multiple intelligent individuals [2–4]. In this system, intelligent individuals constantly interact with each other and with their environment. These interactive processes are the basis of multi-agent collaboration and the core of multi-agent related research. Therefore, the study of multi-unmanned aerial vehicle system cooperation is the study of multi-agent system cooperation based on effective information interaction [5–7].

The sharing and transmission of information is the basis and fundamental basis for multi-agent system to make negotiation decision, so the efficiency, integrity, and consistency of information exchange become the key to determine the effectiveness of negotiation decision. Reyhan et al. proposed a motivation-driven information sharing mechanism based on privacy preserving negotiation to solve the asymmetry of information sharing and proposed a general solution [8]. Ivan Marsa Maestre et al. proposed to introduce competitive belief propagation into multi-agent negotiation process and successfully applied it to Wi-Fi negotiation scenario [9]. Dr. Liu Ming studied the characteristics and effectiveness analysis of agents' association, interaction, and cooperation in the time evolution scale [10]. However, its research thinks that the essence of cooperation lies in the cooperative behavior between two agents, which has certain limitations, and the results are more ideal.

Based on the above research contents and results, most of the agent and its interaction models have weak universality; some of the idealized models are out of touch with practical applications; the impact of cluster topology and its information interaction process on multi-agent decision-making is less considered.

Therefore, this paper studies what kind of agent model with corresponding behavior generation ability should be established, and what kind of protocols or rules should be constructed to realize interaction control.

## 12.3 Iterative Cognitive Interaction for Autonomous Operation of Multiple Unmanned Vehicles

### 12.3.1 Unmanned Vehicle Agent Model Based on Iterative Cognitive Experience

In this paper, iterative cognitive experience based agent—an extended BDI agent model—is proposed for the iterative cognitive interaction of multi-vehicle autonomous operation. The ICEBasedAgent has a six-tuple:

ICEBasedAgent{Belief, Desire, Intention, TaskGoal, Institution, CognitiveExperience}

The structure of agent model based on iterative cognitive experience consists of seven modules (Fig. 12.1):

- (1) **Perception Module** is responsible for sensing changes in environmental information, receiving interactive information from other agents, and sending it to the perception preprocessing module;
- (2) **Perceptual Preprocessing Module** will preliminarily analyze the received changes (such as topological relationship changes) and interactive information (such as negotiation proposals) and send them to the decision module;
- (3) **Decision Module** is the key to the iterative cognitive process module, intuition, logic reasoning, based on the change information of a single cognitive inference graph model;
- (4) **Cognitive Experience Module** stores the preferences and estimates of other agents acquired by the decision module in the operation process and provides information for the subsequent update of local cognitive estimation information;
- (5) **Execution Interaction Module** is responsible for executing the decisions generated by the decision module and sending out interactive information;
- (6) **Behavior Rules Module** presets and stores the behavior rules of agents to provide effective constraints for behaviors;
- (7) **Interaction Recording Module** records the processes information of interactions.

### 12.3.2 Multi-unmanned Vehicle Local Environment Dynamic Cognition

The local dynamic cognitive network model for multi-unmanned vehicles is composed of agent cluster topology and local dynamic cognitive map of each agent. The local dynamic cognitive map of each agent is composed of the agent's own cognitive information and the agent's cognitive estimation information of the neighbor

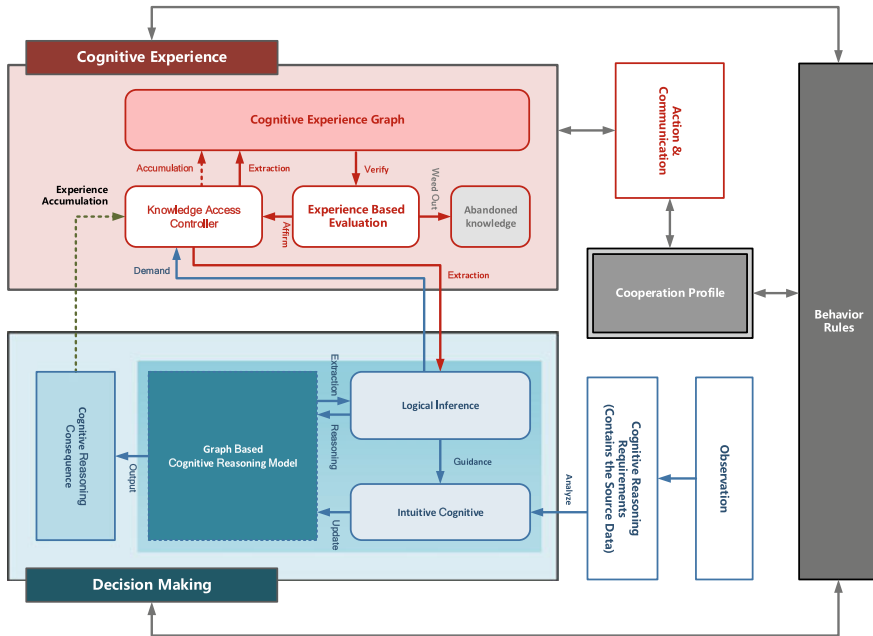


**Fig. 12.1** Structure diagram of agent model based on iterative cognitive experience (including data flow direction)

agents associated with the current topology. It should be noted that, in order to meet the requirements of the scenario, there are two types of processing methods in the processing of new linked nodes:

- (1) When the actual simulation scene needs to maintain the full autonomous cognition of the current agent node to the new connected agent, the current agent does not request the referential cognitive estimation information of the new connected agent from the associated other nodes;
- (2) When actual simulation scenario does not need to keep the current intelligent somite points to the agent of the new league object completely independent cognitive, the agent will be linked to other nodes for the new object coupling agent that may refer to the cognitive estimation information, and according to the actual need simulation scene, the cognitive estimates are associated with integration of information, forming agent cognitive estimation based information of an object.

In a multi-agent cluster, the dynamic cognitive map of an agent is constructed based on the cluster network topology of the agent at the current moment, without considering the connectivity of the nodes within the cluster (i.e., the interaction between the points within the cluster is considered to be reachable, and there is no group dispersion). The structure of multi-agent local dynamic cognitive network

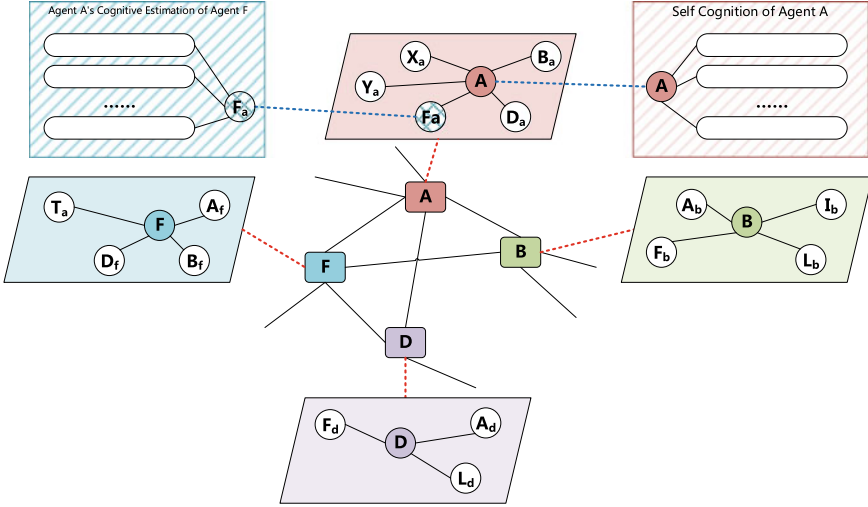


**Fig. 12.2** Schematic diagram of local dynamic cognitive network model for multi-agent

includes the network topology diagram and the associated local dynamic cognitive graph of each agent (Fig. 12.2).

When the information interaction between agents has noise based on probability and observation error, it is necessary to consider whether the information interaction of the cluster can achieve global consistency. In this way, the local dynamic cognitive graph can estimate the global information comprehensively. In the process of information interaction of iterative cognition, the cumulative error of information interaction will be continuously reduced.

Based on the basic Vicsek model [11], when the discrete-time system is composed of  $N$  autonomous individuals (or particles), the set  $\Sigma = \{1, 2, \dots, N\}$  is used to represent the set of all individuals. The initial positions and motion directions of the individuals are randomly distributed. All individuals move freely in the plane region of  $L \times L$ , and the plane region has periodic boundary conditions. When the individual's motion rate is constant at every moment, the individual's cognitive estimation information is updated according to the broadcast information of all neighbors, and there is noise with the mean value of 0 in the broadcast information during the update process. If the mass, shape, and size of an individual are ignored and only regarded as particles, and the cluster individuals have the same perception ability, and each individual can only sense the information of other individuals in the neighborhood, then the neighbor of individual  $i$  is composed of individuals whose Euclidean distance is less than the perception and communication range  $R > 0$ , and whose current position  $\vec{x}_i(t) \in R^2$  is the center (same as above). The neighbor set of individual  $i$  at time  $t$  is represented by  $\Gamma_i(t)$  [12]

$$\Gamma_i(t) = \{j | \|\vec{x}_j(t) - \vec{x}_i(t)\| \leq R, j = 1, 2, \dots, N\} \quad (12.1)$$

where  $\|\vec{x}_j(t) - \vec{x}_i(t)\|$  is the Euclidean distance of vectors. Obviously, the neighbor of individual  $i$  is all individuals in the prototype area with its own position  $\vec{x}_i(t)$  as the center and the perception range  $R$  as the radius. If each individual moves at the same speed  $v_0$ , then the velocity of  $i$  at  $t$  is  $\vec{v}_i(t) = [v_0 \cos \theta_i(t), v_0 \sin \theta_i(t)]^T$  and the direction is  $\theta_i(t) \in (-\pi, \pi]$ . Each individual is updated according to  $\vec{x}_i(t+1) = \vec{x}_i(t) + \vec{v}_i(t)$  mode. The information exchange among individuals is carried out according to the following formula.

$$I_i(t+1) = \langle I_i(t) \rangle_\Gamma + \zeta_i(t) \quad (12.2)$$

where  $\zeta_i(t)$  is the uniformly distributed noise signal on  $[-\eta, \eta]$ ,  $\langle I_i(t) \rangle_\Gamma$  is the weighted average of the confidence estimation of all neighbors based on individual  $i$ , then based on the basic Vicsek model, there must be a certain time  $t_0 > 0$ , so that when  $t \geq t_0$ , there is  $I_i(t) = I_j(t), \forall i, j = 1, 2, \dots, N$ , and the cluster of subject information is consistent, if for any  $I_i(0)$ , at  $t \rightarrow \infty$ , there is

$$\lim_{t \rightarrow \infty} I_i(t) = \lim_{t \rightarrow \infty} I_j(t), \forall i, j \quad (12.3)$$

Then, the cluster can asymptotically achieve the consistency of information interaction. Therefore, no matter whether there is a discrete subgraph in the topological relationship of the group at the current moment, the attenuation and distortion noise among information interactions can achieve the consistent cognition of the same information interaction in the cluster on the uniform distribution after a certain amount of time information accumulation.

### 12.3.3 Task Scheduling Method for Unmanned Vehicles Based on Iterative Cognitive Interaction Network

In this paper, for multi-taxi autonomous scheduling system, a dynamic scheduling model based on iterative cognitive interaction network is proposed to construct a multi-agent cluster network  $\mathcal{N}_{ICE}(A_{ICE}, E_{ICE})$ , in which  $A_{ICE}$  is the set of agents in the network.  $A_{ICE}$  has three roles—{Normal Car, Taxi, Passenger}.  $E_{ICE_{ij}}$  represents the communication connection state between agent node  $i$  and agent node  $j$ . If  $E_{ICE_{ij}}$  exists, its weight value represents the ability of information interaction. Thus, we can get the adjacency matrix  $M_{ICE}$  of this network.

Without considering the unidirectional transmission of communication connection—when  $\mathcal{N}_{ICE}$  is an undirected network, the degree of agent node  $A_{ICE-u}$  is  $k_u = |N(u)| = |\{i \sim (u, i) \in E_{ICE}\}| = \sum_{u \in A_{ICE}} \mathbb{I}_{\{(u, i) \in E_{ICE}\}}$ , which indicates the information connection of all agents connected with  $A_{ICE-u}$ , where  $\mathbb{I}_{[K]}$  is the Kronecker function or indicator function.

The evaluation coefficient of information aggregation ability of each agent is defined as follows: the evaluation of information aggregation ability coefficient of a

single agent (taxi or ordinary vehicle) is determined by the information of neighbor nodes and the estimated distance from passengers. Therefore, the information aggregation ability coefficient  $c_u$  of a vehicle node  $A_{ICE-u}$  is comprehensively measured by the distance evaluation coefficient  $c_{E(u)}$  and the topological interaction coefficient  $c_{B(u)}$ .

$$c_u = b_E c_{E(u)} + b_B c_{B(u)} \quad (12.4)$$

where

$$c_{E(u)} = \frac{k_i}{\sum_{u=1}^r k_u} \quad (12.5)$$

$$c_{B(u)} = \frac{\prod_{j \neq u} \text{Distance}_{j \rightarrow p}}{\sum_{u=1}^r \prod_{s \neq u} \text{Distance}_{s \rightarrow p}} \quad (12.6)$$

At a certain time of  $t_0 > 0$ , according to the information confidence of  $r$  vehicles in the neighborhood,  $A_{ICE-u}$  estimates the passenger position  $\vec{p}$  as

$$\vec{p}_u = \sum_{i=1}^r c_i \times \vec{p}_i = \sum_{i=1}^r \left( \frac{b_E (k_i - 1)}{\sum_{i=1}^r (k_i - 1)} + \frac{b_B \prod_{j \neq u} \text{Distance}_{j \rightarrow p}}{\sum_{i=1}^r \prod_{s \neq i} \text{Distance}_{s \rightarrow p}} \right) \times \vec{p}_i \quad (12.7)$$

According to the structure of ICEBasedAgent model, the following behavior rules are designed in advance for the agent models of three roles (Table 12.1):

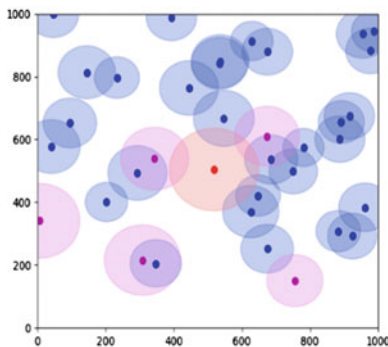
## 12.4 Simulation Verification

For the tasks dynamic scheduling method of unmanned vehicles based on the iterative cognitive interaction network, simulation experiments were carried out in this paper. The simulation scene consisted of 30 ordinary vehicles, 5 taxis, and 1 passenger. In Fig. 12.3a, the blue dot represents the position of ordinary vehicles, and the blue circle represents the observation range and information interaction range of ordinary vehicles. In the same way, the color of purple represents the role of taxi. Either observation range or information interaction orientation were set by simulation. By iterating the location information of passengers (the red dot) to complete cognitive interaction, taxis can successfully find the location of passengers through the weighted estimation of neighborhood information and realize autonomous scheduling (Fig. 12.3b show tracks of taxis and the passenger).

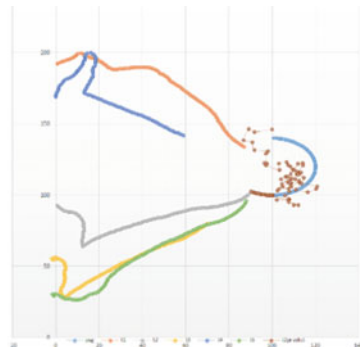


**Table 12.1** Behavior rules for agent roles

Agent roles	Institutions
Normal car	(A) According to the observation, the estimated information of passengers' position is transmitted to the neighbor vehicles (including ordinary vehicles and taxis) losslessly
	(B) When it is within the range of directly observed passenger position, the estimation of passenger position only includes the true value of passenger position
	(C) When it is not within the range of directly observed passenger location, the following location estimation method is used according to the passenger location information notified by neighbor nodes;
	(D) It does not affect its own trajectory because of the passenger's position information, and only broadcast its own passenger position estimation in the neighborhood
Taxi	(A) According to the observation, the passenger's position estimation information is transmitted to the neighbor vehicles (including ordinary vehicles and taxis) in a lossy way
	(B) When it is within the range of directly observing the passenger's position, it directly moves to the passenger in the shortest path and sends the passenger's position misleading information to the nodes in the neighborhood
	(C) When it is not within the range of directly observed passenger location, the following location estimation method is used according to the passenger location information notified by neighbor nodes
Passenger	(A) The location truth value is transmitted to all vehicles in the neighborhood losslessly
	(B) The trajectory is not affected by vehicle position
	(C) When a taxi arrives at its location, the passengers stop sending their location information to the neighboring nodes



(a) Motion diagram of taxis dispatching simulation



(b) tracks of taxis and the passenger

**Fig. 12.3** Schematic diagram of simulation experiments

## 12.5 Conclusion and Prospect

Focusing on the dynamic change of multi-agent cluster observation results, this paper proposes an iterative interactive task dynamic scheduling decision-making method for multi-unmanned vehicles. This method is based on the study of the process characteristics of human cognitive reasoning and introduces a knowledge-driven decision-making process that integrates experience memory into the agent. The simulation results show that this method can achieve the consistency of information cognition in the cluster through dynamic information interaction in the iterative process of local information interaction. In this paper, the behavior and decision-making process of multi-vehicle in aspects of cognition, interaction, and association are analyzed and studied on a time scale, so as to provide ideas for solving the continuous autonomous operation of multi-vehicle system in a high-dynamic environment. The method proposed in this paper has theoretical basis and practical value to extend to multiple application fields.

## References

1. Porru, S., Misso, F.E., Pani, F.E., et al.: Smart mobility and public transport: opportunities and challenges in rural and urban areas. *J. Traffic Transp. Eng. (Engl. Ed.)* **7**(1), 88–97 (2020)
2. Jennings, N.R., Sycara, K., Wooldridge, M.: A roadmap of agent research and development. *Auton. Agent. Multi-Agent Syst.* **1**(1), 7–38 (1998)
3. Jennings, N.R., Faratin, P., Lomuscio, A.R., et al.: Automated negotiation: prospects, methods and challenges. *Group Decis. Negot.* **10**(2), 199–215 (2001)
4. Doran, J.E., Franklin, S., Jennings, N.R., et al.: On cooperation in multi-agent systems. *Knowl. Eng. Rev.* **12**(3), 309–314 (1997)
5. Zartman, I., Berman, M.: *The Practical Negotiator*. Yale University Press, New Haven (1982)
6. Lopes, F., Wooldridge, M., Novais, A.Q.: Negotiation among autonomous computational agents: principles, analysis and challenges. *Artif. Intell. Rev.* **29**(1), 1–44 (2008)
7. Güneş, T.D., Arditi, E., Reyhan, A.: Collective voice of experts in multilateral negotiation. In: *International Conference on Principles & Practice of Multi-agent Systems*. Springer, Cham (2017)
8. Aydoğan, R., Öztürk, P., Razeghi, Y.: Negotiation for incentive driven privacy-preserving information sharing. In: *International Conference on Principles and Practice of Multi-agent Systems*. Springer, Cham (2017)
9. Marsa-Maestre, I., Gimenez-Guzman, J.M., de la Hoz, E., et al.: Competitive belief propagation to efficiently solve complex multi-agent negotiations with network structure. In: *International Conference on Autonomous Agents and Multiagent Systems*, pp. 1–16. Springer, Cham (2017)
10. Xu, Y., et al.: Modeling and simulation of complex network attributes on coordinating large multiagent system. *Sci. World J.* (2014)
11. Vicsek, T., Czirok, A., Ben-Jacob, E., et al.: Novel type of phase transition in a system of self-driven particles (2006)
12. Duan, H.B., Qiu, X.H.: *Unmanned Aerial Vehicle Swarm Autonomous Control Based on Swarm Intelligence*. China Science Publishing & Media Ltd., Beijing (2018)

# Chapter 13

## Event Sequence T-Way Test Strategy for Events Driven System



Yuqi Liu, Daming Pei, and Shiyuan Fang

**Abstract** Event-driven softwares (EDS) are now widely developed and used. Common example of Event-driven software span multiple domains from embedded systems to web and GUI applications. Testing methods based on event executing permutation is common in software testing field. Combinatorial method has been applied to generate sequence coverage array (*SCA*) such as t-seq algorithm developed by Kuhn et al. The *SCA* generated was aimed at  $n$  distinct events which occurs exactly once in sequence. However, event may be repeatable in test sequence, because, for most reactive or event driven systems, events occur multiple times in the course of practical use. Existing sequence coverage array generated by combinatorial method may exist redundancy for repeatable events. Therefore, we propose a reduction algorithm for removing the unwanted subsequence of *SCA*. Furthermore, we introduced a direct construction method to generate one-row test sequence, which satisfy t-way permutations coverage of  $n$  events.

### 13.1 Introduction

Event-driven system taken events such as the buttons response to mouse click and commands input from keyboard as the inputs. Software reacts to event so that state is changed and then ready to the next event. Therefore, event-driven software needs to handle different kinds of events and, in theory, any event response permutations are possible. Some unexpected operation may lead to software failure. Postulate that event A and event B occupy the same resource. If event A is triggered when the resources was not released by event B, the execution sequence of B-A may cause the system failure. However, it is difficult to ensure the coverage of test sequence by designing a lot of testing combination of input order under the limited resources.

---

Y. Liu (✉) · D. Pei  
China Institute of Marine Technology & Economy, Beijing 100081, China  
e-mail: [hityql@163.com](mailto:hityql@163.com)

S. Fang  
Beijing Special Engineering and Design Institute, Beijing 100081, China

© The Author(s), under exclusive license to Springer Nature Singapore Pte Ltd. 2022  
T.-Y. Wu et al. (eds.), *Advances in Smart Vehicular Technology, Transportation, Communication and Applications*, Smart Innovation, Systems and Technologies 250,  
[https://doi.org/10.1007/978-981-16-4039-1\\_13](https://doi.org/10.1007/978-981-16-4039-1_13)

Existing t-way strategies are very useful to detect interaction fault between parameters especially when higher interaction strength but still lack of support for testing the sequence of events or parameters occurrence. Kuhn [7] provides efficient strategy using combinatorial methods but events can only happen once in one row of *SCA*. The repeatable events are very common in event driven system such as testing API call of graphical user interfaces (GUI) applications including web browser, web applications, mobile APP, etc. So considering these redundancy, generating a set of smaller test sequences on the condition of satisfying the T-way coverage requirement is meaningful.

Using combinatorial methods for generating test sequences of events was discussed in [3, 14–17] indicated the progress and achievements in t-way conventional testing and point out that all of the existing t-way strategies do not support conventional t-way testing in addition to the quick and dirty (QnD) strategy. Answer Set Programming (ASP) was used to generating event sequence test cases. [1] presents three constraint programming models from different viewpoints of sequence covering arrays and answer set programming program of the incidence matrix model for finding optimal sequence covering arrays. The approach based on an effective combination of ASP solvers and the incidence matrix can greatly improve the existing bounds of many arrays but still have limitation of huge computation work. [2] introduced a new approach that uses answer-set programming for generating *SCAs*. The event sequence obtained using ASP are significantly smaller than those generated using the greedy algorithm of Kuhn et al. [8]. [4] introduced an event sequence generation algorithm for the testing of event-driven systems in particular Android applications, which presented the method of automatically producing event sequences that result in high coverage. Farchi et al. [5] extended the classic combinatorial model to be an ordered combinatorial model that include both value and order requirements. The new model also support both parameter values and parameter orders restrictions which satisfy a wide range of testing problems. Heuristic algorithm for event sequence testing was developed. [6] presents a sequence-based interaction testing strategy using a heuristic search algorithms (Bees Algorithm) and discussed the implementation, present and compare the results with existing sequence covering array algorithm. Comparing with the test sets produced by QnD algorithm [8], the BA algorithm shown a smaller size or at least similar size. [12] did a large number of experiments using Simulated Annealing (SA) algorithm for Event Driven Input Sequence Testing to achieve optimum or near optimum test cases. The applicability of test suite generated by SA technique still need to be evaluated. [11] presents a new t-way strategy called Flower Strategy that addresses both sequence and sequence-less test generation. Experimental results, in most cases, outperform those existing t-seq [8], BA [6], and ASP [2] strategies.

Test Suite Reduction method and bounds for event sequencing testing was researched. [10] presents an algorithm and criteria for inter-window interactions based reduction, including 2way combinatorial coverage, 2way consecutive-sequence combinatorial coverage, and 2way sequence-based combinatorial coverage criteria. The reduced test suite provide promising fault-finding effectiveness. Lower and upper bounds on the size of the array given in [8] were researched by Margalit [9].

## 13.2 Background

T-way sequence iteration coverage made it possible to provide greater confidence that the system would function correctly regardless of possible dependencies between events. For testing event sequences with non-repeating events, Kuhn [7] provides efficient test sequence using combinatorial methods. A sequence-covering array,  $SCA(N, S, t)$  was defined as an  $N \times S$  matrix, which is a set of tests that ensure all t-way sequences of events have been tested. Every t-length permutation occurs in at least one row in the array and the t symbols in the permutation are not required to be adjacent.  $SCA$  is applicable for event driven systems that may exist a great many of events, where events may occur multiple times but testing multiple occurrences can not bring obvious benefits and test efficiency should have priority. Among algorithms of t-way sequence test generation were investigated, the most classical algorithm of generating sequence covering arrays were named t-seq [7]. Greedy strategy was taken to generate a large number of tests, which chooses the highest scoring test by comparing the number of previously uncovered sequences it covers. In order to explain how  $SCA$  works, taking an embedded interrupt system with four events a, b, c, d for instance. Events that each have priority in embedded system, where external interruption can have higher priority. Interruption events may happen in any time when system is running, so events can happen in any sequences. But bugs may happen when dependent relationship exist between events.

The 3-way sequence coverage is to cover all permutations of 3-length sequences [a-b-c], [a-b-d], [a-c-d], [b-c-d]. One subset of 3-way sequence is [b, c, d], which can be arranged in six permutations: [b-c-d], [b-d-c], [c-b-d], [c-d-b], [d-b-c], [d-c-b]. A test that covers the permutation [d-b-c] is: [a-d-b-c], [d-a-b-c], [d-b-a-c] or [d-b-c-a]. Table 13.1 illustrates the  $SCA$  example generated by the tool of sequence covering array generator, which can be download on the website [13].

As we can see from Table 13.1, eight tests were generated for 3-way permutation coverage of 4 events. Because of extensive human and resource involvement, the time cost for each tests is huge. But  $SCA$  testing significantly reduced test cost by reducing the number of tests.

**Table 13.1** 3-Way sequence for 4 events

Test	Event sequence			
1	a	b	c	d
2	d	c	b	a
3	c	a	d	b
4	b	d	a	c
5	c	b	d	a
6	a	d	b	c
7	d	a	c	b
8	b	c	a	d

### 13.3 The Reduction of Sequence Covering Arrays

Events may be repeatable for many types of event driven systems such as communication system and embedded control system. For repeatable events, test sequences generated by t-seq [7] may exist redundancy. Based on the rule of that failures generally triggered in the condition of whether or not a particular event had occurred prior to the other one and they are not necessary to be adjacent. Things that events occurred multiple times in one test is actually possible in practice. Consider the problem of testing four events, a, b, c and d, 8 tests generated based on 3-way interaction strength was shown in Table 13.1.

---

#### Algorithm 1 Reduction Strategy for SCA.

---

**Input:** SCA, a  $N \times S$  matrix;

//N means number of tests;

//S means event number form event set; **Output:** one row test sequence *Seq*;

```

1:  for number of reduction  $i$  from  $S - 1$  to 1 do
2:      for traverse  $j$  test from 1 to  $N - 1$  do
3:          extract the beginning and ending of  $i$  length subsequence
           frontsubseq and behindsubseq;
4:          detect whether the beginning or the ending subsequence
           of  $j + 1$  to  $N$  test is the same with  $j$  test;
5:          if exist a test that can be merged then
6:              combine two test to be a new test;
           remove the reduced test form SCA;
7:          end if
8:      end for
9:  end for
10:  combine the rest of tests together to be one test Seq;
11: return Seq;

```

---

Taking the third test [c-a-d-b] and the sixth test [a-d-b-c] for example, both test contains the subsequence [a-d-b]. that two test can be reduced to one test [c-a-d-b-c] by with removing the same subsequence, which was in the side of the test sequence and where symbols included was adjacent. Compared with these two test, the combined test covers the same number of uncovered sequence with just 5 events. To reduce the subsequence redundancy, We proposed a Max-Reduction strategy for t-seq covering array. Test cost can be reduced by reducing the events number of tests. The reduction strategy that reduces event of test by removing sequences that do not contribute to a coverage requirement is shown in Algorithm 1.

**Reduction Criteria:** We adopt the greedy strategy to achieve the maximum reduction. Tests contains the longer length of subsequence have the priority to be combined. The reduction algorithm need up to  $n-1$  times iteration for reduce from  $n-1$  to 1 length sequence. Both side of sequence will be detected for the presence of sequence that can be reduced.

Event sequence [d-c-b-a-b-c-d-c-b-d-a-c-b-c-a-d-b-c] can be generated by the algorithm I. Event number of test sequence is 18 comparing to 32 events of 8 test in Table 13.1. *SCA*(8, 5, 3) [13] can be reduced to one-row sequence [b-a-e-d-c-b-a-b-c-d-e-a-c-b-d-e-a-d-a-e-b-c-e-a-d-b-c-a-e] with a reduction of over 27% of the event redundancy. Time and material cost can be reduced for the decrease in even number of test.

---

#### Algorithm 2 Direct Construction Strategy .

---

**Input:** event number  $n$ , iteration strength  $t$ ;

**Output:** one-row test sequence  $Seq$ ;

- 1: generate initial test sequence by listing  $n$  events in one row;
  - 2: judge the number of covering t-way sequence and mark on the covered sequence;
  - 3: **while** all t-way sequences not covered **do**
  - 4:     construct candidate solution: append every event of  $n$  event set behind of the current test sequence to be  $n$  candidate sequence  $seq_i$ ;
  - 5:     select the best candidate sequence from  $seq_n$  that cover more sequences;
  - 6: **end while**
  - 7: **return**  $Seq$ ;
- 

### 13.4 Sequence Coverage Algorithm

Even if the event number of *SCA* has been decreased by the reduction algorithm, there still have redundancy in tests for events which are repeatable in one test. The reduction algorithm only removed duplicate subsequence at the sides of sequences. A direct construction algorithm for generating t-way sequence were produced by greedy strategy. As is shown in Algorithm 2, candidate solution that covers most uncovered sequences will be chosen to be the current best solution during the construction of one-row sequence.

Tables 13.2 and 13.3 respectively, show the 3-way sequence and 4-way sequence test generated by using Algorithm 2. The event number of *SCA* tests generated by t-seq method, tests produced by *SCA* reduction strategy and tests given by direct construction method was compared in Table 13.4.

Event number of *SCA* generated by the t-seq algorithm was given in [7], and the benchmark of t-way sequence tests for 3-way and 4-way permutation coverage are available on the web site [13].

The events number of *SCA* reduction in Table 13.4 was calculated based on the sequence generated by reducing the *SCA* benchmark. Events number of Sequence was counted by the sequence generated by algorithm II. It is surprising that the generated events sequence has a strong regularity in the structure. One-row

**Table 13.2** 3-way sequence generated by direct construction strategy

Events	3-way sequence
5	a-b-c-d-e-a-b-c-d-a-e-b-c
6	a-b-c-d-e-f-a-b-c-d-e-a-f-b-c-d
7	a-b-c-d-e-f-g-a-b-c-d-e-f-a-g-b-c-d-e
8	a-b-c-d-e-f-g-h-a-b-c-d-e-f-g-a-h-b-c-d-e-f

**Table 13.3** 4-way sequence generated by direct construction strategy

Events	4-way sequence
5	a-b-c-d-e-a-b-c-d-e-a-b-c-d-a-e-b
6	a-b-c-d-e-f-a-b-c-d-e-f-a-b-c-d-e-a-f-b-c
7	a-b-c-d-e-f-g-a-b-c-d-e-f-g-a-b-c-d-e-f-a-g-b-c-d
8	a-b-c-d-e-f-g-h-a-b-c-d-e-f-g-h-a-b-c-d-e-f-g-a-h-b-c-d-e

**Table 13.4** Number of events for 3-way and 4-way sequence

Events	t-way seq		SCA reduction		Seq		Events	t-way seq		SCA reduction		Seq	
	3-seq	4-seq	3-seq	4-seq	3-seq	4-seq		3-seq	4-seq	3-seq	4-seq	3-seq	4-seq
5	40	145	29	13	74	17	19	418	2432	404	2287	55	73
6	60	228	47	154	16	21	20	440	2680	422	2523	58	77
7	84	350	67	277	19	25	21	462	2814	443	2664	61	81
8	112	448	77	337	22	29	22	484	3080	470	2928	64	85
9	126	612	114	489	25	33	23	552	3358	534	3192	67	89
10	140	720	128	609	28	37	24	576	3504	557	3347	70	93
11	154	858	143	746	31	41	25	600	4108	582	3647	73	97
12	192	1032	180	917	34	45	26	624	4320	611	3947	76	101
13	208	1196	197	1070	37	49	27	702	4536	684	4156	79	105
14	224	1400	213	1272	40	53	28	728	4814	712	4369	82	109
15	270	1620	254	1486	43	57	29	754	4980	732	4646	85	113
16	288	1792	277	1653	46	61	30	780	7920	764	4800	88	117
17	340	2006	322	1865	49	65	40	1280	10700	1261	7742	85	121
18	360	2196	347	2059	52	69							

sequence based on 3-way sequence of 5 events can be split to 3 sections: a-b-c-d-e a-b-c-da-e-b-c. Compared with 3-way sequence of 6 events, the one-row sequence is a-b-cd-e-f a-b-c-d-e a-f-b-c-d. Meanwhile, the 4-way sequences have the similar rules. 4-way sequence of 5 events is a-b-c-d-e a-b-c-d-e a-b-c-d-a-e-b. 5-way sequence of 6 events is a-b-c-d-e-f a-b-c-d-e-f a-b-c-d-e-f a-b-c-d-e a-f-b (Fig. 13.1).

According to the above examples, t-way sequence of n events can be generated by the combination of 3 subsequence: first subsequence is the repetition of n events arranged in same order for  $t_2$  times; the second is the front  $n_1$  events of n events in



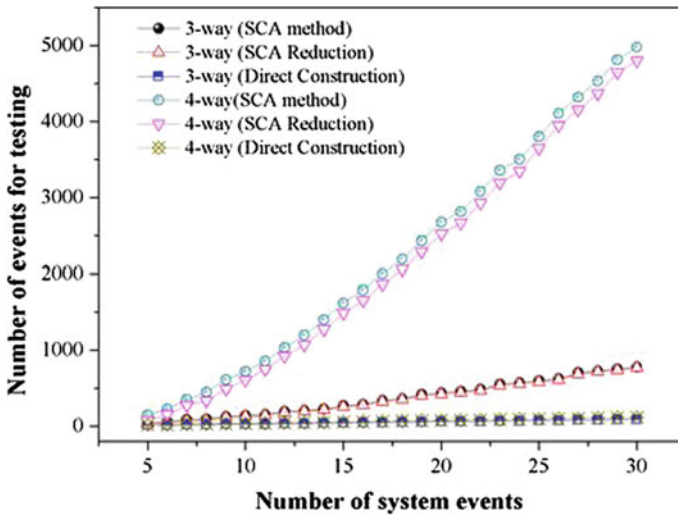


Fig. 13.1 The comparison of events number between *SCA* generated by t-seq algorithm, the reduction of *SCA* and direct construction sequence

the same order; the third subsequence is the front  $n_{t+1}$  events of  $n$  events sequence and the last event is inserted into the second place.

It can be found from Table 13.4 that the reduction strategy was efficient to a certain extent, but very finite in reducing the number of events. However, the direct construction method shows an obvious decrease in event number. In order to show the growth in the number of test events generated by the three methods with the increase in events under test, Fig. 13.1 is given.

### 13.5 Conclusions and Future Work

We have presented a reduction strategy to reduce the sequence coverage redundancy of *SCA* and a direct construction method to generate t-way testing sequence for event driven system, where a large number of events are repeatable in one test. The proposed strategy had shown a promising result. Test cost was reduced by decreasing the event number of test sequences, and it will save the time cost of testing especially systems that require manual or physical operation.

Future work will expand to improve the algorithm so that it could support not only uniform strength sequence interaction, but also to support variable strength. Another direction is that we are currently extending the algorithm to support sequence constraints. Finally, we are exploring the test case generation method for the fault localization of order-faults.

**Acknowledgements** The authors would like to thank Kuhn, D. Richard for providing the tool of Sequence Covering Array Generator.

## Appendix: Verify T-Way Coverage of Sequence Generated by Direct Construction Method

To verify t-way coverage of the sequence generated by direct construction method, taken the 3-way sequence of 4 events as example. In order to satisfy 3-way order coverage requirement of 4 events, [a-b-c], [a-c-b], [b-a-c], [b-c-a], [c-b-a], [c-a-b], [a-b-d], [a-d-b], [b-a-d], [b-d-a], [d-b-a], [d-a-b], [a-c-d], [a-d-c], [c-a-d], [c-d-a], [d-c-a], [d-a-c], [b-c-d], [b-d-c], [c-b-d], [c-d-b], [d-c-b], [d-b-c] must be covered. [a-b-c-d-a-b-c-a-d-b] is the result given by algorithm II based on the direct construction strategy. It is easy to verify that all the 3-length sequences listed above are covered by the sequence.

## References

1. Banbara, M., Tamura, N., Inoue, K.: Generating event-sequence test cases by answer set programming with the incidence matrix (2012)
2. Barin, M., Erdem, E., Inoue, K., Oetsch, J., Puhner, J., Tompits, H., Yilmaz, C., Yilmaz, C.: Event-sequence testing using answer-set programming. *Int. J. Adv. Softw.* **5**(3 and 4), 237–251 (2012)
3. Brooks, P.A., Memon, A.M.: Introducing a test suite similarity metric for event sequence-based test cases. In: *IEEE International Conference on Software Maintenance*, pp. 243–252 (2009)
4. Capsper, A.M., Jensen, S., Prasad, R.: Automated testing with targeted event sequence generation. In: *International Symposium on Software Testing and Analysis*, pp. 67–77 (2013)
5. Farchi, E., Segall, I., Tzoref-Brill, R., Zlotnick, A.: Combinatorial testing with order requirements. In: *2014 IEEE Seventh International Conference on Software Testing, Verification and Validation Workshops (ICSTW)*, Los Alamitos, CA, USA, Apr 2014, pp. 118–127. IEEE Computer Society
6. Hazli, M., Zamli, K.Z., Othman, R.R.: Sequence-based interaction testing implementation using bees algorithm. In: *2012 IEEE Symposium on Computers and Informatics (ISCI)* (2012)
7. Kuhn, D.R., Higdon, J.M., Lawrence, J.F., Kacker, R.N., Lei, Y.: Combinatorial methods for event sequence testing. *IEEE Comput. Soc.* (2012)
8. Kuhn, D.R., Higdon, J.M., Lawrence, J.F., Kacker, R.N., Lei, Y.: Efficient methods for interoperability testing using event sequences. *Crosstalk J. Defense Softw. Eng.* (2012)
9. Margalit, O.: Better bounds for event sequencing testing. In: *2013 IEEE Sixth International Conference on Software Testing, Verification and Validation Workshops*, pp. 281–284 (2013)
10. Mayo, Q., Michaels, R., Bryce, R.: Test suite reduction by combinatorial-based coverage of event sequences. In: *2014 IEEE Seventh International Conference on Software Testing, Verification and Validation Workshops*, pp. 128–132 (2014)
11. Nasser, A.B., Hujainah, F., Alsewari, A., Zamli, K.Z.: Sequence and sequence-less t-way test suite generation strategy based on flower pollination algorithm. In: *2015 IEEE Student Conference on Research and Development (SCORED)* (2016)

12. Rahman, M., Othman, R.R., Ahmad, R.B., Rahman, M.M.: Event driven input sequence t-way test strategy using simulated annealing. In: 2014 5th International Conference on Intelligent Systems, Modelling and Simulation, pp. 663–667 (2014)
13. Richard, K.D.: Sequence Covering Array Library. Available at: <http://cs.nyu.edu/totok/professional/software/tpcw/tpcw.html>
14. Wang, W., Sampath, S., Yu, L., Kacker, R.: An interaction-based test sequence generation approach for testing web applications. In: 2008 11th IEEE High Assurance Systems Engineering Symposium (2008)
15. Xun, Y., Cohen, M.B., Memon, A.M.: Covering array sampling of input event sequences for automated GUI testing. In: 22nd IEEE/ACM International Conference on Automated Software Engineering (ASE), Atlanta, Georgia, USA, 5–9 Nov 2007
16. Xun, Y., Memon, A.M.: Generating event sequence-based test cases using GUI runtime state feedback. *IEEE Trans. Softw. Eng.* **36**(1), 81–95 (2010)
17. Zamli, K.Z., Othman, R.R., Zabil, M.: On sequence based interaction testing. *Comput. Inform.* 662–667 (2011)

**Part III**  
**Artificial Intelligence**

# Chapter 14

## QUasi-Affine TRansformation Evolutionary Algorithm for Feature Selection



Zhi-Gang Du, Tien-Szu Pan, Jeng-Shyang Pan, and Shu-Chuan Chu

**Abstract** QUasi-Affine TRansformation Evolutionary Algorithm (QUATRE) is a currently emerging meta-heuristic evolutionary algorithm. QUATRE has the ability to balance exploitation and exploration in the optimization process, and the algorithm optimization uses matrix operations to greatly reduce the time complexity for solving the same problem. This series of advantages makes this algorithm adopted by a large number of researchers. In this paper, QUATRE is used to optimize the Feature Selection (FS) of the wrapper method. K-Fold Cross-Validation (KFCV) method is also used to divide the test set and training set of the sample, and then use the K Nearest Neighbor (KNN) algorithm for feature classification. In the optimization process, we use a threshold (*choice*) for feature identification to select useful features. Finally, the 9 standard test data sets in UCI are used to verify the effectiveness of the QUATRE algorithm.

---

Z.-G. Du · J.-S. Pan · S.-C. Chu (✉)

College of Computer Science and Engineering, Shandong University of Science and Technology, Qingdao 266590, China

e-mail: [15254200640@163.com](mailto:15254200640@163.com)

T.-S. Pan

Department of Electronic Engineering, National Kaohsiung University of Science and Technology, Kaohsiung, Taiwan

e-mail: [tpan@nkust.edu.tw](mailto:tpan@nkust.edu.tw)

J.-S. Pan

College of Information Science and Technology, Dalian Maritime University, Dalian 116026, China

S.-C. Chu

College of Science and Engineering, Flinders University, 1284 South Road, Clovelly Park, SA 5042, Australia

## 14.1 Introduction

In machine learning, the curse of dimensionality will appear as the sample dimensionality increases [23, 33]. However, in today's information society, there are thousands of pieces of information generated at all times [25]. This has led researchers to use various methods to select valuable data information from these data, and discard features that are not important or relevant in pattern recognition and machine learning [7]. Therefore, it is becoming more and more important to reduce sample dimensions from the original data set and feature selection methods with higher accuracy [42]. Feature selection generally includes three methods: Wrapper, Embedded, and Filter. The filter is the process of feature selection is integrated with the process of classifier learning, and feature selection is performed during the learning process. The most common use of L1 regularization for feature selection. According to the objective function, the wrapper selects several features or excludes several features at a time until the best subset is selected. Embedding). First, use some machine learning algorithms and models for training to obtain the weight coefficients of each feature, and select the features from large to small according to the coefficient. Similar to the filter method, but through training to determine the pros and cons of features.

In real life, an object often has many features (also called attributes), which are mainly divided into related features, irrelevant features, and redundant features. Feature selection is to select  $M$  ( $M < N$ ) sub-features from  $N$  features, and in the  $M$  sub-features, the criterion function can reach the optimal solution. That is to say, by choosing as few sub-features as possible, the effect of the model will not decrease significantly, and the category distribution of the results is as close to the real category as possible [14]. For a sample data with  $N$  features,  $2^N - 1$  feature subsets can be generated, and feature selection is to select the best subset for a specific task from these. Feature selection is also an NP problem. That is, when  $N$  increases infinitely, there is no method other than an exhaustive search that can guarantee the optimal feature subset. Feature selection mainly includes four steps: generating candidate feature subsets, evaluating the quality of feature subsets, deciding when to stop, and whether the feature subsets are valid [10, 13].

The meta-heuristic algorithm is also called a kind of uncertainty algorithm proposed relative to the optimized deterministic algorithm [15, 22, 24]. Uncertainty refers to when the optimization algorithm of a problem can determine the optimal solution of the problem [5, 15], and the meta-heuristic algorithm is an algorithm based on intuition or empirical construction [16], which can spend an acceptable cost referring to the calculation time A feasible solution of the problem is given under (and space), and the degree of deviation of the feasible solution from the optimal solution may not be predicted in advance [2, 40]. However, as the dimensions of problems, in reality, continue to increase, deterministic optimization methods are often computationally time-consuming [4, 9]. Moreover, the problems to be optimized in reality often have various limitations, such as non-differentiation. In order to break through this limitation, the meta-heuristic algorithm came into being [1, 27].

After decades of development, many classic algorithms have been widely used in real life problems [31, 35]. Researchers were inspired by the foraging behavior of birds to generate particle swarm optimization (PSO) [3, 12], which mainly solves continuous problems in real life. Ant Colony Optimization (ACO) simulates the pheromone release of ant colonies in the process of searching for food to guide subsequent ants to foraging behavior, mainly to solve the discrete problem in the real world [6, 41]. Cat Swarm Optimization (CSO) is inspired by the group behavior of cats preying on prey [8, 37, 38]. Meta-heuristic evolutionary algorithms also include Cuckoo Search Algorithm (CSA) [30], Differential Evolution (DE) [20, 26, 29, 39], Artificial Bee Colony (ABC) [18, 32, 36], etc.

QUasi-Affine TRansformation Evolutionary Algorithm (QUATRE) is a meta-heuristic algorithm with a new evolutionary structure proposed by Z. Meng and others [11, 19, 21]. QUATRE overcomes the shortcomings of the existing algorithms, such as the reduction of population diversity as the evolution progresses, and the premature convergence of the algorithm into a local optimum [17, 28, 34]. This paper uses the excellent convergence performance of the QUATRE algorithm for feature selection. We mark each feature by using a threshold. When the dimension representing each feature is greater than the threshold, we consider the feature to be a relevant feature. Otherwise, it is redundant or irrelevant features. Then, perform K-fold cross-validation on the selected samples and use KNN to evaluate the selected features.

The rest of this paper will be discussed in the following parts. Section 14.2 briefly introduces the QUATRE algorithm, the KNN algorithm and the K-fold cross-validation method. Section 14.3 discusses in detail the main architecture for feature selection using the QUATRE algorithm. Section 14.4 presents and analyzes the experimental results of 9 benchmark test data sets based on UCI. Finally, we give relevant conclusions.

## 14.2 Related Work

### 14.2.1 QUasi-Affine TRansformation Evolutionary

The QUATRE algorithm simulates the process of quasi-affine transformation from one affine space to another affine space in the geometric space. Equation 14.1 gives the evolution formula of QUATRE.

$$\mathbf{X} \Leftarrow \mathbf{M} \otimes \mathbf{X} + \bar{\mathbf{M}} \otimes \mathbf{B}, \quad (14.1)$$

where  $\mathbf{X} = [\mathbf{x}_1, \mathbf{x}_2, \dots, \mathbf{x}_{ps}]^T$  is the population position matrix,  $\mathbf{x}_i = (x_{i1}, x_{i2}, \dots, x_{iD})$  is the position vector of the  $i$ th particle,  $ps$  is the population size,  $D$  is the dimension of the problem space and  $\otimes$  represents the multiplication operator by the corresponding

**Table 14.1** Seven generation schemes of evolution matrix **B**.

No.	QUATRE/x/y	Equation
1	QUATRE/rand/1	$\mathbf{B} = \mathbf{X}_{r1} + F \times (\mathbf{X}_{r2} - \mathbf{X}_{r3})$
2	QUATRE/best/1	$\mathbf{B} = \mathbf{X}_{\text{gbest}} + F \times (\mathbf{X}_{r1} - \mathbf{X}_{r2})$
3	QUATRE/target/1	$\mathbf{B} = \mathbf{X} + F \times (\mathbf{X}_{r1} - \mathbf{X}_{r2})$
4	QUATRE/target-to-best/1	$\mathbf{B} = \mathbf{X}_{\text{gbest}} + F \times (\mathbf{X}_{\text{gbest}} - \mathbf{X}) + F \times (\mathbf{X}_{r1} - \mathbf{X}_{r2})$
5	QUATRE/rand/2	$\mathbf{B} = \mathbf{X}_{r1} + F \times (\mathbf{X}_{r2} - \mathbf{X}_{r3}) + F \times (\mathbf{X}_{r4} - \mathbf{X}_{r5})$
6	QUATRE/best/2	$\mathbf{B} = \mathbf{X}_{\text{gbest}} + F \times (\mathbf{X}_{r1} - \mathbf{X}_{r2}) + F \times (\mathbf{X}_{r3} - \mathbf{X}_{r4})$
7	QUATRE/target/2	$\mathbf{B} = \mathbf{X} + F \times (\mathbf{X}_{r1} - \mathbf{X}_{r2}) + F \times (\mathbf{X}_{r3} - \mathbf{X}_{r4})$

position (the ‘.\*’ operation in Matlab). **B** is a mutation matrix, and there are seven generation methods as shown in Table 14.1.

Where  $\mathbf{X}_{r1}, \mathbf{X}_{r2}, \mathbf{X}_{r3}, \mathbf{X}_{r4}, \mathbf{X}_{r5}$  are five different matrices that perform random row transformation on the **X** matrix.  $\mathbf{X}_{r1} - \mathbf{X}_{r2}$  is the difference matrix of the two matrices of  $\mathbf{X}_{r1}$  and  $\mathbf{X}_{r2}$ .  $F$  is the coordination coefficient, which is set to 0.7.  $\mathbf{X}_{\text{gbest}} = [\mathbf{x}_{\text{gbest}}, \mathbf{x}_{\text{gbest}}, \dots, \mathbf{x}_{\text{gbest}}]^T$  is the optimal position matrix, and  $\mathbf{x}_{\text{gbest}}$  is the position vector of the current optimal individual.

**M** is the contribution matrix, and its matrix elements have only two values, 0 and 1.  $\bar{\mathbf{M}}$  is the binary inverse operation matrix of the corresponding bit inversion of the **M** matrix. The inverse of the 0 is 1, and the corresponding relationship between 0, **M** and  $\bar{\mathbf{M}}$  is shown in Eq. 14.2.

$$\mathbf{M} = \begin{bmatrix} 0 & 0 & 1 \\ 1 & 0 & 0 \\ 1 & 1 & 0 \end{bmatrix} \quad \bar{\mathbf{M}} = \begin{bmatrix} 1 & 1 & 0 \\ 0 & 1 & 1 \\ 0 & 0 & 1 \end{bmatrix} \quad (14.2)$$

When the population number  $ps$  is greater than the dimension  $D$  (if  $ps = A \times D + C$ ), the **M** matrix will be initialized first. It is composed of  $D \times D$  lower triangular matrices of and the first  $C$  rows of the lower triangular matrix. Then, perform random row transformation to form the **M** matrix.

### 14.2.2 *K Nearest Neighbor (KNN) Method*

KNN is to judge the category of unknown samples. Its implementation principle is based on the samples of all known categories as a reference, calculates the distance between the unknown sample and all known samples, and selects the  $K$  known samples closest to the unknown. Obey the majority-voting rule, and classify the unknown sample and the  $K$  nearest neighbor samples into one category. Since the KNN Nearest Neighbor classification algorithm only determines the category of the sample to be classified based on the category of the nearest one or several samples



in the classification decision, rather than relying on the method of discriminating the class domain to determine the category, so for the class domain KNN method is more suitable than other methods for the sample sets to be divided with more crossover or overlap.

The key to the realization of the KNN algorithm has the following three points: (1) All the characteristics of the sample must be quantified comparatively. If there are non-numerical types in the sample characteristics, measures must be taken to quantify them into numerical values. For example, the sample feature contains color, and the distance calculation can be realized by converting the color to gray value. (2) Sample features need to be normalized. The sample has multiple parameters, each of which has its own domain and value range. Their influence on distance calculation is different. For example, the influence of a larger value will cover the parameter with a smaller value. Therefore, the sample parameters must be scaled. The simplest way is to normalize the values of all features. (3) A distance function is needed to calculate the distance between two samples. The commonly used distance functions are Euclidean distance, cosine distance, Hamming distance, Manhattan distance, etc. Euclidean distance is generally selected as the distance metric, but this Yes only applies to continuous variables. In the case of discontinuous variables such as text classification, Hamming distance can be used as a metric. Under normal circumstances, if some special algorithms are used to calculate the metric, the accuracy of K Nearest Neighbor classification can be significantly improved, such as the use of large edge nearest neighbor method or nearest neighbor component analysis method.

Taking the calculation of the distance between  $\mathbf{A} : (x_1, x_2, \dots, x_D)$  and  $\mathbf{B} : (y_1, y_2, \dots, y_D)$  in a D-dimensional space as an example, Eqs. 14.3 and 14.4 give the calculation formulas of Euclidean distance and Manhattan distance, respectively.

$$\text{Euc}_D = \left( \sum_{i=1}^D (x_i - y_i)^2 \right)^{\frac{1}{2}} \quad (14.3)$$

$$\text{Man}_D = \sum_{i=1}^D |x_i - y_i| \quad (14.4)$$

### 14.3 QUATRE Algorithm for Feature Selection

In the optimization process of feature selection, the fitness function is very important for the classification result. In the process of designing the fitness function, we should pay attention to two performance indicators, one is the error value  $\text{KE}(\cdot)$  obtained through K-fold cross-validation for  $\mathbf{x}'$ , and the other is the number  $T$  of selected features. Fitness function as shown in Eq. 14.5.

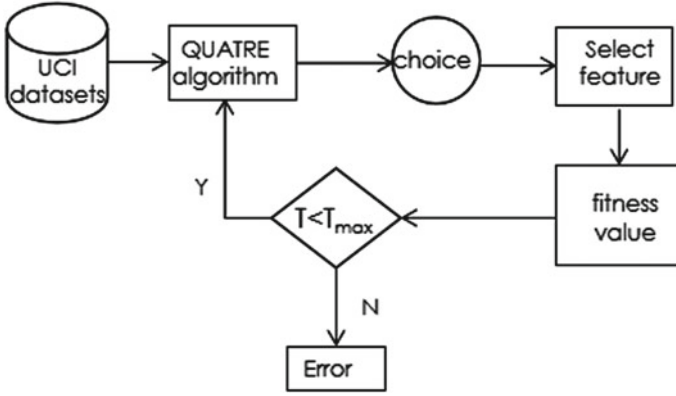


**Fig. 14.1** QUATRE's flow chart for feature selection

$$F = c_1 \times \text{KE}(\mathbf{x}') + c_2 \times \frac{T}{N}, \quad (14.5)$$

where  $N$  is the total number of features,  $c_1$  and  $c_2$  are two coefficients, which are set to 0.99 and 0.01, respectively.  $\mathbf{x}'$  is the feature label vector determined for  $\mathbf{x}$  according to the threshold choice. When the correlation dimension is 0, it means it is irrelevant to the feature, and when it is 1, it is relevant. The conversion rule is shown in formula 5.

$$b_{ij} = \begin{cases} 1, & \text{if } x_{ij} \geq \text{choice} \\ 0, & \text{others} \end{cases}, \quad (14.6)$$

where  $\mathbf{x}'_i = (b_{i1}, \dots, b_{ij}, \dots, b_{iD})$  and  $\mathbf{x}_i = (x_{i1}, \dots, x_{ij}, \dots, x_{iD})$  ( $j = 1, 2, \dots, D$ ) are the mark feature vector and the vector generated by the QAUTRE algorithm, respectively. The overall architecture of QUATRE algorithm applied to FS is shown in Fig. 14.1.

## 14.4 Experimental Results

There are several key parameters that need to be set in the experimental simulation of feature selection of QUATRE and other comparison algorithms. The population size  $ps$  of several comparison algorithms is set to 100, the maximum number of iterations  $T_{\max}$  is set to 100, the number of classifications  $K1$  in KNN is set to 2, and the number of sub-sets  $K2$  in  $K$  cross-validation is set to 5. In the feature selection application, the search boundary range of all comparison algorithms is  $[0, 1]$ , and we can also consider this value as the probability that the feature corresponding to the dimension is a related feature. The specific descriptions of the nine test sets in the UCI used are shown in Table 14.2.

**Table 14.2** Description of the 9 test sets in UCI

No.	Name	Instances	Number of features ( $D$ )
1	Breast	277	9
2	Glass	214	9
3	Heart	303	13
4	Ionosphere	351	34
5	Vehicle	846	18
6	Vote	435	16
7	Wine	178	13
8	Wpbc	198	33
9	Zoo	101	16

**Table 14.3** The average of 10 experimental results of feature selection between QUATRE and other compared algorithms

Name	QUATRE	DE	PSO	GA
Breast	<b>0.216112716</b>	0.281320626	0.329546216	0.385940329
Glass	<b>0.29341433</b>	0.372776467	0.38884776	0.445346747
Heart	<b>0.146052551</b>	0.222789059	0.322111333	0.379684368
Ionosphere	<b>0.100254148</b>	0.147363906	0.185015907	0.205239107
Vehicle	<b>0.252163121</b>	0.324223987	0.389910862	0.463097432
Vote	<b>0.036285345</b>	0.115308332	0.191776519	0.242430897
Wine	<b>0.042358686</b>	0.105133173	0.197194362	0.276414434
Wpbc	<b>0.173772727</b>	0.252651809	0.335215409	0.393911591
Zoo	<b>0.035011139</b>	0.122521627	0.128078693	0.136345532

In order to better demonstrate the excellent performance of QUATRE algorithm in feature selection, PSO, DE, and GA algorithms are used for comparison experiments. Each algorithm is run 10 times independently based on 9 benchmark test data sets and averaged. The corresponding results are given in Table 14.3.

From the comparison data in table, we can clearly see that the QAUTRE algorithm is more accurate than the other three compared algorithms in the application of feature selection.

## 14.5 Conclusion

This paper uses the QUATRE algorithm for feature selection, and the search space is between 0 and 1. The features corresponding to each dimension are distinguished between related and irrelevant features by means of thresholds. The use of thresh-

old reduces the continuous variables of each dimension to two values of 0 and 1. This work also uses KNN with K-fold cross-validation to calculate related classification feature errors. By using the method of reducing the error value to improve the accuracy of feature selection. Compared with other algorithms in the application of feature selection, the experimental effects show that QAUTRE algorithm has a powerful convergence advantage.

In future work, we will further analyze numerous optimization approaches of intelligent algorithms to cope with increasingly complex real-world problems. We also need to further improve the feature selection model framework and improve the accuracy of feature selection.

## References

1. Chai, Q.w., Chu, S.C., Pan, J.S., Hu, P., Zheng, W.m.: A parallel WOA with two communication strategies applied in dv-hop localization method. *EURASIP J. Wirel. Commun. Netw.* **2020**(1), 1–10 (2020)
2. Chai, Q.W., Chu, S.C., Pan, J.S., Zheng, W.M.: Applying adaptive and self assessment fish migration optimization on localization of wireless sensor network on 3-d terrain. *J. Inf. Hiding Multimed. Signal Process.* **11**(2), 90–102
3. Chang, J.F., Roddick, J.F., Pan, J.S., Chu, S.: A parallel particle swarm optimization algorithm with communication strategies. *J. Inf. Sci. Eng.* **21**, 809–818 (2005)
4. Chu, S.C., Du, Z.G., Pan, J.S.: Symbiotic organism search algorithm with multi-group quantum-behavior communication scheme applied in wireless sensor networks. *Appl. Sci.* **10**(3), 930 (2020)
5. Chu, S.C., Huang, H.C., Roddick, J.F., Pan, J.S.: Overview of algorithms for swarm intelligence. In: *International Conference on Computational Collective Intelligence*, pp. 28–41. Springer (2011)
6. Chu, S.C., Roddick, J.F., Pan, J.S.: Ant colony system with communication strategies. *Inf. Sci.* **167**(1–4), 63–76 (2004)
7. Chu, S.C., Roddick, J.F., Su, C.J., Pan, J.S.: Constrained ant colony optimization for data clustering. In: *Pacific Rim International Conference on Artificial Intelligence*, pp. 534–543. Springer (2004)
8. Chu, S.C., Tsai, P.W., Pan, J.S.: Cat swarm optimization. In: *9th Pacific Rim International Conference on Artificial Intelligence*, pp. 854–858. Springer (2006)
9. Chu, S.C., Xue, X., Pan, J.S., Wu, X.: Optimizing ontology alignment in vector space. *J. Internet Technol.* **21**(1), 15–22 (2020)
10. Du, Z.G., Pan, J.S., Chu, S.C., Chiu, Y.J.: Improved binary symbiotic organism search algorithm with transfer functions for feature selection. *IEEE Access* **8**, 225730–225744 (2020)
11. Du, Z.G., Pan, J.S., Chu, S.C., Luo, H.J., Hu, P.: Quasi-affine transformation evolutionary algorithm with communication schemes for application of RSSI in wireless sensor networks. *IEEE Access* **8**(2020)
12. Eberhart, R., Kennedy, J.: Particle swarm optimization. In: *Proceedings of the IEEE International Conference on Neural Networks*, vol. 4, pp. 1942–1948 (1995)
13. Gao, M., Pan, J.S., Li, J.p., Zhang, Z.p., Chai, Q.W.: 3-d terrains deployment of wireless sensors network by utilizing parallel gases Brownian motion optimization. *J. Internet Technol.* **22**(1), 13–29 (2021)
14. Hu, P., Pan, J.S., Chu, S.C.: Improved binary grey wolf optimizer and its application for feature selection. *Knowl.-Based Syst.* 105746 (2020)

15. Hu, P., Pan, J.S., Chu, S.C., Chai, Q.W., Liu, T., Li, Z.C.: New hybrid algorithms for prediction of daily load of power network. *Appl. Sci.* **9**(21), 4514 (2019)
16. Li, W., Yan, W., Ding, Q., Zhang, R., Chen, Y.C.: Discrete synchronization method for continuous chaotic systems and its application in secure communication. *J. Netw. Intell.* **5**(2), 62–76 (2020)
17. Liu, N., Pan, J.S., Wang, J., Nguyen, T.T.: An adaptation multi-group quasi-affine transformation evolutionary algorithm for global optimization and its application in node localization in wireless sensor networks. *Sensors* **19**(19), 4112 (2019)
18. Luo, R., Pan, T.S., Tsai, P.W., Pan, J.S.: Parallelized artificial bee colony with ripple-communication strategy. In: 2010 Fourth International Conference on Genetic and Evolutionary Computing, pp. 350–353. IEEE (2010)
19. Meng, Z., Pan, J.S.: Quasi-affine transformation evolution with external archive (QUATRE-EAR): an enhanced structure for differential evolution. *Knowl.-Based Syst.* **155**, 35–53 (2018)
20. Meng, Z., Pan, J.S., Tseng, K.K.: Pade: an enhanced differential evolution algorithm with novel control parameter adaptation schemes for numerical optimization. *Knowl.-Based Syst.* **168**(9), 80–99 (2019)
21. Meng, Z., Pan, J.S., Xu, H.: Quasi-affine transformation evolutionary (QUATRE) algorithm: a cooperative swarm based algorithm for global optimization. *Knowl.-Based Syst.* **109**, 104–121 (2016)
22. Nguyen, T.T., Pan, J.S., Dao, T.K.: A compact bat algorithm for unequal clustering in wireless sensor networks. *Appl. Sci.* **9**, 1973 (2019)
23. Nguyen, T.T., Pan, J.S., Dao, T.K.: An improved flower pollination algorithm for optimizing layouts of nodes in wireless sensor network. *IEEE Access* **7**, 75985–75998 (2019)
24. Pan, J.S., Hu, P., Chu, S.C.: Novel parallel heterogeneous meta-heuristic and its communication strategies for the prediction of wind power. *Processes* **7**(11), 845 (2019)
25. Pan, J.S., Li, J.B., Lu, Z.M.: Adaptive quasiconformal kernel discriminant analysis. *Neuro-computing* **71**(13–15), 2754–2760 (2008)
26. Pan, J.S., Liu, N., Chu, S.C.: A hybrid differential evolution algorithm and its application in unmanned combat aerial vehicle path planning. *IEEE Access* **8**, 17691–17712 (2020)
27. Pan, J.S., Meng, Z., Chu, S.C., Xu, H.R.: Monkey king evolution: an enhanced ebb-tide-fish algorithm for global optimization and its application in vehicle navigation under wireless sensor network environment. *Telecommun. Syst.* **65**(3), 351–364 (2017)
28. Pan, J.S., Meng, Z., Xu, H., Li, X.: Quasi-affine transformation evolution (QUATRE) algorithm: A new simple and accurate structure for global optimization. In: International Conference on Industrial, Engineering and Other Applications of Applied Intelligent Systems, vol. 9799, pp. 657–667 (2016)
29. Pan, J.S., Meng, Z., Xu, H., Li, X.: A matrix-based implementation of de algorithm: the compensation and deficiency. In: International Conference on Industrial, Engineering and Other Applications of Applied Intelligent Systems, pp. 72–81. Springer (2017)
30. Pan, J.S., Song, P.C., Chu, S.C., Peng, Y.J.: Improved compact cuckoo search algorithm applied to location of drone logistics hub. *Mathematics* **8**(3), 333 (2020)
31. Pan, J.S., Tsai, P.W., Liao, Y.B.: Fish migration optimization based on the fishy biology. In: 2010 Fourth International Conference on Genetic and Evolutionary Computing, pp. 783–786. IEEE (2010)
32. Song, P.C., Pan, J.S., Chu, S.C.: A parallel compact cuckoo search algorithm for three-dimensional path planning. *Appl. Soft Comput.* **94**, 106443 (2020)
33. Sun, C., Jin, Y., Cheng, R., Ding, J., Zeng, J.: Surrogate-assisted cooperative swarm optimization of high-dimensional expensive problems. *IEEE Trans. Evol. Comput.* **21**(4), 644–660 (2017)
34. Sun, X.X., Pan, J.S., Chu, S.C., Hu, P., Tian, A.Q.: A novel pigeon-inspired optimization with quasi-affine transformation evolutionary algorithm for dv-hop in wireless sensor networks. *Int. J. Distrib. Sens. Netw.* **16**(6), 1550147720932749 (2020)
35. Tian, A.Q., Chu, S.C., Pan, J.S., Cui, H., Zheng, W.M.: A compact pigeon-inspired optimization for maximum short-term generation mode in cascade hydroelectric power station. *Sustainability* **12**(3), 767 (2020)

36. Tsai, P.W., Khan, M.K., Pan, J.S., Liao, B.Y.: Interactive artificial bee colony supported passive continuous authentication system. *IEEE Syst. J.* **8**(2), 395–405 (2012)
37. Tsai, P.W., Pan, J.S., Chen, S.M., Liao, B.Y.: Enhanced parallel cat swarm optimization based on the Taguchi method. *Expert Syst. Appl.* **39**(7), 6309–6319 (2012)
38. Tsai, P.W., Pan, J.S., Chen, S.M., Liao, B.Y., Hao, S.P.: Parallel cat swarm optimization. In: 7th International Conference on Machine Learning and Cybernetics, vol. 6, pp. 3328–3333. IEEE (2008)
39. Wang, H., Rahnamayan, S., Wu, Z.: Parallel differential evolution with self-adapting control parameters and generalized opposition-based learning for solving high-dimensional optimization problems. *J. Parallel Distrib. Comput.* **73**(1), 62–73 (2013)
40. Wang, K.H., Chen, C.M., Fang, W., Wu, T.Y.: A secure authentication scheme for internet of things. *Pervas. Mob. Comput.* **42**, 15–26 (2017)
41. Wu, J.M.T., Zhan, J., Lin, J.C.W.: Ant colony system sanitization approach to hiding sensitive itemsets. *IEEE Access* **5**, 10024–10039 (2017)
42. Xue, X., Liu, J.: Collaborative ontology matching based on compact interactive evolutionary algorithm. *Knowl.-Based Syst.* **137**, 94–103 (2017)

# Chapter 15

## Advanced QUasi-Affine TRansformation Evolutionary (QUATRE) Algorithm and Its Application for Neural Network



Pei Hu, Jeng-Shyang Pan, and Shu-Chuan Chu

**Abstract** The QUasi-Affine TRansformation Evolution (QUATRE) was first proposed by Meng et al. in 2016. It has the characteristics of few parameters and fast convergence. This paper brings two methods to improve its solution quality. The opposite position and comprehensive learning greatly advance the ability of jumping out of local traps when the QUATRE falls into stagnation. Their performance is verified by 23 benchmark functions. In the end, they succeed to train the parameters of neural network and predict the long-term traffic flow in Qingdao.

### 15.1 Introduction

In the past few decades, the methods of operational research and heuristic have been greatly developed, but the actual optimization problems are very complex and difficult to solve with traditional approaches. Scholars develop meta-heuristic algorithms by simulating certain natural phenomena processes and laws [1–3]. Compared with traditional mathematical programming, meta-heuristics do not require analyzing the specific problems and have little dependence on the problems [4]. However, the final solution acquired by the meta-heuristic is not necessarily the global optimal solution, and it just obtains a more satisfactory solution in a short time and space [5]. Meta-heuristics mainly include evolutionary algorithms and swarm intelligence [6].

Meta-heuristics have been widely used in various fields [7–11]. In the neural network (NN), Hu et al. combined shuffled frog leaping algorithm (SFLA) with grey

---

P. Hu · J.-S. Pan (✉) · S.-C. Chu

College of Computer Science and Engineering, Shandong University of Science and Technology, Qingdao 266590, China

e-mail: [huxiaopei163@163.com](mailto:huxiaopei163@163.com)

P. Hu

School of Computer and Software, Nanyang Institute of Technology, Nanyang 473004, China

S.-C. Chu

College of Science and Engineering, Flinders University, Sturt Road, Bedford Park, SA 5042, Australia

wolf optimizer (GWO) and differential evolution (DE), and adopted parallel heterogeneous algorithm to train neural network [12]. The proposed scheme successfully realized the predictions of wind power and daily load. Huang et al. adopted tabu search (TS) to optimize the quality of watermarked image and its robustness [13]. Chu et al. brought a constrained ant colony optimization (CACO) to handle the troubles of clusters with outliers or arbitrary shapes and bridges between clusters [14]. Meng et al. proposed an adaptive learning DE and succeeded to solve the inconvenience in the selection of control parameters [15]. Pan, Nguyen and Kong applied genetic algorithm (GA) and cat swarm optimization (CSO) to optimize the wireless sensor network (WSN) [16–18]. Nguyen et al. adopted bat algorithm (BA) to build an optimal cluster, while minimizing the communication distance [19]. Hu et al. and Zhao et al. utilized grey wolf optimizer (GWO) and particle swarm optimization (PSO) to implement the classification [20, 21]. Xue et al. and Chu et al. optimized ontology alignment through meta-heuristics [22–24]. Zhuang et al. improved the flower pollination algorithm (FPA) and applied it in the capacitated vehicle routing problem (CVRP) [25]. To reduce the evaluation time of complex objective function, Sun et al. proposed a cooperative swarm optimization algorithm based on surrogate-assisted model and a fitness approximation assisted competitive swarm optimizer to solve large scale expensive problems [26, 27]. Zhang et al. suggested quantum GA and learning vector quantization neural network to predict short-term traffic flow [28]. Wu et al. offered an advanced ant colony algorithm (ACO) to obtain a large number of high-utility items within a limited time [29]. Wang et al. utilized firefly algorithm (FA) to improve the solution quality and reduce the calculation time [30].

Pan et al. and Song et al. proposed new meta-heuristics to suitable for the different applications [31–33].

Although QUATRE is a new algorithm, it has powerful search ability. This paper proposes two methods to avoid QUATRE from falling into local traps and verifies their superiority through experiments. Finally, the improved methods are successfully applied to long-term traffic flow prediction.

## 15.2 Related Work

QUasi-Affine TRansformation Evolution (QUATRE) is a co-evolutionary architecture algorithm of quasi-affine transformation [34, 35]. It overcomes the slow convergence of PSO. QUATRE also belongs to a DE algorithm with fewer parameters and conquers the representative bias of the high-dimensional perspective in the DE. It achieves a more reasonable search from the perspective of statistics and probability theory.

In geometry, the affine transformation from affine space  $X$  to  $Y$  is  $Y = MX + B$ , and the QUATRE algorithm uses its evolutionary architecture.

$$X = MX + \bar{M}B \quad (15.1)$$



$M$  is derived from a lower triangular matrix through random row and column conversions and  $\bar{M}$  is the inverse operation of  $M$ .  $B$  is calculated by the following equation:

$$B = X_{\text{gbest}} + c * (X_{r1} - X_{r2}) \quad (15.2)$$

where  $c$  is the coefficient factor of the differential matrix and the value is 0.7.  $X_{r1}$  and  $X_{r2}$  are generated by randomly arranging the row vectors of the matrix  $X$ .

### 15.3 The Advanced QUATRE Algorithm

QUATRE has few parameters and fast convergence, but it lacks measures to avoid local optima. This section proposes two effective methods to detect and avoid local traps.

Each particle uses Eq. (15.1) to move to a new position. After the evaluation is completed by fitness function, it is judged whether the value is improved. If there is no development, the following determination is made:

$$\text{stag}_i = \begin{cases} 0 & \text{if}(f_i(n+1) < f_i(n)) \\ \text{stag}_i + 1 & \text{else} \end{cases} \quad (15.3)$$

If the fitness value of  $i$  does not improve compared with the previous time, the stagnation value increases 1, or else the value is reset to 0. Once the stagnation value exceeds  $T$ , where  $T$  is the stagnation threshold with a value of 5. It means that the particle has not moved toward the optimal solution for a long time and it may fall into the local optimum or the search direction will deviate. In this case, it is necessary to force the change of the position. This paper adopts the strategy based on the opposite position to stay away from the current position. UB and LB are the upper and lower limits of the particle's position, and  $X_i$  is the position of  $i$ . The updating position is:

$$X_i = \text{UB} + \text{LB} - X_i \quad (15.4)$$

There is a chance to jump out of the local trap and search for the optimal solution after the particle is updated.

When the particles do not find a better solution, they need to learn from the surrounding particles to obtain great performance. The particle cannot study from one to prevent loss of population diversity and several particles with the same search path. The new position equation is defined as follows:

$$X_i^j = X_r^j \quad (15.5)$$

For each dimension,  $r$  is a randomly selected particle.

The complexity of the algorithms is only a few more judgments than the original QUATRE, and they do not increase the fitness function call. The performance is greatly improved when the amount of calculation is not much different.

## 15.4 Experimental Results and Discussion

In this section, 23 benchmark functions are used to test the performance. Their detailed descriptions can be referred to [12, 20]. O-QUATRE uses the opposite position method and C-QUATRE adopts the comprehensive learning approach. The population size is 20, and the maximum number of iterations is 500. Each function runs 30 times. Table 15.1 shows the experimental results of the algorithms. *AVG* is the average of the best solutions of the 30 times and *STD* is their variance.

**Table 15.1** The statistical results

Function	QUATRE		O-QUATRE		C-QUATRE	
	AVG	STD	AVG	STD	AVG	STD
$f_1$	4.73E-03	2.54E-02	5.25E-07	4.09E-07	2.80E-07	4.10E-07
$f_2$	2.13E-03	8.90E-03	7.11E-05	3.40E-05	3.44E-05	1.29E-05
$f_3$	1.42E+04	2.53E+03	1.62E+04	3.98E+03	1.26E+04	4.77E+03
$f_4$	1.42E+01	4.96E+00	1.13E+00	3.93E-01	1.75E+00	1.60E+00
$f_5$	7.94E+01	4.29E+01	4.34E+01	3.15E+01	8.75E+01	1.13E+02
$f_6$	2.06E-06	2.74E-06	4.62E-06	2.36E-06	3.58E-07	4.76E-07
$f_7$	5.65E-02	2.18E-02	2.60E-02	8.09E-03	2.33E-02	8.77E-03
$f_8$	-1.11E+04	3.62E+02	-1.12E+04	3.15E+02	-1.15E+04	5.67E+02
$f_9$	5.23E+01	1.14E+01	3.59E+01	1.05E+01	3.87E+01	1.45E+01
$f_{10}$	6.38E-01	1.19E+00	1.64E-04	7.21E-05	1.37E-04	1.21E-04
$f_{11}$	8.96E-03	1.13E-02	2.93E-03	1.15E-02	4.60E-03	6.54E-03
$f_{12}$	3.23E-01	5.67E-01	4.04E-03	1.87E-02	2.07E-02	4.15E-02
$f_{13}$	3.73E-02	1.60E-01	7.62E-03	1.83E-02	1.10E-03	3.30E-03
$f_{14}$	3.94E+00	3.91E+00	4.47E+00	3.54E+00	3.79E+00	2.94E+00
$f_{15}$	3.78E-03	7.42E-03	3.87E-03	7.39E-03	3.72E-03	7.45E-03
$f_{16}$	-1.03E+00	1.03E-05	-1.03E+00	3.84E-04	-1.03E+00	8.76E-08
$f_{17}$	3.98E-01	1.06E-04	3.98E-01	1.33E-07	3.98E-01	4.00E-08
$f_{18}$	3.00E+00	3.88E-05	3.00E+00	6.07E-09	3.00E+00	3.63E-05
$f_{19}$	-3.86E+00	8.78E-10	-3.86E+00	3.35E-09	-3.86E+00	1.43E-09
$f_{20}$	-3.27E+00	5.93E-02	-3.28E+00	5.73E-02	-3.27E+00	5.89E-02
$f_{21}$	-5.64E+00	3.12E+00	-5.95E+00	2.92E+00	-6.05E+00	3.26E+00
$f_{22}$	-5.21E+00	3.05E+00	-6.90E+00	3.60E+00	-7.85E+00	3.21E+00
$f_{23}$	-5.37E+00	3.49E+00	-8.00E+00	3.37E+00	-6.19E+00	3.64E+00

**Table 15.2** The Wilcoxon rank sum test based on QUATRE

Function	O-QUATRE	C-QUATRE	Function	O-QUATRE	C-QUATRE
$f_1$	5.83E-03	4.44E-07	$f_{13}$	3.51E-02	2.83E-08
$f_2$	4.51E-02	4.20E-10	$f_{14}$	3.51E-01	8.47E-01
$f_3$	7.98E-02	1.37E-01	$f_{15}$	1.88E-01	7.84E-01
$f_4$	3.02E-11	3.69E-11	$f_{16}$	6.00E-01	6.03E-01
$f_5$	2.32E-02	4.04E-01	$f_{17}$	9.00E-01	8.84E-02
$f_6$	1.11E-06	6.53E-08	$f_{18}$	5.06E-01	7.14E-01
$f_7$	3.65E-08	5.46E-09	$f_{19}$	6.32E-01	5.86E-01
$f_8$	1.81E-01	5.19E-02	$f_{20}$	5.32E-01	8.04E-01
$f_9$	2.88E-06	2.68E-04	$f_{21}$	7.93E-01	9.82E-01
$f_{10}$	3.82E-09	6.72E-10	$f_{22}$	1.40E-01	3.69E-03
$f_{11}$	2.49E-06	3.03E-03	$f_{23}$	4.70E-03	4.91E-01
$f_{12}$	1.75E-05	5.60E-07			
<=>	1/11/11	0/12/11			

It can be seen from Table 15.1 that O-QUATRE and C-QUATRE have greatly improved the performance of the QUATRE and perform well in the test functions. O-QUATRE only has poor performance in the  $f_3, f_6, f_{14}, f_{15}$  and  $f_{20}$ , and it finishes perfectly in 14 test functions. While C-QUATRE completes unsatisfactorily in the  $f_5$  and does well in 17 test functions. The algorithms have the same results in the  $f_{16}-f_{19}$ . This is because the functions have low dimension and complexity. It reveals that O-QUATRE and C-QUATRE have stronger search space capabilities, and the improved strategies assist the QUATRE to escape local traps. The data obtained by C-QUATRE is better than O-QUATRE, which shows that the comprehensive learning can better learn evolutionary information from the surrounding particles. Through the above analysis, the solution quality of O-QUATRE and C-QUATRE wins QUATRE (Table 15.2).

Table 15.3 is the Wilcoxon rank sum test based on QUATRE, which is used to judge whether they have statistical differences. It can be found that O-QUATRE is not as good as QUATRE only on  $f_7$ , and it is superior QUATRE in 11 functions. C-QUATRE is also better than QUATRE in 11 functions, and they have the same statistical results in 12 functions. It is shown by Wilcoxon rank sum test that O-QUATRE and C-QUATRE win QUATRE.

### 15.5 Application for Neural Network

The prediction of traffic flow is very important for both government and individuals. Local governments forecast traffic flow in future to guide appropriate traffic measures, such as changing the time of traffic signals or closing certain roads to avoid potential

**Table 15.3** Quantitative value

DATE	Weather	Weekday	DATE	Weather	Weekday
7.5	0.2	0.6	7.10	0.2	0.2
7.6	0.2	0.6	7.11	0.2	0.5
7.7	0.2	0.5	7.12	0.2	0.6
7.8	0.2	0.2	7.13	0.4	0.5
7.9	0.3	0.3	7.14	0.2	0.2

**Table 15.4** The statistical results of the predictions

Index	QUATRE	O-QUATRE	C-QUATRE
Max error (%)	293.26	367.1	379.25
Min error (%)	0.02	0.02	0.02
>= 100	49	27	5
[50–100]	47	42	20
[30–50]	31	38	29

traffic congestion. The predictions are divided into long-term and short-term [36]. The goal of long-term is to predict the traffic flow for one or more days in future.

Neural network is a hot research in the artificial intelligence [37]. A typical neural network has an input layer, one or more hidden layers and an output layer [38–41]. The meta-heuristic algorithm is used to optimize the input weight, output weight and deviation of the neural network, and then the neural network adopts the parameters to implement prediction. This paper forecasts the traffic flow in Qingdao. The format of the data set is as follows: the day before yesterday's traffic flow, the current day's traffic flow, weather condition and weekday. The data of the first seven days is used as the training set and the data of the next three days is the test set. The hidden layer has 8 neurons. The quantitative data of weather and weekday is shown in Table 15.2.

The average prediction errors of QUATRE, O-QUATRE and C-QUATRE are 37.2%, 28.84% and 18.51% at 423 street intersections. O-QUATRE and C-QUATRE outperform QUATRE, especially C-QUATRE achieves the best results. This illustrates that the two algorithms are successfully used in the neural network prediction of long-term traffic flow.

Table 15.4 shows some statistical results of the three algorithms. In the maximum error, QUATRE is better than O-QUATRE and C-QUATRE, and they have the same minimum prediction error. The error numbers of >100%, 50–100% and 30–50% are 49, 47 and 31, respectively, while the numbers of C-QUATRE are only 5, 20 and 29, respectively.

## 15.6 Conclusion

This paper put forward to two novel approaches to improve the QUATRE. The algorithms contain the opposite position and comprehensive learning. Once QUATRE falls into local optimum, they support escaping from the trap. The application of QUATRE extends to neural network. In future work, we can apply QUATRE to other fields.

## References

1. Sun, C., Zeng, J., Pan, J., Xue, S., Jin, Y.: A new fitness estimation strategy for particle swarm optimization. *Inf. Sci.* **221**, 355–370 (2013)
2. Sun, C., Zeng, J., Pan, J.-S.: A modified particle swarm optimization with feasibility-based rules for mixed-variable optimization problems. *Int. J. Innov. Comput. Inf. Control* **7**(6), 3081–3096 (2011)
3. Wang, J., Gao, Y., Liu, W., Sangaiah, A.K., Kim, H.-J.: An improved routing schema with special clustering using PSO algorithm for heterogeneous wireless sensor network. *Sensors* **19**(3), 671 (2019)
4. Wang, H., Wang, W., Cui, Z., Zhou, X., Zhao, J., Li, Y.: A new dynamic firefly algorithm for demand estimation of water resources. *Inf. Sci.* **438**, 95–106 (2018)
5. Wang, J., Cao, J., Simon Sherratt, R., Park, J.H.: An improved ant colony optimization-based approach with mobile sink for wireless sensor networks. *J. Supercomput.* **74**(12), 6633–6645 (2018)
6. Chu, S.-C., Huang, H.-C., Roddick, J.F., Pan, J.-S.: Overview of algorithms for swarm intelligence. In: *International Conference on Computational Collective Intelligence*, pp. 28–41. Springer (2011)
7. Xue, X., Wang, Y.: Optimizing ontology alignments through a memetic algorithm using both MatchFmeasure and unanimous improvement ratio. *Artif. Intell.* **223**, 65–81 (2015)
8. Cai, X., Wang, H., Cui, Z., Cai, J., Yu, X., Wang, L.: Bat algorithm with triangle-flipping strategy for numerical optimization. *Int. J. Mach. Learn. Cybern.* **9**(2), 199–215 (2018)
9. Sun, C.-L., Zeng, J.-C., Pan, J.-s.: An improved vector particle swarm optimization for constrained optimization problems. *Inf. Sci.* **181**(6), 1153–1163 (2011)
10. Tian, J., Sun, C., Tan, Y., Zeng, J.: Granularity-based surrogate-assisted particle swarm optimization for high-dimensional expensive optimization. *Knowl.-Based Syst.* **187**, 104815 (2020)
11. Chen, C.-M., Wang, K.-H., Yeh, K.-H., Xiang, B., Tsu-Yang, W.: Attacks and solutions on a three-party password-based authenticated key exchange protocol for wireless communications. *J. Ambient Intell. Hum. Comput.* **10**(8), 3133–3142 (2019)
12. Pan, J.-S., Pei, H., Chu, S.-C.: Novel parallel heterogeneous meta-heuristic and its communication strategies for the prediction of wind power. *Processes* **7**(11), 845–868 (2019)
13. Huang, H.-C., Chu, S.-C., Pan, J.-S., Huang, C.-Y., Liao, B.-Y.: Tabu search based multi-watermarks embedding algorithm with multiple description coding. *Inf. Sci.* **181**(16), 3379–3396 (2011)
14. Chu, S.-C., Roddick, J.F., Su, C.-J., Pan, J.-S.: Constrained ant colony optimization for data clustering. In: *Pacific Rim International Conference on Artificial Intelligence*, pp. 534–543. Springer (2004)
15. Meng, Z., Pan, J.-S., Kong, L.: Parameters with adaptive learning mechanism (PALM) for the enhancement of differential evolution. *Knowl.-Based Syst.* **141**, 92–112 (2018)
16. Pan, J.-S., Kong, L., Sung, T.-W., Tsai, P.-W., Snášel, V.: A clustering scheme for wireless sensor networks based on genetic algorithm and dominating set. *J. Internet Technol.* **19**(4), 1111–1118 (2018)

17. Nguyen, T.-T., Pan, J.-S., Lin, J.C.-W., Dao, T.-K., Nguyen, T.-X.-H.: An optimal node coverage in wireless sensor network based on whale optimization algorithm. *J. Netw. Intell.* **2**(2), 11–21 (2018)
18. Kong, L., Pan, J.-S., Tsai, P.-W., Vaclav, S., Ho, J.-H.: A balanced power consumption algorithm based on enhanced parallel cat swarm optimization for wireless sensor network. *Int. J. Distrib. Sens. Netw.* **11**(3), 729680 (2015)
19. Ngo, T.-G., Dao, T.-K.: Unequal clustering formation based on bat algorithm for wireless sensor networks. *Knowl. Syst. Eng.* **326**, 667–678 (2015)
20. Pei, H., Pan, J.-S., Chu, S.-C.: Improved binary grey wolf optimizer and its application for feature selection. *Knowl.-Based Syst.* **195** (2020). <https://doi.org/10.1016/j.knosys.2020.105746>
21. Zhao, L., Gai, M., Jia, Y.: Classification of multiple power quality disturbances based on PSO-SVM of hybrid kernel function. *J. Inf. Hiding Multimed. Signal Process.* **10**(1), 138–146 (2018)
22. Xue, X., Chen, J., Chen, D.: Matching biomedical ontologies through compact hybrid evolutionary algorithm. *J. Inf. Hiding Multimed. Signal Process.* **10**(1), 110–117 (2019)
23. Chu, S.-C., Xue, X., Pan, J.-S., Xiaojing, W.: Optimizing ontology alignment in vector space. *J. Internet Technol.* **21**(1), 15–22 (2020)
24. Xue, X., Liu, J.: Collaborative ontology matching based on compact interactive evolutionary algorithm. *Knowl.-Based Syst.* **137**, 94–103 (2017)
25. Zhuang, J., Luo, H., Pan, T.-S., Pan, J.-S.: Improved flower pollination algorithm for the capacitated vehicle routing problem. *J. Netw. Intell.* **5**(3), 141–156 (2020)
26. Sun, C., Jin, Y., Cheng, R., Ding, J., Zeng, J.: Surrogate-assisted cooperative swarm optimization of high-dimensional expensive problems. *IEEE Trans. Evol. Comput.* **21**(4), 644–660 (2017)
27. Sun, C., Ding, J., Zeng, J., Jin, Y.: A fitness approximation assisted competitive swarm optimizer for large scale expensive optimization problems. *Memetic Comput.* **10**(2), 123–134 (2018)
28. Zhang, F., Tsu-Yang, W., Wang, Y., Xiong, R., Ding, G., Mei, P., Liu, L.: Application of quantum genetic optimization of LVQ neural network in smart city traffic network prediction. *IEEE Access* **8**, 104555–104564 (2020)
29. Wu, J.M.-T., Zhan, J., Lin, J.C.-W.: An ACO-based approach to mine high-utility itemsets. *Knowl.-Based Syst.* **116**, 102–113 (2017)
30. Wang, H., Wang, W., Zhou, X., Sun, H., Zhao, J., Xiang, Y., Cui, Z.: Firefly algorithm with neighborhood attraction. *Inf. Sci.* **382**, 374–387 (2016)
31. Pan, J.S., Tsai, P.W., Liao, Y.B.: Fish migration optimization based on the fishy biology. In: 2010 Fourth International Conference on Genetic & Evolutionary Computing, pp. 783–786. IEEE, Shenzhen, China (2010)
32. Song, P.-C., Chu, S.-C., Pan, J.-S., Yang, H.: Phasmatodea population evolution algorithm and its application in length-changeable incremental extreme learning machine. In: 2020 2nd International Conference on Industrial Artificial Intelligence (IAI), pp. 1–5. IEEE (2020)
33. Chai, Q.-W., Chu, S.-C., Pan, J.-S., Zheng, W.-M.: Applying adaptive and self assessment fish migration optimization on localization of wireless sensor network on 3-d terrain. *J. Inf. Hiding Multimed. Signal Process.* **11**(2), 90–102 (2020)
34. Meng, Z., Pan, J.-S.: Quasi-affine transformation evolutionary (QUATRE) algorithm: a parameter-reduced differential evolution algorithm for optimization problems. In: 2016 IEEE Congress on Evolutionary Computation (CEC), pp. 4082–4089. IEEE (2016)
35. Meng, Z., Pan, J.-S.: Quasi-affine transformation evolution with external archive (QUATRE-EAR): an enhanced structure for differential evolution. *Knowl.-Based Syst.* **155**, 35–53 (2018)
36. Zhang, S.-M., Su, X., Jiang, X.-h., Ming, I.C., Wu, T.-Y.: A traffic prediction method of bicycle-sharing based on long and short term memory network. *J. Netw. Intell.* **4**(2), 17–19 (2019)
37. Ye, X., Rong, H.: Fuzzy neural network based energy efficiencies control in the heating energy supply system responding to the changes of user demands. *J. Netw. Intell.* **2**(2), 186–194 (2017)
38. Chan, Z.-M., Lau, C.-Y., Thang, K.-F.: Visual speech recognition of lips images using convolutional neural network in VGG-M model. *J. Inf. Hiding Multimed. Signal Process.* **11**(3), 116–125 (2020)

39. Guo, C., Liu, G., Chen, C.-H.: Air pollution concentration forecast method based on the deep ensemble neural network. *Wirel. Commun. Mob. Comput.* **2020** (2020)
40. Chen, C.-H., Song, F., Hwang, F.-J., Ling, W.: A probability density function generator based on neural networks. *Phys. A: Stat. Mech. Appl.* **541**, 123344 (2020)
41. Chen, C.-H., Chen-Ling, W., Lo, C.-C., Hwang, F.-J.: An augmented reality question answering system based on ensemble neural networks. *IEEE Access* **5**, 17425–17435 (2017)

# Chapter 16

## An QUasi-Affine TRansformation Evolution (QUATRE) Algorithm for Job-Shop Scheduling Problem by Mixing Different Strategies



Qing-Yong Yang, Shu-Chuan Chu, Chien-Ming Chen, and Jeng-Shyang Pan

**Abstract** How to solve the Job-Shop Scheduling problem (JSP) effectively and make the most efficient use of resources has always been the focus of academic and engineering circles. Aiming at the traditional JSP problem, this paper proposes a new QUasi-Affine Transformation Evolution algorithm (QUATRE) to solve it, called QUATRE-SAO for short. The QUATRE-SAO algorithm combines Simulated Annealing (SA) strategy and Opposition-based Learning (OBL) strategy to enhance the algorithm to jump out of local optimum and further improve the optimization performance of the algorithm. Through the comparative experiment of FT and LA series standard test examples, the results show that the QUATRE-SAO algorithm can solve the JSP problem better and can get a better solution.

### 16.1 Introduction

In practical production and scientific research, various optimization problems are often encountered. Optimization problems exist in various fields, and the constraint conditions are also different in different fields [4, 12]. But the ultimate goal is the same, that is, to choose a solution that can achieve the best results according to the actual engineering needs. At present, with the continuous development of practical engineering applications and scientific research, optimization problems have gradually become more complicated. For some NP-hard optimization problems, traditional optimization algorithms have been difficult to provide a relatively satisfactory solution within a reasonable time.

Job-shop Scheduling problem (JSP) has been proved to be a typical NP-hard problem, which is one of the most critical problems in manufacturing and process planning

---

Q.-Y. Yang · S.-C. Chu · C.-M. Chen · J.-S. Pan (✉)  
College of Computer Science and Engineering, Shandong University of Science and Technology,  
Qingdao 266590, China  
e-mail: [qyzide@163.com](mailto:qyzide@163.com)

C.-M. Chen  
e-mail: [chienmingchen@ieee.org](mailto:chienmingchen@ieee.org)



[10]. And it is widely used in many practical production scheduling problems, such as traffic planning [30, 31], manufacturing, automobile assembly line, airport aircraft scheduling and so on. How to design an efficient scheduling algorithm and effectively solve the JSP problem has become a very realistic and urgent problem. The bionic swarm intelligence algorithms have the characteristics of self-adaptability, parallelism and randomness, and can better solve optimization problems [5]. Typical algorithms include Particle Swarm Optimization (PSO) [14, 25], Flower Pollination Algorithm (FPA) [20, 29], Gray Wolf Optimization (GWO) [11, 19], Cuckoo Search Algorithm (CSA) [6, 9, 24], Ant Colony Optimization (ACO) [8, 26] and so on. At present, more and more scholars apply swarm intelligence algorithms to solve the JSP problems [3, 13, 23].

QUasi-Affine Transformation Evolution algorithm (QUATRE) is a new swarm intelligence algorithm proposed by Meng et al. in 2016 [16]. The offset problem of Differential Evolution (DE) [7, 17, 22, 28] and Monkey King Evolution (MKE) [21] in high dimensional space is solved. Iterative search and population evolution of the algorithm are realized by affine transformation which is similar to geometry. At present, there is no research on applying this algorithm to solving the JSP problem. Therefore, this paper tries to apply the QUATRE algorithm to solve the JSP problem. Meanwhile, the Simulated Annealing (SA) [15] strategy and the Opposition-based Learning (OBL) [27] strategy are introduced to avoid the algorithm falling into local optimum. Finally, through relevant examples of the JSP problem, the effectiveness and feasibility of the proposed QUATRE-SAO algorithm are proved.

The remainder of this paper is arranged as follows. The modeling of the JSP problem, the original QUATRE algorithm and the QUATRE-SAO algorithm are introduced in the second section. Related experiments are introduced in the third section and the fourth section is the summary of this paper.

## 16.2 Related Work

In this section, the description of Job-Shop Scheduling problem, the principle of original QUATRE algorithm, and how to use Simulated Annealing (SA) strategy and Opposition-based Learning (OBL) strategy to improve the original QUATRE algorithm are introduced. The encoding scheme of the algorithm is also described in this section.

### 16.2.1 *Job-Shop Scheduling Problem*

The traditional JSP problem can be introduced as: a workshop has  $m$  machining machines, which need to process  $n$  kinds of workpiece, and each workpiece contains different processing procedures and processing time. Among them, the processing process and processing time of each workpiece have been determined in advance.

The goal of scheduling is to determine the processing sequence and the start time of each process on each machine under the constraint, so as to minimize the makespan. The constraints are as follows:

- Each process is processed on the designated machine, and it can only be started after the previous process is finished.
- At a certain time, a machine can only process one workpiece, regardless of machine failure and other random factors.
- Each workpiece can only be processed once on one machine.
- The process sequence and processing time of each workpiece are known, and do not change with the change of processing sequence.

In this paper, we take the shortest makespan as the performance index, the mathematical model is established as follows [1]:

$$\text{Objective : } f^* = \min(\max(C_{ik})), 1 \leq k \leq m; 1 \leq i \leq n \quad (16.1)$$

Subject to:

$$C_{ik} - p_{ik} + H(1 - a_{ihk}) \geq C_{ih}, i = 1, 2, \dots, n; h, k = 1, 2, \dots, m \quad (16.2)$$

$$C_{jk} - C_{ik} + H(1 - x_{ijk}) \geq p_{jk}, i, j = 1, 2, \dots, n; k = 1, 2, \dots, m \quad (16.3)$$

$$C_{ik} \geq 0, i = 1, 2, \dots, n; k = 1, 2, \dots, m \quad (16.4)$$

$$x_{ijk} = \begin{cases} 1, & \text{if workpiece } i \text{ is processed on machine } k \text{ before workpiece } j \\ 0, & \text{else} \end{cases} \quad (16.5)$$

$$a_{ihk} = \begin{cases} 1, & \text{if machine } h \text{ processes workpiece } i \text{ before machine } k \\ 0, & \text{else} \end{cases} \quad (16.6)$$

where, Eq. 16.1 means the objective function. Equation 16.2 shows that the operation sequence of the workpiece is determined by the process constraints, and  $H$  is a large enough positive number. Equation 16.3 represents the sequence of each machine processing each workpiece. Equation 16.4 represents the constraints of completion time variables. In the above equations,  $p_{ik}$  and  $C_{ik}$  represent the processing time and completion time of workpiece  $i$  on machine  $k$ , respectively.  $x_{ijk}$  and  $a_{ihk}$  are indicative variables and indicative coefficients respectively, and Eqs. 16.5 and 16.6 represent their meanings.

## 16.2.2 Quasi-Affine TRansformation Evolution Algorithm

The QUasi-Affine TRansformation Evolution algorithm is a novel swarm intelligence optimization algorithm [16]. There are many variants of the algorithm [18], and the QUATRE-SAO algorithm in this paper is improved on the basis of the original QUATRE algorithm. The original algorithm contains a matrix  $X$  of size  $ps * D$  to represent the population. Where  $ps$  represents the number of individuals in the population, and  $D$  is the dimension. The evolution formula uses affine transformation similar to geometry to update individuals in the population, as shown in Eq. 16.7:

$$X_{\text{new}} = \bar{M} \otimes X_{\text{old}} + M \otimes B \quad (16.7)$$

where  $X_{\text{new}}$  is the updated offspring population,  $X_{\text{old}}$  is the current population. The fitness of individuals in  $X_{\text{new}}$  will be compared with individuals in  $X_{\text{old}}$ , and the winner will be saved to the parent population of the next iteration.  $M$  is the coevolutionary matrix,  $\bar{M}$  is the association matrix of  $M$ , and  $B$  is the evolutionary guidance matrix.  $\otimes$  represents a bitwise multiplication operation of matrix elements.

The generation of matrix  $B$  is shown in Table 16.1.  $X_r$  is the population obtained by randomly arranging the row vectors of  $X$ .  $X_{\text{gbest}}$  is a global optimal population composed of global optimal individuals. The original QUATRE algorithm uses the first method.  $c$  is the scaling factor, usually set to 0.7.

The matrix  $M$  is derived from a lower triangular matrix  $M_{\text{init}}$  of  $ps * D$ . The change is divided into two steps: the first step is to arrange each row vector element in  $M_{\text{init}}$  randomly to obtain matrix  $M'_{\text{init}}$ ; the second is to arrange all row vectors of matrix  $M'_{\text{init}}$  randomly to obtain matrix  $M$ . The matrix  $\bar{M}$  is obtained by taking the inverse of the members of the matrix  $M$ . The element with value 1 in matrix  $M$  is 0 in  $\bar{M}$ . The element that is 0 in  $M$  is 1 in  $\bar{M}$ .

**Table 16.1** Eight methods of calculating matrix **B**

No.	QUATRE/x/y	Equation
1	QUATRE/best/1	$\mathbf{B} = \mathbf{X}_{\text{gbest}} + c * (\mathbf{X}_{r1} - \mathbf{X}_{r2})$
2	QUATRE/target/1	$\mathbf{B} = \mathbf{X} + c * (\mathbf{X}_{r1} - \mathbf{X}_{r2})$
3	QUATRE/rand/1	$\mathbf{B} = \mathbf{X}_{r1} + c * (\mathbf{X}_{r2} - \mathbf{X}_{r3})$
4	QUATRE/target-to-best/1	$\mathbf{B} = \mathbf{X} + c * (\mathbf{X}_{\text{gbest}} - \mathbf{X}) + c * (\mathbf{X}_{r1} - \mathbf{X}_{r2})$
5	QUATRE/target-to-rand/1	$\mathbf{B} = \mathbf{X} + c * (\mathbf{X}_{r1} - \mathbf{X}) + c * (\mathbf{X}_{r2} - \mathbf{X}_{r3})$
6	QUATRE/best/2	$\mathbf{B} = \mathbf{X}_{\text{gbest}} + c * (\mathbf{X}_{r1} - \mathbf{X}_{r2}) + c * (\mathbf{X}_{r3} - \mathbf{X}_{r4})$
7	QUATRE/target/2	$\mathbf{B} = \mathbf{X} + c * (\mathbf{X}_{r1} - \mathbf{X}_{r2}) + c * (\mathbf{X}_{r3} - \mathbf{X}_{r4})$
8	QUATRE/rand/2	$\mathbf{B} = \mathbf{X}_{r1} + c * (\mathbf{X}_{r2} - \mathbf{X}_{r3}) + c * (\mathbf{X}_{r4} - \mathbf{X}_{r5})$

### 16.2.3 The QUATRE-SAO Algorithm Combining Simulated Annealing and Opposition-Based Learning Strategies

This subsection will introduce how to apply the SA and OBL strategies to improve the original QUATRE algorithm, so as to jump out of the local optimum. The following is an introduction to the two strategies.

#### 1. Simulated Annealing strategy

The SA algorithm was proposed by Kirkpatrick et al. in 1983 [15], derived from the principle of solid annealing. The algorithm consists of two parts: Metropolis criterion and annealing process. The Metropolis criterion describes how to accept the new state with probability instead of using completely determined rules. In this way, the algorithm can avoid falling into local optimum by accepting the difference solution with probability, so as to enhance the search ability of the algorithm. In the QUATRE-SAO algorithm, the strategy is used to update the position of individuals whose fitness is greater than the original fitness, but less than the average of overall fitness. Equation 16.8 is the calculation formula of probability.

$$P = \begin{cases} 1, & \text{fit}_{\text{new}} < \text{fit}_{\text{old}} \\ e^{-\frac{\text{fit}_{\text{new}} - \text{fit}_{\text{old}}}{T}}, & \text{fit}_{\text{new}} > \text{fit}_{\text{old}} \end{cases} \quad (16.8)$$

#### 2. Opposition-based Learning strategy

The thought of opposite learning was first proposed by Tizahoosh et al. [27]. It is currently applied to a variety of intelligent optimization algorithms to improve the performance of the algorithms. Equation 16.9 is the equation for solving the opposite point in  $D$  dimensional space.

$$X'_i = \text{ub}_i + \text{lb}_i - X_i, \quad i = 1, 2, \dots, D \quad (16.9)$$

where  $\text{ub}_i$  is the maximum of the  $i$ th dimension of the current search space and  $\text{lb}_i$  is the minimum. In this paper, this strategy is applied to the global optimal individual which has not been updated for a long time in a certain algebra interval. If the fitness of the individual after the opposition learning is better than that of the current individual, it will replace the original individual.

### 16.2.4 Coding Scheme

In order to be able to apply the QUATRE-SAO algorithm and the original QUATRE algorithm to solving the JSP problems, this paper uses process-based coding rules [2] to code the population individuals. Each individual is a sequence with a length of  $n \times m$ , which represents a processing sequence plan. For example, a JSP

problem with 3 workpieces and 3 machines. Suppose the sequence of one of the individuals is [2, 1, 1, 3, 1, 2, 3, 3, 2]. Its corresponding processing sequence is [ $J_{2,1}, J_{1,1}, J_{1,2}, J_{3,1}, J_{1,3}, J_{2,2}, J_{3,2}, J_{3,3}, J_{2,3}$ ], where  $J_{i,j}$  represents the  $j$ th process of the  $i$ th workpiece.

### 16.3 Experiment Analysis

For verifying the feasibility and effectiveness of the proposed QUATRE-SAO algorithm in solving the JSP problem, this paper selects the FT and LA series of test examples in the JSP standard problem test library to test it. And it is compared among the original QUATRE algorithm and PSO algorithm.

All algorithms are implemented on MATLAB R2019a. And all simulation experiments are carried out under the Windows 10 system with the processor frequency of 2.1 GHz and the memory of 8.0GB. The population size of each algorithm is 150 and the maximum number of iterations is set to 1000. The interval algebra of the proposed algorithm is set to 10. In the PSO algorithm, the parameter  $\omega$  is set to 0.729,  $C_1$  and  $C_2$  are 2 and 2.1, respectively. Each algorithm solves each sample 20 times.

The experimental results are recorded in Table 16.2. The  $f^*$  column in the table represents the best value obtained so far. The better values of the three algorithms are bolded. As can be seen from the data in Table 16.2, the QUATRE-SAO algorithm is better than the other two algorithms in terms of the mean value and the minimum value of the optimization results. The three algorithms have obtained the theoretical optimal values on FT06, LA01, LA06 and LA11, but the stability of the other two algorithms is weaker than that of the proposed algorithm. Although the QUATRE-SAO algorithm does not obtain the optimal value on the FT10 and FT20 samples, its optimization ability is further improved compared with the original QUATRE algorithm. It can also be seen from Figs. 16.1 and 16.2 that the convergence accuracy of the QUATRE-SAO algorithm is better than the other two algorithms, and it has better ability to jump out of the local optimal solution. However, due to a certain probability to accept the poor solution and the introduction of opposite learning strategy, the QUATRE-SAO algorithm loses a certain convergence speed.

**Table 16.2** Comparison of test results of QUATRE, PSO and the proposed algorithm

Name	Size	$f^*/\min$	QUATRE			PSO			QUATRE-SAO		
			best	mean	Std	Best	Mean	Std	Best	Mean	Std
FT06	6*6	55	<b>55</b>	<b>55.4</b>	0.88258	<b>55</b>	57.1	1.7137	<b>55</b>	<b>55.4</b>	0.82078
FT10	10*10	930	1033	1090.75	27.098	1071	1137.25	38.4925	<b>1028</b>	<b>1086.1</b>	24.7171
FT20	20*5	1165	1352	1404.9	29.1058	1401	1474.75	49.1206	<b>1325</b>	<b>1400.9</b>	31.1953
LA01	10*5	666	<b>666</b>	670.9	7.8264	<b>666</b>	696.9	19.7081	<b>666</b>	<b>666.4</b>	1.1877
LA06	15*5	926	<b>926</b>	<b>926</b>	0	<b>926</b>	935.6	15.6185	<b>926</b>	<b>926</b>	0
LA11	20*5	1222	<b>1222</b>	<b>1222</b>	0	<b>1222</b>	1244.55	21.5394	<b>1222</b>	<b>1222</b>	0

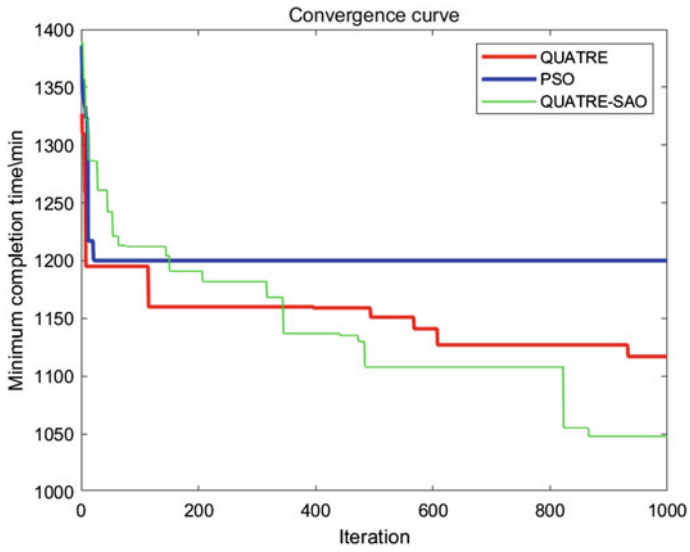


Fig. 16.1 FT10

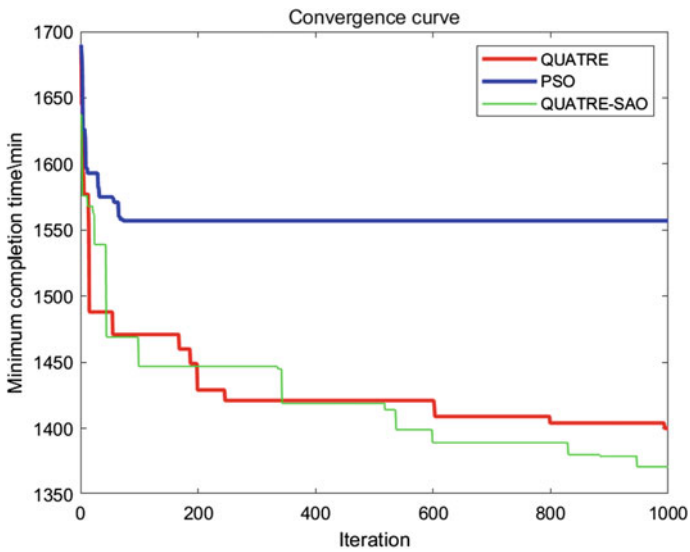


Fig. 16.2 FT20

## 16.4 Conclusions

Aiming at the traditional Job-Shop Scheduling problem, an improved QUATRE algorithm is proposed in this paper to solve it, called QUATRE-SAO for short. The algorithm combines Simulated Annealing (SA) strategy and Opposition-based Learning (OBL) strategy. Through the test, the QUATRE-SAO algorithm is better than the original QUATRE algorithm and the PSO algorithm in solving the JSP problem, but there is a certain decrease in the convergence speed. Therefore, the future direction will focus on how to further accelerate the convergence speed of the algorithm and apply the algorithm to solve other JSP problems.

## References

1. Baker, K.R., Trietsch, D.: Principles of Sequencing and Scheduling. Wiley (2013)
2. Bean, J.C.: Genetic algorithms and random keys for sequencing and optimization. *ORSA J. Comput.* **6**(2), 154–160 (1994)
3. Çaliş, B., Bulkan, S.: A research survey: review of AI solution strategies of job shop scheduling problem. *J. Intell. Manuf.* **26**(5), 961–973 (2015)
4. Chen, Y.Q., Zhou, B., Zhang, M., Chen, C.M.: Using IoT technology for computer-integrated manufacturing systems in the semiconductor industry. *Appl. Soft Comput.* **89**, 106065 (2020)
5. Chu, S.C., Huang, H.C., Roddick, J.F., Pan, J.S.: Overview of algorithms for swarm intelligence. In: *International Conference on Computational Collective Intelligence*, pp. 28–41. Springer (2011)
6. Cui, Z., Zhang, M., Wang, H., Cai, X., Zhang, W.: A hybrid many-objective cuckoo search algorithm. *Soft Comput.* **23**(21), 10681–10697 (2019)
7. Das, S., Suganthan, P.N.: Differential evolution: a survey of the state-of-the-art. *IEEE Trans. Evolut. Comput.* **15**(1), 4–31 (2010)
8. Dorigo, M., Birattari, M., Stutzle, T.: Ant colony optimization. *IEEE Comput. Intell. Mag.* **1**(4), 28–39 (2006)
9. Gandomi, A.H., Yang, X.S., Alavi, A.H.: Cuckoo search algorithm: a metaheuristic approach to solve structural optimization problems. *Eng. Comput.* **29**(1), 17–35 (2013)
10. Garey, M.R., Johnson, D.S., Sethi, R.: The complexity of flowshop and jobshop scheduling. *Math. Oper. Res.* **1**(2), 117–129 (1976)
11. Hu, P., Pan, J.S., Chu, S.C.: Improved binary grey wolf optimizer and its application for feature selection. *Knowl.-Based Syst.* **195**, 105746 (2020)
12. Huang, H.C., Chu, S.C., Pan, J.S., Huang, C.Y., Liao, B.Y.: Tabu search based multi-watermarks embedding algorithm with multiple description coding. *Inf. Sci.* **181**(16), 3379–3396 (2011)
13. Huang, K.L., Liao, C.J.: Ant colony optimization combined with taboo search for the job shop scheduling problem. *Comput. Oper. Res.* **35**(4), 1030–1046 (2008)
14. Kennedy, J., Eberhart, R.: Particle swarm optimization. In: *Proceedings of ICNN'95—International Conference on Neural Networks*, vol. 4, pp. 1942–1948. IEEE (1995)
15. Kirkpatrick, S., Gelatt, C.D., Vecchi, M.P.: Optimization by simulated annealing. *Science* **220**(4598), 671–680 (1983)
16. Meng, Z., Pan, J.S.: Quasi-affine transformation evolutionary (QUATRE) algorithm: a parameter-reduced differential evolution algorithm for optimization problems. In: *2016 IEEE Congress on Evolutionary Computation (CEC)*, pp. 4082–4089. IEEE (2016)
17. Meng, Z., Pan, J.S., Kong, L.: Parameters with adaptive learning mechanism (PALM) for the enhancement of differential evolution. *Knowl.-Based Syst.* **141**, 92–112 (2018)

18. Meng, Z., Pan, J.S., Li, X.: The quasi-affine transformation evolution (QUATRE) algorithm: an overview. In: *The Euro-China Conference on Intelligent Data Analysis and Applications*, pp. 324–333. Springer (2017)
19. Mirjalili, S., Mirjalili, S.M., Lewis, A.: Grey wolf optimizer. *Adv. Eng. Softw.* **69**, 46–61 (2014)
20. Pan, J.S., Dao, T.K., Pan, T.S., Nguyen, T., Chu, S., Roddick, J.: An improvement of flower pollination algorithm for node localization optimization in WSN. *J. Inf. Hiding Multimed. Signal Process.* **8**(2), 486–499 (2017)
21. Pan, J.S., Meng, Z., Chu, S.C., Xu, H.R.: Monkey king evolution: an enhanced ebb-tide-fish algorithm for global optimization and its application in vehicle navigation under wireless sensor network environment. *Telecommun. Syst.* **65**(3), 351–364 (2017)
22. Pan, J.S., Meng, Z., Xu, H., Li, X.: A matrix-based implementation of de algorithm: the compensation and deficiency. In: *International Conference on Industrial, Engineering and Other Applications of Applied Intelligent Systems*, pp. 72–81. Springer (2017)
23. Sha, D., Hsu, C.Y.: A hybrid particle swarm optimization for job shop scheduling problem. *Comput. Ind. Eng.* **51**(4), 791–808 (2006)
24. Song, P.C., Pan, J.S., Chu, S.C.: A parallel compact cuckoo search algorithm for three-dimensional path planning. *Appl. Soft Comput.* **94**, 106443 (2020)
25. Wang, H., Liang, M., Sun, C., Zhang, G., Xie, L.: Multiple-strategy learning particle swarm optimization for large-scale optimization problems. *Complex Intell. Syst.* 1–16 (2020)
26. Wu, J.M.T., Zhan, J., Lin, J.C.W.: An ACO-based approach to mine high-utility itemsets. *Knowl.-Based Syst.* **116**, 102–113 (2017)
27. Xu, Q., Wang, L., Wang, N., Hei, X., Zhao, L.: A review of opposition-based learning from 2005 to 2012. *Eng. Appl. Artif. Intell.* **29**, 1–12 (2014)
28. Xue, X., Chen, J.: Matching biomedical ontologies through compact differential evolution algorithm with compact adaption schemes on control parameters. *Neurocomputing* (2020)
29. Yang, X.S.: Flower pollination algorithm for global optimization. In: *International Conference on Unconventional Computing and Natural Computation*, pp. 240–249. Springer (2012)
30. Zhang, F., Wu, T.Y., Wang, Y., Xiong, R., Ding, G., Mei, P., Liu, L.: Application of quantum genetic optimization of LVQ neural network in smart city traffic network prediction. *IEEE Access* **8**, 104555–104564 (2020)
31. Zhuang, J., Luo, H., Pan, T.S., Pan, J.S.: Improved flower pollination algorithm for the capacitated vehicle routing problem. *J. Netw. Intell.* **5**(3), 141–156 (2020)



# Chapter 17

## QUasi-Affine TRansformation Evolution Algorithm for Optimal Power Flow of Integrated Electrical Network Combining Thermal Power with Wind Power



Jianpo Li, Min Gao, Shu-Chuan Chu, Geng-Chen Li, and Jeng-Shyang Pan

**Abstract** With the development of electric power industry, it is of great technical and economic significance to introduce the optimal power flow (OPF) calculation into the economic analysis of electric power market, which can not be realized by the traditional power flow calculation. At present, many researchers have applied evolutionary algorithms to the calculation of optimal power flow. QUasi-Affine TRansformation Evolutionary (QUATRE) algorithm is a new evolutionary algorithm, combined with the OPF model of power market, which has high efficiency and significance for the economic analysis of power market. In this paper, the minimization of generation cost and active power loss is taken as the objective function, and QUATRE is selected as the optimization tool to study the OPF. In this paper, the simulation experiment of this problem is carried out, and compared with Particle Swarm Optimization (PSO), Artificial Bee Colony (ABC) and Moth Swarm Algorithm (MSA). Through the analysis of the experimental results, it can be seen that QUATRE is superior to other algorithms in terms of power generation cost, active power loss and CPU time.

---

J. Li · M. Gao · G.-C. Li

School of Computer Science, Northeast Electric Power University, Jilin 132012, China  
e-mail: [15822553806@163.com](mailto:15822553806@163.com)

S.-C. Chu · J.-S. Pan (✉)

College of Computer Science and Engineering, Shandong University of Science and Technology, Qingdao 266590, China

S.-C. Chu

College of Science and Engineering, Flinders University, Clovelly Park 5042, Australia

J.-S. Pan

Department of Information Management, Chaoyang University of Technology, Taichung, Taiwan

## 17.1 Introduction

Evolutionary algorithm (EA) is a powerful global optimization method, which belongs to the category of meta-heuristic technology [1–4]. Different from traditional mathematical programming techniques, evolutionary algorithms, such as PSO [5, 6], ABC [7] and MSA [8], etc., attempt to find the global optimal population derived from a certain probability distribution through iterative evolution according to a series of evolution and learning mechanisms. Inspired by different species or natural phenomena in nature, these algorithms carry out mathematical modeling according to the characteristics of natural landscape or the behavior of creatures, and finally find the global optimal solution [9–11]. QUATRE, a cooperative swarm based algorithm for global optimization, was first proposed by Meng et al. The QUATRE conquers some weaknesses of DE [12–15]. Since Quatre was proposed, it has received extensive attention from researchers, and has been improved and applied in various fields.

Optimal power flow (OPF) has always been a research hotspot in the field of power. The main purpose of OPF is to minimize the cost of power generation. The traditional OPF problem is only to reduce the fossil energy consumption on the thermal power unit [16–18]. As times have changed, simply reducing the cost of generating electricity is no longer enough to meet the demands of today's power industry. Safety, stability, efficiency, power quality and other aspects are also included in the research [19–21]. Therefore, in order to make the power system run economically and efficiently, the power generation and loss of multiple power sources in the power network must be optimized. The electronically controlled Flexible AC Transmission System (FACTS) can improve power generation and transmission capabilities. It is necessary to add FACTS equipment to the study of power grid [22, 23].

To sum up, this paper proposes an OPF problem for power system combining thermal power generation and wind power generation using QUATRE optimization. The work arrangement of other parts is as follows: First, QUATRE is introduced. Second, the objective function of OPF problem combining thermal power and wind power is introduced. In the third part, QUATRE is applied to the model and the experimental results are analyzed. Finally, a summary of the work done is given.

## 17.2 QUasi-Affine TRansformation Evolution

Quatre uses the principle similar to the mapping transformation function in geometry  $f : X \rightarrow Y$ . In the D-dimensional search space,  $X$  represents the coordinate matrix of the particle, and the coordinate matrix of the  $i$ th particle is expressed as:  $X_i = [x_1, x_2, \dots, x_D]$ . The position coordinate matrix of the entire population is expressed as:  $X = [X_1, X_2, \dots, X_{ps}]^T$ . The position update equation of the entire population is as follows:

$$\begin{cases} B = X_{\text{gbest}} + c \times (X_{r1} - X_{r2}) \\ X \mapsto M \otimes X + \overline{M} \otimes B \end{cases} \quad (17.1)$$

where  $X_{\text{gbest}}$  represents the globally optimal population composed of globally optimal individuals, and every individual of  $X_{\text{gbest}}$  is the current globally optimal individual  $X_{\text{gbest}}$ . The global optimal population  $X_{\text{gbest}}$  is disturbed by the difference matrix, and the disturbed global optimal population is represented by  $B$ .  $X_{r1}$  and  $X_{r2}$  are two matrices obtained by random permutation of row vectors of  $X$ . The result of  $X_{r1} - X_{r2}$  represents the difference matrix.  $c$  is the difference matrix coefficient.  $M$  is choosing matrix, as shown in Eq. (17.2),  $M$  is obtained by  $M_{\text{imp}}$  transformation. The transformation process is: First, the line has a  $D \times D$  column along with a column direction tile lower triangular matrix, and then each row vector elements are arranged at random, and finally on the premise of the row vector unchanged on line in the direction of the column vector of random arrangement.  $\otimes$  means multiplying the elements in the corresponding positions in the two matrices.

$$M_{\text{imp}} = \begin{bmatrix} 1 & & & \\ 1 & 1 & & \\ & & \dots & \\ 1 & 1 & \dots & 1 \end{bmatrix} \sim \begin{bmatrix} 1 & 1 & & \\ & \dots & & \\ 1 & 1 & \dots & 1 \\ & & & 1 \end{bmatrix} = M \quad (17.2)$$

### 17.3 FACTS Equipment and Optimal Power Flow Problem for Combining Thermal Power with Wind Power

The FACTS devices developed in recent years have also been widely used in power systems. They can not only improve the steady-state operation characteristics of the system, but also significantly improve the stability of the power system to varying degrees, thus greatly increasing the transmission capacity of the transmission lines. In [24], TCSC, TCPS and SVC equipment are explained in detail, and these three components will also be used for experiments in this paper. In the section, the objective function of operating cost and active power loss of power plant are described.

#### 17.3.1 Operating Costs of Power Plants

The traditional OPF problem usually only considers the fuel cost of thermal power plants, while the research in this paper also considers the cost of wind power plants on the basis of traditional experiments. The direct cost of wind power generation is different from thermal power generation, it does not need fuel. The distribution

of wind speed is mainly modeled by Weibull probability density function (PDF). However, the biggest problem of wind power into the grid is the uncertainty of wind energy. Therefore, according to reference [25], the objective function used in this paper not only considers the generation cost of thermal power units  $C_{Ti}(P_{TGi})$ , but also considers the direct cost  $C_{w,j}(P_{ws,j})$ , reserve cost  $C_{Rwj}(P_{wsj} - P_{wavj})$  and penalty cost  $C_{Pwj}(P_{wavj} - P_{wsj})$  of wind power generation. To sum up, for the improved system including wind farms, the total power generation is:

$$C_{\text{gen}} = \sum_{i=1}^{N_{TG}} C_{Ti}(P_{TGi}) + \sum_{j=1}^{N_{WG}} [C_{wi}(P_{wsj}) + C_{Rwj}(P_{wsj} - P_{wavj}) + C_{Pwj}(P_{wavj} - P_{wsj})] \quad (17.3)$$

### 17.3.2 Loss of Active Power

Due to the inherent resistance of the transmission system, actual power loss is inevitable. The actual power loss to be minimized is expressed as:

$$P_{\text{loss}} = \sum_{q=1}^{nl} G_{q(mn)} [V_m^2 + V_n^2 - 2V_m V_n \cos(\delta_{mn})] \quad (17.4)$$

where  $\delta_{mn} = \delta_m - \delta_n$  is the voltage phase difference between bus  $m$  and  $n$ .  $nl$  is the number of transmission lines.  $G_{q(mn)}$  is connected to the bus  $m$  and  $n$  branch transfer conductance.

## 17.4 Experimental Results and Analysis

To verify the superiority of the QUATRE to optimize the integrated use of thermal power and wind power in terms of cost, power loss and time efficiency, this experiment uses the QUATRE to optimize the results and compare the results of the simulation experiments with PSO, ABC and MSA. The voltage phase angle of all calculation examples in this experiment is degrees, and the voltage amplitude is the standard unit value. This paper uses the QUATRE to solve the OPF model. The specific parameters are: 1000 iterations (*Iteration*) and 20 population size (*Pop*). All experimental results are the average of 20 independent runs. The parameters of each algorithm in this experiment are set as Table 17.1.

**Table 17.1** Parameter setting

Algorithm	Parameter
PSO	$c = 2.0, w = 0.9, Pop = 20, Iteration = 1000$
ABC	Onlooker bees = 20, $Pop = 20, Iteration = 1000$
MSA	Pathfinders = 6, $Pop = 20, Iteration = 1000$
QUATRE	$F = 0.7, Pop = 20, Iteration = 1000$

### 17.4.1 Experimental Results to Minimize Power Generation Costs

Experiment with the lowest total cost. The algorithm used is the QUATRE. The experimental results are shown in Table 17.2 and Fig. 17.1. Table 17.2 shows the OPF results of using the QUATRE to optimize wind power and thermal power integrated systems under the premise of minimizing cost. It is a comparison of the cost (*Cost*) and the time (*Time*) used by the CPU for the QUATRE and other algorithms running 20 times to average. It can be seen from the results that the QUATRE proposed in this article has the lowest cost and the least CPU time. The QUATRE and the ABC show a similar trend in solving cost problems. However, ABC shows worse results in terms of CPU time. This shows that QUATRE is very effective in solving such problems.

Figure 17.1 shows the convergence curve of the QUATRE, PSO, ABC and MSA. The results show that before the number of iterations is 150, and these four algorithms all show positive optimization contributions. However, after iterating to 150, especially the PSO was confused by the local optimum, the algorithm did not find a better result in the end and the cost did not decrease. However, the QUATRE proposed in this paper just solves the defect of PSO falling into the local optimum, and it is better to find a lower cost solution. In particular, the QUATRE is weaker than the optimization result of ABC when the iteration reaches 300 times. When iterated to 300 times, QUATRE showed excellent optimization ability. This shows that the QUATRE has a good advantage of jumping out of the local optimum to find the best result.

**Table 17.2** Comparison of cost and CPU time between QUATRE algorithm and other algorithms

Algorithm	Cost	Time (s)
QUATRE	807.1902471	2703.6273
PSO	863.5147728	2696.5206
ABC	808.3618035	12476.1603
MSA	862.95555	2046.4562

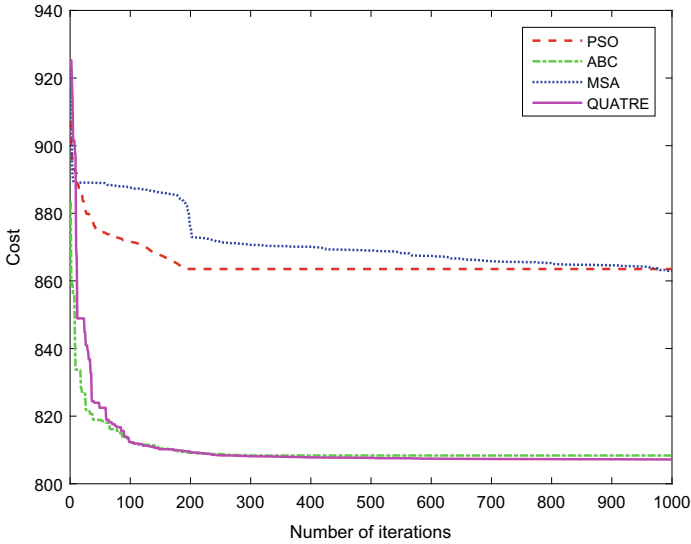


**Fig. 17.1** Convergence curve of IEEE30 bus system based on several algorithms based on the minimum cost

### 17.4.2 Experimental Results of Minimizing Loss of Active Power

Figure 17.2 shows the convergence curve of QUATRE, PSO, ABC and MSA. The results showed that QUATRE and ABC showed a very similar optimization process. This is similar to the optimization process based on the lowest cost. However, as can be seen from Table 17.3, although the optimization capability of ABC is similar to that of QUATRE, it takes a lot of time. However, when PSO reached 100 iterations, it was confused by the local optimum, so that the algorithm did not find a better result in the end so that the power consumption did not decrease. The QUATRE, ABC and MSA proposed in this paper all just solve the defect of PSO falling into the local optimum and find a solution with lower power consumption. However, the QUATRE proposed in this article performs better, especially when the algorithm is iterated to 300, the PSO and ABC basically fall into the local optimum, while the QUATRE is still searching for the best. And the CPU time used by the QUATRE is also relatively small at 3346.150977 s. To sum up, the QUATRE proposed in this article is excellent and effective in solving the integrated OPF problem of wind power and thermal power, and the CPU time is short.

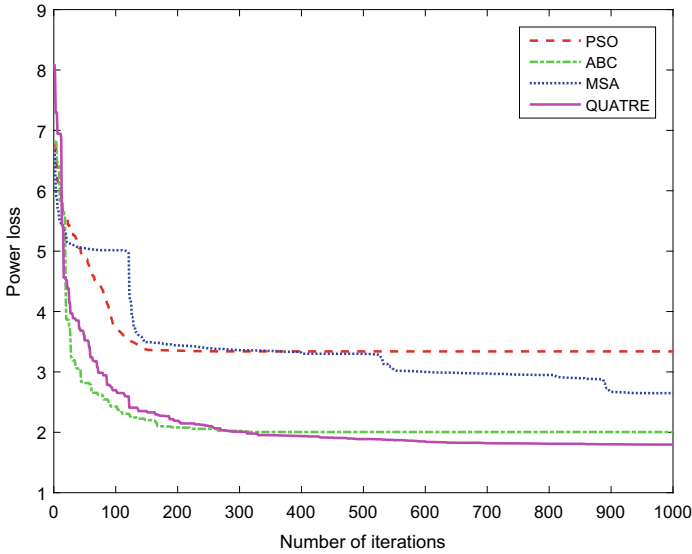


**Fig. 17.2** Convergence curve of IEEE30 bus system based on several algorithms with minimum power consumption as standard

**Table 17.3** Comparison of cost and CPU time between QUATRE algorithm and other algorithms

Algorithm	Power loss	Time (s)
QUATRE	1.79699357374803	3346.0977
PSO	3.33964565872995	3113.2299
ABC	2.00460970889308	4898.7694
MSA	2.64827655091987	3327.0151

### 17.5 Conclusions

In the field of power research, the optimal OPF has been concerned by researchers. This paper introduces the OPF problem of a power system which combines thermal power generation with wind power generation using FACTS equipment. The traditional calculation of power generation cost only considers the cost of thermal power generation. In this study, the direct cost of wind energy, penalty cost and reserve cost are also included in the cost calculation. And joined the FACTS equipment: TCSC, TCPS and SVC. In order to minimize the generation cost and the active power loss, QUATRE is used for optimization. Through the simulation results, we can see that the optimization performance of QUATRE in the system is much better than PSO, ABC and MAS. This shows that QUATRE is effective in solving the OPF problem.

## References

1. Xue, X., Pan, J.-S.: A compact co-evolutionary algorithm for sensor ontology meta-matching. *Knowl. Inform. Syst.* **56**(2), 335–353 (2018)
2. Pan, J.-S., Dao, T.-K., Pan, T.-S., Nguyen, T.T., Chu, S.C., Roddick, J.-F.: An improvement of flower pollination algorithm for node localization optimization in WSN. *J. Inform. Hiding Multimedia Signal Process.* **8**(2), 486–499 (2017)
3. Chu, S.-C., Xue, X., Pan, J.-S., Wu, X.: Optimizing ontology alignment in vector space. *J. Internet Technol.* **21**(1), 15–22 (2020)
4. Gao, M., Pan, J.-S., Li, J.-P., Zhang, Z.-P., Chai, Q.-W.: 3-d terrains deployment of wireless sensors network by utilizing parallel gases Brownian motion optimization. *J. Internet Technol.* **22**(1), 13–29 (2021)
5. Eberhart, R., Kennedy, J.: Particle swarm optimization. In: *Proceedings of the IEEE International Conference on Neural Networks*, vol. 4, pp. 1942–1948. Citeseer (1995)
6. Sun, C., Zeng, J., Pan, J., Xue, S., Jin, Y.: A new fitness estimation strategy for particle swarm optimization. *Inform. Sci.* **221**, 355–370 (2013)
7. Karaboga, D., Basturk, B.: On the performance of artificial bee colony (ABC) algorithm. *Appl. Soft Comput.* **8**(1), 687–697 (2008)
8. Ali Mohamed, A.-A., Mohamed, Y.S., El-Gaafary, A.A.M., Hemeida, A.M.: Optimal power flow using moth swarm algorithm. *Electric Power Syst. Res.* **142**, 190–206 (2017)
9. Chu, S.-C., Huang, H.-C., Roddick, J.F., Pan, J.-S.: Overview of algorithms for swarm intelligence. In: *International Conference on Computational Collective Intelligence*, pp. 28–41. Springer, Berlin (2011)
10. Chu, S.-C., Roddick, J.F., Su, C.-J., Pan, J.-S.: Constrained ant colony optimization for data clustering. In: *Pacific Rim International Conference on Artificial Intelligence*, pp. 534–543. Springer, Berlin (2004)
11. Pan, J.-S., Meng, Z., Chu, S.-C., Xu, H.-R.: Monkey king evolution: an enhanced ebb-tide-fish algorithm for global optimization and its application in vehicle navigation under wireless sensor network environment. *Telecommunication Systems* **65**(3), 351–364 (2017)
12. Du, Z.G., Pan, J.S., Chu, S.C., Luo, H.J., Hu, P.: Quasi-affine transformation evolutionary algorithm with communication schemes for application of RSSI in wireless sensor networks. *IEEE Access* **99**, 1 (2020)
13. Pan, J.-S., Meng, Z., Xu, X., Li, X.: A matrix-based implementation of de algorithm: the compensation and deficiency. In: *International Conference on Industrial, Engineering and Other Applications of Applied Intelligent Systems*, pp. 72–81. Springer, Berlin (2017)
14. Meng, Z., Pan, J.-S.: Quasi-affine transformation evolutionary (quatre) algorithm: a parameter-reduced differential evolution algorithm for optimization problems. In: *2016 IEEE Congress on Evolutionary Computation (CEC)*, pp. 4082–4089. IEEE (2016)
15. Xu, X.-W., Pan, T.-S., Song, P.-C., Hu, C.-C., Chu, S.-C.: Multi-cluster based equilibrium optimizer algorithm with compact approach for power system network. *J. Network Intell.* **6**(1), 117–142 (2021)
16. Chaib, A.E., Bouchekara, H.R.E.H., Mehasni, R., Abido, M. A.: Optimal power flow with emission and non-smooth cost functions using backtracking search optimization algorithm. *Int. J. Electr. Power Energy Syst.* **81**, 64–77 (2016)
17. Li, J., Zhang, Q., Zhang, Z., Yin, Y., Zhang, H.: Congestion control and energy optimization routing algorithm for wireless sensor networks. *J. Northeast Electric Power Univ.* **40**(4), 69–74 (2020)
18. Wu, C., Shang, H.: Qos-aware resource allocation for d2d communications. *J. Northeast Electric Power Univ.* **40**(2), 89–95 (2020)
19. Daryani, N., Hagh, M.T., Teimourzadeh, S.: Adaptive group search optimization algorithm for multi-objective optimal power flow problem. *Appl. Soft Comput.* **38**, 1012–1024 (2016)
20. Wu, T.-Y., Jerry, C.-W.L., Zhang, Y., Chen, C.-H.: A grid-based swarm intelligence algorithm for privacy-preserving data mining. *Appl. Sci.* **9**(4), 774 (2019)



21. Kong, L., Chen, C.-M., Shih, H.-C., Lin, C.-W., He, B.-Z., Pan, J.-S.: An energy-aware routing protocol using cat swarm optimization for wireless sensor networks. In: *Advanced Technologies, Embedded and Multimedia for Human-Centric Computing*, pp. 311–318. Springer, Berlin (2014)
22. Pan, J.-S., Nguyen, T.-T., Dao, T.-K., Pan, T.-S., Chu, S.-C.: Clustering formation in wireless sensor networks: a survey. *J. Netw. Intell.* **2**(4), 287–309 (2017)
23. Sun, Z., Yang, D.: D2d radio resource allocation algorithm based on global fairness. *J. Northeast Electric Power Univ.* **39**(1), 81–87 (2019)
24. Biswas, P.P., Arora, P., Mallipeddi, R., Suganthan, P.N., Panigrahi, B.K.: Optimal placement and sizing of facts devices for optimal power flow in a wind power integrated electrical network. *Neural Comput. Appl.* 1–22 (2020)
25. Biswas, P.P., Suganthan, P.N., Amaratunga, G.A.J.: Optimal power flow solutions incorporating stochastic wind and solar power. *Energy Convers. Manage.* **148**, 1194–1207 (2017)

# Chapter 18

## Hybrid Optimization Algorithm Based on QUATRE and ABC Algorithms



Xin Zhang, Linlin Tang, Shu-Chuan Chu, Shaowei Weng,  
and Jeng-Shyang Pan

**Abstract** Artificial bee colony optimization algorithm (ABC) is an optimization algorithm based on swarm intelligence which is obtained by observing the behavior of bees looking for nectar and sharing food information with bees in the hive. QUasi-Affine TRansformation Evolutionary (QUATRE) is an algorithm that uses quasi-affine transformation as an evolution method because ABC has the shortcoming of weak ability to develop new nectar sources, and QUATRE has weak search ability but strong development ability, so this paper combines these two algorithms to a certain extent and proposes an improved artificial bee colony optimization algorithm (QUA-ABC). QUA-ABC is inspired by the location update formula in QUATRE and proposes a new location update formula suitable for ABC. In this study, experiments were conducted using the internationally used CEC2013 data set. The optimization accuracy and convergence speed of QUA-ABC were compared with the original ABC. The results show that the QUA-ABC algorithm has stronger capabilities and better performance.

---

X. Zhang · S. Weng · J.-S. Pan (✉)

College of Computer Science and Mathematics, Fujian University of Technology, Fuzhou, China  
e-mail: [jspan@ieee.org](mailto:jspan@ieee.org)

X. Zhang

e-mail: [2191905014@smail.fjut.edu.cn](mailto:2191905014@smail.fjut.edu.cn)

S. Weng

e-mail: [wswweiwei@126.com](mailto:wswweiwei@126.com)

S.-C. Chu · J.-S. Pan

College of Computer Science and Engineering, Shandong University of Science and Technology, Qingdao, China

L. Tang

College of Computer Science and Technology, Harbin Institute of Technology, Shenzhen, China  
e-mail: [hittang@126.com](mailto:hittang@126.com)

S.-C. Chu

College of Science and Engineering, Flinders University, Bedford Park, Australia

## 18.1 Introduction

At present, optimization has been the focus of many fields, including computer science, artificial intelligence, and other fields. The traditional optimization method in solving problems, the time required is controlled by the scale of the problem. Moreover, the calculation time gradually increases as the scale of the problem increases, which is very unfavorable for solving complex problems. Swarm intelligence algorithm is a popular algorithm in recent years [22, 23]. It is obtained by studying the intelligent behavior of biological groups in nature [1], such as particle swarm optimization (PSO) [3, 24], differential evolution algorithm (DE) [25], artificial bee colony optimization algorithm (ABC) [26, 27], ant colony algorithm (ACO) [28, 29], etc. Compared with the traditional optimization methods, swarm intelligence algorithm is not limited by whether the search space is continuous or differentiable and can be optimized only by knowing the objective function in the whole optimization process. In addition, it does not need any other information [2].

In 1995, an American professor Seeley discovered the intelligent behaviors of swarms in bee colonies [4]. He proposed a simulation model in which bees are divided into different social classes, and different classes only can complete a single task and then work together to complete more complex tasks by dancing, smelling, and other methods, such as collecting honey by bees. Artificial bee colony optimization algorithm (ABC) was proposed in 2005 by Karaboga of Erciyes University in Turkey. This algorithm simulates the behavior of bees searching for nectar [5].

QUasi-Affine TRansformation Evolutionary algorithm (QUATRE) is a simple and powerful global optimization algorithm. It uses the quasi-radiation transformation method for evolution. It has only one control parameter and is relatively powerful in mathematical logic. It is not only effective in single objective function optimization problems, but also more effective in multi-objective function optimization problems [6–10].

## 18.2 Related Works

### 18.2.1 *Original Artificial Bee Colony Optimization Algorithm*

The employed bee collects honey from its corresponding honey source, searches for better honey source information near the honey source, and then returns to the hive to share its honey source information by dancing swing dance; the observing bee chooses to follow one of the employed bees to collect honey according to the honey source information, and the observing bee will randomly look for the better honey source near the honey source. When neither the employed bee nor the observing bee can find a better honey source nearby, the employed bee will turn into a detective bee and then conduct random search within the searchable range to update the honey source location.

The following is a brief introduction to the motion formula of artificial bee colony optimization algorithm.

Population initialization and scout bee movement formula.

$$x_{ij} = x_j^{\min} + \text{rand} \times (x_j^{\max} - x_j^{\min}) \quad (18.1)$$

In the formula,  $i = 1, 2, \dots, N$ ,  $N$  is the number of populations,  $j = 1, 2, \dots, D$ ,  $D$  is the dimension of the solution, and rand is a random number on  $[0,1]$ . According to formula (18.1) in the solution space, new individuals are randomly generated.

Employed bee movement formula.

$$x_{ij}(t+1) = x_{ij}(t) + \text{rand} \times [x_{ij}(t) - x_{kj}(t)] \quad (18.2)$$

In the formula, rand is a random number on  $[-1, 1]$ ,  $t$  is the number of iterations,  $i \neq k$ . At the beginning of the search, the employed bee searches for a new nectar source according to formula (18.2) and compares the function values of the new nectar source and the original nectar source; if the function value of the new nectar source is better, replace the original nectar source with the new nectar source, otherwise keep the original nectar source.

Observing bee movement formula.

$$P_i = \frac{F(x_i)}{\sum_{k=1}^S F(x_k)} \quad (18.3)$$

In the formula,  $S$  is the number of employed bees,  $F$  is the fitness value, and  $P_i$  is the probability that the observation bee chooses to follow the  $i$ th hired bee. Observing bees select the employed bees to collect honey according to the fitness value of the employed bees calculated by formula (18.3).

### ***18.2.2 Improved Artificial Bee Colony Optimization Algorithm***

In recent years, as people continue to study the ABC algorithm, many researchers have proposed improved bee colony algorithms. Below, we briefly introduce some famous variants of artificial bee colony algorithm.

Literature [11] selects destructive selection strategies, competition selection strategy, level selection strategy, and other new selection strategies. The comparison results show that the improved algorithm is better and avoids premature convergence. Literature [12] proposed a new bee colony algorithm—BeeMiner. Unlike the original bee colony algorithm, BeeMiner can use IHF to guide bees to search in areas with higher fitness values, which can be used to discover classification rules.

Literature [13] proposed a memetic artificial bee colony (MABC) algorithm, which uses random adaptation rules based on NMA and RWDE to control the balance between search and development. Literature [14] obtained a new algorithm (ABC-GSX) through the combination of the greedy sub-path crossover operator, which improved the accuracy of the bee colony algorithm and improved the development ability of the bee colony algorithm.

## 18.3 Method

### 18.3.1 The Basic Idea of QUATRE Algorithm

In geometry, affine transformation, also known as affine mapping, is the transformation from one space to another through the combination of two functions of translation and linear transformation. An affine transformation function that translates  $B$  to vector  $X$  and rotates to enlarge and reduce  $M$  is  $Y = MX + B$ . In the QUATRE algorithm, a quasi-affine change method ( $Y = M \otimes X + \overline{M} \otimes B$ ) is used as its evolution method.

$$\begin{cases} B = X_{\text{gbest}} + c \times (X_{r_1} - X_{r_2}) \\ X \rightarrow M \otimes X + \overline{M} \otimes B \end{cases} \quad (18.4)$$

Formula (18.4) is the position update formula of the QUATRE algorithm. The result of  $X_{r_1} - X_{r_2}$  is regarded as a differential matrix,  $c$  is the coefficient of this differential matrix, and  $X_{\text{gbest}}$  is the coordinate matrix of the global optimal solution.  $M$  is the collaborative search matrix,  $\overline{M}$  is the inverse matrix of matrix  $M$ , the inverse binary operation of 1 is 0, and the inverse binary operation of 0 is 1.

$$\begin{bmatrix} 1 & & & \\ 1 & 1 & & \\ & & \dots & \\ 1 & 1 & \dots & 1 \end{bmatrix} \sim \begin{bmatrix} 1 & & & \\ \dots & & & \\ 1 & & \dots & 1 \\ & & 1 & & 1 \end{bmatrix} = M \quad (18.5)$$

Formula (18.5) is the transformation formula of matrix  $M$ . It can be seen that matrix  $M$  is converted from a lower triangular matrix with all 1 elements. The whole conversion process is divided into two steps: the first step is to randomly replace the lower triangular matrix. Row elements are processed separately for each row; the second step is to randomly replace the row vector of the matrix, and the row elements remain unchanged.

### 18.3.2 The QUA-ABC Algorithm Improvement Idea

Because of ABC's strong search ability and weak development ability, and QUATRE's strong development ability, this study proposes a new improvement strategy. The position update formula of QUATRE algorithm is improved to replace the position update formula of ABC algorithm (18.2), and a new algorithm—QUA-ABC algorithm is obtained.

$$\begin{cases} B_i = X_{\text{gbest}} + \text{rand} \times (X_{r_1} - X_{r_2}) \\ X_i = M_i \otimes X_i + \overline{M}_i \otimes B_i \end{cases} \quad (18.6)$$

$$[1, 1, \dots, 1_{z \times D}, 0, 0, \dots, 0_{(1-z) \times D}] \sim [0, 1, 1, 0, \dots, 1, 0] = M_i \quad (18.7)$$

The position update formula of the new algorithm is shown in formula (18.6), where rand is a random number on  $[-1, 1]$ . In the QUATRE algorithm, it was originally a constant  $c$ . This study changed the constant to a random number, which enhanced the randomness of the algorithm.  $X_i$  is the position of the  $i$ th bee,  $X_{r_1}$  and  $X_{r_2}$  are randomly selected two bees different from  $X_i$ , namely  $X_i \neq X_{r_1} \neq X_{r_2}$ , and  $X_{\text{gbest}}$  is the same as in the QUATRE algorithm, which is the position of the current global optimal solution. As shown in formula (18.7),  $M_i$  is a collaborative search matrix with one row and  $D$  columns,  $D$  represents the dimension,  $z$  is a constant on  $(0, 1)$ , and  $M_i$  is composed of  $z$ -dimensional 1 and  $1-z$ -dimensional 0 after random replacement [15–21].

## 18.4 Experimental Results

This research uses the internationally used CEC2013 data set to test the performance of the QUA-ABC algorithm. The CEC2013 data set contains 28 benchmark functions, which are divided into three categories. Among them:  $f_1$  to  $f_5$  are Unimodal Functions,  $f_6$  to  $f_{20}$  are Basic Multimodal Functions, and  $f_{21}$  to  $f_{28}$  are Composition Functions.

In this experiment, the QUA-ABC algorithm was compared with the original ABC algorithm to verify the performance of the QUA-ABC algorithm proposed in this research. In the moving phase of the employed bee, this experiment sets the parameter  $z$  in the QUA-ABC algorithm to  $1/2$ ; in the moving phase of the observing bee, this experiment sets the parameter  $z$  in the QUA-ABC algorithm to  $3/10$ .

This experiment was performed on Windows10 Home Edition operating system with a 1.60 GHz Intel i5-8265U processor with 8 GB RAM. All algorithms run on Matlab2019a. They will perform 51 independent experiments, which will be less than  $\text{eps} = 1e-14$  fitness errors is set to 0; maxFES is set to  $10e4 * D$ , and  $D$  is the dimension size.

On the CEC2013 test set, this experiment compares the optimization accuracy of the QUA-ABC algorithm and the original ABC algorithm in 10 dimensions, 30 dimensions, and 50 dimensions. The comparison results are summarized in Tables 18.1, 18.2, and 18.3.

Take the average value as the main reference basis, and it can be seen from Table 18.1 that for the 10-dimensional optimization results, 15 of the 28 benchmark functions show that the performance of the QUA-ABC algorithm proposed in this

**Table 18.1** 10-dimensional comparison results under the CEC2013 data set

Algorithms	QUA-ABC		ABC	
	Best	Mean/Std	Best	Mean/Std
$f_1$	0.00E+00	0.00E+00/0.00E+00	0.00E+00	1.34E-14/5.40E-14
$f_2$	5.91E+03	9.88E+04/7.73E+04	2.52E+05	1.34E+06/7.67E+05
$f_3$	1.16E-02	6.85E+06/2.05E+07	8.52E+04	2.22E+06/2.73E+06
$f_4$	9.30E+01	6.40E+02/3.71E+02	7.06E+03	1.17E+04/2.90E+03
$f_5$	0.00E+00	3.12E-14/6.46E-14	0.00E+00	1.11E-13/1.59E-14
$f_6$	1.29E-03	7.12E+00/8.41E+00	1.25E-02	2.01E-01/3.90E-01
$f_7$	2.63E-02	1.42E+01/1.59E+01	1.67E+01	3.45E+01/1.02E+01
$f_8$	2.02E+01	2.03E+01/7.10E-02	2.02E+01	2.04E+01/7.99E-02
$f_9$	3.73E-01	3.29E+00/1.26E+00	3.33E+00	5.09E+00/7.54E-01
$f_{10}$	7.38E-02	4.50E-01/3.90E-01	3.73E-01	1.13E+00/4.22E-01
$f_{11}$	0.00E+00	3.12E-01/5.45E-01	0.00E+00	0.00E+00/0.00E+00
$f_{12}$	2.98E+00	1.60E+01/6.28E+00	1.35E+01	2.49E+01/6.61E+00
$f_{13}$	6.30E+00	2.10E+01/9.77E+00	6.26E+00	3.23E+01/7.65E+00
$f_{14}$	1.87E-01	2.48E+01/4.86E+01	4.15E-09	1.04E-01/5.69E-02
$f_{15}$	2.07E+02	6.65E+02/2.21E+02	3.78E+02	6.70E+02/1.24E+02
$f_{16}$	5.07E-01	1.10E+00/2.45E-01	3.28E-01	5.87E-01/1.33E-01
$f_{17}$	3.78E-02	9.55E+00/3.34E+00	7.83E-01	6.23E+00/4.07E+00
$f_{18}$	1.21E+01	2.20E+01/6.02E+00	2.58E+01	3.44E+01/4.72E+00
$f_{19}$	1.78E-01	5.11E-01/1.65E-01	9.95E-03	4.16E-02/1.85E-02
$f_{20}$	1.48E+00	2.72E+00/5.96E-01	2.29E+00	3.29E+00/3.28E-01
$f_{21}$	1.00E+02	3.73E+02/7.24E+01	3.53E+00	1.25E+02/4.55E+01
$f_{22}$	1.65E+01	1.41E+02/1.07E+02	3.42E+00	9.75E+00/3.37E+00
$f_{23}$	1.14E+02	7.03E+02/3.20E+02	2.75E+02	9.90E+02/2.17E+02
$f_{24}$	2.00E+02	2.11E+02/5.17E+00	1.13E+02	1.29E+02/8.59E+00
$f_{25}$	2.01E+02	2.10E+02/4.97E+00	1.19E+02	1.57E+02/1.94E+01
$f_{26}$	1.06E+02	1.62E+02/4.71E+01	1.13E+02	1.29E+02/8.40E+00
$f_{27}$	3.01E+02	3.86E+02/9.32E+01	3.38E+02	3.88E+02/1.88E+01
$f_{28}$	1.00E+02	3.35E+02/1.12E+02	1.00E+02	1.18E+02/4.64E+01
w/t/1			15/0/13	

**Table 18.2** 30-dimensional comparison results under the CEC2013 data set

Algorithms	QUA-ABC		ABC	
	Best	Mean/Std	Best	Mean/Std
$f_1$	0.00E+00	1.28E-12/6.38E-12	2.27E-13	4.59E-13/8.50E-14
$f_2$	3.67E+05	1.64E+06/1.06E+06	2.18E+06	9.29E+06/3.09E+06
$f_3$	5.99E+05	1.95E+08/3.02E+08	1.05E+07	3.87E+08/3.63E+08
$f_4$	3.28E+02	1.21E+03/5.92E+02	5.79E+04	9.32E+04/1.35E+04
$f_5$	1.14E-13	4.48E-13/5.13E-13	3.41E-13	6.06E-13/9.82E-14
$f_6$	9.18E+00	3.04E+01/2.39E+01	3.90E+00	1.46E+01/4.40E+00
$f_7$	3.11E+01	7.25E+01/3.00E+01	9.06E+01	1.21E+02/1.72E+01
$f_8$	2.08E+01	2.10E+01/4.23E-02	2.07E+01	2.12E+01/5.60E-02
$f_9$	1.45E+01	2.12E+01/3.18E+00	2.25E+01	2.99E+01/2.42E+00
$f_{10}$	1.72E-02	1.96E-01/1.40E-01	8.22E-01	1.46E+00/2.51E-01
$f_{11}$	6.96E+00	2.04E+01/9.74E+00	5.68E-14	5.91E-14/1.11E-14
$f_{12}$	5.77E+01	1.11E+02/2.32E+01	2.02E+02	2.81E+02/3.72E+01
$f_{13}$	8.74E+01	1.64E+02/3.65E+01	2.02E+02	3.18E+02/3.64E+01
$f_{14}$	1.56E+02	6.18E+02/2.75E+02	2.08E-02	2.04E-01/2.89E-01
$f_{15}$	1.74E+03	3.81E+03/7.82E+02	2.98E+03	3.86E+03/3.82E+02
$f_{16}$	1.76E+00	2.32E+00/2.92E-01	5.86E-01	1.05E+00/1.68E-01
$f_{17}$	3.99E+01	5.78E+01/1.00E+01	8.85E+00	3.01E+01/3.03E+00
$f_{18}$	7.49E+01	1.14E+02/2.30E+01	2.17E+02	2.96E+02/3.28E+01
$f_{19}$	2.82E+00	1.07E+01/6.43E+00	1.56E-01	3.60E-01/9.72E-02
$f_{20}$	8.89E+00	1.11E+01/6.89E-01	1.33E+01	1.45E+01/3.08E-01
$f_{21}$	1.00E+02	2.90E+02/8.72E+01	1.08E+02	1.58E+02/3.60E+01
$f_{22}$	3.42E+02	9.87E+02/3.47E+02	1.57E+01	3.03E+01/1.60E+01
$f_{23}$	2.64E+03	4.20E+03/8.19E+02	3.42E+03	4.79E+03/4.39E+02
$f_{24}$	2.41E+02	2.61E+02/9.44E+00	2.71E+02	2.89E+02/6.31E+00
$f_{25}$	2.64E+02	2.79E+02/8.46E+00	2.98E+02	3.09E+02/5.23E+00
$f_{26}$	2.00E+02	2.68E+02/7.62E+01	2.00E+02	2.01E+02/2.33E-01
$f_{27}$	6.89E+02	8.66E+02/8.47E+01	4.00E+02	4.30E+02/1.51E+02
$f_{28}$	1.00E+02	4.21E+02/3.87E+02	1.03E+02	2.11E+02/9.34E+01
w/t/l			16/0/12	

research has improved; from Table 18.2, it can be seen that the 30-dimensional optimization results, among the 28 benchmark functions, 16 functions show that the performance of the QUA-ABC algorithm proposed in this study has improved; from Table 18.3, it can be seen that for the 50-dimensional optimization results, 15 of the 28 benchmark functions show this research; the performance of the proposed QUA-ABC algorithm has been improved. It can be seen from the above three comparison results that the QUA-ABC algorithm proposed in this study has better performance.



**Table 18.3** 50-dimensional comparison results under the CEC2013 data set

Algorithms	QUA-ABC		ABC	
	Best	Mean/Std	Best	Mean/Std
$f_1$	2.27E-13	6.94E-12/1.82E-11	6.82E-13	9.27E-13/1.27E-13
$f_2$	1.90E+06	5.33E+06/2.41E+06	5.92E+06	1.51E+07/3.69E+06
$f_3$	8.71E+07	1.80E+09/1.45E+09	1.91E+08	1.69E+09/1.35E+09
$f_4$	3.53E+02	1.89E+03/1.31E+03	1.25E+05	1.67E+05/1.77E+04
$f_5$	3.41E-13	7.46E-11/4.68E-10	9.09E-13	1.21E-12/1.35E-13
$f_6$	3.08E+01	5.90E+01/2.32E+01	1.47E+01	3.99E+01/6.84E+00
$f_7$	6.74E+01	1.02E+02/2.00E+01	1.29E+02	1.68E+02/1.79E+01
$f_8$	2.10E+01	2.10E+01/3.58E-02	2.10E+01	2.11E+01/3.40E-02
$f_9$	3.14E+01	4.38E+01/5.22E+00	5.57E+01	6.04E+01/2.18E+00
$f_{10}$	2.47E-02	1.30E-01/1.50E-01	8.83E-01	1.34E+00/2.14E-01
$f_{11}$	3.98E+01	1.01E+02/3.56E+01	5.68E-14	1.26E-13/2.62E-14
$f_{12}$	1.49E+02	2.48E+02/5.35E+01	4.85E+02	7.41E+02/8.90E+01
$f_{13}$	2.13E+02	3.95E+02/6.89E+01	45E+02	8.02E+02/8.13E+01
$f_{14}$	9.31E+02	1.71E+03/4.37E+02	6.25E-02	3.51E-01/3.95E-01
$f_{15}$	5.57E+03	7.66E+03/1.03E+03	6.96E+03	7.72E+03/4.10E+02
$f_{16}$	2.17E+00	3.10E+00/3.63E-01	9.49E-01	1.45E+00/2.31E-01
$f_{17}$	1.20E+02	1.99E+02/5.15E+01	5.09E+01	5.10E+01/6.74E-02
$f_{18}$	1.92E+02	2.94E+02/5.99E+01	5.82E+02	7.48E+02/6.63E+01
$f_{19}$	2.81E+01	8.40E+01/4.51E+01	4.72E-01	8.14E-01/1.41E-01
$f_{20}$	1.85E+01	2.05E+01/9.31E-01	2.41E+01	2.45E+01/7.53E-02
$f_{21}$	1.00E+02	7.26E+02/4.26E+02	1.25E+02	1.94E+02/2.33E+01
$f_{22}$	1.81E+03	2.82E+03/5.19E+02	2.53E+01	3.49E+01/4.72E+00
$f_{23}$	6.36E+03	8.38E+03/1.11E+03	8.16E+03	9.88E+03/7.76E+02
$f_{24}$	2.89E+02	3.23E+02/1.43E+01	3.50E+02	3.73E+02/8.73E+00
$f_{25}$	3.32E+02	3.57E+02/1.50E+01	3.88E+02	4.16E+02/1.03E+01
$f_{26}$	2.01E+02	3.93E+02/6.51E+01	2.01E+02	2.02E+02/3.76E-01
$f_{27}$	1.21E+03	1.46E+03/1.12E+02	4.00E+02	1.50E+03/7.51E+02
$f_{28}$	4.00E+02	1.68E+03/1.76E+03	4.00E+02	4.00E+02/1.38E-05
w/t/l			15/0/13	

This experiment also verifies the proposed QUA-ABC algorithm from the perspective of convergence speed. Figure 18.1 is a comparison of the convergence rate curves of the 30-dimensional QUA-ABC algorithm and the original ABC algorithm on the CEC2013 data set. It can be seen that in the functions  $f_4$ ,  $f_9$ ,  $f_{12}$ ,  $f_{13}$ ,  $f_{15}$ ,  $f_{18}$ ,  $f_{20}$ ,  $f_{25}$ , the convergence speed of the QUA-ABC algorithm is better than that of the ABC algorithm.

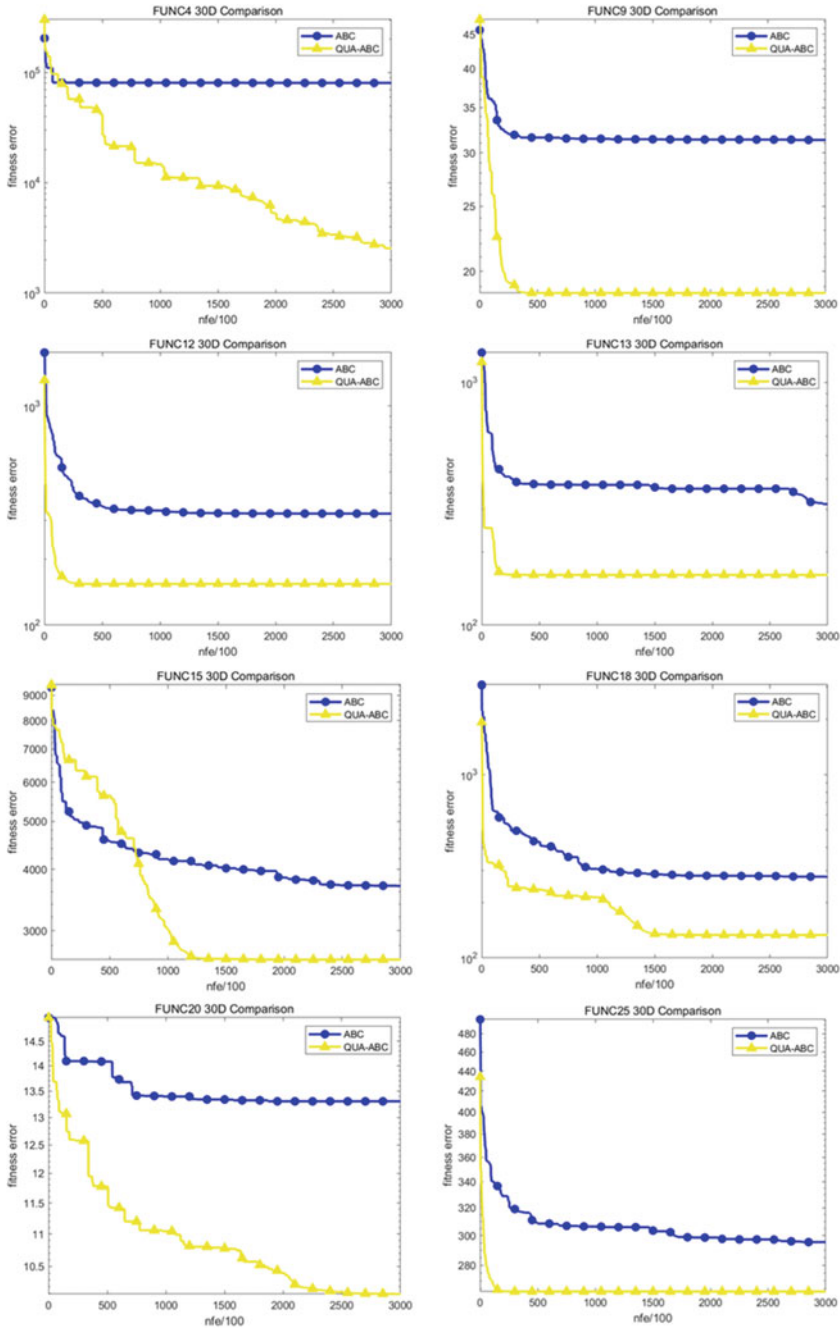


Fig. 18.1 Convergence curve graph in 30 dimensions

## 18.5 Conclusion

This research proposes a new algorithm—QUA-ABC algorithm, which is obtained by changing its position update formula on the basis of the original ABC. The new location update formula is obtained by changing the position update formula of QUATRE algorithm. The original ABC algorithm has the characteristics of weak nectar development ability, and the QUATRE algorithm has the characteristics of strong development ability. The QUA-ABC algorithm obtained by combining these two algorithms to a certain extent has stronger performance than the original ABC algorithm. Through the test of 28 functions in the CEC2013 data set, the QUA-ABC algorithm proposed in this study is better than the original ABC algorithm, whether it is optimization accuracy performance or convergence speed.

## References

1. Bonabeau, E.: Swarm intelligence : from natural to artificial systems. Santa Fe Inst. Stud. Sci. Complexity (1999)
2. Guo, W.: Research and development of algorithm based on swarm intelligence. *J. Henan Mech. Electr. Eng. Col.* (2007)
3. Kennedy, J., Eberhart, R.: Particle swarm optimization. In: Proceedings of IEEE International Conference on Neural Networks, Perth, pp. 1942–1948 (1995)
4. Menzel, R., Fuchs, J., Kirbach, A., et al.: Navigation and communication in honey bees. In: *Honeybee Neurobiology and Behavior*. Springer Netherlands (2012)
5. Karaboga, D., Basturk. B.: A powerful and efficient algorithm for numerical function optimization: artificial bee colony (ABC) algorithm. *J. Global Optim.* **39**(3), 459–471 (2007)
6. Meng, Z., Pan, J.-S., Xu, H.: QUasi-Affine TRansformation evolutionary (QUATRE) algorithm: a cooperative swarm based algorithm for global optimization. *Knowl. Based Syst.* **109**, 104–121 (2016)
7. Meng, Z., Pan, J.-S.: QUasi-Affine TRansformation evolution with external ARchive (QUATRE-EAR): an enhanced structure for differential evolution. *Knowl.-Based Syst.* **155**, 35–53 (2018)
8. Liu, N., Pan, J.-S., Xue, J.Y.: An orthogonal QUasi-Affine TRansformation evolution (O-QUATRE) algorithm for global optimization. *IIH-MSP*. Springer, vol 157, pp 57–66 (2019)
9. Meng, Z., Pan, J.-S.: QUasi-affine TRansformation Evolutionary (QUATRE) algorithm: a parameter-reduced differential evolution algorithm for optimization problems. *CEC* **2016**, 4082–4089 (2016)
10. Pan, J.-S., Meng, Z., Huarong, Xu., Li, X.: QUasi-affine TRansformation evolution (QUATRE) algorithm: a new simple and accurate structure for global optimization. *IEA/AIE* **2016**, 657–667 (2016)
11. Bao, L., Zeng, J.C.: Comparison and analysis of the selection mechanism in the artificial bee colony algorithm. In: ninth international conference on hybrid intelligent systems. *IEEE Computer Society* (2009)
12. Talebi, M., Abadi, M.: BeeMiner: a novel artificial bee colony algorithm for classification rule discovery. In: *Intell. Syst.* *IEEE* (2014)
13. Fister, I., Fister, I., Brest, J., et al.: Memetic artificial bee colony algorithm for large-scale global optimization (2012)
14. Banharnsakun, A., Achalakul, T., Sirinaovakul, B.: ABC-GSX: a hybrid method for solving the traveling salesman problem. In: *Second World Congress on Nature & Biologically Inspired Computing, NaBIC 2010, Kitakyushu, Japan, 15–17 Dec 2010*. *IEEE* (2010)

15. Jiang, B.-Q., Pan, J.-S.: A parallel quasi-affine transformation evolution algorithm for global optimization. *J. Network Intell.* **2**(4), 30–46 (2019)
16. Du, Z.-G., Pan, J.-S., Chu, S.-C., Luo, H.-J., Hu, P.: Quasi-affine transformation evolutionary algorithm with communication schemes for application of RSSI in wireless sensor networks. *IEEE Access* **8**, 8583–8594. <https://doi.org/10.1109/ACCESS.2020.2964783>
17. Liu, N., Pan, J.-S., Wang, J., Nguyen, T.-T.: An adaptation multi-group quasi-affine transformation evolutionary algorithm for global optimization and its application in node localization in wireless sensor networks. *Sensors* **19**(19), 4112 (2019). <https://doi.org/10.3390/s19194112>
18. Zhang, F., Tsu-Yang, Wu., Wang, Y., Xiong, R., Ding, G., Mei, P., Liu, L.: Application of quantum genetic optimization of LVQ neural network in smart city traffic network prediction. *IEEE Access* **8**, 104555–104564 (2020)
19. Chu, S.-C., Chen, Y., Meng, F., Yang, C., Pan, J.-S., Meng, Z.: Internal search of the evolution matrix in QUasi-Affine TRansformation Evolution (QUATRE) algorithm. *J. Intell. Fuzzy Syst.* **38**(5), 5673–5684 (2020)
20. Chen, J.-N., Zhou, Y.-P., Huang, Z.-J., Wu, T.-Y., Zou, F.-M., Tso, R.: An efficient aggregate signature scheme for healthcare wireless sensor networks. *J. Network Intell.* **6**(1):1-15 (2021)
21. Liu, N., Pan, J.-S., Sun, C., Chu, S.-C.: An efficient surrogate-assisted QUasi-affine TRansformation evolutionary algorithm for expensive optimization problems. *Knowl. Based Syst.* (2020) (Accepted)
22. Chu, S.-C., Huang, H.-C., Roddick, J.F., Pan, J.-S.: Overview of algorithms for swarm intelligence. *ICCCI* **1**(2011), 28–41 (2011)
23. Sun, C., Jin, Y., Cheng, R., Ding, J., Zeng, J.: Surrogate-assisted cooperative swarm optimization of high-dimensional expensive problems. *IEEE Trans. Evol. Comput.* **21**(4), 644–660 (2017)
24. Zhao, L., Gai, M., Jia, Y.: Classification of multiple power quality disturbances based on PSO-SVM of hybrid kernel function. *J. Inform. Hiding Multimedia Signal Process.* **10**(1), 138–146 (2019)
25. Nguyen, T.-T., Chu, S.-C., Dao, T.-K., Nguyen, T.-D., Ngo, T.-G.: An optimal deployment wireless sensor network based on compact differential evolution. *J. Network Intell.* **2**(3), 263–274 (2017)
26. Wang, H., Zhijian, Wu., Rahnamayan, S., Sun, H., Liu, Y., Pan, J.-S.: Multi-strategy ensemble artificial bee colony algorithm. *Inf. Sci.* **279**, 587–603 (2014)
27. Pan, J.-S., Wang, H., Zhao, H., Tang, L.-L.: Interaction artificial bee colony based load balance method in cloud computing, in *textit{ICGEC 2014}*, pp 49–57
28. Tang, L., Zhang, Xi., Li, Z., Zhang, Y.: A New hybrid task scheduling algorithm designed based on ACO and GA. *J. Inform. Hiding Multimedia Signal Process.* **9**(6), 1585–1594 (2018)
29. Chu, S.-C., Roddick, J.F., Su, C.-J., Pan, J.-S.: Constrained ant colony optimization for data clustering, in *8th Pacific Rim International Conference on Artificial Intelligence, LNAI 3157* (2004), pp. 534–543

# Chapter 19

## Joint Adaptive Reception Algorithm with Ant Colony Optimization for Asynchronous Cooperation Transmission Systems



Aiyong Zhang, Changjie Liu, and Pengfei Qin

**Abstract** A joint adaptive reception algorithm is proposed for asynchronous cooperation systems, which is aiming at reducing the interference caused by the asynchronous relays, where ant colony optimization algorithm is adopted to enhance the adaptive training process. The coordination node is usually needed for cooperative communication systems, which is employed to apply relays timing synchronization as well as relay selections, thus achieving the diversity order. However, it could be difficult to choose the center, when the requirement is too rigor for some certain system, such as the complexity-limited ones. For this kind of non-centered systems, the relaying nodes usually work asynchronously, so it is necessary to remove the inter-symbol interference (ISI) in the received signal, in order not to degrade the whole transmission performance. As an effective means, equalizer is usually utilized to carry out ISI cancelations, where zero forcing and minimum mean square error are known as the criterions. When channel state information is unavailable, adaptive equalizer can be considered, with which to train the weightings of equalizer. In this paper, to improve the training process of conventional adaptive algorithms, we investigate and modify ant colony optimization to propose a hybrid and combined adaptive architecture, and the converging property can be guaranteed. Computer simulations show that under Rayleigh fading cooperation communication channels, the proposed algorithm has faster convergence speed and can achieve better detecting performance than conventional adaptive equalizer.

---

A. Zhang · C. Liu  
Army, Beijing 32021, China

P. Qin (✉)  
Institute of Telecommunication and Navigation Satellites, China Academy of Space Technology,  
Beijing 100094, China  
e-mail: [qinpf@zju.edu.cn](mailto:qinpf@zju.edu.cn)

Innovation Center of Satellite Communication System, CNSA, Beijing 100094, China

## 19.1 Introduction

Cooperative communications have drawn attentions for years aiming at the scenarios when conventional point-to-point communications have difficulty in providing adequate communication quality, which may even fail to work, considering the limited power supply as well as the extremely bad channel characteristics. Due to the advantages of strong survivability and stability, cooperation among multiple relays has been widely utilized to set up communication links for various kinds of applications, where the source node transmits signal, and then the signal is amplified and forwarded by multiple relay nodes, thus increasing the probability of the signal reaching the destination. Channel property has been regarded as an important factor in conventional communication links, which will be affected by blocking or shadow fading; but in the case of the cooperation scenario, since multiple links can be supplied by the relays, the communication property can be improved dramatically [1].

Least mean square (LMS) is a commonly used adaptive algorithm, which makes use of gradient descent method during the training process. The selection of step size is one of the key points to the algorithm, because the larger step size can promise a quick convergence and the smaller step size can achieve low mean square error (MSE), so the tradeoff between converging speed and MSE property becomes an important research content [2]. Li et al. in [3] investigate the kernel function into the transform of the weighting coefficients and optimize the distance vector of LMS. The quantization error can also affect the performance of adaptive equalizer, which have been studied by the authors in [4], where a steady-state performance is successfully obtained.

Ant colony optimization (ACO) is a swarm intelligence algorithm observed in social species, and intelligent features are exhibited by the intelligent features, so it could also be thought of as an artificial self-organized networking system [5]. The intelligent ACO swarm is able to search the possible solution for many problems, so it has attracted vast attentions from both academia and industry [6]. As an artificial intelligence technique, ACO is studied based on the observations of collective behavior in biological activities such as ant foraging, division of labor, larval sorting, nest building, and cooperative transport [7]. ACO has been applied to routings such as mobile ad hoc networks, wireless sensor networks, or delay tolerant networks, and besides that, ACO is also with a good scalability to other performance analysis [8].

In this paper, we propose a new hybrid adaptive equalizer in cooperative communication systems, by combining ACO together with LMS, where the ACO is adopted to strengthen the local search accuracy, while LMS algorithm is employed as global control to guarantee that the whole system will not fall into local convergence. To the knowledge of the author, there is no work available in reference devoted to improve the non-centered cooperation link by the ACO-aided adaptive equalizer. It should be noted that Ghani et al. have proposed a successive interference cancellation algorithm in [9] using ACO for cooperative communication systems, so that the capacity is improved, while the complexity is reduced, but it is entirely different

from the hybrid equalizer proposed in this paper. The rest of this paper is organized as follows. In Sect. 19.2, system model of cooperative communication is introduced. Conventional LMS, stand ACO, and the proposed ACO-LMS algorithms are given in Sect. 19.3. Simulations are presented in Sect. 19.4, and finally, the paper is concluded in Sect. 19.5.

## 19.2 System Model

The cooperative system model is shown in Fig. 19.1, where the source node transmits the signal to multiple relays, and then relay nodes amplify and forward the signals to the destination node. Since the LOS link between source node and destination node could be blocked or severely deteriorated, we ignore the LOS component here. For simplicity, we use  $h_{SR_l}$  to express the complex channel gain between source node to the  $l$ th relay node and use  $h_{R_lD}$  to stand for the complex channel gain from the  $l$ th relay node to destination node for  $l = 1, 2, \dots, L$ , where  $L$  is the number of the available relays in the systems. Consider that the fixed center node could hardly be established, with which to coordinate the relay nodes for timing and synchronization, so there exists relative delays between the signals forwarded by the multiple relays. To combat the inter block interference caused by the delays, cyclic prefix (CP) is introduced into the system to act as the guard interval, where the length of CP should be no less than the maximal delay among the multiple relays [10].

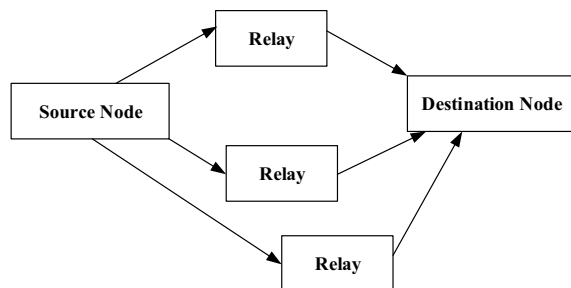
At the transmitter, the constellation mapped signal vector can be written as:

$$\mathbf{s} = [s_1, s_2, \dots, s_k]^T \quad (19.1)$$

where  $k$  denotes the length of block and  $(\cdot)^T$  expresses transpose. After insertion of CP, the baseband transmitted signal is:

$$\mathbf{s}_{CP}(n) = \mathbf{s}(n - P)_k \quad (19.2)$$

**Fig. 19.1** Cooperative communication system model



where  $P$  is the length of CP, which should be larger than that of the maximal delay among the signal forwarded by the relays, and  $(\cdot)_k$  stands for the module- $k$  operation. According to Eq. (19.2), the vector  $[s_{k-P+1}, s_{k-P+2}, \dots, s_k]$  indicates the construction method of CP. When the signal forwarded by the multiple relays arrives at the destination node, after CP removal, the received signal can be expressed as:

$$\mathbf{r} = \mathbf{H}\mathbf{s} + \mathbf{v} \quad (19.3)$$

where  $\mathbf{v}$  is the additive Gaussian noise and  $\mathbf{H}$  is the  $k \times k$  circular matrix, which contains the equivalent gains between the source node to the destination node through all the multiple relays. The circulation format of channel matrix  $\mathbf{H}$  is shown as

$$\mathbf{H} = \begin{bmatrix} h_1 & \cdots & h_3 & h_2 \\ h_2 & h_1 & \cdots & h_3 \\ \cdots & \cdots & \cdots & \cdots \\ 0 & \cdots & h_2 & h_1 \end{bmatrix} \quad (19.4)$$

where the element  $h_l = h_{SR_l}h_{R_lD}$  expresses the equivalent channel gain from source node to destination node through the  $l$ th relay, for  $l = 1, 2, \dots, L$ , and  $L$  is the number of available relays.

$$\mathbf{W}_{ZF} = \mathbf{H}^{-1} \quad (19.5)$$

By utilizing ZF equalizer, the output can be expressed as

$$\mathbf{r}_{ZF} = \mathbf{W}_{ZF}\mathbf{r} = \mathbf{s} + \mathbf{W}_{ZF}\mathbf{v} \quad (19.6)$$

where  $\mathbf{r}_{ZF}$  expresses the output of equalizer, and from Eq. (19.6), the MMSE equalizer is given in the following:

$$\mathbf{W}_{MMSE} = (\mathbf{H}^H\mathbf{H} + \sigma^2\mathbf{I}_k)^{-1}\mathbf{H}^H \quad (19.7)$$

where  $\mathbf{W}_{MMSE}$  denotes the MMSE-rule-based equalizer, and  $\sigma^2$  stands for the variance of noise, and  $\mathbf{I}_k$  is the  $k \times k$  unit matrix.

### 19.3 Proposed ACO-LMS Scheme

In this section, we combine ACO and LMS algorithms to propose the ACO-aided equalizer, and with the hybrid adaptive structure, a fast converging speed can be obtained, and meanwhile, the steady performance can also be acquired.



### 19.3.1 Least Mean Square Adaptive Equalizer

LMS is a widely used adaptive algorithm, which is based on gradient descent method as well as MMSE criteria [6]. In the scheme, the instantaneous square error is used instead of mean square error by approximations, so the computational complexity in achieving the self-correlated matrix is reduced effectively. Suppose that at the  $n$ th time slot, the received vector signal is  $\mathbf{r}(n)$ , and  $\mathbf{w}(n)$  is the equalizer, and  $\mathbf{r}_{eq}(n)$  is the output of equalizer. The LMS algorithm can be summarized in the following.

- Step 1 Initialize the input and output of equalizer;
- Step 2 Initialize the weighting coefficient  $\mathbf{W}$ ;
- Step 3 Weighted filtering, acquire the instantaneous error as:

$$\mathbf{e}(n) = \mathbf{d}(n) - \mathbf{W}\mathbf{r}(n) \tag{19.8}$$

- Step 4 Update the coefficients using:

$$\begin{aligned} \mathbf{w}(n + 1) &= \mathbf{w}(n) + \mu e(n)\mathbf{r}^*(n) \\ n &= n + 1; \end{aligned} \tag{19.9}$$

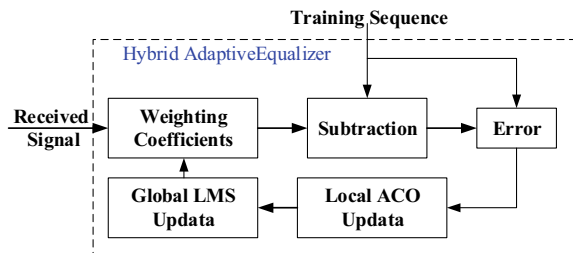
where  $\mu$  is the step size and  $*$  denotes the conjugate transpose;

- Step 5 When the error is small enough, break.

### 19.3.2 Proposed Hybrid ACO-LMS Detector

The diagram of the proposed algorithm is shown in Fig. 19.2, where the “Weighting Coefficients” denote the equalizing operator to the received signal, and  $\mathbf{w}_k$  is used to denote the weighting coefficients of the ACO-LMS hybrid equalizer. In Fig. 19.2, “Substraction” is referred to as the operation to yield the error between the weighted

**Fig. 19.2** Signal processing diagram of the proposed ACO-LMS equalizer



output and the training sequence, which is expressed by the “Error” modular, and it is usually used to update the weighting in conventional LMS mechanism. The weighting error calculation can be described as Eqs. (19.8) and Eqs. (19.9), which are combined together to construct the equalizer. Then, the update of ACO-LMS weighting coefficients is achieved by two stages; during the first stage, we use ACO to strengthen the local convergence of the training, and during the second stage, conventional LMS is applied to ensure an effective global convergence. Finally, when the level of the error is limited to a certain extent, the training process is terminated.

In the new scheme, the received signal at the destination node which is forwarded by multiple relays is firstly weighted using the global weighting coefficients, and then the signal is fed into the ACO updating module. Here, each constellation-mapping symbol forwarded by relays is faded, since the relays retransmit the signal automatically in an asynchronous mode, so the aim for ACO-LMS scheme is to remove the ISI contained in the symbols, by improving the iterative detection process of conventional LMS algorithm. For the proposed one, global optimum solution is regarded as the expected output, after ISI is canceled. Therefore, the goal of the new scheme is to find the coefficients, with which to weight the input signal, and the optimal solution can be achieved. To accomplish that goal, we first simplify the searching process of traditional ACO, where the searching scope is reduced in consideration of the effective global convergence supplied by LMS and then combine it with steep descent method to accomplish the whole training.

At time instant  $n$ ,  $\mathbf{r}(n)$  is the received signal,  $\mathbf{d}(n)$  is the desired signal, and  $\mathbf{w}(n)$  is the weight coefficients of the equalizer. For the ACO module,  $\mathbf{v}$  denotes the update of the ant colony. Then, the proposed hybrid ACO-LMS algorithm can be expressed as follows.

- Step 1 Initialize the input and output of equalizer;
- Step 2 Initialize the weighting coefficient  $\mathbf{W} = \mathbf{0}$ ;
- Step 3 Set and initialize the ant colony as  $\zeta \leftarrow \mu$ , where ants are uniformly distributed in the normalized range interval  $\{0,1\}$ , centered at the initial weighting:

$$P = \{v \in W + c \cdot \{0, 1\}\} \quad (19.10)$$

where  $c$  is a constant;

- Step 4 Select  $v_1, v_2 \in \zeta$  with updates using the uniform distribution mechanism, which meets the probability equation

$$\begin{aligned} \forall v_1, v_2 : f(v_1) \geq f(v_2) \\ \Rightarrow \Pr(\text{select } v_1) \geq \Pr(\text{select } v_2) \end{aligned} \quad (19.11)$$

- Step 5 Update the ant colony with  $z$ , since the solutions should be repeatedly calculated to find the optimal solution, where the randomly distribution of ants can be assumed for  $z$ :

$$z = c_1 \cdot v_1 + c_2 \cdot v_2 \quad (19.12)$$

where  $c_1$  and  $c_2$  are random coefficients, which act as the uniform but random variation of value.

- Step 6 Use the training sequence to represent the global optimization solution, and we can get the equalized output and the corresponding error as:

$$P_v(n) = \mathbf{v} \cdot \mathbf{r}(n) \quad (19.13)$$

$$\mathbf{e}_v(n) = \mathbf{d}(n) - P_v(n) \quad (19.14)$$

- Step 7 Update the ant colony:  $\zeta \leftarrow \{\zeta \cup z\}$ ;  
 Step 8 Choose the best solution from  $\zeta$  which best suits the fitness function and then move on to the next iteration;  
 Step 9 Update the equalization coefficients with LMS as:

$$\mathbf{w}(n+1) = \mathbf{w}(n) + \mu e_v(n) \mathbf{r}^*(n) \quad (19.15)$$

$$n = n + 1;$$

- Step 10 When the error is small enough, break.

## 19.4 Simulation Results

Computer simulations are carried out under the cooperative communication links, where three relays are supposed to forward the signal in the cooperation system, and the channel is supposed to be Rayleigh flat fading. 64QAM is considered as the modulation, and the training process as well as the detection performance of the proposed ACO-LMS is testified.

The converging process of the ACO-LMS is illustrated in Fig. 19.3, compared with that of LMS, where the x-axis denotes the training time, and y-axis stands for the MSE. As can be seen, the proposed hybrid equalizer obtains a faster converging speed than conventional LMS, thus promising a higher training efficiency.

The detection performance is shown in Fig. 19.4, where the x-axis stands for the signal-to-noise ratio (SNR) and y-axis is the bit error rate (BER). It is clear that obvious SNR gain of the proposed scheme can be obtained compared with that of conventional LMS equalizer, and the proposed algorithm can promise a faster decreasing speed in BER.

**Fig. 19.3** Converging property comparisons

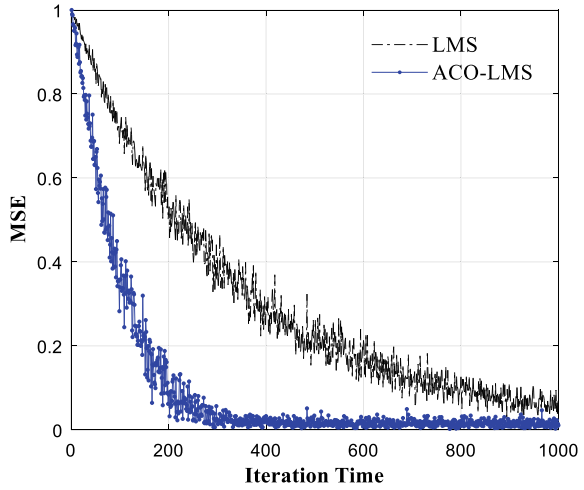
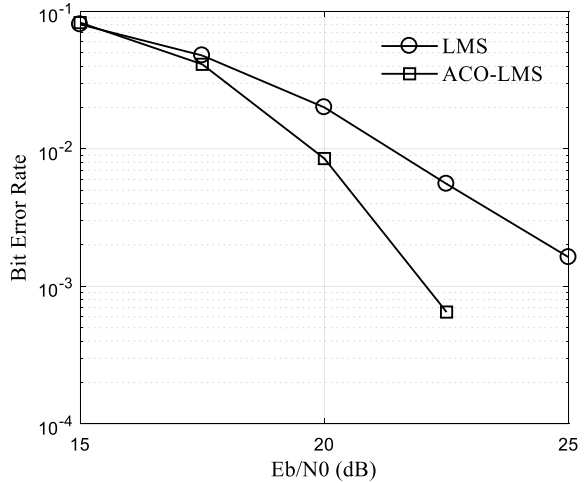


**Fig. 19.4** Bit error rate performance comparisons



### 19.5 Conclusion

Presented in this paper is a new hybrid equalization algorithm, designed for the cooperative communication links, where LOS component of the communication link is not available. We investigate the swarm intelligence ACO algorithm into adaptive LMS and propose the ACO-LMS algorithm, which can converge effectively with low complexity and can acquire comparatively better detecting performance. Computer simulations show that the proposed scheme can surpass conventional LMS adaptive equalizer dramatically.

## References

1. Liu, J., Wang, J., Liu, W., et al.: A novel cooperative physical layer security scheme for satellite downlinks. *Chin. J. Electron.* **27**(4), 860–865 (2018)
2. Song, I., Park, P.G.: A normalized least-mean-square algorithm based on variable-step-size recursion with innovative input data. *IEEE Signal Process. Lett.* **19**(12), 817–820 (2012)
3. Li, K., Principe, J.C.: Transfer learning in adaptive filters: the nearest instance centroid-estimation kernel least-mean-square algorithm. *IEEE Trans. Signal Process* **65**(24), 6520–6535 (2017)
4. Zhu, S., Chen, C., Xu, J., et al.: Mitigating quantization effects on distributed sensor fusion: a least squares approach. *IEEE Trans. Signal Process* **66**(13), 3459–3474 (2018)
5. Bonabeau, E., Dorigo, M., Theraulaz, G.: *Swarm intelligence: from natural to artificial systems*. Oxford University Press (1999)
6. Dorigo, M., Birattari, M., Stutzle, T.: Ant colony optimization-artificial ants as a computational intelligence technique. *IEEE Comput. Intell. Mag.* **1**(4), 28–39 (2006)
7. Zhang, Z., Long, K., Wang, J., et al.: On Swarm intelligence inspired self-organized networking: its bionic mechanisms, designing principles and optimization approaches. *IEEE Commun. Surve. Tutor.* **16**(1), 513–537 (2014)
8. Bai, Y., Zhai, Y., Wang, D.: Research on optimum cooperative relay model for moving targets based on ant colony algorithm. In: *4th International Conference on Information, Cybernetics and Computational Social Systems*, pp. 1–5 (2017)
9. Ghani, H.A., Hamzah, M.H., Syahali, S.: Ant-colony algorithm with interference cancellation for cooperative transmission. *IET Signal Proc.* **10**(6), 603–610 (2016)
10. Wang, J., Xu, Y., Li, Z., et al.: Decision directed multiple-relay diversity detector in asynchronous cooperative communication systems. *Wireless Pers. Commun.* **95**(4), 4931–4946 (2017)

# Chapter 20

## Multiple Data-Dependent Kernel Learning for Circuit Fault Diagnosis



Wang Jianfeng, Wu Meixi, and Li Hanzhi

**Abstract** An analog circuit fault diagnosis method based on multi- data correlation kernel is proposed, and the UCI data set is used to verify the effectiveness of the proposed method. Then, a fault diagnosis method structure of tolerance circuit based on SVM is proposed. Taking Sallen key filter circuit as an example, the specific steps of establishing an analog circuit fault diagnosis model, including fault injection, are introduced: circuit simulation, fault feature extraction, and design of SVM fault classifier based on multi-data correlation kernel. Then, the Sallen key filter circuit and leap frog filter circuit are selected as the diagnosis objects. The HSPICE software is used to inject the fault into the circuit under test and establish the fault simulation model, so as to obtain the circuit data under different circuit states, and the circuit samples are used to establish the fault classifier based on SVM. Finally, the effects of SVM + MK, SVM + DK, and SVM + MDK on the fault classifier diagnosis are compared. The experimental results show that the three methods used in this paper are better than the analog circuit fault diagnosis method based on standard SVM, and the proposed analog circuit fault diagnosis method based on multi-data correlation kernel is the best in terms of diagnosis effect. On this basis, the SVM + MDK algorithm is more effective. The establishment time and diagnosis efficiency of the model are relatively good.

### 20.1 Introduction

With the rapid development of artificial intelligence technology, computer technology, and microelectronics technology, many scholars have conducted in-depth research on electronic circuit fault diagnosis technology. However, there is still a lack of effective diagnosis methods for analog circuit diagnosis. The main reason is that the fault mode is very complex due to the tolerance of analog components, and the inherent characteristics of analog circuit, such as output continuity and input–

---

W. Jianfeng (✉) · W. Meixi · L. Hanzhi

China Institute of Marine Technology and Economy, Beijing 100081, China  
e-mail: [hit08b901005@126.com](mailto:hit08b901005@126.com)

© The Author(s), under exclusive license to Springer Nature Singapore Pte Ltd. 2022  
T.-Y. Wu et al. (eds.), *Advances in Smart Vehicular Technology, Transportation, Communication and Applications*, Smart Innovation, Systems and Technologies 250,  
[https://doi.org/10.1007/978-981-16-4039-1\\_20](https://doi.org/10.1007/978-981-16-4039-1_20)

209

output nonlinearity, increase the complexity of diagnosis and huge amount of calculation. In addition, due to the tolerance of component parameters in analog circuits, the collected circuit samples have the problems of irregular multi-dimensional data and uneven distribution of high-dimensional feature space. And because the output response of the circuit can reflect the working state of the circuit from different angles when the circuit fault occurs, and the dimension of the test space of the circuit fault samples collected from the output response curve is too high, the classifier can not directly classify and identify them effectively, so it needs the method of feature extraction and proposes the meaningful feature information from the output signal. At the same time, the high-dimensional input space of the original circuit data is reduced to a low-dimensional feature space.

For analog circuit fault diagnosis, although the effect of using support vector machine is better than traditional machine learning methods such as neural network, the following problems still exist: in the actual diagnosis process, there are many fault modes in analog circuit, and the separability between different fault modes is very poor, which leads to the unsatisfactory diagnosis effect of standard SVM. The reason is that the standard SVM method maps samples with single kernel function. Because the mapping ability of different kernel functions is not the same, the mapping effect of kernel functions is different for different data sets, and so far there is no perfect theoretical basis for the selection and construction of kernel functions [1, 2]. In addition, the analog circuit fault samples have irregular data or non flat distribution in the high-dimensional feature space, so it is unreasonable to use a single kernel function to map all samples. In recent years, a large number of researches on kernel combination are proposed to solve these problems combination method, namely multi-core learning method [3–8]. This paper focuses on the problem that the classification accuracy of standard support vector machine is not ideal in the above cases, and focuses on the application of multi-core learning method in analog circuit fault diagnosis, and uses the data correlation kernel method to optimize the multi-core matrix, so that the optimized kernel matrix is more suitable for the sample data. Then, it is applied to analog circuit fault diagnosis to solve the problem that the classification accuracy of standard support vector machine for irregular multidimensional data or uneven multidimensional data in circuit samples decreases in the actual diagnosis process.

To solve these problems, the first mock exam circuit is proposed based on multi-data correlation kernel. In order to get the circuit characteristic information of different analog circuits, the feature extraction method of circuit fault data with tolerance characteristics is studied. The fault status and normal state of the circuit can be better separated, and the fault detection and diagnosis can be realized. Taking the international standard analog circuit as the diagnosis object, the HSPICE software is used

to inject faults into the components in the analog circuit, and the circuit data are obtained under different working conditions for classification. The diagnosis model based on support vector machine is established to verify the effectiveness of the proposed method.

## 20.2 Proposed Method

The training set  $S = \{(x_i, y_i)\}_{i=1,2,\dots,m}$ , where  $x_i \in \mathbb{R}^p$ ,  $y_i \in 1, 2, \dots, c$ . Without loss of generality, we suppose the first  $m_1$  samples in the training set belong to  $S_{m_1} = \{(x_i, y_i), y_i = 1_{i=1,2,\dots,m_1}\}$ , and the last  $m_2$  samples belong to  $S_{m_2} = \{(x_i, y_i), y_i = 2, \{i = m_1+1, m_1+2, \dots, m_2\}, m = m_1 + m_2$  represents the total number of samples.  $K$  represents MDK. The expression is

$$k(x, x') = q(x) \sum_{i=1}^I d_i k_{0,i}(x, x') q(x') \quad (20.1)$$

where  $x' \in \mathbb{R}^p$ ,  $k_{0,i}(x, x')$  is the  $i$ th basic kernel function selected from the original kernel, and  $I$  is the number of candidate kernel functions used to combine multiple data-related kernel functions,  $d_i \geq 0$  is the weight of the  $i$ th kernel function,  $q(\cdot)$  is the factor function provided by the following formula:

$$q(x) = \alpha_0 + \sum_{i=1}^n \alpha_i k_1(x, a_i) \quad (20.2)$$

where  $k_1(x, a_i) = e^{-y\|x-a_i\|^2}$ ,  $a_i \in \mathbb{R}^d$  is the coefficient of the kernel function combination. The ‘‘experience center’’  $a_i$ ,  $i = 1, 2, \dots, n$  is selected from the training sample. It is worth noting that the multi-data correlation kernel function  $k(x, x')$  satisfies the Mercer condition,  $k(x, x')$  is still a kernel function because  $k(x, x')$  can also be written as  $k(x, x') = \sum_{i=1}^I d_i [q(x)k_{0,i}(x, x')q(x')]$ , where the conformal transformation of  $k_{0,i}(x, x')$  is  $q(x)k_{0,i}(x, x')q(x')$  and  $k(x, x')$  is a linear combination of kernel functions.

In order to find a balance between computational efficiency and classification accuracy, we need to select some key kernel functions from the candidate kernel functions at the beginning of constructing the multi-data correlation kernel function. In the algorithm, the weight  $d_i = 1, 2, \dots, I$  can be determined by solving the following convex optimization problem:

$$\begin{aligned} & \text{Maximize } A(\mathbf{K}_0, \mathbf{K}^*) \\ & \text{s.t. } \mathbf{K}_0 = \sum_{i=1}^I d_i \mathbf{K}_{0,i} \\ & \text{tr}(\mathbf{K}_0) = 1 \quad d_i \geq 0, \forall i \end{aligned} \quad (20.3)$$



where  $K^* = \begin{cases} 1 & y = y' \\ -1/(Q-1) & \text{other} \end{cases}$  is the ideal target kernel function,  $tr(\cdot)$  is the trace of the matrix,  $Q$  is the number of categories,  $Q \geq 2$ .  $A(\mathbf{K}_0, \mathbf{K}^*) = \frac{\langle \mathbf{K}_0, \mathbf{K}^* \rangle_F}{\|\mathbf{K}^*\|_F \|\mathbf{K}_0\|_F}$ , where  $\langle \cdot, \cdot \rangle_F$  is the Frobenius norm of the two matrices, which is defined as  $\langle \mathbf{D}, \mathbf{E} \rangle_F = \sum_{i=1}^m \sum_{j=1}^m d_{ij} e_{ij} = tr(\mathbf{D}\mathbf{E}^T)$ .

It is easy to find that  $\|\mathbf{K}^*\|_F$  is the corresponding constant for a certain classification task, and the constraint of the matrix trace is to modify the scale invariance of the kernel arrangement. Generally speaking, it is to modify the denominator  $\|\mathbf{K}_0\|_F$  and maximize the numerator  $\langle \mathbf{K}_0, \mathbf{K}^* \rangle_F$ . Let  $\mathbf{H} = [vec(\mathbf{K}_{0,1}) vec(\mathbf{K}_{0,2}) \cdots vec(\mathbf{K}_{0,I})]$ , where  $vec(\cdot)$  is the column vector of the matrix, which can be derived from equation:

$$\begin{aligned} & \text{Minimize } -vec(\mathbf{K}^*)^T \mathbf{H} \mathbf{d} + \gamma_1 \|d\|_2^2 \\ & \text{s.t. } \mathbf{d}^T \mathbf{H}^T \mathbf{H} \mathbf{d} \leq 1 \\ & \quad d_i \geq 0, \forall i \end{aligned} \quad (20.4)$$

where  $d = [d_1 d_2 \cdots d_I]^T$  is the required weight,  $\|d\|_2^2$  is added to the regularized weight to avoid overfitting in the classification process.  $\gamma_1 \in [0, 1]$  is the regularization parameter.

After completing the optimization calculation of the weight  $d_i = 1, 2, \dots, I$ , the following uses Fisher's criterion to calculate the data correlation kernel coefficient  $\alpha_i = 0, 1, \dots, n$ . For the case of multi-classification,  $Q \geq 2$ , we define  $\tilde{x}$  as the mapping value, and  $\tilde{x}$  the center of the entire training data set, respectively. We define  $\tilde{x}_j$  as the center of the  $j$ -th ( $j = 1, 2, \dots, Q$ ) category in the empirical feature space. We get

$$S_b = \frac{1}{m} \sum_{j=1}^Q m_j (\tilde{x}_j - \tilde{x})(\tilde{x}_j - \tilde{x}) \quad (20.5)$$

$$S_w = \frac{1}{m} \sum_{j=1}^Q \sum_{i=1}^{m_j} m_j (\tilde{x}_i^j - \tilde{x}_j)(\tilde{x}_i^j - \tilde{x}_j)^T \quad (20.6)$$

where  $S_b$  is the "inter-category scatter matrix,"  $S_w$  is the "inter-category scatter matrix," and  $\tilde{x}_i^j$  is the  $i$ -th data of the  $j$ -th category.

In the process of constructing multiple data-related kernels, the main task is to determine the weights  $d_i, i = 1, 2, \dots, I$  of the basic kernel function  $k_{0,i}(x, x')$  and the coefficients  $\alpha_i, i = 0, 1, \dots, n$  of the data-related kernels. We use kernel permutation and Fisher discriminant analysis to optimize the weight of the basic kernel function and the coefficient of the data-related kernel, respectively. Figure 20.1 illustrates a schematic diagram of the MDK algorithm process.

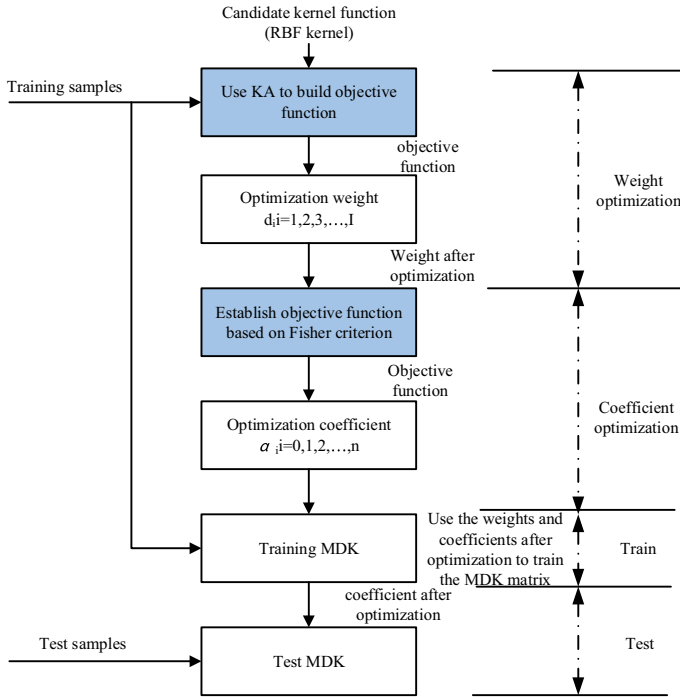


Fig. 20.1 Schematic diagram of MDK algorithm process

## 20.3 Simulation Experiments

### 20.3.1 UCI Dataset

In the verification experiment, the standard support vector machine uses RBF kernel function for classification and uses RBF kernel function as candidate kernel function when combining multiple kernel functions. Each data set should be normalized first, and then randomly divided into three independent parts with the same number of samples. Some of them are used as the experience center set  $\{\alpha_i\}$ . The other two parts are training set and test set. The penalty coefficient  $C$  of SVM has been set before optimization, so that  $C = 10^3$ . Learning rate  $\eta_0$  and iterations  $n$  are set to 0.01 and 200, respectively.

$K_{Gaus}$  in Table 20.1 is for the common Gaussian kernel function used in support vector machine,  $K_{opt\_DK}$  represents that SVM uses the optimized kernel function,  $K_{opt\_MK}$  represents that support vector machine uses multi-kernel function,  $K_{opt\_MDK}$  represents that support vector machine uses multi- data correlation kernel for classification, and training time represents the time that learning machine uses training samples to build model. From the experimental results, we can find that: in terms

**Table 20.1** Comparison of different classifiers for UCI dataset

Methods		Ionosphere	Breast	Liver	Pima	Monks1	Monks2	Monks3
StandardSVM	Accuracy(%)	93.26	96.59	55.17	78.13	87.96	73.39	97.22
	Training time (s)	6.6276	9.7121	4.5978	17.8725	7.7375	8.1907	7.8032
SVM+MK	Accuracy(%)	98.88	99.43	100.00	99.48	100.00	98.17	100.00
	Training time (s)	0.0900	0.2261	0.0749	0.2400	0.0864	0.0908	0.0923
SVM+DK	Accuracy(%)	95.51	97.16	57.17	79.82	92.72	84.63	98.28
	Training time (s)	0.2009	0.3569	0.1926	0.4893	0.1950	0.2852	0.1985
SVM+MDK	Accuracy(%)	100.00	99.43	100.00	100.00	100.00	100.00	100.00
	Training time (s)	0.1642	0.2782	0.1358	0.3067	0.1520	0.1490	0.1622

of classification accuracy, compared with standard SVM and SVM + DK, SVM + MK, and SVM + MDK have better classification accuracy. This is because the latter two use the multi-core learning method. Because the multi-core learning principle takes advantage of the mapping advantages of multiple basic cores, the classification separability of input samples in the composite space is better than that in the single core space. However, due to the optimization algorithm of data correlation kernel in SVM + MDK algorithm, the training time of SVM + MDK algorithm is slightly longer than that of SVM + MK algorithm.

### 20.3.2 Leap Frog Filter Circuit Experiment

Figure 20.2 shows the circuit of the leap frog filter, in which all the resistors are  $10\text{ k}\Omega$ ,  $C_1 = C_4 = 10\text{ nF}$ ,  $C_2 = C_3 = 20\text{ nF}$ , the normal tolerance of resistance is 5%, and the tolerance of capacitance is 10%. As shown in Fig. 20.3, (a) is the circuit response curve in the time domain under the normal working state of the circuit, and (b) is the circuit response curve in the time domain under the normal fault state of the circuit. The data sample is decomposed into approximate part and detail part by using five-level Haar wavelet transform, and the first low frequency coefficient of the approximate part of the five-level Haar wavelet decomposition is selected as the eigenvector of different circuit states. Figure 20.3c shows the result of wavelet

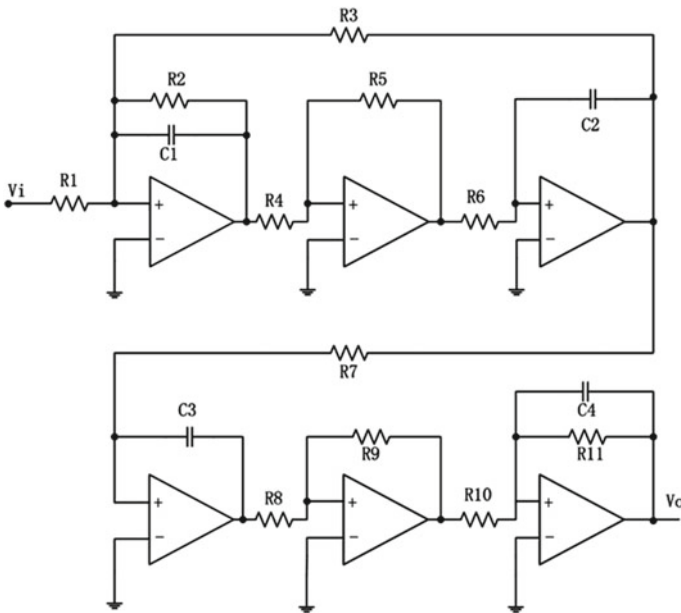
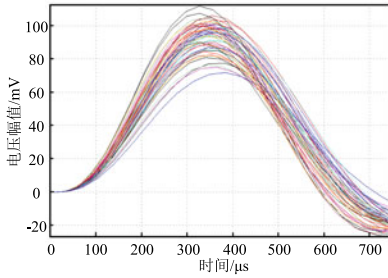
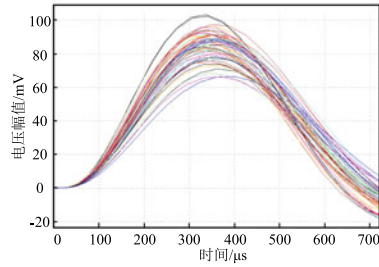


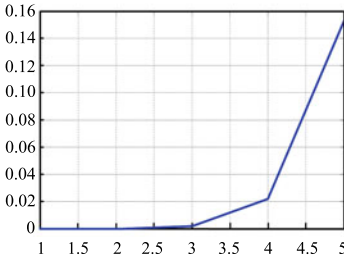
Fig. 20.2 Circuit of leapfrog filter



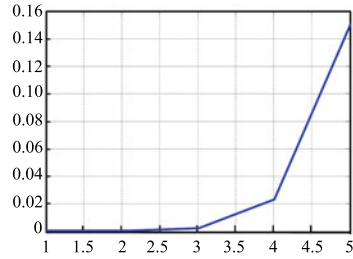
(a) Output response curve of the circuit in normal working state of leapfrog



(b) The output response curve of the circuit under the fault condition of leapfrog



(c) The wavelet decomposition result of the output response curve of the circuit in normal working state of leapfrog



(d) Wavelet decomposition result of output response curve of circuit under fault condition of leapfrog

**Fig. 20.3** Response curves and wavelet decomposition results of the circuit under different working conditions of leapfrog

decomposition of the output response curve under the normal working state of the circuit, and Fig. 20.3d shows the result of wavelet decomposition of the output response curve under the fault state of the circuit. The fault diagnosis classifier based on SVM is constructed by using the above three methods, and fault detection is carried out.

The rest parameters of the diagnosis algorithm are set as follows: in the standard SVM algorithm, RBF kernel is selected for classification, and the grid search method is used to classify the parameters ( $C, \gamma_0$ ) to optimize the standard SVM to achieve the best classification effect. The trained SVM classifier is used to diagnose the circuit test data, and the circuit classification results are given in Table 20.2.

It can be seen from Table 20.2 that for two analog circuits, compared with the other two methods, SVM + MK and SVM + MDK have the best diagnosis effect, because for the same data set, multi-core learning obtains the composition space by combining multiple basic cores in a certain combination form. The advantage of the composition space is that it has the advantage of feature mapping of each basic core, and can be used for diagnosis. The multi-core learning theory avoids the

**Table 20.2** Comparison of circuit diagnosis effects of fault diagnosis systems based on different methods

Classification methods and evaluation index		Sallen key	Leapfrog
StandardSVM	Accuracy(%)	91.11	86.51
	Training time (s)	35.7662	4.9849
SVM+MK	Accuracy(%)	100.00	100.00
	Training time (s)	0.9721	0.1650
SVM+DK	Accuracy(%)	91.56	92.83
	Training Time(s)	1.5351	0.2737
SVM+MDK	Accuracy(%)	100.00	100.00
	Training time (s)	1.5879	0.2323

**Table 20.3** Comparison of test time between SVM + MK and SVM + MDK

	Testing time (s) (Sallen key)	Testing time (s)
SVM+MK	0.0314%	0.0084
SVM+MDK	0.0306%	0.0080

kernel function selection strategy based on grid search and cross validation, which can significantly shorten the training time; the data correlation kernel method is for multi- kernel moments By taking Fisher discriminant analysis as the objective function, the objective function is maximized to make the classification of circuit data better in the empirical feature space, so as to improve the diagnosis effect; in terms of the time of establishing the diagnosis model, the complexity of the algorithm is slightly increased due to the addition of data correlation accounting method to the SVM + MDK algorithm to optimize the multi-core matrix, but the complexity of the algorithm is still low. Compared with SVM + MK, SVM + MDK algorithm has advantages in diagnosis efficiency, that is, the test time is shorter; in terms of diagnosis efficiency, as given in Table 20.3, it can be found that the test time of SVM + MDK is slightly shorter than that of SVM + MK, because the complexity of the diagnosis model established by each algorithm is different. The complexity of SVM model can be evaluated by the number of support vectors. For example, for Sallen key circuit, the number of support vectors found by SVM + MDK method is 16, while the number of support vectors found by SVM + MK method is 16 Using the SVM + MK method, the number of support vectors is 17, so the SVM + MDK diagnosis model is slightly simpler than the SVM + MK diagnosis model, and the diagnosis speed is also slightly faster during the test process.

Finally, because the circuit used in this paper is relatively simple, MDK fault diagnosis method compared with MK method, both achieved 100% diagnostic accuracy. However, from the verification results of standard UCI data sets, we can see that MDK can achieve better classification accuracy for complex problems because it

combines the advantages of multi-core learning and data correlation kernel learning. In the follow-up work, the above methods will be used for fault diagnosis of more complex electronic systems to verify the promotion effect of the method.

### 20.3.3 Conclusion

An analog circuit fault diagnosis method based on multi-data correlation kernel is proposed, and the UCI data set is used to verify the effectiveness of the proposed method. Then, a fault diagnosis method structure of tolerance circuit based on SVM is proposed. Taking Sallen key filter circuit as an example, the specific steps of establishing an analog circuit fault diagnosis model, including fault injection, are introduced. Circuit simulation, fault feature extraction and design of SVM fault classifier based on multi-data correlation kernel. Then, the Sallen key filter circuit and leap frog filter circuit are selected as the diagnosis objects. The HSPICE software is used to inject the fault into the circuit under test and establish the fault simulation model, so as to obtain the circuit data under different circuit states, and the circuit samples are used to establish the fault classifier based on SVM.

## References

1. Huang, Y., Yang, D., Wang, K., Wang, L., Zhou, Q.: Stability analysis of GMAW based on multi-scale entropy and genetic optimized support vector machine. *Measurement* **151**, 107–282 (2019)
2. Martinez-Vargas, J., Duque-Munoz, L., Vargas-Bonilla, F., Lopez, J., Castellanos-Dominguez, G.: Enhanced data covariance estimation using weighted combination of multiple gaussian kernels for improved M/EEG source localization. *Int. J. Neural Syst.* **29**, 1–15 (2019)
3. Aiolli, F., Donini, M.: Easymkl: A scalable multiple kernel learning algorithm. *Neurocomputing* **169**, 215–224 (2015)
4. Akyuz, S.O., Ustunkar, G., Weber, G.W.: Adapted infinite kernel learning by multi-local algorithm. *Int. J. Patt. Recogn. Artif. Intell.* **30**(4), 1651004.1–1651004.21 (2016)
5. Chen, X., Niu, Y.W., Wang, G.H., Yan, G.Y.: Mkrmda: multiple kernel learning-based kronecker regularized least squares for mirna-disease association prediction. *J. Transl. Med.* **15**, (2017)
6. Gautam, C., Balaji, R., Sudharsan, K., Tiwari, A., Ahuja, K.: Localized multiple kernel learning for anomaly detection: one-class classification. *Knowl. Based Syst.* **165**, 241–252 (2019)
7. Guo, Y., Xiao, H.: Multiclass multiple kernel learning using hypersphere for pattern recognition. *Appl. Intell.* (2017)
8. Karimi, A.H.: A summary of the kernel matrix, and how to learn it effectively using semidefinite programming (2017)

# Chapter 21

## Calculation of Spacecraft Transfer Trajectory Based on Modified Differential Evolution Algorithm



Gui-bo Zheng, Qing Yin, Guan-qun Wu, and Ke-yan Huang

**Abstract** Aiming at the optimization problem of spacecraft transfer trajectory, based on differential evolution algorithm, a fast optimization method for transfer trajectory with modified differential algorithm is proposed. The method can quickly find the best transfer trajectory that satisfies the specified constraints through the intelligent optimization based on the population individuals. It avoids the problems of large calculation and low efficiency caused by traditional iteration methods. The actual application of the calculation of the transfer trajectory under certain initial conditions shows that the method can quickly determine the transfer orbit parameters.

### 21.1 Introduction

For more and more space missions, the calculation and optimization of spacecraft rendezvous orbits are becoming more and more common. However, the trajectory optimization problem is usually solved under nonlinear and multi-constrained conditions. According to the traditional iterative solution method, not only the calculation quantity is large, but also the analytical solution of the problem is difficult to obtain, which affects the execution efficiency of the space task. In order to solve the problem of orbit optimization, people continue to use neural networks, genetic algorithms, etc. in the analysis and calculation of the orbit [1–3]. As optimization problems become diversified and complicated, the original optimization algorithm to solve these problems becomes very difficult. Some researchers try to simulate

---

G. Zheng (✉) · Q. Yin · G. Wu · K. Huang  
Beijing Institute of Spacecraft System Engineering, Beijing 100083, China

Q. Yin  
e-mail: [qing48117@163.com](mailto:qing48117@163.com)

G. Wu  
e-mail: [wqwuguanqun@163.com](mailto:wqwuguanqun@163.com)

K. Huang  
e-mail: [thehky@163.com](mailto:thehky@163.com)



the evolutionary process of nature to propose an algorithm that simulates the evolutionary process to solve complex optimization problems. From this, Evolutionary Computing (EC) came into being. Differential evolution algorithm (DE), as a branch of EC, is an intelligent optimization algorithm that uses random search and floating-point vector encoding [4]. It is also an efficient heuristic evolution algorithm. Because of its simplicity principles, fewer control parameters, easy implementation and other characteristics, DE algorithm show great potential in solving optimization problems, excellent performance in experiments on various test problems. And it has become one of the hot topics in evolutionary algorithm research in recent years [5–8].

Based on the differential evolution algorithm (DE), this paper proposes a modified differential algorithm and tries to use it in the fast optimization calculation of the spacecraft transfer orbit under the condition of a fixed speed increase. The complicated and time-consuming parameter calculation is transformed into an independent parameter optimization process to shorten the calculation time and improve calculation accuracy. Based on the modified algorithm, the transfer orbits of the spacecraft in two coplanar elliptical orbits under the condition of a fixed speed increase of 1000 m/s are analyzed and calculated.

## 21.2 Differential Evolution Algorithm

Differential Evolution Algorithm (DE) [4] is a social evolution algorithm based on population differences, which proposed by Storn and Price in 1997. It solves optimization problems through cooperation and competition among individuals in the population. It is essentially an evolutionary algorithm based on real number coding with the idea of preserving superiority.

### 21.2.1 *Basic Principles of Differential Evolution Algorithm*

The basic idea of the differential evolution algorithm is as follow. Firstly, the mutant individuals are formed by the mutation operations between the parent individuals. Secondly the parent individuals and the mutant individuals are cross-operated with a certain probability to generate a trial individual; then the parent individuals and the trial individuals perform greedy selection operations according to their value of fitness, and keep the better ones. Then the evolution of the population is realized.

DE adopts the calculation method similar to the standard evolutionary algorithm, mainly through the three operations of mutation, crossover and selection to perform intelligent search. However, unlike traditional evolutionary algorithms, DE uses random selection of different individuals to generate proportional difference vectors to perturb the contemporary population, and uses the difference between

the candidate solutions to generate new individuals. Compared with other evolutionary algorithms, DE has the advantages of simple structure which has only 3 control parameters, easy implementation, good global search performance and strong robustness.

DE needs to go through the following four basic processes including individual initialization, mutation, crossover, and selection. After the individual is initialized, two individuals in the same population are differentiated and scaled by the most important difference mutation operator in evolution algorithm, and adds another random individual vector in the population to generate the mutant vector, then the vector of the parent individual and the mutant individual uses the crossover operation to obtain the trial individual vector, and finally compare the fitness value of the trial individual vector and the parent individual vector to save the superior to the evolved in the next generation. DE uses differential mutation, crossover, and selection methods to continuously iterate the population to evolve until it meets the stop conditions.

### 21.2.2 Standard Differential Evolution Algorithm Process

**Initialization.** Suppose the current evolutionary generation is  $t$ , the population size is  $NP$ , the spatial dimension is  $D$ , and the current population is  $X(t) = \{x_1^t, x_2^t, \dots, x_{NP}^t\}$ ,  $x_i^t = \{x_{i1}^t, x_{i2}^t, \dots, x_{iD}^t\}^T$  is the  $i$ th individual in the population. In the evolution process, the following three operations are performed in sequence for each individual  $x_i^t$ .

**Mutation operation.** For each individual  $x_i^t$ , a variant individual  $v_i^t = \{v_{i1}^t, v_{i2}^t, \dots, v_{iD}^t\}^T$  is generated as follows:

$$v_{ij}^t = x_{r_1j}^t + F * (x_{r_2j}^t - x_{r_3j}^t) \quad j = 1, 2, \dots, D \quad (21.1)$$

where  $x_{r_1}^t = (x_{r_11}^t, x_{r_12}^t, \dots, x_{r_1D}^t)^T$ ,  $x_{r_2}^t = (x_{r_21}^t, x_{r_22}^t, \dots, x_{r_2D}^t)^T$ ,  $x_{r_3}^t = (x_{r_31}^t, x_{r_32}^t, \dots, x_{r_3D}^t)^T$  are three randomly selected individuals in the population, and  $r_1 \neq r_2 \neq r_3 \neq i$ ;  $x_{r_1j}^t, x_{r_2j}^t, x_{r_3j}^t$  are the  $j$ th dimension components of individual  $r_1, r_2$  and  $r_3$ , respectively;  $F$  is the variation factor, which generally takes the value  $[0,2]$ . In this way, the variant individual  $v_i^t$  is obtained.

**Crossover operation.** From the variant individual  $v_i^t$  and the parent individual  $x_i^t$ , the trial individual  $u_i^t = (u_{i1}^t, u_{i2}^t, \dots, u_{iD}^t)^T$ , then

$$u_{ij}^t = \begin{cases} v_{ij}^t & \text{if rand}[0, 1] \leq CR \text{ or } j = j\_rand \\ x_{ij}^t & \text{if rand}[0, 1] > CR \text{ or } j \neq j\_rand \end{cases} \quad (21.1)$$

Among them, rand[0,1] is a random number between [0,1]; CR is a constant in the range [0,1], called the cross factor, larger value of CR means greater possibility of crossover; j\_rand is an integer randomly selected in [1,D], which guarantees that for the trial individual  $u_i^t$ , at least one element must be obtained from the variant individual  $v_i^t$ . The above mutation operations and crossover operations are collectively referred to as reproduction operations.

**Select operation.** The differential evolution algorithm uses a “greedy” selection strategy, that is, from the parent individual  $x_i^t$  and the trial individual  $u_i^t$ , the next-generation individual  $x_i^{t+1}$  is selected with the best fitness value. The selection operation is:

$$x_i^{t+1} = \begin{cases} x_i^t & \text{if fitness}(x_i^t) < \text{fitness}(u_i^t) \\ u_i^t & \text{otherwise} \end{cases} \tag{21.2}$$

Among them, fitness(·) is the fitness function, and generally the objective function to be optimized is the fitness function.

e iterative calculation is performed by using the above difference algorithm until the fitness function value or the number of iterations of the parent individual  $x_i^t$  and the trial individual  $u_i^t$  meet the requirements.

### 21.2.3 Modified Differential Evolution Algorithm

There are two important operations in the DE algorithm: mutation and crossover. The crossover operation is relatively easy, and the trial individual is generally judged by the cross factor CR taking [0.2, 0.8]. The mutation operation has a great impact on the algorithm. If the distribution range of the mutation individuals is large, it is not conducive to the rapid convergence of the algorithm; if the distribution range of the mutation individuals is small, although it is helpful to improve the convergence speed of the algorithm, it is easy to fall into the local optimum. Therefore, the penalty coefficient  $\lambda$  is introduced when calculating the variant individual and the calculation of the variant individual is performed as follows.

$$v_{ij}^t = x_{r1j}^t + \lambda * (x_{\text{best}}^t - x_{r1j}^t) + F * (x_{r2j}^t - x_{r3j}^t) \quad j = 1, 2, \dots, D \tag{21.3}$$

where  $x_{\text{best}}^t$  is the individual with the best fitness function value of the parent individual  $x_i^t$  and the trial individual  $u_i^t$ .

### 21.3 Transfer Trajectory Optimization Method Based on Modified Differential Algorithm

The application scenario of the transfer trajectory calculation in the paper is as follows. The mission spacecraft releases a sub-spacecraft at a fixed initial speed which direction is adjustable. Through the optimization design of the transfer trajectory, the sub-spacecraft and the target spacecraft can be accurately rendezvous. This calculation scenario can be described as the calculation of the rendezvous transfer trajectory under the condition of a fixed speed increase. The final goal of the calculation is to find an optimal orbit transfer time, under which the sub-spacecraft can achieve the accurate rendezvous with the target spacecraft at the condition of specified speed increase. The specific implementation steps of the transfer orbit calculation based on the DE algorithm are as follows:

- (1) Initialization parameters. Set population size  $NP = 10$ ; mutation factor  $F = 0.6$ ; crossover factor  $CR = 0.5$ ; spatial dimension  $D = 1$ ; initial evolution generation  $t = 0$ .
- (2) Initialize randomly the initial population  $X(t) = \{x_1^t, x_2^t, \dots, x_{NP}^t\}$ , where  $x_i^t = \{x_{i1}^t, x_{i2}^t, \dots, x_{iD}^t\}^T$ . Using the individual  $x_i^t$  in the population as the orbit transfer time  $t_f$ , the Lambert orbit calculation method is used to calculate the velocity vector  $V_1$  required to achieve the rendezvous with the target spacecraft at time  $t_f$ .
- (3) Individual evaluation: Calculate the fitness value of each individual, and use the value of  $V_1 - V_0 - V_m$  as the fitness of the particle, where  $V_0$  is the initial vector of the mission spacecraft, and  $V_m$  is modulus of the spacecraft's velocity increment of sub-spacecraft released by the mission spacecraft.
- (4) Mutation operation: According to formula (4), perform mutation operation on each individual, and get the mutated individual  $v_i^t$ .
- (5) Crossover operation: Perform crossover operation on each individual according to formula (2) to obtain the test individual  $u_i^t$ .
- (6) Selection operation: According to formula (3) to select one from the parent individual  $x_i^t$  and the trial individual  $u_i^t$  as the next generation individual.
- (7) Termination test: the new generation of population  $(t + 1) = \{x_1^{t+1}, x_2^{t+1}, \dots, x_{NP}^{t+1}\}$ , Suppose the optimal individual in  $X(t + 1)$  is  $x_{\text{best}}^{t+1}$ , if the maximum evolution generations is reached or the error requirement is met, the evolution is stopped and  $x_{\text{best}}^{t+1}$  is the optimal solution, otherwise let  $t = t + 1$ , and turn to (3).

Through the above steps, the orbit transfer time  $t_f$  can be quickly calculated. From the orbit transfer time, the required speed for orbit transfer can be calculated by the Lambert method. From the orbit transfer speed and the initial position of the target spacecraft, the orbital elements of the transfer orbit and transfer path can be calculated.

## 21.4 Transfer Trajectory Calculation Under the Condition of Fixed Speed Increase

The initial state of the transfer trajectory calculation under the condition of fixed speed increase is as follows. The target spacecraft and the mission spacecraft operate independently in two polar orbit elliptical orbits with the same orbital height and the same orbital plane. The orbital inclination angles are both  $97.3^\circ$ , and the perigee angles of the two orbits differ by  $180^\circ$ . The schematic diagram of the orbital relationship and transfer process of the two spacecraft is shown in Fig. 21.1.

Orbit 1 is the initial orbit of the mission spacecraft, orbit 2 is the initial orbit of the target spacecraft, point 4 is the initial position of the mission spacecraft, and point 5 is the initial position of the target spacecraft. The mission spacecraft throws the sub-spacecraft at point 4 with speed of 1000 m/s, which will rendezvous with the target spacecraft at point 6 after time  $t_f$ .

The initial position and velocity vectors RV1 and RV2 of the mission spacecraft and the target spacecraft are as follows.

$$\begin{aligned}
 RV1 &= [-1612.1024e3, 413.0029e3, 6670.9961e3, 7.0840e3, 2.2895e3, 1.6230e3]; \\
 RV2 &= [-1613.8025e3, 415.1338e3, 6690.8095e3, 7.0885e3, 2.2766e3, 1.5155e3].
 \end{aligned}$$

From the initial position and velocity vector, the initial orbital number of the two spacecraft can be calculated as shown in Table 21.1.

**Fig. 21.1** Schematic diagram of spacecraft's orbit distribution and transfer

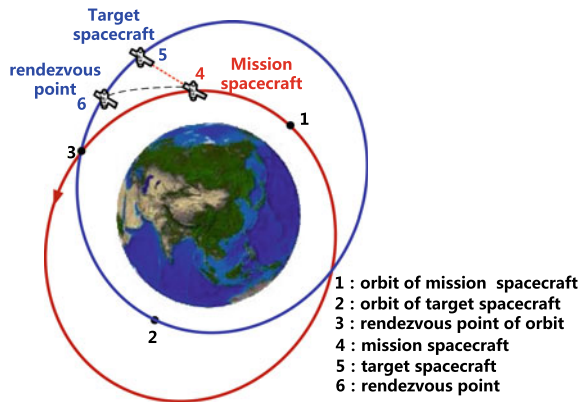
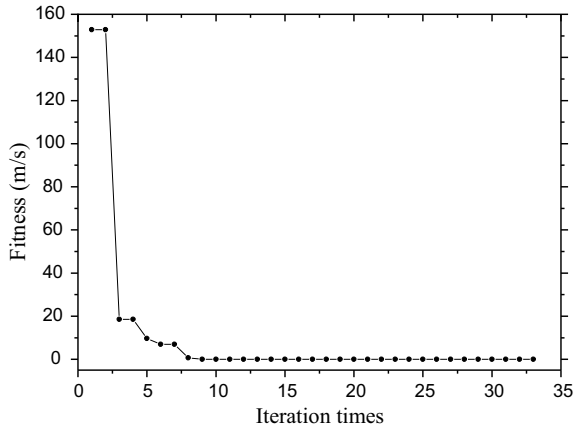


**Table 21.1** The initial orbital elements of the spacecraft

Orbital elements	$\alpha$ (km)	e	$I$ ( $^\circ$ )	$\Omega$ ( $^\circ$ )	$\Omega$ ( $^\circ$ )	$F$ ( $^\circ$ )
Mission spacecraft	6885.6	0.007	97.3	196.3	0	77.2
Target spacecraft	6885.6	0.007	97.3	196.3	180	258.8

**Fig. 21.2** Rendezvous time optimization path



The transfer trajectory calculation method based on modified differential evolution algorithm is programmed for analysis and calculation orbit transfer trajectory. The initial parameters of the MDE algorithm are set as: the fixed velocity increment  $dV_0$  of the sub-spacecraft released by the mission spacecraft is 1000 m/s, the number of particles  $N = 10$ , the particle dimension  $D = 1$ , the maximum number of iterations is set to 1000, and the minimum number of population individuals is set to 1, The maximum value of the population is 50, and the optimization termination error is  $1.0 \times 10^{-6}$ .

According to the above-mentioned initial conditions, the trajectory transfer time  $t_f$  is optimized. It can be seen from the optimization results that after 9 iterations, the fitness (the difference between the theoretical increment rate and the specified increment rate) converges from 152 to 0.03 m/s, and after 33 iterations, the fitness reaches  $9.7376 \times 10^{-7}$  m/s, and the optimal rendezvous time is  $t_f = 18.051096$  s (Fig. 21.2).

The calculation process of the transfer trajectory is as follow:

From the transfer trajectory time  $t_f$ , calculate the position vector of the target spacecraft after  $t_f$  time is  $p_2' = [-1485.53435e3, 456.14493e3, 6716.84006e3]$ ;

With the initial position vector  $p_1 = [-1612.1024e3, 413.0029e3, 6670.9961e3]$  of the mission spacecraft, from  $p_1, p_2'$  and  $t_f$  using the Lambert equation to calculate the orbit transfer speed vector  $V_1 = [6994.3273, 2394.7096, 2613.4869]$  of the transfer orbit passing through the two points  $p_1$  and  $p_2'$  in  $t_f$  time.

The initial position and velocity vector  $RV_1'$  of the transfer trajectory is formed by the initial position vector  $p_1$  of the mission spacecraft and the orbit transfer velocity vector  $V_1$ ;

Calculate the elements of transfer orbits  $\alpha = 7318.7$  km,  $e = 0.146$ ,  $i = 97.3^\circ$ ,  $\Omega = 196.3^\circ$ ,  $\omega = 4.73^\circ$ ,  $f = 57.83^\circ$  by  $RV_1'$ .

Calculate the position vector from  $t_0$  to  $t_f$  from the orbital elements, and then obtain the orbital transfer trajectory.

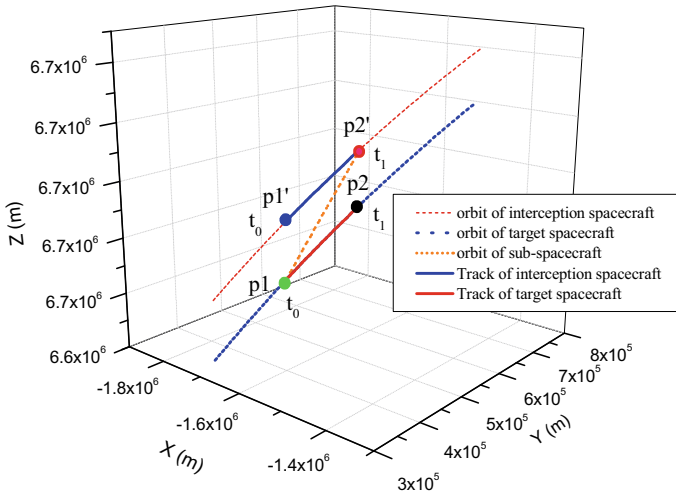


**Fig. 21.3** Orbit transferring process of spacecraft

The data of the position vector of the mission spacecraft, the target spacecraft and the sub-spacecraft are obtained by calculation.

In Fig. 21.3, point  $p_1$  is the initial position of the target spacecraft,  $p_1'$  is the initial position of the target spacecraft,  $t_0$  is the time zero,  $t_1$  is the rendezvous time point,  $p_2'$  is the position of the target spacecraft and the sub-spacecraft during the rendezvous, and  $p_2$  is the mission spacecraft position at the rendezvous. The  $\vec{p_1 p_1'}$  is the trajectory of the sub-spacecraft, and  $\vec{p_1' p_2'}$  is the trajectory of the target spacecraft. To ensure accurate rendezvous, the time from  $p_1'$  to  $p_2'$  of the target spacecraft and the time from  $p_2$  to  $p_2'$  of the sub-spacecraft are equal to the rendezvous time  $t_f$  (18.051096 s).

## 21.5 Conclusion

Aiming at the problem of the optimal transfer trajectory design of the sub-spacecraft under the fixed speed increase constraint, this paper adopts a modified differential algorithm based on swarm intelligence to optimize the transfer trajectory parameters. The calculation results show that the modified differential algorithm can not only obtain the optimal transfer orbit parameters, but also has higher convergence speed and accuracy. It is a better parameter optimization method for nonlinear problems, and can be used for the transfer of complex spacecraft such as multi-objective continuous rendezvous.

## References

1. Jin, H., Zhang, Y., et al.: Optimal design of ANN model in orbit prediction for high-altitude orbit satellite. *J. Geomatics Sci. Technol.* **32**(6), 559–564 (2015)
2. Lin, Z., Yu-ling, Li., et al.: Optimization method research of satellite attaching track planning based on genetic algorithm. *Syst. Eng. Electron.* **38**(5), 1114–1120 (2016)
3. Wu-dong, D., Feng, C., et al.: The genetic-algorithm's application on communication satellite's orbit optimization. *Flight Control Detect.* **3**(3), 57–64 (2020)
4. Storn, R., Price, K.: Differential evolution—a simple and efficient heuristic for global optimization over continuous spaces. *J. Global Optim.* **11**, 341–359 (1997)
5. Xian-li, L., Jin-chu, H., et al.: Based on differential evolution algorithm X fluorescence peak overlapping decomposition. *Spectrosc. Spectral Anal.* **40**(7), 2301–2306 (2020)
6. Yigang, L., Ying-quan, Z., et al.: An improved photovoltaic MPPT algorithm based on differential evolution algorithm. *Acta Energiæ Solaris Sinica* **41**(6), 264–271 (2020)
7. Wu, X., Qi, Y.: Differential evolution algorithm for solving robotic cell scheduling problem with batch-processing machines. *Control Decision* **35**(1), 74–82 (2020)
8. Xu-jian, Y.-L., et al.: Synthesis of sparse rectangular planar arrays with multiple constraints based on dynamic parameters differential evolution algorithm. *J. Electron. Inf. Technol.* **42**(5), 1282–1287 (2020)



# Chapter 22

## Channel Pruning and Quantization-Based Learning for Object Detection with Computing Source Limited Application



Fei Zhao, Huanyu Liu, Moufa Hu, and Yingjie Deng

**Abstract** With the rise of convolutional neural network (CNN) in the field of computer vision, more and more practical applications need to deploy CNN on mobile devices. However, due to the large amount of CNN computing operations and the large number of parameters, it is difficult to deploy on ordinary edge devices. The neural network model compression method has become a popular technology to reduce the computational cost and has attracted more and more attention. We specifically design a small target detection network for hardware platforms with limited computing resources, use pruning and quantization methods to compress, and demonstrate in VOC dataset and RSOD dataset on the actual hardware platform. Experiments show that the proposed method can maintain a fairly accurate rate while greatly speeding up the inference speed. The proposed model designed in this paper achieves 76.74% mAP on the VOC dataset, which is 4.76 times faster than the original model.

### 22.1 Introduction

In recent years, convolutional neural network (CNN) is regarded as one of the best techniques for understanding image content and has shown great performance in image classification [4], segmentation [2], and detection [8] tasks. The features of

---

F. Zhao · M. Hu · Y. Deng

National Key Laboratory of Science and Technology on ATR, College of Electronic Science,  
National University of Defense Technology, Changsha 410073, China  
e-mail: [f\\_z2020@126.com](mailto:f_z2020@126.com)

M. Hu

e-mail: [hu199709\\_200106@sina.com](mailto:hu199709_200106@sina.com)

Y. Deng

e-mail: [447824977@qq.com](mailto:447824977@qq.com)

H. Liu (✉)

School of Electronics and Information Engineering Harbin Institute of Technology, Harbin,  
Heilongjiang 150001, China  
e-mail: [1094963265@qq.com](mailto:1094963265@qq.com)

CNN such as local connection, weight sharing, and pooling operations can effectively reduce the complexity of the network and reduce the number of training parameters. Since the advent of AlexNet [9], most frontrunners in image processing competitions have adopted CNN-based methods.

However, current state-of-the-art CNN cannot adapt well to today's smart mobile devices, especially in tasks with higher complexity like target detection. Therefore, many recent research aims to reduce the model computing operations and model parameters with minimal accuracy losses. However, most model compression methods are performed on classification models. Common classification networks usually have small input resolution and simple model architecture, while detection network usually has a larger input resolution and more complicated architecture. Detection network may also include multiple inputs, as well as some post-processing, which put forward higher requirements for the design of the network compression algorithm. Common compression methods include pruning [10], quantization [3], and distillation. Model pruning methods can usually be divided into two types: structured and unstructured. Unstructured pruning methods usually only work on specific hardware due to the sparsity on neuron level [12]. The structured pruning method usually prunes on the channel level, which can be accelerated on common hardware. Quantization methods can generally be divided into post-training quantization and quantization during training. Quantization converts floating-point numbers to integers symmetrically or asymmetrically according to the quantization bit depth, zero point, and scale parameters. Post-training quantization usually calculates the quantization parameters of each layer on the calibration set. Quantization during training, aka quantization-aware training (QAT), learns and observes weights and quantization parameters at the same time, which can achieve accuracy closer to the floating-point model. The distillation method achieves model compression by transferring the knowledge of the trained large model to a smaller model. Common compression methods usually only demonstrate on large models. However, in order to be able to deploy the CNN on platforms with limited computing resources, choose a small network designed specifically for mobile devices and then use the compression technique to achieve better results. We use channel pruning and quantization methods to compress the small detection network and test inference time on actual hardware.

## 22.2 Proposed Method

In this section, we discuss the details of the methods and principles used to compress the object detection network. First, we describe the architecture of the proposed detection network and then discuss the algorithm of pruning and quantization methods respectively.

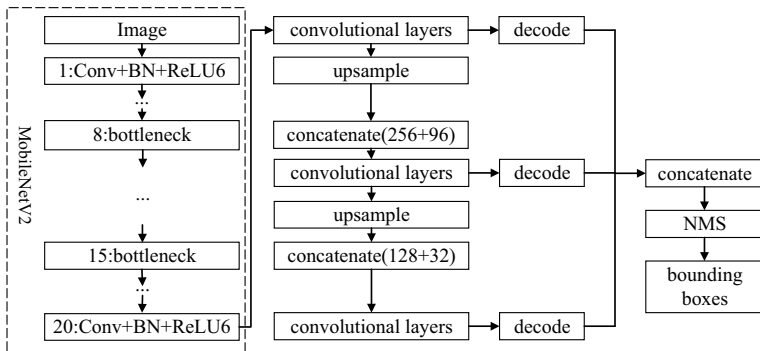


Fig. 22.1 Architecture of the proposed object detection network

### 22.2.1 Network Architecture

The architecture of proposed object detection network is shown in Fig. 22.1. We choose MobileNetV2 as our feature extractor. MobileNetV2 is a small network designed specifically for mobile devices, which maintains high accuracy while having a small amount of operations. MobileNetV2 greatly reduces computing operations through the depth-wise convolutions and inverse residual structure, and is more friendly to CPU. It achieved 72.0% Top-1 accuracy on the ImageNet dataset.

The post-processing of the network is mainly composed of decoding and non-maximum suppression (NMS). Decoding converts the outputs of the convolutional layer into predictive value of the bounding boxes. The shape of the tensor is  $B \times H \times W \times A \times (C + 5)$ , where  $B$  is the batch size;  $H$  and  $W$  are the height and width of the feature map;  $A$  is the number of anchors;  $C$  is the number of categories. The last five values of the last dimension are the offsets from the center of the grid point and one foreground probability, denoted as  $(\hat{x}_{\min}, \hat{y}_{\min}, \hat{x}_{\max}, \hat{y}_{\max}, p_F)$ . Let the grid points of the feature map be  $P_{i,j} = (x_i, y_j) = (i, j)$ ,  $0 \leq i \leq W$ ,  $0 \leq j \leq H$ . The relationship between the decoded coordinates and the outputs of the convolution layer will be:

$$\begin{aligned} (x_{mn}, y_{mn}) &= P + \exp\left(\left(\hat{x}_{\min}, \hat{y}_{\min}\right)\right) + 0.5 \\ (x_{mn}, y_{mn}) &= P + \exp\left(\left(\hat{x}_{\max}, \hat{y}_{\max}\right)\right) + 0.5 \end{aligned} \quad (22.1)$$

We apply NMS on the decoded outputs of detection heads to get the finally bounding boxes. In detection head, we use BCE loss [5] and GIoU loss [7] for classification and box regression.

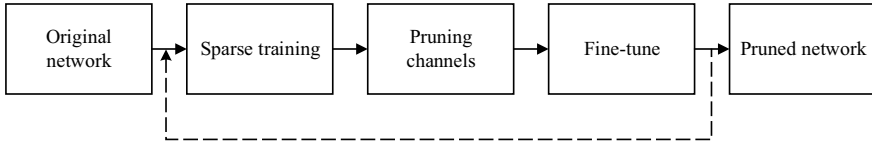


Fig. 22.2 Flowchart of channel pruning

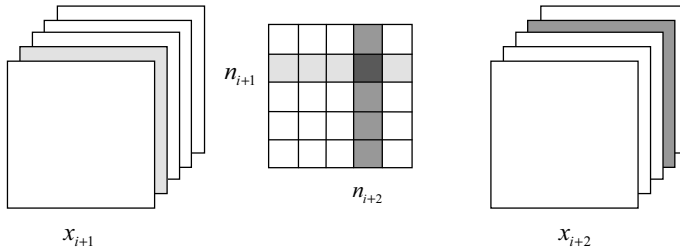


Fig. 22.3 Pruning strategy in general situation

### 22.2.2 Pruning

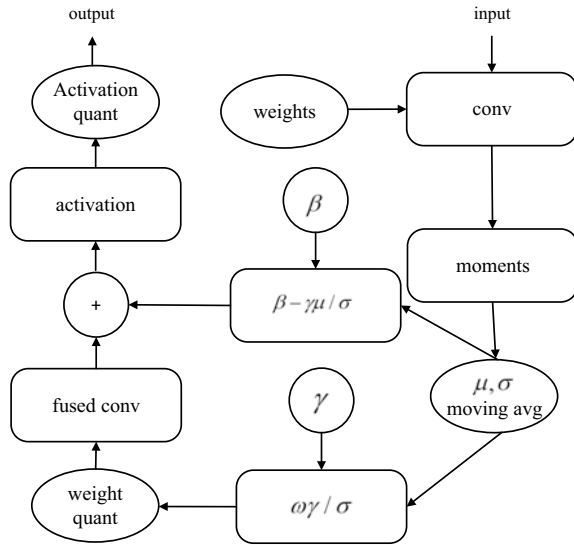
The channel pruning algorithm can be divided into three steps: sparse training, pruning, and fine-tuning, which is shown in Fig. 22.2. The pruning process can be carried out once or multiple times. Sparse training: In the training process, L1 norm penalty is applied to of the BN layer after the convolutional layer that needs to be sparse. The specific steps of sparse training are as follows. Schematic diagram of channel pruning is shown in Fig. 22.3. Let the shape of the current layer convolution kernel be  $(N_{in}, N_{out}, K_h, K_w)$ . Then, the convolution kernel after pruning is shown in Eq. 22.2.

$$F'_x = F_x[M_{in}, M_x, :, :] \tag{22.2}$$

where  $N_{in}, N_{out}, K_h, K_w$  represent the number of input channels, the number of output channels, the convolution kernel height and width, respectively.  $A[M_1, M_2]$  means filtering out and restructuring  $A$  by  $M_1, M_2$  dimension-wise. Colon indicates a mask of all ones. Finally, set current layer's pruning mask  $M_x$  as the next layer's input pruning mask.

Depth-wise convolution: The depth-wise convolution can be seen as a convolution with the same number of groups as the number of input channels and output channels. For this type of convolution, it is only necessary to remove the corresponding convolution kernel according to the input pruning mask  $M_{in}$ , then set the number of output channels and the number of groups to the new number of input channels.

**Fig. 22.4** Computation graph of quantization-aware training



### 22.2.3 Quantization

We have different computation graph during training and inference. The training graph and the inference graph are shown in Fig. 22.4. In training graph, we simulate quantized convolution operation through the fake-quantization module, and fuses the BN layer parameters into the convolution weights to better fit the actual value. We observe the range of values after each convolution and activation to calculate the quantization parameters. We use 8-bit signed integers to quantize the 32-bit floating-point weights, and 8-bit unsigned integers for the activations. Both network input and convolution weights are quantized to 8-bit integers. However, since the biases of convolution are sensitive to errors, 32-bit unsigned integers are used for quantization. The inference graph only contains quantized convolution operations, since batch-normal layers have been fused into pervious convolution weights.

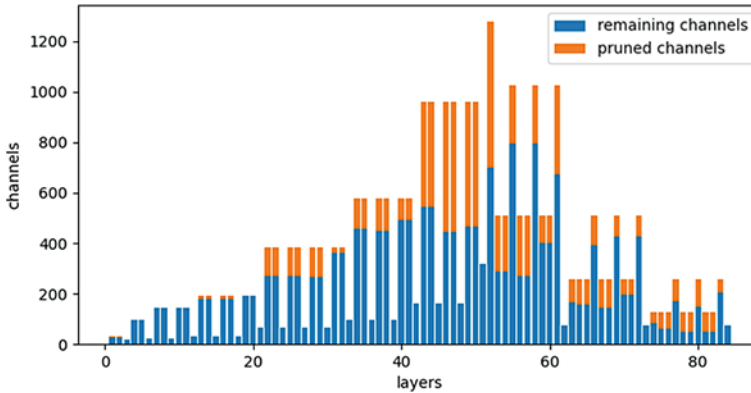
## 22.3 Experiments

This section gives a comparison between proposed network and other state-of-art lightweight detection networks. Then, we show the acceleration of pruning and quantization. We train our model on the VOC dataset. We set training epoch to 80 for all cases, using standard data augment methods, including random cropping and horizontal flipping, and additionally using mixup. Adopting Adam optimization algorithm, cosine annealing learning rate strategy with warming up, the initial learning rate is  $4e-3$ , and the batch size is 16. As a result, proposed model got 78.46% of the test set

**Table 22.1** Comparison of the accuracy, MACs, and number of parameters

Name	mAP (%)	MACs (G)	Params (M)
YOLOv3 [6]	79.2	49.8	59.25
Tiny YOLOv3 [1]	61.3	8.36	8.5
YOLO Nano [11]	71.7	6.92	<b>1.1</b>
Ours	<b>78.46</b>	<b>4.25</b>	6.775

The bold denotes the highest performance among the three methods

**Fig. 22.5** Comparison of the number of channels per layer before and after pruning on VOC dataset

mAP under the input image size of 512–512. FLOPs of our model is 4.25G MACs, and the number of parameters is 6.775M. See Table 22.1 for comparison with other network in terms of accuracy, MACs, and number of parameters.

All model in Table 22.1 was evaluated on the VOC 2007 test set at the input image size of  $512 \times 512$ . By comparison, the proposed model is close to the YOLOv3 in accuracy, but both MACs and the number of parameters are reduced a lot. Compared with Tiny YOLOv3 and YOLO Nano, we still have great advantages in accuracy and MACs.

The hyperparameter settings of sparse training are the same as previous. In sparse training, we set the sparse rate to 0.01. Reached 75.65% mAP on VOC 2007 test set. After pruning 40% of channels and fine-tuning for 20 epochs, it finally reached 75.44% testset mAP, which decreased by 3.0% compared with the unpruned model. MACs was reduced to 2.606G, and the number of parameters was reduced to 2.31M. Compared with the unpruned model, it was reduced by 38.6% and 65.9%, respectively. The number of channels of each layer before and after pruning is shown in Fig. 22.5. See Table 22.2 for detailed comparison.

We then apply quantization on 40% pruned model. Training settings are the same as above. We choose 8-bit quantization, freezing BN layer parameters after 10 epochs, and freezing quantization parameters after 15 epochs. The quantized model achieved 76.74% mAP on testset, a decrease of 1.7% from the original model. We benchmark

**Table 22.2** Comparison between original and pruned model on VOC dataset

Name	mAP (%)	MACs (G)	Params (M)
Original	78.46	4.25	6.775
30% pruned	76.30	3.195	3.463
40% pruned	75.44	2.606	2.308

**Table 22.3** Benchmark for original, pruned, and quantized model on VOC dataset

Name	mAP (%)	MACs (G)	Params (M)	Inference time (ms)	Speedup
Original	78.46	4.25	6.775	126.6	1
40% pruned	75.44	2.606	2.308	102.7	1.23
40% pruned + quantized	76.74	–	–	26.6	4.76

all models on E5-2630 v4 CPU, and the network input is 512–512. The benchmark is performed on the first 100 testset images of VOC dataset. See Table 22.3 for details. After pruning and quantization on original model, we achieved 4.76 times acceleration on CPU, and there is only a small loss of accuracy.

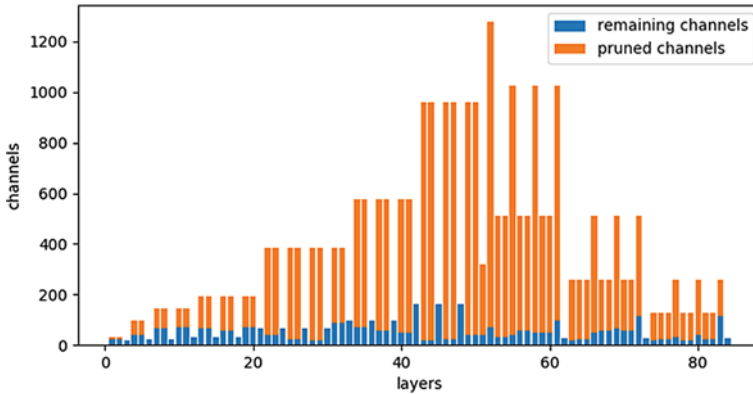
We also experiment on RSOD dataset. The RSOD dataset is an open dataset for object detection in remote sensing images. The dataset includes aircraft, oiltank, playground, and overpass. The image sizes range from 500–500 to 2000–1000. We randomly select 80% of the original images as the training set, 20% as the test set. As a result, the training and test set include 752 images and 187 images, respectively. During training, we randomly crop a 512–512 patch on original images, and then scale it to the size of 320–608. We apply similar augmentation as before, but add horizontal flipping. We pad the test images to nearest multiple of 32 and evaluate on original size. The model is trained by 20k iterations in total, and other training hyperparameter settings is as same as before. In sparse training, we set sparse ratio to 0.1 and round remaining number of channels to multiple of 8. To avoid pruning out all channels, we set the minimum number of channels to 16. As shown in Table 22.4, our model reached 92.59% mAP on test set. We found that 85% of pruning on model greatly reduce FLOPs to 1.335G MACs, and the number of parameters is 180.5K. Nearly  $37\times$  smaller than unpruned model with trivial accuracy drop.

We found that if pruning ratio higher than 85%, mAP drop sharply. The pruning limit is around 0.876 in this case, perhaps that is why. For comparison, we also draw a figure shown the number of channels with and without pruning (see Fig. 22.6). Note that the layers as main stem of residual blocks make up most of FLOPs.

Finally, we quantize the 85% pruned model with QAT. We benchmark 100 images on CPU with 512–512 input. Table 22.5 shows comparison between original, pruned, and quantized model. Our final model is 6.31 times faster than original one. The size of final model is only 253 KB.

**Table 22.4** Comparison between original and pruned model on RSOD dataset

Name	mAP (%)	MACs (G)	Params
Original	92.59	4.248	6.689M
30% pruned	91.76	3.274	3.506M
60% pruned	91.38	2.334	1.085M
80% pruned	90.78	1.650	326.3K
85% pruned	90.81	1.335	180.5K
90% pruned	63.53	1.113	84.9K

**Fig. 22.6** Comparison of the number of channels per layer before and after pruning on RSOD dataset**Table 22.5** Benchmark for original, pruned, and quantized model on RSOD dataset

Name	mAP (%)	MACs (G)	Params	Inference time (ms)	Speedup
Original	92.59	4.248	6.689M	131.3	1
85% pruned	90.81	1.335	180.5K	58.3	2.25
85% pruned + quantized	91.15	–	–	20.8	6.31

## 22.4 Conclusions

We propose a lightweight object detection model for hardware platforms with limited computing resources. We achieved this by designing a small network, channel pruning, and quantization. After pruning and quantization, we benchmark proposed model on VOC dataset and RSOD dataset, which achieved 4.76 and 6.31 times acceleration on common CPU with minor accuracy loss.



## References

1. Gong, H., Li, H., Xu, K., Zhang, Y.: Object detection based on improved yolov3-tiny. In: 2019 Chinese Automation Congress (CAC) (2019)
2. Grzybowski, J., Bragagnolo, L., Rezende, L.R., Silva, R.: Convolutional neural networks applied to semantic segmentation of landslide scars. *Catena* **201**(1), 1 (2021)
3. Krishnamoorthi, R.: Quantizing deep convolutional networks for efficient inference: a whitepaper (2018)
4. Krizhevsky, A., Sutskever, I., Hinton, G.: Imagenet classification with deep convolutional neural networks. In: NIPS (2012)
5. Pan, J., Canton, C., Mcguinness, K., O'Connor, N.E., Giro-I-Nieto, X.: Salgan: Visual saliency prediction with generative adversarial networks (2017)
6. Redmon, J., Farhadi, A.: Yolov3: an incremental improvement. arXiv e-prints (2018)
7. Rezatofighi, H., Tsoi, N., Gwak, J., Sadeghian, A., Reid, I., Savarese, S.: Generalized intersection over union: A metric and a loss for bounding box regression. In: 2019 IEEE/CVF Conference on Computer Vision and Pattern Recognition (CVPR), pp. 658–666 (2019)
8. Sengupta, D.: Deep learning architectures for automated image segmentation (2019)
9. Shermin, T., Teng, S.W., Murshed, M., Lu, G., Sohel, F., Paul, M.: Enhanced Transfer Learning with Imagenet Trained Classification Layer. Springer, Cham (2019)
10. Tian, G., Chen, J., Zeng, X., Liu, Y.: Pruning by training: a novel deep neural network compression framework for image processing. *IEEE Signal Process. Lett.* **28**, 344–348 (2021)
11. Wong, A., Shafi, E., Li, F., Chwyl, B.: Yolo nano a highly compact you only look once convolutional neural network for object detection (2019)
12. Wu, K., Guo, Y., Zhang, C.: Compressing deep neural networks with sparse matrix factorization. *IEEE Trans. Neural Networks Learn. Syst.* **99**, 1–11 (2019)

# Chapter 23

## Retinal Vessels Segmentation Based on Multi-scale Hybrid Convolutional Network



Rui Li, Zuoyong Li, Xinrong Cao, and Shenghua Teng

**Abstract** Retinal fundus image can reveal the information on the early symptoms of diabetes, hypertension, hyperlipidemia and other diseases. Accurate segmentation of retinal vessels can assist the detection and diagnosis of the related diseases. Due to the intricate characteristic information of retinal vessels images, traditional segmentation methods lead to inaccurate segmentation for small vessels and pathological segmentation errors. In this paper, we propose a new multi-scale hybrid convolution U-Net. Firstly, we take the hybrid convolution module by combining dilated convolution and standard convolution as the core structure for feature extraction to obtain more abundant semantic feature information, while expanding the receptive field. Then, we add a multi-scale fusion module to the network encoding and decoding connection part, which fuses the feature information of different layers to reduce the loss of information and enhance the representation ability of the network. We evaluate the performance of the proposed method on two public retinal datasets (DRIVE and CHASE\_DB1). The results of quantitative and qualitative experiments show that the proposed model can improve good accuracy in retinal vessels segmentation.

---

R. Li · S. Teng (✉)

College of Electronic and Information Engineering, Shandong University of Science and Technology, Qingdao 266590, China

e-mail: [shteng@sdust.edu.cn](mailto:shteng@sdust.edu.cn)

Z. Li · X. Cao (✉)

Fujian Provincial Key Laboratory of Information Processing and Intelligent Control, Minjiang University, Fuzhou 350121, China

X. Cao

Fuzhou Digital Healthcare Industry Technology Innovation Center, Minjiang University, Fuzhou 350121, China

## 23.1 Introduction

Retinal fundus images involve valuable biomedical information and play an essential role in the early detection of cardiovascular and ophthalmic diseases. For instance, Hypertensive Retinopathy (HR) [1] is a disease of retina induced by elevated blood pressure, which can be accompanied by blood vessels to bend or narrow. Diabetic Retinopathy (DR) [2] is another usual disease of retina caused by hyperglycemia and can cause retinal vessels swelling. So, segmentation of retinal vessels is one of the most important steps in the quantitative analysis of retinal fundus images. However, if the retinal vessels are segmented manually, it can be a time-consuming and technically demanding task. Although the automatic retinal vessels segmentation has been widely studied, it is still challenging.

In recent years, the emergence of deep learning has promoted the rapid development in the field of biomedicine. In the task of retinal vessels segmentation, convolution neural network (CNN) based on deep learning has been widely used. Fu et al. [3] use CNN to learn rich feature information and combine conditional random fields (CRF) to establish remote interactions between pixels. Different from the traditional CNN, Long et al. [4] established the full convolutional network (FCN) for the first time to achieve end-to-end semantic segmentation. The FCN-based U-Net proposed by Olaf Ronneberger et al. [5] has been very popular in biomedical research. Zhang et al. [6] proposed an attention-guided CNN, and the segmentation results can preserve the structural information of retinal vessels. Guo et al. [7] proposed a SD-Unet network for retinal vessels segmentation by introducing structured dropout blocks [8]. Lv et al. [9] constructed an AA-Unet by combining atrous convolution and attention mechanism for retinal vessels segmentation.

In this work, we use hybrid convolution [10] and feature fusion to form a multi-scale hybrid convolutional neural network, which can extract and fuse the feature information of different layers, and achieve good performance in retinal vessels segmentation.

The main contributions of this paper are as follows:

- (1) We propose an end-to-end segmentation model of retinal vessels based on deep learning network. A hybrid convolution is used as the core structure in the feature extraction stage, which can obtain more abundant semantic information, while expanding the receptive field.
- (2) At the end of the encoder, we add a multi-scale module to fuse the feature information of different layers to detect the morphology of the tiny vessels and achieve the segmentation of the tiny vessels.

The rest of this paper is structured as follows. In Sect. 23.2, the proposed method is introduced, including a context-aware encoder module, a multi-scale fusion module and a feature decoder module. In Sect. 23.3, the datasets, experimental settings and evaluation indicators are described. In Sect. 23.4, the analysis results of the proposed model are compared with those of other models.

## 23.2 Proposed Method

The purpose of this paper is to automatically segment retinal vessels from color fundus images. The deep learning-based U-Net [5] is regarded as an encoder-decoder network structure. The encoding stage mainly carries out feature extraction by continuous convolution and down-sampling, and the decoding stage uses transposed convolution for up-sampling and fuses the feature mapping from the encoding stage to restore the original resolution of the image. We have improved a U-Net-based segmentation algorithm that includes a context-aware encoder module, a multi-scale fusion module and a feature decoder module. The architecture of our network is shown in Fig. 23.1.

### 23.2.1 Context-Aware Encoder Module

Convolution operations play an essential role in the natural language processing and computer vision. Different from the standard convolution, dilated convolution [11] injects holes into the feature map to enlarge the receptive field. We use the hybrid convolution by combining dilated convolution and standard convolution to extract image features, which can obtain further abundant characteristic information, while expanding the receptive field (see Fig. 23.2). Specifically, the inputs are convolved by standard convolution with convolution kernel  $3 \times 3$  and dilated convolution with dilation rate  $2 \times 2$ , respectively, and then the elements of the corresponding positions

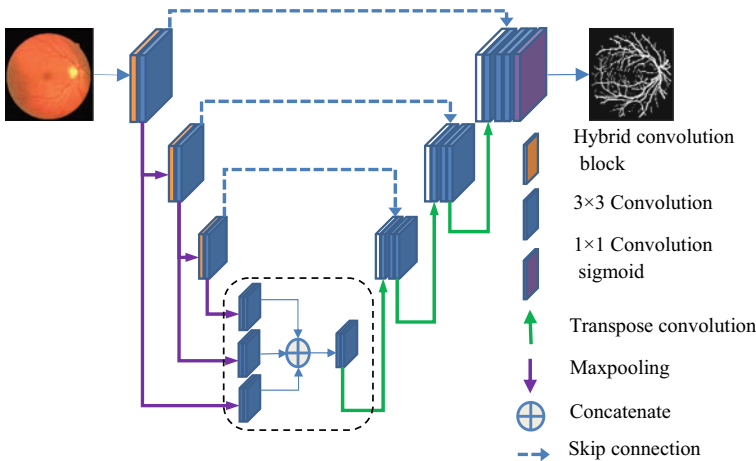
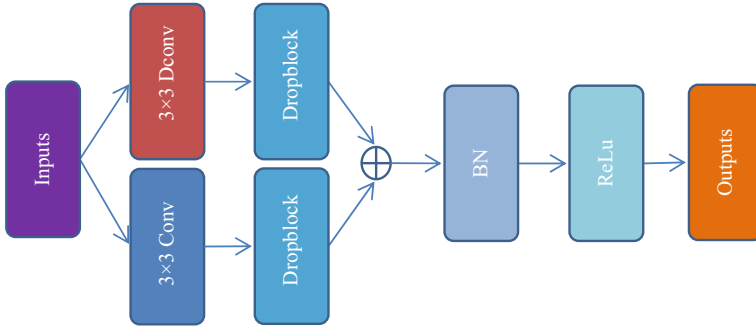
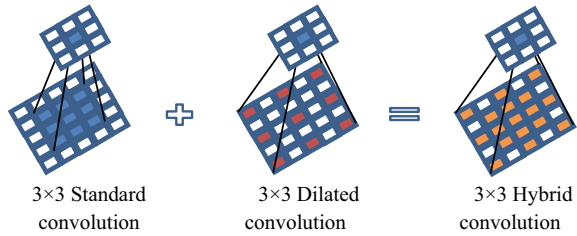


Fig. 23.1 The proposed network architecture

**Fig. 23.2** Hybrid convolution



**Fig. 23.3** Hybrid convolution block

on the feature maps are added. The final output is obtained through the batch normalization (BN) [12] layer and the rectified linear unit (ReLu) [13] layer successively. In Fig. 23.3, we show the structure of the hybrid convolution block.

We use Dropblock [8] instead of Dropout [14] in the convolution layer. Dropblock performs regularization constraints on the convolution layer by randomly dropping contiguous blocks of the feature map. The overfitting phenomenon can be better prevented for the convolution layer. It contains two parameters: *keep\_prob* and *block\_size*. The specific expression of the dropping parameter  $\gamma$  is as follows:

$$\gamma = \frac{1 - keep\_prob}{block\_size^2} \times \left( \frac{w \times h}{(w - block\_size + 1)(h - block\_size + 1)} \right) \quad (23.1)$$

where *keep\_prob* represents the probability that the neuron remains in the classical discarded state, *block\_size* can be interpreted as the size of the region to be dropped, and  $(w - block\_size + 1)(h - block\_size + 1)$  represents the size of valid seed region (where *w* represents the width of the feature map, and *h* represents the height of the feature map).

### 23.2.2 Multi-scale Fusion Module

We add a multi-scale fusion module at the end of the encoder. Because feature maps at different layers contain semantic information in different dimensions, we fuse this information in the form of Concatenate. And then go through two layers of  $3 \times 3$  standard convolution, these convolution layers can learn additional multi-scale information from input feature maps of different layers.

### 23.2.3 Feature Decoder Module

In the encoding stage, the feature of the input image is extracted to generate a smaller and finer feature map, while the decoding stage decodes the feature information by up-sampling and restores the original resolution of the image. Direct up-sampling would result in a large amount of information loss, which is addressed by the deep learning-based U-Net [5] by fusing the feature mapping of the encoders. The premise of fusion is that the feature image from the encoder-decoder has the same size. This feature map fusion method is also used in our proposed network architecture to reduce the feature information loss induced by up-sampling.

### 23.2.4 Loss Function

The loss function used in this algorithm is the binary cross entropy. The definition is as follows:

$$\text{Loss} = -\frac{1}{N} \sum_{i=1}^N y_i \log \hat{y}_i + (1 - y_i) \log(1 - \hat{y}_i) \quad (23.2)$$

where  $y_i$  means ground truth training label,  $\hat{y}_i$  represents the probability that pixel  $i$  belong to retinal vessels.

## 23.3 Experiments

In the following sections, we introduce the experimental datasets and the performance indicators of the evaluation algorithm model, and then introduce the method of data enhancement to expand the training sample data.

### 23.3.1 Datasets and Performance Metrics

For the datasets used in the experiment, we used two public datasets to evaluate the proposed model: DRIVE [15], CHASE\_DB1 [16]. The DRIVE dataset consists of 40 original fundus images with a resolution of  $565 \times 584$ . DRIVE has specified the training set and the test set, each containing 20 fundus images. The CHASE\_DB1 dataset contains 28 fundus images, each with a resolution of  $960 \times 999$ . We selected 20 images to train the model and another 8 images to test the model.

Retinal vessels segmentation is actually a binary classification problem. As a result, there are four categories: TP (True Positive) refers to true positive sample, FP (False Positive) indicates false positive sample, TN (True Negative) refers to true negative sample, FN (False Negative) refers to false negative sample.

For the evaluation indicators, the following four performance metrics are used to evaluate the model: Accuracy (ACC) refers to the ratio of correctly classified pixels to the pixels of the whole image. Sensitivity (SE) refers to the ratio that is correctly divided into retinal vessels. Specificity (SP) represents the ratio that is correctly divided into non-retinal vessels. Area under curve (AUC) refers to the area under receiver operating characteristic (ROC), and higher AUC values indicate better performance of the model. These performance metrics are defined as follows:

$$ACC = \frac{TP + TN}{TP + TN + FP + FN} \quad (23.3)$$

$$SE = \frac{TP}{TP + FN} \quad (23.4)$$

$$SP = \frac{TN}{TN + FP} \quad (23.5)$$

### 23.3.2 Implementation Details

To facilitate training, the original images of two datasets are set to  $592 \times 592$ . Because of the small amount of training sample data, we use data enhancement methods such as adding Gaussian noise, color dithering, changing brightness and contrast to expand the training sample. These data-enhanced images are divided into training set and validation set, accounting for 90% and 10%, respectively. Image enhancement is often used in biomedical related tasks, especially in small datasets, where it can make models more stable. In order to improve the experimental performance to the best, *block\_size* in the Dropblock is set to 7, and the *keep\_prob* are set to 0.82 and 0.87 on DRIVE dataset and CHASE\_DB1 dataset, respectively.

**Table 23.1** The results of different models on DRIVE

Model	ACC	SE	SP	AUC
U-Net [5]	0.9672	0.7866	0.9845	0.9786
AG-Net [6]	0.9692	0.8100	0.9848	0.9856
SD-Unet [7]	0.9674	0.7891	0.9848	0.9836
AA-Unet [9]	0.9558	0.7941	0.9798	0.9847
Ours	<b>0.9697</b>	<b>0.8171</b>	<b>0.9852</b>	<b>0.9866</b>

**Table 23.2** The results of different models on CHASE\_DB1

Model	ACC	SE	SP	AUC
U-Net [5]	0.9715	0.8145	0.9820	0.9663
AG-Net [6]	0.9661	0.8132	0.9814	0.9863
SD-Unet [7]	0.9738	0.7559	<b>0.9900</b>	0.9872
AA-Unet [9]	0.9608	0.8176	0.9704	0.9865
Ours	<b>0.9746</b>	<b>0.8267</b>	0.9845	<b>0.9888</b>

## 23.4 Results and Analysis

In Tables 23.1 and 23.2, we summarize the segmentation performance of our method and several state-of-the-art models on DRIVE and CHASE\_DB1 datasets, highlighting the best of each indicator in bold. The data in the tables demonstrate that our proposed model has achieved better performance. Specifically, our proposed method has 98.66%/98.88% AUC (0.10%/0.16% higher than the second performance) and 81.71%/82.67% sensitivity (0.71%/0.91% higher than the second performance). The highest accuracy and specificity are comparable. In Fig. 23.4, we show the example results of the segmentation of the models on two datasets. It can be seen from figure that our proposed model can segment even tiny retinal vessels.

## 23.5 Conclusion

In this paper, we proposed a multi-scale hybrid convolutional network for the segmentation of retinal vessels. Specifically, the hybrid convolution by combining dilated convolution and standard convolution is the core module of encoder feature extraction, which allows more feature information to be extracted, while extending the received domain. At the end of the encoder, we capture smaller details of the retinal vessel structure by fusing multi-scale feature information, which enhances the ability of the network to segment tiny retinal vessels. Finally, the fine vessel segmentation mask is reconstructed by the feature decoder and skip connections. Our proposed



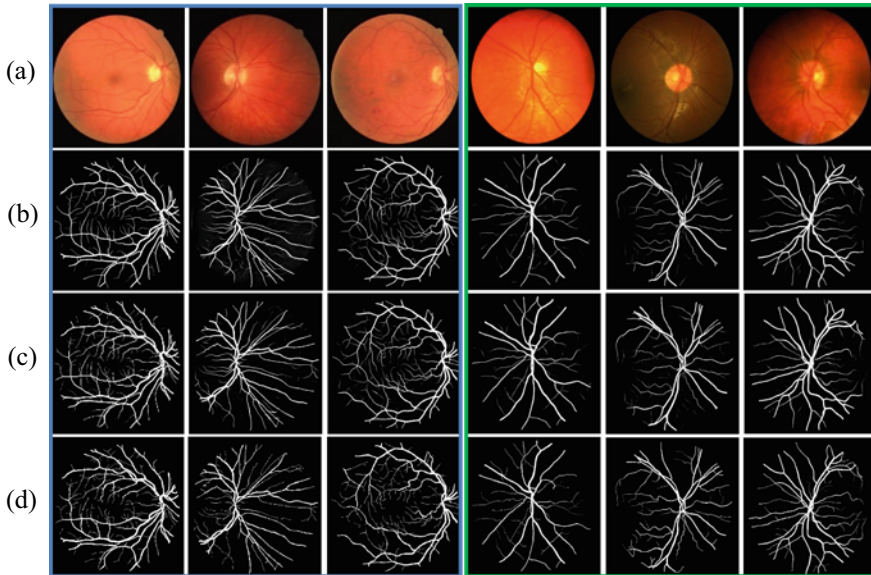


**Fig. 23.4** Segmentation results on DRIVE (blue border) and CHASE\_DB1 (green border). **a** Original images, **b** U-Net segmented images, **c** Our segmented images, **d** Ground truth

model was demonstrated on DRIVE and CHASE\_DB1 datasets, and the experimental analysis shows that our proposed model improves the segmentation accuracy of retinal vessels.

**Acknowledgements** This work is partially supported by National Natural Science Foundation of China (61972187), Natural Science Foundation of Fujian Province (2020J02024), Guangdong Provincial Key Laboratory of Cyber-Physical Systems(2020B1212060069), National&Local Joint Engineering Research Center of Intelligent Manufacturing Cyber-Physical Systems, and Fuzhou Science and Technology Project (2020-RC-186).

## References

1. Irshad, S., Usman Akram, M.: Classification of retinal vessels into arteries and veins for detection of hypertensive retinopathy. In: Proceedings of the Biomedical Engineering Conference (CIBEC), pp. 133–136. IEEE (2014)
2. Jacobs, I.S., Bean, C.P.: Fine particles, thin films and exchange anisotropy. *Spin Arrang. Crystal Struct. Domains Micromagn.* **330**(7), 271–350 (1963)
3. Fu, H., Xu, Y., Lin, S., et al.: DeepVessel: retinal vessel segmentation via deep learning and conditional random field. In: Proceedings of the International Conference on Medical Image Computing and Computer-Assisted Intervention, pp. 132–139 (2016)
4. Long, J., Shelhamer, E., et al.: Fully convolutional networks for semantic segmentation. *IEEE Trans. Pattern Anal. Mach. Intell.* **39**(4), 640–651 (2015)

5. Ronneberger, O., Fischer, P., et al.: U-net: convolutional networks for biomedical image segmentation. In: Proceedings of the International Conference on Medical Image Computing and Computer-Assisted Intervention, pp. 234–241 (2015)
6. Zhang, S., Fu, H., Zhang, Y., et al.: Attention guided network for retinal image segmentation. In: Proceedings of the International Conference on Medical Image Computing and Computer Assisted Intervention, pp. 797–805 (2019)
7. Guo, C., Szemenyei, M., Pei, Y., et al.: SD-Unet: a structured dropout U-Net for retinal vessel segmentation. In: Proceedings of the IEEE 19th International Conference on Bioinformatics and Bioengineering (BIBE), pp. 439–444 (2019)
8. Ghiasi, G., Lin, T.-S., Le Quoc, V.: DropBlock: a regularization method for convolutional networks. In: Proceedings of the Neural Information Processing Systems, pp. 1–11 (2018)
9. Lv, Y., Ma, H., Li, J., et al.: Attention guided U-Net with atrous convolution for accurate retinal vessels segmentation. *IEEE Access* **8**, 32826–32839 (2020)
10. Ting, F., Chuansheng, W., Xinwei, C., et al.: URNet: A U-Net based residual network for image dehazing. *Appl. Soft Comput.* **102**, 1–9 (2020)
11. Yu, F., Koltun, V.: Multi-scale context aggregation by dilated convolutions. In: Proceedings of the International Conference on Learning Representations, pp. 1–9 (2016)
12. Ioffe, S., Szegedy, C.: Batch Normalization: accelerating deep network training by reducing internal covariate shift. In: Proceedings of the 32nd International Conference on International Conference on Machine Learning, pp. 448–456 (2015)
13. Glorot, X., Bordes, A., Bengio, Y.: Deep sparse rectifier neural networks. In: Proceedings of the 14th International Conference on Artificial Intelligence and Statistics (AISTATS), pp. 315–323 (2011)
14. Tompson, J., Goroshin, R., et al.: Efficient object localization using convolutional networks. In: Proceedings of the IEEE Conference on Computer Vision and Pattern Recognition (CVPR), pp. 648–656 (2015)
15. Staal, J., Abramoff, M.D., Niemeijer, et al.: Ridge-based vessel segmentation in color images of the retina. *IEEE Trans. Med. Imaging* **23**(4), 501–509 (2004)
16. Owen, C.G., Rudnicka, A.R., Mullen, R., Barman, S.A., et al.: Measuring retinal vessel tortuosity in 10-year-old children: validation of the computer-assisted image analysis of the retina (CAIAR) program. *Invest. Ophthalmol. Vis. Sci.* **50**(5), 2004–2010 (2009)

## Chapter 24

# Location Optimization of Service Centers for Seniors Based on an Improved Particle Swarm Optimization Algorithm



Wei-Feng Wang , Ruo-Bin Wang , Shuo Yin , Zhi-Wei An ,  
and Lin Xu 

**Abstract** The world's population is gradually aging, and the construction of Service Centers for Seniors (SCS) has become an important issue worthy of concern. In this paper, a particle swarm optimization algorithm with random weight and synchronous learning factor (RSPSO) is proposed to optimize the location and compared with three improved PSO algorithms. Experimental results show that RSPSO bears a faster convergence with better improvements on global searching. Furthermore, it can effectively avoid falling into the local optimal solution. The results also demonstrate the superiority of RSPSO over PSO in location optimization of SCS.

## 24.1 Introduction

In light of the gradual aging of world's population, the United Nations released the World Population Aging Report [1], and it has shown the population of seniors over 60 will be 20% of the total population by the mid-twenty-first century. The population of seniors over 60 in China had reached 255 million by 2020, accounting for 17.8%. By 2050, it will reach 483 million, accounting for 34.1% [2].

Hence, the construction of Services Center for Seniors (SCS) aims to relieve the pressure on offspring and satisfy the senior's requirements, but where to build SCS is an issue worthy of discussion. It is difficult for the traditional location planning to find the optimal solution. With the development of swarm intelligence optimization algorithms, some researchers have made valuable achievements on the location optimization issue. This paper attempts to propose a PSO with random

---

W.-F. Wang · R.-B. Wang (✉) · S. Yin · Z.-W. An  
North China University of Technology, Beijing 100043, China  
e-mail: [wrb@ncut.edu.cn](mailto:wrb@ncut.edu.cn)

L. Xu (✉)  
University of South Australia, Adelaide 5095, Australia  
e-mail: [xuyly032@mymail.unisa.edu.au](mailto:xuyly032@mymail.unisa.edu.au)

Fuzhou Institute of Technology, Fuzhou 350506, China

weight and synchronous learning factor (RSPSO) algorithm and apply to the location optimization of SCS.

The main contributions of our research are summarized as follows:

- Our improvements on PSO algorithm include two aspects, (1) improving the random weight to balance the searching capability between the local search and the global search; (2) improving the learning factor to combine the self-cognitive and social-cognitive part of particles, so as to improve the results of group cooperation and knowledge sharing among particles.
- Test the effectiveness of RSPSO, we proposed by comparing the performances of different algorithms on the same fitness functions. The experimental results reveal the superiority of RSPSO over PSO and the other two modified PSO.
- The RSPSO we proposed is applied on the location optimization of SCS, which is a concerned issue in aging society. RSPSO outperforms well than traditional location planning.

The organization of this article is as follows: Sect. 24.2 discusses the related works. Section 24.3 introduces the mathematical model of SCS. Section 24.4 describes the RSPSO. Section 24.5 presents the findings of the experiment and discusses the experimental results. Finally, Sect. 24.6 concludes the outcome of the research.

## 24.2 Related Works

Because of its conciseness and effectiveness, the PSO algorithm is widely employed in many fields. Such as location selection, UAV path planning, deep learning and so on. At present, the research and improvements of PSO can be roughly divided into three categories: Inertia weight, hybrid algorithm, and parallel technology.

**Inertia Weight.** Ren et al. [3] applied the improved PSO to wireless sensor networks. By introducing the optimal fitness change rate to control the inertia weight; Hua et al. [4] averaged particle spacing as guidance factor of population diversity is employed to establish nonlinear inertia weight and arccosine function is adopted to design nonlinear symmetric acceleration coefficient in order to control the balance of global search and local search for distribution center location problem. Ji et al. [5] introduce the PSO to solve the location of distribution center problem of optimal solution, the empirical results show that the PSO algorithm can reduce the iteration times and time, and can improve the optimization precision of location selection problem, reduce the total cost.

**Hybrid algorithm.** Tang et al. [6] introduced a simulated annealing algorithm into PSO and applied it to UAV path planning so that the particles can jump out of the local extremum, which improved the global optimization ability of PSO, but there are still limitations in the local search ability; Wang et al. [7] aimed to solve the UAV path planning problem, the chemotactic operation, and migration operation of the bacteria foraging algorithm is introduced in the PSO to improve its optimization

ability. Due to the introduction of two operators, the hybrid algorithm increases a certain amount of computation, which leads to the total time consumption higher than the traditional algorithm, but the overall efficiency is improved compared with the traditional PSO.

**Parallel Technology.** Chai et al. [8] proposed a parallel whale optimization algorithm. It contains two information exchange strategies between groups and it significantly enhances global search ability and population diversity of algorithm, and it was adopted to optimize the localization of WSN; Song et al. [9] proposed an improved cuckoo search algorithm based on compact and parallel techniques for three-dimensional path planning problems. The parallel scheme can increase the accuracy and achieve faster convergence. The parallel scheme can increase the accuracy and achieve faster convergence; Jiang et al. [10] proposed a new parallel QUATRE algorithm. The P-QUATRE enhance the overall performance of the former QUATRE algorithm by incorporating a parallel mechanism and use to tackle tough real-parameter optimization problems.

The improvement of inertia weight requires more data experiments that results to the algorithm in poor flexibility; the hybrid algorithm improves the convergence speed of iteration, but it increases the space and time complexity; the parallel technology finds too many optimal solutions which increases a lot of computation. Based on the above analysis, an improved algorithm-RSPSO is proposed, and apply it to location optimization of SCS.

### 24.3 Mathematical Model of SCS

#### 24.3.1 Problem Definition

Taking a city as an example, the number of seniors in the region is counted, and the maximum capacity of the SCS is estimated by investigating the personnel structure of the SCS that had been built and the number of seniors who need to be served every day. Finally, it is estimated that several SCSs for seniors need to be built in this area. Therefore, the equation for determining the number of SCS is as follows:

$$\begin{aligned}
 N_1 &= \frac{M * C}{S * k_1 + W * k_2 + R * k_3}, \lambda = 0 \\
 N_2 &= \frac{\varepsilon * M * C}{S * k_1 + W * k_2 + R * k_3}, 0 < \lambda \leq 2 \\
 N &= N_1 + N_2
 \end{aligned}
 \tag{24.1}$$

where,  $N$  is the number of SCS to be built;  $S$  is the number of senior;  $k_1$  is the supply of various services for each senior;  $w$  is the number of worker;  $k_2$  is the supply for worker;  $R$  is the Number of fixed beds, generally take 10 (the upper limit of the

SCS is 10 due to the influence of the policy);  $k_3$  is the supply for bed;  $M$  is the total number of the senior in the region;  $C$  is the average space occupied by each senior;  $\lambda$  is the impact factor ( $0 \leq \lambda \leq 2$ ).

### 24.3.2 Determine the Objective Function

This paper studies the location optimization of SCS in a region. According to the principle of the shortest distance, the objective function is established:

$$F(a_0, b_0) = \sum_{i=1}^N \left( \sqrt{(a_0 - a_i)^2 + (b_0 - b_i)^2} \right) \tag{24.2}$$

$$\text{subject to } \sqrt{(a_0 - a_i)^2 + (b_0 - b_i)^2} - d_i \leq 0, i = 1, 2, 3, \dots, N \tag{24.3}$$

The objective function (24.2) and constraints (24.3) constitute the location model of the SCS with time constraints, which indicates that the location goal of the shortest distance principle should be considered when seniors are in the scope of service and the service efficiency is high.

## 24.4 The Improved Particle Swarm Optimization

### 24.4.1 Traditional Particle Swarm Optimization

PSO was proposed by Eberhart and Kenndy [11] in 1995 based on the foraging behavior of birds. In the PSO algorithm, each individual is called a particle, representing a potential solution. In the search space, let all particles constitute a group. Each particle has two attributes of velocity and position. The particle iterates through the fitness function to find the optimal solution. In each iteration, the velocity and position information of particles are updated according to the following equation:

$$v_{id}^{k+1} = wv_{id}^k + c_1r_1(p_{id} - z_{id}^k) + c_2r_2(p_{gd} - z_{id}^k) \tag{24.4}$$

$$x_{id}^{k+1} = x_{id}^k + v_{id}^{k+1} \tag{24.5}$$

where,  $k$  is the number of iterations,  $c_1$  and  $c_2$  are the learning factor,  $r_1$  and  $r_2$  are a uniform random number in the range of  $[0,1]$ , and  $w$  is the inertia weight factor.

### 24.4.2 Improved Particle Swarm Optimization

In the iterative process, if one particle finds the optimal position, other particles will approach it. However, if the position is a local optimum, the whole PSO will fall into a state of local optimum. Aiming at the defects of premature convergence, slow search speed, and ease to fall into local optimum of PSO, this paper adds random weight and synchronous learning factor into PSO. The advantage of random weight is that when the starting position of particles is close to the best, it may produce a smaller weight, and it will not easily fall into the local optimal solution, so it can better balance the local and global search ability. The random weight method obeys the normal distribution, and the formula is defined as follows:

$$\begin{cases} w = \mu + \sigma * N(0, 1) \\ \mu = \mu_{\min} + (\mu_{\max} - \mu_{\min}) \text{rand}(0, 1) \end{cases} \quad (24.6)$$

The synchronous learning factor is to combine the self-cognitive and social-cognitive part of particles, so as to better reflect the group cooperation and knowledge sharing among particles. The equation of synchronous learning factor is defined as follows:

$$c_1 = c_2 = c_{\max} - (c_{\max} - c_{\min}) \frac{i}{k} \quad (24.7)$$

The pseudocode of the RPSO algorithm is shown in Table 24.1.

**Table 24.1** The pseudocode of the RPSO algorithm

Procedure of RPSO
For each particle i
Initialize velocity $V_i$ and position $X_i$ for particle i
Evaluate particle i and set $P_{best_i} = X_i$
End For
Gbest =min{Pbesti}
While not stop
For i=1 to $\Phi N$
Evaluate W and c1 c2
Update the velocity and position of particle i and Evaluate particle i
If fit( $X_i$ )<=fit(Pbesti)
Pbesti= $X_i$ ;
If fit(Pbesti)<=fit(Gbest)
Gbest=Pbesti;
End For
End While
Print Gbest
End procedure

### 24.5 Simulation Experiment

In the process of optimizing the location of SCS, to prove that the performance of RSPSO is better than other improved PSO, this section will carry out simulation research, using MATLAB R2019b. According to the simulation requirements, set up a two-dimensional space area with the size of 100 m × 100 m, mark out several locations with the largest number of the seniors. If the data is real world, we should calculate the number of SCS to be built by Eq. (24.1). This paper set  $N = 1$  under ideal conditions. Finally, determine the SCS location by RSPSO.

Firstly, according to the empirical value, the parameters of RSPSO are set in Table 2.

Secondly, the PSO with random weight (RPSO), the PSO with synchronous learning factor (SPSO), and the RSPSO are simulated, and the comparison of their convergence rates are shown in Fig. 24.1.

Finally, to ensure the effectiveness of the experiment, each algorithm uses the same parameters. Table 24.3 shows that RSPSO also can take the least time to find the best fitness value. In solving SCS optimization problem, RSPSO has better performance.

**Table 24.2** RSPSO parameter settings

Parameter	Value
Number of particle, $\Phi N(\Phi = 10, \Phi \text{ is integer})$	10
Maximum iterations, $T$	30
Number of dimensions	2
Maximum/minimum inertial weight	0.9/0.4
Maximum/minimum learning factor	2.0/0.8

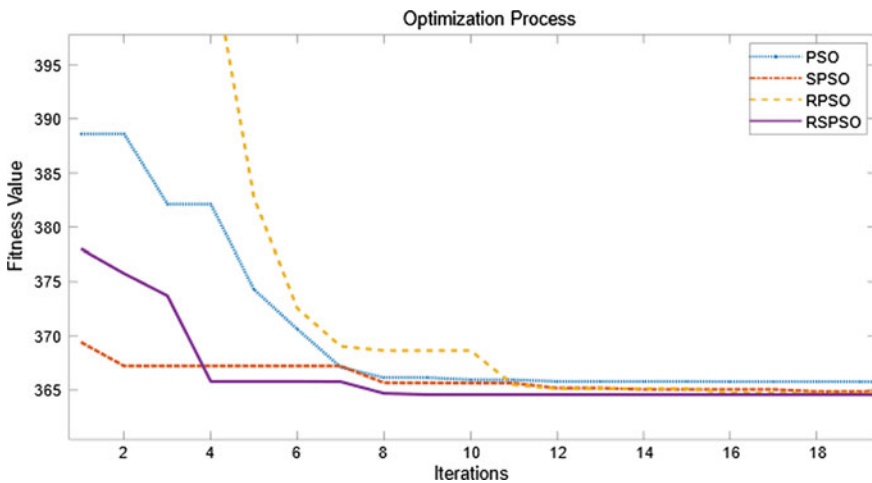


**Fig. 24.1** Convergence rate comparison



**Table 24.3** Experimental results

Algorithm	Rate of convergence	Fitness value	Optimal coordinate
PSO [11]	22	365.2	(50.2575, 58.2080)
RPSO [4]	21	364.6	(50.3740, 58.6431)
SPSO [5]	18	364.9	(50.5213, 58.7126)
RSPSO (ours)	9	364.6	(50.3655, 58.6435)

## 24.6 Conclusion

In this paper, based on an in-depth analysis on the location optimization problem of SCS, a mathematical model of SCS location is established, and then the RSPSO is proposed to effectively address the optimal issue of the SCS location. The simulation results show that the improvements on inertia weight and learning factor can effectively improve the stability of the algorithm. Therefore, it can improve the optimization accuracy of the location issue. Similar engineering issues can be addressed by changing some statements, and it is worthy of generalization to apply in other fields of location optimization. The paper achieve location optimization through single-swarm calculation. The future work will employ parallel technology to solve location optimization problems.

## References

1. Liu, Q.: United Nations releases multiple issues. Attention Paid to World Population Aging Problems **26**(05), 96 (2017). (Chinese)
2. Mou, F.Z.: Suggestions on the strategic design of the system and mechanism to deal with the aging population. *Int. J. Educ. Manage.* **5**(2), 28–30 (2020)
3. Ren, P.Y., Chen, L.R., Kong, J.S.: WSN node localization technology research based on improved PSO. In: Yang, G.H. (ed.) *Proceedings of 2014 IMSS International Conference on Future Mechatronics and Automation*, Vol. 1, pp. 101–105 (2014)
4. Hua, X., Hu, X., Yuan, W.: Research optimization on logistics distribution center location based on adaptive particle swarm algorithm. *Optik-Int. J. Light Electron. Opt.* **127**(20), 8443–8450 (2016)
5. Ji, M.J.: Study on location selection and optimization of logistics center based on particle swarm optimization. *Int. Core J. Eng.* **6**(9), 282–287 (2020)
6. Tang, H., Peng, S., Sun, J., Liu, X.: 3-D route planning of UAV based on SAPSO algorithm. *Tactical Missile Technol.* **2**, 62–68 (2017). (Chinese)
7. Wang, Y.H., Wang, S.M.: UAV path planning based on improved particle swarm optimization. *Comput. Eng. Sci.* **42**(09), 1690–1696 (2020). (Chinese)
8. Chai, Q.W., Chu, S.C., Pan, J.S.: A parallel WOA with two communication strategies applied in DV-Hop localization method. *Wirel. Com Netw.* **2020**, 50 (2020)
9. Song, P.C., Pan, J.S., Chu, S.C.: A parallel compact cuckoo search algorithm for three-dimensional path planning. *Appl. Soft Comput.* **94** (2020)

10. Jiang, B.Q., Pan, J.S.: A parallel quasi-affine transformation evolution algorithm for global optimization. *J. Netw. Intell.* **4**(2), 30–46 (2019)
11. Kennedy, J.: Particle swarm optimization. In: Sammut, C., Webb, I.G. (eds.) *Proceedings of 1995 IEEE International Conference on Neural Networks*, Vol. 4, pp. 1942–1948 (2011)

# Chapter 25

## IBPO: Solving 3D Strategy Game with the Intrinsic Reward



Huale Li, Rui Cao, Xiaohan Hou, Xuan Wang, Linlin Tang, Jiajia Zhang, and Shuhan Qi

**Abstract** In recent years, deep reinforcement learning achieves great success in many fields, especially in the field of games, such as AlphaGo, AlphaZero and AlphaStar. However, reward sparsity is still a problem in the 3D strategy games with a higher dimension of state space and more complex game scenarios. To solve this problem, in this paper, we propose an intrinsic-based policy optimization algorithm (IBPO) for reward sparsity. The IBPO incorporates the intrinsic reward into the traditional policy, which composed by the differential fusion mechanism and the modified value network. The experimental results show our method can obtain better performance than the previous methods on the VizDoom.

### 25.1 Introduction

Deep reinforcement learning (DRL) has achieved great success in the field of computer games in recent years [1, 2]. And many new testing platforms have emerged to verify the intelligence of the agent in complex strategy games, such as StarCraft and VizDoom. Since the strategy game contains rich game scenarios and a considerable game state space [3, 4], it becomes a kind of ideal platform to verify relevant DRL-based methods. In view of the great success achieved by the DRL in past years, researchers have investigated intensively on solving strategy games through the DRL methods in more complex games. In 2019, AlphaStar became the first agent that defeated a professional human player in StarCraft, which has been viewed as a milestone in the advancement of artificial intelligence [5].

---

H. Li · R. Cao · X. Hou · X. Wang · L. Tang · J. Zhang (✉) · S. Qi (✉)  
School of Computer Science and Technology,  
Harbin Institute of Technology, Shenzhen 518055, China  
e-mail: [zhangjiajia@hit.edu.cn](mailto:zhangjiajia@hit.edu.cn)

S. Qi  
e-mail: [shuhanqi@cs.hitsz.edu.cn](mailto:shuhanqi@cs.hitsz.edu.cn)

© The Author(s), under exclusive license to Springer Nature Singapore Pte Ltd. 2022  
T.-Y. Wu et al. (eds.), *Advances in Smart Vehicular Technology, Transportation, Communication and Applications*, Smart Innovation, Systems and Technologies 250,  
[https://doi.org/10.1007/978-981-16-4039-1\\_25](https://doi.org/10.1007/978-981-16-4039-1_25)

257

Although the DRL-based methods have made certain achievements in the research of solving the strategy games, there are still many problems that have to be solved. The DRL-methods highly rely on the reward to update the model during the training process. Reasonable and instant reward not only makes the training process converge quickly, but also makes the learned model more robust. In the game scenario where the reward is sparse, the speed of the convergence will be slow down seriously and even more, resulted in a divergent model finally. In the 3D strategy games with a higher dimension of state space and more complex game scenarios, the reward sparsity problem will become more severe. Although there is a clear reward (e.g., the score of the game) in such game scenarios, most of the final goal need to be achieved by defining a series of subgoals in the early stage. Most of subgoals may not get rewards in time unless they are finished. The reward sparsity problem will make the training process much more difficult and slower due to it cannot get a timely and effective reward. To solve this problem, many solutions such as reward reshaping, hierarchical DRL and curriculum learning are proposed in recent years [6–8]. However, in the process of practical application, these methods require carefully designed rewards for related problems or additional training data, which greatly limits the applicability of related methods. Therefore, these methods can not deal with the problem of sparse reward very well.

To deal with the problem of reward sparsity, this paper improves the traditional strategy optimization DRL methods by introducing intrinsic reward mechanism. We proposed an intrinsic-based policy optimization algorithm (IBPO), which improves the exploration performance of the agent in the 3D scene with the sparse reward. In this algorithm, the intrinsic reward is used to combined with the traditional strategy optimization. The experimental results tested on the VizDoom show our method has a better performance than the previous methods. We summarize our contributions as follows:

- We proposed a method, intrinsic-based policy optimization algorithm (IBPO), to study the reward sparsity problem in the 3D games with imperfect information.
- The IBPO effectively improves the exploration performance of the agent by combining the intrinsic reward and the traditional strategy optimization method.
- Extensive experimental results show that the performance of our method IBPO is significantly improved on VizDoom, compared with the previous methods.

## 25.2 The Proposed Method

In this section, we seek a method of training the agent that can address the reward sparsity in the 3D game with complex environment. Intrinsic-based policy optimization (IBPO) is proposed by introducing an intrinsic reward mechanism.

### 25.2.1 Intrinsic-Based Policy Optimization (IBPO)

Due to the sparse reward problem in 3D strategy games, it is very difficult for the agent to carry out policy iteration and update. To overcome this problem, in this paper, we introduce the concept of intrinsic rewards, which can provide auxiliary reward information for the agent to update its policy. That is to say, here, we employ an IIML (as shown in Fig. 25.1) model. In this model, there are not only external rewards from the environment, but also intrinsic rewards that are generated by a designed intrinsic reward generation module. In addition, to adopt the intrinsic reward into the traditional policy optimization framework, we propose an Intrinsic-Based Policy Optimization (IBPO) algorithm, in which the intrinsic reward generation module can be integrated with the policy optimization framework seamlessly.

**The Generation of Intrinsic Reward** We describe how the intrinsic reward is designed. As mentioned above, the IIML contains the external reward and the intrinsic reward. The external reward is feedback from the environment, which cannot be obtained sometimes. When the agent sinks into a situation of lacking external reward, the intrinsic reward plays a key role in helping the agent to continue to update its policy. Especially, in the 3D game, if an external reward is sparse, the agent will easily fall into the problem of lingering in a local region. Therefore, to avoid the local region problem, the agent should increase its curiosity to explore unseen scenes. Based on this consideration, this paper constructs the intrinsic reward by estimating the novelty degree of the state. The state novelty here indicates that if the state is the agent has never gone through. A certain degree given to the new state can be viewed as the intrinsic reward, and the agent has a chance to overcome the local region problem.

Based on the above assumption, here, we design the intrinsic reward generation module as follows. The intrinsic reward generation module is composed of a dual-network structure as shown in Fig. 25.1 a. In this structure, there is a target mapping network and a prediction network. Here, we set the target mapping network as a fixed

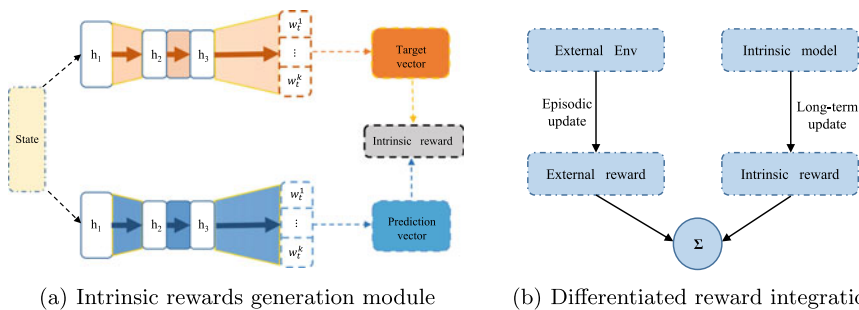


**Fig. 25.1** The structure of the IBPO (in the subfigure a, there are two channels: one is to output the target vector, the other is to output the prediction vector, which forms the intrinsic reward through the combination of them. The subfigure b is the reward integration of the two rewards)

network and the prediction network as a trainable network. Then, the intrinsic reward value is adopted as the similarity between the output vector of the target mapping network and prediction network. The input of these two networks is the current state of the game. That is to say, if the game state is novel, then the intrinsic reward will be a large value and vice versa. The main reason for this is to make the agent tend to explore unseen states in the environment. In the initial training phase, the agent has a smaller range of motion and there are more unfamiliar states in the game. In this case, the output vector of the two networks is less similar, thus the calculated intrinsic reward value is larger. When the action policy is updated, the agent takes intrinsic reward as the main source of the reward.

Here, we describe the detail of constructing the target mapping network and the prediction network. A three layers convolutional neural network is used to extract features from the input state and finally a vector represented with a fixed dimension is output. The same network structure is adopted to reduce the error effect of different network structures on computing the similarity of the vector. The loss function  $L_{IR}$  of the intrinsic reward generation module is defined as follows:

$$L_{IR} = \frac{1}{n} \sum_{i=1}^n (P - T)^2 + \lambda_{IR} \sum_{j=1}^k \|\theta_j\|^2 \quad (25.1)$$

where  $P$  and  $T$  are the output vector of the prediction vector and the target vector, respectively.  $\theta_j$  is the regularization term and  $\lambda_{IR}$  is the penalty factor of regular term.  $n$  and  $j$  is the time steps.

**Integrate the intrinsic reward into policy optimization** To train the intrinsic reward prediction network, adequate samples of the agent are necessary. Meanwhile, the agent's action in the environment is always driven by the policy optimization algorithm. In this way, it is a key to combine the intrinsic reward generation module with the policy gradient or policy optimization algorithm.

For traditional policy optimization algorithm, the update of the policy mainly depends on the external rewards generated via the interaction with the environment. Therefore, to deal with the external reward and the intrinsic reward is the key point of adapting the intrinsic reward mechanism to policy optimization algorithm. In this paper, we adopt a combination of long-term intrinsic reward and episodic external reward, as shown in Fig. 25.1b. The long-term reward can give the agent a goal. Meanwhile, it may lead to the reward sparse problem, which makes the strategy unable to converge or converge slow down. Therefore, the intrinsic reward is introduced through the continuous incentive agent to explore, which will continue to support the agent to achieve its goal.

## 25.3 Experimental Results

In this section, we first introduce the VizDoom. Secondly, implementation details are described. Finally, we conduct experiments to evaluate the performance of the IBPO.

### 25.3.1 Description of VizDoom

VizDoom is a first-person shooter game [3], which is a platform capable of training agents to explore 3D environments. In this paper, experiments were conducted based on VizDoom’s pathfinding and survival scenarios. **Pathfinding Scenario:** Rewards are sparse in the pathfinding scenario. The agent can only get the reward at the target, but not at any other location. The entire map is made up of several different opaque rooms with only one fixed target spot in a specific room. In this scenario, the agent can move freely but the starting position is far away from the target. The agent needs to pass through rooms with different contents to obtain rewards at the target spot. **Survival Scenario:** There are mazes in the survival scenario, which block the agent from seeing a wide range of scenes. Moreover, the agent may continue to lose the life value during movement in this scenario. Therefore, it acquires the agent to explore and motion as efficiently as possible in the maze; otherwise, the training round would end when the life value turns 0. Besides, drug packages can restore life value appear randomly in the scenes. The agent needs to collect as many drug packages as possible to survive longer.

### 25.3.2 Implementation Details

The network structure of the adjusted policy optimization is shown in Tab. 25.1. The NN1 includes the actor network and the critic network [9], both of which share part of the hidden layer neurons. The critic network designed in this paper has two independent reward output heads to offer independent supervision information to the external reward and the intrinsic reward [10].

The intrinsic reward generation model makes up for the lack of the external reward when updating. The model includes a target mapping network and a prediction network, both of which have the same network structure. In Table 25.1, NN2 states the network structure of the intrinsic reward generation model [11].

In addition, the development platform of this research is Linux server with Ubuntu 16.04-5.4.0 system; the CPU is Intel (R) Xeon (R) Silver 4110 CPU @ 2.10 GHz, with 32 virtual cores; the GPU is NVIDIA Tesla P100, with 16GB video memory; the development language is based on Python 3.6.3.

**Table 25.1** The network structure

NN1	Parameter	NN2	Parameter
conv	Conv(64,3,3)	conv	Conv(128,3,3)
conv	Conv(32,3,3)	conv	Conv(32,3,3)
active	Relu	active	BN
transform	Flatten	active	Relu
fc	Linear(288,256)	transform	Flatten
fc	Linear(256,256)	fc	Linear(288,256)
Actor	Linear(256,4),a		
Critic	Linear(256,1),r		
Critic	Linear(256,1),r		

### 25.3.3 The Performance of the IBPO

The IBPO is tested in the pathfinding scenario. The agent starts to explore the entire scene from the starting position and cannot complete the task until it reaches the target position in the pathfinding scenario. This scenario is an extremely challenging training map in the Vizdoom platform because there is only an external reward signal at the target. Another issue is that random agents have difficulty reaching the target position with limited action steps. Consequently, we test the IBPO algorithm in the pathfinding scenario.

In the pathfinding scenario, the evaluation indicators are the average reward value and average action steps. The average reward value is defined as the ratio of the number of the agent that reached the target position within the specified steps to the number of all trained agents currently, indicating the pathfinding success rate of the agents. The average action step is defined as the average number of action steps for 100 verifiable interactions between the environment and the agent after the algorithm converges, which indicates the stability of the agent’s action policy.

We train different RL agents with IBPO, DRQN [12], and DFP [13], respectively, in the pathfinding scenario to prove the effectiveness of the IBPO by comparing their evaluation indicators. The experiments verify the intrinsic reward can give agents assistance in updating policy effectively without the environmental reward feedback. The DFP and the DRQN are the methods used by the second and third-place agents in the 2017 VizDoom competition. In this competition, there is a map similar to the pathfinding scenario. The DRQN utilizes the game information provided by the simulator. The DFP owns supplementary processing modules for the state and the reward information. These two algorithms are dominant in the pathfinding scenario. Figure 25.2 illustrates the performance curves using the IBPO, DFP, DRQN in the pathfinding scenario.

We can find that the IBPO reached an average reward value of 0.92, which outperforms the DRQN and the DFP, whose average reward values are 0.79 and 0.86, respectively. The closer the average reward value is to 1, the more effective the pol-



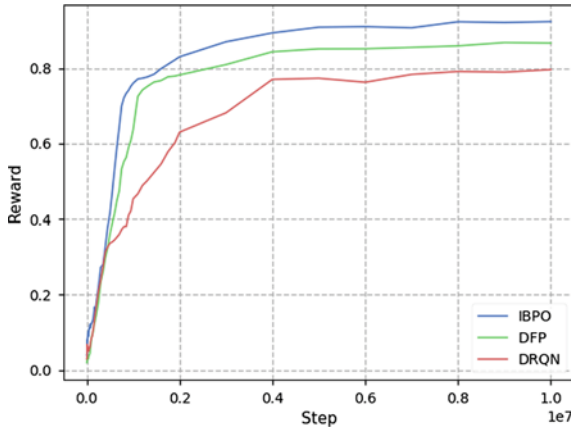


**Fig. 25.2** Experimental results of the IBPO in the pathfinding scenario (The y-axis represents the average reward value obtained by the DRL agents in the pathfinding scenario, and the x-axis represents the timestep during training. The greater the reward, the better the method.)

**Table 25.2** Experimental results of the IBPO (the bold is the best)

Evaluation criteria	IBPO	DFP	DRQN
Average reward value	<b>0.92</b>	0.86	0.79
Average action steps	<b>61.8</b>	69.3	75.7

icy learned by the method is and the more likely the agent will reach the expected position. The main reason for this result is the deficiency of environmental rewards in the pathfinding scenario. The intrinsic rewards in the IBPO make up for the lack of positive reward values in experience replay memory, thus promoting the learning of exploration policy. The above comparative experiments demonstrate that the DRL agent trained by the IBPO has plentiful and efficient performance in exploring the 3D pathfinding scenarios.

Table 25.2 summarizes the average reward value and average action step in the pathfinding experiments. The first row corresponds to the reward in Fig. 25.2, and the second row shows action steps required by different agents to reach the target position. We can find that the IBPO performs the best among the three methods with a minimum average action steps 61.8. It indicates the agent trained by the IBPO can find the path to the target faster with a more steady action policy.

To sum up, the value generated by the intrinsic reward module provide auxiliary signals for the agent’s policy update, which helps the agent to learn effective exploration policy in sparse reward scenarios. Through comparative experiments with the DRQN and the DFP, we conclude that the IBPO outperforms these two methods in the average reward value and average action step indicators.

## 25.4 Conclusions

We have presented a novel approach, named IBPO, for the reward sparsity problem in 3D games. Unlike existing DRL-based methods, an agent of our approach can learn the intrinsic reward, which uses the differential fusion mechanism and the modified value network. The experimental results based on the VizDoom platform show the effectiveness of the proposed approach.

**Acknowledgements** This research was funded by National Natural Science Foundation of China (No. 61902093), Natural Science Foundation of Guangdong (No. 2020A1515010652), Shenzhen Foundational Research Funding Under Grant (No. 20200805173048001), key fields R&D project of Guangdong Province, Research and Application of Imperfect information Game Key Technology Driven by Super AI Computing Power (No. 2020B0101380001), PINGAN-HITsz Intelligence Finance Research Center, Ricoh-HITsz Joint Research CenterGBaseHITsz Joint Research Center.

## References

1. Mnih, V., Kavukcuoglu, K., Silver, D., Rusu, A.A., Veness, J., Bellemare, M.G., Graves, A., Riedmiller, M., Fidjeland, A.K., Ostrovski, G., et al.: Human-level control through deep reinforcement learning. *Nature* **518**(7540), 529 (2015)
2. Silver, D., Schrittwieser, J., Simonyan, K., Antonoglou, I., Huang, A., Guez, A., Hubert, T., Baker, L., Lai, M., Bolton, A., et al.: Mastering the game of go without human knowledge. *Nature* **550**(7676), 354 (2017)
3. Kempka, M., Wydmuch, M., Runc, G., Toczek, J., Jaśkowski, W.: Vizdoom: a doom-based ai research platform for visual reinforcement learning. In: Proceedings of the 2016 IEEE Conference on Computational Intelligence and Games, pp. 1–8. IEEE (2016)
4. Shao, K., Zhu, Y., Zhao, D.: Starcraft micromanagement with reinforcement learning and curriculum transfer learning. *IEEE Trans. Emerg. Topics Comput. Intell.* **3**(1), 73–84 (2018)
5. Vinyals, O., Babuschkin, I., Chung, J., M.: Grandmaster level in starcraft II using multi-agent reinforcement learning. *Nature* **575**(7782), 350–354 (2019)
6. Kulkarni, T.D., Narasimhan, K., Saeedi, A., Tenenbaum, J.: Hierarchical deep reinforcement learning: integrating temporal abstraction and intrinsic motivation. In: Proceedings of the Advances in Neural Information Processing Systems, pp. 3675–3683 (2016)
7. Song, S., Weng, J., Su, H., Yan, D., Zou, H., Zhu, J.: Playing fps games with environment-aware hierarchical reinforcement learning. In: Proceedings of the 28th International Joint Conference on Artificial Intelligence, pp. 3475–3482. AAAI Press (2019)
8. Pathak, D., Agrawal, P., Efros, A.A., Darrell, T.: Curiosity-driven exploration by self-supervised prediction. In: Proceedings of the International Conference on Machine Learning, pp. 2778–2787 (2017)
9. Mnih, V., Badia, A.P., Mirza, M., Graves, A., Lillicrap, T., Harley, T., Silver, D., Kavukcuoglu, K.: Asynchronous methods for deep reinforcement learning. In: Proceedings of the International Conference on Machine Learning, pp. 1928–1937 (2016)
10. Zhang, S., Su, X., Jiang, X., Chen, M., Wu, T.: A traffic prediction method of bicycle-sharing based on long and short term memory network. *J. Network Intell.* **4**(2), 17–29 (2019)
11. Wang, Y., Wang, J., Deng, C., Zhu, H., Wang, S.: L1–L2 norms based target representation for visual tracking. *J. Network Intell.* **3**(2), 102–112 (2018)
12. Lample, G., Chaplot, D.S.: Playing fps games with deep reinforcement learning. In: Proceedings of the 31st AAAI Conference on Artificial Intelligence, pp. 2140–2146 (2017)
13. Dosovitskiy, A., Koltun, V.: Learning to act by predicting the future. In: Proceedings of the International Conference on Learning Representations, pp. 637–645 (2017)

# Chapter 26

## An Operation with Crossover and Mutation of MPSO Algorithm



Yuxin Zhong, Yuxin Chen, Chen Yang, and Zhenyu Meng

**Abstract** As an efficient and simple optimization algorithm, particle swarm optimization (PSO) has been widely applied to solve various real optimization problems in expert systems. However, avoiding premature convergence and balancing the global exploration and local exploitation capabilities of the PSO remains an open issue. To overcome these drawbacks and strengthen the ability of PSO in solving complex optimization problems, a modified PSO using adaptive strategy called MPSO is proposed, although MPSO has achieved excellent performance, and its convergence and stability are still some defects. In this paper, we presented a new variant of MPSO algorithm which can explore the search space deeper than the previous method, and better performance can be achieved under CEC2013 test suite.

### 26.1 Introduction

Global optimization has been widely used in real word. By mimicking a flock of birds' foraging behavior, particle swarm optimization (PSO) algorithm was first proposed by Kennedy and Eberhart in 1995 [1], PSO is a simple but promising evolutionary technique. Since its inception, PSO has attracted great interest from researchers [2], the performance of PSO has been improved significantly in the past two decades, but there are still a few challenges [3]. So many variants of PSO have been proposed to improve the performance of PSO [4]. Shi and Eberhart first proposed inertial weights-iwPSO [5]. Liang et al. proposed the comprehensive learning particle swarm optimizer—CLPSO [6, 7]. Nasir et al. proposed a dynamic neighbor learning based PSO for global numerical optimization—DNLPSO [8]. Moreover, Cheng et al. proposed self-learning particle swarm optimization algorithm for scalable optimization—SLPSO [9, 10]. Dr Nandar Lynn proposed a new PSO variant

---

Y. Zhong (✉) · Y. Chen · C. Yang · Z. Meng

Fujian Provincial Key Lab of Big Data Mining and Applications, Fujian University of Technology, Fuzhou, China

© The Author(s), under exclusive license to Springer Nature Singapore Pte Ltd. 2022  
T.-Y. Wu et al. (eds.), *Advances in Smart Vehicular Technology, Transportation, Communication and Applications*, Smart Innovation, Systems and Technologies 250,  
[https://doi.org/10.1007/978-981-16-4039-1\\_26](https://doi.org/10.1007/978-981-16-4039-1_26)

265

which is called ensemble particle swarm optimizer—EPSO [11]. Hao et al. proposed a modified particle swarm optimization using adaptive strategy—MPSO [12], the particles are mainly updated based on the use of chaotic nonlinear inertial weights, in additions, an adaptive position updating strategy and terminal replacement mechanism is adopted to enhance the ability of PSO to solve complex optimization problems in expert systems. Although these PSO variants can achieve some goal optima, PSO still has a lot of space to improved [13]. Inspired by MPSO, in this paper, we proposed a new PSO variants to enhance MPSO performance.

The remainder of this paper is organized as follows. In Section 26.2, swarm-based evolutionary algorithms are briefly introduced. In Section 26.3, we presents a detailed description of the new variant of PSO. In Section 26.4, we present the comparison with other algorithm. Finally, conclusion is described in Sect. 26.5.

## 26.2 Swarm Based Evolutionary Algorithms

In this section, the canonical PSO algorithm and several famous PSO variants are reviewed. A detailed description is mainly focused on several PSO variants, in current generation  $G$ , the following two vectors are related to the  $i$ th particle ( $i=1,2,\dots,ps$ ). In a  $D$ -dimensional hyperspace, one is the velocity vector  $V_{i,G} = (v_i^1, v_i^2, \dots, v_i^d, \dots, v_i^D)_G$ , and the other is the position vector  $X_{i,G} = (x_i^1, x_i^2, \dots, x_i^d, \dots, x_i^D)_G$ , where  $d \in [1, D]$ , during movement each particle modifies its position according to its own best position ( $X_{pbest}$ ), as well as the global best location of the population denotes ( $X_{gbest}$ ).

### 26.2.1 Original PSO

In PSO, the initial population generate by random solutions, and a randomized velocity is attach to each potential solution of the population, then the potential solution flow through the search space. Equation 26.1 illustrate how the velocity and position update.

$$\begin{cases} V_{i,G} = V_{i,G} + c_1 \cdot r_1 \cdot (X_{pbest_{i,G}} - X_{i,G}) + c_2 \cdot r_2 \cdot (X_{gbest_G} - X_{i,G}) \\ X_{i,G} = X_{i,G} + V_{i,G} \end{cases} \quad (26.1)$$

where  $c_1$  and  $c_2$  are called the acceleration coefficients.  $r_1$  and  $r_2$  is one uniformly distributed random numbers in range  $[0,1]$ .

### 26.2.2 CLPSO

To overcome the premature convergence problem, CLPSO is proposed. In CLPSO, it is mainly to change the particle update structure. The neighbor particle' personal best position is employed to enhance exploration, different dimensions of one particle may learn from different neighbor particles. The velocity of CLPSO is updated according to Eq. 26.2:

$$\begin{cases} V_{i,G} = \omega \cdot V_{i,G} + c \cdot r_{i,G} \cdot (X_{\text{pbest}_{f_i,G}} - X_{i,G}) \\ V_{i,G} = \min(V_{\text{max},G}, \max(V_{i,G}, V_{\text{min},G})) \\ X_{i,G} = X_{i,G} + V_{i,G} \end{cases} \quad (26.2)$$

It is possible the  $f_i = i$ . An inertia weight determination strategy was introduced in which the value of  $\omega$ :

$$\omega = \omega_{\text{max}} - \frac{\text{gen}}{\text{gen}_{\text{max}}} (\omega_{\text{max}} - \omega_{\text{min}}). \quad (26.3)$$

### 26.2.3 DNLPSO

To improve the disadvantages that CLPSO cannot always offer a better value in every dimension, so DNLPSO is proposed. The learning mechanisms in the DNLPSO is shown in Eq. 26.4:

$$\begin{cases} V_{i,G} = \omega \cdot V_{i,G} + c_1 \cdot r_1 \cdot (X_{\text{pbest}_{f_i,G}} - X_{i,G}) + c_2 \cdot r_2 \cdot (X_{\text{gbest}_G} - X_{i,G}) \\ X_{i,G} = X_{i,G} + V_{i,G} \end{cases} \quad (26.4)$$

### 26.2.4 SLPSO

In order to address the problems for PSO, Cheng et al. proposed SLPSO[?][?]. The key step in SLPSO changes the particle update structure. The main process of SLPSO is described as follows in Eq. 26.5–26.7:

$$X_{i,j}^{t+1} = \begin{cases} X_{i,G} + \Delta X_{i,G}, & \text{if } P_{i,G} \leq P_{i,L} \\ X_{i,G} & \text{otherwise} \end{cases} \quad (26.5)$$

$$\Delta X_{i,G} = r_{1,G} \cdot \Delta X_{i,G} + r_{2,G} \cdot I_{i,G} + r_{3,G} \cdot \epsilon \cdot C_{i,G} \quad (26.6)$$

$$\begin{cases} I_{i,G} = X_{k,G} - X_{i,G} \\ C_{i,G} = \bar{X}_G - X_{i,G} \end{cases} \quad (26.7)$$

where a particle learns from a better  $X_k (i \leq k \leq ps)$ ,  $\Delta X_{i,G}$  is the behavior correction.  $r_1, r_2$  and  $r_3$  are random of  $[0,1]$ .  $\epsilon$  is the society influence factor calculated,  $\beta$  is a predefined parameter, and it defines a learning probability  $P_{i,L}$  for each particle, also  $P_{i,G}$  is a randomly generated probability.

### 26.2.5 MPSO

In MPSO, in order to avoid the premature convergence phenomenon of PSO and improve its performance on complex problems, not only the parameters of the weighting factor are modified, but the update structure of the particles is also adjusted. In MPSO, mainly four major step: (1) Stochastic and mainstream learning strategies are devised to replace the self and global learning strategies, and an adaptive position updating strategies is introduced to further balance the exploration and exploitation process:

$$V_{i,G} = \omega(i) \cdot V_{i,G} + r_1 \cdot c_1 \otimes (X_{lbest_{i,G}} - X_{i,G}) + r_2 \cdot c_2 \otimes (X_{Mbest,G} - X_{i,G}) \tag{26.8}$$

$$X_{i,G} = \begin{cases} \omega(t) \cdot X_{i,G} + (1 - \omega(i)) \cdot V_{i,G} + X_{gbest,G} & p_i > \text{rand} \\ X_{i,G} + V_{i,G} & \text{otherwise} \end{cases} \tag{26.9}$$

where  $X_{lbest}$  is mean the final stochastic personal best,  $X_{Mbest}$  is defined as the mean of the  $X_{pbest}$  of all particles, and  $\otimes$  denotes the element-wise product of two vectors. (2) A novel terminal replacement mechanism is introduced to enhance the performance of MPSO.

Although these PSO variants were famous and powerful in optimization competition, especially the MPSO, but the inborn weakness in PSO still existed in these variants. So how to choose an appropriate speed update strategy and parameters are still important problems to improve MPSO algorithm.

## 26.3 The Proposed CM-MPSO Algorithm

In this section, we propose a new version of MPSO algorithm. In this algorithm, the mutation operator is introduced, and not only the updating strategy of speed and position is adjusted, but also the crossover algorithm is added to the adaptive position strategy of MPSO algorithm. The evolution operations of the proposed algorithm can be introduced as follows:

1. The main parameters include  $ps, c_1$  and  $c_2$  (equal to 1.49445 and 2),  $bc$ (mutation parameters equal to 0.5),  $D, V_{max}, V_{min}, ps, c_{max}, nfe, nfe_{max}, X_{max}, X_{min}, \omega_{min}, \omega_{min}, gen, nfe, nfe_{max}, f$ ;
2. When  $Nfe < G_h * \max\_Nfe$ :

- The initialized particle is mutated;
- Before the mutation operation, the fitness value of the current particle was sorted, the particles ranked in the bottom half of the fitness value were updated by SLPSO operation, and the speed and position of the particles ranked in the top half of the fitness value were updated by MPSO. The concept of neighborhood topology structure was introduced into the speed update formula, and the specific speed update formula is:

$$V_{i,G} = V_{\text{MPSO}} + c_1 \cdot r_1 \cdot (\text{FIP} - X_{i,G}) \quad (26.10)$$

where  $V_{\text{MPSO}}$  representative Formula (26.8).

- For the terminal replacement mechanism of MPSO, the crossover operator is introduced into the terminal replacement mechanism, where the crossover probability is 0.9, and its specific formula is as follows:

$$X_{i,G} = X_{\text{gbest},G} + 0.5 \cdot r_1 \cdot X_{\text{pbest}_{r_1,G}} - X_{\text{pbest}_{r_2,G}} \quad (26.11)$$

end When.

3. Remaining operations are same as MPSO.

## 26.4 Experiment Analysis

All experimental results have been conducted on PC with an Intel(R) Core(TM) i5-8265U 1.8GHz CPU and Microsoft Windows 10 Enterprise SPA 64-bit operating system. In order to test CM-MPSO algorithm performance and compare with other PSO variants, set the algorithm to carry out 51 independent runs for all test functions. The comparison results under our test suite on 10D optimization and 30D optimization. In Tables 26.1 and 26.2,  $w/d/l$  represent the sums of the comparison results ( $>$ ,  $\approx$ ,  $<$ ) on all the benchmarks under sign test [14]. From the comparison results, we can see that: (1) our CM-MPSO algorithm obtains 19 performance improvements in comparison with PSO; it also obtains 14 performance improvements and 1 similar results in comparison CLPSO; obtains 24 performance improvements in comparison with DNLPSO; obtains 13 performance improvements and 2 similar results in comparison SLPSO; obtains 13 performance improvements and 3 similar results in comparison MPSO on 10-D optimization under benchmark  $f_{a_1} - f_{a_{28}}$ . (2) our CM-MPSO algorithm obtains 25 performance improvements in comparison with PSO; it also obtains 19 performance improvements and 1 similar results in comparison CLPSO; obtains 22 performance improvements in comparison with DNLPSO; obtains 13 performance improvements and 2 similar results in comparison SLPSO; obtains 17 performance improvements in comparison MPSO on 30-D optimization

Table 26.1 Comparisons results of the proposed algorithm and several famous variants under  $f_{a_1} - f_{a_{28}}$  in CEC2013

ID	PSO		CLPSO		DNLPSO		SLPSO		MPSO		Proposed algorithm	
	Mean/Std.	Mean/Std.	Mean/Std.	Mean/Std.	Mean/Std.	Mean/Std.	Mean/Std.	Mean/Std.	Mean/Std.	Mean/Std.	Mean/Std.	
$f_{a_1}$	1.291E-03/3.213E-03(<)	0/0(≈)	3.522E+02/8.091E+01(<)	0/0(≈)	3.522E+02/8.091E+01(<)	0/0(≈)	0/0(≈)	0/0(≈)	0/0(≈)	0/0(≈)	0/0	0/0
$f_{a_2}$	1.410E+05/2.120E+05(<)	1.330E+06/1.330E+06(<)	2.263E+06/1.855E+05(<)	1.312E+05/1.176E+05(>)	2.263E+06/1.855E+05(<)	1.312E+05/1.176E+05(>)	6.574E+04/8.175E+04(>)	6.574E+04/8.175E+04(>)	6.574E+04/8.175E+04(>)	6.574E+04/8.175E+04(>)	1.752E+05/1.741E+05	1.752E+05/1.741E+05
$f_{a_3}$	3.828E+08/8.523E+08(<)	2.298E+07/2.298E+07(<)	3.552E+08/1.695E+08(<)	3.052E+05/1.256E+06(<)	3.552E+08/1.695E+08(<)	3.052E+05/1.256E+06(<)	7.989E+03/6.255E+03(<)	3.140E+03/1.089E+03(>)	3.140E+03/1.089E+03(>)	3.140E+03/1.089E+03(>)	6.087E+04/2.476E+05	6.087E+04/2.476E+05
$f_{a_4}$	8.548E+02/1.484E+03(>)	9.722E+03/9.722E+03(<)	2.505E+03/8.933E+02(>)	2.505E+03/8.933E+02(>)	2.505E+03/8.933E+02(>)	2.505E+03/8.933E+02(>)	4.458E-15/2.229E-14(<)	3.877E-12/1.346E-11(<)	3.877E-12/1.346E-11(<)	3.877E-12/1.346E-11(<)	5.552E+03/2.424E+03	5.552E+03/2.424E+03
$f_{a_5}$	2.088E+00/4.378E+00(<)	1.921E-11/1.107E-11(<)	5.584E+01/1.263E+01(<)	4.458E-15/2.229E-14(<)	5.584E+01/1.263E+01(<)	4.458E-15/2.229E-14(<)	2.175E+00/0.822E-01(>)	6.387E+00/4.696E+00(>)	6.387E+00/4.696E+00(>)	6.387E+00/4.696E+00(>)	7.764E+00/7.957E+00	7.764E+00/7.957E+00
$f_{a_6}$	1.607E+01/2.228E+01(<)	3.572E+00/2.010E+00(>)	4.269E+01/1.519E+01(<)	4.269E+01/1.519E+01(<)	4.269E+01/1.519E+01(<)	4.269E+01/1.519E+01(<)	4.255E-02/9.680E-02(>)	2.037E+00/2.155E+00(<)	2.037E+00/2.155E+00(<)	2.037E+00/2.155E+00(<)	4.380E-01/1.509E+00	4.380E-01/1.509E+00
$f_{a_7}$	4.843E+01/2.226E+01(<)	2.153E+01/6.369E+00(<)	2.994E+01/1.010E+01(<)	2.994E+01/1.010E+01(<)	2.994E+01/1.010E+01(<)	2.994E+01/1.010E+01(<)	2.037E+01/7.253E-02(<)	8.719E+00/2.008E+00(<)	8.719E+00/2.008E+00(<)	8.719E+00/2.008E+00(<)	3.256E+00/1.410E+00	3.256E+00/1.410E+00
$f_{a_8}$	2.032E+01/8.757E-02(>)	2.036E+01/6.993E-02(<)	6.044E+00/1.524E+00(<)	4.897E+00/6.785E-01(<)	2.032E+01/8.757E-02(>)	2.036E+01/6.993E-02(<)	6.471E+00/1.142E+00(<)	8.719E+00/2.008E+00(<)	8.719E+00/2.008E+00(<)	8.719E+00/2.008E+00(<)	3.256E+00/1.410E+00	3.256E+00/1.410E+00
$f_{a_9}$	6.044E+00/1.524E+00(<)	4.897E+00/6.785E-01(<)	1.537E+00/3.132E-01(<)	3.748E+01/1.171E+01(<)	6.044E+00/1.524E+00(<)	4.897E+00/6.785E-01(<)	3.748E+01/1.171E+01(<)	2.202E-01/1.925E-01(>)	2.202E-01/1.925E-01(>)	2.202E-01/1.925E-01(>)	4.671E-01/4.113E-01	4.671E-01/4.113E-01
$f_{a_{10}}$	2.881E+00/3.192E+00(<)	1.101E-07/1.780E-07(>)	4.812E+01/6.249E+00(<)	4.812E+01/6.249E+00(<)	2.881E+00/3.192E+00(<)	1.101E-07/1.780E-07(>)	4.812E+01/6.249E+00(<)	2.653E+00/1.315E+00(>)	2.653E+00/1.315E+00(>)	2.653E+00/1.315E+00(>)	1.064E+01/6.014E+00	1.064E+01/6.014E+00
$f_{a_{11}}$	2.486E+01/1.144E+01(<)	1.682E+01/3.114E+00(<)	3.227E+01/1.535E+01(<)	1.682E+01/3.114E+00(<)	2.486E+01/1.144E+01(<)	1.682E+01/3.114E+00(<)	4.846E+01/5.871E+00(<)	9.409E+00/1.827E+00(>)	9.409E+00/1.827E+00(>)	9.409E+00/1.827E+00(>)	1.661E+01/8.837E+00	1.661E+01/8.837E+00
$f_{a_{12}}$	3.227E+01/1.535E+01(<)	1.682E+01/3.114E+00(<)	4.963E+01/1.385E+01(<)	1.841E+01/4.992E+00(<)	3.227E+01/1.535E+01(<)	1.682E+01/3.114E+00(<)	4.963E+01/1.385E+01(<)	9.908E+00/4.453E+00(>)	9.908E+00/4.453E+00(>)	9.908E+00/4.453E+00(>)	1.790E+01/7.656E+00	1.790E+01/7.656E+00
$f_{a_{13}}$	4.963E+01/1.385E+01(<)	1.841E+01/4.992E+00(<)	7.663E+02/2.711E+02(>)	9.013E+00/4.815E+00(>)	4.963E+01/1.385E+01(<)	1.841E+01/4.992E+00(<)	7.663E+02/2.711E+02(>)	2.395E+02/3.436E+02(<)	2.395E+02/3.436E+02(<)	2.395E+02/3.436E+02(<)	1.380E+03/2.264E+02(<)	1.380E+03/2.264E+02(<)
$f_{a_{14}}$	7.663E+02/2.711E+02(>)	9.013E+00/4.815E+00(>)	9.567E+02/2.605E+02(>)	1.381E+03/1.393E+02(=)	7.663E+02/2.711E+02(>)	9.013E+00/4.815E+00(>)	9.567E+02/2.605E+02(>)	1.384E+03/2.350E+02(<)	1.384E+03/2.350E+02(<)	1.384E+03/2.350E+02(<)	1.231E+03/1.674E+02(>)	1.231E+03/1.674E+02(>)
$f_{a_{15}}$	9.567E+02/2.605E+02(>)	1.381E+03/1.393E+02(=)	5.280E-01/1.872E-01(>)	1.282E+00/2.323E-01(<)	9.567E+02/2.605E+02(>)	1.381E+03/1.393E+02(=)	5.280E-01/1.872E-01(>)	1.186E+00/2.294E-01(>)	1.186E+00/2.294E-01(>)	1.186E+00/2.294E-01(>)	1.170E+00/2.068E-01(>)	1.170E+00/2.068E-01(>)
$f_{a_{16}}$	5.280E-01/1.872E-01(>)	1.282E+00/2.323E-01(<)	3.939E+01/1.273E+01(<)	1.192E+01/5.035E-01(>)	5.280E-01/1.872E-01(>)	1.282E+00/2.323E-01(<)	3.939E+01/1.273E+01(<)	2.183E+01/3.681E+00(>)	2.183E+01/3.681E+00(>)	2.183E+01/3.681E+00(>)	3.042E+01/5.782E+00(>)	3.042E+01/5.782E+00(>)
$f_{a_{17}}$	3.939E+01/1.273E+01(<)	1.192E+01/5.035E-01(>)	4.001E+01/1.396E+01(<)	3.837E+01/4.563E+00(>)	3.939E+01/1.273E+01(<)	1.192E+01/5.035E-01(>)	4.001E+01/1.396E+01(<)	2.960E+01/3.239E+00(>)	2.960E+01/3.239E+00(>)	2.960E+01/3.239E+00(>)	3.851E+01/3.881E+00(>)	3.851E+01/3.881E+00(>)
$f_{a_{18}}$	4.001E+01/1.396E+01(<)	3.837E+01/4.563E+00(>)	1.716E+00/8.275E-01(>)	3.600E-01/1.346E-01(>)	4.001E+01/1.396E+01(<)	3.837E+01/4.563E+00(>)	1.716E+00/8.275E-01(>)	1.886E+00/2.058E-01(>)	1.886E+00/2.058E-01(>)	1.886E+00/2.058E-01(>)	2.214E+00/7.096E-01	2.214E+00/7.096E-01
$f_{a_{19}}$	1.716E+00/8.275E-01(>)	3.600E-01/1.346E-01(>)	3.401E+00/5.354E-01(>)	3.618E+00/2.010E-01(<)	1.716E+00/8.275E-01(>)	3.600E-01/1.346E-01(>)	3.401E+00/5.354E-01(>)	3.540E+00/2.943E-01(<)	3.540E+00/2.943E-01(<)	3.540E+00/2.943E-01(<)	3.517E+00/2.394E-01	3.517E+00/2.394E-01
$f_{a_{20}}$	3.401E+00/5.354E-01(>)	3.618E+00/2.010E-01(<)	4.067E+02/6.194E+01(>)	2.238E+02/6.256E+01(>)	3.401E+00/5.354E-01(>)	3.618E+00/2.010E-01(<)	4.067E+02/6.194E+01(>)	4.002E+02/0.000E+00(<)	4.002E+02/0.000E+00(<)	4.002E+02/0.000E+00(<)	3.963E+02/2.803E+01(≈)	3.963E+02/2.803E+01(≈)
$f_{a_{21}}$	4.067E+02/6.194E+01(>)	2.238E+02/6.256E+01(>)	9.845E+02/2.706E+02(>)	1.236E+02/3.478E+01(<)	4.067E+02/6.194E+01(>)	2.238E+02/6.256E+01(>)	9.845E+02/2.706E+02(>)	1.691E+02/2.962E+02(<)	1.691E+02/2.962E+02(<)	1.691E+02/2.962E+02(<)	1.325E+03/2.726E+02(<)	1.325E+03/2.726E+02(<)
$f_{a_{22}}$	9.845E+02/2.706E+02(>)	1.236E+02/3.478E+01(<)	1.256E+03/3.410E+02(>)	1.178E+03/3.110E+02(>)	9.845E+02/2.706E+02(>)	1.236E+02/3.478E+01(<)	1.256E+03/3.410E+02(>)	1.128E+03/2.705E+02(>)	1.128E+03/2.705E+02(>)	1.128E+03/2.705E+02(>)	1.056E+03/2.933E+02	1.056E+03/2.933E+02
$f_{a_{23}}$	1.256E+03/3.410E+02(>)	1.178E+03/3.110E+02(>)	2.191E+02/4.242E+00(<)	1.500E+02/9.762E+00(>)	1.256E+03/3.410E+02(>)	1.178E+03/3.110E+02(>)	2.191E+02/4.242E+00(<)	2.226E+02/1.332E+00(<)	2.226E+02/1.332E+00(<)	2.226E+02/1.332E+00(<)	2.036E+02/6.699E+00(<)	2.036E+02/6.699E+00(<)
$f_{a_{24}}$	2.191E+02/4.242E+00(<)	1.500E+02/9.762E+00(>)	2.173E+02/1.508E+01(<)	1.729E+02/1.968E+01(>)	2.173E+02/1.508E+01(<)	1.500E+02/9.762E+00(>)	2.173E+02/1.508E+01(<)	2.222E+02/1.934E+00(<)	2.222E+02/1.934E+00(<)	2.222E+02/1.934E+00(<)	2.029E+02/3.990E+00(<)	2.029E+02/3.990E+00(<)
$f_{a_{25}}$	2.173E+02/1.508E+01(<)	1.729E+02/1.968E+01(>)	2.295E+02/2.114E+01(<)	1.358E+02/2.406E+00(>)	2.295E+02/2.114E+01(<)	1.358E+02/2.406E+00(>)	2.295E+02/2.114E+01(<)	2.033E+02/2.301E+01(<)	2.033E+02/2.301E+01(<)	2.033E+02/2.301E+01(<)	1.619E+02/6.466E+01(<)	1.619E+02/6.466E+01(<)
$f_{a_{26}}$	2.295E+02/2.114E+01(<)	1.358E+02/2.406E+00(>)	5.215E+02/7.292E+01(<)	3.841E+02/2.037E+01(<)	2.295E+02/2.114E+01(<)	1.358E+02/2.406E+00(>)	5.215E+02/7.292E+01(<)	5.218E+02/2.760E+01(<)	5.218E+02/2.760E+01(<)	5.218E+02/2.760E+01(<)	3.443E+02/5.934E+01(<)	3.443E+02/5.934E+01(<)
$f_{a_{27}}$	5.215E+02/7.292E+01(<)	3.841E+02/2.037E+01(<)	4.863E+02/2.093E+02(<)	2.224E+02/5.184E+01(>)	4.863E+02/2.093E+02(<)	2.224E+02/5.184E+01(>)	4.863E+02/2.093E+02(<)	3.000E+02/0.000E+00(<)	3.000E+02/0.000E+00(<)	3.000E+02/0.000E+00(<)	3.828E+02/1.497E+02(<)	3.828E+02/1.497E+02(<)
$f_{a_{28}}$	4.863E+02/2.093E+02(<)	2.224E+02/5.184E+01(>)	9/0/19	13/1/14	4.863E+02/2.093E+02(<)	2.224E+02/5.184E+01(>)	9/0/19	13/2/13	13/2/13	13/2/13	12/3/13	12/3/13
w/d/l	9/0/19	13/1/14	4/0/24	13/2/13	9/0/19	13/1/14	4/0/24	13/2/13	13/2/13	13/2/13	12/3/13	12/3/13



**Table 26.2** Comparisons results of the proposed algorithm and several famous variants under  $f_{a1} - f_{a28}$  in CEC2013

30D NO.	PSO		CLPSO		DNLPSO		SLPSO		MPSO		Proposed algorithm	
	Mean/Std.	Mean/Std.	Mean/Std.	Mean/Std.	Mean/Std.	Mean/Std.	Mean/Std.	Mean/Std.	Mean/Std.	Mean/Std.	Mean/Std.	
$f_{a1}$	2.586E+03/1.360E+03(<)	2.274E-13/0.000E+00(<)	6.196E+03/8.009E+02(<)	1.382E-13/1.121E-13(<)	1.962E-13/7.902E-14(<)	1.080E+06/5.170E+05(>)	4.600E+07/6.294E+07(<)	2.980E+06/1.793E+06	0/0			
$f_{a2}$	3.856E+07/2.123E+07(<)	2.085E+07/6.080E+06(<)	9.530E+07/1.854E+07(<)	1.391E+06/1.619E+06(<)	1.080E+06/5.170E+05(>)	4.600E+07/6.294E+07(<)	2.980E+06/1.793E+06	0/0				
$f_{a3}$	3.277E+10/1.757E+10(<)	1.078E+09/4.708E+08(<)	1.903E+10/8.321E+09(<)	7.107E+06/9.058E+06(>)	4.600E+07/6.294E+07(<)	2.980E+06/1.793E+06	0/0					
$f_{a4}$	3.260E+04/1.222E+04(<)	3.396E+04/5.508E+03(<)	1.737E+04/4.341E+03(>)	3.652E+03/1.249E+03(>)	9.470E+02/7.446E+03(>)	2.398E+04/5.501E+03	0/0					
$f_{a5}$	8.740E+02/4.856E+02(<)	1.374E-11/5.634E-12(<)	1.233E+03/3.090E+02(<)	1.137E-13/0.000E+00(<)	1.012E-09/1.741E-09(<)	4.043E+01/2.333E+01	0/0					
$f_{a6}$	2.864E+02/1.077E+02(<)	5.608E+01/1.551E+01(<)	6.537E+02/1.069E+02(<)	4.789E+01/2.779E+01(<)	3.140E+01/2.586E+01(>)	4.043E+01/2.333E+01	0/0					
$f_{a7}$	2.045E+02/4.308E+01(<)	7.634E+01/1.018E+01(<)	1.324E+02/2.248E+01(<)	1.288E+00/1.024E+00(<)	4.018E+01/1.903E+01(<)	4.043E+01/2.333E+01	0/0					
$f_{a8}$	2.092E+01/5.655E-02(>)	2.094E+01/4.921E-02(≈)	2.093E+01/2.093E+01(>)	2.094E+01/5.241E-02(≈)	2.094E+01/4.838E-02(<)	2.094E+01/4.241E-02	0/0					
$f_{a9}$	3.317E+01/2.625E+00(<)	2.816E+01/1.836E+00(<)	3.618E+01/2.679E+00(<)	9.223E+00/2.318E+00(>)	2.130E+01/2.755E+00(>)	2.437E+01/4.657E+00	0/0					
$f_{a10}$	5.505E+02/1.734E+02(<)	4.719E+00/1.266E+00(<)	8.914E+02/1.309E+02(<)	2.665E-01/1.358E-01(>)	1.487E+00/2.963E-01(>)	2.774E+00/1.529E+00	0/0					
$f_{a11}$	3.305E+02/8.643E+01(<)	2.622E-04/3.861E-04(>)	3.022E+02/3.022E+02(<)	1.338E+01/4.109E+00(>)	5.650E+01/1.842E+01(<)	3.460E+01/1.40E+01	0/0					
$f_{a12}$	3.380E+02/7.233E+01(<)	1.277E+02/1.594E+01(<)	3.093E+02/2.468E+01(<)	1.597E+02/9.119E+00(<)	5.889E+01/1.740E+01(<)	9.541E+01/3.656E+01	0/0					
$f_{a13}$	4.023E+02/8.994E+01(<)	1.542E+02/1.690E+01(<)	3.148E+02/2.079E+01(<)	1.593E+02/8.055E+00(<)	1.207E+02/2.749E+01(<)	9.541E+01/3.656E+01	0/0					
$f_{a14}$	4.383E+03/5.924E+02(<)	3.023E+02/8.428E+01(>)	2.079E+01/2.959E+02(>)	3.128E+02/1.466E+02(<)	5.717E+03/1.826E+03(<)	2.925E+03/1.861E+03	0/0					
$f_{a15}$	4.806E+03/6.726E+02(<)	5.920E+03/3.249E+02(<)	7.225E+03/7.225E+03(<)	4.791E+03/2.489E+03(<)	3.709E+03/9.522E+02(>)	4.251E+03/1.488E+03	0/0					
$f_{a16}$	1.476E+00/4.350E-01(>)	2.500E+00/2.653E-01(>)	2.411E+00/2.314E-01(>)	2.456E+00/2.749E-01(>)	2.433E+00/2.683E-01(>)	2.529E+00/2.842E-01	0/0					
$f_{a17}$	4.498E+02/7.499E+01(<)	4.544E+01/2.193E+00(>)	5.557E+02/3.679E+01(<)	1.600E+02/1.507E+01(<)	8.589E+01/2.349E+01(<)	7.829E+01/2.528E+01	0/0					
$f_{a18}$	4.308E+02/8.525E+01(<)	2.128E+02/1.209E+01(<)	5.628E+02/3.933E+01(<)	1.913E+02/8.112E+00(<)	1.626E+02/5.438E+01(>)	1.756E+02/5.928E+01	0/0					
$f_{a19}$	6.706E+02/2.113E+03(<)	3.167E+00/4.295E-01(>)	4.518E+02/2.179E+02(<)	3.267E+00/5.518E-01(>)	4.899E+00/1.564E+00(>)	5.013E+00/1.310E+00	0/0					
$f_{a20}$	1.336E+01/8.738E-01(>)	1.367E+01/4.566E-01(>)	1.336E+01/2.109E-01(>)	1.317E+01/1.566E+00(>)	1.394E+01/1.121E+00(<)	1.393E+01/1.014E+00	0/0					
$f_{a21}$	1.348E+03/3.899E+02(<)	3.138E+02/1.406E+01(<)	1.252E+03/2.694E+02(<)	3.158E+02/8.062E+01(<)	3.352E+02/8.202E+01(<)	2.990E+02/7.547E+01	0/0					
$f_{a22}$	5.465E+03/8.767E+02(<)	8.491E+02/1.900E+02(>)	2.694E+02/5.078E+02(>)	3.103E+02/1.453E+02(>)	2.571E+03/1.194E+03(<)	2.175E+03/1.663E+03	0/0					
$f_{a23}$	5.732E+03/7.860E+02(<)	6.543E+03/4.020E+02(<)	7.639E+03/3.754E+02(<)	2.949E+02/3.336E+03(>)	3.831E+03/1.127E+03(>)	5.614E+03/1.842E+03	0/0					
$f_{a24}$	2.989E+02/7.630E+00(<)	2.690E+02/6.615E+00(<)	3.062E+02/8.064E+00(<)	2.196E+02/1.058E+01(<)	2.387E+02/1.245E+01(<)	2.155E+02/1.432E+01	0/0					
$f_{a25}$	3.082E+02/1.008E+01(<)	2.943E+02/5.226E+00(<)	3.377E+02/6.141E+00(<)	2.842E+02/1.150E+01(<)	2.723E+02/1.214E+01(>)	2.731E+02/1.422E+01	0/0					
$f_{a26}$	3.493E+02/7.314E+01(<)	2.024E+02/7.055E-01(>)	2.888E+02/9.125E+01(<)	2.472E+02/5.266E+01(<)	2.738E+02/7.040E+01(<)	2.295E+02/4.819E+01	0/0					
$f_{a27}$	1.180E+03/7.394E+01(<)	8.793E+02/2.401E+02(<)	1.294E+03/6.013E+01(<)	3.959E+02/1.014E+02(<)	7.195E+02/1.148E+02(<)	4.243E+02/1.029E+02	0/0					
$f_{a28}$	2.958E+03/7.190E+02(<)	3.063E+02/1.391E+01(<)	1.964E+03/1.334E+02(<)	3.000E+02/2.743E-13(≈)	3.376E+02/2.321E+02(<)	3.000E+02/2.982E-13	0/0					
w/d/1	3/0/25	8/1/19	6/0/22	13/2/13	11/0/17							

under benchmark  $f_{a_1} - f_{a_{28}}$ . All parameter settings of other algorithms conform to the recommended values of the original paper. The results of 51 independent runs are summarized in Tables 26.1 and 26.2. And the result shows that our approach have better performance compared with PSO, CLPSO, DNLPSO, SLPSO, and MPSO.

## 26.5 Conclusion

An variant of MPSO was presented in this paper—CM-MPSO. The performance of our algorithm is compared with other PSO variants algorithm, the experimental results show that our algorithm introduces mutation operator, and not only adjusts the updating strategy of speed and position, but also adds crossover algorithm to the MPSO algorithm's adaptive position strategy, which improves the performance of the original MPSO algorithm. Some optimization methods  $f_{a_{15}} - f_{a_{20}}$  may be employed to further improve the efficiency of the proposed scheme in the future work.

## References

1. Kennedy, J., Eberhart, R.: Particle swarm optimization. In: Proceedings of ICNN'95—International Conference on Neural Networks, Perth, WA, Australia, vol. 4, pp. 1942–1948 (1995)
2. Meng, Z., Pan, J.S.: Monkey king evolution: a new memetic evolutionary algorithm and its application in vehicle fuel consumption optimization. *Knowl. Based Syst.* **97**, 144–157 (2016)
3. Du, B., Zhu, J., Ding, Q.: Optimization of multi-scale kernel chaotic time series prediction method based on the joint parameters were optimized with variable particle swarm. *J. Netw. Intell* **3**(4), 291–304 (2018)
4. Meng, Z., Pan, J.S., Tseng, K.K.: PaDE: an enhanced differential evolution algorithm with novel control parameter adaptation schemes for numerical optimization. *Knowl.-Based Syst.* **168**, 80–99 (2019)
5. Shi, Y., Eberhart, R.: Parameter selection in particle swarm optimization. In: *Evolutionary Programming VIZ: Proceedings EP98*, pp. 591–600. Springer, New York (1998)
6. Liang, J.J., Qin, A.K., Suganthan, P.N., et al.: Comprehensive learning particle swarm optimizer for global optimization of multimodal functions. *IEEE Trans. Evolution. Comput.* **10**(3), 281–295 (2006)
7. Meng, Z., Pan, J.S., Xu, H.: QUasi-Affine TRansformation evolutionary (QUATRE) algorithm: a cooperative swarm based algorithm for global optimization. *Knowl. Based Syst.* **109**, 104–121 (2016)
8. Nasir, M., Das, S., Maity, D., et al.: A dynamic neighborhood learning based particle swarm optimizer for global numerical optimization. *Inform. Sci.* **209**, 16–36 (2012)
9. Cheng, R., Jin, Y.: A social learning particle swarm optimization algorithm for scalable optimization. *Inform. Sci.* **291**, 43–60 (2015)
10. Meng, Z., Pan, J.S., Kong, L.: Parameters with adaptive learning mechanism (PALM) for the enhancement of differential evolution. *Knowl.-Based Syst.* **141**, 92–112 (2018)
11. Lynn, N., Suganthan, P.N.: Ensemble particle swarm optimizer. *Knowl.-Based Syst.* **55**, 533–548 (2017)
12. Liu, H., Zhang, X.W., Tu, L.P.: A modified particle swarm optimization using adaptive strategy. *Expert Syst. Appl.* **152**, 113353 (2020)

13. Meng, Z., Pan, J.S.: QUasi-Affine TRansformation evolution with external ARchive (QUATRE-EAR): an enhanced structure for differential evolution. *Knowl.-Based Syst.* **155**, 35–53 (2018)
14. Meng, Z., Pan, J.S.: HARD-DE: hierarchical ARchive based mutation strategy with depth information of evolution for the enhancement of differential evolution on numerical optimization. *IEEE Access* **7**, 12832–12854 (2019)

# Chapter 27

## Deep Learning on 3D Point Cloud for Semantic Segmentation



Zhihan Ning, Linlin Tang, Shuhan Qi, and Yang Liu

**Abstract** In this paper, a method by applying deep learning method onto the point clouds data for semantic segmentation is proposed. Three convolutional neural networks, PointNet, PointNet++, and DGCNN, are replicated, designed, and analyzed. In order to avoid problems introduced by some other methods due to the preprocessing step, here, PointNet, PointNet++, and DGCNN are directly used onto the 3D point cloud. Experiments verified the effect of these neural networks on point clouds for semantic segmentation. Methods based on PointNet and PointNet++ show good results, while DGCNN-based reached state-of-the-art performance.

### 27.1 Introduction

In recent years, with the continuous development of 3D scanning equipment technology, the related research based on 3D point cloud data has been developed rapidly. At the same time, with the continuous proposal of smart city, autonomous driving, virtual reality, and other related technical concepts, semantic segmentation as the basis of 3D scene understanding and analysis [1] has become the research focus in other fields such as computer vision and pattern recognition, which has more advantages than traditional methods. It has wide application prospect and value. Semantic segmentation means that the target image is divided into several groups of pixel regions with certain semantic meaning, and the category of each region is identified. Finally, an image with pixel semantic annotation is obtained, which makes the image easier to understand and analyze. Scene segmentation can be used in automatic driving, streetscape recognition, magnetic lasso, and other fields. At present, research of semantic segmentation based on 2D image has been relatively mature, but the occlusion problem of 2D image affects effect of semantic segmentation, so researchers turn their attention to 3D point cloud data.

---

Z. Ning · L. Tang (✉) · S. Qi · Y. Liu  
Harbin Institute of Technology, Shenzhen 518055, China  
e-mail: [hittang@126.com](mailto:hittang@126.com)

3D point cloud is an essential type of geometric data captured by 3D scanners. There are three characteristics for this kind of data: the segmentation network should be insensitive to its input order; distance measurement determines different characteristics of the local neighborhood; a rigid transformation of the point cloud should not affect the understanding of the segmentation network.

Semantic segmentation refers to dividing target image into several groups of pixel areas with a specific semantic meaning, identifying each area's category, and finally obtaining an image with pixel semantic annotation to make the image easier to understand and analyze. With the continuous improvement of 3D scanning technology, research on the 3D point cloud data has developed rapidly. As the concept of smart city, autopilot, and virtual reality were put forward, technology related to semantic segmentation as a 3D scene understanding and analysis [1] has become the basis of research in the field of computer vision and pattern recognition, etc. Semantic segmentation on point cloud has broad application prospects and can be used in many areas such as autonomous driving, street view recognition, and magnetic lasso.

At present, researches on semantic segmentation based on 2D images have been relatively mature. However, occlusion occurs in 2D images, so researchers are paying more and more attention to 3D point cloud data. Compared with the 2D image data, 3D point cloud packets contain more information, which brings opportunities for scene segmentation and introduces new challenges in the data processing at the same time. Scene segmentation based on point cloud has a broad application area and development prospects.

## 27.2 Related Work

There has been two main methods in point cloud segmentation: voxelization and multi-view, before the introduction of PointNet, which consumes point cloud directly.

Brock et al. [2] introduced a voxel-based method for image segmentation based on point cloud. This method voxelize disordered 3D point cloud data, which changes it into a regular structure so that it can be trained just as deep learning methods applied on 2D images. The authors developed methods for training voxel-based variational autoencoders, and they also gave a user interface for exploring the latent space learned by the autoencoder, and also a deep convolutional neural network architecture for object classification was shown. Voxelization makes data unnecessarily large and may cause related spatiotemporal problems. Considering computational cost for the voxelization of point cloud data, the available resolution of the voxel grid is limited. Thus low-resolution grids make it difficult to distinguish similar shapes, affecting the segmentation accuracy.

Inspired by the research of 2D image processing, Su et al. [3] created 2D images from 3D data through projection from different perspectives. They train a convolution neural network model with those 2D images as the training data. Firstly, a

standard CNN architecture is trained to recognize the shapes' rendered views independently of each other, and then, results are shown that a 3D shape can be recognized even from a single view at an accuracy far higher than using state-of-the-art 3D shape descriptors. Recognition rates further increase when multiple views of the shapes are provided. Compared with methods with traditional handcraft characteristics, multi-view models achieve better results, despite some geometry space loss, which decreases the final segmentation accuracy.

Point cloud is a set of points with spatial coordinates, RGB colors, etc. In this paper, only the spatial coordinate feature of point cloud data is considered, as (27.1):

$$\{p_i = (x_i, y_i, z_i) \mid i = 1, 2, \dots, n\} \tag{27.1}$$

Here,  $p_i$  is the  $i$  th point concerning the 3D coordinate information.  $x_i, y_i, z_i$ , respectively, represent the coordinates of the first point in the input point cloud data of the point.

For semantic segmentation of point cloud, each point  $p_i$  can be recognized as a specific category. Therefore, we need to find a segmentation function to calculate probability distribution of each point on each category:

$$\{p_{r_i} \mid i = 1, 2, \dots, n\} = \{f_s(p_i) \mid i = 1, 2, \dots, n\} \tag{27.2}$$

In function (27.2),  $p_{r_i}$  represents the probability distribution of  $p_i$  over each category. Then each point is recognized as the class of the highest probability.

### 27.3 Proposed Method

Three models are used here: PointNet [4], PointNet++ [5], and DGCNN [6] in this paper. We will introduce those models in brief.

As shown in the above Fig. 27.1, PointNet is a novel neural network that consumes point cloud directly regardless of its input order. This network provides a unified

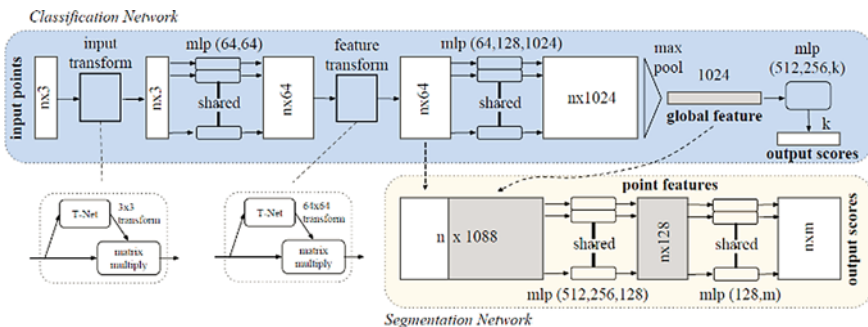


Fig. 27.1 PointNet architecture [4]

architecture for semantic segmentation. It is very efficient and performs equally as or even better than methods based on voxelization and multi-view. These deep neural networks can directly train PointNet-based point cloud segmentation without prior dimensionality reduction preprocessing, which can effectively prevent the information loss caused by dimension reduction, such as the loss of a large amount of geometric space information, affecting the final segmentation accuracy. Simultaneously, compared with volume pixel of disordered 3D point cloud data, making it a regular structure and applying voxelization method of deep learning, PointNet will not make data unnecessarily large and will not cause related space–time problems. Therefore, PointNet shows great improvement in point cloud semantic segmentation compared with some other traditional methods such as dimensionality reduction and voxelization.

PointNet has shown impressive performance on some benchmarks. However, it cannot capture local point cloud features at different scales. PointNet++ (Fig. 27.2) layered feature learning framework can solve this problem well. The new architecture of PointNet++ builds a layered set of points and gradually extracts larger and larger local areas along the hierarchy. Its hierarchy consists of several collection extraction layers. A set of points is processed and extracted within each layer to produce a new set with fewer elements. The point set extraction layer consists of three key layers: sampling layer, grouping layer, and PointNet layer (the PointNet mentioned above).

DGCNN stands for dynamic graph convolutional neural network. As Fig. 27.3, inspired by PointNet, DGCNN adds EdgeConv (edge convolution) to achieve a better understanding of point cloud local features. EdgeConv refers to the convolution of edges between points. Instead of using individual points like PointNet, DGCNN utilizes local geometry structure by constructing local neighborhood graph and applies operations similar to convolution on edges connecting adjacent point pairs in the spirit of the graph neural network. This operation, called EdgeConv, has properties that fall between the translational invariance and non-locality. Unlike graph convolutional neural network (graph CNNs), graph used by DGCNN is not fixed but dynamically and will be updated after each network layer.

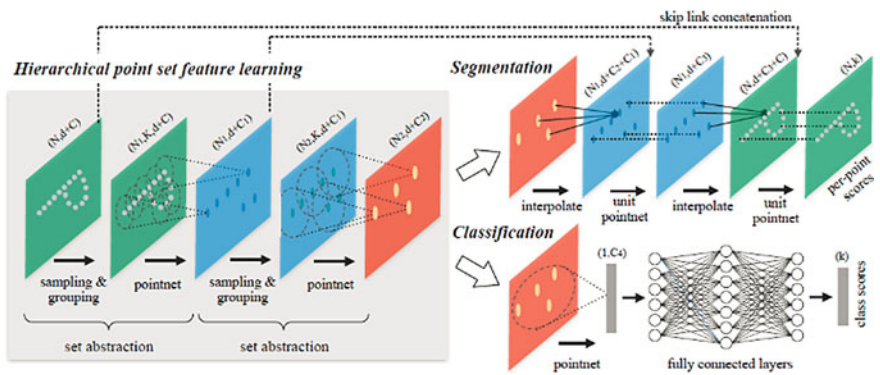


Fig. 27.2 PointNet++ hirarchy architecture [5]

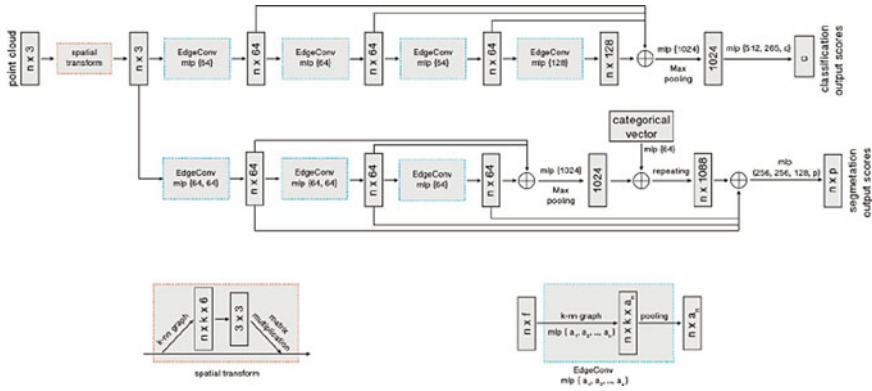


Fig. 27.3 DGCNN architecture [6]

### 27.4 Experiments

We evaluate PointNet, PointNet++, DGCNN on Stanford Large-Scale 3D Indoor Spaces Dataset (S3DIS) [7] for a semantic scene segmentation task, as shown in Fig. 27.4. We used one NVIDIA 2080Ti GPU for training. One of the best multi-view models, MS + CU (multi-scale block features with consolidation units), achieved 79.2% accuracy. One of the best voxelization models, G + RCU (the grid-blocks with recurrent consolidation units), achieved 81.1% in this semantic segmentation task [8].

For DGCNN training 3D point cloud data, the following parameters are used: max\_Epoch = 50, batch\_Size = 6, learning\_Rate = 0.001, decay\_Step = 300,000, decay\_Rate = 0.5. Select batch here\_Size = 6 is because the NVIDIA geforce RTX 2080ti single video card is in too large a batch\_Under size training, the video memory will overflow.

For the 3D semantic analysis dataset of Stanford University, PointNet has the following accuracy rates, as shown in Table 27.1.

Finally, the accuracy of PointNet scene segmentation based on the overall test dataset is 88.46%.

It can be seen that DGCNN has a very good scene segmentation effect. Compared with PointNet (+7.90%) and PointNet++ (+7.23%), it has a great performance improvement.

As shown in Table 27.2, PointNet achieved a precision of 80.56%, PointNet++ achieved 81.23%, and DGCNN achieved 88.46%. PointNet shows comparable performance as multi-view (+1.36% than MS + CU) and voxelization (-0.54% than G + RCU) models. Based on PointNet, Pointnet++ focused on learning local features with increasing contextual scales. Therefore, it has a better result (+0.67% than PointNet) and surpasses the MS + CU as well as the G + RCU models. Comparing with PointNet and PointNet++ DGCNN has the best performance (+7.90% than Pointnet, +7.23% than PointNet++).



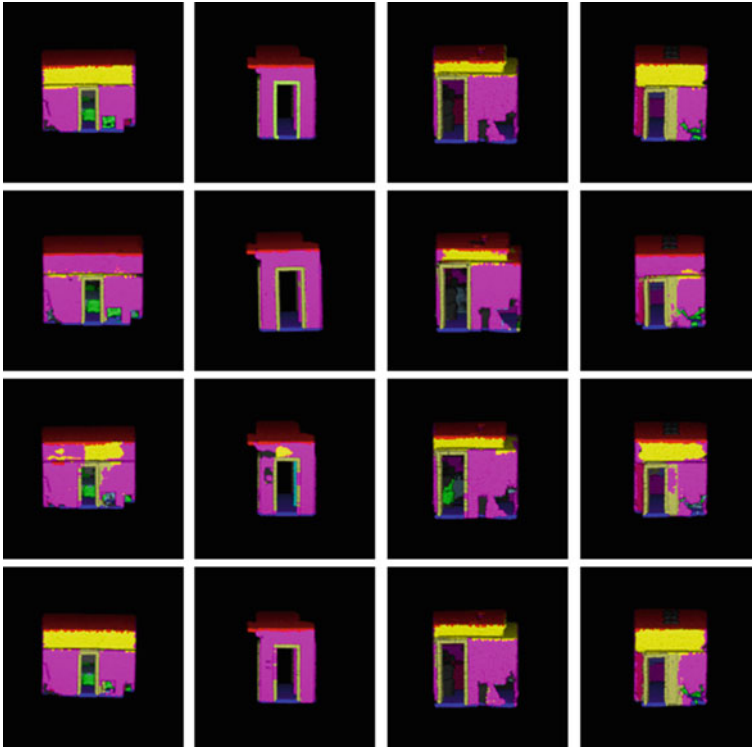


**Fig. 27.4** Visualization of semantic segmentation

From top to bottom are ground truth, PointNet, PointNet++, and DGCNN. From left to right are conference room, hallway, office, and pantry.

## 27.5 Conclusion

In this paper, we mainly applied three deep learning models, PointNet, PointNet++, and DGCNN, for point cloud semantic segmentation. PointNet provides a unified approach for 3D semantic segmentation and achieves 80.56% accuracy. PointNet++ introduces a hierarchical neural network that applies PointNet recursively on a nested partitioning of the input point set. It has higher precision of 81.23%. DGCNN incorporates local neighborhood information and learns global shape properties. Moreover, it captures semantic characteristics over potentially long distances in the original embedding. DGCNN achieved an accuracy of 88.46% as a state-of-the-art method. In the future, it is worth thinking that color and other point cloud data features can bring advantages for deep learning on point cloud for semantic segmentation.

**Table 27.1** Partial scene segmentation performance of DGCNN

Type	Accuracy	Type	Accuracy	Type	Accuracy
ConferenceRoom_1	0.952	ConferenceRoom_2	0.801	CopyRoom_1	0.868
Hallway_1	0.956	Hallway_2	0.914	Hallway_3	0.975
Hallway_4	0.923	Hallway_5	0.959	Hallway_6	0.874
Hallway_7	0.915	Hallway_8	0.835	Office_10	0.857
Office_11	0.912	Office_12	0.878	Office_13	0.930
Office_14	0.834	Office_15	0.898	Office_16	0.907
Office_17	0.899	Office_18	0.944	Office_19	0.926
Office_1	0.951	Office_20	0.887	Office_21	0.912
Office_22	0.882	Office_23	0.946	Office_24	0.952
Office_25	0.939	Office_26	0.931	Office_27	0.910
Office_28	0.888	Office_29	0.861	Office_2	0.869
Office_30	0.791	Office_31	0.783	Office_3	0.917
Office_4	0.934	Office_5	0.915	Office_6	0.922
Office_7	0.857	Office_8	0.931	Office_9	0.929
Pantry_1	0.891	WC_1	0.968		

**Table 27.2** Accuracy of deep learning models for semantic segmentation

Model	Accuracy (%)
MS + CU	79.2
G + RCU	81.1
PointNet	80.56
PointNet++	81.23
DGCNN	88.46

**Acknowledgements** This work was supported by Shenzhen Science and Technology Plan Fundamental Research Funding JCYJ20180507183527919 and Shenzhen Foundational Research Funding JCYJ20180306171938767.

## References

1. Zhang, X., Liu, J., Shi, Z., Wu, Z., Wang, Z.: Review of deep learning-based semantic segmentation. *Laser Optoelectron. Prog.* **56**(15), 150003 (2019)
2. Brock, A., Lim, T., Ritchie, J.M., et al.: Generative and discriminative voxel modeling with convolutional neural networks. *Comput. Vis. Pattern Recogn.* (2016)
3. Su, H., Maji, S., Kalogerakis, E., et al.: Multi-view convolutional neural networks for 3D shape recognition. In: *International Conference on Computer Vision*, pp. 945–953 (2015)

4. Qi, C.R., Su, H., Mo, K., et al.: Pointnet: deep learning on point sets for 3d classification and segmentation. In: *IEEE Conference on Computer Vision and Pattern Recognition*, pp. 652–660 (2017)
5. Qi, C.R., Yi, L., Su, H., et al.: Pointnet++: deep hierarchical feature learning on point sets in a metric space. In: *Advances in Neural Information Processing Systems*, pp. 5099–5108 (2017)
6. Wang, Y., Sun, Y., Liu, Z., et al.: Dynamic graph CNN for learning on point clouds. *ACM Trans. Graph. (TOG)*, **38**(5), 146 (2019)
7. Armeni, I., Sener, O., Zamir, A.R., Jiang, H., Brilakis, I., Fischer, M., Savarese, S.: 3d semantic parsing of large-scale indoor spaces. In: *Proceedings of the IEEE International Conference on Computer Vision and Pattern Recognition*, Las Vegas, NV, USA, pp. 1534–1543 (2016)
8. Engelmann, F., et al.: Exploring spatial context for 3D semantic segmentation of point clouds. In: *International Conference on Computer Vision*, pp. 716–724 (2017)

# Chapter 28

## An Improved Arithmetic Optimization Algorithm with a Strategy Balancing Exploration and Exploitation



Ruo-Bin Wang , Shuo Yin , Wei-Feng Wang , Zhi-Wei An ,  
and Lin Xu 

**Abstract** With the increasing complexity and difficulty of practical problems, higher requirements are put forward to optimization techniques, especially the improvement on reliability and performance of meta-heuristic algorithm. In this paper, an improved arithmetic optimization algorithm (IAOA) is proposed, and it is compared with two algorithms—particle swarm optimization (PSO) and arithmetic optimization algorithm (AOA) on 13 benchmark functions. Experimental results show that the proposed algorithm performed better than the compared algorithms in solving particle problems in most cases.

---

R.-B. Wang (✉)

Key Laboratory of Nondestructive Testing, Fuqing Branch of Fujian Normal University, Fuqing 350300, China

e-mail: [wrb@ncut.edu.cn](mailto:wrb@ncut.edu.cn)

R.-B. Wang · S. Yin · W.-F. Wang · Z.-W. An

North China University of Technology, Beijing 100043, China

L. Xu (✉)

University of South Australia, Adelaide 5095, Australia

e-mail: [xuyly032@mymail.unisa.edu.au](mailto:xuyly032@mymail.unisa.edu.au)

Fuzhou Institute of Technology, Fuzhou 350506, China

## 28.1 Introduction

In recent decades, the rapid development of information science leads to higher performance requirements of optimization algorithm, especially meta-heuristic optimization algorithms. There are four categories of meta-heuristic algorithms: evolution-based algorithms, swarm intelligence algorithms, physics-based algorithms and human-based method heuristic [1]. Arithmetic optimization algorithm (AOA) is a kind of physics-based algorithm. The main inspiration of AOA comes from the use of arithmetic operators in solving arithmetic problems. In this algorithm, mathematical operators are employed as mathematical optimizations to determine the best element that meets a particular criterion from a set of candidate options. However, in view of the fact that the specific meaning of Math Optimizer Probability (MOP) in AOA is not completely consistent with the actual requirement, which will spoil the performance of the algorithm, therefore, we propose an improved AOA (IAOA).

The main contributions of this research are summarized as follows:

- Proposing an improved AOA with a strategy balancing between exploration and exploitation.
- Testing the effectiveness of IAOA on 13 benchmark functions.
- Comparing and demonstrating the superiority of IAOA against the other three algorithms.

The remainder of the paper is structured as follows: Sect. 28.2 provides the related works. Section 28.3 describes the basic idea of IAOA. Section 28.4 presents the findings of the experiment. Finally, Sect. 28.5 concludes the outcome of the research.

## 28.2 Related Works

**Swarm intelligence algorithms.** Swarm intelligence algorithms are group of meta-heuristics, which simulates the behavior of animals in movement or hunting groups. Kennedy et al. [2] proposed a particle swarm optimization (PSO) algorithm, which is a global random search algorithm based on swarm intelligence. It is inspired by the research findings of artificial life and simulates the migration and clustering behavior of birds in the process of foraging. Song et al. [3] proposed a nest of cuckoo represents a possible solution in the algorithm, which is combined with Lévy flight to constantly update the position of the nest to find a potentially better solution to be a new cuckoo's nest. Okwu and Tartibu [4] proposed a butterfly optimization algorithm (BOA), which is a unique algorithm inspired by nature. The algorithm replicates the behavior of the natural butterfly which can be described to perform a cooperative movement while navigating toward its food source and position. Hu et al. [5] proposed a binary gray wolf optimizer (BGWO). It is a new swarm intelligence algorithm mimicking the

behaviors of gray wolves. Its abilities include fast convergence, simplicity and easy realization.

Diversity preservation is often employed to improve performance in many multi-population algorithms. Regardless of the strategy used, the balance between knowledge transfer and diversity maintenance should always be considered when dealing with environmental changes.

**Physics-based algorithms.** The physics-based algorithm is another group of optimization algorithm. This group derives from real-life laws of physics and typically describes the communication of search solutions based on rules of control that are ingrained in the physical methods. Mirjalili and Lewis [6] proposed a gravitational search algorithm (GSA), and it was inspired by the gravitational forces between masses in nature. This algorithm has demonstrated superior performance among other well-known heuristic algorithms such as particle swarm optimization and genetic algorithm. However, slow exploitation is a major weakness that might result in degraded performance when dealing with real engineering problems. Meshkat and Parhizgar [7] proposed a novel population-based optimization algorithm called sine cosine algorithm (SCA) for solving optimization problems. The SCA creates multiple initial random candidate solutions and requires them to fluctuate outward or toward the best solution using a mathematical model based on sine and cosine functions. Laith et al. [8] proposed an AOA. It makes use of the distribution characteristics of the main arithmetic operators (multiplication (m), division (d) and subtraction) in mathematics. However, the accuracy of algorithm optimization and the ability of mining stage need to be improved.

## 28.3 The Improved Arithmetic Optimization Algorithm (IAOA)

### 28.3.1 The Basic Idea of AOA

The particle position update idea of the AOA is consistent with PSO. A vector of “similar velocity” is calculated for each particle and added to the current position of the particle to form the coordinates of the next iteration.

MOP is a parameter that controls the magnitude of change, and the definition of MOP is shown in formula (28.1). As the number of iterations increases, the MOP value gradually decreases, so that the magnitude of change in the later iterations will also decrease accordingly to meet the needs of the later exploitation stage of the algorithm.

$$\text{MOP}_{\text{Iter}} = 1 - \left( \frac{\text{Iter}}{\text{MAX\_Iter}} \right)^\alpha \quad (28.1)$$

The  $\alpha$  is a hyperparameter of the algorithm. The best value of  $\alpha$  is 0.2 measured by experiments. There are four formulas for updating particle positions based on MOP and MOA, which are two important parameters in AOA. The four update formulas correspond to four basic mathematical operations (+ add; – subtract;  $\times$  multiplication;  $\div$  division).

$$x_{i,j} = \begin{cases} x_{\text{best},j} \times \text{MOP} \times \text{ABS}_{\text{step}}, r_1 < \text{MOA}, r_2 \geq 0.5 \\ x_{\text{best},j} \div (\text{MOP} + \varepsilon) \times \text{ABS}_{\text{step}}, r_1 < \text{MOA}, r_2 < 0.5 \\ x_{\text{best},j} + \text{MOP} \times \text{ABS}_{\text{step}}, r_1 \geq \text{MOA}, r_3 \geq 0.5 \\ x_{\text{best},j} - \text{MOP} \times \text{ABS}_{\text{step}}, r_1 \geq \text{MOA}, r_3 < 0.5 \end{cases} \quad (28.2)$$

### 28.3.2 Improved AOA

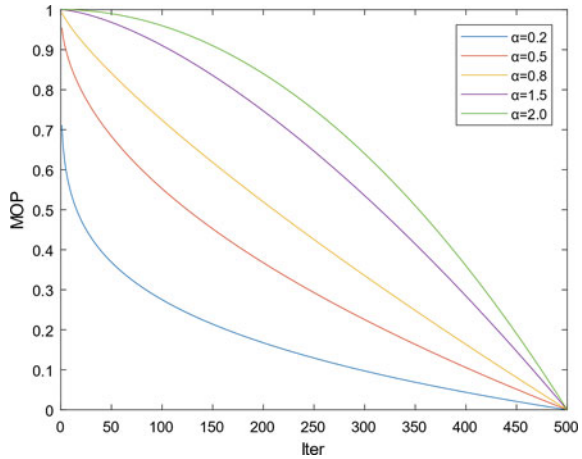
The AOA is a group optimization algorithm. Each individual is a possible optimal solution. The  $X$  vector is used to represent the position of each individual. Every component of a particle is based on the current round of iteration. Each component of the sub-optimal solution undergoes a certain degree of change. The method and magnitude of this change are determined by the two parameters of MOA and MOP, respectively. MOA is a parameter that linearly increases and changes from  $\text{MOA}_{\text{MIN}}$  to  $\text{MOA}_{\text{MAX}}$ . The specific calculation is illustrated in the formula (28.3), where  $\text{MOA}_{\text{MIN}}$  and  $\text{MOA}_{\text{MAX}}$  are preset values. When the random number  $r_1$  is greater than the MOA, the global optimal possible area is explored, and when  $r_2$  is less than the MOA, the local minimum is deeply mined.

$$\text{MOA}(\text{Iter}) = \text{MOA}_{\text{MAX}} + \text{Iter} \times \left( \frac{\text{MOA}_{\text{MAX}} - \text{MOA}_{\text{MIN}}}{\text{MAX\_Iter}} \right) \quad (28.3)$$

Iter represents the current number of iterations, starting from 1 and increasing until the maximum number of iterations- MAX\_ Iter.

One of the super parameters in this algorithm is  $\mu$ , which controls the “absolute step size” of each update of the algorithm. Since the objective function and  $\mu$  are given at the beginning,  $\text{ABS}_{\text{step}}$  will not change during the entire iteration, so it can also be interpreted as a fixed “reference displacement”. Only under the control of  $\mu$ , can the size of this “reference displacement” be calculated. The  $\varepsilon$  in the update formula using division in the formula (28.2) is to avoid errors of division by zero. The small amount designed is approximately equal to  $2.2204e - 16$ . The  $r_2$  and  $r_3$  are random numbers between  $[0, 1]$ , and  $x_{i,j}$  represents the  $j$ -th dimension of the  $i$ -th individual in next iteration.  $x_{\text{best},j}$  is the  $j$ -th dimension component of the optimal solution in the current iteration round, and the  $\text{ABS}_{\text{step}}$  represents the constant absolute-step. The definition is shown in formula (28.4).

**Fig. 28.1** MOP changed by the iteration in multiple  $\alpha$



$$ABS_{step} = (UB - LB) \times \mu + LB \tag{28.4}$$

In the original paper of AOA, only the case where  $0 < \alpha < 1$  is fully discussed. After considering the actual meaning of MOP: the “absolute step size” of the control coordinate update, we decide to improve the MOP parameters in the AOA.

According to formula (28.1), it can be known that when  $0 < \alpha < 1$ , MOP decreases with the increase in the number of iterations, and the speed of decline is fast at first and then becomes slow. When  $\alpha > 1$ , MOP decreases with the increase in the iterations times, but the difference is that the rate of decline is slow at first and then becomes faster. The image when  $\alpha = 0.2$  to  $\alpha = 2$  is shown in Fig. 28.1. It can be seen that when  $0 < \alpha < 1$ , MOP’s function with respect to iteration is convex, and when  $\alpha > 1$ , MOP’s function of iteration is concave.

We decide to use  $\alpha$  larger than 1 to improve the AOA. In this case, MOP is a concave function for iteration, which is conducive to sufficient exploration of the algorithm in the early stage, rather than quickly converging to a possible region found. Changing the parameter of MOP can improve the accuracy and convergence effect of the algorithm. The experimental results are shown in Table 28.4.

The pseudocode of the IAOA algorithm is shown in Table 28.1.

## 28.4 Experiments

We chose 13 benchmark functions in the literature as test functions to compare the performance of AOA, PSO and IAOA. Population was uniformly set as 30, and the number of cycles was set as 500. For the 13 test functions, F1–F13, we chose to use 30 dimensions for the test, and the solution space was the same (the upper and lower bounds of each dimension of the solution were the same). The setting



**Table 28.1** The pseudocode of the IAOA algorithm**Algorithm 1:** IAOA**Output:** best solution:  $x_{best}$ 


---

```

1: Initialize the solutions randomly. ( $x_i, i = 1, 2, \dots, N$ )
2: Set super parameters.  $\mu = 0.499, \alpha = 2.0$ 
3: for (1 to  $MAX\_Iter$ ) do
4:   Calculate function values of all the individuals
5:   Get the best solution:  $x_{best}$ .
6:   Calculate MOP and MOA.
7:   Calculate  $ABS_{step}$ 
8:   for ( $i = 1$  to  $N$ ) do
9:     for ( $j = 1$  to  $x$ 's dimension) do
10:      Set three random number between  $[0,1]$  ( $r_1, r_2, r_3$ )
11:      if  $r_1 < MOA$  then
12:        if  $r_2 < 0.5$  then
13:          Apply the Multiplication( $\times$ ) Strategy
14:        else
15:          Apply the Division( $\div$ ) Strategy
16:        end if
17:      else
18:        if  $r_3 < 0.5$  then
19:          Apply the Addition( $+$ ) Strategy
20:        else
21:          Apply the Subtraction( $-$ ) Strategy
22:        end if
23:      end if
24:    end for
25:  end for
26: end for

```

---

of these parameters could ensure the validity of the experiment. At the same time, we execute 10 experiments for each objective function to take the mean value and standard deviation to compare the mean value of different algorithms, so as to ensure the fairness of comparison.

### 28.4.1 Unimodal Test Functions

The performance of the algorithm on the unimodal function (F1–F7) is shown in Table 28.2. The experimental result shows that IAOA has a significantly improved fitness value over AOA, which represents a better effectiveness in the exploitation stage. Meanwhile, the standard deviation of the experimental results also indicates that IAOA has a high availability.

**Table 28.2** Unimodal test functions

Function	Description	LB	UB	$f_{\min}$
F1	$f(x) = \sum_{i=1}^n x_i^2$	-100	100	0
F2	$f(x) = \sum_{i=1}^n  x_i  + \prod_{i=1}^n  x_i $	-10	10	0
F3	$f(x) = \sum_{i=1}^n \left( \sum_{j=1}^i x_j \right)$	-100	100	0
F4	$f(x) = \max\{ x_i , 1 \leq i \leq n\}$	-100	100	0
F5	$f(x) = \sum_{i=1}^{n-1} \left[ 100(x_i^2 - x_{i+1})^2 + (1 - x_i)^2 \right]$	-30	30	0
F6	$f(x) = \sum_{i=1}^n ([x_i + 0.5])^2$	-100	100	0
F7	$f(x) = \sum_{i=0}^n i x_i^4 + \text{random}[0, 1)$	-1.28	1.28	0

### 28.4.2 Multimodal Test Functions

Multimodal functions (F8–F13) having many local minima are often regarded as being difficult to optimize. The performance of PSO, AOA and IA OA in multimodal test functions is shown in Table 28.3. From F8 to F10, it can be seen that IA OA is significantly improved compared with AOA and PSO, and the F11 function represents that IA OA is more effective in the exploitation stage.

Results of all experiments are shown in Table 28.4. In the table, the bold part is the best experimental data.

## 28.5 Conclusions

In this paper, an improved optimization algorithm based on AOA is proposed. The parameter of MOP is redesigned as a concave function instead of a convex function. The comprehensive experiments are conducted to validate the performance of the proposed IA OA. In all 13 test functions, our newly proposed IA OA performed strictly better than the AOA on 9 test functions, and the results in F1–F4 showed its better effects on the unimodal function. And the improvement in the F8 function revealed its stronger global optimization capacity. In future work, we will employ the parallel method to further optimize the AOA and try to apply it in the actual tasks [9, 10].

**Table 28.3** Multimodal test functions

Function	Description	LB	UB	$f_{\min}$
F8	$f(x) = \sum_{i=1}^n (-x, \sin(\sqrt{ x_i }))$	-500	500	-418.9826 × n
F9	$f(x) = \sum_{i=0}^n [x_i^2 - 10 \cos(2\pi x_i) + 10]$	-5.12	5.12	0
F10	$f(x) = -20 \exp\left(-0.2 \sqrt{\frac{1}{n} \sum_{i=1}^n x_i^2}\right) - \exp\left(\frac{1}{n} \sum_{i=1}^n \cos(2\pi x_i)\right) + 20 + e$	-32	32	0
F11	$f(x) = 1 + \frac{1}{4000} \sum_{i=1}^n x_i^2 - \prod_{i=1}^n \cos\left(\frac{x_i}{\sqrt{i}}\right)$	-600	600	0
F12	$f(x) = \frac{\pi}{n} \{10 \sin(\pi y_1)\} + \sum_{i=1}^{n-1} (y_i - 1)^2 [1 + 10 \sin^2(\pi y_i + 1) + \sum_{j=1}^n u(x_j, 10, 100, 4)]$ , where $y_i =$ $1 + \frac{x_i+1}{4}, u(x_i, a, k, m) \begin{cases} K(x_i - a)^m & x_i > a \\ 0 & -a \leq x_i \leq a \\ K(-x_i - a)^m & -a \leq x_i \end{cases}$	-50	50	0
F13	$f(x) =$ $0.1(\sin^2(3\pi x_1) + \sum_{i=1}^n (x_i - 1)^2 [1 + \sin^2(3\pi x_i + 1)] + (x_n - 1)^2 + \sin^2(2\pi x_n)) + \sum_{i=1}^n u(x_i, 5, 100, 4)$	-50	50	0

**Table 28.4** Results of all experiments

F	PSO		AOA		IAOA	
	Ave	Std	Ave	Std	Ave	Std
F1	7.56E - 03	1.05E - 02	4.90E - 06	1.43E - 06	<b>0.00E + 00</b>	0.00E + 00
F2	2.02E + 00	4.00E + 00	1.95E - 03	1.66E - 03	<b>0.00E + 00</b>	0.00E + 00
F3	3.47E + 03	2.81E + 03	1.17E - 03	6.62E - 04	<b>0.00E + 00</b>	0.00E + 00
F4	6.28E + 00	1.55E + 00	1.53E - 02	1.06E - 02	<b>0.00E + 00</b>	1.85E - 68
F5	9.12E + 03	2.70E + 04	2.79E + 01	2.13E - 01	<b>5.36E - 02</b>	1.42E - 01
F6	3.33E - 02	7.71E - 02	3.07E + 00	2.84E - 01	<b>9.72E - 06</b>	3.33E - 01
F7	4.52E - 02	1.17E - 02	5.44E - 05	5.18E - 05	<b>5.40E - 05</b>	2.14E - 05
F8	- 8.43E + 03	5.99E + 02	<b>- 5.41E + 03</b>	3.60E + 02	- 7.91E + 02	3.88E + 02
F9	6.49E + 01	1.74E + 01	1.51E - 06	1.33E - 06	<b>0.00E + 00</b>	0.00E + 00
F10	7.08E - 01	6.25E - 01	4.16E - 04	1.20E - 04	<b>8.88E - 16</b>	0.00E + 00
F11	3.70E - 02	2.94E - 02	2.70E - 05	9.57E - 06	<b>0.00E + 00</b>	4.04E + 01
F12	1.74E - 01	2.55E - 01	7.41E - 01	3.18E - 02	<b>3.11E - 01</b>	5.44E - 02
F13	4.33E - 01	8.58E - 01	2.97E + 00	7.96E - 06	<b>7.27E - 02</b>	5.64E - 02

**Acknowledgements** This work is funded by the Key Laboratory of Nondestructive Testing in Fuqing Branch of Fujian Normal University, Fujian Province, under grants # S2-KF1901.

## References

1. Abualigah, L., Hehab, M., Shinwan, M.: Salp swarm algorithm: a comprehensive survey. *J. Neur. Comput. Appl.* **32**(15), 11195–11215 (2020)
2. Kennedy, J.: Particle swarm optimization. In: Sammut, C.I., Webb, G. (eds.) *Proceedings of 1995 IEEE International Conference on Neural Networks*, vol. 4, pp. 1942–1948 (2011)
3. Song, P.C., Pan, J.S., Chu, S.C.: A parallel compact cuckoo search algorithm for three-dimensional path planning. *J. Appl. Soft Comput.* **94** (2020)
4. Okwu, M., Tartibu, L.: Butterfly optimization algorithm. In: *Metaheuristic Optimization: Nature-Inspired Algorithms Swarm and Computational Intelligence, Theory and Applications*, Chapter: 105–114. Springer, Cham (2020)
5. Hu, P., Pan, J.S., Chu, S.C.: Improved binary grey wolf optimizer and its application for feature selection. *J. Knowl.-Based Syst.* 195 (2020)
6. Mirjalili, S., Lewis, A.: Adaptive gbest-guided gravitational search algorithm. *J. Neur. Comput Appl.* **25**(7–8), 1569–1584 (2014)
7. Meshkat, M., Parhizgar, M.: A novel sine and cosine algorithm for global optimization. In: *2017 7th International Conference on Computer and Knowledge Engineering (ICCKE)*, vol. 96, pp. 120–133 (2017)
8. Abualigah, L., Diabat, A., Mirjalili, S.: The Arithmetic optimization algorithm. *Comput. Methods Appl. Mech. Eng.*, 376 (2021)

9. Zhuang, J., Luo, H., Pan, T.-S., Pan, J.-S.: Improved flower pollination algorithm for the capacitated vehicle routing problem. *J. Netw. Intell.* **5**(3), 141–156 (2020)
10. Trong, N., Jeng, P., Tsu, W., Thi, D., Trinh, N.: Node coverage optimization strategy based on ions motion optimization. *J. Netw. Intell.* **4**(1), 1–9 (2019)

**Part IV**  
**Networks and Security**

# Chapter 29

## MPSiam: A Fast Multiplexing Siamese Tracking Network



Donghao Li, Ce Shen, Jinxing Hu, and Diping Yuan

**Abstract** Siamese trackers have achieved remarkable performance in accuracy. However, the high memory cost and inference speed have restricted the deployment of the state-of-the-art trackers in mobile applications. To address this issue, this paper presents a backbone consisting of multiplexing convolution blocks that newly proposed by us, which combine the spatial multiplexing operation and channel multiplexing operation. The spatial multiplexing operation is inspired by the subpixel convolution in super-resolution tasks. The channel multiplexing operation is inspired by the channel shuffle in ShuffleNet. These two modules can be used to effectively optimize the multiply–accumulate (MACC) operation, by multiplying the number of operations and then adding it to a network. We employ this new module to build a novel lightweight backbone for the SiamRPN++ tracker. We trained this model and evaluated its performances on the VOT2018 and OTB2015 datasets. Our model is compressed to 43 MB, the inference time was 83 FPS, and the experiments were carried out in a single NVIDIA 2080Ti GPU. Our model is superior to MobileNetv2-SiamRPN++, which has a model size of 58 MB and the inference time of 55 FPS, and our method also managed to reduce the MACC from 1.2 to 0.5 B. Compared with SiamRPN++ with Resnet50 backbone, our model achieved a compression rate of  $4.8\times$  and speedup of  $3.3\times$ , just losing 3% EAO.

---

D. Li · C. Shen · J. Hu (✉) · D. Yuan

Shenzhen Institute of Advanced Technology, Chinese Academy of Sciences, Shenzhen, People's Republic of China

e-mail: [jinxing.hu@siat.ac.cn](mailto:jinxing.hu@siat.ac.cn)

D. Li · C. Shen

University of Chinese Academy of Sciences, Beijing, China

D. Yuan

Shenzhen Urban Public Safety and Technology Institute Co. Ltd., Shenzhen, China

## 29.1 Introduction

Object tracking is a fundamental vision task. Given with only an unknown target's location in the first frame, object tracking aims to infer its location in the next video sequence. It has wide practical applications, such as automatic driving [1], indoor obstacle avoidance [2], and disaster response [3]. In recent years, many efforts have been made to improve the performance of visual trackers. However, developing an accurate, fast, and robust tracker is still extremely challenging because of the vast amounts of deformations, motions, and occlusions that often occur on video objects with complex backgrounds.

Recent years have witnessed various approaches of Siamese network proposed to handle the visual tracking tasks because these approaches can achieve balance between accuracy and speed. In the pioneering work SiamFC [4], a simple yet effective tracking framework is proposed, which converts the tracking task to template matching using the similarity metric. This framework can be easily combined with other techniques. Some real-time trackers [5, 6] have been proposed to improve the accuracy using various techniques. Along with this line, a recently proposed tracker SiamRPN++ [7] has achieved significant improvement of accuracy and high speed (25 FPS in Titan X GPU) by applying a region proposal network (RPN) to directly regress the position and scale of objects. This method is likely to become the next baseline to further improve the performance real-time tracking due to its high speed and impressive accuracy.

Despite being studied extensively with remarkable progresses achieved, the Siamese network-based visual trackers generally faces a conflict between the high memory cost and the strict constraints on memory budget in real-world applications, especially for SiamRPN++ whose model size is up to 206.11 MB. The high memory cost makes these methods of Siamese network undesirable in practical mobile visual tracking applications, such as the accurate trackers running real time on a drone. How to reduce the memory cost of Siamese trackers without remarkable loss of the tracking accuracy is one of the key issues that need to be addressed in order to put the academic algorithms into practical applications. Furthermore, by reducing the model size, the computational cost will be will directly decreased, which can produce a faster tracker.

To address this issue, we propose a method to achieve both great performance and high speed of convolutional layers. To this end, we introduce multiplexing convolution, which can improve the efficiency of DW-convolution [8] or group-wise convolutional layers by reducing their MACCs. Multiplexing convolution uses two components to achieve this purpose: spatial multiplexing operation and channel multiplexing operation. Our spatial multiplexing utilizes the spatial shuffle to extract the feature map, process the feature information through the group-wise convolution layers and then assemble the feature map back together. While our channel multiplexing operation is inspired by the channel shuffle operation of ShuffleNet [9]. This component is designed to enhance the flow of information between channels by using the shuffle operation. Jointly, these two components can boost the information



fusion ability of model in different dimensions, and mitigate the burden of MACC computation in our network.

The main contributions of this work are twofold. (1) We combine the two operations of spatial multiplexing and channel multiplexing, and propose a new lightweight block called the multiplexing convolution block. Then, we build a new backbone based on this block and apply it to a Siamese tracker. (2) We trained this new Siamese network on the Tiny-ImageNet and COCO2017 datasets, achieved the compression rates of more than  $4.8\times$  and speedup of  $3.3\times$ , and only lost 3% of expected average overlap (EAO) compared with the baseline method.

## 29.2 Related Work

In this section, we review related work on the Siamese trackers and the multi-scale mechanism.

**Siamese Trackers:** SINT [1] and SiamFC [4] firstly applied the Siamese networks to train a similarity metric between the target and the candidate images. Then, to improve the detection accuracy, SiamRPN [10] introduced a region proposal network (RPN), which was derived from the Faster R-CNN [11]. SiamRPN can capture the scale changes with the anchor boxes. SiamRPN and the previous networks can only use shallow network like AlexNet [12]. Recently, SiamRPN++ [7] was proposed, which allows the Siamese trackers to utilize deeper backbone networks by changing the sampling method, such as ResNet [13]. Siam-Mask [14] incorporates segmentation into tracking because the rectangular bounding box has limited the accuracy. Our work is related to SiamRPN++, and this network can be integrated into our backbone.

**Multi-scale:** Different forms of multi-scale processing have been utilized in the convolutional neural networks, including the multi-resolution feature maps designed for object detection [15], CondenseNet [16] with multi-scale processing. These method has enhanced predictive ability for large models. In contrast, our multiplexing convolution method uses multi-scale processing to enhance the ability of information fusion in a lightweight model, which can be deployed in environments with constrained resources. Notably, multiplexing convolution uses a pixel operation similar to subpixel convolution in [17] to change the feature maps. The channel shuffle component is inspired by [18].

## 29.3 Methodology

We designed a new fully convolutional lightweight backbone for our Siamese network. As shown in Fig. 29.1, the proposed framework consists of a multiplexing convolution backbone for feature extraction and two branches for classification and regression. This backbone is composed of four components: normal convolution,

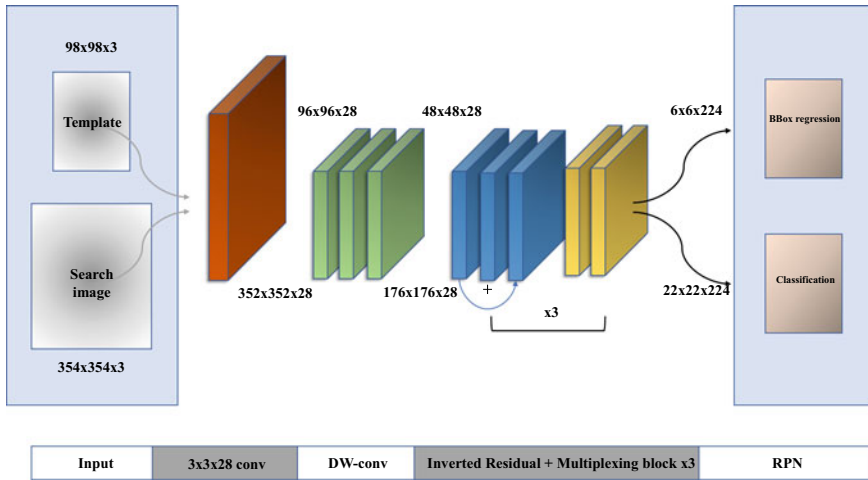


**Fig. 29.1** Multiplexing Siamese framework (MPSiam)

depth-wise separable convolution inverted residual bottleneck, and multiplexing convolutional block.

### 29.3.1 Spatial Multiplexing Operation

The spatial multiplexing operation is a three-dimension scaling operation, which maps the spatial information into multi-scale channels. Specifically, given a feature map  $x \in R^{C \times H \times W}$ , the channels are divided into three groups of  $(C_1, C_2, C_3)$ , such that  $C = C_1 + C_2 + C_3$ . A sub-operation (sub-op) is carried out for the first part of channels, and the third part is subject to a super-operation (super-op). We define sub-op as follows: we parameterize the sub-op by  $r$ . The feature maps are mapped to  $r^2$  channels. Each  $r \times r$  window matches a unique location. Generally, the sub-op maps the first part of size  $C \times H \times W$  to features of size  $r^2 C \times \frac{H}{r} \times \frac{W}{r}$ . Then, we define super-op in the same way: super-op maps the third part of size  $C \times H \times W$  to features of size  $\frac{C}{r^2} \times rH \times rW$ . Super-op is the reverse operation of sub-op. These operations enable the down-scaled and up-scaled spatial information to be multiplexed with the channel information. Then, the three parts are convolved separately by a group convolution. The output feature maps are reshaped back to the same dimensions as the input feature maps by reversing sub-op or super-op. Full view of spatial multiplexing operation is shown in Fig. 29.2a. Collectively, these two operations enable the flow of spatial information across channels through pixel manipulation.

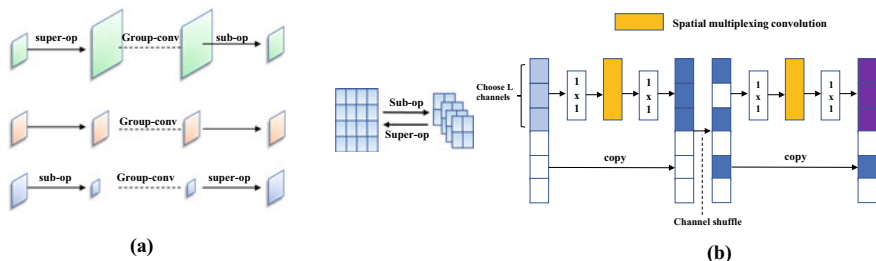


Fig. 29.2 **a** Spatial multiplexing operation. **b** Multiplexing block

### 29.3.2 Channel Multiplexing Operation

Spatial multiplexing operation is effective, but it still has some limitations. Firstly, the group convolution has higher computational complexity than the depth-wise separable convolution which it replaces. Secondly, information cannot flow across groups when group convolution is used. To overcome these drawbacks, we designed the channel multiplexing operation to reduce the computational burden of spatial multiplexing. We achieved it in two steps, namely selective processing and channel shuffling. An illustration of this operation is shown in Fig. 29.2b. Our method is different from ShuffleNet on two aspects: (1) ShuffleNet shares the processed channel information in different groups using shuffling, but we use shuffling to blend both the unprocessed and processed channel information. (2) We choose  $L$  channels ( $L$  is a hyperparameter) to split, instead of choosing half of the channels like in ShuffleNet.

## 29.4 Experiments

### 29.4.1 Implementation Details

**Training and Testing:** Our network backbone was pretrained on a subset of Tiny-ImageNet (20 classes) to provide good initialization for other tasks. When we trained the backbone for classification, we changed the stride of first convolutional layer into 2 to fit the input size of  $224 \times 224$ . The last block will output a feature map of  $7 \times 7 \times 224$ . Then, we added a fully connected layer after this block for classification. This model converged well within 80–100 epochs, which was adopted in the subsequent object tracking task. Next, we changed the stride of first convolutional layer into 1, and used two branches (the classification branch and regression branch) instead of the fully-connected layer. We trained the complete network on the COCO2017 dataset, and enabled the network to measure the similarities between the target and searched images. We used 98 pixels for the template object and 354 pixels for the searching regions. For evaluation, we focused on the short-term single object tracking

on OTB2015 and VOT2018. Then, the backbone of SiamRPN++ [17] was replaced with the proposed backbone to demonstrate the performance our method, while the other settings were the same as in SiamRPN++.

### 29.4.2 Comparison and Ablation Study

**Result on VOT2018:** The VOT2018 dataset is the best-known dataset in the field of single object tracking, which includes 60 video sequences with different challenging goals. Following the evaluation protocol of VOT2018, we adopt the Expect Average Overlap (EAO), Accuracy ( $A$ ), and Robustness ( $R$ ) as the criteria to compare the performances of different trackers. The details are listed in Table 29.1. The model size and FPS are shown in Table 29.2. The reported FPS is evaluated on a machine with a single NVIDIA 2080Ti GPU. From the two tables, we observe that our method has a smaller model size and a higher efficiency than the ResNet-based and MobileNet-based Siamese Networks, and MPSiam just lost 3% EAO compared to ResNet-Siam and 1.5% EAO compared to MobileNetv2-Siam.

**Result on OTB2015:** OTB2015 consists of approximately 100 video sequences. It has two evaluation criteria: precision and success rate. We define the precision as the proportion of frames with tracking results of 20 pixels within the target in the total frames, and we define the success rate the proportion of the frames with larger overlap than current threshold in the total frames when the overlap threshold changes from 0 to 1. In both the success plot and precision plot, the Area Under Curve (AUC) is used to evaluate the performances of algorithms. Figure 29.3 shows the success plot and precision plot.

**Ablation Study:** We tested the cases without spatial multiplexing (SM) and without channel shuffling (CS) on VOT2018. DW-conv was used to replace spatial multi-

**Table 29.1** Result on VOT2018

	$A$	$R$	EAO
Resnet50-Siam	0.601	0.234	0.415
MobileNetv2-Siam	0.586	0.229	0.410
MPSiam (ours)	0.591	0.236	0.404

**Table 29.2** Result on VOT2018

	Size	FPS (MB)	MACC (B)
Resnet50-Siam	206	25	4.5
MobileNetv2-Siam	58	55	1.2
MPSiam (ours)	43	83	0.5

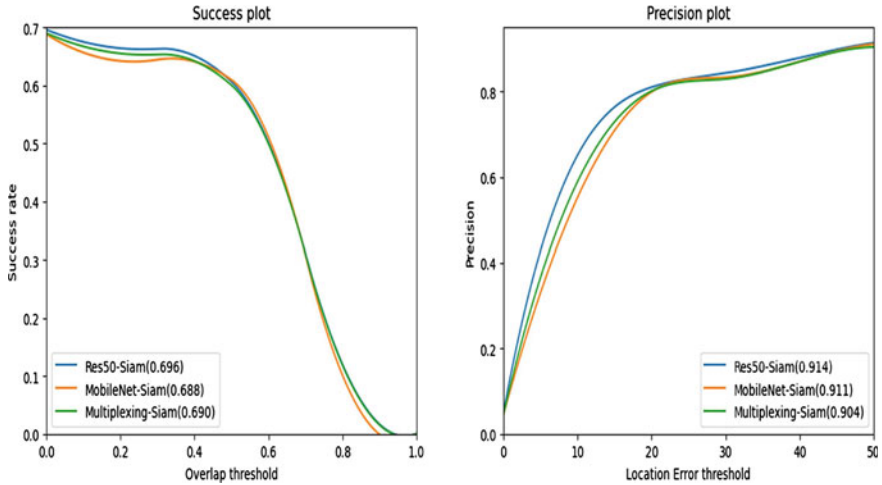


Fig. 29.3 Success and precision plot

Table 29.3 Ablation study

	MACC (B)	FPS	EAO
MPSiam	0.5	83	0.404
MPSiam\SM	0.7	70	0.403
MPSiam\CS	1.0	59	0.411
MPSiam\SM\CS	1.2	40	0.408

plexing, no shuffling operation was used, and all channels were treated as the same. The results of ablation study are given in Table 29.3. According to the results, both the SM and CS operations have an impact on the MACC, and because CS can reduce the EAO, its speed-up effect is more obvious.

### 29.5 Conclusion

To compress and speed up the Siamese network, we propose the two operations of spatial multiplexing (SM) and channel shuffling (CS) which can effectively reduce MACC and combine them into a new block. Then, we build a backbone with this block for SiamRPN++ to infer the feature map efficiently. We achieved trade-off among the factors of accuracy, model size and speed. The experimental results suggest that our method is  $3.3\times$  faster than the typical ResNet-SiamRPN++, and ours compression rates reach  $4.8\times$ . Our model only has 0.5 B MACCs and just lost 3% EAO.

**Acknowledgements** The research was funded by Shenzhen Science and Technology Program (No. KCXFZ202002011007040), National Key Research and Development Program of China (No. 2019YFC0810704), and Key Area Research and Development Program of Guangdong Province (No. 2019B111102002).

## References

1. Lee, K.-H., Hwang, J.-N.: On-road pedestrian tracking across multiple driving recorders. *IEEE Trans. Multimedia* **17**(9), 1429–1438 (2015)
2. M. Odelga, P. Stegagno, N. Kochanek, H.H. Bühlhoff, A selfcontained teleoperated quadrotor: on-board state-estimation and indoor obstacle avoidance. In: *Proceedings of the IEEE International Conference on Robotics and Automation (ICRA)*, pp. 7840–7847 (2018)
3. Yuan, C., Liu, Z., Zhang, Y.: Aerial images-based forest fire detection for firefighting using optical remote sensing techniques and unmanned aerial vehicles. *J. Intell. Robot. Syst.* **88**(2–4), 635–654 (2017)
4. Bertinetto, L., Valmadre, J., Henriques, J.F., Vedaldi, A., Torr, P.H.: Fully convolutional Siamese networks for object tracking. In: *ECCV*, pp. 850–865 (2016)
5. Valmadre, J., Bertinetto, L., Henriques, J. F., Vedaldi, A., Torr, P.H.S.: End-to-end representation learning for correlation filter based tracking. In: *CVPR* (2017)
6. Huang, C., Lucey, S., Ramanan, D.: Learning policies for adaptive tracking with deep feature cascades. In: *ICCV* (2017)
7. Li, B. Wu, W., Wang, Q., Zhang, F., Xing, J., Yan, J. SiamRPN++: evolution of Siamese visual tracking with very deep networks. In: *CVPR*, pp. 4282–4291 (2019)
8. Chollet, F.: Xception: deep learning with depthwise separable convolutions. In: *IEEE Conference on Computer Vision and Pattern Recognition (CVPR)* (2017)
9. Zhang, X., Zhou, X., Lin, M., Sun, J.: Shufflenet: an extremely efficient convolutional neural network for mobile devices. In: *IEEE Conference on Computer Vision and Pattern Recognition (CVPR)* (2018)
10. Li, B., Yan, J., Wu, W., Zhu, Z., Hu, X.: High performance visual tracking with Siamese region proposal network. In: *CVPR* (2018)
11. Ren, S., He, K., Girshick, R., Sun, J.: Faster R-CNN: towards real-time object detection with region proposal networks. In: *International Conference on Neural Information Processing Systems*, pp. 91–99 (2015)
12. Krizhevsky, A., Sutskever, I., Hinton, G.E.: ImageNet classification with deep convolutional neural networks. *Adv. Neural Inf. Process. Syst.* **25**(2), 2012 (2012)
13. He, K., Zhang, X., Ren, S., Sun, J.: Proceedings of the IEEE Conference on Computer Vision and Pattern Recognition (CVPR), pp. 770–778 (2016)
14. Wang, Q., Zhang, L., Bertinetto, L., Hu, W., Torr, P.H.: Fast online object tracking and segmentation: a unifying approach. In: *CVPR* (2019)
15. Lin, T.-Y., Dollár, P., Girshick, R., He, K., Hariharan, B., Belongie, S.: Feature pyramid networks for object detection. In: *IEEE Conference on Computer Vision and Pattern Recognition (CVPR)* (2017)
16. Huang, G., Liu, S., Van der Maaten, L., Weinberger, K.Q.: Condensenet: an efficient densenet using learned group convolutions. In: *IEEE Conference on Computer Vision and Pattern Recognition (CVPR)* (2018)
17. Shi, W., Caballero, J., Huszár, F., Totz, J., Aitken, A.P., Bishop, R., Rueckert, D., Wang, Z.: Real-time single image and video super-resolution using an efficient sub-pixel convolutional neural network. In: *IEEE Conference on Computer Vision and Pattern Recognition (CVPR)* (2016)
18. Ma, N., Zhang, X., Zheng, H.-T., Sun, J.: Shufflenet v2: practical guidelines for efficient CNN architecture design. In: *European Conference on Computer Vision (ECCV)* (2018)

# Chapter 30

## A Single-Phase-to-Ground Fault Location Method Based on Deep Belief Network



Jia-Min Li, Shi-Jian Liu, Xiang Shao, and Jeng-Shyang Pan

**Abstract** When a single-phase-to-ground (SPG) fault occurs in a resonant grounding distribution system, the amplitude of the transient zero-sequence current waveform at the upstream detection node of the fault point is greater than the amplitude of the transient zero-sequence current waveform at the downstream detection node, and the two polarities are opposite. The transient zero-sequence currents at the detection nodes on the same side of the fault point are very similar. Based on this, the paper proposes a new method of SPG fault location based on a deep belief network (DBN). Firstly, this method uses the fault transient zero-sequence current waveform obtained from each detection node in the simulation model as the input of DBN, and the deep features of the fault signals are extracted. Secondly, the deep features are divided into upstream detection nodes category and downstream detection nodes category by a supervised classifier. And then, the fault location is implemented by analyzing the network structure of fault detection nodes. Finally, the testing results of the simulation data prove that the algorithm has high recognition accuracy under different fault grounding points, different initial phase angles of faults, different grounding resistances, and different types of faults, and has certain practical engineering application value.

---

J.-M. Li · S.-J. Liu · J.-S. Pan (✉)

College of Computer Science and Mathematics, Fujian University of Technology, Fuzhou, China  
e-mail: [jspan@ieee.org](mailto:jspan@ieee.org)

J.-M. Li

e-mail: [ljm113156@126.com](mailto:ljm113156@126.com)

S.-J. Liu

e-mail: [liusj2003@126.com](mailto:liusj2003@126.com)

X. Shao

College of Electrical Engineering and Automation, Fuzhou University, Fuzhou, China  
e-mail: [fjsdy158\\_shao@163.com](mailto:fjsdy158_shao@163.com)

J.-S. Pan

College of Computer Science and Engineering, Shandong University of Science and Technology, Qingdao, China

## 30.1 Introduction

In China, resonant grounding is widely applied in medium voltage distribution networks. When an SPG fault occurs, the coil will generate a corresponding inductive current to offset the capacitive current to earth caused by the fault to suppress the arc. However, the symmetrical relationship of the system phase-to-phase voltage still keeps symmetry, and it can be allowed to keep operating for 1–2 h [1]. However, the rise in the voltage of the non-fault phase will greatly threaten the insulation of the system and may cause insulation breakdown in severe cases. It is quite necessary to find the fault location and eliminate the fault in a short time. Therefore, it is important to further carry out the study of the SPG fault location of the resonant grounding distribution system.

The existing methods of SPG fault location can be divided into active location methods [2, 3] and passive location methods. Taking into account the equipment requirements, economy, and safety of operation, research on passive fault location is becoming more and more popular. The passive fault location methods are to analyze the fault characteristics of the fault original signal adopted by the zero-sequence current transformer, to complete the fault location without the injection equipment. Then, the passive location methods can be divided into location methods based on steady component [4, 5] and transient component [6–9] according to the different adopted fault signals. However, the transient component of the fault signal can be several times or even dozens of times larger than the steady component [10], and the fault location methods based on the fault steady component is easily affected by unbalanced current and transition resistance. Therefore, the location methods based on the fault transient component have become mainstream.

In [6], a 10 kV boundary switch controller based on the first half-wave method is designed, which judges the faults inside or outside the section, and realizes fault isolation according to the direction of zero-sequence voltage, zero-sequence current, and reactive power. In [7], a fault location method for radial distribution networks based on traveling wave and network theory is proposed. The method performs high accuracy in the testing. However, the actual traveling wave is difficult to obtain, which causes the method to perform a low actual application value. Paper [8] determines the fault section by comparing the similarity of the transient currents of the Feeder Terminal Units (FTU) at adjacent switches. If the two transient currents are very similar, the zone is regarded as a non-fault section; otherwise, it is regarded as a fault section. In [9], a method for SPG fault location based on multi-criteria clustering analysis is designed, which integrates zero-sequence current polarity, inherent modal energy, and the difference of phase current mutations to generate a set of fault features, and uses *K*-means clustering to cluster the obtained sets to realize the fault location.

With the progress and adhibition of the artificial intelligence technology, deep learning methods (such as expert systems, SVM [11–13], fuzzy theory [14, 15],



neural network [16, 17], etc.) are gradually applied to the study of SPG fault detection in distribution networks. The fault location process of the traditional fuzzy clustering method of features can be divided into artificially fault signal selecting, artificially mathematical analysis methods selecting, and artificially clustering methods selecting. However, the deep learning method can adaptively extract the fault features and realize intelligent classification, avoiding the shortcoming of a single fault feature selected artificially. DBN is one of the common deep learning methods, which has an unsupervised self-learning function.

Therefore, this paper provides a new method of SPG fault location based on DBN. The main contents of each chapter are planned as follows. Section 30.1 introduces the background and research status of SPG fault location. In Sect. 30.2, the simulation model of a 10 kV resonant grounding distribution system is introduced and its fault characteristics are analyzed. Section 30.3 introduces the basic theory and model structure of DBN and RBN in detail, as well as the network training process of DBN. In Sect. 30.4, a new method of SPG fault location based on DBN is proposed. Section 30.5 is to verify the method proposed in this paper under different conditions. Section 30.6 gives the conclusion.

### 30.2 Fault Characteristic Analysis

Power Systems Computer Aided Design (PSCAD) is electromagnetic transient simulation software widely used in the world. Electromagnetic Transients including DC (EMTDC) is the core of its simulation calculation, and PSCAD provides a graphical operation interface for EMTDC [18]. Therefore, PSCAD/EMTDC is used to build a 10 kV resonant grounding distribution system model, as shown in Fig. 30.1a, where  $O_L$  is the length of the overhead feeder,  $C_L$  is the length of the cable feeder, and  $R_f$  is the grounding resistance. The simulation network parameters and equipment selection are referenced in [19].

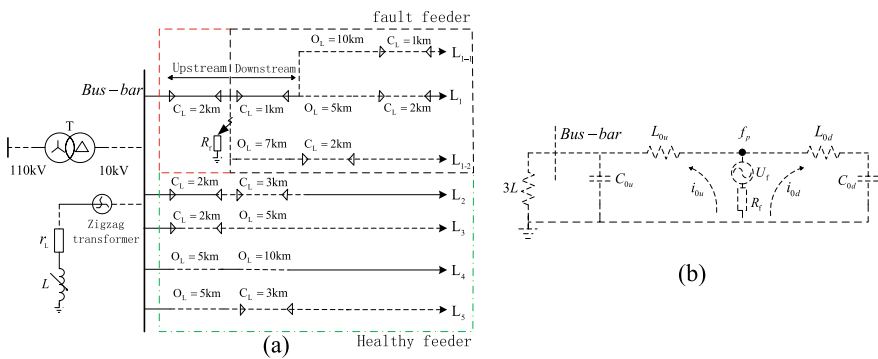


Fig. 30.1 Simulation model of a 10 kV resonant. a Simulation model. b Transient equivalent circuit

When an SPG fault occurs, its transient equivalent circuit is shown in Fig. 30.1b. Among them,  $f_p$ ,  $U_f$ , and  $R_f$ , respectively, represent the fault point, fault voltage, and fault transition resistance.  $i_{0u}$ ,  $L_{0u}$ , and  $C_{0u}$ , respectively, are the sum of the zero-sequence current, zero-sequence inductance, and zero-sequence distributed capacitance of the upstream feeder of the fault point and all healthy feeders.  $i_{0d}$ ,  $L_{0d}$ , and  $C_{0d}$ , respectively, are the sum of the zero-sequence current, zero-sequence inductance, and distributed capacitance of the downstream feeders of the fault point. The upstream and downstream feeders are displayed in the dotted frame in Fig. 30.1a.

Because the oscillation frequency of the transient process after the fault is high, the arc-suppression coil cannot immediately compensate for the fault transient zero-sequence current. At the moment, the transient zero-sequence current of the upstream detection node is the sum of the distributed capacitive currents of its upstream feeder and all healthy feeders, with a large amplitude, and the direction is from the feeder to the bus; the one of the downstream detection node or healthy feeder detection node is the sums of the capacitance currents of its downstream feeder, with a small amplitude, and the direction is from the bus to the feeder. Therefore, the amplitude of the transient zero-sequence current waveform at the upstream detection node is greater than the one at the downstream detection node, and the polarities are opposite [19]. But the transient zero-sequence current difference between the two detection nodes located on one side of the fault point is only the line-to-earth capacitive current between the two detection nodes, and the amplitude difference is small. Based on this, there is a big difference between the transient zero-sequence current of the upstream detection node and the transient zero-sequence current of the downstream detection node, while the transient zero-sequence currents of the detection node on one side of the fault point have similarities [20]. The detection node on the non-fault branch is classified as the downstream detection node.

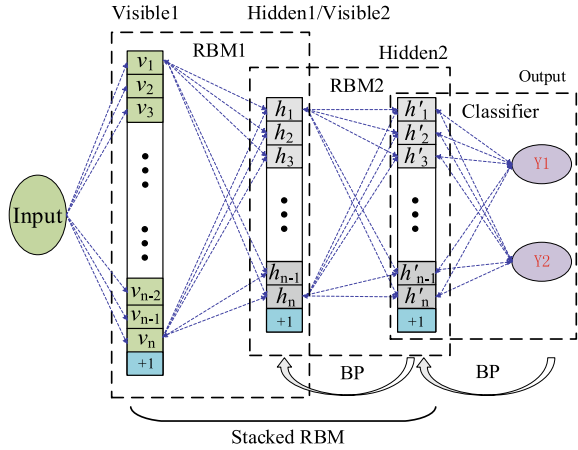
### 30.3 Deep Belief Network

In 2006, the Hinton research group proposed DBN in “Science” and optimized the connection weight and threshold of the DBN layer by layer through an unsupervised greedy learning algorithm. DBN can use the characteristics of its network structure to extract features from the original input to obtain a good feature expression. Its model is composed of multiple Restricted Boltzmann Machines (RBM) and a classifier.

#### 30.3.1 Structure of DBN

As shown in Fig. 30.2, this paper employs a four-layer DBN model, including two visible layers, two hidden layers, and one output layer, forming two stacked RBMs. The DBN algorithm includes two parts: network training and fault data testing. In the network training process, the original sample with labeled data is input into the visible

**Fig. 30.2** Structure diagram of DBN and RBM



layer of RBM1, and the deep features of the original sample are extracted, which are passed to the hidden layer of RBM1. The layer-by-layer RBM structure is realized by using the hidden layer of the previous layer as the input of the visible layer of the next layer. The hidden layer of RBM1 is as the input of the visible layer of RBM2, and a higher level of feature expression is obtained, which is passed to the hidden layer of RBM2. Then input the extracted features of the original sample into the supervised classifier, compare the classification results with the labels of the original sample, and propagate the error to each RBM through the Back Propagation Algorithm (BP) to realize the self-adjustment and optimization process of the parameter. When an SPG fault happens, input the collected fault signal into the trained DBN to quickly complete the classification for upstream and downstream detection nodes.

### 30.3.2 Structure of RBM

RBM is the main component of DBN. Each RBM contains a visible layer and a hidden layer. Both layers are composed of stochastic binary units. There is no connection between the units at the same layer. The units from different layers are connected through a weight matrix in both directions. Each unit has two states, active or inactive, represented by 1 or 0.

The activation state of RBM is determined by the energy function. The lower the energy, the higher the activation probability. Assuming that the visible layer of an RBM contains  $m$  units, the state is  $v_i$ , and the bias is  $a_i$  ( $i = 1, 2, 3, \dots, m$ ); the hidden layer contains  $n$  units, the state is  $h_j$ , and the bias is  $b_j$  ( $j = 1, 2, 3, \dots, n$ );  $W_{ij}$  is the weight matrix between the visible unit  $i$  and the hidden unit  $j$ , and the energy function is

$$E(v, h) = - \sum_{i=1}^m a_i v_i - \sum_{j=1}^n b_j h_j - \sum_{j=1}^n \sum_{i=1}^m w_{ij} v_i h_j \quad (30.1)$$

The joint probability distribution between the visible layer and the hidden layer is

$$p(v, h) = \frac{e^{-E(v, h)}}{Z} \quad (30.2)$$

Among them,  $Z = \sum_v \sum_h e^{-E(v, h)}$  is the normalization constant.

Because there is no interconnection between the RBM units at the same layer, and the units at different layers are connected in both directions,

$$\begin{cases} p(h|v) = \prod_j p(h_j|v) \\ p(v|h) = \prod_i p(v_i|h) \end{cases} \quad (30.3)$$

For an input signal  $v$ , the probability that the corresponding hidden unit  $h_j$  is activated is

$$P(h_j = 1|v) = \sigma \left( b_j + \sum_{i=1}^I w_{i,j} v_i \right) \quad (30.4)$$

In the formula, the activation function is the Sigmoid function,  $\sigma(x) = \frac{1}{1+e^{-x}}$ .

Due to the bidirectional connection between layers, the visible unit can also be activated by the hidden unit, and the state of each visible unit  $v_i$  is reconstructed as

$$P(v_i = 1|h) = \sigma \left( a_j + \sum_{j=1}^J w_{i,j} h_j \right) \quad (30.5)$$

Therefore, the update of weight and bias between the visible layer and the hidden layer of the RBM is as follows

$$W^{(1)} = W^{(0)} + \lambda [P(h^{(0)} = 1|v^{(0)})v^{(0)T} - P(h^{(1)} = 1|v^{(1)})v^{(1)T}] \quad (30.6)$$

$$b^{(1)} = b^{(0)} + \lambda [P(h^{(0)} = 1|v^{(0)}) - P(h^{(1)} = 1|v^{(1)})] \quad (30.7)$$

$$a^{(1)} = a^{(0)} + \lambda [v^{(0)} - v^{(1)}] \quad (30.8)$$

Among them,  $\lambda$  is the learning rate,  $a^{(0)}$ ,  $b^{(0)}$ ,  $W^{(0)}$ ,  $v^{(0)}$ ,  $h^{(0)}$  are the parameters before the update, and  $a^{(1)}$ ,  $b^{(1)}$ ,  $W^{(1)}$ ,  $v^{(1)}$ ,  $h^{(1)}$  are the updated data.

### 30.3.3 Forward Iteration and Back Propagation

The training process of DBN is completed by tuning training for each RBM individually. Taking RBM1 as an example, its tuning training needs to use forward iteration to obtain a certain output value from the input, and then use the output value to reconstruct the input value [21].

The forward iteration is as follows

$$h = \sigma(W * v + b) \quad (30.9)$$

$$v' = \sigma(W^T * h + a) \quad (30.10)$$

where  $v'_1$  is the visible layer state after reconstruction.

The BP algorithm with the Minimization Criterion of Mean-Square Error (MMSE) is utilized to update the parameters of the entire network. The iterative termination condition of RBM1's training is that the number of iterations exceeds 200 or  $\text{Cost}(x, y)$ , the error cost function, is less than the set threshold  $10^{-3}$ .

$$\text{Cost}(v, v') = \frac{1}{n} \sum_{i=1}^n |v_i - v'_i|^2 \quad (30.11)$$

Then, the reverse error propagation of the entire DBN is as follows

$$W^l = W^{l-1} - \lambda \frac{\partial \cos T}{\partial (W^{l-1})} \quad (30.12)$$

$$a^l = a^{l-1} - \lambda \frac{\partial \cos T}{\partial (a^{l-1})} \quad (30.13)$$

$$b^l = b^{l-1} - \lambda \frac{\partial \cos T}{\partial (b^{l-1})} \quad (30.14)$$

## 30.4 The SPG Fault Location Method

When an SPG fault is detected in the system, the DBN with self-learning fault features is used to extract the deep characteristics of the first cycle transient zero-sequence current waveform from each detection node. Then, the deep features are distinguished by a supervised classifier. Therefore, the upstream and downstream detection nodes of the fault point are divided into two categories, and the fault location is selected.

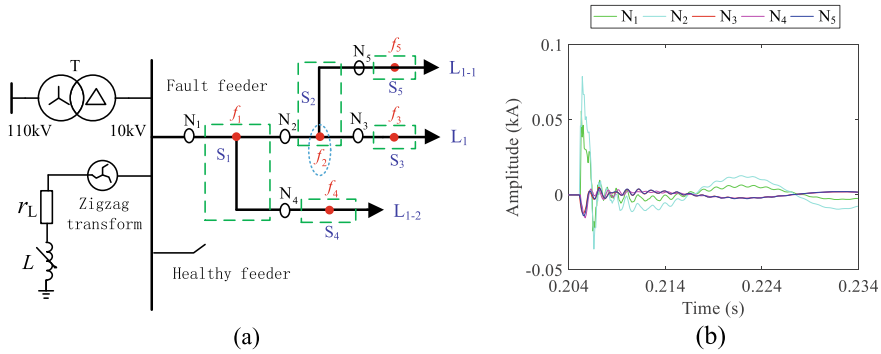


**Fig. 30.3** An SPG fault in a 10 kV resonant grounding system. **a** Simplified simulation model. **b** Transient zero-sequence current waveform of each detection node

### 30.4.1 Acquisition of Transient Zero-Sequence Current Waveform

As shown in Fig. 30.3a, for the convenience of explanation, take the installation of 5 detection nodes on line 1 as an example, which is divided into 5 sections, namely  $S_i, i = 1, 2, \dots, 5$ . Each section is set to 1 fault point  $f_i, i = 1, 2, \dots, 5$ .

When the SPG fault occurs in phase A, the fault point is  $f_2$ , the initial phase angle of the fault is  $60^\circ$ , the fault grounding resistance is  $100 \Omega$ , and the fault transient zero-sequence current at each detection node is shown in Fig. 30.3b. As demonstrated in the figure, the amplitude of the transient zero-sequence current waveforms at the upstream detection nodes  $N_1$  and  $N_2$  of the fault point is greater than the ones at the downstream detection nodes  $N_3, N_4$ , and  $N_5$ . And the polarities of the two are almost opposite. At the same time, the similarity between the transient zero-sequence current waveforms of the detection nodes ( $N_1, N_2$ ) or ( $N_3, N_4, N_5$ ) on the same side of the fault point is high, which is consistent with the theoretical analysis results.

### 30.4.2 DBN-Based Feature Extraction and Classification of Fault Waveform

Through a large amount of experimental data testing and verification, it is determined that the DBN model adopts a two-layer stacked RBM model, which contains 2 visible layers, 2 hidden layers, and an output layer. The parameter configuration for each layer is shown in Table 30.1.

The fault transient zero-sequence current waveform at each detection node is normalized by Eq. (30.15) and used as the input of DBN. After repeated iterative of RBM1 and RBM2, the reconstructed output waveform is infinitely close to the input waveform. Then obtain the features of the transient zero-sequence current waveform

**Table 30.1** Parameter configuration of the DBN

Model	Number of nodes	Learning rate	Number of batch training
$V_1$	200	0.005	10
$H_1/V_2$	50		
$H_2$	50		
Output	2		

of each detection node from the hidden layer of RBM2, and input them into the classifier to realize intelligent classification.

$$(x_i^j)' = \frac{x_i^j - \min\{X\}}{\max\{X\} - \min\{X\}} \tag{30.15}$$

Among them,  $X = \{X^1, X^2, \dots, X^j, \dots, X^N\}$  is the data set of fault transient signals from all detection nodes.  $X^j$  ( $j = 1, 2, \dots, N$ ) is the transient zero-sequence current of the  $j$ -th detection node.  $N$  is the number of detection nodes.  $x_i^j$  is the  $i$ -th element of  $X^j$ .

### 30.4.3 Judgment Basis for Fault Location

As shown in Fig. 30.4a, there is no branch in the section between detection nodes  $N_1$  and  $N_2$ . If the classification result determines that  $N_1$  is the upstream detection node and  $N_2$  is the downstream detection node, the fault occurs in  $S_1$ . The section between  $N_2, N_3$ , and  $N_4$  is at the branch of the line. If it is determined that the fault occurs in  $S_2$ , the classification result needs to be judged that  $N_2$  is the upstream detection node and  $N_3, N_4$  are both judged as the downstream detection nodes. For the end sections  $S_3$  and  $S_4$ , only  $N_3$  or  $N_4$  needs to be judged as the upstream detection node.

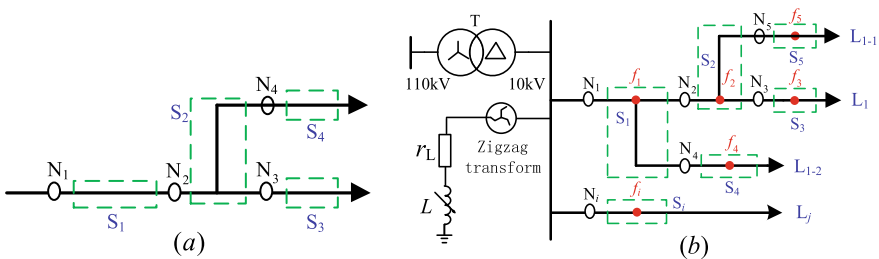


**Fig. 30.4** Judgment and verification for fault location. **a** Schematic diagram of fault location. **b** Schematic diagram of fault detection nodes installation and section division

**Table 30.2** Test results of software simulation data

	$f_i$	$\theta$ ( $^\circ$ )	$R_f$ ( $\Omega$ )	$T_n$	$C_n$	$\varphi$ (%)
Training data	$f_1-f_9$	0, 30, 60, 90	0, 10, 100, 1000	144	/	/
Testing data	$f_1-f_9$	10, 20, 40, 50, 70, 80	0, 10, 100, 1000	216	216	100
	$f_1-f_9$	0, 30, 60, 90	0, 50, 500, 5000	144	144	100
	$f_1-f_9$	20, 50, 80	0, 200, 1000	81	81	100

According to the judgment basis of the fault section location, the identification result of the fault example in this paper is  $S_2$ , which is consistent with the actual situation.

### 30.5 Verification by Software Simulation

As displayed in Fig. 30.4b, in order to ensure the adaptability of the proposed algorithm, a detection node  $N_i$  ( $i = 6, 7, 8, 9$ ) is set on each line  $L_j$  ( $j = 2, 3, 4, 5$ ). In the simulation model of the 10 kV resonant grounding distribution system, different fault grounding points, different initial phase angles of faults, different fault grounding resistances, and different types of faults are simulated. The results of the proposed algorithm are shown in Table 30.2. It can be seen that the proposed algorithm has higher recognition accuracy, which has certain practical engineering application value.

In the table,  $f_i$  is the fault point,  $\theta$  is the initial phase angle of fault,  $R_x$  is the grounding resistance, and  $\varphi$  represents the accuracy of the location method, as shown in Eq. (30.16).

$$\varphi = \frac{C_n}{T_n} \times 100\% \quad (30.16)$$

where  $C_n$  is the number of the faults correctly located, and  $T_n$  is the total number of the faults.

### 30.6 Conclusion

The DBN is used in the research of fault location and performs a higher accuracy rate. The test results of different fault types under software simulation show that:

- (1) The DBN with self-learning fault characteristics can adaptively extract the SPG fault signal characteristics, avoid the manual feature selection and classifier selection required by traditional fault location methods.



- (2) The DBN can better distinguish the upstream detection node and the downstream detection node, and improve the similarity between the transient zero-sequence current waveforms from the detection nodes at the same side.
- (3) Due to the ideal situation of the software simulation model, it is difficult to prove the adaptability of the proposed algorithm in the field. Therefore, the algorithm proposed in this paper still needs to be further tested by actual field fault data.

**Acknowledgements** This work is supported by the National Natural Science Foundation of China (No. 61872085), Collaborative Education Program of Industry and Education of Ministry of Education (No. 201901052008), Scientific Research Project of Fujian Education Department (No. JAT190069, No. JK2017029), and Scientific Research Project of Fujian University of Technology (No. XF-X19017).

## References

1. Zhang, S., He, Z.-Y., Lin, S., et al.: Fault location based on charge and discharge transient characteristic of the single-phase fault in the resonant grounding system. *Power Syst. Prot. Control* **41**(9), 13–20 (2013)
2. Qi, Y.-L., Zhao, J.-Y., Du, Q.-S.: Research on location of single-phase earth fault based on pulse injection method in distribution network. In: 2009 9th International Conference on Electronic Measurement and Instruments. IEEE (2009)
3. Li, Z.-T., Ye, Y.-Q., Ma, X., et al.: Single-phase-to-ground fault section location in flexible resonant grounding distribution networks using soft open points. *Int. J. Electr. Power Energy Syst.* **122**, 106198 (2020)
4. Orozco-Henao, C., Bretas, A.S., Chouhy-Leborgne, R., et al.: Active distribution network fault location methodology: a minimum fault reactance and fibonacci search approach. *Int. J. Electr. Power Energy Syst.* **84**, 232–241 (2017)
5. Grajales-Espinal, C., Mora-Flórez, J., Pérez-Londoño, S., et al.: Advanced fault location strategy for modern power distribution systems based on phase and sequence components and the minimum fault reactance concept. *Electr. Power Syst. Res.* **140**, 933–941 (2016)
6. Liu, M.-Y., Lv, L.-P., Ding, D., et al.: Study of the small current neutral grounding fault based on TDFT sampling method of first half wave. *Electr. Meas. Instrum.* **55**(23), 22–33 (2018)
7. Dwivedi, A., Yu, X.-H.: Fault location in radial distribution lines using travelling waves and network theory. In: 2011 IEEE International Symposium on Industrial Electronics. IEEE (2011)
8. Li, T.-Y., Xue, Y.-D., Li, J.-J.: A New Single Phase Fault Location Method of Noneffectively Grounded Networks for DA Systems, pp. 0582–0582 (2013)
9. Lu, S.-Y., Ding, X.-H., Su, B.-L.: A novel location method for single-phase grounding fault in small current grounding distribution network based on difference of phase current fault component between fault and non-fault phases. In: 2020 IEEE Texas Power and Energy Conference (TPEC). IEEE (2020)
10. Li, J.-P., Zhang, G.-Q., Li, H.-B., et al.: A review of fault location methods for small current grounding systems. *IOP Conf. Ser. Mater. Sci. Eng.* **677**(5) (2019)
11. Li, Y.-F., Li, J.-B., Pan, J.-S.: Hyperspectral image recognition using SVM combined deep learning. *J. Int. Technol.* **20**(3), 851–859 (2019)
12. Gao, F.-Y., Hsieh, J.-G., Jeng, J.-H.: A study on combined CNN-SVM model for visual object recognition. *J. Inform. Hiding Multimedia Sig. Process.* **10**(4), 479–487 (2019)

13. Song, Q., Qin, T.: Load forecasting based on wavelet submodel and LS-SVM. *J. Netw. Intell.* **5**(3), 102–112 (2020)
14. Pan, J.-S., Chu, S.-C., Dao, T.-K., et al.: Improved performance of wireless sensor network based on fuzzy logic for clustering scheme. In: *VTCA 2018*, pp. 104–113
15. Tu, T.N., Hoang, H.N., Van, T.V., et al.: Enhancing remote sensing image contrast based on combination of fuzzy logic and local approach. *J. Inf. Hiding Multimedia Sig. Process.* **10**(4), 488–499 (2019)
16. Hu, P., Pan, J.-S., Chu, S.-C., et al.: New hybrid algorithms for prediction of daily load of power network. *Appl. Sci.* **9**, 4514 (2019)
17. Pan, J.-S., Pei, Hu., Chu, S.-C.: Novel parallel heterogeneous meta-heuristic and its communication strategies for the prediction of wind power. *Processes* **7**(11), 845 (2019)
18. Woodford, D., Irwin, G., Gudmundsdottir, U.S.: PSCAD/EMTDC. In: *Numerical Analysis of Power System Transients and Dynamics*, pp. 135–167. IET (2015)
19. Guo, M.-F., Yang, N.-C.: Features-clustering-based earth fault detection using singular-value decomposition and fuzzy *C*-means in resonant grounding distribution systems. *Int. J. Electr. Power Energy Syst.* **93**, 97–108 (2017)
20. Xie, W., Wang, X.-W., Zhang, H.-X., et al.: Application case of transient energy method in location of single phase to ground fault. In: *2020 IEEE/IAS Industrial and Commercial Power System Asia (I&CPS Asia)*. IEEE (2020)
21. Fan, Q.-W., Guo, Y.-L., Shao-En, Wu., et al.: Two-level diagnosis of heating pipe network leakage based on deep belief network. *IEEE Access* **7**, 182983–182992 (2019)

# Chapter 31

## A Data Fusion Scheme in Wireless Sensor Network Based on Optimizing Parameters of Neural Network



Thi-Kien Dao, Trong-The Nguyen, Van-Dinh Vu, and Truong-Giang Ngo

**Abstract** This study suggests a scheme of data fusion strategy in wireless sensor networks (WSNs) based on optimizing the neural network (NN) to decrease data redundancy, increase data transmission, and save communication energy consumption in WSN. The optimal parameters are optimized by applying the bat algorithm (BA). The optimized neural network (NNBA) is used to fuse captured data in cluster head (CH) and then forwards the combined data to the base station (BS) of a WSN. The simulation experiment is implemented in several scenarios to test the proposed scheme performance. The proposed scheme's results show that the proposed algorithm can save sensor node energy consumption, extend the lifetime, and increase the data fusion accuracy of WSN.

### 31.1 Introduction

A multi-hop wireless sensing network consisting of several sensor nodes is a wireless sensor network (WSNs) [1]. It is commonly used in national military and defense, monitoring hospital health, monitoring atmosphere, industrial and marine applications [2]. The correlation and redundancy of data are extreme since the monitoring

---

T.-K. Dao · T.-T. Nguyen (✉)

School of Computer Science and Mathematics, Fujian Province, Fujian University of Technology, Fuzhou 350118, China

e-mail: [thent@uit.edu.vn](mailto:thent@uit.edu.vn)

T.-T. Nguyen

Multimedia Communications Lab, University of Information Technology, VNU-HCM, Ho Chi Minh City, Vietnam

V.-D. Vu

Information Technology Faculty, Electric Power University, Hanoi, Vietnam

e-mail: [dinhvv@epu.edu.vn](mailto:dinhvv@epu.edu.vn)

T.-G. Ngo

Faculty of Computer Science and Engineering, Thuyloi University, Hanoi, Vietnam

e-mail: [giangnt@tlu.edu.vn](mailto:giangnt@tlu.edu.vn)

range of sensor nodes overlaps with each other [3], contributing to the energy waste of base station (BS) nodes [4] and affecting the lifespan of the network [5]. Many researchers have done a lot of in-depth research on WSN data fusion routing algorithms and obtained some research results to increase energy usage and reduce energy consumption [3, 6].

Data fusion schemes for WSNs are primarily divided into cluster-based data fusion and data fusion for tree-based data [7, 8]. The former, the cluster-based data fusion algorithms, such as LEACH [9], TEED [10], and routing algorithms, are primarily used in cluster-based data fusion [6]. The cluster-based data fusion scheme offers the benefits of node comfort. The management and node cooperation complexity are low, but the cluster's maintenance cost is high [11]. The latter, tree-based data fusion, is difficult to construct an optimal data fusion tree [4].

In addition, intelligent algorithms are primarily used to build the purchase and selling number of data fusion, such as genetic algorithm (GA) [12]. It is predominantly suitable for acquiring and monitoring small static network data but requires a lot of energy and a low-efficiency network for a large-scale network [13]. Some scholars are trying to apply the neural network to the data fusion application of WSN with the development of the artificial intelligence algorithm and have achieved good results [14]. However, the network weight and threshold significantly influence the BP neural network in practical implementation [15].

Bat algorithm (BA) is a new metaheuristic of swarm intelligence algorithms that can dynamically control the conversion process between local search and global search, avoid the algorithm falling into local optimum, and have better convergence [16]. In order to reduce the amount of data transmitted by sensor nodes, the utilization rate of node energy could be improved, the survival time of WSN would be prolonged, and a data fusion strategy is proposed based on applied BA for neural optimization network (NN-BA).

## 31.2 Energy Consumption Model of Wireless Sensor

According to the node perceived energy model, the node energy consumption is analyzed, and the energy consumption formula of node packet transmission is defined as

$$E_{\text{send}} = E_{\text{trans}} \times l + E_{\text{amp}} \times d^2 \quad (31.1)$$

where  $E_{\text{trans}}$  is the total energy consumption of transmitting 1-bit data,  $l$  is the size of data packets sent by sensing nodes,  $E_{\text{amp}}$  is the circuit loss after signal amplification, and  $D$  is the communication distance between sensing nodes.

The energy consumption formula of received signal is as follows:

$$E_{\text{receive}} = E_{\text{rec}} \times m \quad (31.2)$$

Here,  $E_{rec}$  represents the energy consumed by receiving 1 bit, and  $M$  represents the number of packets sent by the node.

### 31.3 Optimizing Backpropagation NN with Bat Algorithm

#### 31.3.1 Backpropagation Neural Network

The neural network (NN) of backpropagation (BP) is a kind of multilayer feedforward NN that has the input, hidden, and output layers [15]. It means that the upper and lower layers are fully connected with the error backpropagation used to train a multilayer feedforward network. The figure's neural network has  $n$  input nodes,  $j$  output nodes, and  $k$  neurons in the hidden layer.  $x_1, x_2, \dots, x_n$  is the actual input of the network,  $y_1, y_2, \dots, y_j$  is the actual output of the network, the connection weight from  $x_n$  to  $R_i$  is  $w_{ni}$ , the connection weight from  $R_i$  to  $y_j$  is  $w_{ij}$ , the transfer functions can be such as the sigmoid or tan functions. A linear function is the transfer function of the output layer. The gradient steepest descent approach is the basic concept of the BP learning algorithm, and the fundamental idea is to change the weight to make the network. The complex's total error is the lowest.

#### 31.3.2 Bat's Algorithm

The bat's echolocation algorithm is used to optimize the numerical problems through echolocation of bats [16]. Assuming that the location of the  $i$ th individual bat at time  $t$  is  $x_i^t$  and the velocity is  $v_i^t$ , then the updating formula of position  $x_i^{t+1}$  and position  $v_i^{t+1}$  at time  $t + 1$  is expressed [16].as follows

$$Q_i = Q_{\min} + (Q_{\max} - Q_{\min})\beta \quad (31.3)$$

$$v_i^{t+1} = v_i^t + (x_i^t - x_*)Q_i \quad (31.4)$$

The frequencies of updating the speed equation of the bat algorithm are expressed as follows

$$v_i^{t+1} = wv_i^t + (x_* - x_i^t)Q_i \quad (31.5)$$

where  $Q_1$ ,  $Q_{\max}$ , and  $Q_{\min}$  are the frequencies of the sound waves emitted by the  $i$ th bat and the maximum and minimum values of the frequency, respectively;  $\beta$  is the number generated randomly between 0 and 1;  $x_*$  is the current global optimal solution.

$$x_i^{t+1} = x_i^t + v_i^{t+1} \quad (31.6)$$

Once the optimal solution is produced, the new position of the individual bat is as follows:

$$x''(i) = x' + \varepsilon AV^t \quad (31.7)$$

where  $x'$  is a randomly selected solution from the current optimal solution,  $AV^t$  is the average loudness of bat population, and  $\varepsilon$  is a random vector between  $-1$  and  $1$ .

The loudness  $a(1)$  and emission rate  $R(1)$  in BA are updated with the iteration.

$$A^{t+1}(i) = \alpha A^t(i) \quad (31.8)$$

$$R^{t+1}(i) = R_0(i) \times [1 - \exp(-\gamma t)] \quad (31.9)$$

### 31.3.3 Optimizing Backpropagation NN with Bat Algorithm

The downside of slow convergence speed and easy to fall into optimal local solution is the conventional BP neural network algorithm. The initial neural network parameters decide performance experience accuracy. For this reason, BA is used to refine the BP neural network's structure and parameters to solve this problem, which can increase the convergence speed of the BP neural network and solve the shortcomings of the conventional BP neural network.

Assuming that the monitoring node  $i$  sends the collected initially data to node  $j$ , the correlation coefficient of the collected data node is defined as

$$\rho(i, j) = 1 - H(i|j)/H(j) \quad (31.10)$$

where  $H(i)$  is the size of data packets sent by sensing node  $i$ , and  $H(i, j)$  is the size of data volume after data fusion. The data fusion model is based on the typical inversion model, which assumes that the correlation of the collected data is inversely proportional to the distance between the nodes, but the Gaussian random field model in other data fusion models considers that the correlation between the data and the distance between nodes is exponentially decreasing, and the mathematical relationship is as follows.

$$\rho(i, j) = \exp(-\alpha d^2(i, j)) \quad (31.11)$$

Among them,  $\alpha$  is the correlation coefficient. The greater the  $\alpha$  is, the smaller the correlation of the data is, and on the contrary, the greater the correlation.

The details are as follows.

- (1) Initialization parameters of bat population: the number of bats  $m$ , the maximum pulse frequency  $R(i)$  and the maximum pulse sound intensity  $a(i)$  of the individual bat  $i$  were set, and the increase coefficient of bat frequency was set as  $\gamma$ , the attenuation coefficient of sound intensity  $\alpha$ , the maximum iteration number  $nmax$  and the search accuracy  $\epsilon$ ;
- (2) The position of bat individuals was randomly initialized  $x(i = 1, 2)$ . Besides, individuals of  $X^*$  bats in the best position were searched;
- (3) Generate random number  $R1$ , if  $R1$  is less than  $R(i)$ , update the bat's current position according to formula (31.4); otherwise, disturb the bat's current position, and the disturbing position will replace the current position;
- (4) If  $R2$  is less than  $a(i)$  and the bat's current position is optimized and changed, the bat will fly to the updated position;
- (5) If the bat individual  $i$  is better than the best bat in the individual, the best bat individual should be replaced, and the pulse frequency  $R1$  and pulse intensity  $a(i)$  should be adjusted according to Eqs. (31.8) and (31.9);
- (6) To find out the best position of bats and the best time of their running;
- (7) If the preset search precision is satisfied or the maximum search times are reached, then turn to step (8), otherwise turn to step 3, and then search for the optimal individual;
- (8) The optimal global solution and optimal individual value of the output function are used as the weights and thresholds of the BP neural network;
- (9) Judge whether the ending conditions are met. Suppose the number of iterations reaches the given BP neural network's preset maximum value or meets the minimum error requirement. In that case, the network outputs the optimal value and stops counting.
- (10) Otherwise, turn to step (2).

The algorithm's idea is the first to make clusters of the entire network of sensors, and second, the cluster head sensing node in each region receives the data detected by each sensor node in the region. Like the leach clustering algorithm, the member nodes extract the correlation data's characteristics and take the same portion. In order to improve network efficiency and minimize network energy consumption, the BA is used to optimize the neural network for data fusion between clusters. Figure 31.1 shows a schematic diagram of the model structure of the NN-BA scheme.

## 31.4 Simulation Experiment

The parameters of the bat algorithm are:  $Q_{max} = 1$ ,  $q = 0_{min}$ ,  $\alpha = 0.9$ ,  $\gamma = 0.9$ . The initial loudness and initial emission rate are randomly generated in the interval  $[0,1]$ , and the initial frequency is 0. The population number is set as 50, the maximum iteration number is 500, the maximum inertia coefficient  $W_{max} = 1.2$  and the minimum

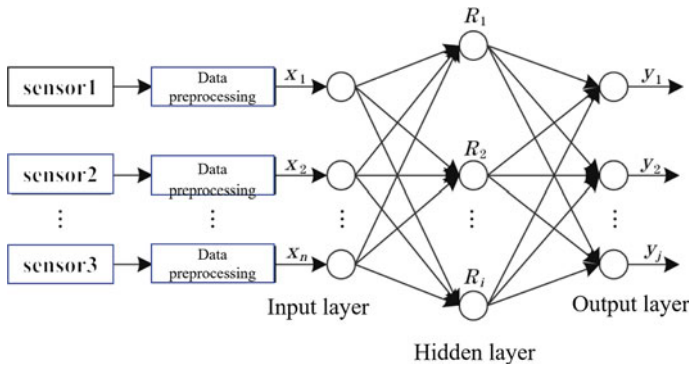


**Fig. 31.1** Schematic diagram of the model structure of NN-BA scheme

**Table 31.1** Simulation experiment parameters setting for data fusion in WSN

Parameters	Value	Parameters	Value
Network specifications	$M \times M$ (100, 200) m	Receive energy consumptions	30 nj/bit
Number of nodes	N (100,150, 200)	Packet size	100 bytes
Initial energy	0.5 J	Polling times	2000
Communication range	20 m	Simulation times	500 s
Transmission energy consumptions	50 nj/bit		

inertia coefficient  $w_{\min} = 0.1$  [2, 4]. The node parameter settings of the simulation experiment are shown in Table 31.1.

The obtained results of the proposed scheme of the NN-BA are compared with the backpropagation neural network (BP-NN) [15], naive Bayes [6], and neural network multi-verse optimizer (NN-MVO) [3] for the data fusion experiments. The proposed scheme’s performances are comprehensively analyzed in terms of surviving number of nodes, the total remaining energy consumption of nodes, the number of sink nodes received, the number of rounds of dead nodes, and the degree of data fusion.

Figure 31.2 shows the number of network-aware nodes surviving with the number of network simulation polling. As can be seen from Fig. 31.2, when the number of network simulation polling is about 780, the number of network surviving nodes of the Bayes algorithm begins to decrease; at 830, the number of surviving nodes of the BP algorithm begins to decrease; at about 890, the number of surviving nodes of NN-MVO algorithm also decreases, while NN-BA algorithm calculates that the number of surviving nodes in NN-BA is also decreasing gradually at 960 polling times. It can be seen from the change of the number of surviving nodes that the NN-BA node has the longest survival time.



**Fig. 31.2** Comparison of network node survival

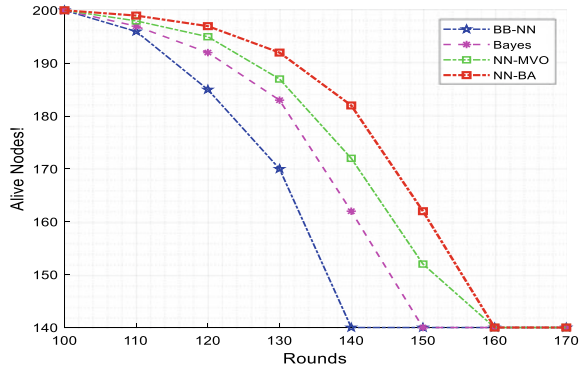


**Table 31.2** Comparison of the proposed scheme with the other methods in terms of the dead node rounds

Fusion algorithm	Number of death rounds for the first node	Half of the node death rounds	Number of death rounds of all nodes
BP-NN [15]	784	939	1189
Bayes [6]	832	1026	1252
NN-MVO [3]	891	1063	1327
<b>NN-BA</b>	926	1095	1425

Table 31.2 shows a comparison of the number of dead nodes of the proposed scheme NN-BA with the other schemes, e.g., the BP-NN [15], naive Bayes [6], and NN-MVO [3] schemes. As can be seen from the data in Table 31.2, the NN-BA algorithm has the most extended number of first node rounds. The clustering scheme of BP-NN has the least number of simulation rounds when half and all nodes are dead, followed by the NN-MVO [3] and NN-BA.

The network convergence efficiency of different algorithms changes with the number of nodes, as shown in Fig. 31.3. As shown in Fig. 31.3, with the increase of the number of nodes in the network, the network’s data fusion efficiency is also gradually improved. The main reason is that with the increase of the number of sensing nodes, there are a lot of neighbor nodes around the sensing nodes, and these data are sent to sink nodes through these neighbor nodes through the multi-hop method.

When these neighbor nodes are gradually fused and sent to sink nodes, the network’s fusion efficiency is improved. NN-BA algorithm is higher than the NN-MVO algorithm [3] and BP neural network [15], and the fusion accuracy is the best. When  $\alpha = 0.01/m^2$ , the network fusion efficiency ratio is  $\alpha = 0.001/m^2$ . When  $\alpha = 0.001$ , the efficiency of data fusion is small when the data fusion algorithm is 0.001. The proposed scheme can effectively extract a small amount of feature data from data fusion data and then send the extracted feature data to sink, which reduces the amount of data transmission and improves the network lifetime.

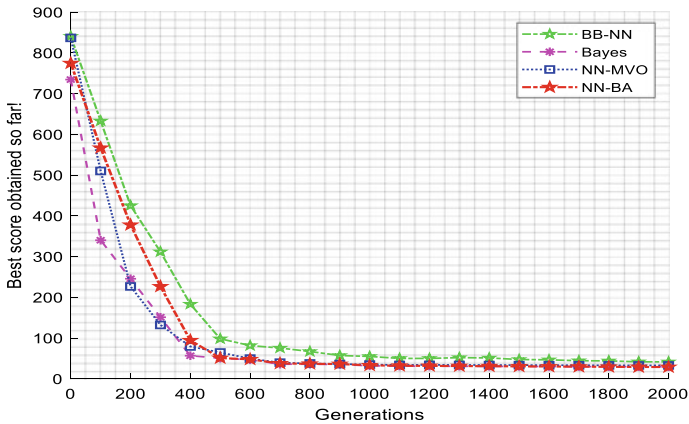


**Fig. 31.3** The performance comparison of data fusion rate

## 31.5 Conclusion

This paper proposed a data fusion strategy based on a hybridized bat algorithm and a neural network (NN-BA) to deploy wireless sensor networks (WSNs). The neural network parameters optimized by the bat algorithm (BA) were used to fuse captured data in cluster head (CH) and then forward the fused data to the base station (BS) of a WSN. Several scenarios have been experimented with to test the proposed scheme performance. The proposed scheme's results show that the proposed algorithm provides decreased data redundancy, increased data transmission, node energy consumption, extended lifetime, and improved data fusion accuracy of WSN.

## References

1. Nguyen, T.-T., Dao, T.-K., Horng, M.-F., Shieh, C.-S.: An energy-based cluster head selection algorithm to support long-lifetime in wireless sensor networks. *J. Netw. Intell.* **01**, 23–37 (2016)
2. Pan, J.-S., Nguyen, T.-T., Dao, T.-K., Pan, T.-S., Chu, S.-C.: Clustering formation in wireless sensor networks: a survey. *J. Netw. Intell.* **02**, 287–309 (2017)
3. Dao, T., Yu, J., Nguyen, T., Ngo, T.: A Hybrid improved MVO and FNN for identifying collected data failure in cluster heads in WSN. *IEEE Access* **8**, 124311–124322 (2020). <https://doi.org/10.1109/ACCESS.2020.3005247>
4. Dao, T., Nguyen, T., Pan, J., Qiao, Y., Lai, Q.: Identification failure data for cluster heads aggregation in WSN based on improving classification of SVM. *IEEE Access* **8**, 61070–61084 (2020). <https://doi.org/10.1109/ACCESS.2020.2983219>
5. Nguyen, T.T., Pan, J.S., Dao, T.K.: An improved flower pollination algorithm for optimizing layouts of nodes in wireless sensor network. *IEEE Access* **7**, 75985–75998 (2019). <https://doi.org/10.1109/ACCESS.2019.2921721>
6. Chu, S.C., Dao, T.K., Pan, J.S., Nguyen, T.T.: Identifying correctness data scheme for aggregating data in cluster heads of wireless sensor network based on naive Bayes classification.

- Eurasip J. Wirel. Commun. Netw. **52**(1–16) (2020). <https://doi.org/10.1186/s13638-020-01671-y>
7. Nguyen, T.-T., Pan, J.-S., Lin, J.C.-W., Dao, T.-K., Nguyen, T.-X.-H.: An optimal node coverage in wireless sensor network based on whale optimization algorithm. *Data Sci. Pattern Recognit.* **02**, 11–21 (2018)
  8. Nguyen, T.-T., Wang, H.-J., Dao, T.-K., Pan, J.-S., Liu, J.-H., Weng, S.-W.: An improved slime mold algorithm and its application for optimal operation of cascade hydropower stations. *IEEE Access* **8**, 1 (2020). <https://doi.org/10.1109/ACCESS.2020.3045975>
  9. Heinzelman, W.B., Chandrakasan, A.P., Balakrishnan, H.: An application-specific protocol architecture for wireless microsensor networks. *IEEE Trans. Wirel. Commun.* **1**, 660–670 (2002). <https://doi.org/10.1109/TWC.2002.804190>
  10. Manjeshwar, A., Agrawal, D.P.: TEEN: a routing protocol for enhanced efficiency in wireless sensor networks. In: *Proceedings 15th International Parallel and Distributed Processing Symposium*, pp. 2009–2015 (2001). <https://doi.org/10.1109/IPDPS.2001.925197>
  11. Pan, T.-S., Nguyen, T.-T., Dao, T.-K., Chu, S.-C.: An optimal clustering formation for wireless sensor network based on compact genetic algorithm. In: *Proceedings—2015 3rd International Conference on Robot, Vision and Signal Processing, RVSP 2015* (2016). <https://doi.org/10.1109/RVSP.2015.77>
  12. Srinivas, M., Patnaik, L.M.: Genetic algorithms: a survey. *Computer (Long. Beach. Calif.)*. **27**, 17–26 (1994). <https://doi.org/10.1109/2.294849>
  13. Nguyen, T.-T., Pan, J.-S., Wu, T.-Y., Dao, T.-K., Nguyen, T.-D.: Node coverage optimization strategy based on ions motion optimization. *J. Netw. Intell.* **4** (2019)
  14. Nguyen, T.-T., Pan, J.-S., Chu, S.-C., Roddick, J.F., Dao, T.-K.: Optimization localization in wireless sensor network based on multi-objective firefly algorithm. *J. Netw. Intell.* **1**, 130–138 (2016)
  15. Hecht-Nielsen, R.: Theory of the backpropagation neural network. In: *Neural networks for Perception*, pp. 65–93. Elsevier (1992)
  16. Yang, X.-S., Hossein Gandomi, A.: Bat algorithm: a novel approach for global engineering optimization. *Eng. Comput. Int. J. Comput. Eng. Softw.* **29**, 464–483 (2012). <https://doi.org/10.1108/02644401211235834>

# Chapter 32

## Cluster-Based Two-Level Mesh Routing Protocol for Wireless Sensor Network



Qi-yuan Zhang, Bo Sun, Jian-ming Xu, Jian He, and Ji-liang Mu

**Abstract** Wireless sensor networks (WSNs) have broad application scenarios in military and civilian fields. How to reduce the energy consumption of network communication and extend the life cycle of the network has always been a research focus of WSN. Clustering is one of the important methods to extend the network life cycle. However, the existing clustering routing protocol has room for further optimization of the connection mode between the common node and the cluster head node, the network topology structure and the communication mode between nodes. In this paper, a cluster-based two-level mesh (CTM) routing protocol for WSN is proposed, which supports common nodes to connect to the cluster head and communicate with any node in a multi-hop manner. It also specifies the topological structure of the two-level mesh and two communication modes. Finally, simulations on the OMNeT++ platform verify that the protocol can effectively reduce network and energy costs.

---

Q. Zhang · J. He · J. Mu (✉)

Science and Technology on Electronic Test and Measurement Laboratory, North University of China, 030051 Taiyuan, China

e-mail: [mujiliang@nuc.edu.cn](mailto:mujiliang@nuc.edu.cn)

J. He

e-mail: [drhejian@nuc.edu.cn](mailto:drhejian@nuc.edu.cn)

B. Sun

China Academy of Space Technology, 100094 Beijing, China

e-mail: [sunboo2002@sina.com](mailto:sunboo2002@sina.com)

J. Xu

State Key Laboratory of Space Power Technology, Shanghai Institute of Space Power-Sources, 200245 Shanghai, China

e-mail: [xujianming1127@163.com](mailto:xujianming1127@163.com)

## 32.1 Introduction

The wireless sensor network (WSN) is a wireless communication network formed by a large number of sensor nodes through self-organization and multi-hop communication [1]. Therefore, it has very broad application prospects in the field of civil Internet of Things and military monitoring [2–4]. Because sensor nodes have higher requirements for power consumption control, how to reduce the energy consumption of network communication and extend the network life cycle has always been a research hotspot of WSN [5]. Node clustering can optimize the network topology and reduce the communication volume of nodes, which is one of the important methods to extend the life cycle of the network [6, 7]. However, in the routing protocols based on classic clustering algorithms such as Low-Energy Adaptive Clustering Hierarchy (LEACH) and its improved clustering algorithm, ordinary nodes and cluster head nodes use single-hop communication, and the communication between nodes must be completed through cluster head forwarding [8–10]. The protocol also does not support information exchange between arbitrary sensor nodes. There is a room for further optimization of link selection and network topology in special occasions. In this paper, a cluster-based two-level mesh (CTM) routing protocol for WSN is proposed. By specifying the topological structure and information transmission mode of the two-level mesh WSN, the link between nodes is optimized, and the network life cycle is extended. It also enhances the ability of the network to integrate with other networks.

## 32.2 Protocol Design

The sensor nodes of the entire sensor network are divided into ordinary nodes and cluster head nodes. Nodes can become ordinary nodes or cluster head nodes during the election process. Ordinary nodes and cluster head nodes can form a secondary mesh network through low-transmit power communication. The cluster head nodes form a primary level mesh network through high-transmit power communication. The schematic diagram of the network topology is shown in Fig. 32.1.

The protocol stipulates two information transmission modes, namely long-distance transmission and short-distance transmission. They need establish a short-distance link and a long-distance link, respectively. The short-distance transmission uses the primary mesh network, and the long-distance transmission uses both the primary mesh network and the secondary mesh network. Figure 32.2 is a schematic diagram of short-distance transmission and long-distance transmission.

The complete long-distance link is divided into three parts: the part between the source node and the cluster head (s-c link), the part between the cluster head and the cluster head (c-c link), and the part between the cluster head and the target node (c-t link). In order to make the network more flexible, any node can be used as the source node or the target node to communicate, so the long-distance link may not consist

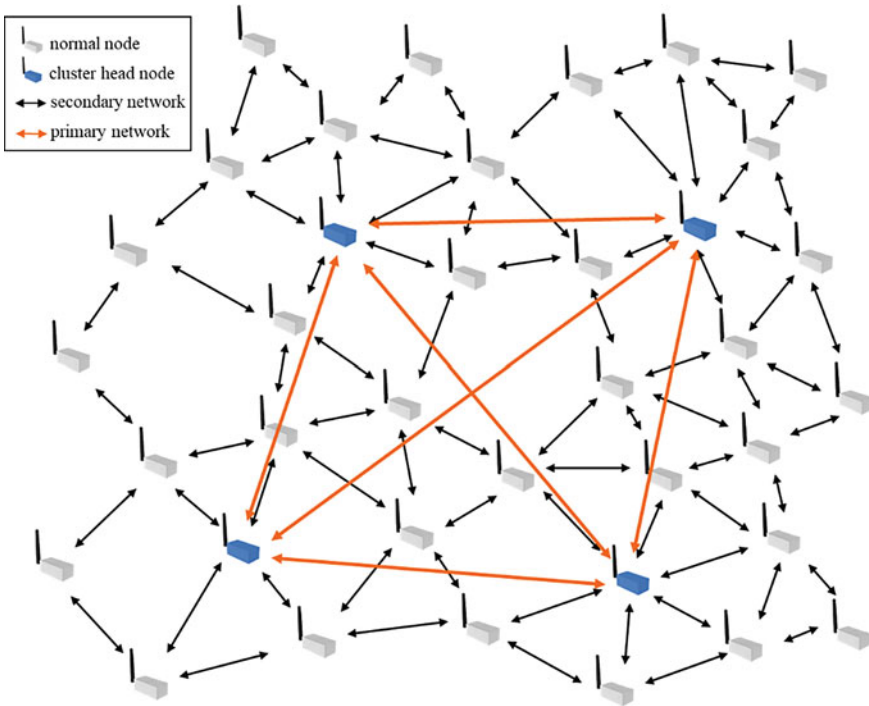
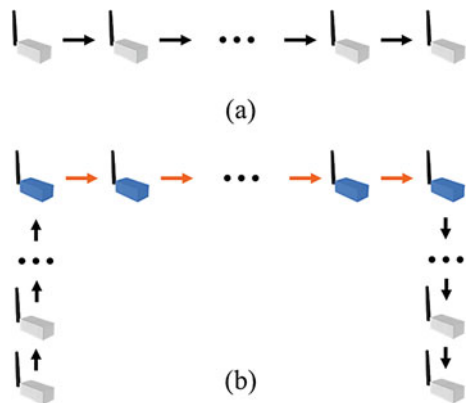


**Fig. 32.1** Schematic diagram of network topology

**Fig. 32.2** Schematic diagram of transmission mode: **a** short-distance transmission; **b** long-distance transmission



of a complete three-part. The s-c link and c-t link specify the maximum number of hops which is consistent with the maximum number of hops for short-distance transmission. The c-c link also limits the maximum number of hops. The maximum number of hops can be customized according to the range of the cluster and the size

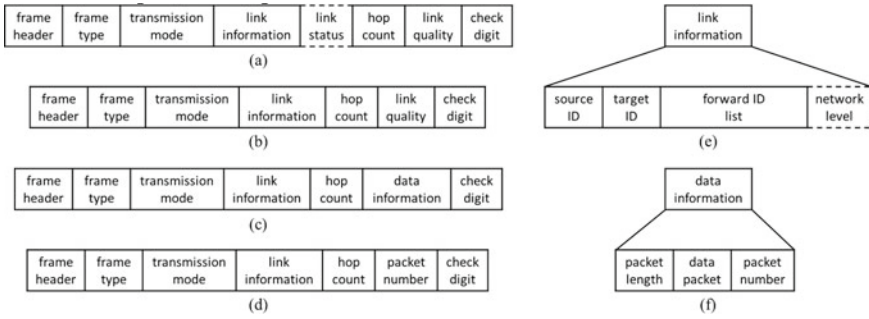


**Fig. 32.3** The frame format specified by the protocol: **a** frame format of link establishment request; **b** frame format of link establishment ack; **c** frame format of transmission data; **d** frame format of data reception ack; **f** structure of link information; **e** structure of data information

of the entire wireless sensor network, which can realize communication between all nodes, while limiting the network resources occupied when establishing routes.

The protocol stipulates four basic frames, namely link establishment request, link establishment ack, data transmission, and data reception ack. The format of the frame is shown in Fig. 32.3. Among them, the frame type is used to distinguish different frames and further read the data according to its format for corresponding processing. The transmission mode describes the transmission mode used by the frame. Link information contains link-related information such as the address of the source node, target node, and transit node. The address information of the forwarded node is recorded when the link request is established, and the node will check the address information when receiving the request to avoid loops. After the forwarding condition is met, the address of the node will be added. The link information of other types of frames records the complete link which cannot be modified, and the node only needs to forward and receive frames according to the link. If it is a long-distance transmission mode, the link information will also record which level of network communication is used between each node. The link status is only found in the frame of link establishment request by long-distance transmission. There are three status corresponding to the three parts of the long-distance link. It is used to ensure that the established link contains only one c-c link. The hop count is used to record the number of times the frame is forwarded during the transmission process, combined with link information to determine whether the node meets the forwarding or acceptance conditions. In the frame of link establishment request by long-distance transmission, in addition to recording the total hop count, the hop count of each part of the long-distance link is also recorded to avoid exceeding the maximum hop count. Link quality is included in link establishment request and link establishment ack, and its value is determined by the number of hops, received signal strength, and node power. When a node receives multiple link establishment ack within the specified time, it will select the link with the highest link quality and save it. The data information includes data packet length, data packet, and data packet number.

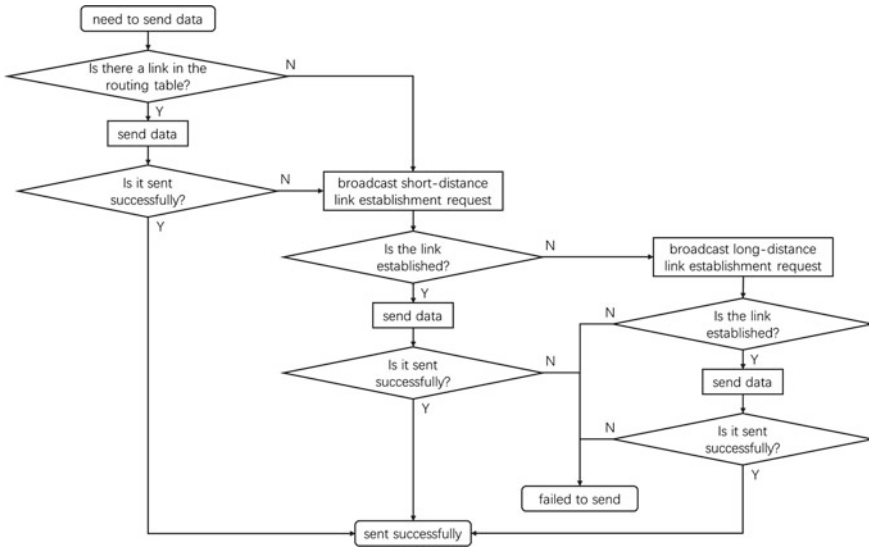


Fig. 32.4 Flow chart of node sending data

The data packet number is used in the reception confirmation, and the data packet number will not be repeated for a period of time.

In order to save hardware resources and adapt to the changing network topology, the protocol is designed in the form of an on-demand routing protocol [11]. Figure 32.4 shows the process when a node transmits data to other nodes. First of all, the node will query whether there is a link information of the target node in the routing table maintained by itself, send data if it has, or broadcast a link establishment request if it is not. If sending data fails, the link information of the target node in the routing table will be deleted and a link establishment request will be broadcast. In order to save network resources as much as possible, the node first broadcasts a request to establish a short-distance link. If the target node is not found, then broadcast the request to establish a long-distance link. After finding the target node, record the link information and send data to the target node.

The judgment process when the node receives the frame of link establishment request is shown in Fig. 32.5. If the node is the target, the link establishment ack will be sent to the source node. Otherwise, it will be judged whether to forward according to whether the maximum number of hops has been reached and whether the node information is already in the frame. When the forwarding conditions are met, if the node is a cluster head, it will use both the primary network and the secondary network for broadcasting, otherwise only the primary network will be used.



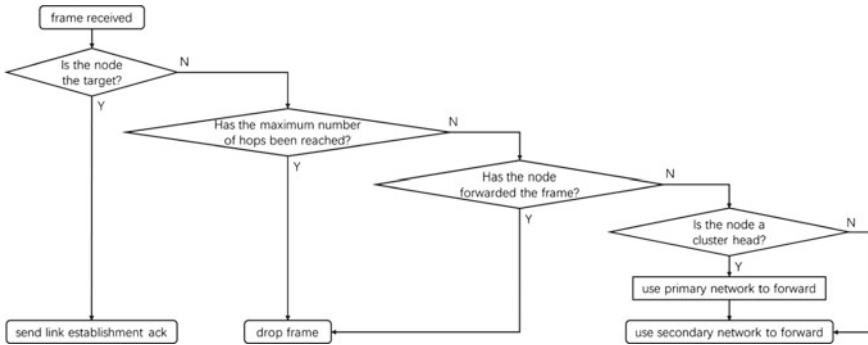


Fig. 32.5 Flow chart of judgment when a frame is received

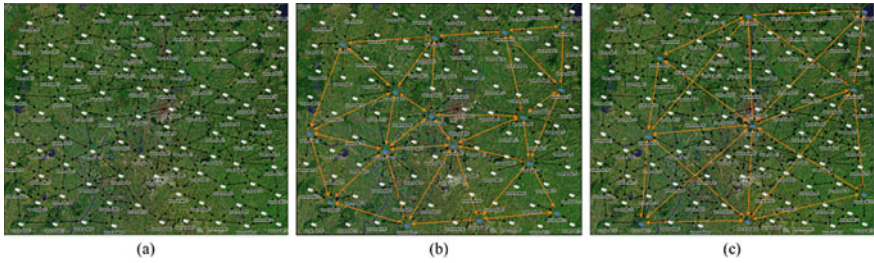
### 32.3 Results and Discussion

OMNeT++ is used as a simulation platform to build a WSN. According to the protocol, the network topology and the communication mode of nodes were simulated and compared with the performance of other protocols. Compared with the classic clustering routing protocol for WSN, CTM routing protocol for WSN has no obvious cluster boundary in the communication process, and the cluster head node does not need forwarding when communicating between two adjacent clusters. Therefore, network resources and node energy are saved. The comparison of links is shown in Fig. 32.6.

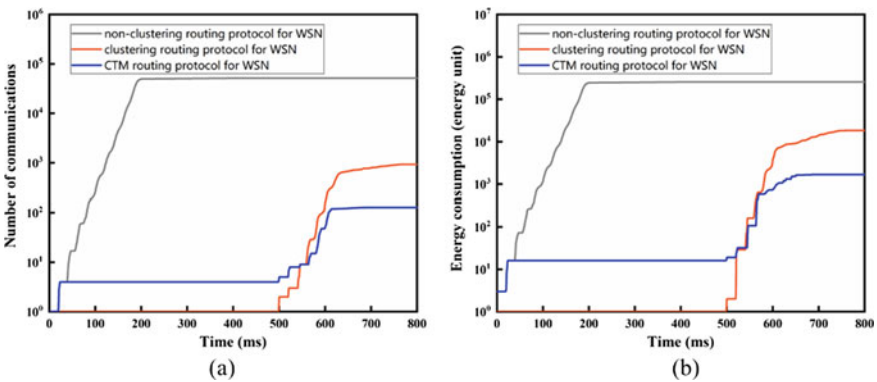
In OMNeT++ platform, the non-clustering WSN, the classical clustering WSN, and CTM Mesh WSN were built, respectively, as shown in Fig. 32.7. Through simulation, the number of communications and energy consumption of the entire network were calculated when there were communications between the distant nodes. The model of energy consumption is  $P \propto R^2$ . Where  $P$  is the transmit power,  $R$  is the transmission distance. The consumption of low-power transmission is 1 energy unit. The energy consumption of high-power transmission is  $(2h + 1)^2$  energy units, where  $h$  is the maximum number of hops of the link between the ordinary node and the



Fig. 32.6 Comparison of the links between adjacent nodes in adjacent clusters: a Use the classic clustering routing protocol for WSN; b Use CTM routing protocol for WSN



**Fig. 32.7** The wireless sensor network constructed by the simulation platform: **a** non-clustering WSN; **b** classical clustering WSN; **c** CTM mesh WSN



**Fig. 32.8** Simulation results: **a** total number of network communication; **b** total network energy consumption

cluster head node. The comparison of the total number of the communication and energy consumption of a complete data transmission is shown in Fig. 32.8. Almost, all of the network costs and energy costs are used for link establishment. It can be seen from figure that CTM routing protocol for WSN has obvious advantages in network costs and energy costs when maintaining the routing table.

### 32.4 Conclusions

In summary, a cluster-based two-level mesh routing protocol for WSN is proposed. Compared with other clustering routing protocols for WSN, CTM routing protocol for WSN supports ordinary nodes to connect to the cluster head through multi-hop, which expands the range of clusters and reduces the number of cluster heads. The protocol supports mutual communication between arbitrary nodes, which enhances the flexibility of the network and the ability to integrate with other networks. The protocol stipulates a two-level mesh topology and two communication modes, which

optimizes the links between cluster boundary nodes, reduces the network costs and energy costs required to maintain the routing table, and extends the network life cycle. Finally, the OMNeT++ platform was used to build a WSN and simulate the protocol. The results show that CTM routing protocol for WSN has better performance than the classic WSN routing protocol.

## References

1. Marinho, J., Monteiro, E.: Cognitive radio: survey on communication protocols, spectrum decision issues, and future research directions. *Wirel. Netw.* **18**(2), 147–164 (2012)
2. Bayrakdar, M.E.: Energy-efficient technique for monitoring of agricultural areas with terrestrial wireless sensor networks. *J. Circ. Syst. Comp.* **29**(9), 2050141 (2020)
3. Chan, F.K.W., So, H.C.: Accurate distributed range-based positioning algorithm for wireless sensor networks. *IEEE Trans. Sig. Process.* **57**(10), 4100–4105 (2009)
4. Lan, X.L., Zhang, Y.M., Cai, L., Chen, Q.C.: Adaptive transmission design for rechargeable wireless sensor network with a mobile sink. *IEEE Internet Things* **7**(9), 9011–9025 (2020)
5. Azarhava, H., Niya, J.M.: Energy efficient resource allocation in wireless energy harvesting sensor networks. *IEEE Wirel. Commun. Lett.* **9**(7), 1000–1003 (2020)
6. Bagci, F.: Energy-efficient communication protocol for wireless sensor networks. *Ad Hoc Sens. Wirel. Netw.* **30**(3–4), 301–322 (2016)
7. Kundaliya, B.L., Hadia, S.K.: Routing algorithms for wireless sensor networks: analysed and compared. *Wirel. Pers. Commun.* **110**(1), 85–107 (2020)
8. Xie, P.H., Lv, M., Zhao, J.J.: An improved energy-low clustering hierarchy protocol based on ensemble algorithm. *Concurrency Comput. Pract. Experience.* **32**(7), e5575 (2020)
9. Radhika, M., Sivakumar, P.: Energy optimized micro genetic algorithm based LEACH protocol for WSN. *Wirel. Netw.* **27**(1), 27–40 (2021)
10. Heinzelman, W.B., Chandrakasan, A.P., Balakrishnan, H.: An application-specific protocol architecture for wireless microsensor networks. *IEEE Trans. Wirel. Commun.* **1**(4), 660–670 (2002)
11. Khaleghnasab, R., Bagherifard, K., Nejatian, S., Parvin, H., Ravaei, B.: A new energy-efficient multipath routing in internet of things based on gray theory. *Int. J. Inf. Tech. Decis.* **19**(6), 1581–1617 (2020)

# Chapter 33

## PD Detection and Analysis of Cross-Bonded Cable Based on Broadband Sensor and Three-Phase Amplitude Relation Analysis Method



Liwei Wang, Bingwei Liu, Bin Wang, Xutao Han, Zhentao Liu, and Wei Sun

**Abstract** The power cable is one of the most important transmission equipment. The long cable common use the cross-bonded grounding method to reduce the loss of shielding layer and decrease the voltage rise at the end of cable. Therefore, it is difficult to diagnosis the PD detection result of cross-bonded cable in field because the PD signals will be influenced by both the environment electromagnet interference and the interference among different phases. The broad band sensor is used to detect the PD of cross-bonded cable in field in this paper. The waveform of the PD pulse, PRPD, and 3PARD diagrams are analyzed to diagnose the results. The results have shown that the broadband sensor can anti the environment electromagnet interference because it can obtain more information of PD signal. The 3PARD diagrams can division the interference among different phases.

### 33.1 Introduction

With the development of power system, XLPE cable has been widely used in transmission lines and urban distribution network. When the cable line is long (more than 1 km), the three-phase cross-bonded transmission cable is adopted [1–3]. The cable line is divided into several large sections, and each large section is divided into three

---

L. Wang

Henan Jiuyu Enpai Power Technology Co., Ltd, Zhengzhou, China

B. Liu

Sanmenxia Power Supply Company of Henan Electric Power Company, Sanmenxia, China

B. Wang

State Grid Henan New Energy Co., Ltd, Zhengzhou, China

X. Han · W. Sun (✉)

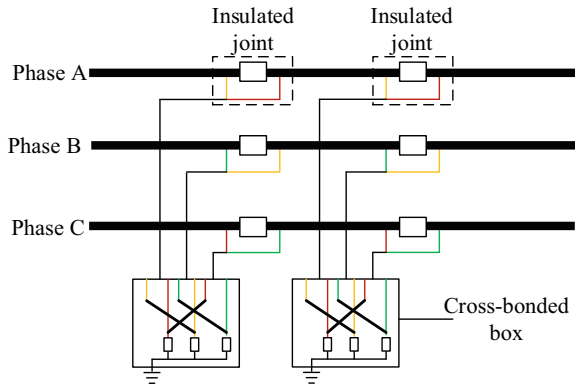
Xidian University, Xi'an, China

e-mail: [wsun@xidian.edu.cn](mailto:wsun@xidian.edu.cn)

Z. Liu

Xi'an University of Posts and Telecommunications, Xi'an, China

**Fig. 33.1** Diagram of cross-bonded grounded



small sections of equal length. The insulated joints are installed between each small section. On both sides of the insulated joints, the metal shields of different phases are transposed by coaxial cross interconnection lines, as shown in Fig. 33.1.

Some insulation defects are inevitable in the process of manufacture and operation of high-voltage XLPE cable. Partial discharge occurs due to the concentration of electric field at the defect. Long-term discharge process will lead to deterioration and aging of cables, and eventually lead to cable insulation failure and power failure [4–7]. The insulation fault can be effectively prevented by detecting the partial discharge signal of the cable.

However, for the cross-bonded cable system, when partial discharge occurs in the main insulation of a phase cable, the partial discharge signal will propagate through the conductor layer of the phase cable to the next layer and continue to propagate. As a result, the discharge signals of three phases interfere with each other. Therefore, the field partial discharge detection of cross-bonded cable is not only interfered by the external electromagnetic signals, but also is interfered with each other of the three-phase signals, which increases the difficulty of judging and analyzing the detection results.

At present, many researches on the PD propagation characteristics of cross-bonded cable have been conducted by the simulation or test methods in the laboratory [4–7]. The current sensors are common used in the field PD detection of cross-bonded cable. However, the frequency band of the current sensor is lower than 1 MHz which is easy to be interfered by external signals. The pulse separation of different phases can be realized by multi-channel joint detection. The three-phase amplitude phase correlation spectrum (3PRPD) has been widely used in transformers. In this paper, aiming at the difficulty of PD signal detection of cross-bonded cable in the field, the partial discharge is measured by broadband sensor, and the detection results are identified and analyzed by the discharge pulse waveform, discharge PRPD spectrum, and 3PRPD spectrum. The results of this paper are beneficial to the detection of PD signals of cross-bonded cable in the field.

### 33.2 Three-Phase Amplitude Phase Relationship Analysis Method

As shown in Fig. 33.1, when a partial discharge pulse signal occurs in a certain phase of the cross-bonded cable system, the PD signal can be detected in the three phases at the same time, as shown in Fig. 33.2.

In order to ensure the correlation of three-phase partial discharge signals, it is generally considered that the signals collected in the time range of 1–2 μs are the partial discharge signals in the same period. After the partial discharge signals corresponding to three phases are determined, the measured three pulse amplitudes are mapped into three pulse vectors with original amplitude and phase of 0°, 120°, and 240°, respectively, as shown in Eqs. (33.1) to (33.3).

$$\vec{q}_A = |\vec{q}_A| \angle 0^\circ \tag{33.1}$$

$$\vec{q}_B = |\vec{q}_B| \angle 120^\circ \tag{33.2}$$

$$\vec{q}_C = |\vec{q}_C| \angle 240^\circ \tag{33.3}$$

$$\vec{q} = \vec{q}_A + \vec{q}_B + \vec{q}_C \tag{33.4}$$

Finally, a partial discharge pulse vector can be obtained by adding the three vector vectors, as shown in Eq. (33.4), which is a PD point in 3PRPD diagram. The calculation process is shown in Fig. 33.3.

The partial discharge signal and interference signal in phase A can be distinguished by 3PRPD technology. When the partial discharge occurs in phase A, the amplitude of partial discharge detected on phase A must be the largest. After superimposed with the partial discharge signal vector of the other two phases, the partial discharge

Fig. 33.2 Discharge pulse of three phases

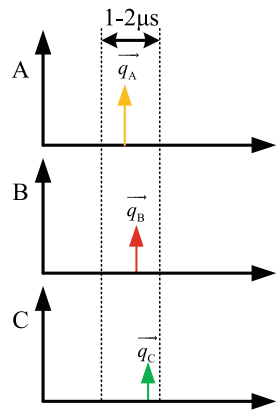
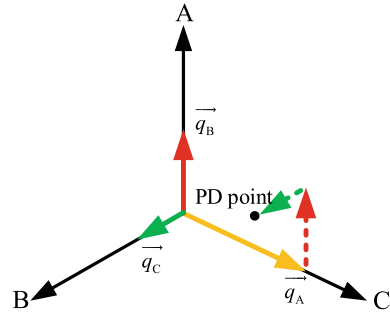


**Fig. 33.3** Composing principle of 3PARD



point will fall on the coordinate axis of phase A. If the amplitude difference between phase A and the other two phases is large, at the same time the superimposed vector is far away from the coordinate origin, it indicates that the actual position of partial discharge is phase A. The signals detected by other two phases are the crosstalk results of phase A PD. When the amplitude of the three-phase pulse is the same and the partial discharge point after vector superposition is located at the coordinate origin, it indicates that the partial discharge signal detected at this time is actually external interference signal.

When 3PRPD technology is used in practice, the pulse point after vector superposition is not strictly located on the coordinate axis and coordinate origin. This is because the actual PD signal is affected by the attenuation of propagation path and the superposition of interference which leads to its distortion. As a result, it makes the PD signal after vector superposition be a pulse cluster, in which the pulse cluster of real partial discharge signal is around a certain phase coordinate axis, while the pulse cluster of interference signal is located near the coordinate origin.

### 33.3 Field PD Detection and Analysis of Cross-Bonded Cable

#### 33.3.1 Field Detection System

The field detection system of cross-bonded cable is shown in Figs. 33.4 and 33.5. The PD signals are detected by the three same high-frequency current sensor (HFCT) with the frequency band of 100 kHz–20 MHz and the sensitivity of 2.5 V/A. The phase information is obtained by measurement of the induced voltage.

Compared with the traditional sensors, the system can obtain a wider frequency distribution signal. The signal can be separated by detecting the frequency characteristics of the signal. The detection system can detect the discharge signals with different frequencies, such as 2 MHz, 6 MHz, 10 MHz, and 12 MHz.

**Fig. 33.4** Detection diagram of cross-bonded cable

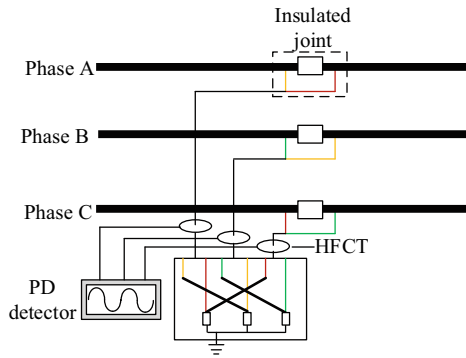
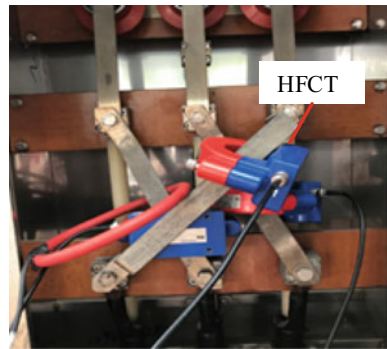


**Fig. 33.5** Picture of filed detection



### 33.3.2 Results of Low Frequency

The field detection results of 2 MHz are shown in Fig. 33.6. It can be seen that the signals are covered by the interference signals. It hardly gets the characteristics of the patterns. In addition, all the sensors of three phases detect the signals. However,

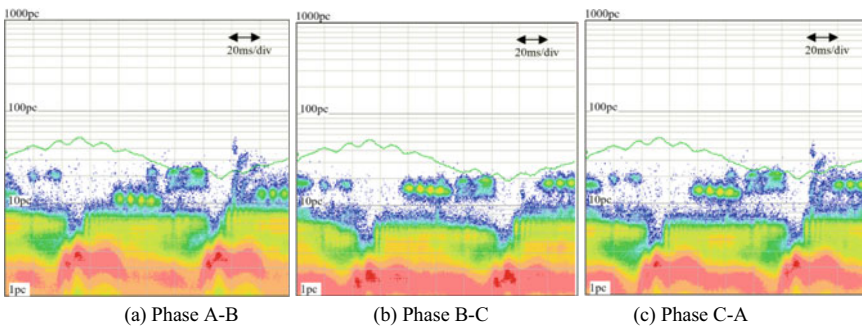
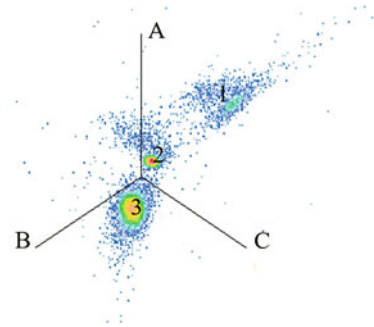


**Fig. 33.6** PRPD pattern of 2 MHz



**Fig. 33.7** 3PRPD pattern of 2 MHz



it cannot determine the PD phase due to the interference of environment and cross-bonded system.

The 3PRPD pattern of 2 MHz is shown in Fig. 33.7. It can be seen from the figure that there are three clusters of signals. Signal 2 and signal 3 are close to the origin, indicating that the amplitude difference of phase A, B, and C signals is not big. Therefore, the signal should be external interference signal. The signal 1 is close to the A and C phases. It illustrates that this cluster of signals is the discharge signals from A and C phases, and the signals have the characteristics of floating defects.

### 33.3.3 Detection Results of High Frequency

The 3PRPD pattern of 6 MHz is shown in Fig. 33.8. At this time, there is two clusters of signals. One of them is near the origin. The other is between the phase A and C. Therefore, this cluster of signals is the PD signals.

The detection result of higher frequency is shown in Fig. 33.9 which presents the 3PRPD pattern of 10 MHz. It can be seen that there is only one cluster of signals. It very close to phase A. Therefore, it is the PD occurs in phase A.

When the frequency is further increased, the interference signal is smaller. The 3PRPD pattern of 12 MHz is shown in Fig. 33.10. At this time, there is only one cluster signals which is located at phase A.

**Fig. 33.8** 3PRPD pattern of 6 MHz

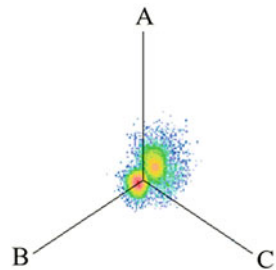


**Fig. 33.9** 3PRPD pattern of 10 MHz

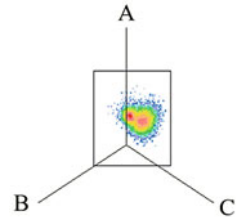


**Fig. 33.10** Change curves of number of photons and change rate of photon number

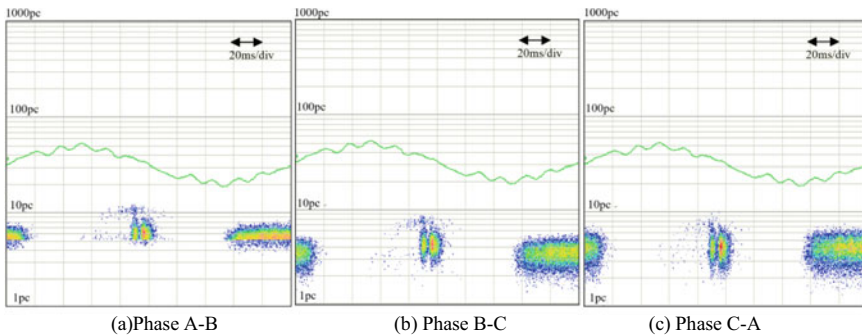
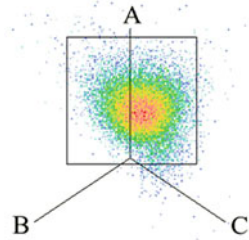


**Fig. 33.11** PRPD pattern of 12 MHz

The PRPD patterns of 12 MHz are shown in Fig. 33.11. Because the interference signals under high frequency is very small, the detected signals are mainly PD signals. From the patterns, it can be concluded that the discharge source is floating defect.

### 33.4 Conclusions

The PD signals in the cross-bonded cable system is measured by using broadband current sensor. In addition, the detection results are analyzed and diagnosed according to PRPD and 3PRPD patterns. The results have shown that more detailed discharge information can be obtained by using wideband current sensor, which is beneficial to

remove the influence of external electromagnetic interference signal on the detection results. The 3PRPD pattern can effectively separate the discharge signals, and consequently, it can eliminate the crosstalk between the three-phase signals. It is helpful to determine the position of the discharge source in field.

**Acknowledgements** This work was supported by National Nature Science Foundation of China (NSFC) under Grants No. 61671356, Science and Technology Program of Shaanxi Province under Grants No. 2020GY-136 and 2019ZDLGY14-02-03.

## References

1. Petzold, F., Schlapp, H., Gulski, E.: Advanced solution for on-site diagnosis of distribution power cables. *IEEE Trans. Dielectr. Electr. Insul.* **15**(6), 1584–1589 (2008)
2. He, W., Wang, Q., Huang, C., et al.: A novel noise elimination method for PD measurement of on-site MV cable using frequency-tuned resonant system. In: *2016 International Conference on Condition Monitoring and Diagnosis (CMD)*, Xi'an, China (2016)
3. Putter, H.T., Gotz, D., Petzold, F., et al.: Innovative solutions for on-site diagnosis of distribution power cables. In: *Transmission & Distribution Conference & Exposition*. IEEE (2012)
4. Koltunowicz, W., Plath, R.: Synchronous multi-channel PD measurements. *IEEE Trans. Dielectr. Electr. Insul.* **15**(6), 1715–1723 (2008)
5. Kraetge, A., Hoek, S., Hummel, R., et al.: De-noising approaches for partial discharge measurements—a comparison of methods and their practical application. In: *International Conference on Condition Monitoring and Diagnosis*. IEEE (2013)
6. Yin, Y., Li, Z.: Research on a practical de-noising method and the characterization of partial discharge UHF signals. *IEEE Trans. Dielectr. Electr. Insul.* **21**(5), 2206–2216 (2014)
7. Henseler, J., Chin, W.W.: A comparison of approaches for the analysis of interaction effects between latent variables using partial least squares path modeling. *Struct. Eqn. Model. Multi. J.* **17**(1), 82–109 (2010)

# Chapter 34

## A Dynamic and Fair Timeout Heartbeat Detection Technique for Server Clusters Using Nginx Reverse Proxy



Beiping Ma and Wei Zhang

**Abstract** In recent years, more and more SMEs use their existing equipment enterprises to form server clusters for the internal welfare platform of enterprises through Nginx reverse proxy. For this kind of platform, the health detection mechanism of nodes in the server cluster plays a very important role in ensuring the high availability of the system. Nginx's native health detection mechanism is very weak. The widely used Tengine provides Nginx with a separate health detection module, but it still fails to consider the problem of different node performance caused by heterogeneous hardware and uneven load on software, and uses a unified heartbeat detection strategy, which leads to the problem that Nginx cannot detect the faulty node in time or mistakenly determines the "Fake dead" node as the faulted node. In this paper, node performance parameters such as CPU utilization and IO utilization are selected to construct a weight calculation model by entropy method to quantify node performance, and then a node fault misjudgment loss model is constructed to optimize the accuracy of node fault judgment. Finally, a dynamic fair timeout algorithm based on Nginx is proposed to make Nginx's heartbeat timeout strategy more fair and real-time. Experiments show that compared with the heartbeat detection technology before improvement, the algorithm proposed in this paper improves the accuracy of node fault detection by 18%, and this algorithm is an effective technology to improve the high availability of cluster.

### 34.1 Introduction

Due to the rapid development of Internet technology in recent years, most businesses use the cluster to provide services now. The overall service provided by clusters greatly improves the continuous stability of the service and avoids the unavailability

---

B. Ma · W. Zhang (✉)  
The Computer School, Beijing Information Science and Technology University, Beijing, China  
e-mail: [zhwei@bistu.edu.cn](mailto:zhwei@bistu.edu.cn)

B. Ma  
e-mail: [2018021004@mail.bistu.edu.cn](mailto:2018021004@mail.bistu.edu.cn)

of the service caused by the downtime of a single server [1]. However, a cluster with 10,000 servers with high reliability still has one server failure almost every day in 30 years of statistics, and 1–5% of disk drives are damaged every year [2]. Therefore, the problem of node failure in the cluster cannot be ignored, especially for scene above. The first thing to do is to detect the faulty node. Heartbeat detection, as a common and important means of detecting the failure of the back-end node, is an object worth studying.

## 34.2 Nginx's Fault Detection Mechanism

### 34.2.1 *Nginx's Native Health Check*

Nginx is a high-performance http server, reverse proxy server and mail server developed by Russian Igor Sysoev. It was officially opened source in 2004. After the open source, its ecology has been continuously developed and improved. At present, many well-known Internet enterprises at home and abroad, such as Tencent, Alibaba, GitHub and Facebook, all use Nginx servers [3–6]. When used as a reverse proxy server Nginx, the need for back-end server node health monitoring, to ensure timely detection unavailable node, avoid forwarding requests to unavailable nodes. Nginx's native health check can be achieved by modifying the upstream module in `nginx.conf` in the configuration file, and it uses service forwarding as a detection packet [3].

### 34.2.2 *Tengine's Heartbeat Detection*

Tengine is a software developed by Taobao team in China based on Nginx, which adds many advanced functions and features on the basis of Nginx, including `nginx_upstream_check_module`, which uses the mechanism of heartbeat detection. In a cluster, the heartbeat detection mechanism sends heartbeat information to each other between the heartbeat modules of the main control node and the common node so as to detect whether the network connection or node machine is normal [7, 8]. Compared with Nginx, Tengine has changed from passive health examination to active health examination, thus improving node fault detection and real-time performance. However, Tengine does not take into account the problem of different node performance during the running of the system. It used a unified configuration and standard for each node, which is obviously unreasonable [3, 9].

### 34.3 Dynamic and Fair Timeout Algorithm Based on Nginx

#### 34.3.1 Fair Misjudgment Loss Algorithm

FMJL is a Hadoop-based algorithm proposed by Guan Guodong, Faye Ting and others in 2015 to calculate the job timeout of each node in heterogeneous clusters. The algorithm can calculate the appropriate job timeout time of each node by inputting data such as node failure probability, short job execution time and node processing rate ratio. Because there are many differences between Nginx and Hadoop, this paper will propose a dynamic fair timeout algorithm based on Nginx based on fair misjudgment loss algorithm and considering that nodes are constantly changing at runtime.

#### 34.3.2 Dynamic and Fair Timeout Algorithm Based on Nginx

**Dynamic weight design.** This paper argues that each node should be given a certain weight according to its performance, and then the appropriate heartbeat timeout strategy should be calculated according to the weight. In this paper, CPU utilization rate ( $C_{cpu}$ ), memory utilization rate ( $C_{men}$ ), network bandwidth utilization rate ( $C_{net}$ ) and IO utilization rate ( $C_{io}$ ) are selected as the weight important elements to evaluate the current node. The value of the system run-time weighting factor is constantly changing, the weights of elements within a record period  $T$  and score draw  $C_{t_{cpu}}, C_{t_{men}}, C_{t_{net}}$  and  $C_{t_{io}}$ .  $R_{cpu}, R_{men}, R_{net}$  and  $R_{io}$  are used to represent the weight coefficients of the above four factors, and the weight coefficients represent the influence degree of these important elements on the weight. Let the default weight of all nodes be  $W_{de}$  and the weight of a node  $i$  be  $W_i$ , then the formula for calculating  $W_i$  is as follows:

$$W_i = (C_{t_{cpu}} \times R_{cpu} + C_{t_{men}} \times R_{men} + C_{t_{net}} \times R_{net} + C_{t_{io}} \times R_{io}) \times W_{de} \quad (34.1)$$

$$R_{cpu} + R_{men} + R_{net} + R_{io} = 1 \quad (34.2)$$

**Entropy method.** Entropy method uses entropy to measure uncertainty, which is inversely proportional to the amount of information. Entropy method, as an objective evaluation weighting method, has been widely used in determining the factor weight in the construction of evaluation indicators. The calculation steps are as follows [3]:

- (1) Select  $m$  servers,  $n$  important factors, then  $x_{ij}$  ( $i = 1, 2, \dots, m; j = 1, 2, \dots, n$ ) is the value of the  $j$ -th weight important element of the  $i$ -th server.
- (2) Since the index units of these indicators are uncertain and known, it is necessary to convert the absolute value of the indicators to the relative value before

calculating the comprehensive index: positive indicators:

$$x'_{ij} = \frac{x_{ij} - \min\{x_{1j}, x_{2j}, \dots, x_{mj}\}}{\max\{x_{1j}, x_{2j}, \dots, x_{mj}\} - \min\{x_{1j}, x_{2j}, \dots, x_{mj}\}} \quad (34.3)$$

Negative indicators

$$x'_{ij} = \frac{\max\{x_{1j}, x_{2j}, \dots, x_{mj}\} - x_{ij}}{\max\{x_{1j}, x_{2j}, \dots, x_{mj}\} - \min\{x_{1j}, x_{2j}, \dots, x_{mj}\}} \quad (34.4)$$

The normalized result is recorded as  $x_{ij}$ .

- (3) Calculate the proportion of the value of the  $i$ -th server under the  $j$ -th weight important element index to the index:

$$P_{ij} = \frac{x_{ij}}{\sum_{i=1}^m x_{ij}}, \quad i = 1, \dots, m; j = 1, \dots, n \quad (34.5)$$

- (4) Calculate the entropy value of the  $j$ -th weight important element

$$e_j = -k \sum_{i=1}^m p_{ij} \ln(p_{ij}), \quad j = 1, 2, \dots, n$$

where  $k = 1/\ln(m) > 0$ , satisfying  $e_j \geq 0$  (34.6)

- (5) Calculating information entropy redundancy

$$d_j = 1 - e_j, \quad j = 1, 2, \dots, n \quad (34.7)$$

- (6) Calculate the weight of each weight important element

$$R_i = \frac{d_j}{\sum_{j=1}^n d_j}, \quad j = 1, 2, \dots, n \quad (34.8)$$

**Failure probability of node.** Assuming that the probability of failure of nodes obeys a negative exponential distribution [6], the probability of node failure is regarded as a Poisson distribution with a failure event arrival rate of  $\lambda_{pc}$  [10]. According to life experience, the arrival rate of failure events of node  $I$  has a certain relationship with the performance of node  $i$ , and the performance of node  $i$  can be judged by referring to the weight  $W_i$ . Therefore, given an initial arrival rate  $\lambda_{fi}$ , it's assumed that the failure time arrival rate of each node is the product of the initial arrival rate and the weight:

$$\lambda_i = \lambda_{fi} \times W_i \quad (34.9)$$

Poisson distribution is a discrete probability distribution, which is used to describe the probability of  $\gamma$  events occurring within a period of time  $[0, t]$ . It assumes that events arrive at a constant rate, then the probability of events occurring in  $[0, t]$  is:

$$\text{Error}_y(t) = \frac{e^{-\lambda_i t} \times (\lambda_i t)^\gamma}{\gamma!} \quad (34.10)$$

If  $\gamma = 0$ , that is, the event does not occur within the time period  $[0, t]$ , according to formula (34.10). It can be seen that the probability that the event does not occur can be expressed as:  $\text{Error}_{\gamma=0} = e^{-\lambda_i t}$ . Let an index period be  $T$ , combined with Formula (34.9), it can be seen that the probability of node  $I$  failure within the job execution time  $[0, t]$  is:

$$\text{PF}_i = 1 - e^{-\lambda_{fi} \times W_i \times T} \quad (34.11)$$

**Node's Misjudgment Loss Model.** Since this article uses the heartbeat module of Tengine, a few parameters must be covered: INTE (heartbeat detection packet transmission interval), FALL (the number of times a node fails to receive a heartbeat response continuously), TOUT (timeout time of a heartbeat detection packet).

**Definition (1) Lost Connected State:** Assuming that the Nginx server and a node at the back-end keep their heartbeat normal until they do not receive a heartbeat reply for the first time, the node is considered to be in a lost connected state at this time. Then, the time from the last received heartbeat to the lost state is recorded as  $T_{iout}$ . The waiting time is defined as  $2 \times T_{iout}$ . For node  $i$ , the total length of cardiac overshoot was recorded as  $T_{tall}(i)$  ( $3 \times T_{iout}$ ), and the total length of a single heartbeat period is  $T_{iout}(i)$ . The parameters to be introduced in this model are:  $N$ : indicates the number of back-end servers to which Nginx is connected;  $\alpha$ : equation coefficient;  $\rho$ : the minimum accuracy requirement of cluster fault judgment;  $S_i$ : the rate at which requests are processed by node  $i$  AFD <sub>$i$</sub> : (accuracy of fault diagnosis), the accuracy of fault diagnosis for node  $i$ ; PMJ <sub>$i$</sub> : (probability of misjudgment), probability of misjudgment for node  $i$ . If a node is disconnected, at this time, the node may be in a down state or a suspended animation state. If it is in a down state, all service requests on the node will fail. It can be considered that the number of requests that node  $I$  made mistakes during downtime is the number of requests that node  $I$  accepted during  $T_{iout}$ :  $S_i \times T_{iout}$ . Here, it is stipulated that the  $T_{tall}$  time cannot exceed two default times,  $T_{tall}(i) \leq 120$  s, so  $T_{iout}(i) \leq 40$  s. Assume that performance of the best nodes have not received the heart in 120 s, the failure rate is 100%, while for some nodes with poor performance, even if the TALL time is not 120 s, the failure accuracy of the node can reach 100%. The waiting time of Nginx can be used as a criterion to determine whether a node fails or not, if Nginx judges that the probability of server failure and the waiting time  $t$  satisfy the value of the function  $\text{Pt} = 0.5 - 0.5 \times \cos(t)$ , which is related to the failure probability of the node in the whole period. Therefore, let  $\theta = \alpha \times \text{PF}_i$ , so the accuracy rate of Nginx judges the failure of node  $i$  is:



$$AFD_i(t) = 0.5 - 0.5 \times \cos(\alpha \times PF_i \times t) \quad 0 < t \leq 120 \quad (34.12)$$

It is assumed that for the node  $e$  with the best performance, if  $t = 120$  s,  $AFD_e(120) = 1$ , if the weight of the node is known, the failure arrival rate of the node can be obtained, and the time period  $T$  is known, then the coefficient can be obtained:  $\alpha = \pi / (1 - e^{-\lambda_e \times T}) / 120$ . It can also be known that  $AFD_i + PMJ_i = 1$ . Therefore, the probability of misjudgment is:

$$PMJ_i(t) = 1 - AFD_i(t) \quad (34.13)$$

**Definition (2) Misjudgment loss:** The loss of computing resources caused by Nginx misjudging a node  $i$  as a failure node by the back end is the loss caused by misjudgment (LCMJ). The misjudgment loss can be considered as the product of the misjudgment probability and the number of requests that have been forwarded to the node  $i$ :

$$LCMJ_i = PMJ_i(\text{TALL}) \times S_i \times T_{IOUT} \quad \text{TALL} \leq 120 \quad (34.14)$$

**Definition (3) Principle of fairness (POF):** If node  $I$  and node  $J$  are out of connection at the same time and Nginx judges that the node fails, the LCMJ caused by Nginx to each node is equal [11].

$$LCMJ_i = LCMJ_j \quad (34.15)$$

According to formulas (34.11)–(34.15), the calculation method of  $T_{iout}(i)$  can be summarized  $T_{iout}(i) = 1/\alpha/PF_i \times \arccos(2 \times PMJ_e \times S_e/S_i - 1)/3$  ( $S_i > PMJ_e \times S_e$ ) **Minimum fault judgment accuracy requirement:** the setting of TALL, the total heartbeat overdue length of the node, needs to meet the requirement that the node fault accuracy judgment rate is not less than  $\rho$ . Therefore, a node that satisfy the POF but does not satisfy  $AFD_i \geq \rho$ , set  $AFD_i = \rho$ ; a node that does not meet the POF, the fault judgment accuracy of the node is also made to be  $\rho$ , so it can be known that:  $T_{iout}(i) = \arccos(1 - 2 \times \rho)/\alpha/PF_i/3$  ( $AFD_i < \rho$  or does not meet the POF). In addition, since  $T_{iout}(i) \leq 40$  is specified above, the calculation formula of the actual heartbeat overdue total length of each node is:  $T'_{iout}(i) = \min\{T_{iout}(i), 120\}$ .

**Dynamic Fair Timeout Algorithm Based on Nginx.** According to the above, a dynamic fair timeout algorithm based on Nginx can be summarized. The expression of the algorithm needs to introduce the following set.

- (1) Weight set of nodes  $w = \{w_1, w_2, \dots, w_i\}$
- (2) The set of accident arrival rates of nodes  $\lambda = \{\lambda_1, \lambda_2, \dots, \lambda_i\}$
- (3) Processing rate set of nodes  $S = \{S_1, S_2, \dots, S_I\}$
- (4) Single node heartbeat period  $T_{iout} = \{T'_{iout}(1), T'_{iout}(2) \dots T'_{iout}(i)\}$

Algorithm Input:  $w, S, T_{iou}(1), \rho, T, \lambda_{fi}$

Output:  $T_{iou}$

- (1) Perform steps (2) to (16) at intervals  $T$
- (2)  $PF_1 = 1 - e^{-\lambda_{fi} \times W_1 \times T}$
- (3)  $\alpha = \pi / (1 - e^{-\lambda_{fi} \times W_1 \times T}) / 120$
- (4)  $AFD_1(T_{iou}(1)) = 0.5 - 0.5 \times \cos(\alpha \times PF_1 \times T_{iou}(1))$
- (5)  $PMJ_1 = 1 - AFD_1$
- (6) *for*(*int*  $i = 2; 1 \leq N; i + +$ )
- (7)  $\{PF_i = 1 - e^{-\lambda_{fi} \times W_i \times T}$
- (8)     *if* ( $S_i > PMJ_1 \times S_1$ )
- (9)          $\{ T_{iou}(i) = 1/\alpha/PF_i \times \arccos(2 \times PMJ_1 \times S_1/S_i - 1)/3$
- (10)          $AFD_i(T_{iou}(i)) = 0.5 - 0.5 \times \cos(\alpha \times PF_i \times T_{iou}(i))$
- (11)         *if* ( $AFD_i < \rho$ )
- (12)          $\{ T_{iou}(i) = \arccos(1 - 2 \times \rho)/\alpha/PF_i/3$
- (13)         } *else*
- (14)          $\{ T_{iou}(i) = \arccos(1 - 2 \times \rho)/\alpha/PF_i/3\}$
- (15)  $T'_{iou}(i) = \min\{T_{iou}(i), 120\}$
- (16) *return*  $T_{iou}$

**Implementation of Dynamic and Fair Timeout Algorithm Based on Nginx.** In this paper, MATLAB software is used for simulation. Firstly, the running values of each index in the experiment are obtained as training data, and  $W_i$  are calculated. It is then up to Nginx to periodically collect performance metrics for the back-end server. Nginx calculates the  $T_{iou}$  of each node according to the above algorithm at every interval  $T$  cycle and writes it into the corresponding array to assign the corresponding parameter.

### 34.4 Construction and Testing of Experimental Environment

In this experiment, five servers are built in the VMware virtual machine, and the configuration and functions are as follows (Table 34.1).

By collecting performance data from Server1 to Server3 many times, use the entropy method to simulate in MATLAB, the weight can be calculated. Use siege tools (500 concurrent numbers last for ten minutes) to test the path pressure test from the client to Nginx and then to one of the nodes. According to the test results, the problem processing rate ratio of each node is obtained. In this experiment, the period selected is 5 min, the  $W_{de}$  is 10, the coefficient is 0.2, and the  $T_{iou}$  of Server1 node is set for 30 s, then each node calculates the weight every 5 min and sends it to Nginx. Test scheme: Siege is continuously used to send static page access requests at a concurrent frequency of 100, 200 and 500 for 3 periods each, and the service of one of the servers is randomly stopped for 1 min in the period, and the total amount

**Table 34.1** Server node software and hardware configuration

Node	Memory	CPU	Operating system	Network adapter (Mb/s)
Client	2g	1 single core processor	CentOS7	1000
Nginx	2g	1 double core processor	CentOS7	1000
Server1	2g	1 single core processor	CentOS7	1000
Server2	4g	1 double core processor	CentOS7	1000
Server3	6g	2 double core processor	CentOS7	1000

**Table 34.2** The test results

Period	Concurrency	Total before improvement	Total number of failed node forwarding before improvement	Total after improvement	Total number of failed node forwarding after improvement
1	100	623,180	198,487	640,537	180,488
2	100	629,660	195,903	655,979	199,256
3	100	651,599	205,709	592,422	173,797
4	300	611,875	184,599	622,155	167,468
5	300	644,548	201,989	601,889	170,502
6	300	638,130	198,782	633,256	169,112
7	500	553,599	180,590	573,546	148,773
8	500	588,369	184,103	580,989	150,332
9	500	580,540	178,452	578,437	149,876

of requests forwarded to “down” nodes before and after improvement in the nine periods is counted (Table 34.2).

The fault detection promotion rate is defined as the difference between the total number of forwarding of failed nodes before and after improvement and the total number of previous tests, Then the improved fault detection accuracy is increased by 7% at 100 concurrent numbers, 12% at 300 concurrent numbers, and 18% at 500 concurrent numbers. Therefore, experiments can prove that the dynamic fair timeout heartbeat algorithm based on Nginx effectively improves the fault detection accuracy of nodes.

## 34.5 Conclusions

Aiming at the problems existing in the existing health check mechanism of heterogeneous clusters based on Nginx reverse proxy, this paper considers the characteristics of heterogeneous clusters and uneven load that lead to different performance

and dynamic changes, and proposes a dynamic fair timeout algorithm based on Nginx. The implementation and proof show that the failure detection rate of nodes is increased by 18% compared with that before improvement. However, only detecting failed nodes does not have an effective and reliable failover mechanism, nor can it improve the fault tolerance of the cluster system, nor can it improve the high availability of the cluster. Therefore, the next goal of this paper is to study the failover strategy of Nginx to improve the high availability of the cluster.

The main contribution of this paper is to implement the platform transplantation of the fair timeout algorithm, and to improve it based on the Nginx platform, so the fault detection of Nginx has been improved to a certain extent. It is an improvement for such a widely used Nginx server.

## References

1. Ramana, K., Ponnaivaikko, M.: A multi-class load balancing algorithm (MCLB) for heterogeneous web cluster. *Stud. Inf. Control* **27**(4), 443–452 (2018)
2. Zheng, Q.: Improving MapReduce fault tolerance in the cloud. In: 2010 IEEE International Symposium on Parallel and Distributed Processing. IEEE (2010). <https://doi.org/10.1109/IPDPSW.2010.5470865>
3. Baohua, W.: Research and optimization of server cluster load balancing strategy based on Nginx. Nanchang University (2020)
4. Chen, W.: Research and improvement of server cluster load balancing strategy based on Nginx. South China University of Technology (2020)
5. Yuan, G.: Research on load balance strategy of web server based on Nginx. Hainan University (2019)
6. Dean, J., Ghemawat, S.: MapReduce: simplified data processing on large clusters. *Commun. ACM* **51**(1), 107–113 (2008)
7. Xunzhi, X.: Research on cluster management system. Beijing University of Posts and Telecommunications (2018)
8. Jing, Z., Hongrui, N., Xiucui, Y., Xiaorong, J., Yao, H.: A spatial correlation based partial coverage scheduling scheme in wireless sensor networks. *J. Netw. Intell.* **5**(2), 34–43 (2020)
9. Yuxing, Z.: Source code research and systematic module encapsulation based on nginx. Nanjing University of Posts and Telecommunications (2020)
10. Zhiyi, L., Zhexing, L., Lei, G.: I/O performance comparison of apache and Nginx in high concurrence environment. *Comput. Syst. Appl.* **22**(06), 204–208 (2013)
11. Guodong, G., Fei, T., Yan, Y.: Real-time fault-tolerant technology for Hadoop based on heartbeat expired time mechanism. *J. Comput. Appl.* **35**(10), 2784–2788 (2015)

# Chapter 35

## Visually Meaningful Image Encryption Algorithm Based on Parallel Compressive Sensing and Cellular Neural Network



Renxiu Zhang , Donghua Jiang , Wei Ding , Ya Wang , Yanan Wu ,  
Yerui Guang , and Qun Ding 

**Abstract** At present, most image encryption algorithms protect the image by converting the original image into a visually meaningless noise-like image. However, the noise-like image can easily attract the attention of attackers, which increases the risk of being deciphered. Thus, a novel meaningful image encryption algorithm based on parallel compressive sensing and cellular neural network is proposed in this paper. In our scheme, the image is processed by three modules, namely, compression, encryption and hiding. Among them, the compression module is utilized to compress the plain images in parallel. After that, the encryption module converts the compressed image into a meaningless noise-like image by diffusion and scrambling. Finally, the hiding module realizes the visualization of the encrypted image by embedding the encrypted image into a carrier image, which helps reduce the interest of attacker in deciphering cipher images. Experimental results and analysis indicate that the proposed algorithm has satisfactory performance and can effectively protect

---

R. Zhang · W. Ding · Y. Wang · Y. Wu · Y. Guang · Q. Ding (✉)  
Electronic Engineering College, Heilongjiang University, Harbin 150080, China  
e-mail: [qunding@aliyun.com](mailto:qunding@aliyun.com)

R. Zhang  
e-mail: [2191297@s.hlju.edu.cn](mailto:2191297@s.hlju.edu.cn)

W. Ding  
e-mail: [2191266@s.hlju.edu.cn](mailto:2191266@s.hlju.edu.cn)

Y. Wang  
e-mail: [2201740@s.hlju.edu.cn](mailto:2201740@s.hlju.edu.cn)

Y. Wu  
e-mail: [2201734@s.hlju.edu.cn](mailto:2201734@s.hlju.edu.cn)

Y. Guang  
e-mail: [2201708@s.hlju.edu.cn](mailto:2201708@s.hlju.edu.cn)

D. Jiang  
School of Information Engineering, Chang'an University, Xi'an 710064, China  
e-mail: [jiangdonghua@chd.edu.cn](mailto:jiangdonghua@chd.edu.cn)

image information from being leaked under the premise of reducing computational overhead.

## 35.1 Introduction

In recent years, the field of image encryption chaos-based has attracted the attention of many scholars. For instance, Ref. [1] proposed a new secure transmission system for images based on the diffusion-permutation structure. In particular, in the permutation stage, the system uses a chaos generator to generate the initial value of the improved 2D Cat map, which makes the transmission system obtain higher security. Then, Ref. [2] presented an image encryption method, which employed the simple chaotic map, lightweight computation and parallel structure to encrypt the plain image into a noise-like image. Experiments have proved that this method has qualified security. However, there are some issues that need to be resolved. (i) when the volume of images that need to be encrypted is very large, it will consume a lot of resources and computational costs; (ii) low-dimensional chaotic map has defects such as small key space and poor unpredictability; (iii) converting images containing confidential information into meaningless noise-like images greatly arouses the interest of attackers in cracking cipher images, thereby increasing the risk of confidential information leakage.

To address these issues, a novel meaningful image encryption algorithm based on parallel compressive sensing and cellular neural network is proposed in this paper, which is mainly composed of three modules. Wherein, in order to reduce the consumption of resources and computation, the first module adopts the compressive sensing technology to simultaneously encrypt and compress images. Next, the second module uses 6-D CNN and Hilbert curve to encrypt the compressed image to further improve the security. Finally, to protect the appearance security of image, the third module hides the encrypted images into the carrier images to attain the visual cipher images. Extensive experimental results and analysis indicate that the proposed algorithm can not only reduce computational overhead but also has satisfactory security performance.

## 35.2 Preliminaries

### 35.2.1 *Parallel Compressive Sensing*

To reduce the overhead of computation and the consumption of space, the compressive sensing (CS) is adopted to sample and measure the plain image by column. For an image  $\mathbf{z}$  sized of  $M \times N$ ,  $z_i$  are the pixel values of the  $i$ -th column of  $\mathbf{z}$ . Then the measurement process of compressive sensing is expressed as Eq. (35.1).

$$y_i = \Phi \times z_i, \quad i = 1, 2, 3, \dots, N. \tag{35.1}$$

$y = [y_1, y_2, \dots, y_N]$  is measurement value matrix sized of  $M \times N$ .  $\Phi \in \mathbb{R}^{M \times N}$  is defined as measurement matrix. Moreover, the CS reconstruction theory shows that when  $\Phi$  satisfies the restricted isometry property and  $z_i$  is sparse, it is possible for  $z_i$  to be reconstructed from  $y_i$ . However, in general, the natural signal is sparse only in certain transform domains. When  $z_i = \Psi \times s_i$  and  $\|s_i\|_0 = k$ ,  $z_i$  is considered to be  $k$ -sparse on  $\Psi$ . At this point, the measurement process can be expressed as Eq. (35.2).

$$y_i = \Phi \times z_i = \Phi \times \Psi \times s_i = \Theta \times s_i \tag{35.2}$$

It is difficult to judge whether the matrix  $\Phi$  satisfies the RIP constraints. However, if  $\Phi$  independent of the sparse representation basis  $\Psi$ , the reconstructed sparse signal  $s_i$  can be converted to a problem solved by the  $l_1$  norm according to Eq. (35.3). Then, the original image is restored through the inverse transform of sparse representation.

$$\min \|s_i\|_1 \quad \text{s.t. } y_i = \Theta \times s_i \tag{35.3}$$

### 35.2.2 Image Encryption Based on “diffusion-Scrambling”

**The 6-D CNN.** Reference [3] describes and analyzes the hyperchaos phenomenon of the 6-D cellular neural network system in detail. Its mathematical model is described in Eq. (35.4).

$$\begin{cases} \dot{x}_1 = -x_3 - x_4 \\ \dot{x}_2 = 2x_2 + x_3 \\ \dot{x}_3 = 14x_1 - 14x_2 \\ \dot{x}_4 = 100x_1 - 100x_4 + 200p_4 \\ \dot{x}_5 = 18x_2 + x_1 - x_5 \\ \dot{x}_6 = 4x_5 - 4x_6 + 100x_2 \end{cases} \tag{35.4}$$

In Eq. (35.4),  $p_4 = (lx_4 + 1 - lx_4 - 1)/2$ . When  $t \rightarrow \infty$ , its Lyapunov exponents are  $\lambda_1 = 2.7481$ ,  $\lambda_2 = -2.9844$ ,  $\lambda_3 = 1.2411$ ,  $\lambda_4 = -14.4549$ ,  $\lambda_5 = -1.4123$  and  $\lambda_6 = -83.2282$ . Two of them are positive, which indicates that this system is hyperchaotic [4]. Additionally, the partial phase diagram of 6-D CNN obtained by Runge–Kutta method is plotted in Fig. 35.1.

**Scrambling with Hilbert curve.** Hilbert curve is the filled curve which has the property of being able to traverse all points in a square area on the plane. By using this property, the pixel position of the image can be shuffled to obtain a scrambled image. As shown in Fig. 35.2a, the pixels of the image matrix are scanned sequentially

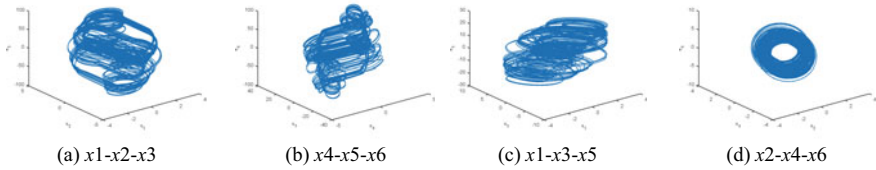
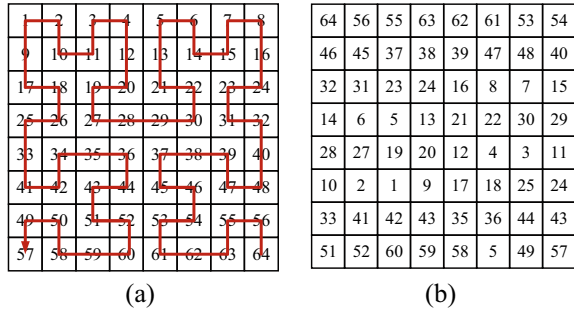


**Fig. 35.1** The 6-D CNN chaotic attractors

**Fig. 35.2** Hilbert curve. **a** Scanning trajectory of Hilbert curve. **b** The scrambled matrix



according to the traversal sequence of the 2D Hilbert curve, and the results are stored in a 1D sequence. Then, the pixels of the image are rearranged to obtain the pixel matrix of the scrambled image, as shown in Fig. 35.2b.

### 35.3 The Proposed Algorithm

The encryption flow chart proposed in this paper is shown in Fig. 35.3, which mainly includes three stages. In the first stage, i.e., the compression module, the measurement matrix produced by the 2-dimensional logistic map [5] is utilized to compress the wavelet coefficients of the original image in parallel. Then, in the encryption module, the compressed image is further encrypted by the diffusion sequence generated by 6-D CNN chaotic system and Hilbert scrambling algorithm. In the last stage, the encrypted image is embedded into the alpha channel of the carrier image. Moreover, for the sake of generality, it is assumed that the size of plain image  $PI$  and host image  $H$  is  $M \times N$ . Next, the encryption steps of the proposed algorithm are described in detail as follows.



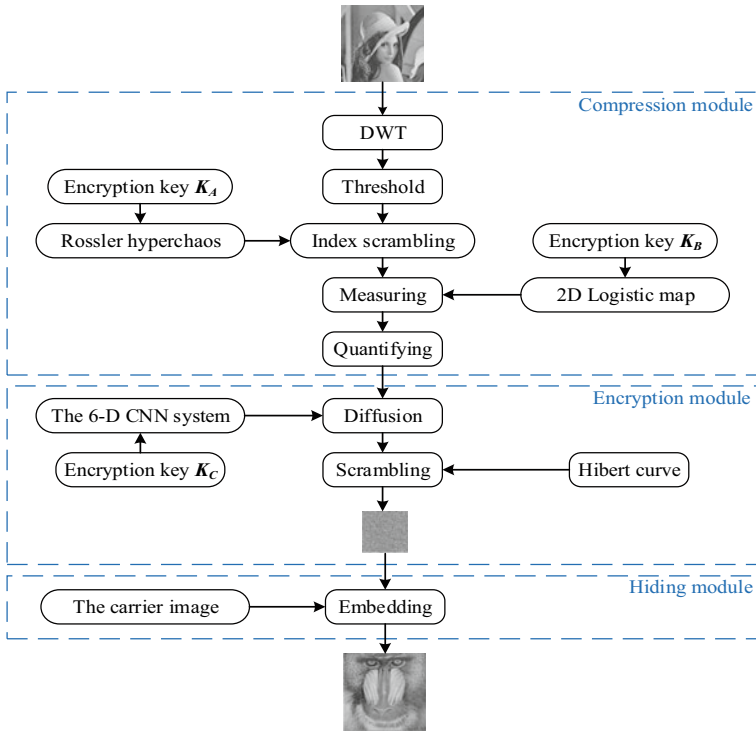


Fig. 35.3 The encryption flow

### 35.3.1 Compression Module

Step 1. The plain image  $P1$  is sparsed by 2-D discrete wavelet transform to obtain the coefficient matrix  $P2$ .

Step 2. All elements in matrix  $P2$  whose absolute values are less than or equal to the threshold  $T_s$  are assigned to 0. And the matrix after threshold processing is defined as  $P3$ .

Step 3. The encryption key  $K_A$  is used as the initial value of the Rossler hyperchaos [6], and iterate it  $500 + MN$  times to obtain the hyperchaotic trajectories  $[X, Y, Z] \in \mathbb{R}^{MN \times 3}$ .

Step 4. The sequence  $X$  is sorted to obtain the keystream  $Tx$  used for index scrambling. Then, according to Eq. (35.5), the matrix  $P3$  is scrambled.

$$P4_i = P3_{Tx(i)} \tag{35.5}$$

Step 5. The key-controlled measurement matrix  $\mathbf{Phi}$  was generated by the 2D Logistic map, where  $\mathbf{Phi} \in \mathbb{R}^{CN \times N}$ ,  $CN = CR \times M$ , and the matrix  $\mathbf{P4}$  was measured in parallel to obtain the compressed matrix  $\mathbf{P5}$ . This process can be expressed by Eq. (35.6).

$$\mathbf{P5} = \mathbf{Phi} \times \mathbf{P4} \quad (35.6)$$

Step 6. The matrix  $\mathbf{P5}$  is linearly quantized according to Eq. (35.7) to produce the compressed image  $\mathbf{P6}$ . The parameters max and min of the quantization, respectively, represent the maximum and minimum in matrix  $\mathbf{P5}$ . Also, round( $\cdot$ ) means to round the elements in parentheses.

$$\mathbf{P6} = \text{round}\left(255 \times \frac{\mathbf{P5} - \min}{\max - \min}\right) \quad (35.7)$$

### 35.3.2 Encryption Module

Step 1. The compressed image  $\mathbf{P6}$  is divided into six non-overlapping units  $\mathbf{C}_i$ . Using the encryption keys as the initial values of the 6-D CNN. Then, six chaotic sequences  $\mathbf{S}_i$  are generated after iteration, and the diffused image  $\mathbf{DI}$  is obtained by Eq. (35.8).

$$\mathbf{DI} = \mathbf{S}_i \oplus \mathbf{C}_i \quad (35.8)$$

Step 2. The Hilbert curve is utilized to scramble and reposition the pixel positions of the diffused image  $\mathbf{DI}$  to complete the scrambled image  $\mathbf{SI}$ .

### 35.3.3 Hiding Module

Step 1. The encrypted image  $\mathbf{SI}$  is segmented to obtain the matrices  $\mathbf{SI}_1$ ,  $\mathbf{SI}_2$  and  $\mathbf{SI}_3$  according to Eq. (35.9).

$$\begin{cases} \mathbf{SI}_1 = \text{fix}(\mathbf{SI}/100) \\ \mathbf{SI}_2 = \text{mod}(\text{fix}(\mathbf{SI}/10), 10) \\ \mathbf{SI}_3 = \text{mod}(\mathbf{SI}, 10) \end{cases} \quad (35.9)$$

Step 2. Construct the matrix  $\mathbf{A} \in \mathbb{N}^{M \times N}$  with element values of 246. Then, matrix  $\mathbf{SI}_1$ ,  $\mathbf{SI}_2$  and  $\mathbf{SI}_3$  are embedded into the matrix  $\mathbf{A}$ , respectively, by Eq. (35.10), and

the processed matrix is defined as  $AI$  where  $i = 1, 2, 3, \dots, 0.25 MN$ .

$$\begin{cases} A^i = 246 + SI_1^i \\ A^{(0.25M \times N)+i} = 246 + SI_2^{(0.25M \times N)+i} \\ A^{(0.5M \times N)+i} = 246 + SI_3^{(0.5M \times N)+i} \end{cases} \quad (35.10)$$

Step 3. The cipher image  $C$  is generated synchronously with the carrier image using the matrix  $AI$  as the alpha channel.

## 35.4 Experimental Results and Analysis

### 35.4.1 Key Space

Insufficient key space may cause the algorithm to be brute forcefully cracked by decipherers. Thus, a sufficiently extensive key space is one of the essential conditions for encryption algorithms to resist the brute force attacks. In the proposed scheme, the key is derived from the initial values of Rossler hyperchaos, 6D CNN and logistic map. Moreover, assuming that the calculation accuracy is  $10^{-15}$ , then the key space of our scheme reach to  $10^{165}$ , which is large enough that the attackers cannot brute force it.

### 35.4.2 Correlation

The attacker can make statistical analysis of the cipher image by taking advantage of the concentrated distribution of adjoining pixels in the image to achieve the purpose of deciphering. Therefore, the encryption algorithm should cut down the correlation between adjoining pixels as far as possible. The pixel distribution of the original image and the generated cipher image are plotted in Fig. 35.4. It can be observed that the adjoining pixels of the original image are concentrated in the diagonal area and are closely related, while the pixels of the cipher image are irregularly distributed in the whole area. It can be concluded that the algorithm can effectively decrease the correlation between the adjoining pixels of the image. Furthermore, the correlation between adjoining pixels can be qualitatively judged by Eq. (35.11).

$$r_{xy} = \frac{\text{cov}(x, y)}{\sqrt{D(x)D(y)}} \quad (35.11)$$

where  $x$  and  $y$  represent the gray values of two adjoining pixels in the image. The test results are listed in Table 35.1. It can be seen that the adjoining pixels in original

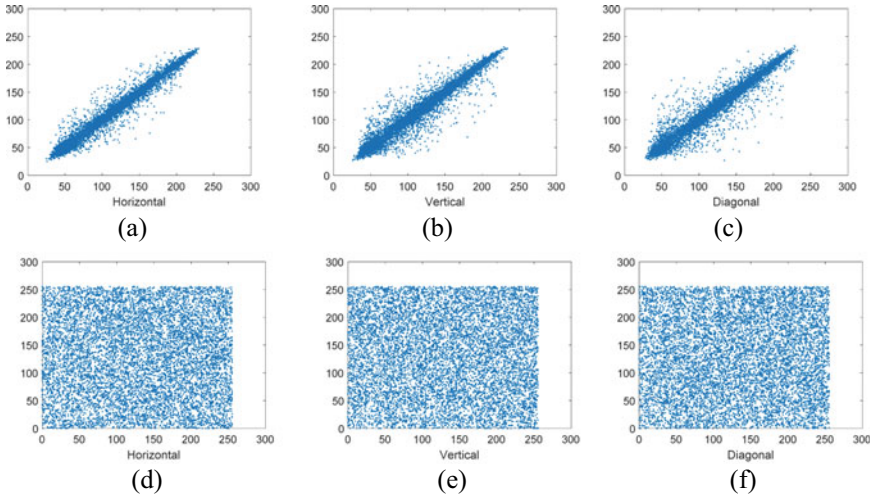


**Fig. 35.4** The pixel distribution of the plain image and the cipher image. **a** The horizontal pixel distribution of the plain image. **b** The vertical pixel distribution of the plain image. **c** The diagonal pixel distribution of the plain image. **d** The horizontal pixel distribution of the cipher image. **e** The vertical pixel distribution of the cipher image. **f** The diagonal pixel distribution of the cipher image

**Table 35.1** The correlation tests of the original image and the encrypted image

Image	Correlation		
	Horizontal	Vertical	Diagonal
Original Lena	0.9849	0.9689	0.9661
Encrypted Lena	0.0033	0.0044	0.0110

Lena are high correlated, while the correlation of adjoining pixels in encrypted Lena tends to 0.

### 35.4.3 Visual Security

The difference between the steganographic images and the carrier images determines the visual security of the encryption algorithm. The smaller the difference, the higher the visual security of the algorithm. The visual security of the proposed algorithm is quantitatively measured by calculating the peak signal-to-noise ratio (PSNR) between the steganographic images and the carrier images. The PSNR is mathematically represented as Eq. (35.12), where  $O(i, j)$  and  $D(i, j)$  represent the original image and the decrypted image sized of  $M \times N$ , respectively.

**Table 35.2** PSNR tests of the plain image and the carrier image

Plaintext image	Carrier image	PSNR (dB)	
		Ours	Ref. [7]
Lena (256 × 256)	Peppers (256 × 256)	36.5021	31.7986
Barbara (256 × 256)	Bridge (256 × 256)	36.3017	31.7397

**Table 35.3** PSNR tests of the plaintext image and the decrypted image

Plain image	Carrier image	PSNR (dB)	
		Ours	Ref. [8]
Barbara (512 × 512)	Peppers (512 × 512)	30.19	28.55
Barbara (512 × 512)	Lena (512 × 512)	30.19	28.55

$$PSNR = 10 \times \log \frac{255^2}{\frac{1}{M \times N} \sum_{i=1}^M \sum_{j=1}^N (O(i, j) - D(i, j))^2} \text{ (dB)} \quad (35.12)$$

The larger the value of PSNR, the smaller the difference between the two images. The plain image Lena sized of 256 × 256 and the carrier image Peppers sized of 256 × 256 are placed to the proposed encryption algorithm. The PSNR values obtained are listed in Table 35.2. The comparative analysis further illustrates that the embedding method proposed in this paper has satisfactory visual security.

### 35.4.4 Quality of Decryption

In the compression stage, due to the loss of energy, the image will inevitably be damaged, which will lead to a decline in quality. Therefore, it is necessary to analyze the quality of a decrypted image by calculating the PSNR value of the original image and decrypted image. As shown in Table 35.3, the PSNR value obtained by the proposed algorithm is 30.19 dB, which has satisfactory decryption quality.

## 35.5 Conclusion

This paper presents a visual digital image encryption algorithm with good security effect. In this algorithm, first, the compression module encrypts and compresses the image synchronously, which greatly reduces the computational cost. Second, the encryption module diffuses and scrambles the compressed image data to further improve the security, thereby transforming the image into a visually meaningless noise-like image. To protect the appearance security of image information, the final hiding module realizes the visual processing of the noise-like image. By hiding the

encrypted noise-like image into the carrier image, a visual cipher image is formed, which greatly reduces the attacker's intention to crack the cipher image. Extensive experimental results and analysis manifest that the proposed algorithm has the properties of extensive key space, low correlation, high visual security and satisfactory decryption quality. Moreover, it can effectively protect the image information from being leaked while reducing the computational cost.

## References

1. Assad, S.E., Farajallah, M.: A new chaos-based image encryption system. *Sig. Process. Image Commun.* **41**, 144–157 (2016)
2. Lee, W.K., Phan, R.C.W., Yap, W.S., Goi, B.M.: SPRING: a novel parallel chaos-based image encryption scheme. *Nonlinear Dyn.* **92**, 575–593 (2018)
3. Qing, D., Xiao, S., Fang, Y.: Hyperchaos in a simple CNN. *Int. J. Bifurcat. Chaos* **16**, 2453–2457 (2006)
4. Koçak, H., Palmer, K.: Lyapunov exponents and stability in interval maps. *Sema J.* **51**(1), 79–82 (2010)
5. Kumar, V., Girdhar, A.: A 2D logistic map and Lorenz-Rosler chaotic system based RGB image encryption approach. *Multimed. Tools Appl.* **80**, 3749–3773 (2021)
6. Malik, D.S., Shah, T.: Color multiple image encryption scheme based on 3D-chaotic maps. *Math. Comput. Simul.* **178**, 646–666 (2020)
7. Zhu, L., Song, H., Zhang, X., et al.: A robust meaningful image encryption scheme based on block compressive sensing and SVD embedding. *Sig. Process.* **175**, 107629 (2020)
8. Chai, X.: An efficient visually meaningful image compression and encryption scheme based on compressive sensing and dynamic LSB embedding. *Opt. Lasers Eng.* **124**(1), 105837 (2020)

# Chapter 36

## Comments on “A Robust User Authentication Protocol with Privacy-Preserving for Roaming Service in Mobility Environments”



Xinglan Guo, Lei Yang, Tsu-Yang Wu, Lili Chen, and Chien-Ming Chen

**Abstract** Roaming service under the global mobile network (GLOMONET) means that users who use mobile devices can still use mobile devices in other regions or countries after leaving their region or country. When mobile users use roaming services, the communication information transmitted by wireless channels is easy to be tampered with and eavesdropped on by attackers. These attacks may expose the identity and location of remote users. Thus, mutual authentication among mobile users, foreign agents, and home agents play an important role. To ensure a secure roaming service in a mobile network, it is necessary to design an efficient and secure solution. Recently, Shashidhara et al. proposed a user authentication protocol for roaming service in the GLOMONET. In this paper, we find that there are some security vulnerabilities in their protocol, including perfect forward secrecy (PFS), key compromise impersonation attacks (KCIA), and known-session-specific temporary information attacks (KTIA).

### 36.1 Introduction

The rapid development of wireless networks [11] has brought great convenience to people's lives, in which there is a special network environment called global mobility network (GLOMONET) [1, 2, 9, 10, 14]. GLOMONET refers to a new network environment that can provide global roaming service for communication. With the rapid development of communication technologies, mobile users can access the services through roaming technologies. In this environment, the mobile user registers with the home agent. To obtain the service of the foreign network, it needs the help of the home agent to realize the authentication and establish a session secret key [6, 18–20] between the mobile user and the foreign agent. However, the communication transmitted in the mobile network environment is easily vulnerable to various attacks [4]. Thus, it is necessary to protect the privacy of users as well as

---

X. Guo · L. Yang · T.-Y. Wu (✉) · L. Chen · C.-M. Chen  
College of Computer Science and Engineering, Shandong University of Science and Technology,  
Qingdao 266590, China

to design authentication protocols to ensure the realization of secure communication [5, 7, 12, 15–17, 21].

In 2009, Chang et al. [3] proposed an enhanced authentication protocol to maintain the anonymity of mobile users for roaming services in global mobile networks. However, this protocol cannot guarantee anonymity and confidentiality. To improve their protocol, Zhou et al. [23] proposed a secure authentication protocol. Unfortunately, their protocol is also vulnerable to forgery attacks, replay attacks, and insider attacks. In 2016, Gope et al. [8] proposed an effective authentication protocol. However, the cost of this protocol is computationally expensive. Xu et al. [22] analyzed Gope et al.'s protocol and found that the protocol is vulnerable to replay attacks and clock synchronization problems. Then, a new user authentication protocol is proposed.

Recently, Shashidhara et al. [13] analyzed Xu et al.'s protocol and found that the protocol is vulnerable to denial of service attacks, privileged-insider attacks, and impersonation attacks. To solve these security problems, they further proposed a lightweight user authentication protocol with privacy preservation. In this paper, we analyze Shashidhara et al.'s authentication protocol and point out its security vulnerabilities, including perfect forward secrecy (PFS), key compromise impersonation attacks (KCI), and known-session-specific temporary information attacks (KSTIA).

## 36.2 Review of Shashidhara et al.'s Protocol

In this section, we review the initialization phase, registration phase, login phase, and authentication phase of the protocol. The symbols used in this protocol are described in Table 36.1.

**Table 36.1** Notations

Symbol	Description
$PSW_{MU}$	Password of the mobile user
$ID_{MU}, ID_{HA}, ID_{FA}$	Identities of MU, HA and FA
$SK_F$	Shared-secret key of HA and FA
$SK_H$	Secret key of HA
$K_{MU}$	Counter value of MU
SK	Session key
A	Adversary



### 36.2.1 Initialization Phase

The protocol includes three roles. Mobile User (MU), Foreign Agent (FA), and Home Agent (HA). In the initialization phase, FA obtains a dynamic Diffie–Hellman secret key  $SK_F$  from HA, where  $SK_F = h(ID_{FA} \parallel SK_H)$ .

### 36.2.2 Registration Phase

The registration phase of the protocol is that MU registers with HA. The registration of MU follows the following steps.

- (1) MU selects identity  $ID_{MU}$ , password  $PSW_{MU}$  and randomly generates a random number  $R_M$ , then MU computes a pseudo identity  $AID = h(ID_{MU} \parallel R_M)$ , and sends  $M_m = \{AID\}$  to HA through secure channel.
- (2) HA computes  $RID = h(AID \parallel SK_H)$  after receiving message  $M_m$  from MU, and initializes  $K_{MU}$  to 0. Then, HA stores  $\{AID, K_{MU}\}$  in its own database. Finally, HA sends  $M_h = \{RID, K_{MU}, h(\cdot)\}$  to MU through secure channel.
- (3) After MU receives the message  $M_h$  from HA, MU computes two values:  $AC = RID \oplus h(PSW_{MU} \parallel R_M)$ ,  $LA = h(ID_{MU} \parallel PSW_{MU} \parallel R_M)$ . Finally, MU stores  $\{AC, LA, R_M, K_{MU}\}$  in the smart card.

### 36.2.3 Login and Mutual Authentication Phase

This is an authentication protocol based on three parties. When MU wants to access a foreign network through roaming service, to ensure secure communication, MU and FA need to be authenticated by HA. The authentication steps are as follows.

- (1) First of all, MU enters its own  $ID_{MU}$  and password  $PSW_{MU}$  in the smart device, and computes  $LA^* = h(ID_{MU} \parallel PSW_{MU} \parallel R_M)$  through the  $R_M$  obtained from the smart card, then MU verifies  $LA^* \stackrel{?}{=} LA$ . If equal, login to smart card is successful. Otherwise, the login fails.
- (2) After successful login, MU generates a random number  $N_{MU}$ , and computes  $RID = AC \oplus h(PSW_{MU} \parallel R_M)$ ,  $A_M = h(ID_{MU} \parallel R_M) \oplus N_{MU}$ ,  $V_1 = h(RID \parallel K_{MU}) \oplus N_{MU}$ . Finally, MU transmits the login request  $M_1 = \{A_M, V_1, ID_{HA}\}$  to FA through public channel.
- (3) After receiving the message  $M_1$  from MU, FA generates a random number  $N_{FA}$ , and computes  $B_M = h(A_M \parallel SK_F) \oplus N_{FA}$ ,  $V_2 = h(B_M \parallel SK_F \parallel V_1)$ . FA transmits authentication request  $M_2 = \{B_M, V_1, V_2, ID_{FA}\}$  to HA through public channel.
- (4) After receiving the message  $M_2$  from FA, HA verifies the  $ID_{FA}$ , and if it exists, HA finds the  $SK_F = h(ID_{FA} \parallel SK_H)$  associated with the  $ID_{FA}$ . HA computes

$V_2^* = h(B_M \parallel SK_F \parallel V_1)$ , and verifies  $V_2^* \stackrel{?}{=} V_2$ . If equal, HA believes that FA is legal. Otherwise, the certification is terminated. HA computes  $RID^* = h(AID \parallel SK_H)$ ,  $N_{MU}^* = h(RID^* \parallel K_{MU}) \oplus V_1$ ,  $V_1^* = h(RID^* \parallel K_{MU}) \oplus N_{MU}^*$  and verifies  $V_1^* \stackrel{?}{=} V_1$ . If equal, HA believes that MU is legal. Otherwise, authentication is terminated. HA computes  $A_M^* = (AID \parallel R_M) \oplus N_{MU}^*$ ,  $N_{FA}^* = h(A_M^* \parallel SK_F) \oplus B_M$ ,  $N_M^* = h(RID^* \parallel N_{MU}^*) \oplus N_{FA}^*$ ,  $V_3 = h(ID_{HA} \parallel A_M^* \parallel SK_F)$ ,  $V_4 = h(RID^* \parallel ID_{FA} \parallel K_{MU})$ . Then HA updates  $K_{MU} = K_{MU} + 1$  and stores in database of HA. Finally, HA transmits authentication request  $M_3 = \{N_M^*, V_3, V_4\}$  to HA.

- (5) After receiving authentication request  $M_3$  from HA, FA computes  $V_3^* = h(ID_{HA} \parallel A_M \parallel SK_F)$ , and verifies  $V_3^* \stackrel{?}{=} V_3$ . If it is equal to  $V_3$ , FA believes that HA and MU are legal. Otherwise, the communication will be terminated. Then, FA computes  $SK = h(N_{FA} \parallel A_M \parallel ID_{HA})$ , and finally FA transmits message  $M_4 = \{N_M^*, V_4\}$  to MU.
- (6) After receiving message  $M_4$  from FA, MU computes  $V_4^* = h(RID \parallel ID_{FA} \parallel K_{MU})$ , and verifies  $V_4^* \stackrel{?}{=} V_4$ . If equal, MU believes that FA and HA are legal. Otherwise, the certification is terminated. Then, MU computes  $N_{FA} = h(RID \parallel N_{MU}) \oplus N_M^*$ ,  $SK = h(N_{FA} \parallel A_M \parallel ID_{HA})$ , and finally MU updates  $K_{MU} = K_{MU} + 1$  and stores it in the smart card.

### 36.3 Statement of the Problem

This paper is about the protocol of Shashidhara et al. In this section, we analyze the protocol and point out three security vulnerabilities, violation of perfect forward secrecy (PFS), key compromise impersonation attacks (KCIA), and known-session-specific temporary information attacks (KTIA). PFS means that although the server's long-term private key is compromised by the adversary ( $A$ ), the former session keys can also be protected. KCIA refers to that if  $A$  can obtain a long-term private key of the user, then  $A$  can impersonate as another legitimate user. KTIA means that the exposure of the random number will lead to the exposure of the session key.

In this paper, we suppose  $A$  has the following abilities.  $A$  can access the public communication channel. And  $A$  may obtain a dynamic Diffie–Hellman secret key  $SK_F$  from HA, where  $SK_F = h(ID_{FA} \parallel SK_H)$ , and direct access a random number  $N_{FA}$ .

#### 36.3.1 Perfect Forward Secrecy

To compute the session key,  $A$  may follow the following steps.

- (1)  $A$  can first intercept the login request  $M_1 = \{A_M, V_1, ID_{HA}\}$  and authentication request  $M_2 = \{B_M, V_1, V_2, ID_{FA}\}$  transmitted on the public channel.  $A$  can

obtain parameters  $\{A_M, ID_{HA}, B_M, ID_{FA}\}$  from the two requests for subsequent computation of session key.

- (2)  $A$  uses  $\{ID_{FA}, B_M, A_M\}$  in intercepted message  $M_2$  and  $SK_H$  to compute  $SK_F = h(ID_{FA} \parallel SK_H)$ ,  $N_{FA} = h(A_M \parallel SK_F) \oplus B_M$  to get the value  $N_{FA}$  required for session key computation.
- (3) Finally,  $A$  can successfully compute  $SK = h(N_{FA} \parallel A_M \parallel ID_{HA})$ .

Therefore, the protocol of R. Shashidhara et al. cannot provide PFS.

### 36.3.2 Key Compromise Impersonation Attacks

To impersonate as a legitimate FA,  $A$  may follow the following steps.

- (1) Firstly,  $A$  can intercept the authentication request  $M_2 = \{B_M, V_1, V_2, ID_{FA}\}$  and login request  $M_1 = \{A_M, V_1, ID_{HA}\}$  transmitted on the public channel, and compute  $SK_F^* = h(ID_{FA} \parallel SK_H)$  with  $SK_H$  obtained by  $A$ .
- (2) Then,  $A$  generates a random number  $N'_{FA}$ , and computes  $B'_M = h(A_M \parallel SK_F^*) \oplus N'_{FA}$ ,  $V'_2 = h(B'_M \parallel SK_F^* \parallel V_1)$ .  $A$  can form an effective authentication request  $M'_2 = \{B'_M, V_1, V'_2, ID_{FA}\}$  and send it to HA.
- (3) After receiving the message  $M'_2$  from  $A$ , HA verifies the  $ID_{FA}$ , and if it exists, HA finds the  $SK_F^* = h(ID_{FA} \parallel SK_H)$  associated with the  $ID_{FA}$ . HA computes  $SK_F^* = h(ID_{FA} \parallel SK_H)$ ,  $V_2^* = h(B'_M \parallel SK_F^* \parallel V_1)$ , and verifies  $V_2^* \stackrel{?}{=} V'_2$ . If equal, HA believes that  $A$  is a legal FA. Otherwise, the certification is terminated. HA computes  $RID^* = h(AID \parallel SK_H)$ ,  $N^*_{MU} = h(RID^* \parallel K_{MU}) \oplus V_1$ ,  $V_1^* = h(RID^* \parallel K_{MU}) \oplus N^*_{MU}$  and verifies  $V_1^* \stackrel{?}{=} V_1$ . If equal, HA believes that MU is legal. Otherwise, authentication is terminated. HA computes  $A^*_M = h(ID_{MU} \parallel R_M) \oplus N^*_{MU}$ ,  $N'_{FA} = h(A^*_M \parallel SK_F^*) \oplus B'_M$ ,  $N'_M = h(RID^* \parallel N^*_{MU}) \oplus N'_{FA}$ ,  $V'_3 = h(ID_{HA} \parallel A^*_M \parallel SK_F^*)$ ,  $V'_4 = h(RID^* \parallel ID_{FA} \parallel K_{MU})$ . Then, HA updates  $K_{MU} = K_{MU} + 1$  and stores in database of HA. Finally, HA transmits authentication request  $M'_3 = \{N'_M, V'_3, V'_4\}$  to HA.
- (4) After receiving authentication request  $M'_3$  from HA,  $A$  computes  $V_3^* = h(ID_{HA} \parallel A_M \parallel SK_F^*)$ , and verifies  $V_3^* \stackrel{?}{=} V'_3$ . If it is equal to  $V'_3$ ,  $A$  believes that HA and MU are legal. Otherwise, the communication will be terminated. Then,  $A$  computes  $SK = h(N'_{FA} \parallel A_M \parallel ID_{HA})$  and transmits message  $M'_4 = \{N'_M, V'_4\}$  to MU.
- (5) After receiving message  $M'_4$  from  $A$ , MU computes  $V_4^* = h(RID \parallel ID_{FA} \parallel K_{MU})$ , and verifies  $V_4^* \stackrel{?}{=} V'_4$ . If equal, MU believes that  $A$  and HA are legal. Otherwise, the communication is terminated. Then, MU computes  $N'_{FA} = h(RID \parallel N_{MU}) \oplus N'_M$ ,  $SK = h(N'_{FA} \parallel A_M \parallel ID_{HA})$ , updates  $K_{MU} = K_{MU} + 1$ , and stores it in the smart card. So  $A$  can get the session key  $SK$  by impersonating FA.

Therefore, the protocol of R. Shashidhara et al. is vulnerable to KCIA.

### 36.3.3 *Known-session-specific Temporary Information Attacks*

To compute the session key,  $A$  may follow the following steps.

- (1)  $A$  can first intercept the login request  $M_1 = \{A_M, V_1, ID_{HA}\}$  transmitted on the public channel.  $A$  can obtain parameters  $\{A_M, ID_{HA}\}$  from the request for subsequent computation of session key.
- (2)  $A$  can obtain a random number  $N_{FA}$  generated by FA.
- (3) Finally,  $A$  can successfully compute  $SK = h(N_{FA} \parallel A_M \parallel ID_{HA})$ .

Therefore, the protocol of R. Shashidhara et al. is vulnerable to KTIA.

## 36.4 Conclusion

This paper is about the protocol of Shashidhara et al. We carefully analyze their proposed protocol and point out three security vulnerabilities, including PFS, KCIA, and KTIA. It is contrary to the protocol of Shashidhara et al. that the protocol is unable to resist some well-known attacks and cannot guarantee secure communications. We hope that this research can guide researchers to design a more secure protocol for roaming services in mobile environments.

## References

1. Alveras, D., Grotchel, M., Jonas, P., Paul, U.: Survivable mobile phone network architectures: models and solution methods. *IEEE Commun. Mag.* **36**(3), 88–93 (1998)
2. Buttyan, L., Gbaguidi, C.: Extensions to an authentication technique proposed for the global mobility network. *IEEE Trans. Commun.* **48**(3), 373–376 (2000)
3. Chang, C.C., Lee, C.Y., Chiu, Y.C.: Enhanced authentication scheme with anonymity for roaming service in global mobility networks. *Comput. Commun.* **32**(4), 611–618 (2009)
4. Chen, C.M., Xu, L., Wang, K.H., Liu, S., Wu, T.Y.: Cryptanalysis and improvements on three-party-authenticated key agreement protocols based on chaotic maps. *J. Int. Technol.* **19**(3), 679–687 (2018)
5. Chen, C.M., Wang, K.H., Fang, W., Wu, T.Y., Wang, E.K.: Reconsidering a lightweight anonymous authentication protocol. *J. Chin. Inst. Eng.* **42**(1), 9–14 (2019)
6. Chen, C.M., Xiang, B., Wang, K.H., Yeh, K.H., Wu, T.Y.: A robust mutual authentication with a key agreement scheme for session initiation protocol. *Appl. Sci.* **8**(10), 1789 (2018)
7. Chen, C.M., Xiang, B., Wang, K.H., Zhang, Y., Wu, T.Y.: An efficient and secure smart card based authentication scheme. *J. Int. Technol.* **20**(4), 1113–1123 (2019)
8. Gope, P., Hwang, T.: Lightweight and energy-efficient mutual authentication and key agreement scheme with user anonymity for secure communication in global mobility networks. *IEEE Syst. J.* **10**(4), 1370–1379 (2016)
9. Hwang, K.F., Chang, C.C.: A self-encryption mechanism for authentication of roaming and teleconference services. *IEEE Trans. Wirel. Commun.* **2**(2), 400–407 (2003)

10. Karuppiyah, M., Saravanan, R.: A secure authentication scheme with user anonymity for roaming service in global mobility networks. *Wirel. Pers. Commun.* **84**, 2055–2078 (2015)
11. Lee, C.C., Hwang, M.S., Liao, I.E.: Security enhancement on a new authentication scheme with anonymity for wireless environments. *IEEE Trans. Ind. Electron.* **53**(5), 1683–1687 (2006)
12. Lee, C.C., Yang, C.C., Hwang, M.S.: A new privacy and authentication protocol for end-to-end mobile users. *Int. J. Commun. Syst.* **16**(9), 799–808 (2003)
13. Shashidhara, R., Bojjagani, S., Maurya, A.K., Kumari, S., Xiong, H.: A robust user authentication protocol with privacy-preserving for roaming service in mobility environments. *Peer-to-peer networking and applications* **13**, 1943–1966 (2020)
14. Suzuki, S., Nakada, K.: An authentication technique based on distributed security management for the global mobility network. *IEEE J. Sel. Areas Commun.* **15**(8), 1608–1617 (1997)
15. Tzeng, Z.J., Tzeng, W.G.: Authentication of mobile users in third generation mobile systems. *Wirel. Pers. Commun.* **16**, 35–50 (2001)
16. Wang, Y., Liu, Y., Ma, H., Ma, Q., Ding, Q.: The research of identity authentication based on multiple biometrics fusion in complex interactive environment. *J. Netw. Intell.* **4**(4), 124–139 (2019)
17. Wu, T.Y., Lee, Y.Q., Chen, C.M., Tian, Y., Al-Nabhan, N.A.: An enhanced pairing-based authentication scheme for smart grid communications. *J. Ambient Intell. Hum. Comput.* (2021), <https://doi.org/10.1007/s12652-020-02740-2>
18. Wu, T.Y., Lee, Z., Obaidat, M.S., Kumari, S., Chen, C.M.: An authenticated key exchange protocol for multi-server architecture in 5g networks. *IEEE Access* **8**, 28018–28096 (2020)
19. Wu, T.Y., Lee, Z., Yang, L., Luo, J.N., Tso, R.: Provably secure authentication key exchange scheme using fog nodes in vehicular ad hoc networks. *J. Supercomput.* (2021). <https://doi.org/10.1007/s11227-020-03548-9>
20. Wu, T.Y., Wang, T., Lee, Y.Q., Zheng, W., Kumari, S., Kumar, S.: Improved authenticated key agreement scheme for fog-driven IoT healthcare system. *Secur. Commun. Netw.* **2021**, 6658041 (2021)
21. Wu, T.Y., Yang, L., Lee, Z., Chen, C.M., Islam, S.H.: Improved ECC-based three-factor multi-server authentication scheme. *Secur. Commun. Netw.* **2021**, 6627956 (2021)
22. Xu, G., Liu, J., Lu, Y., Zeng, X., Zhang, Y., Li, X.: A novel efficient MAKKA protocol with desynchronization for anonymous roaming service in global mobility networks. *J. Netw. Comput. Appl.* **107**, 83–92 (2018)
23. Zhou, T., Xu, J.: Provable secure authentication protocol with anonymity for roaming service in global mobility networks. *Comput. Netw.* **55**(1), 205–213 (2011)

**Part V**  
**Video, Image, and Others**

# Chapter 37

## Research on Construction Method of Massive Geographic Image Database for Power Grid EIA



Yu Wu, Zun Li, Yang Guo, Songyang Zhang, Zhiguo Zhang, Zhentao Liu, Xutao Han, and Wei Sun

**Abstract** With the continuous development of science and technology, the capacity of data is also showing a geometric increase. Therefore, this paper mainly studies how to store query, change, and replace a large number of geographic images. The text uses SQL server platform and ArcGIS geographic software processing platform. It solves the problem of processing limit exceeding the database in the face of massive database, insufficient network bandwidth compared with massive images, slow image display speed, storage problem of massive image data, and so on.

### 37.1 Overview

#### 37.1.1 Background

Traditional database and data processing technology no longer meet the requirements of image data. With the extensive use of massive volume image data, if we use traditional database technology to deal with massive image data, it will inevitably lead to problems such as excessive image data. Beyond the limits of database processing and bandwidth shortage, display speed is too slow to store massive image data [1–7].

---

Y. Wu · Z. Li · S. Zhang  
State Grid He-Nan Electric Power Company, Zhengzhou, China

Y. Guo  
Henan Jiuyu Enpai Power Technology Co., Ltd, Zhengzhou, China

Z. Zhang · X. Han · W. Sun (✉)  
Xidian University, Xi'an, China  
e-mail: [wsun@xidian.edu.cn](mailto:wsun@xidian.edu.cn)

Z. Liu  
Xi'an University of Posts and Telecommunications, Xi'an, China

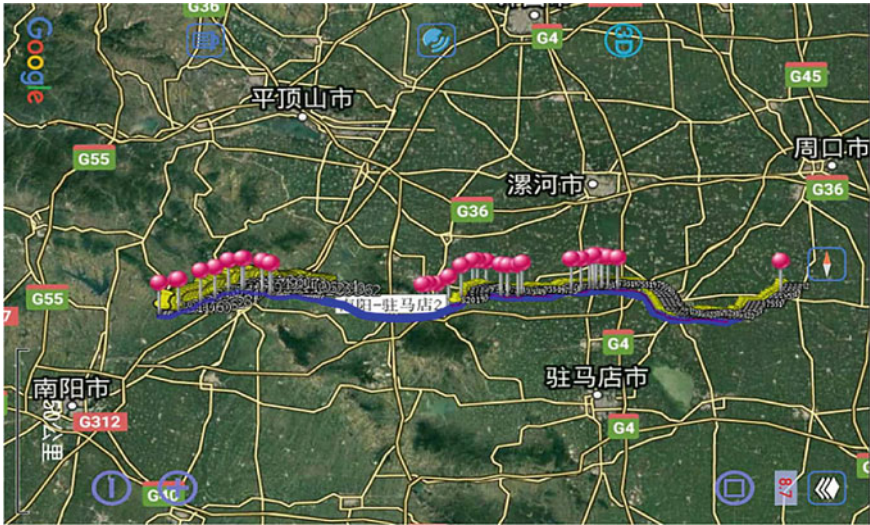


Fig. 37.1 Whole route given in OVI map

## 37.1.2 *Surveying and Mapping Project of Henan Electric Power Company of State Grid*

### 37.1.2.1 **Overview of Surveying and Mapping Project of Henan Electric Power Company of State Grid**

On the basis of the existing three-dimensional panoramic decision support platform for large power grid, on the one hand, the land spatial planning module of power grid construction projects is added, and relevant environmental sensitive areas, land use planning, and urban and rural planning are incorporated into the platform, so as to provide comprehensive and scientific decision-making basis for site selection and route selection of power grid construction projects; on the other hand, environmental intelligent exploration and information optimization module are added for construction. Taking UHV project as an example, it collects data, images, and video data of different historical periods in the construction process, carries out intelligent analysis and image optimization processing, and provides data support for EIA, completion acceptance, and litigation that may be faced in the later stage (Fig. 37.1).

### 37.1.2.2 **Working Equipment**

In surveying and mapping project of Henan Electric Power Company of State Grid, the following equipment is mainly used: “Wu 2,” “M100,” “Spirit 4pro,” and other UAVs (Fig. 37.2).





**Fig. 37.2** Working equipment

### ***37.1.3 Construction Method of Massive Image Database***

The total time of field measurement is 15 days and 2 batches, and the total sensitive points of the project are 31. The first field exploration time is 4 days for preliminary survey, and the second field exploration time is 11 days for precise measurement. The survey route starts from the north of Nanyang City in the West and ends in the west of Zhoukou City in the East, with a total length of 166.8 km. There are more than 1 W photos taken in the project. There are 24 ecological sensitive sites in total, and a total of 24 sensitive points are taken by aerial photography. The setting of aerial photography points is shown in Fig. 37.3. The total area of the model is about 2.1 million square meters [1, 8, 9].



**Fig. 37.3** Selection of aerial photography points for ecological sensitive points

We use ArcGIS platform for data management. First of all, we need to apply for registration of a quota of ArcGIS platform in ArcGIS platform to obtain the use right of a massive image database, and create a remote database connection platform in ArcGIS.

Secondly, in the SQL server platform, a database platform that can store massive data is established to store various massive data. After that, the SQL server database is typed into ArcGIS, and the data is managed and improved by ArcCatalog software. Finally, ArcCatalog software is combined with ArcGIS server to form Web accessible results.

The main software involved in this paper is ArcGIS and SQL server. Among them, ArcGIS catalog and ArcGIS map, as well as independent ArcGIS server software, are mainly used.

## **37.2 ArcGIS Software and Its Platform**

### ***37.2.1 Overview of ArcGIS***

Whether using GIS in a stand-alone or online environment, users can use ArcCatalog, ArcMap and ArcToolbox of ArcGIS to complete their work. ArcCatalog can be used for spatial database content management, database design, and metadata recording and browsing; ArcMap can be used for map compilation, editing, and analysis; ArcToolbox can be used for data conversion and geographic processing. Through the coordination of these three applications, users can complete various GIS tasks from simple to complex, including mapping, data management, spatial analysis, data editing, and geographic processing [2, 3, 10] (Fig. 37.4).

### ***37.2.2 Database Comparison***

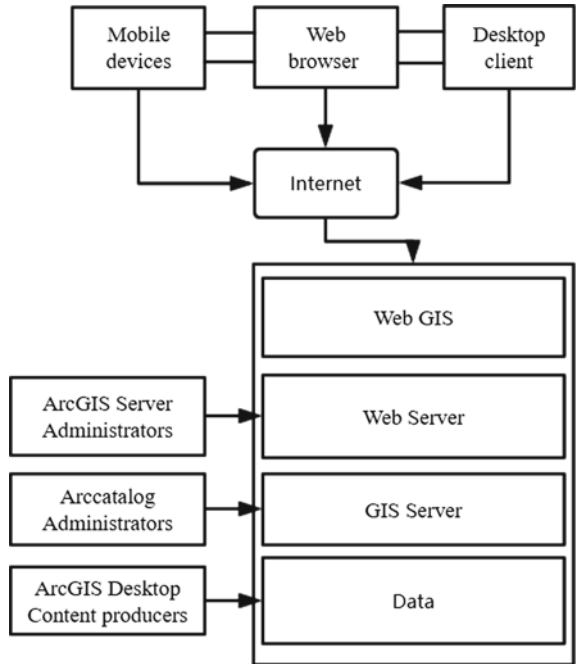
There are three types of geographic databases:

File geographic database: stored in the file system as a folder. Each dataset is saved as a file, which can be expanded to a maximum of 1 TB.

Personal geographic database: all data sets are stored in Microsoft Access data file, and the maximum size of the data file is 2 GB.

ArcSDE geographic database is also known as multi-user geographic database. This type of database is stored in a relational database using Oracle, Microsoft SQL server, IBM DB2, IBM Informix, or PostgreSQL. These geographic databases require ArcSDE, and there are no restrictions on the size and number of users (Table 37.1).

**Fig. 37.4** ArcGIS server architecture



### 37.3 Query and Release of Engineering Aerial Data

#### 37.3.1 Release of Engineering Aerial Data

Firstly, the collected engineering aerial data are classified, including image data, GPS data, etc.

Then, the data are input in the SQL server platform. The large positive image is used as the raster data set, the original small image is used as the mosaic data set, and the GPS and other data are input in the form of table.

After inputting each data into SQL server platform, it is necessary to read and verify the new input data in ArcCatalog data platform.

Finally, the data can be published through the Web in ArcGIS server platform.

All the data of engineering aerial photography can be released in the three platforms SQL server, ArcGIS server, and ArcCatalog.

#### 37.3.2 Publishing Selection of Different Types of Images

In the massive database, there are roughly two types of images. One is the mosaic map, which is orthophoto map. One is the original data map, which is the aerial

**Table 37.1** Database comparison

Key features	Number of users	Storage form	Size limit	Platform	Management tool	Security and permissions
Arcsde database	Multiple users	Oracle/Db2/Informix/SQL	DBMS	Windows, Unix, Linux	Backup, recovery, replication	DBMS
File geographic database	Smaller working groups	Separate document. The folder used to save its dataset files	1 TB	Cross-platform	File system management	Operating file system security
Personal geographic database	Single user and smaller working groups	Save in a single Microsoft access file (.MDB)	2 GB	Windows	Windows	Windows



**Fig. 37.5** Shimantan orthophoto image

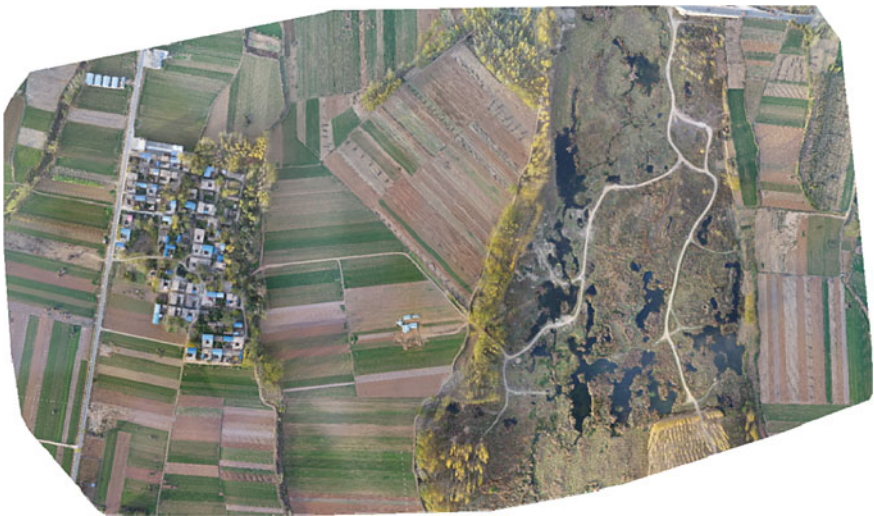


**Fig. 37.6** Aerial orthophoto image

original map. Because of different types of images and different needs, the storage of images is not the same (Figs. 37.5 and 37.6).

### ***37.3.3 Engineering Aerial Data Query***

For the query of aerial data, it can be seen that data storage exists in SQL server, ArcGIS server, and ArcCatalog in the three platforms. Therefore, there are several ways to query the engineering aerial data.

1. In SQL server platform, local query can be done through windows identity, or login and query through remote data connection using mixed mode.

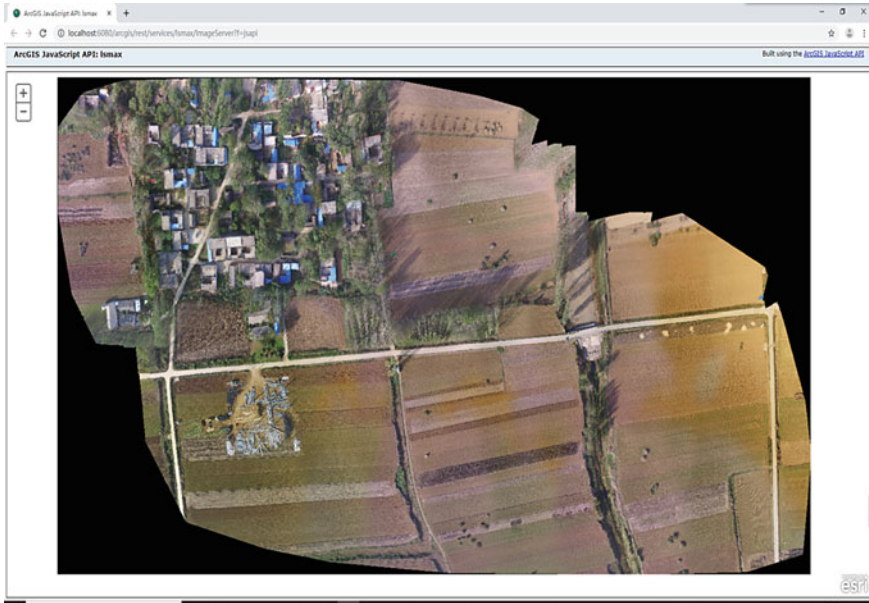


Fig. 37.7 Web geographic information data query

2. You can preview and query the published data through ArcCatalog. This operation can also be queried locally or by remote administrator.
3. You can query the published data on the web through ArcGIS server software, as shown in Fig. 37.7.

### 37.4 Conclusion

In this paper, the design and implementation of massive image database system are studied in detail. The main work is as follows: a convenient operation method for massive image database storage is studied and can be classified into categories to store the required valid data. And on this basis, a convenient operation method for massive image database query is studied. Through multi-path and multi-mode data query, the massive data can be stored and displayed in a clear way.

**Acknowledgements** This work was supported by National Nature Science Foundation of China (NSFC) under Grants No. 61671356, Science and Technology Program of Shaanxi Province under Grants No. 2020GY-136 and 2019ZDLGY14-02-03.

## References

1. Arnas, D., Rodríguez, M.: Range searching in multidimensional databases using navigation metadata. *Appl. Math. Comput.* **386** (2020)
2. McIntyre, R.S., Millson, B., Power, G.S.: Burden of treatment resistant depression (TRD) in patients with major depressive disorder in Ontario using Institute for Clinical Evaluative Sciences (ICES) databases: economic burden and healthcare resource utilization. *J. Affect. Disord.* **277** (2020)
3. Li, Y., Chang, Y., Cheng, M., Feng, T.: Multi-value private information retrieval with colluding databases via trace functions. *Inf. Sci.* **543** (2021)
4. Müller, F., Gorr, B., Christ, H.-J., Chen, H., Kauffmann, A., Laube, S., Heilmaier, M.: Formation of complex intermetallic phases in novel refractory high-entropy alloys NbMoCrTiAl and TaMoCrTiAl: thermodynamic assessment and experimental validation. *J. Alloy. Compd.* **842** (2020)
5. Cao, M., Yan, X., Yang, N., Fu, Q., Xue, T., Zhao, S., Hu, J., Li, Q., Song, L., Zhang, X., Su, B., Li, C.: Genome-wide characterization of toll-like receptors in black rockfish *Sebastes schlegelii*: evolution and response mechanisms following *Edwardsiella tarda* infection. *Int. J. Biol. Macromol.* **164** (2020)
6. Paliwal, S., Yenuganti, S.: Design and simulation of digital output MEMS pressure sensor. *Arab. J. Sci. Eng.* **45**(8) (2020)
7. Zhang, Y., Pu, S., Lv, X., Gao, Y., Ge, L.: Global trends and prospects in microplastics research: a bibliometric analysis. *J. Hazard. Mater.* **400** (2020)
8. Saga, R., Uchida, T., Takino, Y., Kondo, Y., Kobayashi, H., Kinoshita, M., Saitoh, D., Ishigami, A., Makishima, M.: Radiation-induced gastrointestinal syndrome is exacerbated in vitamin C-insufficient SMP30/GNL knockout mice. *Nutrition* **81** (2021)
9. Fang, Y., Zheng, T., Zheng, X., Peng, H., Wang, H., Xin, J., Zhang, B.: Assessment of the hydrodynamics role for groundwater quality using an integration of GIS, water quality index and multivariate statistical techniques. *J. Environ. Manag.* **273** (2020)
10. Ghobadi, M., Nasri, M., Ahmadipari, M.: Land suitability assessment (LSA) for aquaculture site selection via an integrated GIS-DANP multi-criteria method; a case study of Lorestan province, Iran. *Aquaculture* **530** (2021)

# Chapter 38

## Automatic Director of Live Sport Based on Motion State



Juan Wang and Longfei Zhang

**Abstract** This paper introduces automatic director method of live sport based on motion state. The method is to combine the video frames of multi-channel cameras and use larger and more complete panoramic video for video content analysis and semantic event detection. Then, through the state analysis of the sport, it is determined whether the match at that moment is in Play or Break state. If the match is in Play state, it is adopted to place the motion target in the center of the guide screen. If the game is in the Break state, the sliding window method is adopted to build a HCRF model to mine the potential feature relationship between multimodal semantic clues and semantic events, so as to realize the detection of specific semantic events in sports videos, and to smoothly track the guide screen for extraction. We have done experiments on football match videos, and the results show that our method can generate coherent edited videos in line with audience psychology and achieve good visual effects, which also lays a foundation for the application of artificial intelligence to the automatic director of sports events.

### 38.1 Introduction

In recent years, the rapid development of artificial intelligence vision technology has brought a new solution to the work of director editing in the era of convergence media. The broadcast of major international sports events has entered a stage of standardization of television public signal production, and an automatic editing framework needs to be provided to assist the director of sports events. Previous researchers have been studying how to choose a good way from multiple original cameras and automatically synthesize the broadcast video [1, 2]. It always needs the cameraman to capture the wonderful picture in time, which cannot truly realize

---

J. Wang · L. Zhang (✉)  
Beijing Institute of Technology, Beijing, China  
e-mail: [longfeizhang@bit.edu.cn](mailto:longfeizhang@bit.edu.cn)

J. Wang  
e-mail: [3120181092@bit.edu.cn](mailto:3120181092@bit.edu.cn)

© The Author(s), under exclusive license to Springer Nature Singapore Pte Ltd. 2022  
T.-Y. Wu et al. (eds.), *Advances in Smart Vehicular Technology, Transportation, Communication and Applications*, Smart Innovation, Systems and Technologies 250,  
[https://doi.org/10.1007/978-981-16-4039-1\\_38](https://doi.org/10.1007/978-981-16-4039-1_38)

381



automatic director. Moreover, with the diversified and personalized needs of users, the number of cameras needs to increase, which increases the difficulty of director of sports events. This paper proposes automatic director method (see Fig. 38.1). Firstly, multi-channel video frames are stitched for panoramic video. Secondly, the video state is used to judge whether the game is in Play or Break state [3, 4]. If it is in the Play state, football target is selected as the focus of the guide screen. Through the detection and tracking of the football target, the appropriate screen is selected for the broadcast. If it is in Break state, the analysis of video semantic structure is selected to extract multimodal semantic cues of football video. Then, by constructing a model based on HCRF to mine the potential feature relationship between multimodal semantic clues and semantic events, the detection of exciting events in the football video is realized, and the hot spots are successfully obtained for real-time director. In this cycle, the final editing video is formed.

Our contributions are as follows:

1. Combine machine learning with live broadcast of sports events. Most of the previous studies are focused on the rebroadcast video of sports events. However, we applied machine learning to live broadcast, and obtained considerable experimental results, which provides a good prospect for the development of live broadcast of sports events.
2. This paper proposes an automatic director framework. Our proposed framework will really separate the photographer and the director from the heavy work, and automatically retrieve and rebroadcast the wonderful events of the game through the framework.

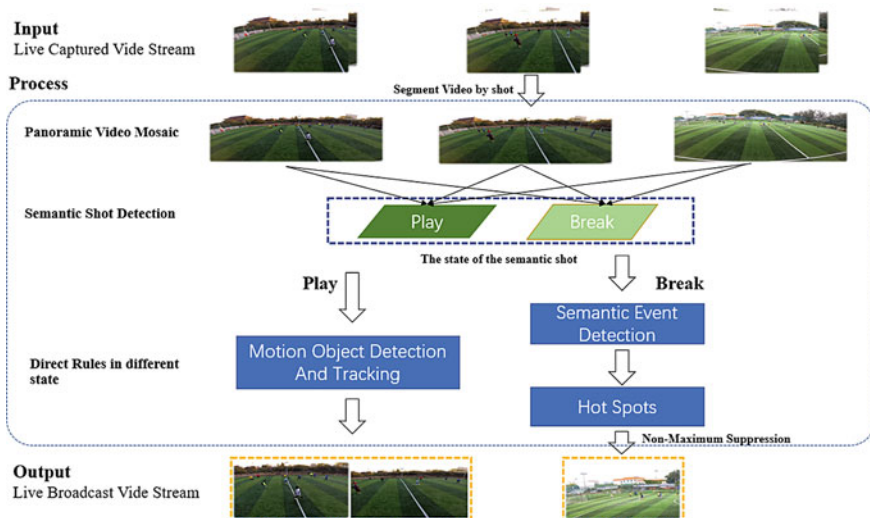


Fig. 38.1 Framework automatic director of sports game based on motion state

3. For the first time, according to the game state in Play–Break state, different director decisions are taken to better meet the requirements of director.

## 38.2 Semantic Shot Detection

Sports event video has a long duration and a large amount of data, and the features of the starting and ending points of semantic events are not obvious. It is a difficult point in the field of sports video analysis to determine a reasonable and effective analysis unit, which helps to define the boundary of semantic events. After the research of many scholars, a semantic analysis method of sports video based on Play–Break segments has attracted more and more attention. The main idea is to retrieve the Play–Break fragments in the video data stream through automatic extraction and analysis of low-level features, the semantic features of Play–Break fragments are extracted and finally realize the detection and location of semantic events. The Play segment mainly refers to that when the motion object is located in the match field and the match is in progress, the director should present the match from the main perspective of the motion object. The Break segment represents the state when the match is interrupted by a specific semantic event, such as a goal or foul, etc. The director should present the specific details of the semantic event with a partial shot. Therefore, different rule of the director should be adopted to select the appropriate picture in the two states. In this paper, the optical flow field algorithm is used to calculate the moving optical flow field of the motion object and players [5, 6], and the motion vector field is further analyzed. It is analyzed that the semantic shot belongs to Play state or Break state.

1. The original video stream of multiple cameras is obtained in real time, and the panoramic video frame sequence is obtained by video mosaic technology [7–12], and then the sport field is extracted based on HIS color model and K-means clustering algorithm [13].
2. Use optical flow algorithm to obtain the moving optical flow field of football and players, respectively.
3. Carry out vector analysis on the moving optical flow field, including the motion speed analysis of the main body of the vector field.
4. Set the speed thresholds of football and players and judge whether the semantic shot belongs to Play or Break state.

## 38.3 Guide Rules Establishment

### 38.3.1 Guide Rules in Play State

When the football game is in Play state, the attacker will seek to shoot through various strategies and techniques, and the defender will defend the players closely,

and even try to seize the football. There will be fierce confrontation between the two teams, and the main focus will be on the football. Therefore, when judging that the semantic shot is in Play state, this paper chooses the football as the focus of the guide and conducts the guide by choosing the appropriate screen. In order to effectively realize the detection and tracking of football target, it is necessary to recognize and classify the extracted football field, extract the candidate football target, and then track the football target further. In this paper, football recognition method based on target shape and soccer tracking method based on particle filter are adopted.

### **Object Recognition Based on Target Shape**

Shape analysis [14, 15] is a hot topic in the field of computer vision. The main idea is to extract the feature information of the target area from the image and store it in a specific data structure for subsequent operations such as comparison, recognition, classification, and retrieval. The football target in video is round, small in area, and single in color. Therefore, this paper defines the area, perimeter, roundness, and length–width ratio of external rectangle as the screening conditions.

### **Motion Object Tracking Method Based on Particle Filter**

After the football recognition, there will be some candidate footballs, including the real football and the areas that looks very similar to football. At the same time, because the players often appear some occlusion when they move with the ball, the football tracking effect is not ideal. Because the idea of particle filter is to approximate the probability density function of state variables with some discrete random sampling particles, which can well approximate the posterior probability density function, and then estimate the position of football. This paper uses a particle filter tracking algorithm based on color features for football tracking in football matches. Firstly, the color feature of the football in the first frame sequence is extracted and used as a feature template, which is integrated into the framework of particle filter algorithm. Then, the particle filter algorithm is applied to track each candidate football, and the sample features of the particles are compared with the template features, and the candidate ball with the highest similarity is marked with a rectangular window. Set the height of panoramic video as  $H$  and the width as  $L$ , and take the tracked football target as the guide center. According to the definition of the guide screen, the system sets the height of a rectangular window as the height of panoramic video  $H$ , and the width is  $4/3H$ , so as to output the final guide screen.

### **38.3.2 Guide Rules in Break State**

When the attacking team looks for the right opportunity to shoot, a goal may be scored, the goalkeeper may save the ball, the ball may fly off the goal line, or there are certain semantic events such as corner kick, red and yellow card events, the game will be interrupted and come into Break. This will be followed by a number of local,

close-up, or off-field shots. Multiple low-level semantic features [16–19] constitute important clues for the detection of specific semantic events.

### Semantic Event Extraction

The structure and characteristics of football video are deeply analyzed, and according to the contained semantic information, 11 kinds of low-level features are defined as multimodal semantic clues [20]. The potential rules of video are mined from two aspects of audio and video, and all aspects of video clips are comprehensively described. The features are as follows: frame motion intensity, field ratio, red and yellow cards, audio energy, referee ratio, penalty area, corner area, number of players, and the position of ball.

Multimodal semantic clues are used as attributes of concept lattice to construct formal background. For the features represented by frames and shots, the mean value is taken as the attribute value.

$$\text{att}_i = \frac{1}{n} \sum_{b=1}^n \text{att}_a(b) \quad (38.1)$$

where  $n$  is the total number of frames and  $\text{att}_a(b)$  represents the attribute values of the  $a$ -th video and the  $b$ -th frame. The concept lattice processing needs to binarize the attributes in the formal background, and select the mean value of each feature as the threshold value, which is greater than the threshold value of 1, otherwise it is 0.

After clustering based on concept lattice, nine kinds of multimodal semantic cues are automatically clustered to generate a unique emotional feature combination for each event. The emotional feature combination of goal event is: audio energy, penalty area, and the position of the ball; the combination of corner event is: penalty area, corner area, and the position of the ball; the combination of penalty kick events is the position of the ball and the number of players; the combination of red and yellow card events is the intensity of frame movement and the proportion of referees.

Based on the clustering results, the characteristic value weighting method is used to establish the emotional incentive model:

$$A_u = \lambda_1 \times F_{\mu 1} + \lambda_2 \times F_{\mu 2} + \dots \quad (38.2)$$

Among them, the corner mark of  $F_{\mu h}$  represents the  $h$ -th emotional incentive feature of the  $u$ -th event.  $F_{\mu h} = \{F_{11}, F_{12}, F_{13}, F_{21}, \dots\}$ , ( $\mu = 1, \dots, 4; h = 1, \dots, 4$ ).  $\lambda_h$  represents the weighted value of the  $n$ -th emotional incentive feature.  $A_u$  Indicates the emotional incentive value of category  $u$  event. Weight coefficient  $\lambda_1, \lambda_2$ , and  $\lambda_3$  represents the weight of each observation, It is determined by the following formula:

$$\begin{cases} \alpha_i = \frac{\text{mean}_H - \text{mean}_N}{\text{mean}_i}, & i = 1, 2, 3 \\ \lambda_i = \frac{\alpha_i}{\alpha_1 + \alpha_2 + \alpha_3} \end{cases} \quad (38.3)$$

Among them,  $i = 1, 2, 3$ , respectively, represent three kinds of emotional motivation characteristics,  $\text{mean}_H$  is the average value of emotional motivation in specific semantic shot,  $\text{mean}_N$  is the mean value of emotional stimulation in non-semantic shot, and  $\text{mean}$  is the mean value of all shot segments of this kind of emotional stimulation feature.

HCRF [16, 21, 22] is an undirected graph model with hidden state and probability as output. We use this model to recognize semantic events.

### Guide Screen Select

After the establishment of panoramic video mosaic model and direct rule model, we generate panoramic video according to the input multi-channel original video signal, and the system automatically sets a “sliding window” to detect semantic events and detects the best picture for direct. The specific implementation steps are as follows:

For each frame of panoramic video image, the size of “sliding window” is automatically set according to the height and width of panoramic video. Set the height of the panoramic video as  $H$  and the width as  $L$ . According to the definition of the direct screen, the system sets the height of the sliding window as the height of the panoramic video  $h$ , and the width is  $4/3H$ .

Slide the detection window in  $S$  (detection window width  $1/20$ ) step each time to detect the semantic events that each window belongs to, and multiple windows may have semantic events.

Using the idea of non-maximum inhibition, only the box with the maximum probability is reserved for multiple windows with wonderful semantic events detected, so as to determine the semantic events selected this time and output the final direct screen.

## 38.4 Experiment

This paper uses the psychological measurement method in performance evaluation for reference and analyzes the audience’s experience and feelings in the process of watching the video by means of questionnaire, based on the self-report of the subjects and indirectly obtain the evaluation results of the framework.

In order to evaluate the performance of the automatic editing framework comprehensively, a total of 200 viewers, aged 18–55, were recruited. A total of 13 evaluation questions are set from the four dimensions of lens switching, video quality, lens selection, and audience satisfaction. The audience scored the above thirteen questions with five levels of Likert scale (the full score is 5), with the rating from “totally opposed” to “totally agreed,” and allowed the audience to add explanatory answers to specific questions.

In order to facilitate the subsequent analysis, this paper uses the consistency principle to set the evaluation questions, the higher the score of each question, the better the visual effect of the clip video, and the higher the performance of the frame. After all the audiences have completed the questionnaire and scoring, the proportion

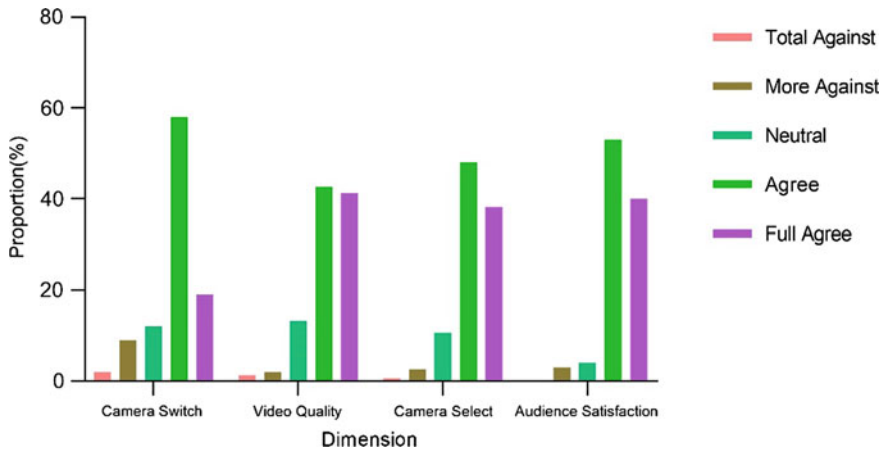


Fig. 38.2 Percentage of people in rating level

of the number of people scored in each dimension of the five grades in the evaluation is counted, and the results are shown in Fig. 38.2.

From the data of the figure, it can be concluded that 77% of the audience think that the delay of shot switching has little impact on the visual effect (score > 3) and that the shot switching is logical and continuous, only 8 people who often watch football games can feel the delay; 83.3% of the audience think that the clarity and esthetic feeling of the video are in line with the visual habits and esthetic taste of the audience, and the audio and picture can reach the standard 87.3% of the audience think that the shot selection can meet the professional requirements in accuracy, detail presentation, and picture design satisfaction; 93% of the audience think that the editing video can meet their requirements in rhythm and appeal. The above experimental results show that the video clips generated by the frame have good visual effect, so the automatic editing frame proposed in this paper can replace the director to edit football match to some extent.

## 38.5 Summary

The preliminary experimental results show that our framework can effectively determine the most appropriate shot image at the current moment of the game from the multi-channel original video without editing, and generate the final edited video, which can achieve the visual effect that meets the requirements of the audience, which also verifies the feasibility of the combination of artificial intelligence and sports event broadcasting. The framework is only a rudiment of automatic broadcast, and the future work will also involve the evaluation of editing video, and the evaluation results will be fed back to the generation model to generate new and better

editing video, and then the evaluation again; in addition, it will also involve the game tactics detection and behavior prediction, so as to generate the editing video which can reflect the sports charm and meet the audience's aesthetic.

**Acknowledgements** This work has been supported by National Key R&D Program of China under Grant NO.2018YFB1403905.

## References

1. Wang, J., Xu, C., Chng, E., Lu, H., et al.: Automatic composition of broadcast sports video. *Multimedia Syst.* **14**(4), 179–193 (2008)
2. Leake, M., Davis, A., Truong, A., et al.: Computational video editing for dialogue-driven scenes. *ACM Trans. Graphics* **36**(4CD), 1–14 (2017)
3. Tjondronegoro, D., Chen, Y.P.: Knowledge-discounted event detection in sports video. *IEEE Trans. Syst. Man Cybern. Part A Syst. Humans* **40**(5), 1009–1024 (2010)
4. Bovik, A.: The essential guide to video processing. *J. Electron. Imaging* **19**(1), 9901 (2007)
5. Horn, B.K.P., Schunck, B.G.: Determining optical flow. *Artif. Intell.* **17**(1–3), 185–203 (1981)
6. Bouguet, J.-Y.: Pyramidal implementation of the Affine Lucas Kanade feature tracker description of the algorithm. *Intel Corporation* **5**, 1–10 (2001)
7. Brown, M., Lowe, D.G.: Automatic panoramic image stitching using invariant features. *Int. J. Comput. Vision* **74**(1), 59–73 (2007)
8. Zitová, B., Flusser, J.: Image registration methods: a survey. *Image Vision Comput.* **21**(11), 977–1000 (2003)
9. Bay, H.: Surf: speeded up robust features. *Comput. Vis. Image Underst.* **110**(3), 404–417 (2006)
10. Bay, H., Ess, A., Tuytelaars, T., et al.: Speeded-up robust features (surf). *Comput. Vis. Image Underst.* **110**(3), 346–359 (2008)
11. Luo, J., Oubong, G.: A comparison of SIFT, PCA-SIFT and SURF. *Int. J. Image Process.* **3**(4), 143–152 (2009)
12. Perez, P., Gangnet, M., Blake, A.: Poisson image editing. *ACM Trans. Graphics (TOG)* **22**(3), 313–318 (2003)
13. Wang, X., Chen, R., Yan, F.: High-dimensional data clustering using K-means subspace feature selection. *J. Netw. Intell.* **4**(3), 80–87 (2019)
14. Loncaric, S.: A survey of shape analysis techniques. *Pattern Recogn.* **31**(8), 983–1001 (1998)
15. Wu, C.-C., Wu, S.-L.: Research and implementation of road traffic sign identification system. *J. Netw. Intell.* **4**(2), 47–57 (2019)
16. Shimawaki, T., Sakiyama, T., Miura, J., et al.: Estimation of ball route under overlapping with players and lines in soccer video image sequence. In: *18th International Conference on Pattern Recognition 2006*, vol. 1, pp. 359–362. IEEE, China (2006)
17. Xu, M., Duan, L.Y., Xu, C.S., et al.: A fusion scheme of visual and auditory modalities for event detection in sports video. In: *International Conference on Multimedia and Expo*. IEEE, USA (2003)
18. Zhong, D., Chang, S.F.: Real-time view recognition and event detection for sports video. *J. Vis. Commun. Image Represent.* **15**(3), 330–347 (2004)
19. Wang, J., Song, W.M., Sun, X.Y., et al.: Annotation method to improve the mapping between image features and high level semantic expression. *J. Netw. Intell.* **5**(4), 211–217 (2020)
20. Gong, Y.: Automatic parsing of TV soccer programs. In: *Icmcs*, p. 167 (1995)
21. Soullard, Y., Artières, T.: Hybrid HMM and HCRF model for sequence classification. In: *European Symposium on Esann* (2016)

22. Xu, G., Ma, Y.F., Zhang, H.J., et al.: Motion based event recognition using HMM. In: *16th International Conference on Pattern Recognition*, vol. 2, pp. 831–834. IEEE, Canada (2002)



# Chapter 39

## Image Dehazing Network Based on Multi-scale Feature Extraction



Ting Feng, Fuquan Zhang, Zhaochai Yu, and Zuoyong Li

**Abstract** To remove image haze and make haze image scene clear, we proposed an image dehazing network based on multi-scale feature extraction (MSFNet) in this paper. The MSFNet first directly performs feature extraction on hazy images with three different resolutions to obtain fine feature maps and concatenates them with the rough feature maps extracted in the downsampling process for fusing and obtaining richer image information. Then, the fused feature maps are put into a network module composed of ResNeXt building blocks for network learning. Next, the feature maps extracted by upsampling are sequentially concatenated with the feature maps learned by the ResNeXt module for obtaining the residual image. Finally, the learned residual image is added to the input hazy image to obtain the image dehazing result. The experimental results on the SOTS dataset show that the MSFNet improves effectiveness of image dehazing.

### 39.1 Introduction

In recent years, the increasingly serious air pollution has led to the frequent occurrence of haze weather, which has caused the poor quality of the images taken, and the required information cannot be obtained from it. Hazy images have affected the application of computer vision, such as remote sensing images and target recognition. Therefore, image dehazing is still an important research direction in computer vision. The image dehazing method is mainly composed of the prior-based method [1, 2] and the deep learning-based method [3, 4].

The prior-based method is designed for the imaging principle of hazy images, and the image dehazing results are generated through the physical model [5]. Tarel

---

T. Feng · F. Zhang · Z. Yu · Z. Li (✉)

Fujian Provincial Key Laboratory of Information Processing and Intelligent Control, College of Computer and Control Engineering, Minjiang University, Fuzhou 350121, China  
e-mail: [fzulzytdq@126.com](mailto:fzulzytdq@126.com)

T. Feng

College of Mathematics and Computer Science, Fuzhou University, Fuzhou 350108, China

et al. [6] used median filtering to estimate the hazy concentration and then used the physical model to generate image dehazing results. He et al. [7] estimated the rough transmission map based on the dark channel prior and then employed the physical model to obtain the dehazing results. Zhu et al. [8] calculated the depth of the scene based on the color attenuation prior and then generated a dehazing image through the physical model. The time complexity of this kind of method is low, but the a priori information proposed is not universal, and the dehazing performance is unstable.

Convolutional neural networks (CNNs) have made great progress in some tasks in these years [9–11], so some researchers use them to design image dehazing methods and achieve better results. Cai et al. [12] proposed DeHazeNet to estimate the image transmission and then used the physical model to obtain the image dehazing results. Li et al. [13] proposed that AOD-Net directly obtains the image dehazing result, which is an end-to-end dehazing method. This type of method reduces the interference of human factors, and the dehazing effect is better.

Therefore, the MSFNet is an end-to-end image dehazing method based on deep learning. When the image is downsampling, part of the information will be lost. Therefore, extracts the rough feature map during downsampling at each layer, modifies the size of the input image to be the same as the rough feature map, performs convolution to obtain a fine feature map at the same times, and merges the rough feature map and the fine feature map to obtain richer image information and then put the spliced feature map into the ResNeXt [14] module to further learn image features. Next, the feature maps obtained by upsampling are spliced with the modules learned by the ResNeXt module to obtain the residual image. Finally, added the input image and residual image to get the image dehazing result.

The contributions of the MSFNet are as follows:

1. We proposed an end-to-end network based on multi-scale feature extraction named as MSFNet for image dehazing.
2. The MSFNet concatenates three different resolutions feature maps to obtain richer image information.
3. The experimental results on SOTS show that the MSFNet improves the effectiveness of image dehazing.

## 39.2 Related Works

The MSFNet is a deep learning-based method for image dehazing. This type of method can be subdivided into two categories according to whether the physical model is used.

One is to use the combination of the physical model and convolutional neural network. This type of method mainly uses the CNN to obtain the required parameters and then substitute the parameters into the physical model to obtain the dehazing results. Ren et al. designed a multi-scale CNN architecture to learn image features (MSCNN) [15]. The MSCNN first estimates the rough scene transmission map and

then refines the map by fine-scale. MSCNN uses physical methods to obtain atmospheric light values, substituting parameters into the physical model to obtain the dehazing result.

The other is the end-to-end image dehazing method. This type of method is to directly generate the image dehazing result after inputting the hazy image without using the physical model. Ren et al. designed a gated fusion network (GFN) based on the encoding–decoding structure [16]. The GFN first performs preprocessing operations on the image to obtain three processed images. Then, processed images are used as network input, and the corresponding feature map is generated through the network. Finally, the processed images are fused with corresponding feature maps to get the final dehazing results.

### 39.3 Proposed Method

The MSFNet proposed in this paper uses the generative adversarial network [17] framework. First, the network uses an effective encoding–decoding structure in the generator to get the dehazing result. Then the generator result and the corresponding label image are input to the discriminator for discrimination. Finally, the obtained discrimination result is fed back to the generator to continue training the model. Figure 39.1 is the architecture of the MSFNet in this paper. Next, we will introduce the architecture of MSFNet, feature extraction, and ResNeXt.

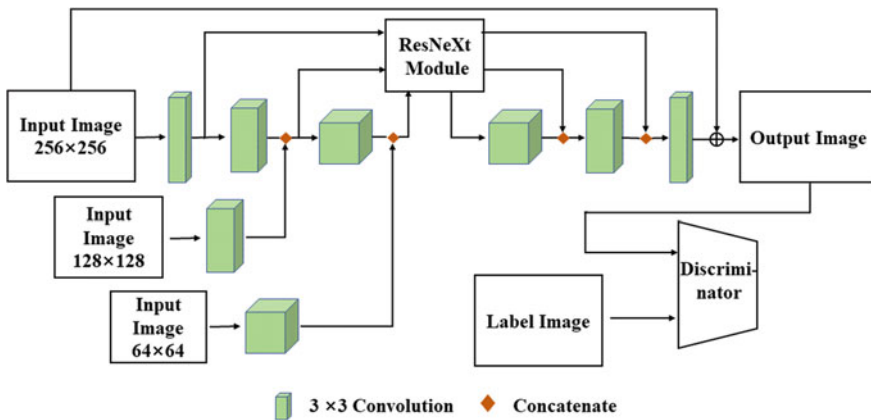


Fig. 39.1 Architecture of MSFNet

### 39.3.1 Architecture

The MSFNet method includes two parts: generator and discriminator. The MSFNET uses different sizes of hazy images for feature extraction in different downsampling layers of the generator and stitches the feature maps obtained in each layer with the feature maps obtained in the downsampling layer to get more detailed information. Next, put the fused feature map into the ResNeXt module for learning. Then stitch the feature maps obtained by the ResNeXt module with the corresponding upsampling feature maps to achieve feature fusion. After, the residual image is obtained by upsampling, and the input image is added to get the dehazing result. Finally, the image dehazing result generated by the generator and the real haze-free result are input to the discriminator for discrimination, and the discrimination result guide generator continues training.

### 39.3.2 Feature Extraction

The image dehazing task is an image restoration task, which restores the damaged image, that is, the hazy image is restored to the label image. In the image restoration task, learn as many features as possible, and the restored image quality will be better. For this reason, when extracting image features, the input images of different scales are extracted with corresponding layers. When the image features are extracted by downsampling, the rough feature map is obtained. Therefore, when the feature map is obtained after downsampling, the input image is changed to the same size as the feature map, and the fine feature map is obtained through convolution and then concatenate the fine and rough feature map. The input image of the network is to crop the  $256 \times 256$  area in the middle of the hazy image, that is, the size of the input image is  $256 \times 256$ . The size of the rough feature map obtained after the first downsampling is  $128 \times 128$ . At the same time, the size of the  $256 \times 256$  input image is resized as  $128 \times 128$ , and convolution is performed to obtain the fine feature map of the same layer, and then the rough feature map is combing with the fine feature map to achieve feature fusion to obtain more image features. The second downsampling is still the same, and the rough feature map of  $64 \times 64$  is concatenated with the fine feature map.

### 39.3.3 ResNeXt

Generally, the accuracy of the model is improved by deepening or widening the network, but this will increase the hyperparameters, thereby increasing the difficulty and overhead of network design. The ResNeXt [14] structure improves model accuracy without increasing parameter complexity. At the same time, ResNeXt has the

same topological structure and reduced hyperparameters, thereby improving network performance without increasing network complexity. The formula of ResNeXt is as follows:

$$y = x + \sum_{i=1}^C T_i(x) \quad (39.1)$$

where  $C$  is the base of simplified Inception,  $x$  is the input image, and  $T(x)$  is the transformation of  $x$ .

## 39.4 Experiment

In the previous section, the MSFNet is introduced in detail. To further show the effectiveness, the MSFNet is compared qualitatively and quantitatively with the existing six methods: DCP [7], CAP [8], DeHazeNet [12], MSCNN [15], AOD-Net [13], and GFN [16]. This section first conducts a quantitative analysis on the indoor and outdoor images of the SOTS dataset [18] and then conducts a qualitative analysis on the indoor and outdoor images of the SOTS dataset.

### 39.4.1 Dataset and Evaluation Measure

The MSFNet uses the indoor training set and the outdoor training set of RESIDE [18] as the training set of the network and synthetic objective testing set (SOTS) as the testing set. This paper uses peak signal-to-noise ratio (PSNR) and structural similarity (SSIM) as qualitative evaluation measures. The higher the evaluation means the dehazing effect better. The formulas of PSNR and SSIM are as follows:

$$\text{PSNR} = 20 \times \log\left(\frac{255}{\sqrt{\text{MSE}}}\right) \quad (39.2)$$

$$\text{MSE} = \frac{1}{W \times H} \sum_{i=0}^{W-1} \sum_{j=0}^{H-1} \|G(i, j) - I(i, j)\|^2 \quad (39.3)$$

$$\text{SSIM} = \frac{(2\mu_G\mu_I + C_1)(2\delta_{G,I} + C_2)}{(\mu_G^2 + \mu_I^2 + C_1)(\delta_G^2 + \delta_I^2 + C_2)} \quad (39.4)$$

where  $W$  and  $H$  are the width and height of the image, respectively,  $G$  represents the haze-free image (label),  $I$  represents the obtained image dehazing result,  $\mu$  and  $\delta$  represent the mean and variance of the image, respectively,  $\delta_{G,I}$  represents the

covariance between the haze-free image  $G$  and the image dehazing result  $I$ , and  $C_1$  and  $C_2$  are constants.

### 39.4.2 Quantitative Results

Table 39.1 and 39.2 show the quantitative evaluation results of the indoor dataset and outdoor dataset on the SOTS, and the highest value is shown in bold. It can be seen from Table 39.1, and the MSFNet has the highest PSNR value (25.93) and SSIM value (0.938), indicating that the MSFNet has the best dehazing effect in the indoor dataset. The values of the MSFNet on the SOTS indoor dataset are significantly higher than the other six image dehazing methods. Among the six image dehazing methods, the value of GFN is slightly higher than other methods, ranking second. The value of CAP, DeHazeNet, and AOD-Net is in the middle. While the value of DCP and MSCNN is lower, ranking in last. Table 39.2 shows that it has the highest PSNR value (27.58) and SSIM value (0.930), indicating that the MSFNet has the best dehazing effect in the outdoor dataset. Among the six image dehazing methods, DeHazeNet's PSNR value is significantly higher than other methods, ranking second. AOD-Net's SSIM value is second; CAP and GFN values are in the middle, while DCP and MSCNN's value is lower, ranking last. In summary, the experimental results prove that the MSFNet has a better dehazing effect than the other six image dehazing methods on the SOTS datasets, showing that the MSFNet has the best image dehazing effect.

**Table 39.1** Quantitative comparison on average evaluation values of indoor dataset in the SOTS [18]

	DCP [7]	CAP [8]	MSCNN [15]	DeHazeNet [12]	AOD-Net [13]	GFN [16]	MSFNet
PSNR	18.87	21.31	20.01	22.66	21.01	22.99	<b>25.93</b>
SSIM	0.794	0.825	0.791	0.833	0.837	0.903	<b>0.938</b>

**Table 39.2** Quantitative comparison on average evaluation values of outdoor dataset in the SOTS [18]

	DCP [7]	CAP [8]	MSCNN [15]	DeHazeNet [12]	AOD-Net [13]	GFN [16]	MSFNet
PSNR	18.54	23.95	21.73	26.84	24.08	23.67	<b>27.58</b>
SSIM	0.710	0.869	0.831	0.826	0.873	0.836	<b>0.930</b>

### 39.4.3 Qualitative Results

To further prove the image dehazing performance, the MSFNet is combined with six image dehazing methods for qualitative evaluation. Figures 39.2 and 39.3 show the visible dehazing results of the six representative indoor and outdoor synthetic hazy images.

It can be seen from Fig. 39.2 that the indoor image dehazing results of seven image dehazing methods. The DCP method has hazy residue, and the dehazing image has

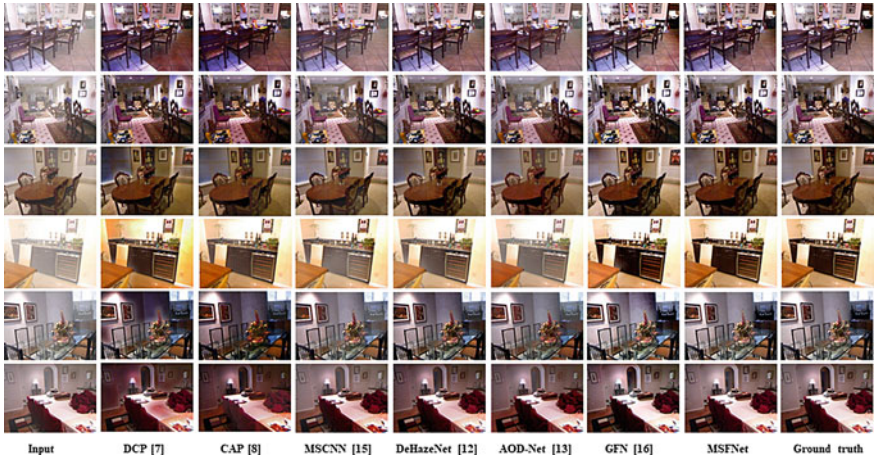


Fig. 39.2 Qualitative evaluation of six indoor synthetic hazy images of STOS [18]

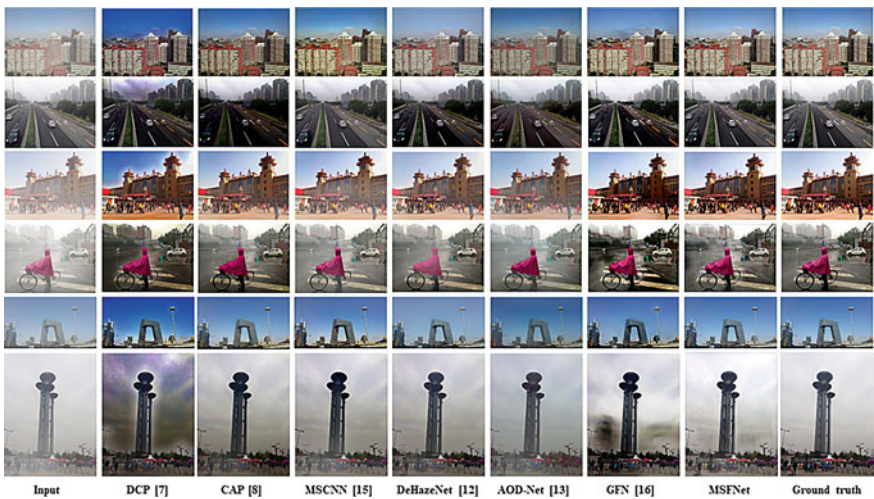


Fig. 39.3 Qualitative evaluation of six outdoor synthetic hazy images of STOS [18]

a deviation compared with the haze-free image. The color of the dehazing image of the MSCNN and AOD-Net method is closer to the label, but there is obvious residual hazy. Compared with the previous three methods, the CAP and DeHazeNet methods have less hazy residue, but the color of dehazing result is darker. The degree of hazy removal and the color restoration after dehazing by GFN and MSFNet is closer to a label image.

Figure 39.3 also gets similar conclusions. There are many sky areas in Fig. 39.3, and it can be seen that there is a large area of obvious distortion in the sky area after dehazing using the DCP, as shown in the second image. MSCNN and AOD-Net methods have higher hazy residue after dehazing, while CAP and DeHazeNet methods have less hazy residue after dehazing. The image after GFN dehazing is clearer, but the image after dehazing is darker than the label image. The dehazing image obtained by the MSFNet is closer to the dehazing image regardless of the overall color or the degree of hazy removal, which shows that the MSFNet has a better dehazing effect.

## 39.5 Conclusion

Inspired by GAN and ResNeXt, we proposed an image dehazing network based on multi-scale feature extraction. The MSFNet first concatenates fine feature maps with rough feature maps in the downsampling process to obtain more detailed information. Then, the MSFNet introduces the ResNeXt module to further learn image features for preventing the gradient disappearing and improving the performance of the proposed model. The feature maps learned by the ResNeXt module are concatenated with the feature maps obtained by upsampling to obtain residual image and subsequent image dehazing result. The experimental results on the SOTS dataset show that the MSFNet obtains better image dehazing performance than other comparison methods.

**Acknowledgements** This work is partially supported by National Natural Science Foundation of China (61972187), Natural Science Foundation of Fujian Province (2020J02024), Fuzhou Science and Technology Project (2020-RC-186), and the Opening Foundation Projects of Fujian Provincial Key Laboratory of Information Processing and Intelligent Control (Minjiang University) (MJUKF-IPIC201914).

## References

1. Bui, T.M., Kim, W.: Single image dehazing using color ellipsoid prior. *IEEE Trans. Image Process.* **27**(2), 999–1009 (2017)
2. Huang, L.: The algorithm of segmenting the prior neighborhood of dark channel in the single image dehazing. *J. Geo-Inf. Sci.* **20**(2), 224–228 (2018)



3. Yang, D., Sun, J.: Proximal dehaze-net: A prior learning-based deep network for single image Dehazing. In: Proceedings of the European Conference on Computer Vision (ECCV), pp. 702–717 (2018)
4. Li, Y., Miao, Q., Ouyang, W., et al.: LAP-Net: level-aware progressive network for image Dehazing. In: Proceedings of the IEEE International Conference on Computer Vision (ICCV), pp. 2276–2285 (2019)
5. Narasimhan, S., Nayar, S.K.: Contrast restoration of weather degraded images. *IEEE Trans. Pattern Anal. Mach. Intell.* **25**(6), 712–724 (2002)
6. Tarel, J.P., Hautiere, N.: Fast visibility restoration from a single color or gray level image. In: Proceedings of the IEEE Conference on Computer Vision and Pattern Recognition, pp. 2201–2208 (2009)
7. He, K.M., Sun, J., Tang, X.O.: Single image haze removal using dark channel prior. In: Proceedings of the IEEE Conference on Computer Vision and Pattern Recognition, pp. 1956–1962 (2009)
8. Zhu, Q., Mai, J., Shao, L.: A fast single image haze removal algorithm using color attenuation prior. *IEEE Trans. Image Process.* **24**(11), 2522–2522 (2015)
9. Zhang, S.M., Su, X., Jiang, X.H., et al.: A traffic prediction method of bicycle-sharing based on long and short term memory network. *Netw. Intell.* **4**(2), 17–29 (2019)
10. Zhang, Y.J., Fan, H.Y., Lu, Z.M.: A digital watermarking scheme for protecting weights of convolutional neural networks. *Netw. Intell.* **5**(3), 157–165 (2020)
11. Tan, F.G., Zhou, F.M., Liu, L.S., et al.: Detection of wrong components in patch component based on transfer learning. *Netw. Intell.* **5**(1), 1–9 (2020)
12. Cai, B., Xu, X., Jia, K., et al.: DehazeNet: an end-to-end system for single image haze removal. *IEEE Trans. Image Process.* **25**(11), 5187–5198 (2016)
13. Li, B.Y., Peng, X.L., Wang, Z.Y., et al.: AOD-net: all-in-one Dehazing network. In: Proceedings of the IEEE International Conference on Computer Vision (ICCV), pp. 4770–4778 (2017)
14. Xie, S., Girshick, R., Dollár, P., et al.: Aggregated residual transformations for deep neural networks. In: Proceedings of the IEEE Conference on Computer Vision and Pattern Recognition (CVPR), pp. 1492–1500 (2017)
15. Ren, W.Q., Liu, S., Zhang, H., et al.: Single image Dehazing via multi-scale convolutional neural networks. In: Proceedings of the European Conference on Computer Vision (ECCV), pp. 154–169 (2016)
16. Ren, W.Q., Ma, L., Zhang, J.W., et al.: Gated fusion network for single image Dehazing. In: Proceedings of the IEEE Conference on Computer Vision and Pattern Recognition (CVPR), pp. 2252–2261 (2018)
17. Goodfellow, I., Pouget-Abadie, J., Mirza, M., et al.: Generative adversarial nets. In: Proceedings of the Advances in Neural Information Processing Systems, pp. 2672–2680 (2014)
18. Li, B.Y., Ren, W.Q., Fu, D.P., et al.: RESIDE: a benchmark for single image Dehazing. *CLASS FILES* **14**(8), 1–11 (2015)

# Chapter 40

## Research on the Challenges and Strategies of Enterprises in Reverse Logistics Cost Control Under B2C Mode



Chengxiao Ju

**Abstract** Generally speaking, B2C e-commerce enterprises have a high-sales return rate, resulting from the nature of the industry, and sales return means the increase in reverse logistics cost. Through the research on the composition of reverse logistics information system and reverse logistics process, it is found that B2C e-commerce enterprises face some problems in reverse logistics cost control, such as imperfect reverse logistics information system, unreasonable value utilization of returned and exchanged goods, huge storage cost and incomplete third-party logistics utilization. In order to achieve competitive advantage in the fierce market, e-commerce enterprises should establish a perfect reverse logistics information system, optimize the reuse value of returned and exchanged goods, endeavor to reduce the storage cost and fully introduce the third-party logistics. The countermeasures can provide some reference for e-commerce enterprises to do well in reverse logistics cost management under B2C mode. In this way, the enterprises can reduce reverse logistics cost and obtain healthy and sustainable development.

### 40.1 Introduction

#### 40.1.1 Research Background and Significance

As modern information network technology develops rapidly, B2C e-commerce obtains a solid economic and technological foundation, and the developing e-commerce opens a new door for reverse logistics economy. In the fierce e-commerce market competition, unconditional return and exchange policy have become an important means for e-commerce enterprises to attract customers for secondary consumption, accompanied by higher and higher return cost. Too frequent return and exchange are the primary reason to increase the reverse logistics cost and reduce the overall profit level. When the cost control is close to the bottleneck, many e-commerce

---

C. Ju (✉)

City College of Dongguan University of Technology, Dongguan 523419, China

enterprises find the importance of reverse logistics cost control, and gradually adopt and recognize the concept of reverse logistics. In China, the reverse logistics cost of e-commerce enterprises accounts for more than 20% of the total cost, far higher than the average level of 4% in developed countries, directly reducing the profits of cross-border e-commerce enterprises.

### ***40.1.2 Domestic and Foreign Research Status***

Stock [1] first put forward reverse logistics in 1992, which “covers a series of logistics activities, such as product return, parts replacement, commodity reproducing, waste disposal and repair.” However, he did not elaborate and clearly define its functions and activities and others. In 1998, Rogers and Tibben [2] redefined reverse logistics as “an activity to efficiently plan, implement and control the flow of raw materials, process inventory, products and related information from commodity consumption to reproducing in operation and cost, so as to reuse the commodity and effectively deal with various wastes.” It is also a definition that has been fully accepted so far.

Domestic research on reverse logistics started a little late. Xiang [3] first introduced to China the concept of reverse logistics, and explored the close relationship between reverse logistics and ecological protection and the building criteria of reverse logistics supply chain. Xu [4] compared the three modes of reverse logistics operation: self-operation, joint operation and outsourcing, pointed out their respective strengths, weaknesses and suitable type of enterprise.

In recent years, the problems existing in e-commerce reverse logistics cost management have attracted much attention. Xiang [5] pointed out that the B2C model is, as one of the earliest e-commerce models in China, characterized by small sales volume, uneven consumer distribution and large return volume. B2C is an online shopping mode, so it inevitably encounters return due to its uncontrollability. B2C e-commerce enterprises should attach importance to reverse logistics cost management. Ding [6] believed that for return reverse logistics, consumers concerned the indicators of “return process,” “payment of return expenses,” “distribution efficiency” and “service attitude” in most cases. Facing a sharp rise in the return rate, B2C e-commerce enterprises should optimize reverse logistics management, which has become key to reduce the return rate and logistics expenses and improve customer satisfaction.

## **40.2 Reverse Logistics Information System and Processing Flow**

### ***40.2.1 Reverse Logistics Cost***

Reverse logistics cost means the monetary performance of all kinds of manpower and materialized labor consumed by goods in reverse space or time movement. To be specific, it is the sum of manpower, material resources and financial resources lost in the process of physical movement such as packaging, loading and unloading, transportation, storage, processing and distribution. For enterprises, it is the necessary expenditure to do a good job in return logistics operation, and the prerequisite to reduce commodity consumption and improve consumer services.

### ***40.2.2 Composition of Reverse Logistics Information System***

For B2C e-commerce enterprises, reverse logistics information management is the key to the reasonable and effective return logistics management. In order to increase the competitive advantage, most enterprises adopt preferential return policies and accept all returns, which attract many consumers' attention to a certain extent. However, the increase in returns also makes it harder to manage information. In the event of return, enterprises need to carry out a series of complex communication and negotiation with consumers. In other words, enterprises need to analyze whether the return meets their return conditions stipulated, negotiate in accordance with the return time and return method of customers, select the mode of transportation and return method, and determine the return waiting time. This series of process takes a long time, so that it needs a strong reverse logistics information system to support.

It can be seen from Fig. 40.1 that reverse logistics information system is composed of four main bodies: merchants, online shopping platforms, consumers and logistics companies. When the corporate information flow circulates among these four main bodies, the information is easily distorted. The information distortion in any link may pose a great negative impact on other links. In the normal return process, the customer who needs to return goods directly inform the merchant of the return information, and then the merchant passes the information to the logistics company, which can minimize the transfer process and avoid errors. However, some enterprises outsource customer service to third-party customer service companies. In other words, the reverse logistics information system built does not include the reverse logistics information of online shopping platform. The customer's return information is collected by the third-party customer service and then forwarded to the merchant. This process takes a long time, and requires many people to handle, which is easy to cause the "bullwhip" effect.

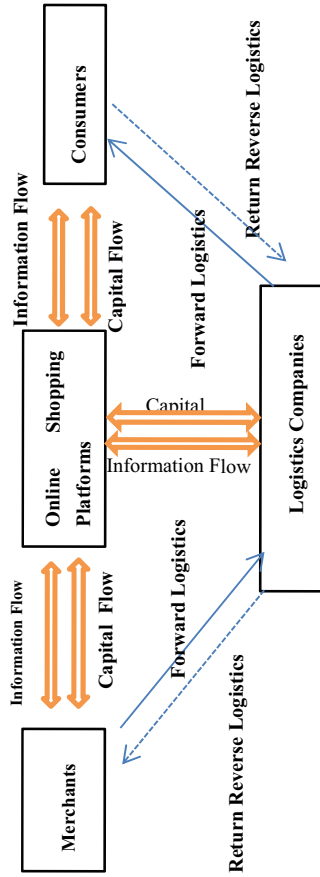


**Fig. 40.1** Analysis chart of reverse logistics information system

### 40.2.3 Return Reverse Logistics Process

Enterprises should deal with returned goods in the correct way. Enterprises should first classify them. The goods that can be sold again directly should be immediately arranged for secondary sale; the goods that need to be reprocessed should be arranged to enter the reprocessing center; the goods that can be disassembled for reuse of parts should be disassembled in order to avoid wasting resources, and the wastes should be treated without pollution. From the perspective of B2C e-commerce enterprises, the smaller the return rate is, the better it is definitely, after all, customer return means the decrease in revenue and the increase in cost. However, from another point of view, sales return may not be good for nothing. Customer return can promote enterprises to find out the shortcomings of products for sales, understand customer demands, and strengthen technological innovation, and improve product quality, so as to better maintain customer loyalty. In addition to the unreasonable return, the returned goods are more representative of the new consumer demands and the new trend of product technological improvement. The complete return reverse logistics process is shown in Fig. 40.2.

Under normal circumstances, after dealing with returned goods in accordance with the process shown in Fig. 40.2, enterprises can give a reasonable treatment scheme for the returned goods, so as to minimize the cost loss and maximize the resource utilization. But the whole process takes time and resource.

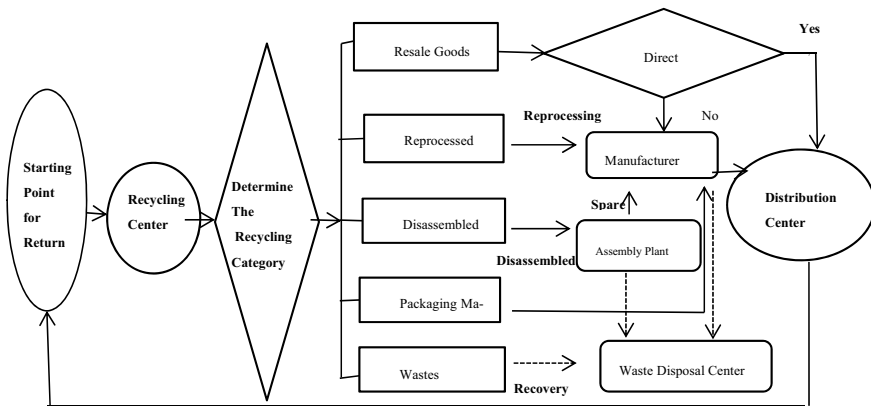


Fig. 40.2 Return reverse logistics process

## **40.3 The Challenges of Enterprises in Reverse Logistics Cost Control Under B2C Mode**

### ***40.3.1 Imperfect Reverse Logistics Information System***

Information management plays a very important role in the reverse logistics of B2C e-commerce enterprises. Some e-commerce enterprises fail to build reverse logistics information system matching with the supply chain as a result of large business volume, numerous consumers and uneven distribution. Even if the enterprises achieve an effective reverse logistics information system, they fail to correctly and effectively deal with the conflict between forward logistics and reverse logistics in the operation process. In addition, the information of normal delivery and return is complex, and the existing reverse logistics information system cannot accurately provide return information. Therefore, sales return cannot be treated timely, which leaves a bad impression on consumers. The imperfect reverse logistics information system aggravates the “bullwhip” effect. When dealing with the return information in each link of the supply chain, the enterprises suffer from the increase in transportation cost, inventory cost and operation cost, due to excessive return detention time, information distortion and incorrect return processing.

### ***40.3.2 Unreasonable Value Utilization of Returned Goods***

E-commerce enterprises generally believe that return is the biggest resistance to increase incomes. Therefore, in the face of the customers who tend to return goods, some enterprises first make unconditional concession, and make up for their dissatisfaction by means of large amount of cash back for subsidy, so as to dispel their ideas of giving medium and negative feedback. As a result, although the customers do not return the goods and give a negative comment, they will not plan to make secondary consumption. In addition, the large amount of cash back offsets selling profits, and even leads to negative profit. In other words, an order wastes manpower, material resources and financial resources. Most e-commerce enterprises offer a cash back range of 20–100%, which varies in accordance with the severity of the return problem.

### ***40.3.3 High Storage Cost***

According to data, Amazon’s storage cost accounts for about 20% of the reverse logistics cost, while the storage cost of China’s state-owned e-commerce enterprises accounts for more than 40%. There are three main problems in the storage cost management of e-commerce enterprises: firstly, the warehouse construction cost is

high. In order to timely deliver goods, some large e-commerce enterprises have established their own warehouses in major transportation hubs, which are not applied to outsource services. Due to the high price of land, land use, labor cost and building materials in these transportation hubs, the enterprises bear heavy costs. In the off-season, the sales volume greatly reduces, so that the warehouse is idle and resources are wasted. Secondly, the storage technology cannot meet the requirements of inventory storage. Because the goods are special, some e-commerce enterprises have higher requirements on storage management level, or it is easy to cause damage. Storage management is a systematic and professional activity. Thirdly, the storage operation is disordered. There is no unified operation standard of storage management, leading to unclear division of responsibilities, the loose work attitude and the low-operation efficiency.

#### ***40.3.4 Incomplete Utilization of Third-Party Logistics***

E-commerce return under B2C mode is characterized by small number of single return, scattered recycling locations and different transportation distances, which bring huge obstacles to return. Some enterprises build their own logistics system to store, transport and distribute the main commodities, but they have to invest a lot in the system. In addition, they lack professional logistics management personnel, and thus fail to establish a perfect logistics system. Compared with the traditional self-built logistics, the third-party logistics can reduce the cost of land, labor and construction of the logistics infrastructure to a certain extent, and provide good value-added services such as order processing, transshipment, inventory management and after-sales maintenance. Most e-commerce enterprises introduce third-party logistics, but only limited to the basic logistics transportation, storage and distribution services. In other words, they do not make good use of the additional value-added services provided by third-party logistics companies.

### **40.4 The Strategies of Enterprises in Reverse Logistics Cost Control Under B2C Mode**

#### ***40.4.1 Establishment of Perfect Reverse Logistics Information System***

The enterprises should first make the centralized analysis of return information. The data of goods such as quantity, date of purchase, shelf life, and inventory quantity should be included in the reverse logistics information system. In the process of building their own reverse logistics information system, the enterprises should, on the premise of fully considering the information characteristics of reverse logistics,



make full use of and perfect the existing forward logistics system, and gradually build a sound reverse logistics information system. In order to ensure that the reverse logistics information system can work accurately under the premise of high efficiency and low cost, the enterprises can connect their internal departments with the reverse logistics system into a complete internal supply chain system, and classify and code the return information through wireless network technology, automation technology, GPS technology and bar code technology. This is conducive to directly tracking the location and process of returns reduces the workload of manual picking of returned goods.

#### ***40.4.2 Optimization of the Reuse Value of Returned Goods***

Under the B2C e-commerce mode, the reverse logistics network focuses on recovering the returned goods from customers, and then deliver to the reprocessing location or send back to the warehouse after pretreatment. At the reprocessing center, the returned goods should be first properly classified. Some goods with reuse value should be reprocessed; some goods that can be sold at a discount instead of being reprocessed should be delivered to nearby outlets for discount promotion; other goods that have been completely scrapped and the remaining waste of the reprocessing center should be directly sent to the destruction site for pollution-free destruction. In different links of reverse logistics, the degree of return and reuse of goods is different. In the event of return, the enterprises should immediately do a good job in public relations, appease customers, understand the reason involved, find out the problems of goods or services, strengthen technical improvement based on the problems, and rationalize the reprocessing of goods.

#### ***40.4.3 Endeavor to Reduce Storage Cost and Create New Profit Growth Points***

In order to reduce the storage cost of reverse logistics, the enterprises should achieve the following four points. Firstly, the enterprises should make rational use of external storage system. As the business scope continuously expands to other provinces and cities, the original storage system fails to meet the requirements, but the cost of self-built warehouse is huge. The enterprises can strengthen internal and external contact with others, and establish cooperative storage system with local enterprises based on the local actual situation. Secondly, the enterprises should improve the use level of modern storage information. The ERP information system should be applied to record the storage information, automatically connect purchasing, logistics and sales system, facilitate the information communication between the storage department and other

departments, automatically and timely update the storage data information, and effectively control the inventory management information system. Thirdly, the enterprises should comprehensively introduce high-tech storage management technology. Good storage management improves storage service efficiency through storage technology and machinery and equipment, such as forklift, modern goods shelf, bar code technology and stacker. The modern storage machinery and equipment can maximize the storage space. Fourthly, the enterprises should adopt the standard operation system. On the one hand, they should strengthen staff quality training, correct their work attitude and improve work efficiency. On the other hand, based on their actual storage level, they should formulate reasonable operation standards, realize standardized operation, maximize storage efficiency and reduce storage cost. In order to avoid the return and exchange of goods, the warehouse management personnel should strictly control the quality of the products in and out of the warehouse, and refuse to deliver the products with problems out of the warehouse.

#### ***40.4.4 Full Introduction of Third-Party Logistics***

The reverse logistics make higher requirements on the logistics management technology, electronic information technology, and the comprehensive quality of employees and others. Therefore, from the perspective of sharing the B2C e-commerce operation risk and ensuring the service level of reverse logistics, it is a good choice to outsource the reverse logistics business to professional logistics enterprises. If B2C e-commerce enterprises introduce third-party reverse logistics, they can not only obtain professional logistics services, but also improve the distribution efficiency and quality of goods, so as to reduce their logistics cost and enhance profits. The third-party logistics with complete service functions can provide the enterprises with comprehensive and integrated logistics services, such as order processing, inventory management, recycling and processing, and free them from seeking multi-party cooperation. With the help of third-party reverse logistics, on the one hand, reverse logistics information can be highly shared. B2C e-commerce enterprises can obtain the logistics information of returned goods in each link at any time, effectively reduce the reverse logistics cost, minimize the return time, improve the return efficiency, establish a good image, and achieve a strong competitive advantage in the electronic market.

### **40.5 Conclusion**

With the rapid development of science and technology, more and more investors invest in e-market economy, which promotes B2C e-commerce enterprises to develop steadily. But at the same time, the B2C e-commerce enterprises face more and more fierce competition. In order to survive in the fierce electronic market competition,

e-commerce enterprises should constantly increase revenue and reduce expenditure, analyze the composition of operating costs, and find out the controllable operating costs. B2C e-commerce enterprises should correctly understand the significance of reverse logistics cost control and improve economic benefits by reducing reverse logistics cost.

**Remarks** Project fund: This paper is one of the research results of the provincial quality engineering project “Financial Management” specialty (156R106870) of the 2020 project (the third batch) of “Strengthening the University through Innovation” by Department of Education of Guangdong Province.

## References

1. Stock, J.R.: Reverse logistics. Council of Logistics Management, Oak, 22–25 (1992)
2. Rogers, S., Tibben-Lembke, S.: Going backwards: Reverse logistics trends and practices. Reverse Logistics Executive Council (1999)
3. Xiang, S.: Reverse logistics and environmental protection. *Logistics Technol.* **01**, 44–45 (2001)
4. Xu, J., Zhang, Y., Jin, Y.: Research on the mode decision of reverse logistics of waste electronic products. *Logistics Sci. Technol.* **04**, 14–16 (2006)
5. Xiang, L., Chen, J.: Problems and countermeasures of e-commerce reverse logistics. *Econ Trade Pract.* **16**, 188–188 (2017)
6. Ding, H., Deng, Q., Guo, Y.: Analysis of reverse logistics of small returns. *J. Shaoxing Univ. Arts Sci.* **8**, 66–70 (2017)

# Chapter 41

## Research on the Training Path of Big Data Application-Oriented Talents in Chinese Colleges and Universities



Xiaohong Ju

**Abstract** The big data technology is undergoing fast development around the world, and the market requirement for related talents is growing, while the insufficient supply of application-oriented talents has become an urgent issue that needs to be addressed. By analyzing the current situation of talent need in China's big data industry and the training of big data application-oriented talents in Chinese colleges and universities, this paper innovatively proposes the "three-integration training path" of big data application-oriented talents for colleges and universities. The "three-integration training path" mainly consists of the following three aspects: First, building the soft environment for talent training through "Integration of interdisciplinary"; Second, meeting the diversified needs of talents through "Integration between teaching and employment"; Third, developing multi-field practice scenarios through "integration between education and industry". The "three-integration training path" can urge colleges and universities to conduct internal governance and reform by combining the industrial need, and provide valuable references for colleges and universities to train of big data application-oriented talents.

### 41.1 Introduction

#### 41.1.1 Research Background and Significance

In recent years, big data has triggered significant economic and social reform. "Big data is the new oil and mineral in future" has become a new global consensus [1]. From the "dispensable" margin, big data has evolved into a core that "must be acquired," which has also generated huge social value and industrial space. The report "big data: Seizing Opportunities. Preserving Values" of the United States points out that big data can bring great value in many fields [2]. In the new stage of information development, the research and application of big data have become a new "catalyst" for the

---

X. Ju (✉)

City College of Dongguan University of Technology, Dongguan 523419, China

development of information industry, which have generated unexpected degree and scale of influences on the economic development, social order, national governance and people's lives. In particular, with the emergence of construction projects such as Digital China and New Smart City, big data application has become an important tool for the government and corporations to make intelligent decisions. Data-driven enterprises perform better, the survey shows that the average productivity and profitability of enterprises using data-driven decision-making are 5% and 6% higher than those of their competitors [3], and for every 10% improvement of enterprise data quality, the roe of public utilities, aviation, telecommunications, petroleum and petrochemical industries will increase by more than 200% [4].

### ***41.1.2 Domestic and Foreign Research Status***

Big data is an information asset that needs efficient and innovative information processing mode to enhance insight, decision-making power and optimization processing ability [5]. Big data application is a brand new challenge to human being from their mode of thinking to their lifestyles, which has also raised new requirements for talent training by colleges and universities. The establishment and application of massive data platforms have increased the number of application-oriented posts of big data technology, and the data collection, cleaning, mining, analysis and intelligent decision all require many application-oriented talents. As important organizations to train and deliver application-oriented talents for the big data industry, colleges and universities must conduct in-depth analysis of the development and talent requirement of big data industry. In addition, they also need to conduct research and practice on the aspects of post requirement, training goal, training plan, curricula construction and teacher training of big data application-oriented talents, provide innovative design of the training model of application-oriented talents for the emerging industry of "big data."

Colleges and universities cooperate with the big data industry to lead enterprises and industry associations, make the industrial chain and professional chain docking, and comprehensively explore the mode, power, mechanism, problems and countermeasures of big data industry talent training become the research focus. Du Hui and Xiong Yanfang (2017) proposed to rely on cooperation between school and enterprise to establish and improve the flexible curriculum system, promote the reform of teaching methods with market orientation, track the market demand, realize the development and application of big data teaching and feedback platform, and explore a new mode of talent training in many aspects; AI Xusheng (2018) pointed out that in the era of big data, colleges and universities must reform the IT talent training mode, and colleges and universities at different levels need to reasonably position the training objectives; Yi [11] pointed out that the development of big data science cannot do without multidisciplinary collaboration, and the construction of teaching team needs to consider the diversity of teaching staff. Wang Xinmin (2019) pointed out that the cultivation of compound big data talents needs the close combination

of government, industry, universities, research and application; Hu Yanli (2020) proposed the mode of integrating knowledge construction and practice innovation, and cultivated the practice innovation ability of big data talents through the teaching design of “practice-driven knowledge construction” and “problem-oriented practice innovation.”

## **41.2 Current Talent Requirement of Big Data Industry**

### ***41.2.1 Talent Need is Transforming from Academic Orientation to Application Orientation***

From the perspectives of the knowledge structure and professional development of big data talents, the big data talents can be classified into the two categories of academic-oriented and application-oriented talents. For the academic-oriented talents, we mainly need to examine their understanding and application of related models in the data science; for the application-oriented talents, we need to test their ability to utilize related ideas and methods of big data to solve specific application problems. Generally speaking, many mid-to-high-end academic-oriented talents are required during the data application stage and early development stage of research and development, while during the later stage; many application-oriented talents are required to undertake the work at the posts of big data technology application. Analysis shows that during the start-up stage of a big data company, the proportions of employees with a Doctor’s degree and a Master’s degree are relatively higher, which are 14.7% and 29%, respectively. Such high proportions are closely related to the fact that the company requires a lot of technological research and development during the start-up stage. However, with the expansion of corporate scale, the proportions of employees with a Doctor’s degree and a Master’s degree will gradually decline, stabilized at the levels of 2.4 and 12.6%, while the proportion of employees with a Bachelor’s degree is steady at the high level of 60% [6]. According to the development characteristics of big data industry at current stage, the big data applications in both the traditional and emerging industries are in urgent need of many application-oriented talents.

### ***41.2.2 Open-Source Technology is Becoming a Core Element in the Ability Composition***

The big data industry is growing in a stunning speed, and IDC (2018) predicts that the total amount of global data will increase from 33 zb in 2018 to 175 zb in 2025[7]. Many organizations are forced to find new creative methods to control the massive operational data and deeply mine the value of data, so as to quickly improve their

working and operational efficiency. The open-source technology can enable more and more projects to directly adopt the big data technology, and the open-source technology is becoming a core element in the ability composition of big data talents. According to related investigation, from the small start-up companies to the industrial giants, the suppliers of various scales are all using the open-source technology to process big data and conduct prediction and analysis. Based on the open-source and cloud computing technologies, the start-up companies are able to contend against big manufacturers on many aspects. Among the ability requirements for big data-related positions, the open-source technologies of Python, Java and Hadoop are among the top three. The industry generally adopts the open-source technologies to build the big data platform and develop big data applications, and these technologies are generally reflected by the positions requiring application-oriented talents, such as data crawling, data cleaning, data analysis and big data platform maintenance [8].

### ***41.2.3 The Requirement for Interdisciplinary Talents is Increasingly Strong***

The development of big data industry both in scope and in depth and its horizontal expansion have triggered change in talent demand, and from the perspective of positions, an important trend is the transformation from demand for high-end experts to mid-level interdisciplinary talents. Data services are often accompanied with the integration application. The integration application can reflect the value and connotation of big data, which vividly embodies the in-depth combination between the big data technology and the physical industry, and it can also practically increase the work efficiency of industry and cooperation, reduce their cost, and improve the government's social governance level and its ability to serve people's livelihood. The early application of big data technology was mainly concentrated on the aspects of big data platform establishment, big data development and algorithm design, while current big data applications will be more combined with the industrial characteristics, and the big data technology will be applied into the service fields such as finance, education and medicine. Therefore, the big data application-oriented talents not only need to understand the logic of technology, but also need to know the logic of services, and the interdisciplinary talents with outstanding specialized ability and the ability to coordinate services among different fields will be increasingly more favored.

## **41.3 Main Problems Existing in the Training of Big Data Application-Oriented Talents**

### ***41.3.1 Slow Construction of Training Environment for Interdisciplinary Collaboration***

The training of big data talents required coordinated support of interdisciplinary integration. However, during the actual educational work, the construction of training environment for interdisciplinary collaboration is slow within various colleges and universities, which causes the training of application-oriented talents by colleges and universities to lag behind the growth of industrial development demand. From the disciplinary perspective, the training of big data talents requires computer science, mathematics and statistics as the basic supporting disciplines, and requires biology, medicine, environmental sciences, economics, social science and management as the extended disciplines. The critical specialized knowledge and skills, such as big data collection, storage, management, analysis and application, can only be effectively trained under the condition of interdisciplinary collaboration [9]. Under the influence of the traditional concept of discipline and specialty construction, colleges and universities tend to focus on construction of specialty and specialty group within the scope of a discipline, the discipline construction and development involves serious selfish departmentalism, and the interdisciplinary collaboration construction mechanism is not sufficiently flexible and complete.

### ***41.3.2 Gap Between the Training of Big Data Talents and the Market Requirement***

During education, colleges and universities tend to emphasize the importance of general talents, focus on the training of specialized basic theoretical system and application ability of students, and fail to meet the diverse requirements in the job market or provide flexible curricular setting. As a result, there is a gap between the talent output standard and the diverse job requirements of employers. For example, for skill training of big data application-oriented talents, the open-source technology practice and application level of students cannot sufficiently satisfy the market demand. There is a gap between the training of big data talents and the market demand, and it is caused by the following reasons. Colleges and universities fail to do a great job in analyzing the job demand for big data talents, the investigation is not broad, deep or comprehensive enough, and some core elements of ability are directly ignored. As a result, the logical relationship among job ability, training goal and curricular setting is not completely sorted out during the formulation of talent training plan, which has caused various realistic problems, for example, the intensity of curriculum system



reform is not sufficient, the coverage of ability training is not very comprehensive, and the improvement of core qualities is not significant.

### ***41.3.3 Difficulty to Obtain Actual Scenarios of Multiple Fields During the Training Process***

The big data application scenario is essentially the data service application scenario, which is the specific embodiment of data and data analysis in actual activities [10]. However, it is difficult to colleges and universities to obtain actual data scenarios, which results in low achievement of goal to train interdisciplinary talent to handle cross-field services. The selection of most application scenarios is based on the quality, type, source and scale of data, and the data realization value and data service target need to be considered, which are the necessary conditions and important resources to train interdisciplinary talent. Acquisition of classic, demonstrative and diverse big data application conditions poses difficulty to colleges and universities, and the construction of a real-time dynamic teaching environment is even more difficult. Therefore, there is a lack of pertinent training under actual data scenarios during the training of adaptation, flexibility and leaning ability of big data interdisciplinary talent by colleges and universities, as a result, the students have low-learning efficiency when using the big data technology integration to address problems, and they mainly focus on the abstract concepts.

## **41.4 Construction of “Three-Integration Training Path”**

The design of “three-integration” training path for application-oriented talents in the big data industry by colleges and universities is a training path for application-oriented and interdisciplinary talent under the new engineering background. In this training path, colleges and universities are the dominant force of reform. By actively responding to the government’s industrial policy and development program, and coordinating with related institutions, organizations and leading companies in the big data industry, colleges and universities conduct survey of talent demand by working with corporations. With classic application-oriented jobs in big industry as the analytic target, based on in-depth study of the typical tasks and core technical requirements for application-oriented jobs in big industry, colleges and universities construct the training path for application-oriented interdisciplinary talents according to the ideas of “Integration of interdisciplinary,” “Integration between teaching and employment” and “integration between education and industry.” (Fig. 41.1)

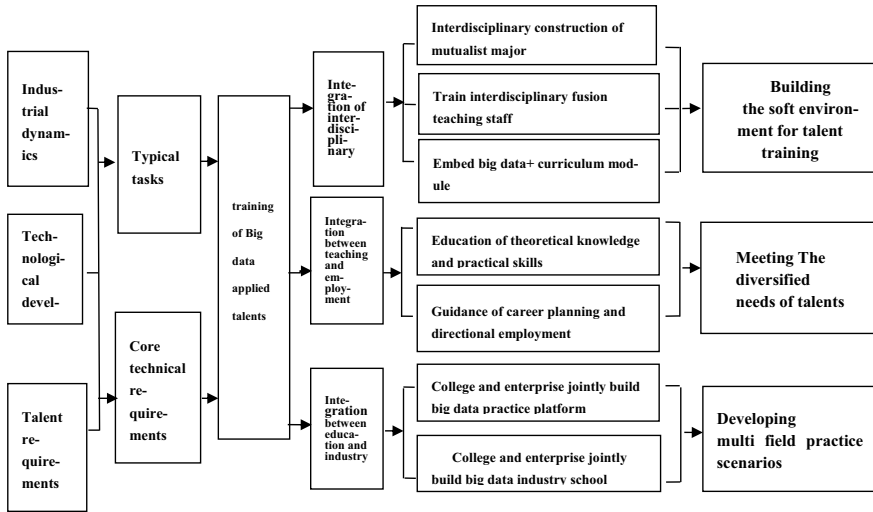


Fig. 41.1 “Three-fusion training path” diagram of big data application-oriented talents

## 41.5 Main Practice Points of “Three-Integration Training Path”

### 41.5.1 Building the Soft Environment for Talent Training Through “Integration of Interdisciplinary”

To train application-oriented talents of big data, the campus disciplinary and specialized resources should be fully integrated, and to forward looking and interdisciplinary soft environment for talent training should be designed by combining the new knowledge structure required by applications in the big data industry. The training of application-oriented talents of big data requires coordination among multiple disciplines, including professional integration development, diversity construction of teaching staff, and embedded reform of curriculum. Colleges and universities should further deepen the comprehensive reform of disciplines and majors, explore the integrated construction of the traditional majors and the big data major, and create a batch of “interdisciplinary” mutualistic majors. During the construction of teaching staff, they not only need to consider the rationality of discipline coverage, but also emphasize the introduction and training of teachers with interdisciplinary background. Based on comprehensive investigation of big data talent training plan and curricular setting in both Chinese and foreign colleges and universities, colleges and universities should extract core ability curriculum module for big data application-oriented talents in different industries, and try to embed the curriculum module into the curriculum system of related majors, so as to rapidly expand the channels to train big data application-oriented talents in various industries.

### ***41.5.2 Meeting the Diversified Needs of Talents Through “Integration Between Teaching and Employment”***

Based on innovation construction mechanism of “integration between teaching and employment” for school-based teachers and enterprise instructors, it can provide theoretical and practical conditions to train the core abilities required by key jobs in various industries, and ensure that the talent output can better meet the diverse requirement of market. The mechanism of “integration between teaching and employment” is based on the concept of integration of production and education, and by designing the educational and guidance path for students with industrial application as the center, organic integration between the school-based leaning and the industrial practice and application can be effectively promoted. In the mechanism of “integration between teaching and employment”, the industry and enterprises will choose experienced engineers to work as instructors for students on campus. Under the joint guidance from the school-based teachers and enterprise instructor team, the students can determine their future work field in advance and make career plan, and independently choose industrial instructors from related fields, so that the teaching model of directional training and planned employment can be formed. In the teaching model of directional training and planned employment, the school-based teachers focus on training the specialized and basic qualities of students, while the industrial instructors mainly instruct the students to obtain the practical skills of related techniques, service, management and operational skills. For example, by training the open-source practice ability required by different industries, it can enable the students to adapt to the actual scenarios of future jobs in advance, and improve the students’ ability to meet the requirements of critical jobs.

### ***41.5.3 Developing Multi-Field Practice Scenarios Through “integration Between Education and Industry”***

Based close cooperation with various industrial organizations, colleges and universities can establish the coordinated educational model of “integration between education and industry” by jointly building practical resource platform and industry school, so that the multi-field big data practice and learning scenarios can be maximally developed and applied, which can create a high-quality practice platform to train the practice ability of interdisciplinary talents. During cooperative education, colleges and industrial entities can choose conduct deep integration with multiple industries and enterprises, continuously combine and integrate the industrial standards and enterprise requirements into the specific links of cooperative education, jointly build related practice platform, teaching base and laboratory based on cooperation between school and enterprise, and cooperatively establish practical data centers, such as e-commerce big data, traffic big data, finance big data, advertisement big data and agricultural big data. On the basis of in-depth coordinated education and

mature conditions on various aspects, efforts can be made to start construction of industry school of big data direction. By integrating and utilizing the advantages and resources of colleges and universities, government and industry, industrial certification and industrial ecological resource development and sharing can be developed in depth, which can provide multi-field practice scenarios to train more interdisciplinary talents for big data industry.

## 41.6 Conclusion

By analyzing the current situation of talent needs in China's big data industry and the training of big data application-oriented talents in Chinese colleges and universities, this paper innovatively proposes the "three-integration training path" of big data application-oriented talents for colleges and universities, which can urge colleges and universities to conduct internal governance and reform by combining the industrial need, and provide valuable references for colleges and universities to training of big data application-oriented talents. "Three-integration training path" is beneficial exploration for the purpose of providing application-oriented talent support for the development of current digital economy, which is also an important way to train application-oriented talents for big data-related industries and companies. Colleges and universities can actively refer to the "three-integration training path" to design reform ideas, carry out the research and practice of big data talent training mode, and strive to open up a new direction for promoting the transformation and development of new engineering.

Ju Xiaohong, female Master Lecturer at City College of Dongguan University of Technology, focusing on the research fields of higher education management and human resource management.

**Fund program** Specialty Construction Project of *Software Engineering* under 2017 Quality Engineering Project Approval by Department of Education of Guangdong Province.

## References

1. Office of Science and Technology Policy Executive Office of the President: Big Data Research and Development Initiative (2012)
2. Executive Office of the President: Big Data: Seizing Opportunities. Preserving Values (2014)
3. McAfee, A., Brynjolfsson, E.: Big data: the management revolution. *Harv. Bus. Rev.* **90**(10), 60–66 (2012)
4. Barua, A., Mani, D., Mukherjee, R.: Measuring the Business Impacts of Effective Data (2010)
5. Sicular, S.: Gartner's Big Data Definition Consists of Three Parts, Not to Be Confused with Three "V" s [EB/OL] (2013-3-27) [2018-10-15]
6. <https://www.forbes.com/sites/gartnergroup/2013/03/27/Gartners-big-data-definition-consists-of-three-parts-not-to-be-confused-with-three-vs/>

7. Big Data Industry Ecological Alliance: 2019 White Paper on the Development of China's Big Data Industry. China Information World (2019)
8. Reinsel, D., Gantz, J., Rydning, J.: The Digitization of the World from Edge to Core. IDC (2018)
9. Meng, W.: Analysis of current skilled talent demand and talent training in big data application industry I. Sci. Technol. Inf. **17**, 20–21 (2020)
10. Kui, Z., Bin, W.: Construction of college innovative experiment curriculum system combining big data platform I. Comput. Educ. **1**, 138–143 (2020)
11. Yi, T.: Analysis and thinking of the big data talent training model. Inner Mongolia Sci. Technol. Econ. **18**, 30–32 (2019)

**Ju Xiaohong**, female, Master, Lecturer at City College of Dongguan University of Technology, focusing on the research fields of higher education management and human resource management.

# Author Index

## A

An, Zhi-Wei, 249, 283

## C

Cao, Rui, 257  
Cao, Xinrong, 239  
Chen, Chien-Ming, 167, 361  
Chen, Dingjun, 27  
Chen, Hao, 39  
Chen, Junxi, 3, 11  
Chen, Lili, 361  
Chen, Lulu, 125  
Chen, Xiao, 11  
Chen, Yuxin, 265  
Chu, Shu-Chuan, 147, 157, 167, 177, 187

## D

Dao, Thi-Kien, 77, 315  
Deng, Yingjie, 229  
Ding, Qun, 351  
Ding, Wei, 351  
Du, Zhi-Gang, 147

## F

Fang, Shiyuan, 135  
Feng, Ting, 391

## G

Gao, Min, 177  
Gao, Yueqing, 125  
Guang, Yerui, 351

Guo, Xinglan, 361

Guo, Yang, 371

## H

Han, Xutao, 333, 371  
Hanzhi, Li, 209  
He, Jian, 325  
Hou, Xiaohan, 257  
Huang, Ke-yan, 219  
Hu, Jinxing, 295  
Hu, Moufa, 229  
Hu, Pei, 157

## J

Jia, Furong, 19  
Jianfeng, Wang, 209  
Jiang, Donghua, 351  
Ju, Chengxiao, 401  
Ju, Xiaohong, 411

## K

Kan, Chenyan, 27

## L

Lee, Chang-Der, 67  
Lee, Hung-Peng, 77  
Lei, Jinglan, 11  
Li, Donghao, 295  
Li, Geng-Chen, 177  
Li, Huale, 257  
Li, Jia-Min, 303

- Li, Jianpo, 177  
 Lin, Dong-Cherng, 67  
 Li, Rui, 239  
 Liu, Bingwei, 333  
 Liu, Changjie, 199  
 Liu, Huanyu, 229  
 Liu, Shi-Jian, 303  
 Liu, Wenbo, 99  
 Liu, Yang, 275  
 Liu, Yi, 11, 19  
 Liu, Yuqi, 135  
 Liu, Zhentao, 333, 371  
 Li, Xueqin, 39  
 Li, Zun, 371  
 Li, Zuoyong, 239, 391  
 Luo, Xuan, 87  
 Lv, Miaomiao, 55
- M**  
 Ma, Beiping, 341  
 Meixi, Wu, 209  
 Meng, Xin, 125  
 Meng, Zhenyu, 265  
 Mu, Ji-liang, 325
- N**  
 Ngo, Truong-Giang, 77, 315  
 Nguyen, Trong-The, 67, 77, 315  
 Ning, Zhihan, 275
- P**  
 Pan, Jeng-Shyang, 67, 147, 157, 167, 177, 187, 303  
 Pan, Jinshan, 3  
 Pan, Tien-Szu, 147  
 Pei, Daming, 135
- Q**  
 Qin, Pengfei, 199  
 Qi, Shuhan, 257, 275  
 Qiu, Mingyue, 87
- R**  
 Ren, Zhang, 113
- S**  
 Shao, Xiang, 303  
 Shen, Ce, 295  
 Shen, Yuting, 113, 125  
 Sun, Bo, 325  
 Sun, Lin, 19  
 Sun, Wei, 99, 333, 371
- T**  
 Tang, Linlin, 187, 257, 275  
 Teng, Shenghua, 239
- V**  
 Vu, Van-Dinh, 77, 315
- W**  
 Wang, Bin, 333  
 Wang, Juan, 381  
 Wang, Kaixuan, 113, 125  
 Wang, Liwei, 333  
 Wang, Ruo-Bin, 249, 283  
 Wang, Wei-Feng, 249, 283  
 Wang, Wenxian, 39  
 Wang, Xuan, 257  
 Wang, Ya, 351  
 Weng, Shaowei, 187  
 Wu, Guan-qun, 219  
 Wu, Kangjie, 3  
 Wu, Qianqian, 19  
 Wu, Tsu-Yang, 361  
 Wu, Yanan, 351  
 Wu, Yu, 371
- X**  
 Xu, Jian-ming, 325  
 Xu, Lin, 249, 283
- Y**  
 Yang, Can, 55  
 Yang, Chen, 265  
 Yang, Lei, 361  
 Yang, Qing-Yong, 167  
 Yang, Shiwei, 55  
 Yang, Yao, 27  
 Yao, Qingchen, 55  
 Yin, Qing, 219  
 Yin, Shuo, 249, 283  
 Yin, Tingyu, 87  
 Yuan, Diping, 295  
 Yue, Mengyuan, 55  
 Yu, Jianglong, 113  
 Yu, Kaihan, 3  
 Yu, Zhaochai, 391

**Z**

- Zhang, Aiyong, [199](#)  
Zhang, Fuquan, [113](#), [125](#), [391](#)  
Zhang, Jiajia, [257](#)  
Zhang, Jin, [87](#)  
Zhang, Longfei, [381](#)  
Zhang, Qi-yuan, [325](#)  
Zhang, Renxiu, [351](#)  
Zhang, Songyang, [371](#)  
Zhang, Wei, [341](#)  
Zhang, Xin, [187](#)  
Zhang, Zhiguo, [371](#)  
Zhan, Zichen, [11](#), [19](#)  
Zhao, Fei, [229](#)  
Zheng, Gui-bo, [219](#)  
Zhong, Yuxin, [265](#)  
Zhou, Min, [39](#)  
Zhu, Hongxing, [87](#)  
Zhuo, Liang, [113](#)